5-1-2004

Flexural Strength and Ductility of Highway Bridge I-Girders Fabricated from HPS-100W Steel

Emad Said Salem

Richard Sause

FLEXURAL STRENGTH AND DUCTILITY OF HIGHWAY BRIDGE I-GIRDERS FABRICATED FROM HPS-100W STEEL

by

Emad Said Salem

Richard Sause

Sponsored by the Federal Highway Administration (Contract No. DTFH61-99-C00062) and the Pennsylvania Infrastructure Technology Alliance through a grant from the Pennsylvania Department of Community and Economic Development

ATLSS Report No. 04-12

May 2004

ATLSS is a National Center for Engineering Research on Advanced Technology for Large Structural Systems

117 ATLSS Drive
Bethlehem, PA 18015-4728

Phone: (610)758-3525
Fax: (610)758-5902

www.atlss.lehigh.edu
Email: inatl@lehigh.edu

FLEXURAL STRENGTH AND DUCTILITY OF HIGHWAY BRIDGE I-GIRDERS FABRICATED FROM HPS-100W STEEL

by

Emad Said Salem, Ph.D.
Formerly, Graduate Research Assistant
Lehigh University

Richard Sause, Ph.D.
Joseph T. Stuart
Professor of Structural Engineering
Lehigh University

Sponsored by the Federal Highway Administration (Contract No. DTFH61-99-C00062) and the Pennsylvania Infrastructure Technology Alliance through a grant from the Pennsylvania Department of Community and Economic Development

ATLSS Report No. 04-12

May 2004

ATLSS is a National Center for Engineering Research on Advanced Technology for Large Structural Systems

117 ATLSS Drive
Bethlehem, PA 18015-4728

Phone: (610)758-3525
Fax: (610)758-5902

www.atlss.lehigh.edu
Email: inatl@lehigh.edu

Acknowledgments

This research was conducted at the Advanced Technology for Large Structural Systems (ATLSS) Center and the Department of Civil and Environmental Engineering, Lehigh University, Bethlehem, Pennsylvania.

The authors appreciate the effort of Mr. John Hoffner, Mr. Edward Tomlinson, Mr. Frank Stokes, and the technical staff under their direction at ATLSS during the experimental phase of this research. The authors would like to thank Mr. Peter Bryan for providing the necessary computer support, Mr. Larry Fahnestock for providing previous experimental data, Mr. Pholdej Therdphithakvanij for his assistance with the residual stress measurements, and Mr. Daming Yu for his assistance during the experimental testing.

This research was sponsored by the Federal Highway Administration (Contract No. DTFH61-99-C00062), and the Pennsylvania Infrastructure Technology Alliance (PITA) through a grant from Pennsylvania Department of Community and Economic Development. The first author would like to extend his appreciation to the Egyptian government for financial support. Special thanks to the Civil Engineering Department at AL-AZHAR University, Cairo, Egypt, for their support.

The findings, opinions, and conclusions presented in this dissertation are the authors and do not necessarily reflect the views of those acknowledged herein.

Table of Contents

List of Tables

List of Figures

Abstract

High performance steel (HPS) for highway bridges has high strength in addition to good weldability, fracture toughness, and corrosion resistance. This research investigates the flexural strength and ductility of bridge I-girder made from HPS-100W, with a yield strength of 100 ksi (690 MPa). The AASHTO LRFD specifications limit the nominal flexural strength of steel I-girders made from steel with specified yield strength greater than 70 ksi (485 MPa) to the yield moment. This limit applies to HPS-100W I-girders and hinders the use of HPS-100W in highway bridges, and this study investigates whether this limit can be eliminated.

The experimental part of this research included testing of five I-girder specimens fabricated from HPS-100W steel. These I-girders were tested to failure under three-point loading simulating the condition of negative flexure at an interior pier of a continuous-span bridge girder. The experimental research included careful measurement of residual stresses and geometric imperfections before testing, and detailed analysis of the experimental data to study the complex stresses that developed in the specimens at failure.

The analytical part of this research included finite element simulations. The purpose of these finite element simulations is to accurately predict both the strength and ductility of these I-girders. A parametric study was performed using finite element simulations to study the effect of various parameters on the flexural strength and ductility.

Comparison of the flexural strength of the experimental and parametric specimens with the nominal flexural strength, M_n, calculated according to the Draft 2004 AASHTO LRFD specifications shows that these specifications are also applicable for calculating the nominal flexural strength of HPS-100W I-girders when the strength is controlled by inelastic web and flange local buckling. Therefore, the AASHTO LRFD specification provision limiting the negative flexural strength of HPS-100W I-girders to the yield moment can be elimeninated.

CHAPTER 1 Introduction

With the development and application of high performance steel (HPS) for highway bridges, a close examination of the applicability of current standard highway bridge design provisions to HPS is needed. To safely utilize the strength of HPS in bridge girders, a comprehensive understanding of the strength and ductility of HPS bridge girders should be developed as part of this examination. HPS has high strength in addition to good weldability, fracture toughness, and corrosion resistance. Since 1991, the Advanced Technology for Large Structural Systems (ATLSS) Center at Lehigh University has been involved with the development of HPS, testing of HPS, and the structural testing of HPS bridge girder prototypes [Gross et al. 1998].

In the current ASTM specifications [ASTM 2004], there are two grades of HPS for highway bridge construction, namely, HPS-50W and HPS-70W. HPS-50W has a specified minimum yield strength of 50 ksi (345 MPa), and HPS-70W has a specified minimum yield strength of 70 ksi (485 MPa). Recent research by Gross and Stout [2001] has resulted in a new grade of HPS, HPS-100W steel, with a specified minimum yield strength of 100 ksi (690 MPa). The flexural strength and ductility of highway bridge girders fabricated from this steel are the subject of the present research.

1.1 Overview

In the 1996 American Association of State Highway Transportation Officials (AASHTO) Load and Resistance Factor Design (LRFD) Bridge Design Specifications [AASHTO 1996], the nominal flexural strength of steel I-girders with a specified minimum yield strength greater than 50 ksi (345 MPa) was limited to the yield moment rather than the plastic moment. However, studies performed by Barth et al. [2000] and Yakel et al. [2002], developed knowledge that enabled this limit for the specified minimum yield strength to be raised to 70 ksi (485 MPa), as is now implemented in the 2001 AASHTO LRFD specifications [AASHTO 2001] and in the Draft 2004 AASHTO LRFD specifications [AASHTO 2004]. This change allows HPS-70W to be used more economically. In general, limiting the flexural strength to the yield moment hinders the economical use of HPS in highway bridge girders. The present research is aimed at developing knowledge to enable the current limit in the AASHTO LRFD specifications to be eliminated, enabling more economic use of HPS-100W.

The main focus of the present study is to investigate the flexural strength and ductility of bridge I-girders in negative flexure, under conditions that occur at the pier of a continuous-span bridge. The flexural strength of I-girders that are classified either as compact or noncompact sections according to the 2001 AASHTO LRFD specifications [AASHTO 2001] is investigated. The flexural strength of these sections

is controlled by local buckling of the compression flange and web. Flexural strength controlled by fracture of the tension flange is not investigated in this study.

The HPS-100W steel used in the present study is a new high performance steel with a nominal yield strength of 100 ksi (690 MPa). The steel used to fabricate girder experimental specimens tested by Fahnestock and Sause [1998] (also called HPS-100W) had a different chemical composition than the steel used in the present study. The chemical composition of the HPS-100W steel used in this study is given by Gross and Stout [2001] and is shown in Table 1.1. The chemical composition of the steel used in the previous study by Fahnestock and Sause [1998] is given by Nickerson [1997] and is also shown in Table 1.1.

Highway bridge I-girders are usually designed with web slenderness above the limit for compact sections and flange slenderness near or below the limit for compact sections. Previous studies that considered I-girders in these web and flange slenderness ranges are relevant to the present study on highway bridge I-girder. Relevant previous studies that integrate experimental testing and finite element simulations were conducted by Barth [1996] and Yakel et al. [2002]. Barth [1996] investigated the flexural strength and ductility of bridge I-girders fabricated from ASTM A572 Grade 50 steel. Yakel et al. [2002] investigated the flexural strength of ASTM A709 HPS-70W I-girders. Other previous studies which focus mainly on finite element simulations are Earls et al. [2002], and Greco and Earls [2003]. Previous studies which focus mainly on experimental testing are Schilling and Morcos [1988] and Fahnestock and Sause [1998]. These previous studies used steel that had different stress-strain characteristics than the steel used in the present study.

In many of the previous studies, geometric imperfections and residual stresses were not measured and were assumed in the finite element simulations. The present study overcomes these limitations by integrating experiments and finite element simulations to provide better understanding of the flexural strength and ductility of HPS-100W bridge I-girders, as controlled by local buckling of the compression flange and web.

To characterize the experimental specimens and better correlate the experimental results with the finite element simulation results, the following steps were followed: (1) the steel stress-strain properties, and the specimen residual stresses and geometric imperfections were measured before the experiments were performed, (2) an instrumentation plan to measure the detailed results required for correlating the finite element simulation results with the experimental results was developed and implemented, (3) a plane stress plasticity program was developed to convert the experimentally measured strains into stresses for the purpose of comparing with finite element simulation results.

1.2 Research Objectives

The objectives of this research are as follows:

- To investigate the flexural strength and ductility of highway bridge I-girders fabricated from HPS-100W steel and investigate the applicability of the 2001 AASHTO LRFD specifications [AASHTO 2001] and the Draft 2004 AASHTO LRFD specifications [AASHTO 2004] for calculating the flexural strength and ductility of HPS-100W I-girders in negative flexure.
- To provide experimental data on the flexural strength and ductility of bridge I-girders fabricated from HPS-100W steel.
- To develop a finite element model capable of simulating the inelastic flexural behavior of HPS-100W bridge I-girders, as controlled by local buckling in the inelastic range.
- To use the calibrated finite element model in a parametric study of the flexural strength and ductility of HPS-100W I-girders in negative flexure, and compare with the flexural strength and ductility calculated according to the 2001 AASHTO LRFD specifications [AASHTO 2001] and the Draft 2004 AASHTO LRFD specifications [AASHTO 2004].

1.3 Research Scope

This research integrated experiments, finite element simulations, and a simplified theoretical model to provide better understanding of the flexural strength and ductility of HPS-100W bridge I-girders, as controlled by local buckling of the compression flange and web.

Experiments on five HPS-100W I-girder specimens were conducted. The five experimental specimens were half-scale models of the pier regions of continuous-span bridge I-girders with main spans in the range of 150 ft to 350 ft (46 m to 107 m). The HPS-100W I-girder specimens were tested to failure under three-point loading simulating the condition of negative flexure at an interior pier. The experimental specimens were carefully chosen to represent an appropriate range of web slenderness, flange slenderness, and cross section aspect ratio. Prior to selecting the experimental specimen geometry, the actual thickness and material properties of the steel plates used in fabricating these specimens were determined. The geometry of each experimental specimen was then selected and finite element simulations were conducted to evaluate the experimental behavior. After fabricating the specimens, measurements of residual stresses and geometric imperfections were conducted.

ABAQUS [2002] was used in this study to conduct finite element simulations of the local buckling behavior of bridge I-girders under flexure. The purpose of these finite element simulations is to accurately predict both the strength and ductility of

these I-girders as they are influenced by compression flange and web local buckling after the cross-section yields. The finite element models used in the present study were developed using ideas given by Green [2000], however, improvements to these ideas were made. These finite element models were verified using the experimental specimens tested by Fahnestock and Sause [1998]. Prior to fabrication of the experimental specimens of the present study, preliminary finite element simulations were performed to gain more insight into the behavior of each specimen.

The preliminary finite element simulations of the experimental specimens provided information about local buckling modes and location. Guided with this information, strain gage locations were selected to capture the local buckling behavior of the experimental specimens. Strain gages, including rosettes to measure shear stresses, were clustered on the upper surface of the top flange around the expected failure region. At the junction between the web and compression flange, strain gages were used to observe interaction between the web and compression flange.

Finite element simulations of the tests of the experimental specimens, and specimens tested previously by Fahnestock and Sause [1998], were performed. Comparisons between the experimental results and the finite element simulation results were made for each specimen. A plane stress plasticity program was developed to convert the experimentally measured strains into stresses. These stresses enabled comparisons, at selected locations, between the experimental and finite element simulation results.

After achieving good correlation between the experimental results and the finite element simulation results, a parametric study was performed to study the effect of different parameters on the strength and ductility of bridge I-girders fabricated from HPS-100W steel. These parameters are flange slenderness, web slenderness, and cross section aspect ratio.

The flexural strength of the experimental specimens and the parametric specimens was compared with the nominal flexural strength calculated using two versions of the AASHTO LRFD specifications, namely, the Draft 2004 AASHTO LRFD specifications [AASHTO 2004] and the 2001 AASHTO LRFD specifications [AASHTO 2001]. For each specification version, the nominal flexural strength was calculated twice, with and without taking into consideration the limitation related to the yield strength of the steel to investigate whether the limit related to the steel yield strength can be lifted. Also, the plastic rotation capacity calculated using the Draft 2004 AASHTO LRFD specifications [AASHTO 2004] was compared with the results from the finite element simulations for the parametric specimens and the experimental results for the experimental specimens.

1.4 Organization of Report

Chapter 2 presents background information about the AASHTO LRFD specifications and previous research related to the present study. In Chapter 3, the development of the finite element model, to predict both the strength and ductility of bridge I-girders influenced by flange and web local buckling, is explained. Experimental results from Fahnestock and Sause [1998] are used to calibrate the finite element model. Chapter 4 presents the design and fabrication of the experimental specimens and setup, along with the specimen instrumentation. The measured material properties, residual stresses in the web and flanges, and the web and compression flange imperfections are reported in Chapter 4.

In Chapter 5, test results for the experimental specimen are discussed. Finite element simulations of the experimental specimens are presented in Chapter 6, along with comparisons with the experimental results. The comparisons are presented in terms of load versus midspan vertical deflection and moment versus end rotation. Comparisons of stresses are also made. The flexural strength and ductility of HPS-100W bridge I-girders are discussed in Chapter 7. A parametric study of the effect of the flange slenderness, web slenderness, and cross section aspect ratio on the flexural strength and ductility of bridge I-girders fabricated from HPS-100W steel is presented in Chapter 7. The flexural strength (of the experimental and parametric specimens) is also compared with the nominal flexural strength calculated using the two versions of the AASHTO LRFD specifications in Chapter 7. Also, the plastic rotation capacity (for the experimental and parametric specimens) is compared with the plastic rotation capacity calculated using the Draft 2004 AASHTO LRFD specifications [AASHTO 2004]. Chapter 8 presents a summary, conclusions, and future work.

Table 1.1 Chemical compositions of HPS-100W bridge steel used in the present and previous studies

	C	Mn	P	S	Si	Ni	Cu	Cr	Mo	V	Cb	Al	Ti	B	N
Present study	0.060	0.990	0.005	0.002	0.270	0.750	0.980	0.510	0.500	0.059	0.020	0.035	--	--	--
Previous study [Fahnestock and Sause 1998]	0.110	0.850	0.015	0.003	0.300	0.850	0.330	0.540	0.460	0.039	--	0.032	0.027	0.001	0.005

CHAPTER 2 Background

2.1 Introduction

The background related to the present study is reviewed in this chapter. The procedures for calculating the ultimate flexural strength of bridge I-girders from two different versions of the AASHTO LRFD Bridge Design Specifications are reviewed. These two versions are the Draft 2004 AASHTO LRFD Bridge Design Specifications [AASHTO 2004] and 2001 AASHTO LRFD Bridge Design Specifications [AASHTO 2001]. The present study considers only the flexural strength and ductility of I-girders controlled by local buckling of the compression flange and web. Therefore, only the relevant parts of the AASHTO LRFD specifications are reviewed. The procedures from the Draft 2004 AASHTO LRFD specifications will be reviewed in some detail since these procedures are not currently in use. The procedures from the 2001 AASHTO LRFD specifications will not be reviewed in detail since these procedures are currently available in print. Previous research related to the flexural strength and ductility of I-girders will be also presented. Finally a review of the theory of plasticity, which is used in the analytical part of the present study, will be presented.

2.2 Draft 2004 AASHTO LRFD Bridge Design Specifications

This section presents the equations related to flexural strength from the Draft 2004 AASHTO LRFD specifications [AASHTO 2004] in detail since these equations are not currently available for the designers and may not be included in the final specification version.

2.2.1 Article 6.10.8

For composite sections in negative flexure and noncomposite sections in positive or negative flexure with a web that satisfies the noncompact slenderness limit given by Equation 2.1, the flexural strength may be determined according to Appendix A of the Draft 2004 AASHTO LRFD specifications [AASHTO 2004]. Otherwise, the flexural strength is determined according to Article 6.10.8. The flexural strength of sections controlled by the compression flange strength or stability is given by Equation 2.2.

$$\frac{2D_c}{t_w} \le 5.7\sqrt{\frac{E}{F_{yc}}} \tag{2.1}$$

$$M_{nc} = F_{nc}\, S_{xc} \tag{2.2}$$

where:

D_c = Depth of the web in compression in the elastic range
t_w = Web thickness
E = Young's modulus
F_{yc} = Specified minimum yield strength of the compression flange
F_{nc} = Nominal flexural resistance of the compression flange
S_{xc} = Elastic section modulus for the compression flange about the major axis
M_{nc} = Nominal flexural resistance based on the compression flange

In Article 6.10.8, F_{nc} is taken the smaller of the local buckling resistance and lateral torsional buckling resistance, calculated as shown in the following sections.

2.2.1.1 Local Buckling Resistance of Compression Flange

For the compression flange, the local buckling resistance is determined as follows:

1. If $\bar{\lambda}_f \le \lambda_{pf}$, then:

$$F_{nc} = R_b\, R_h\, F_{yc} \tag{2.3-a}$$

2. Otherwise:

$$F_{nc} = \left[1 - \left(1 - \frac{F_{yr}}{R_h\, F_{yc}} \right) \left(\frac{\bar{\lambda}_f - \lambda_{pf}}{\lambda_{rf} - \lambda_{pf}} \right) \right] R_b\, R_h\, F_{yc} \tag{2.3-b}$$

where:

$\bar{\lambda}_f$ = Compression flange slenderness = $\dfrac{bf}{2t_f}$

λ_{pf} = Compact flange slenderness limit = $0.38\sqrt{\dfrac{E}{F_{yc}}}$

λ_{rf} = Noncompact flange slenderness limit = $0.56\sqrt{\dfrac{E}{F_{yr}}}$

R_b = Web load shedding factor

R_h = Hybrid factor (from Article 6.10.1.10.1, but 1.0 for the present study)

F_{yr} = Compression-flange stress at the onset of nominal yielding

= $0.7F_{yc} \le F_{yw}$

F_{yc} = Specified minimum yield strength of the compression flange

F_{yw} = Specified minimum yield strength of the web

b_f = Flange width

t_f = Flange thickness

The web load-shedding factor, R_b, is calculated as follows:

If the web is longitudinally stiffened, or if:

$$\frac{2D_c}{t_w} \le \lambda_{rw}$$

then, R_b shall be taken as 1.0.

Otherwise:

$$R_b = 1 - \left(\frac{a_{wc}}{1200 + 300\, a_{wc}} \right) \left(\frac{2D_c}{t_w} - \lambda_{rw} \right) \le 1.0 \tag{2.4}$$

where:

λ_{rw} = Noncompact web slenderness limit = $5.7\sqrt{\frac{E}{F_{yc}}}$

a_{wc} = $\frac{2D_c\, t_w}{b_f\, t_f}$

2.2.1.2 Lateral Torsional Buckling Resistance of Compression Flange

For the compression flange, the local buckling resistance is determined as follows:

1. If $L_b \le L_p$, then:

$$F_{nc} = R_b\, R_h\, F_{yc} \tag{2.5}$$

2. If $L_p < L_b \leq L_r$, then:

$$F_{nc} = C_b \left[1 - \left(1 - \frac{F_{yr}}{R_h F_{yc}} \right) \left(\frac{L_b - L_p}{L_r - L_p} \right) \right] R_b R_h F_{yc} \leq R_b R_h F_{yc} \quad (2.6)$$

where:

L_b = Unbraced length

L_p = Maximum unbraced length for yield as the flexural resistance

$$= r_t \sqrt{\frac{E}{F_{yc}}}$$

L_r = Minimum unbraced length for elastic buckling as the flexural resistance

$$= \pi r_t \sqrt{\frac{E}{F_{yr}}}$$

r_t = Effective radius of gyration for lateral torsional buckling

$$= \frac{b_f}{\sqrt{12\left(1 + \frac{1}{3}\frac{D_c t_w}{b_f t_f}\right)}}$$

Note that the definitions of L_r and r_t are different in the Draft 2004 AASHTO LRFD specifications than those in the 2001 AASHTO LRFD specifications.

2.2.2 Appendix A

Appendix A of the Draft 2004 AASHTO LRFD specifications [AASHTO 2004)] applies to composite sections in negative flexure and noncomposite sections in positive or negative flexure with compact or noncompact webs. These sections should satisfy the following requirements:

1. The minimum specified yield strengths of the flanges and web do not exceed 70 ksi (485 MPa)
2. The web satisfies the noncompact slenderness limit given in Equation 2.1

For the present study, the equations from Appendix A are applied to the HPS-100W I-girders under study, even though they violate the first requirement. The purpose is to determine if Appendix A applies to HPS-100W I-girders.

2.2.2.1 Web Plastification Factor

For compact web sections, the web slenderness ratio satisfies the following:

$$\frac{2D_{cp}}{t_w} \le \lambda_{pw}(D_{cp})$$

where:

D_{cp} = Depth of web in compression at M_p

$\lambda_{pw}(D_{cp})$ = Maximum slenderness ratio for a compact web based on $2D_{cp}/t_w$

$$= \frac{\sqrt{\frac{E}{F_{yc}}}}{\left(0.54\frac{M_p}{R_h M_y}\right)}$$

In this case, the web plastification factor, R_{pc}, is as follows:

$$R_{pc} = \frac{M_p}{M_{yc}} \tag{2.7}$$

For noncompact web sections, the web slenderness ratio satisfies the following:

$$\lambda_{pw}(D_c) < \bar{\lambda}_w \le \lambda_{rw}$$

where:

$\lambda_{pw}(D_c)$ = Maximum slenderness ratio for a compact web based on $2D_c/t_w$

$\bar{\lambda}_w$ = Slenderness ratio for the web based on the elastic moment

$$= \frac{2D_c}{t_w}$$

In this case, the web plastification factor is as follows:

$$R_{pc} = \left[1 - \left(1 - \frac{R_h M_{yc}}{M_p} \right) \left(\frac{\lambda_w - \lambda_{pw}(D_c)}{\lambda_{rw} - \lambda_{pw}(D_c)} \right) \right] \frac{M_p}{M_{yc}} \leq \frac{M_p}{M_{yc}} \tag{2.8}$$

2.2.2.2 Local Buckling Resistance of Compression Flange

For the compression flange the local buckling resistance is determined as follows:

1. If $\bar{\lambda}_f \leq \lambda_{pf}$, then:

$$M_{nc} = R_{pc} M_{yc} \tag{2.9}$$

2. Otherwise:

$$M_{nc} = \left[1 - \left(1 - \frac{F_{yr} S_{xc}}{R_{pc} M_{yc}} \right) \left(\frac{\bar{\lambda}_f - \lambda_{pf}}{\lambda_{rf} - \lambda_{pf}} \right) \right] R_{pc} M_{yc} \tag{2.10}$$

where:

λ_{rf} = Noncompact flange slenderness limit = $0.95\sqrt{\frac{E k_c}{F_{yr}}}$

k_c = Flange local buckling coefficient = $\frac{4}{\sqrt{\frac{2D_c}{t_w}}}$

S_{xc} = Elastic section modulus for the compression flange about the major axis of the section

Note that λ_{rf} in this section was defined differently than in Section 2.2.1.1.

2.2.2.3 Lateral Torsional Buckling Resistance of Compression Flange

For the compression flange the local buckling resistance is determined as follows:

1. If $L_b \leq L_p$, then:

$$M_{nc} = R_{pc}\, M_{yc} \tag{2.11}$$

2. If $L_p < L_b \le L_r$, then:

$$M_{nc} = C_b \left[1 - \left(1 - \frac{F_{yr}\, S_{xc}}{R_{pc}\, M_{yc}} \right) \left(\frac{L_b - L_p}{L_r - L_p} \right) \right] R_{pc}\, M_{yc} \le R_{pc}\, M_{yc} \tag{2.12}$$

2.3 2001 AASHTO LRFD Bridge Design Specifications

An I-girder with a compact compression flange, compact web, and sufficient compression flange bracing is expected to develop the plastic moment M_p as its flexural strength and maintain M_p through an inelastic rotation capacity that is sufficient for plastic design [AASHTO 2001]. An I-girder with a noncompact web or a noncompact flange is expected to reach the yield moment, M_y as its flexural strength, with a possible reduction for shedding of compressive stresses by the web.

The web slenderness limit for a compact section is given by [AASHTO 2001]:

$$\frac{2D_{cp}}{t_w} \le 3.76 \sqrt{\frac{E}{F_{yw}}} \tag{2.13}$$

The flange slenderness limit for a compact section is given by [AASHTO 2001]:

$$\frac{b_f}{2\, t_f} \le 0.382 \sqrt{\frac{E}{F_{yc}}} \tag{2.14}$$

The web-flange interaction formula for web and flange slenderness limit for a compact section reduces the limits given in Equation 2.13 and Equation 2.14 to:

$$\frac{2D_{cp}}{t_w} + 9.35 \frac{b_f}{2\, t_f} \le 6.25 \sqrt{\frac{E}{F_{yc}}} \tag{2.15}$$

When the compression flange bracing satisfies the requirements for a compact section but the web or the compression flange or both do not satisfy the respective slenderness limits, the 2001 AASHTO LRFD specifications [AASHTO 2001] give an optional Q formula for calculating the nominal flexural resistance of a steel I-girder, as follows:

$$M_n = \left[1 - \left(1 - \frac{0.7}{M_p / M_y}\right)\left(\frac{Q_p - Q_{fl}}{Q_p - 0.7}\right)\right] M_p \le M_p \tag{2.16}$$

For symmetrical sections:

$$Q_p = 3.0 \tag{2.17}$$

If the compression flange is compact, $\frac{b_f}{2t_f} \le 0.382\sqrt{\frac{E}{F_{yc}}}$, then:

$$Q_{fl} = \frac{30.5}{\sqrt{\frac{2D_{cp}}{t_w}}} \tag{2.18}$$

otherwise:

$$Q_{fl} = \frac{4.45}{\left(\frac{b_f}{2t_f}\right)^2 \sqrt{\frac{2D_{cp}}{t_w}}} \frac{E}{F_{yc}} \tag{2.19}$$

Note that all the above equations apply only for steels having a specified minimum yield strength not exceeding 70 ksi (485 MPa) [AASHTO 2001]. For I-girders fabricated from steel having a specified minimum yield strength that exceeds 70 ksi (485 MPa), the nominal flexural strength is determined using the noncompact section compression-flange slenderness provisions of Article 6.10.4.1.4 [AASHTO 2001], which limit the flexural strength to the yield moment. However, for the present study, the restriction that the specified minimum yield strength does not exceed 70 ksi (485 MPa) was not considered. The purpose is to determine if the optional Q formula for calculating the nominal flexural resistance of a steel I-girder in the 2001 AASHTO LRFD specifications [AASHTO 2001] applies to HPS-100W I-girders.

2.4 Previous Research

The present study focuses on the flexural strength and ductility of highway bridge I-girders fabricated from high performance steel with a nominal yield stress of 100 ksi (690 MPa), that is, HPS-100W. Previous research related to the present study includes investigation of both conventional and high strength steel I-shaped members. The following sections summarize the research relevant to this study. To easily

compare different research results, the data are presented in tables, which contain the parameters controlling the behavior.

The following are the definitions of symbols used to summarize the research results:

h_w = Web height
t_w = Web thickness
b_f = Width of compression flange
t_f = Thickness of compression flange
E = Young's modulus
σ_{yf} = Actual yield strength of the compression flange
σ_{yw} = Actual yield strength of the web
λ_f = Normalized flange slenderness = $(\frac{b_f}{2 \cdot t_f}\sqrt{\frac{\sigma_{yf}}{E}})$
λ_w = Normalized web slenderness = $(\frac{h_w}{t_w}\sqrt{\frac{\sigma_{yw}}{E}})$
L_{b1} = First unbraced length measured from maximum moment location
r_y = Minimum radius of gyration of steel section with respect to the vertical axis
M_u = Maximum moment from experiment
M_p = Plastic moment
M_y = Yield moment

2.4.1 McDermott [1969]

The earliest study of the strength and ductility of I-shaped members fabricated from high strength steel was performed by McDermott [1969]. This study investigated the inelastic behavior of I-shaped beams fabricated from ASTM A514 steel. This steel has a nominal yield strength of 100 ksi (690 MPa). The actual yield strength of the steel used in this study ranged from 128 ksi (883 MPa) to 115 ksi (793 MPa). These yield strengths are similar to those of HPS-100W steel. However, λ_w and λ_f considered by McDermott are quite different than those considered in the present study. Table 2.1 summarizes the geometry and strength of these specimens.

Nine specimens were tested; five of them were rolled wide-flange beams and four welded plate I-shaped beams. Specimens 1 through 7 were symmetrically loaded by two jacks to produce a constant bending moment region between the loading points. Specimens A and B were loaded by one central jack to produce a moment gradient between the loading point and the supports.

Failure of Specimens 1 through 5 was by local buckling of the compression flange. Specimen 6 and Specimen 7 failed by a combination of local and lateral buckling of the compression flange. The failure of Specimens 1 through 7 occurred within the region of constant moment. Specimen A and Specimen B failed by rupture of the tension flange.

McDermott concluded that premature plastic buckling of A514 steel I-shaped members will not occur if $b_f/2t_f$ is less than 5 and the ratio L_{b1}/r_y is limited to 21 for uniform moment and to 36 for moment gradient regions.

2.4.2 Croce [1970]

Eight continuous I-shaped plate girders were tested. The main objective was to study the static strength of plate girders with unstiffened slender webs and investigate the maximum web slenderness for the use in plastic design. The specimens were welded I-girders fabricated from ASTM A36 steel with a nominal yield strength of 36 ksi (248 MPa). The specimens were three-span continuous I-girders with varying span lengths and loading configurations.

The normalized flange slenderness, λ_f, ranged from 0.131 to 0.338 and the normalized web slenderness, λ_w, ranged from 2.13 to 4.35. Table 2.2 summarizes the geometry and strength of these specimens. The failure modes of the majority of the test specimens involved shear buckling of the web rather than local buckling of the compression flange and/or web.

Several of the web slenderness values considered by Croce are in the range of interest of the present study. However, the flange slenderness values were much less than those considered in the present study.

2.4.3 Holtz and Kulak [1973]

Ten welded I-shaped specimens were tested at the University of Alberta to determine a suitable limit for the web slenderness of compact beams. The specimens were fabricated from CSA G40.12 steel, with a nominal yield strength of 44 ksi (303 MPa). All specimens were simply supported and loaded symmetrically in four-point loading. To prevent premature lateral buckling, the compression flange of each specimen was laterally braced with a spacing meeting the requirements for plastic design.

Eight specimens have a normalized flange slenderness, λ_f, of 0.377, and two specimens have slightly stockier flanges with λ_f of 0.312. The normalized web slenderness, λ_w, for the specimens ranged from 3.02 to 5.45. Table 2.3 summarizes the geometry and strength of these specimens. Also, the plastic rotation capacity, θ_{pc}, of

the specimens which reached or exceeded M_p is provided in Table 2.3. θ_{pc} is the plastic rotation at which the flexural strength of the I-girder falls below M_p, as shown in Figure 2.1. The ultimate flexural strength, M_u, for four of the specimens exceeded M_p. The data for θ_{pc} versus λ_w for these specimens is shown in Figure 2.2, with the label H&K.

2.4.4 Schilling and Morcos [1988]

Three I-girders were tested with the aim of developing moment versus rotation curves for noncompact plate girders. The specimens were fabricated from ASTM A572 Grade 50 steel, with an actual yield strength of 58.8 ksi (405 MPa) for the flanges and 56.2 ksi (388 MPa) for the web. Each specimen was tested as a simply supported beam in three-point loading. This loading arrangement simulated the condition of negative flexure at the pier of a continuous-span bridge.

The normalized flange slenderness, $\lambda_{f,}$ ranged from 0.295 to 0.300 and the normalized web slenderness, $\lambda_{w,}$ ranged from 3.55 to 6.76. Table 2.4 summarizes the geometry and strength of these specimens. Also, the plastic rotation capacity, θ_{pc}, of the specimens which reached or exceeded M_p is provided in Table 2.4. The ultimate flexural strength, M_u, for two of the specimens exceeded M_p. The data for θ_{pc} versus λ_w is shown in Figure 2.2, with the label S&M. The failure modes of the three specimens involved a complex interaction of local flange buckling, local web buckling, and lateral buckling.

2.4.5 Barth [1996]

Six specimens were tested at Purdue University to investigate the flexural strength and ductility of bridge I-girders fabricated from ASTM A572 Grade 50 steel, with an actual yield strength of 62 ksi (427 MPa) for the flanges and 70 ksi (485 MPa) for the web. The specimens were tested to failure under three-point loading, which simulated the condition of negative flexure at the pier of a continuous-span bridge.

λ_f ranged from 0.291 to 0.391 and λ_w ranged from 4.79 to 6.23. A summary of the geometry, yield strength, normalized web and flange slenderness, the ratio of the maximum moment to the plastic moment, and θ_{pc} is given in Table 2.5. The slenderness of the six specimens is within the range of interest for the present study. The plastic rotation capacity, θ_{pc}, of Specimen 6, which reached M_p, is provided in Table 2.5. The data for θ_{pc} versus λ_w for this specimen is shown in Figure 2.2, with the label B. The failure modes of all specimens involved a complex interaction of local flange buckling, local web buckling, and lateral buckling.

2.4.6 Fahnestock and Sause [1998]

Two specimens were tested at Lehigh University to investigate the flexural strength and ductility of bridge I-girders fabricated from HPS-100W steel, with a nominal yield strength of 100 ksi (790 MPa). Note this steel is somewhat different than the steel used in the present study as discussed in Chapter 1. The specimens were tested to failure under three-point loading. Specimen 1 was designed to have compact flange and web, and Specimen 2 was designed to have a compact flange and a noncompact web. Both specimens were designed according to interim 1996 AASHTO LRFD specifications [AASHTO 1996], which do not include the web-flange slenderness interaction formula, given by Equation 2.15, that is included in more recent AASHTO LRFD specifications [AASHTO 2001].

The normalized flange slenderness, $\lambda_{f,}$ for Specimen 1 and Specimen 2 are 0.399 and 0.401, respectively, and normalized web slenderness, $\lambda_{w,}$ for Specimen 1 and Specimen 2 are 3.63 and 5.35, respectively. Table 2.6 summarizes the geometry and strength of the two specimens. Also, the plastic rotation capacity, θ_{pc}, is provided in Table 2.6. The data for θ_{pc} versus λ_w for Specimen 1 is shown in Figure 2.2, with the label F&S.

Both specimens failed by local buckling of compression flange and web. Specimen 1 reached an ultimate moment greater than M_p by 3%, and Specimen 2 reached an ultimate moment less than M_p by 3%.

It was concluded that the 1996 AASHTO LRFD specifications for the flexural strength of I-girders with compact or noncompact sections were applicable to I-girders fabricated from HPS-100W steel.

2.4.7 Yakel, Mans, and Azizinamini [2002]

Four I-girders were tested at University of Nebraska-Lincoln to address the limitations in the AASHTO LRFD specifications on the flexural strength of ASTM A709 HPS-70W I-girders. Prior to 2001, the nominal flexural strength of I-girders with yield strength greater than 50 ksi (345 MPa) was limited to the yield moment. The first pair of specimens was fabricated using ASTM A709 HPS-70W with a nominal yield strength of 70 ksi (485 MPa). The two specimens had the same compact flanges. One specimen had a compact web and the other specimen had a noncompact web. To compare the behavior of a girder fabricated from HPS-70W with that of a girder fabricated from ASTM A572 Grade 50 steel, the second pair of specimens was designed such that both specimens have noncompact webs and noncompact compression flanges. Due to limited availability of HPS-70W steel, ends of the specimens, which were expected to remain elastic, were fabricated from ASTM A572

Grade 50 steel. All specimens were simply supported and loaded with a single point load at midspan.

The normalized flange slenderness of the specimens, $\lambda_{f,}$ ranged from 0.262 to 0.444 and the normalized web slenderness, $\lambda_{w,}$ ranged from 3.90 to 5.05. A summary of the geometry, yield strength, normalized web and flange slenderness, the ratio of the maximum moment to the plastic moment, and θ_{pc} is shown in Table 2.7. The data for θ_{pc} versus λ_w is shown in Figure 2.2, with the label Y. The slenderness of the four specimens is within the range of interest for the present study.

The experimental results showed that both of the first pair of specimens, fabricated from HPS-70W, were able to reach and exceed the theoretical plastic moment capacity, M_p. For the second pair of specimens, one specimen was fabricated from ASTM A572 Grade 50 and the other specimen was fabricated from HPS-70W. Both of the second pair of specimens were able to exceeding the yield moment capacity as required by the AASHTO LRFD Bridge Design Specifications for noncompact sections. It was concluded that noncompact I-girders fabricated from ASTM A572 Grade 50 and ASTM A709 HPS-70W steel exhibit similar behavior. As a result, the equations used for A572 Grade 50 I-girders were considered applicable to A709 HPS-70W I-girders.

2.5 Review of Theory of Plasticity

Converting strains into stresses in the elastic range can be done using the elasticity matrix. However, after the material yields, plasticity theory is needed to convert strains into stresses. In order to apply the theory of plasticity, three main elements of the theory have to be defined, namely, the yield criterion, the flow rule, and the hardening rule. In the following sections a brief explanation of each of these elements of the theory are introduced. The algorithm used in the present research for determining stresses from strains using plane stress plasticity with nonlinear hardening will be presented in Appendix A, of the report.

2.5.1 Yield Criterion

The yield criterion defines a surface, which represents the boundary of the elastic region. If the stress state lies within this boundary, no plastic deformation will take place. On the other hand, when the stress state lies on the boundary, plastic deformation will occur. The most widely used yield criterion for steel is Von Mises. For plane stress conditions, the Von Mises yield criterion for a nonlinear hardening material is defined by [Crisfield, 1991]:

$$f = \sqrt{\sigma^2{}_{11} + \sigma^2{}_{22} - \sigma_{11}\,\sigma_{22} + 3\,\sigma^2{}_{12}} - \sigma_y(\varepsilon_{ps}) \tag{2.20}$$

$$f = \sigma_e - \sigma_y(\varepsilon_{ps}) \tag{2.21}$$

$$\sigma_e = \sqrt{\sigma^2{}_{11} + \sigma^2{}_{22} - \sigma_{11}\,\sigma_{22} + 3\,\sigma^2{}_{12}} = \sqrt{3J_2} \tag{2.22}$$

where:

σ_e = Effective stress
J_2 = Second invariant of stresses
ε_{ps} = Equivalent plastic strain
$\sigma_y(\varepsilon_{ps})$ = Yield stress as a function of the equivalent plastic strain

As the yield criterion must be invariant with respect to the choice of axes used to represent the state of stress, σ_e is a function of the second invariant of stresses.

2.5.2 Hardening Rule

The most widely used rule is the isotropic hardening rule, which is based on the assumption that the initial yield surface expands uniformly without distortion or translation as plastic flow occurs. This expansion of the yield surface is a function of the equivalent plastic strain. In other words, the yield stress is defined as a function of the equivalent plastic strain, $\sigma_y(\varepsilon_{ps})$ as will be shown in detail in Appendix A.

2.5.3 Flow Rule

The flow rule defines the kinematic assumption for plastic deformation or plastic flow. It provides the relative magnitudes of the plastic strain components for an increment of plastic strain. These relative magnitudes define the direction of the plastic strain increment. The simplest flow rule is defined when the yield function and plastic potential function coincide. This flow rule is called the associated flow rule. For plane stress conditions, the associated flow rule is as follows:

$$d\varepsilon_{ij}^{p} = d\lambda\left(\frac{\partial f}{\partial \sigma_{ij}}\right) \tag{2.23}$$

$$\frac{\partial f}{\partial \sigma_{ij}} = \frac{1}{2\sigma_e}\begin{pmatrix} 2\sigma_{11} - \sigma_{22} \\ 2\sigma_{22} - \sigma_{11} \\ 6\sigma_{12} \end{pmatrix} \tag{2.24}$$

$$d\varepsilon_{ij}^{p} = \begin{pmatrix} d\varepsilon_{11}^{p} \\ d\varepsilon_{22}^{p} \\ d\varepsilon_{12}^{p} \end{pmatrix} = \frac{d\lambda}{2\sigma_e} \begin{pmatrix} 2\sigma_{11} - \sigma_{22} \\ 2\sigma_{22} - \sigma_{11} \\ 6\sigma_{12} \end{pmatrix} \tag{2.25}$$

where $\frac{\partial f}{\partial \sigma_{ij}}$ is the normal to the yield surface and $d\lambda$ is the plastic strain rate multiplier, a positive constant. The equivalent plastic strain is given by:

$$\varepsilon_{ps} = \int d\varepsilon_{ps} \tag{2.26}$$

which is an accumulation of the equivalent plastic strain increment [Crisfield, 1991].

$$d\varepsilon_{ps} = \frac{2}{\sqrt{3}} (d\varepsilon_{11}^{p\,2} + d\varepsilon_{22}^{p\,2} + d\varepsilon_{11}^{p}\, d\varepsilon_{22}^{p} + \frac{1}{4} d\gamma_{12}^{p\,2})^{1/2} \tag{2.27}$$

Table 2.1 Specimens tested by McDermott [1969]

Specimen	h_w (in)	t_w (in)	b_f (in)	t_f (in)	σ_{yw} (ksi)	σ_{yf} (ksi)	λ_w	λ_f	h_w/b_f	L_{b1}/r_y	M_u/M_p	θ_{pc} (rad)
1	7.23	0.294	8.780	0.370	125	125	1.61	0.779	0.82	11.60	0.78	———
2	7.11	0.347	7.910	0.491	128	128	1.36	0.535	0.90	9.00	0.97	———
3	7.23	0.386	6.700	0.554	115	115	1.18	0.381	1.08	7.30	1.01	NA
4	7.22	0.382	5.580	0.560	118	118	1.21	0.318	1.29	6.00	1.02	NA
5	7.22	0.386	4.450	0.557	119	119	1.20	0.256	1.62	5.40	1.02	NA
6	8.09	0.256	3.970	0.624	116	120	2.00	0.205	2.04	24.90	1.02	NA
7	8.14	0.267	5.940	0.619	116	119	1.93	0.307	1.37	23.90	1.00	NA
A	8.05	0.258	3.970	0.614	116	120	1.97	0.208	2.03	37.50	1.17	NA
B	7.99	0.259	5.970	0.619	116	119	1.95	0.309	1.34	35.40	1.14	NA

Table 2.2 Specimens tested by Croce [1970]

Specimen	h_w (in)	t_w (in)	b_f (in)	t_f (in)	σ_{yw} (ksi)	σ_{yf} (ksi)	λ_w	λ_f	h_w/b_f	L_{b1}/r_y	M_u/M_p	θ_{pc} (rad)
1	15.89	0.179	5.970	0.322	43	39	3.42	0.338	2.66	45.8	1.20	NA
2	15.96	0.186	6.040	0.527	40	35	3.17	0.200	2.64	41.7	1.15	NA
3	15.92	0.186	6.050	0.527	40	35	3.17	0.200	2.63	41.7	1.15	NA
4	15.82	0.177	5.990	0.773	43	33	3.44	0.131	2.64	79.5	1.02	NA
5	16.03	0.250	6.050	0.527	42	35	2.44	0.200	2.65	43.8	1.30	NA
6	22.00	0.375	5.970	0.507	38	35	2.13	0.205	3.69	53.6	1.09	NA
7	22.00	0.264	5.970	0.506	38	35	3.02	0.205	3.69	32.5	1.24	NA
8	22.00	0.188	5.940	0.507	40	35	4.35	0.204	3.70	30.3	1.16	NA

Table 2.3 Specimens tested by Holtz and Kulak [1973]

Specimen	h_w (in)	t_w (in)	b_f (in)	t_f (in)	σ_{yw} (ksi)	σ_{yf} (ksi)	λ_w	λ_f	h_w/b_f	L_{b1}/r_y	M_u/M_p	θ_{pc} (rad)
WS-1	20.00	0.250	7.250	0.375	44	44	3.12	0.377	2.76	31.78	1.02	0.027
WS-2	24.97	0.250	7.250	0.375	44	44	3.89	0.377	3.44	33.68	0.98	———
WS-3	29.97	0.250	7.250	0.375	44	44	4.67	0.377	4.13	30.95	0.89	———
WS-4	35.00	0.250	7.250	0.375	44	44	5.45	0.377	4.83	27.86	0.86	———
WS-6	23.47	0.250	7.250	0.375	44	44	3.66	0.377	3.24	33.14	0.88	———
WS-7-P	21.00	0.250	6.000	0.375	44	44	3.27	0.312	3.50	30.68	0.99	———
WS-8-P	23.50	0.250	6.000	0.375	44	44	3.66	0.312	3.92	31.56	0.95	———
WS-9	19.41	0.250	7.250	0.375	44	44	3.02	0.377	2.68	23.66	1.08	0.028
WS-10	20.94	0.250	7.250	0.375	44	44	3.26	0.377	2.89	21.49	1.15	0.052
WS-11	22.97	0.250	7.250	0.375	44	44	3.58	0.377	3.17	16.44	1.07	0.017

Table 2.4 Specimens tested by Schilling and Morcos [1988]

Specimen	h_w (in)	t_w (in)	b_f (in)	t_f (in)	σ_{yw} (ksi)	σ_{yf} (ksi)	λ_w	λ_f	h_w/b_f	L_{b1}/r_y	M_u/M_p	θ_{pc} (rad)
S	17.002	0.211	6.972	0.523	56.20	58.80	3.55	0.300	2.44	———	1.11	0.059
M	23.953	0.204	6.961	0.527	56.20	58.80	5.16	0.297	3.44	———	1.02	0.025
D	30.384	0.198	6.924	0.528	56.20	58.80	6.76	0.295	4.39	———	0.90	———

Table 2.5 Specimens tested by Barth [1996]

Specimen	h_w (in)	t_w (in)	b_f (in)	t_f (in)	σ_{yw} (ksi)	σ_{yf} (ksi)	λ_w	λ_f	h_w/b_f	L_{b1}/r_y	M_u/M_p	θ_{pc} (rad)
1	25.08	0.198	8.590	0.508	70	62	6.22	0.391	2.92	45.46	0.91	———
2	25.23	0.199	8.570	0.510	70	62	6.23	0.388	2.94	33.47	0.93	———
3	25.21	0.205	7.200	0.562	70	62	6.04	0.296	3.50	40.65	0.93	———
4	25.22	0.210	8.550	0.510	70	62	5.90	0.388	2.95	67.80	0.80	———
5	19.80	0.203	8.560	0.507	70	62	4.79	0.390	2.31	46.99	0.95	———
6	19.75	0.202	7.170	0.569	70	62	4.80	0.291	2.75	42.45	1.00	0.035

Table 2.6 Specimens tested by Fahnestock and Sause [1998]

Specimen	h_w (in)	t_w (in)	b_f (in)	t_f (in)	σ_{yw} (ksi)	σ_{yf} (ksi)	λ_w	λ_f	h_w/b_f	L_{b1}/r_y	M_u/M_p	θ_{pc} (rad)
1	24.00	0.388	9.813	0.775	100	115	3.63	0.399	2.45	18.38	1.03	0.020
2	36.00	0.395	9.813	0.770	100	115	5.35	0.401	3.67	16.23	0.97	———

Table 2.7 Specimens tested by Yakel et al.[1999, 2000]

Specimen	h_w (in)	t_w (in)	b_f (in)	t_f (in)	σ_{yw} (ksi)	σ_{yf} (ksi)	λ_w	λ_f	h_w/b_f	L_{b1}/r_y	M_u/M_p	θ_{pc} (rad)
A	34.00	0.390	16.250	1.530	82	71	4.64	0.263	2.09	30.23	1.12	0.063
D	28.75	0.393	16.250	1.540	82	71	3.90	0.262	1.77	33.99	1.19	0.099
C50	35.25	0.330	14.844	0.770	65	50	5.05	0.400	2.37	48.16	0.91	———
C70	29.81	0.331	12.688	0.760	85	82	4.87	0.444	2.35	34.24	0.91	———

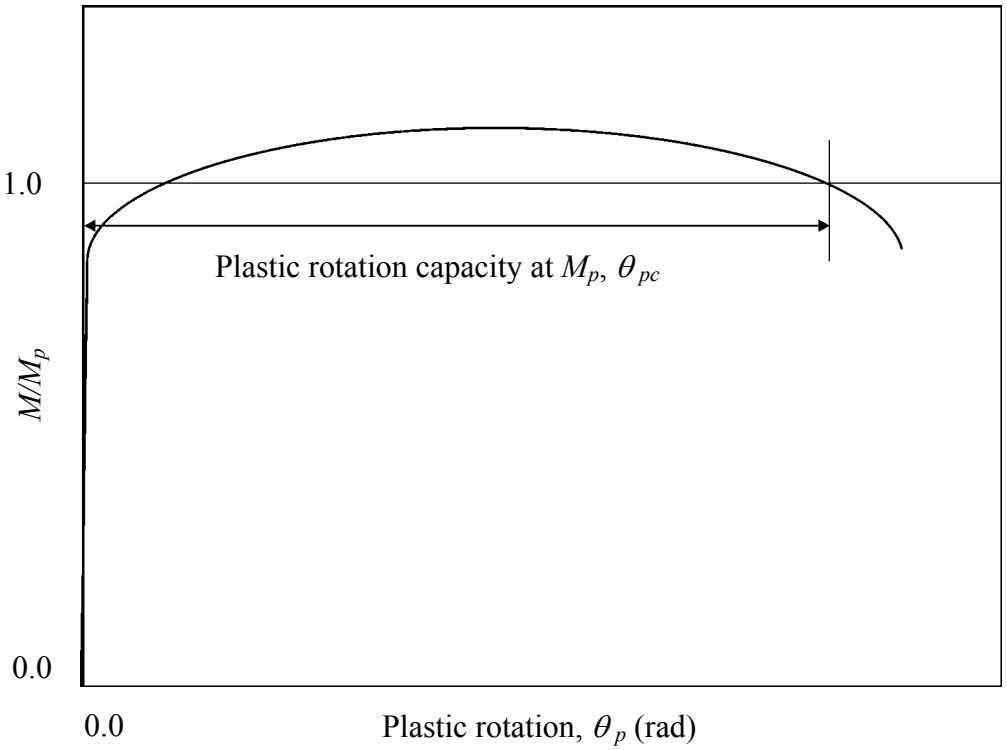

Figure 2.1 Normalized moment versus plastic rotation

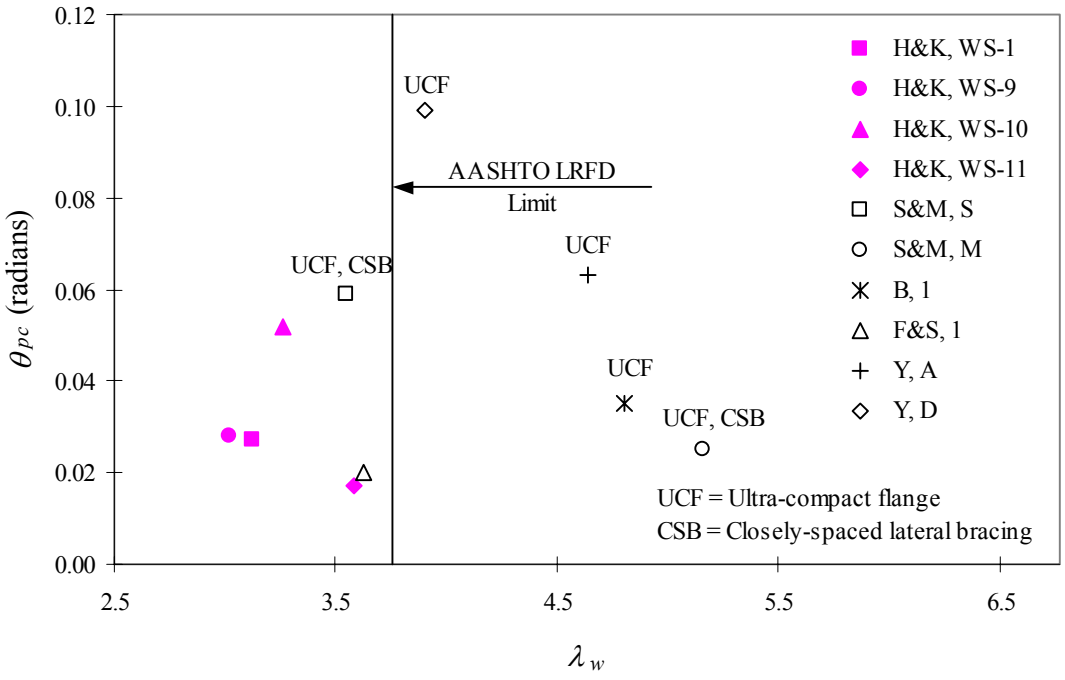

Figure 2.2 Plastic rotation capacity at M_p versus normalized web slenderness

CHAPTER 3 Finite Element Model for I-Girder Local Buckling

3.1 Introduction

The commercially general-purpose finite element program, ABAQUS [2002], was used in this study to model local buckling behavior of I-girders, fabricated from HPS-100W steel. The purpose of these finite element simulations is to accurately predict both the strength and ductility of these I-girders as they are influenced by flange and web local buckling after the cross-section yields. Two HPS-100W I-girder specimens tested at Lehigh University by Sause and Fahnestock [2001] were used to calibrate the finite element model. As shown in Figure 3.1, the loading conditions for these two experimental specimens simulated negative moment conditions at the pier of a continuous span girder. The failure mode of these specimens was an interaction of local flange instability, web instability, and lateral instability. To accurately model this failure mode, the nonlinear geometry and nonlinear material capabilities of the ABAQUS [2002] program were used. The shell element used in the model is a general-purpose shell element that can provide accurate solutions for both thin and thick shell problems. In the formulation of this element, the change in thickness as a function of in-plane deformation is included.

Previous research related to the influence of local buckling on the flexural strength and ductility of I-girders fabricated from high performance steel, includes investigations by Barth [1996], Green [2000], Barth et al. [2000], Earls et al. [2002], Yakel et al. [2002], and Greco and Earls [2003]. The finite element modeling used in the present study began with ideas given by Green [2000], however, improvements to these ideas were made.

The most important step in conducting nonlinear finite element simulation of steel I-girder local buckling is developing appropriate finite element models. The accuracy of the finite element models is governed by many variables, including element type, which determines the element kinematic assumptions, initial geometry, mesh density, material constitutive models, loading, and boundary conditions. The accuracy of the finite element simulation depends on these variables, and the solution method employed to control the simulation.

Experimental data is needed to develop accurate finite element models. Through comparison with experimental results, it is possible to develop an accurate model, however, close agreement between selected results from a finite element simulation and an experimental data is not the only factor that determines the accuracy of the model. For example, the use of a coarse finite element mesh could require unreasonably large imperfections to get good correlation with the experimental results. In this case the increased imperfection amplitudes will offset the increased stiffness of the finite element model from the coarse mesh, resulting in close agreement between

the simulation results and the experimental results. Thus it is a challenge to determine an appropriate combination of finite element model variables that enable the local buckling behavior of steel I-girders to be accurately simulated.

3.2 Physical Model

Two specimens tested at Lehigh University by Sause and Fahnestock [2001] were used to develop the finite element model in the present study. Each specimen, Specimen 1 and Specimen 2, approximates a half-scale model of the pier negative-moment region of a continuous-span bridge girder as shown in Figure 3.1 and Figure 3.2. These specimens were fabricated from HPS-100W steel, which has different properties than the HPS-100W steel used in the present study as explained in Chapter 1. The geometry of these specimens along with their lateral brace locations is shown in Figure 3.2. To reduce the friction between the braces and the girder, Teflon sheets were attached to both the girder flange tips and the brace member in contact with the flanges [Fahnestock and Sause 1998]. A gap was intentionally left between the brace members and the flange tips, which was about 1/16 in (2 mm). The tensile coupon test results for the steel plate material used to fabricate the specimens are shown in Figure 3.3.

3.3 Main Parameters Affecting I-girder Local Buckling Finite Element Simulations

Many variables affect local buckling simulations from finite element models [Green 200]. Some of these variables are: element type, mesh density, material constitutive models, load, boundary conditions, geometric imperfections, residual stresses, and solution method. Most of these variables were studied to assess their effects on the finite element simulation of the local buckling of Specimen 1 and Specimen 2. The commercially available general-purpose finite element program, ABAQUS [2002] was used to develop the models and conduct the simulations.

To evaluate the finite element model, the applied load versus midspan vertical deflection and the midspan moment versus total end rotation from the experimental results were compared with those obtained from the finite element simulations.

3.3.1 Element Type

A four-node doubly curved general-purpose, reduced integration with hourglass control, shell element [ABAQUS 2002] was used to create the finite element models. This element assumes that the transverse shear strain is constant over the element. As a result, all four stiffness integration locations will have the same transverse shear strain, transverse shear section force, and transverse shear stress. This element is a general-purpose shell element for both thin and thick shell problems. The element includes change in thickness as a function of in-plane deformation.

The number of integration points through the thickness was set to five. Increasing the number of integration points to seven did not affect the global behavior in terms of midspan vertical deflection and total end rotation.

3.3.2 Material Constitutive Model

The finite element model used a material constitutive model for metals that accounted for differences in the compressive and tensile behavior. The constitutive model uses true stress and natural strain to account for finite deformations. The measured engineering stress-strain data from tensile coupon tests by Fahnestock and Sause [1998] were used to develop a representative curve for the engineering stress-strain behavior up to the ultimate stress. The procedures used to develop the representative engineering stress-strain curve were similar to those developed by Green [2000] with the following exceptions. The strain-hardening region is fit differently as explained in Chapter 5 and the stress-strain curve is treated as linear up to the yield point. The engineering stress-strain curve was then converted to true stress-strain and then true stress versus natural plastic strain as follows:

$$\sigma_{tr} = \sigma_{eng}\,(1 + \varepsilon_{eng}) \tag{3.1-a}$$

$$\varepsilon_{nat} = ln\,(1 + \varepsilon_{eng}) \tag{3.1-b}$$

$$\varepsilon_{nat-pl} = \varepsilon_{nat} - \frac{\sigma_{tr}}{E} \tag{3.1-c}$$

where:

σ_{eng} = Engineering stress
ε_{eng} = Engineering strain
σ_{tr} = True stress
ε_{nat} = Natural strain
ε_{nat-pl} = Natural plastic strain
E = Young's modulus

The true stress versus natural plastic strain curves for the web and flange steel plate material are shown in Figure 3.4. Beyond the ultimate engineering stress, the plot for true stress-natural plastic strain was linearly extended in the tangent direction up to a natural plastic strain of 0.12 as shown by the dotted line in Figure 3.4.

The constitutive model is an isotropic elastic plastic model that uses the Von Mises yield function with an associated flow rule [ABAQUS 2002], to model the material plasticity. Strain hardening is isotropic, assuming that the yield surface

expands uniformly expands without a change in shape. The hardening depends on the plastic deformation, in accordance with the true stress natural plastic strain curve.

3.3.3 Mesh Convergence

A sufficiently refined finite element mesh is needed to obtain accurate results from a finite element simulation. Coarse meshes will yield inaccurate results. The mesh should be determined before the other variables (e.g. geometric imperfection amplitude and location) are modified to achieve closer agreement with the experimental results. The numerical results from the finite element model will tend toward a unique value as the mesh density increases. The mesh is converged when further mesh refinement produces a negligible change in the results. For local buckling simulations, a uniformly fine mesh throughout the structure is rarely used. A fine mesh is used in the regions of high stress or deformation gradients, where local buckling is expected, and a coarser mesh is used in regions of low stress or deformation gradients.

The different finite element meshes that were investigated are shown in Figure 3.5. The detailed geometry of mesh C, which was ultimately selected for the study, is shown in Figure 3.6 and Figure 3.7 for the flange and web, respectively. To show that mesh C was sufficiently refined, the number of the compression flange elements in the middle region of the girder was doubled to produce mesh D as shown in Figure 3.5. The load versus midspan vertical deflection from simulations using mesh C and mesh D are compared with experimental results from Specimen 1 in Figure 3.8. This comparison shows that mesh C was sufficiently refined.

3.3.4 Boundary Conditions, Load Point, and Lateral Bracing

The boundary conditions implemented in the finite element model to simulate those used during the experiments, are two roller supports at bearings of the girder specimens and one pin support at the load point at midspan. The roller supports are located on the bottom flange nodes and the pin support is at a single node at the middle of top flange. The pin support at the midspan of the girder simulates friction under the load application point during the test, which controlled movement in the X (longitudinal) direction. The reaction distribution at bearings was achieved through the bearing stiffeners. The stiffener at the midspan is 1.5 in (38 mm) thick, and the load during the physical experiments was applied at the middle of the midspan stiffener on the top flange. The midspan stiffener and part of the web on each side of the midspan stiffener participated in distributing the applied load to the I-girder.

The tube support element (ITSUNI) from ABAQUS is used in the model to simulate the restraint provided by the lateral braces. This element is a unidirectional element, which acts in a fixed direction in space and is made up of a spring/friction link, as shown in Figure 3.9, and a parallel dashpot. The dashpot is not shown in the figure, since it is not used in the model. The spring behaves as shown in Figure 3.9. When there is no contact between the flange and the brace, no lateral force is

transmitted to the flange by the spring; and when the flange is in contact with the brace, the lateral force increases as the flange displaces laterally. The brace force is therefore a nonlinear function of the lateral displacement of the flange.

This element is attached to each edge of the flange by specifying two nodes at the edge of the flange with the same coordinates (for example, nodes a and b as shown in Figure 3.9(a)). The gap between the flange and brace that was intentionally set for experiments is modeled using this element by specifying the nonlinear behavior of the spring as shown in Figure 3.9.

In the experiments, Teflon sheets were attached to the brace surface in contact with girder flanges and to the girder flange tips to minimize the friction [Fahnestock and Sause 1998]. As a result, no friction was specified in the brace model. A gap of 1/16 in (2 mm) was used in the model. The brace stiffness for elements attached to top flange was estimated to be 156 kip/in (27 kN/mm) from data given by Fahnestock and Sause [1998], while the stiffness for elements attached to the bottom flange was estimated to be 96 kip/in (17 kN/mm).

3.3.5 Geometric Imperfection

Geometric imperfections have a detrimental effect on the local buckling behavior of steel bridge I-girders. As only the maximum web imperfection amplitude and its location were reported by Fahnestock and Sause [1998], an assumption for imperfection shape was made similar to that used by Green [2000].

An imperfection with a sine wave in *x*-direction and cosine wave in *y*-direction was introduced to the web. This imperfection was introduced to the north of the midspan as shown by the hatched region, in Figure 3.10. The imperfection amplitude, z_0, was taken as the maximum imperfection amplitude reported by Fahnestock and Sause [1998], which was 1/16 in (2 mm).

An initial imperfection with a sine wave in the local-x direction and cosine wave in the local-y direction was introduced to the web. The local-x and y coordinate system is shown in Figure 3.10. The geometry of the imperfect region is specified by the following equation:

$$z = \frac{z_0}{2}\left[1 - cos\left(\frac{2\pi x}{A}\right)\right] sin\left(\frac{\pi y}{B}\right) \tag{3.2}$$

where:

A = Length of the imperfect region in the *x*-direction
B = Length of the imperfect region in the *y*-direction
z_0 = Maximum imperfection amplitude at $x = A/2$ and $y = B/2$

3.3.6 Solution Method

In order to trace the post peak behavior of the I-girder specimens failing by local buckling, the modified Riks method [ABAQUS 2002] was used as the solution method. The modified Riks method is one of the arc-length methods. In relation to structural analysis, Riks [1972, 1979] and Wempner [1971] originally introduce the arc-length method with later modification being made by Crisfield [1981, 1983].

3.4 Validation of Finite Element Model

The two specimens, Specimen 1 and Specimen 2, tested at Lehigh University by Fahnestock and Sause [1998], were used to verify the finite element model. Those specimens were fabricated from HPS-100W steel, as discussed previously. Specimen 1 and Specimen 2 were designed as a compact and a noncompact section, respectively using the AASHTO LRFD specifications [AASHTO 1996], but neglecting the limitation on the use of steel with yield strength in excess of 50 ksi (345 MPa). The actual dimensions and material properties of specimens were used as reported in Fahnestock and Sause [1998], as shown in Table 3.1.

For Specimen 1, comparisons between the experimental results and the finite element simulation results are presented in Figure 3.11 and Figure 3.12. Load versus midspan vertical deflection is compared in Figure 3.11 and midspan moment versus average end rotation is compared in Figure 3.12. A plot of the deflected shape from the finite element analysis, at 90% P_u-post peak, where P_u is the ultimate load, and the deflected shape of the experimental specimen after the experiment is shown in Figure 3.13.

From these figures, it is clear that the finite element simulation accurately predicts the experimental specimen behavior. The ultimate load from the finite element simulation is 277 kips (1232 kN), which is higher than the ultimate load from the experiment by 1%.

For Specimen 2, comparisons between the experimental results and the finite element simulation results are presented in Figure 3.14 and Figure 3.15. Load versus midspan vertical deflection is compared in Figure 3.14 and midspan moment versus average end rotation is compared in Figure 3.15. A plot of the deflected shape from the finite element analysis, at 90% P_u-post peak, and the deflected shape of the experimental specimen after the experiment is shown in Figure 3.16.

The ultimate load from the finite element simulation is 290 kips (1290 kN), which is 1% higher than the ultimate load from the experiment.

3.5 Effect of Imperfection Location and Amplitude

The location of the web imperfection in the finite element model was varied as shown in Figure 3.17. The effect of these variations on the load versus deflection behavior of Specimen 1 is shown in Figure 3.18. From this figure, it is clear that the closer the imperfection is to the middle of the span, the faster the specimen will unload.

The effect of the web imperfection amplitude is shown in Figure 3.19 for Specimen 1. Three maximum imperfection amplitudes, 1/16 in (2 mm), 1/8 in (3 mm), and 1/4 in (6 mm) were used. As the imperfection amplitude increases, the specimen unloads earlier.

3.6 Moment and Force Transferred Between Web and Top Flange

When the webs of Specimen 1 and Specimen 2 buckle, primary bending moment is shed to the flanges. In addition, the top flange is subjected to twisting moment and lateral force from the web. The twisting moment disturbs the top flange and increases its local torsional instability, while the lateral force increases its lateral instability. The global and local directions used in the finite element analysis are shown in Figure 3.20.

The following are the available stresses [ABAQUS 2002]:

σ_{11} = Normal stress in the local-1 direction
σ_{22} = Normal stress in the local-2 direction
σ_{12} = Shear stress in the local 1-2 plane
σ_{13} = Transverse shear stress in the local 1-3 plane
σ_{23} = Transverse shear stress in the local 2-3 plane

The following are the available section forces, moments, and transverse shear forces [ABAQUS 2002]:

SF1 = Normal force per unit width in the local-1 direction
SF2 = Normal force per unit width in the local-2 direction
SF3 = In-plane shear force per unit width in the local 1-2 plane
SF4 = Transverse (through thickness) shear force per unit width acting on plane normal to local-1 direction
SF5 = Transverse (through thickness) shear force per unit width acting on plane normal to local-2 direction
SM1 = Bending moment per unit width about the local-2 axis
SM2 = Bending moment per unit width about the local-1 axis
SM3 = Twisting moment per unit width in the local 1-2 plane

The section force and moment resultant per unit length for a shell element of thickness t can be defined as follows [ABAQUS 2002], where x_3 is a dummy variable in the local-3 direction:

$$(SF1, SF2, SF3, SF4, SF5) = \int_{-t/2}^{t/2} (\sigma_{11}, \sigma_{22}, \sigma_{12}, \sigma_{13}, \sigma_{23})\, dx_3 \tag{3.3}$$

$$(SM1, SM2, SM3) = \int_{-t/2}^{t/2} (\sigma_{11}, \sigma_{22}, \sigma_{12})\, x_3\, dx_3 \tag{3.4}$$

Note that the bending moment *SM2* acting on the web produces a twisting moment on the flange and the transverse shear force *SF5* acting on the web produces a lateral force on the flange. The positive directions for the bending moment, *SM2*, and the transverse shear force, *SF5*, transferred between web and top flange are shown in Figure 3.21. The twisting moment and lateral force are plotted in Figure 3.22 and Figure 3.23, respectively, for Specimen 1, and in Figure 3.24 and Figure 3.25, respectively, for Specimen 2. In these figures the horizontal axis represents the distance measured from the midspan of the specimen, X_m, along the specimen length (along the global-X direction). As the twisting moment and lateral force develop from web out-of-plane deformation, they have their greatest effect within a distance equal to the web height, h_w, from the midspan. A vertical line spaced at h_w from the midspan is plotted in Figure 3.22 through Figure 3.25. As a reference to represent the location of first lateral brace, which is a distance L_{b1} from midspan, a vertical line spaced at $0.5\ L_{b1}/L$ from the midspan is plotted in Figure 3.22 through Figure 3.25.

In Figure 3.22 through Figure 3.25, the twisting moment and lateral force are plotted when the load corresponds to P_u. Note that at the middle of the buckled zone, the resultants of the distributed twisting moment and lateral force are in directions to produce the deflected shape shown in Figure 3.13 and Figure 3.16, for Specimen 1 and Specimen 2, respectively. Note that Specimen 1 and Specimen 2 have the same b_f and different h_w. As a result, the cross section aspect ratio, h_w/b_f, for the two specimens is different. Specimen 1 has h_w/b_f = 2.45 and Specimen 2 has h_w/b_f = 3.67. It is clear that for the same b_f and different h_w/b_f, the specimen with larger h_w/b_f will have larger h_w (Specimen 1 has h_w = 24 in (610 mm) and Specimen 2 has h_w = 36 in (914 mm)). In Figure 3.22 through Figure 3.25, by comparing the distance over which the twisting moment and lateral force act at the middle of the buckled zone, it is clear that as the web height increases, this distance increases.

As the local torsional and lateral instabilities interact with each other, one could theoretically separate this interaction by eliminating, say, the lateral instability. The lateral instability can be eliminated in the finite element model by continuously restraining the compression flange against lateral deflection. Figure 3.26 and Figure 3.27 compare results from finite element simulations with the actual bracing spacing

and with continuous bracing of the compression flange, for Specimen 1 and Specimen 2, respectively. Even when the compression flange is continuously braced, there is not much increase in the ductility of the load versus midspan vertical deflection behavior. The reason for this is that lateral bending of the top flange produces tension on one side of the flange and compression on the other side. The tension induced by lateral bending enhances the local torsional stability of one side of the compression flange but the compression induced by lateral bending reduces the local torsional stability of the other side of the compression flange. The increase in flange stability due to the induced tension is offset by the decrease due to the induced compression.

3.7 Effect of Specimen Slenderness

A preliminary parametric study was performed to understand the effect of specimen geometry on the local buckling behavior. Comparing the load versus midspan vertical deflection behavior of Specimen 1 and Specimen 2, Figure 3.11 and Figure 3.14, respectively, shows that Specimen 1 is more ductile. In terms of normalized flange slenderness, λ_f, and normalized web slenderness, λ_w, as defined in Chapter 2, Specimen 1 has $\lambda_f = 0.399$ and $\lambda_w = 3.63$, while Specimen 2 has $\lambda_f = 0.401$ and $\lambda_w = 5.35$. Note that in calculating λ_f and λ_w, the actual flange and web yield strengths, σ_{yf} and σ_{yw}, were used, respectively. Specimen 1 has a nearly compact flange and compact web (CFCW), according to the 1996 interim AASHTO LRFD specifications [AASHTO 1996], while Specimen 2 has a nearly compact flange and noncompact web (CFNCW). The limits for compact web and flange are given by Equation 2.13 and Equation 2.14 in the 1996 interim AASHTO LRFD specifications [AASHTO 1996].

To study the effect of flange slenderness and web slenderness on the load-deflection behavior, two new finite element models were created, as shown in Figure 3.28. For the first model, λ_w of Specimen 2 was changed from 5.35 to 3.63, to match λ_w of Specimen 1. The change in λ_w was achieved by increasing the web thickness. This model is called the CFCW model. Note that the CFCW model has λ_f similar to that of Specimen 1, and λ_w equal to that of Specimen 1, but it has a cross section aspect ratio (h_w/b_f) equal to that of Specimen 2. Figure 3.28 shows that although the normalized strength (P/P_y) of the CFCW model is higher than the original Specimen 2 model (the CFNCW model), the unloading is rapid similar to Specimen 2.

For the second model, λ_f and λ_w of Specimen 2 were changed to an ultracompact flange and compact web (the UCFCW model) as shown in Figure 3.28. The change in λ_f was achieved by increasing the flange thickness, while the change in λ_w was achieved by increasing the web thickness. Even though the normalized strength (P/P_y) of the UCFCW model is similar to that of the CFCW model, the

unloading is less rapid and closer to that of Specimen 1. Note that Specimen 1 has h_w/b_f = 2.45, while that of the CFNCW (Specimen 2), CFCW, and UCFCW models are all 3.67.

From this preliminary parametric study it is clear that not only the flange and web slenderness affect the specimen behavior, but also the cross section aspect ratio, h_w/b_f. This conclusion was reached also by El-Ghazaly [1983] and Barth [1996].

3.8 Contour Plots of Stresses and Resultant Forces and Moments

For Specimen 1, contour plots of stresses on the upper surface of the top flange, σ_{11}, σ_{22}, and σ_{12}, are shown in Figure 3.29 for the load increment corresponding to 90% P_u-post peak. The resultant normal forces, *SF1* and *SF2*, and transverse force, *SF4*, for the top flange are shown in Figure 3.30, and the resultant moments, *SM1*, *SM2*, and *SM3* for top flange are shown in Figure 3.31 for the same load increment.

Similarly, for Specimen 2, contour plots of stresses on the upper surface of the top flange, σ_{11}, σ_{22}, and σ_{12}, are shown in Figure 3.32 for the load increment corresponding to 90% P_u-post peak. The resultant normal forces, *SF1* and *SF2*, and transverse force, *SF4*, for the top flange are shown in Figure 3.33, and the resultant moments, *SM1*, *SM2*, and *SM3* for top flange are shown in Figure 3.34 for the same load increment.

In Figure 3.29, it is important to note that σ_{11} reaches 140 ksi (965 MPa) in compression at 90% P_u-post peak, which is 122% of σ_{yf}. This increase in σ_{11} is a result of a high compression stress in the local-2 direction due to bending deformation about the local-1 axis.

At 90% P_u-post peak, the normal force *SF1* is significantly reduced near the edges of the buckled zone to the north of midspan as shown in Figure 3.30. This reduction is a result of combined action of plate bending, *SM1*, about the local-2 axis, high transverse shear force *SF4*, and lateral flange bending.

Table 3.1 Geometry and material properties of the specimens tested by Fahnestock and Sause [1998]

Specimen	t_f (in)	t_w (in)	b_f (in)	h_w (in)	L (in)	h_w/b_f	h_w/t_w	$b_f/2t_f$	E_f (ksi)	σ_{yf} (ksi)	E_w (ksi)	σ_{yw} (ksi)	λ_f	λ_w
1	0.775	0.388	9.813	24.0	408.0	2.45	61.9	6.33	29000.0	115.0	29000.0	100.0	0.399	3.63
2	0.770	0.395	9.813	36.0	600.0	3.67	91.1	6.37	29000.0	115.0	29000.0	100.0	0.401	5.35

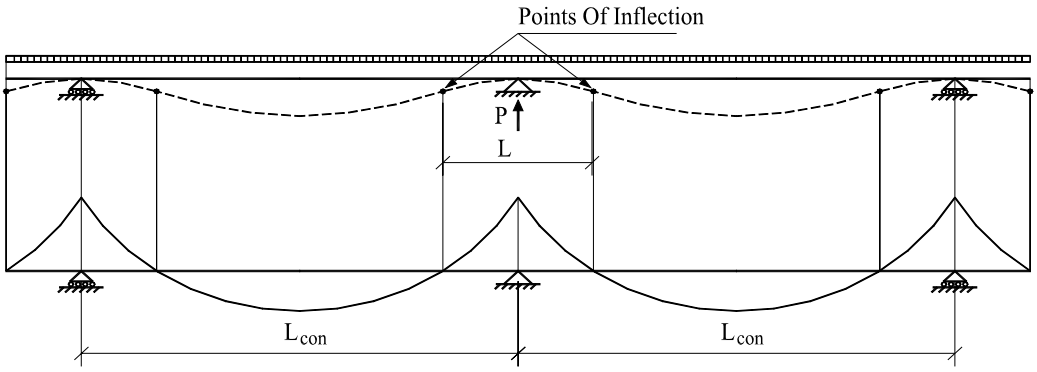

(a) Deflected shape and moment diagram for a continuous-span girder subjected to uniformly distributed load

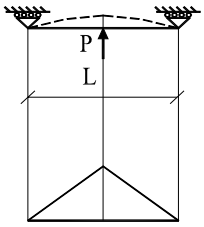

(b) Simply supported girder subjected to concentrated load at midspan

Figure 3.1 Correlation between negative moment region near pier and experimental specimen loading conditions [Fahnestock and Sause 1998]

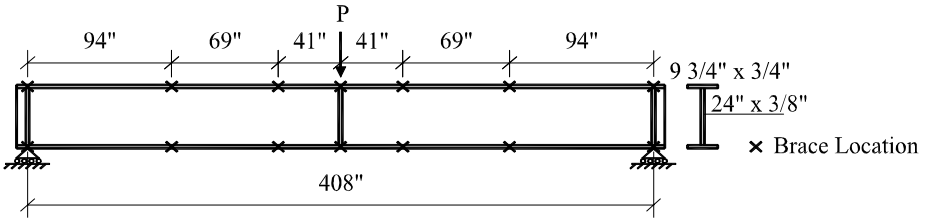

(a) Specimen 1

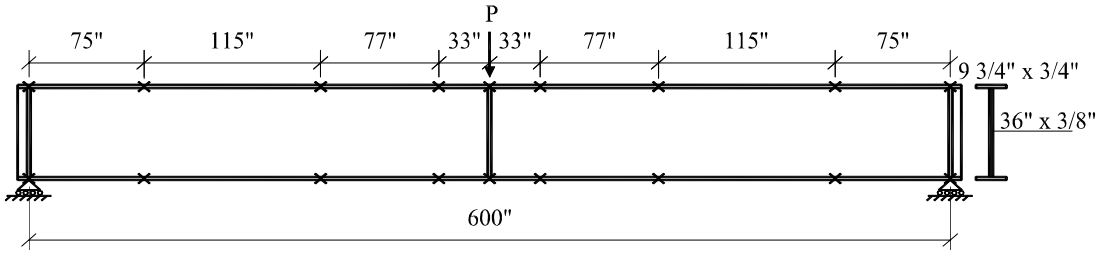

(b) Specimen 2

Figure 3.2 Dimensions and lateral brace locations for Specimens 1 and 2 [Fahnestock and Sause 1998]
(1" = 1 in and 1' = 1 foot)

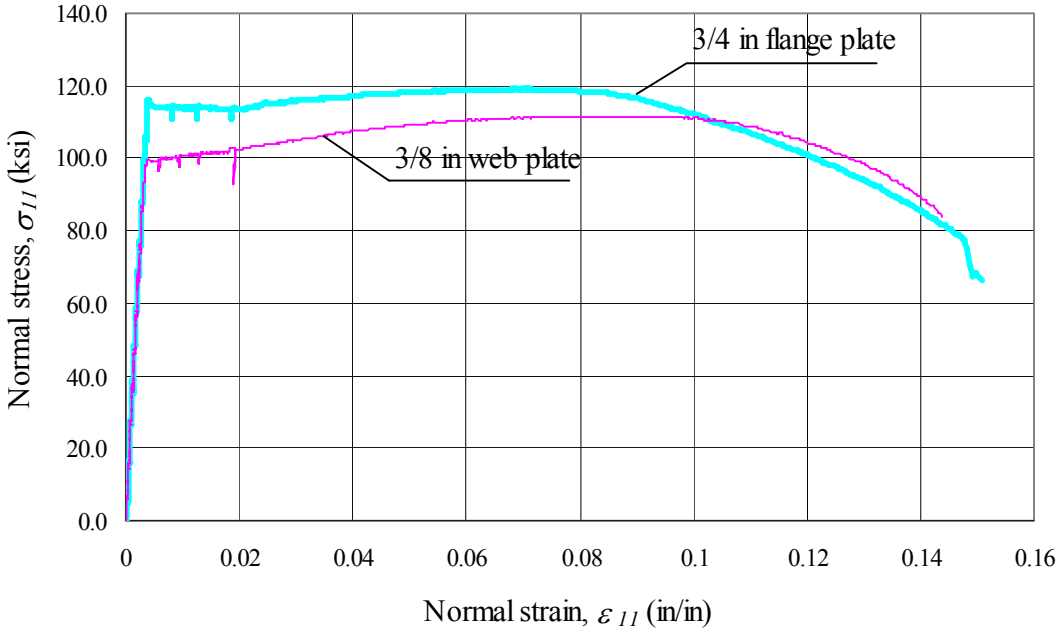

Figure 3.3 Stress versus strain for HPS-100W steel [Sause and Fahnestock 2001]

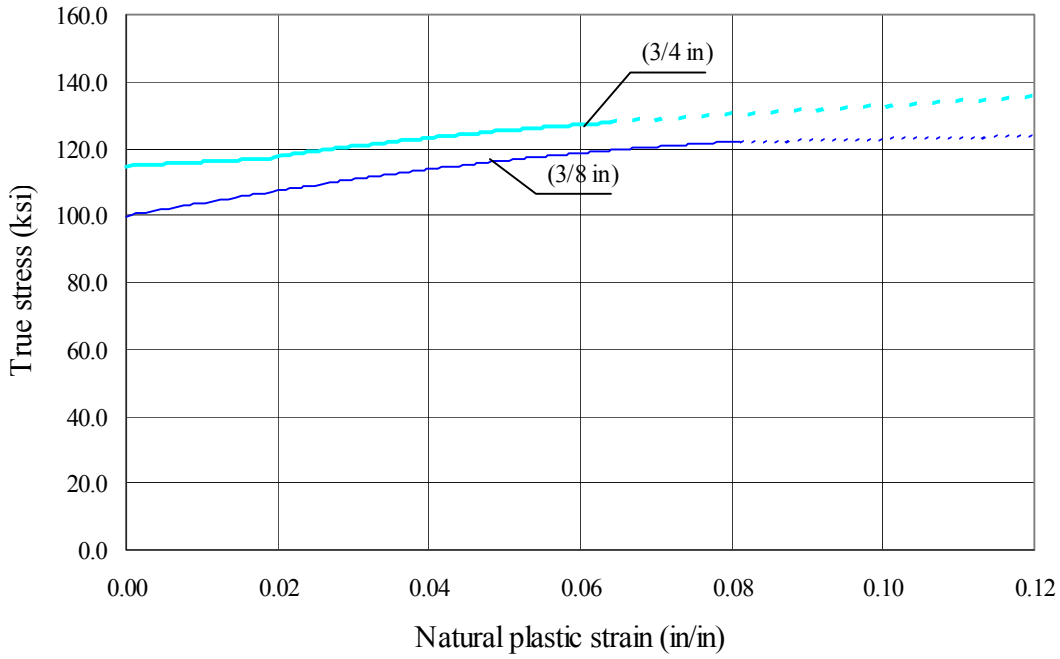

Figure 3.4 True stress versus natural plastic strain for HPS-100W steel

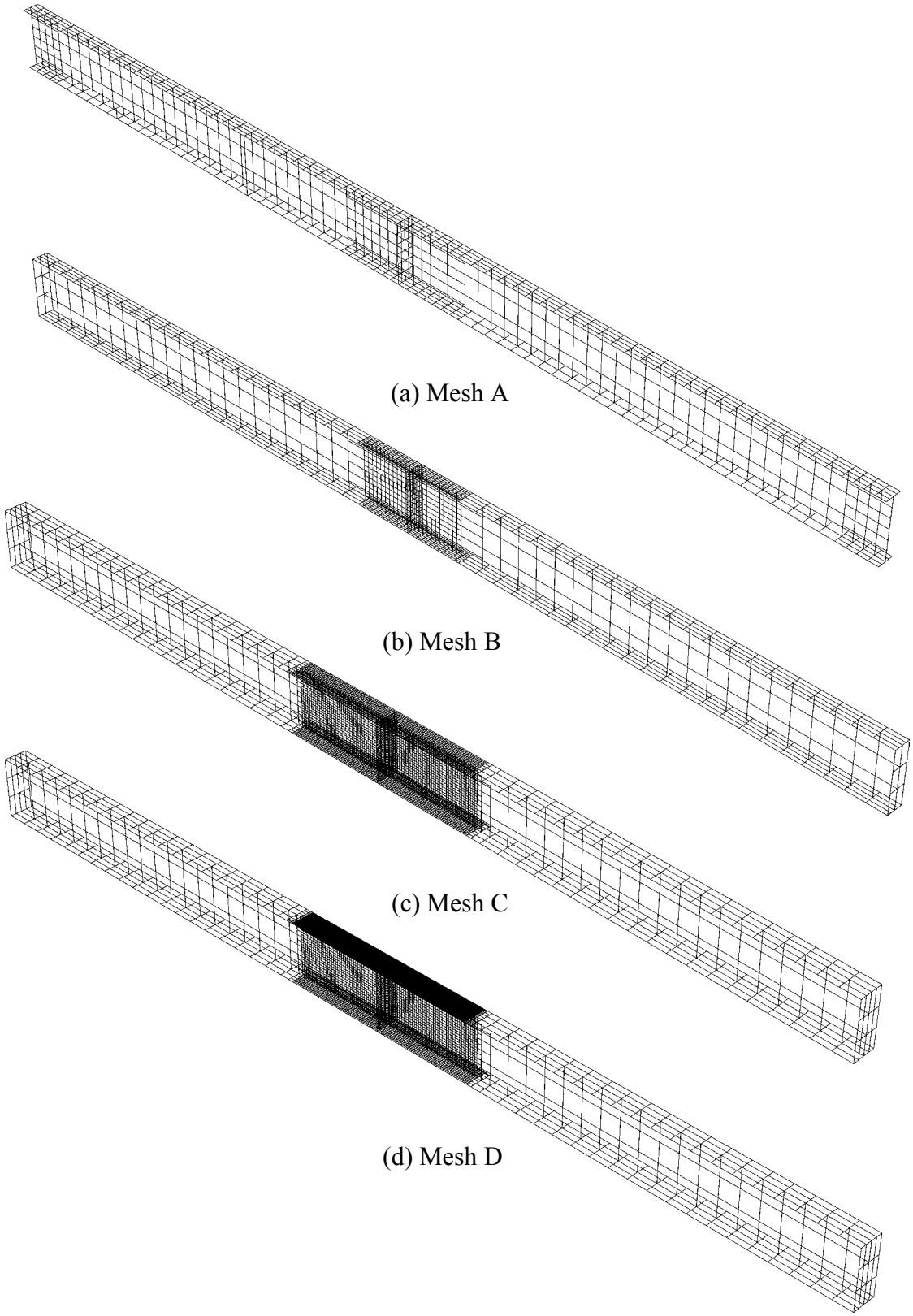

(a) Mesh A

(b) Mesh B

(c) Mesh C

(d) Mesh D

Figure 3.5 Different finite element meshes for Specimen 1

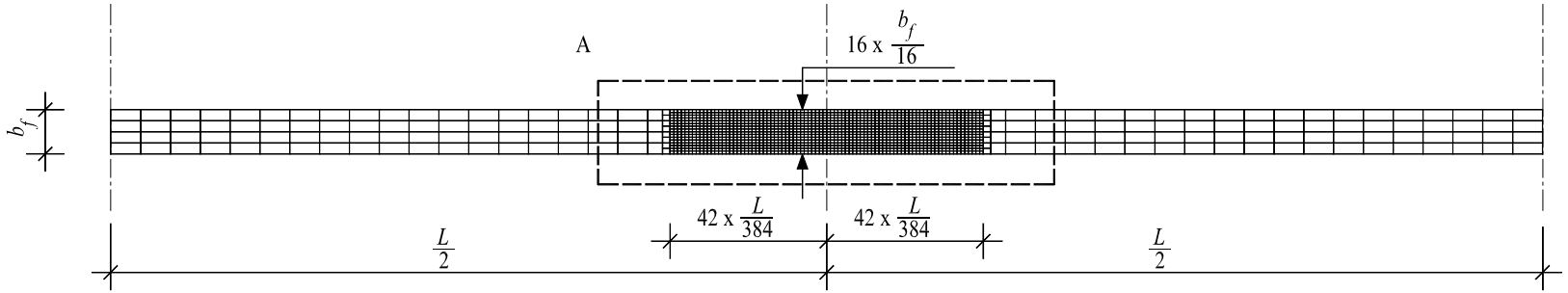

(a) Top flange finite element mesh

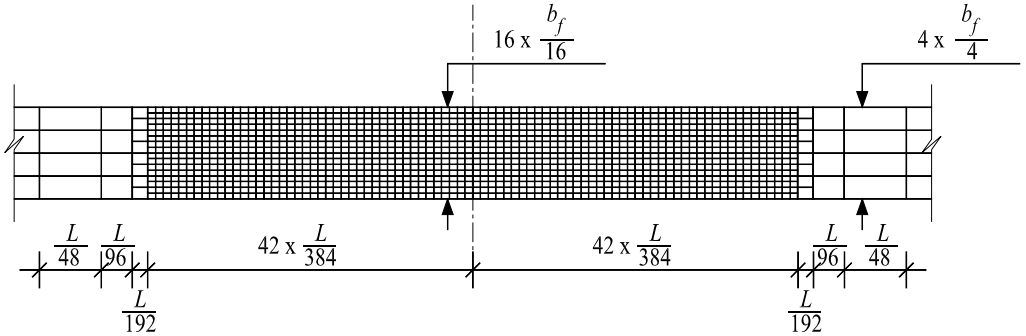

(b) Detail A

Figure 3.6 Details of flange finite element mesh

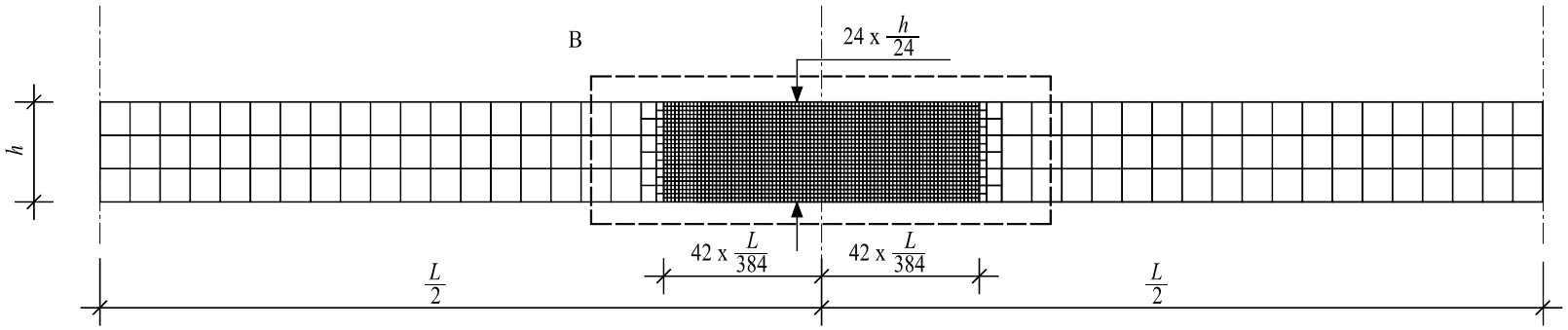

(a) Web finite element mesh

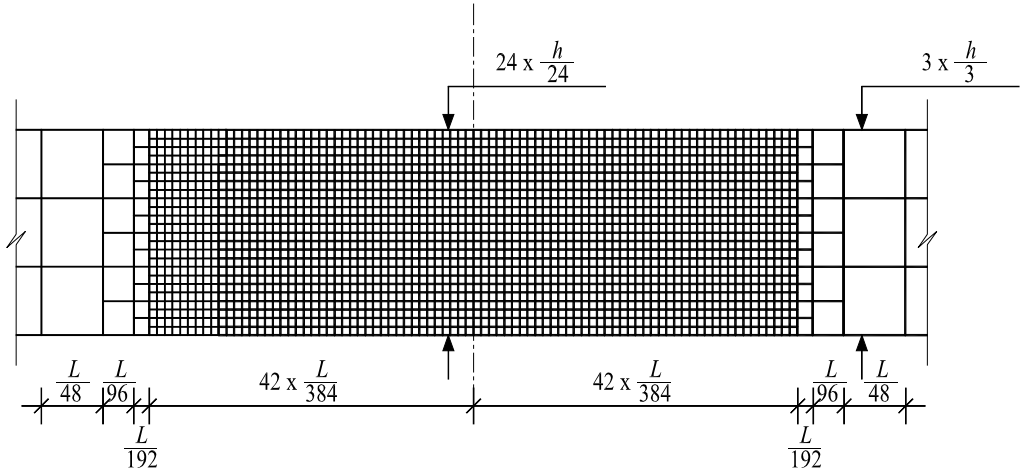

(b) Detail B

Figure 3.7 Details of web finite element mesh

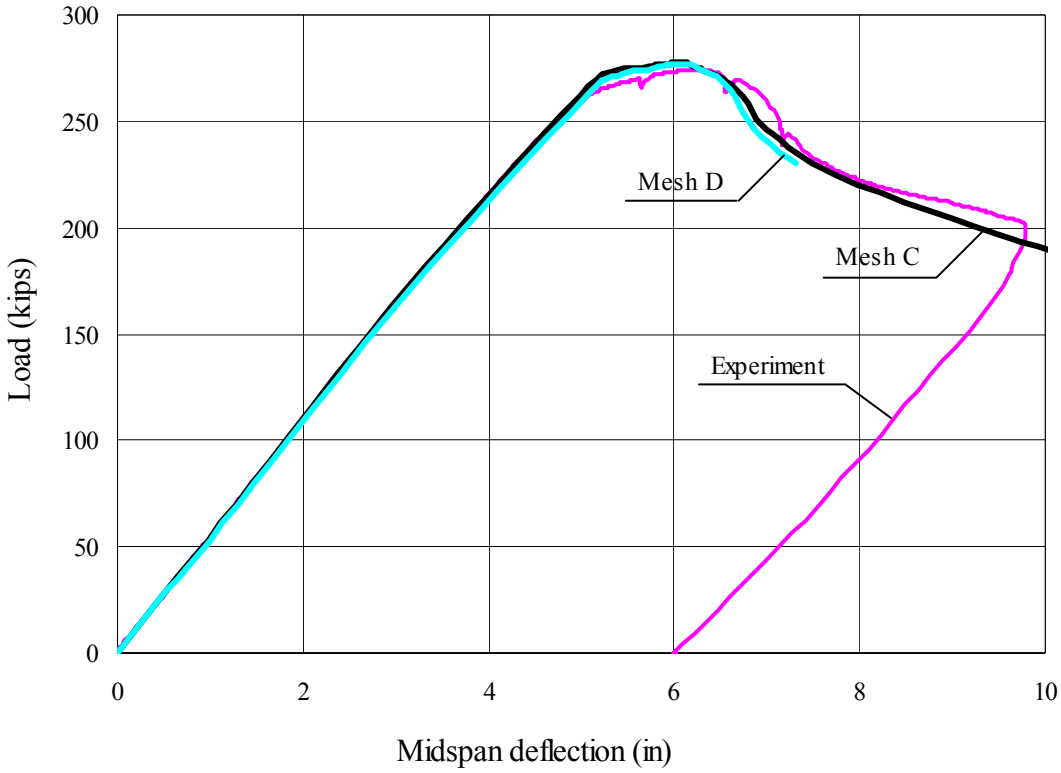

Figure 3.8 Effect of mesh refinement (mesh C and mesh D for Specimen 1)

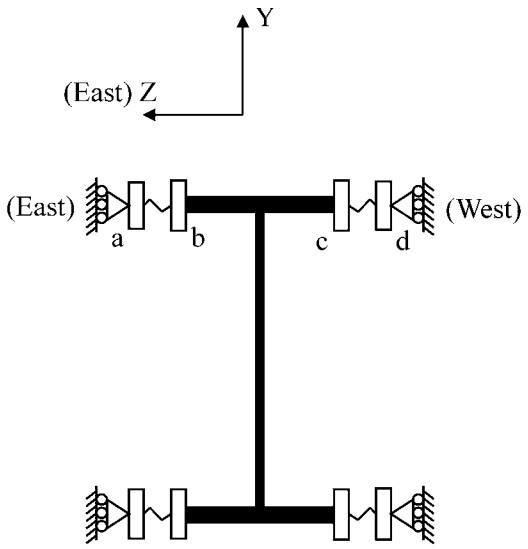

(a) Lateral brace model

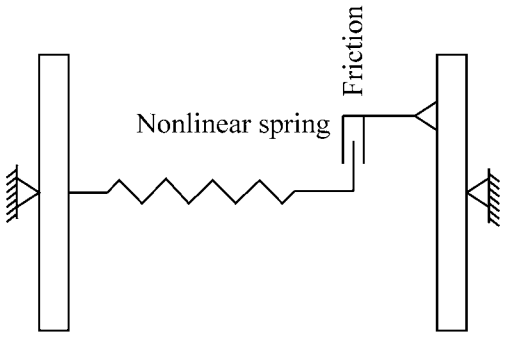

(b) ABAQUS element ITSUNI

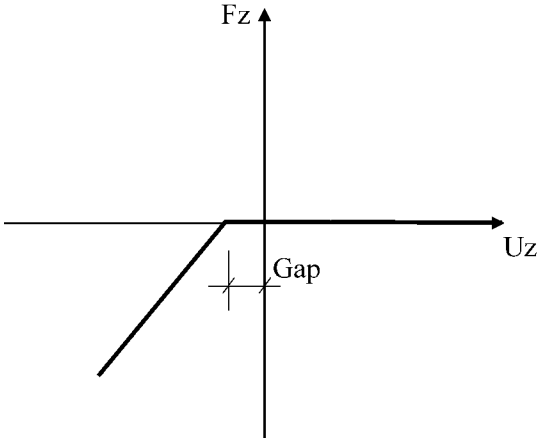

(c) Spring force-relative displacement for brace elements to the west of flanges

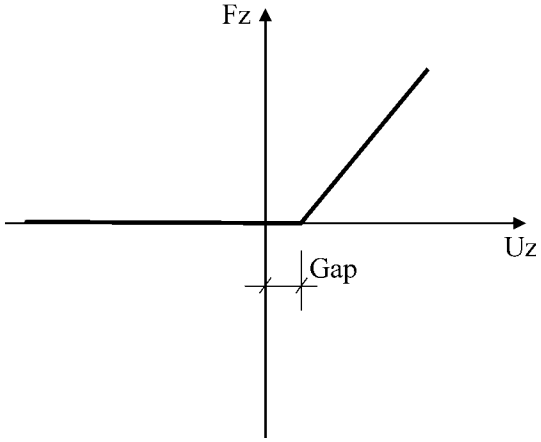

(d) Spring force-relative displacement for brace elements to the east of flanges

Figure 3.9 Lateral brace with gap model using ABAQUS element ITSUNI

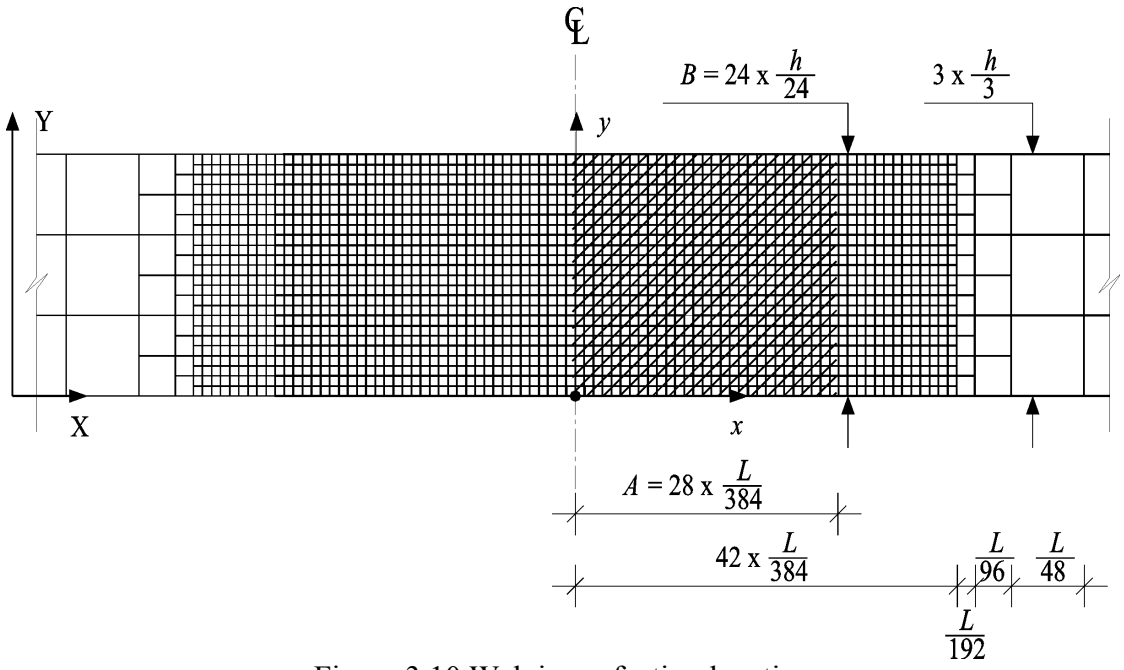

Figure 3.10 Web imperfection location

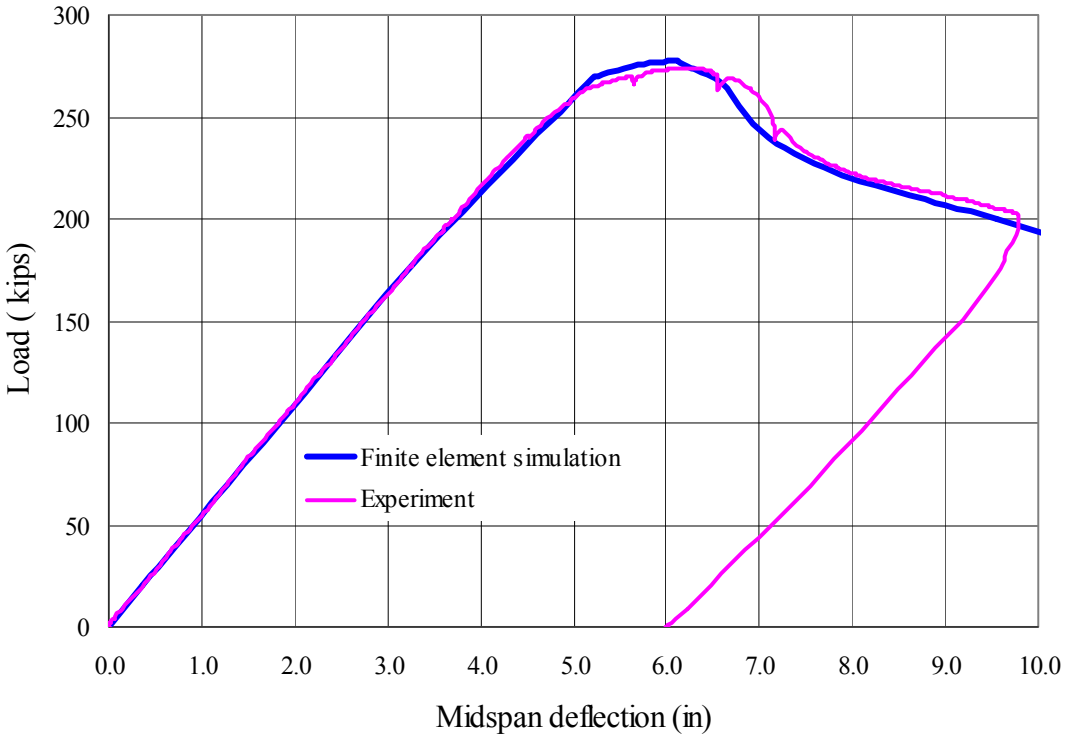

Figure 3.11 Load versus midspan vertical deflection (Specimen 1)

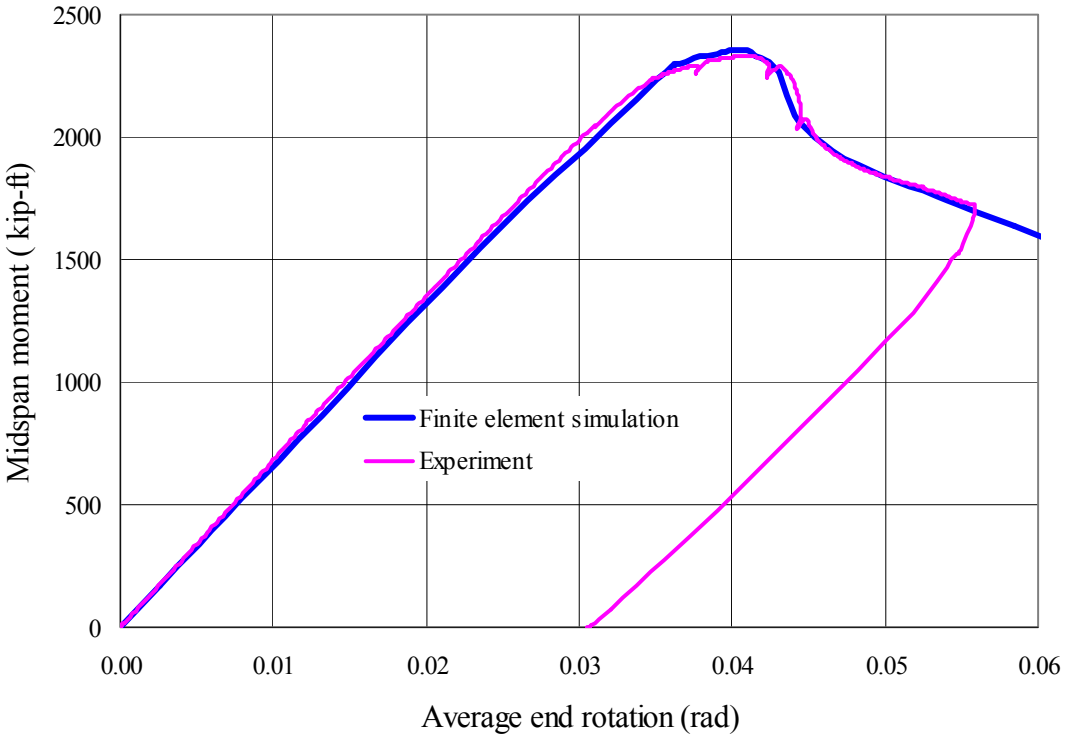

Figure 3.12 Midspan moment versus average end rotation (Specimen 1)

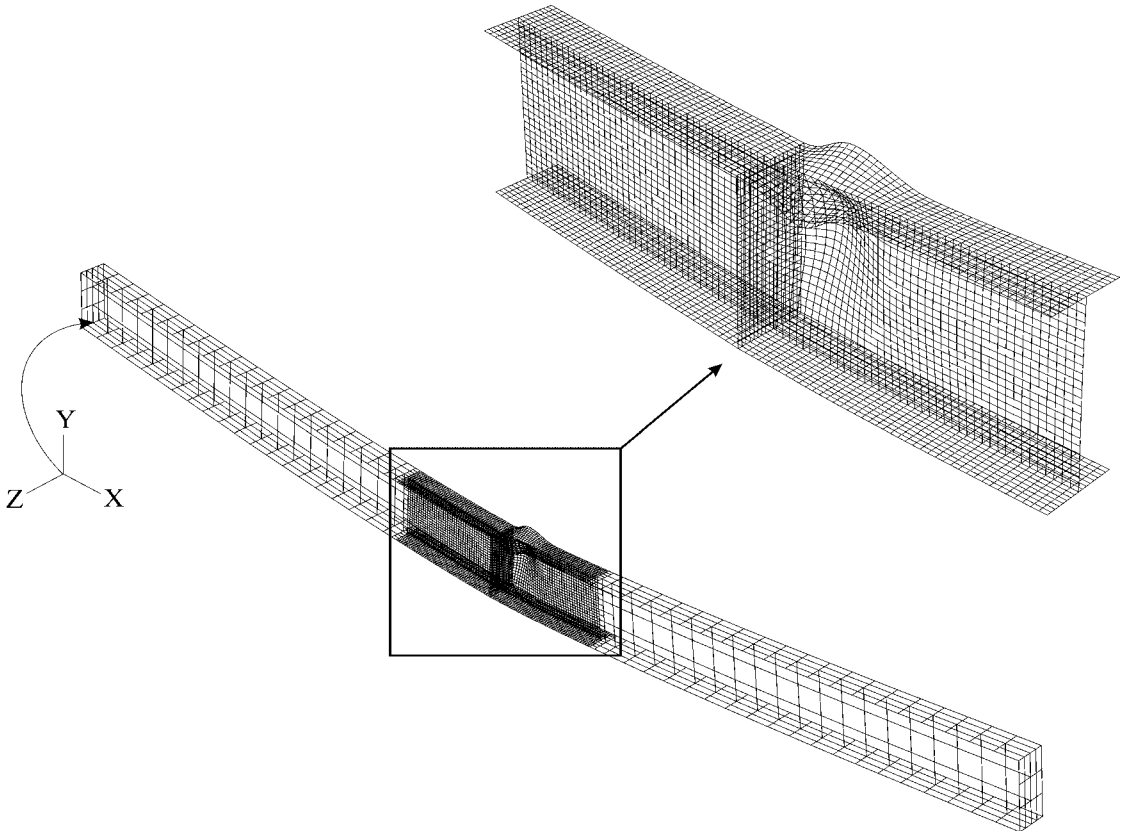

(a) Deflected shape (at 90% P_u-post peak)

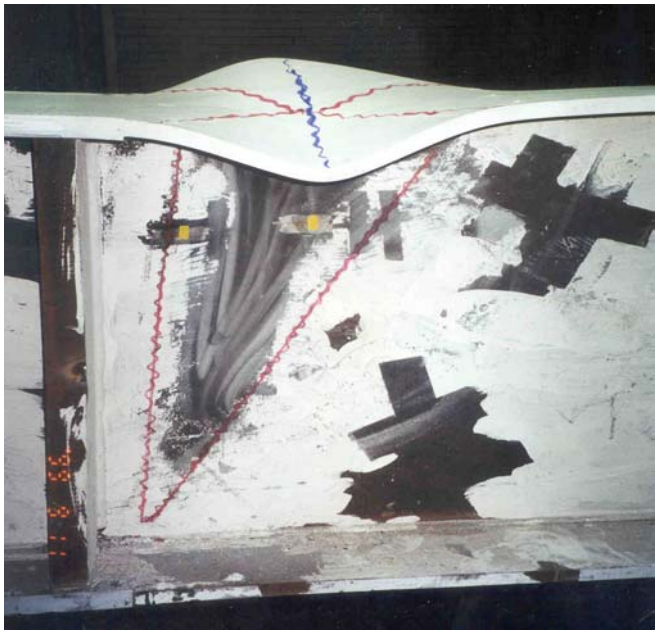

(b) Deflected shape after experiment

Figure 3.13 Deflected shape at 90% P_u-post peak and deflected shape of Specimen 1 after experiment

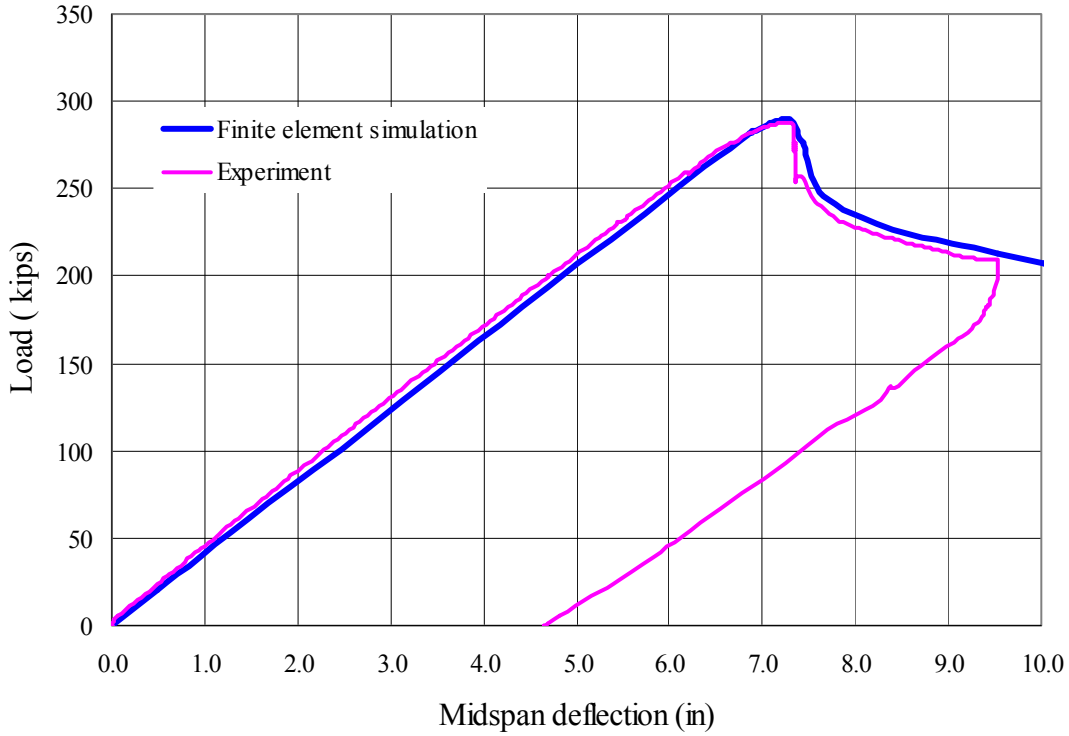

Figure 3.14 Load versus midspan vertical deflection (Specimen 2)

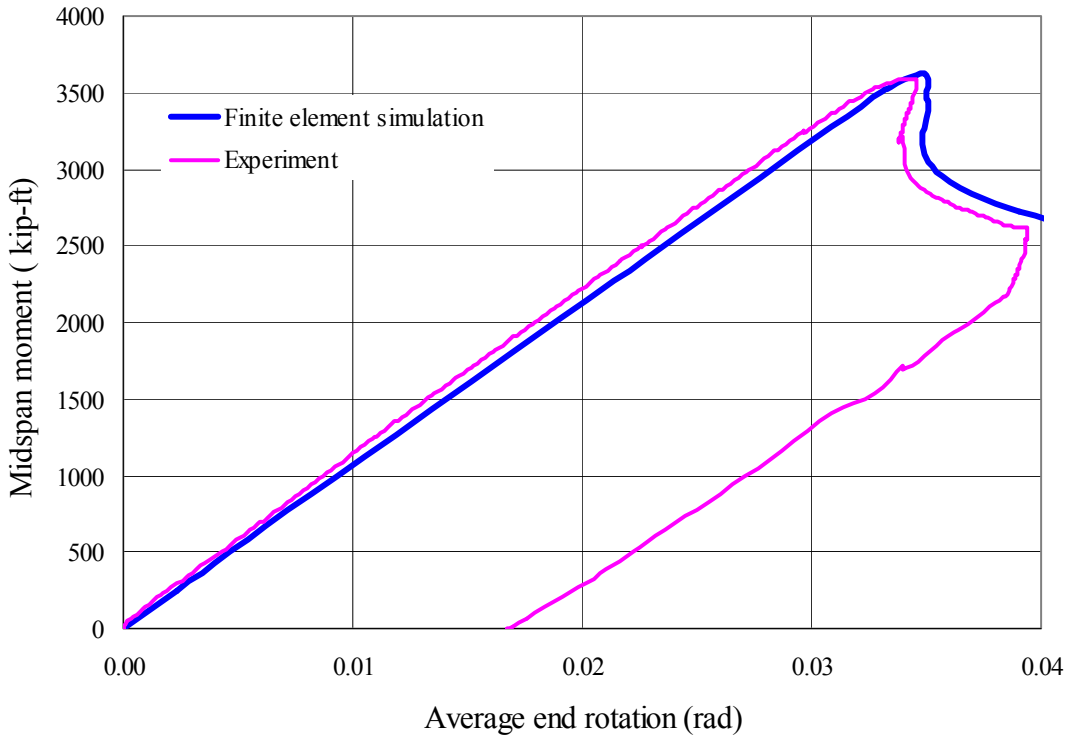

Figure 3.15 Midspan moment versus average end rotation (Specimen 2)

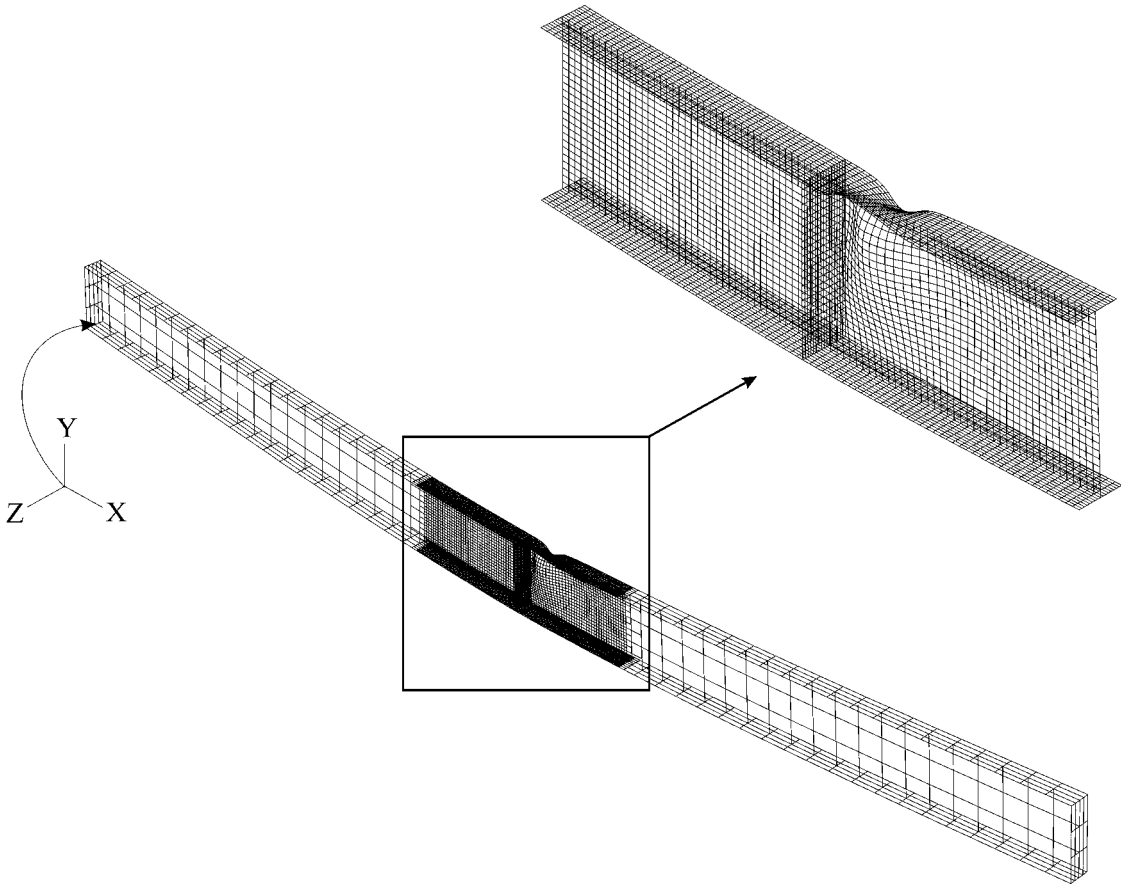

(a) Deflected shape (at 90% P_u-post peak)

(b) Deflected shape after experiment

Figure 3.16 Deflected shape at 90% P_u-post peak and deflected shape of Specimen 2 after experiment

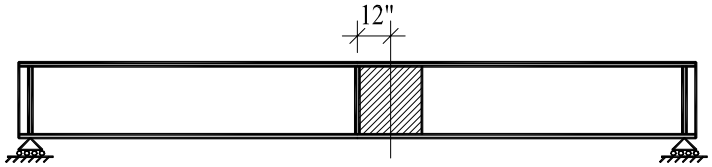

(a) Imperfection location A

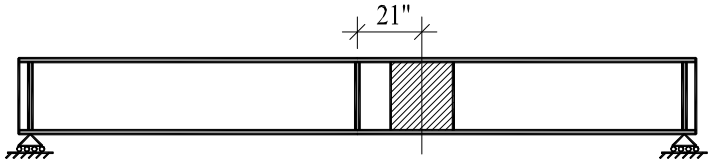

(b) Imperfection location B

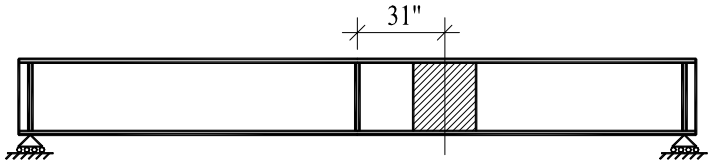

(c) Imperfection location C

Figure 3.17 Web imperfection location
(1" = 1 in and 1' = 1 foot)

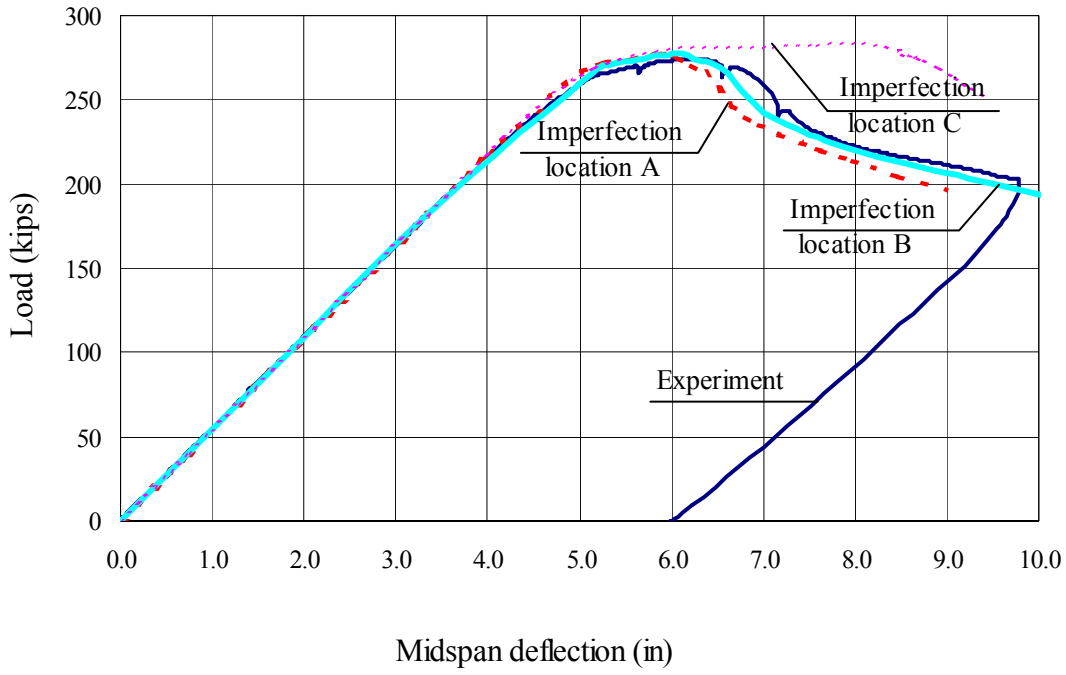

Figure 3.18 Effect of web imperfection location

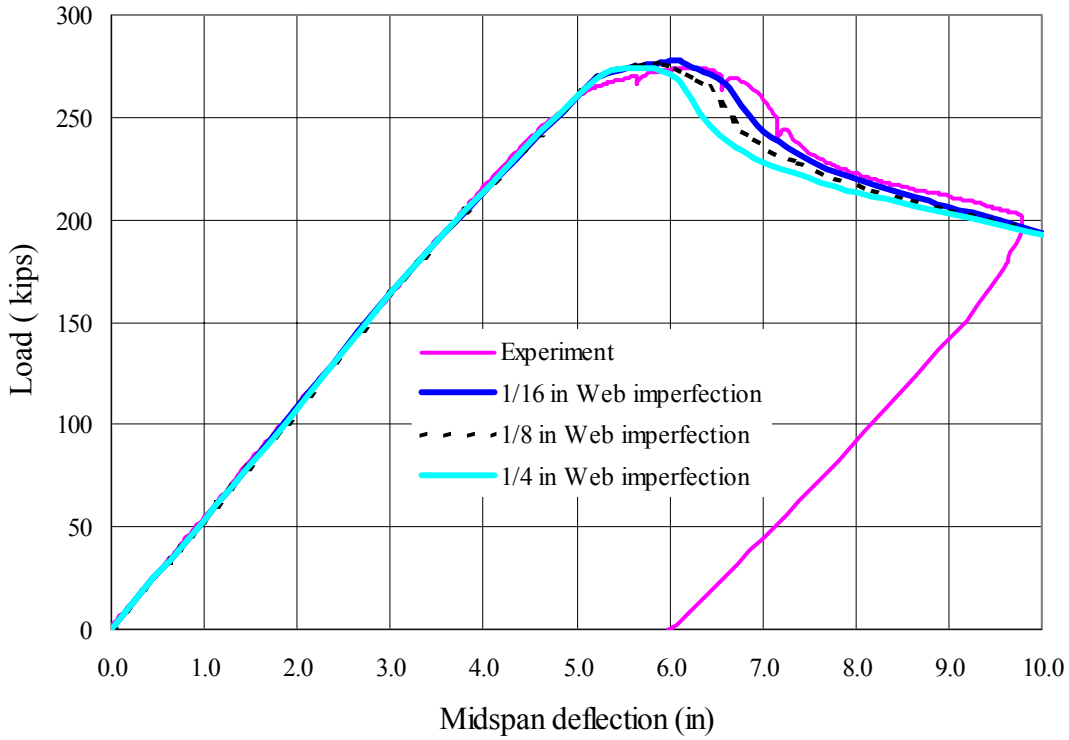

Figure 3.19 Effect of web imperfection amplitude

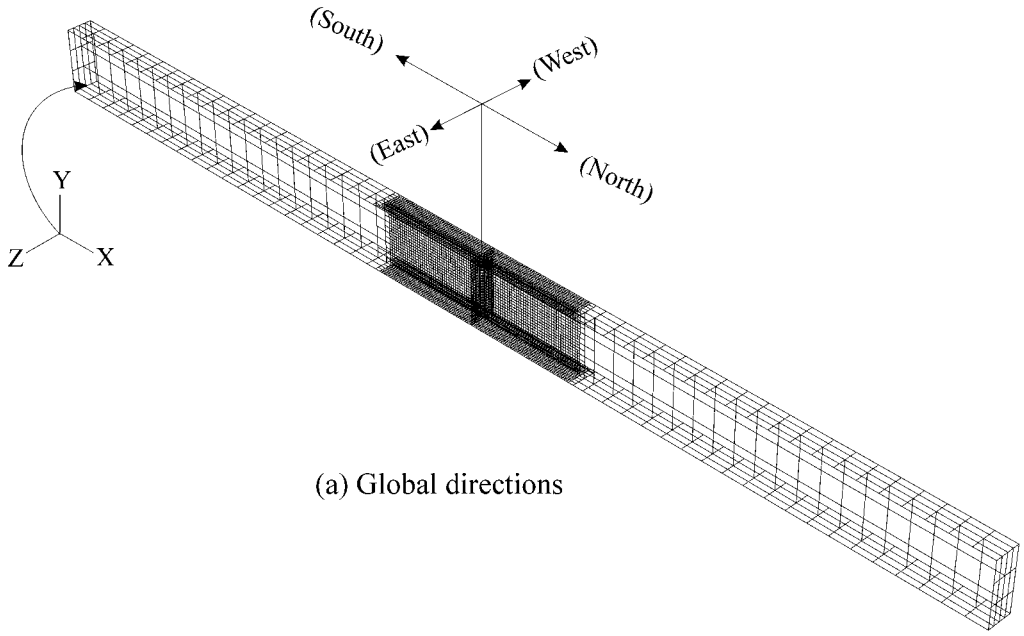

(a) Global directions

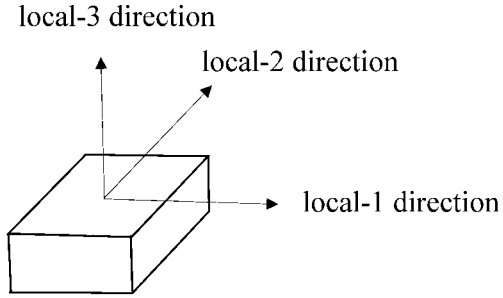

(b) Flange element local directions

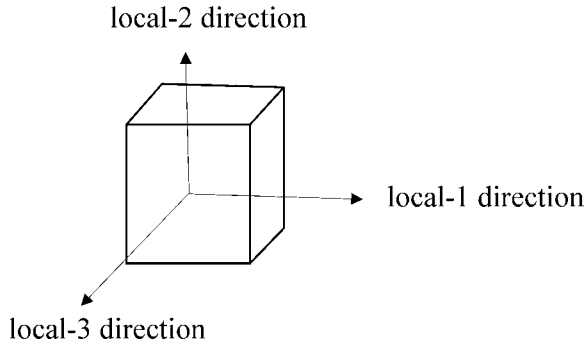

(c) Web element local directions

Figure 3.20 Global and local directions in the finite element model

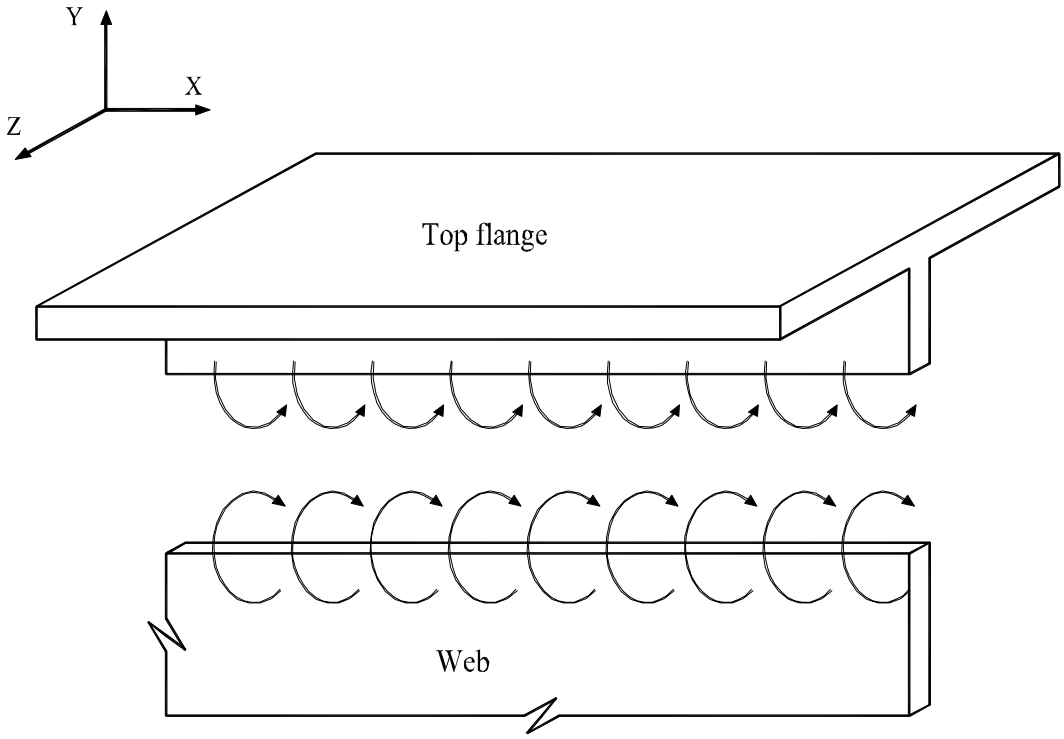

(a) Moment (*SM2*) transferred between web and top flange (positive sign)

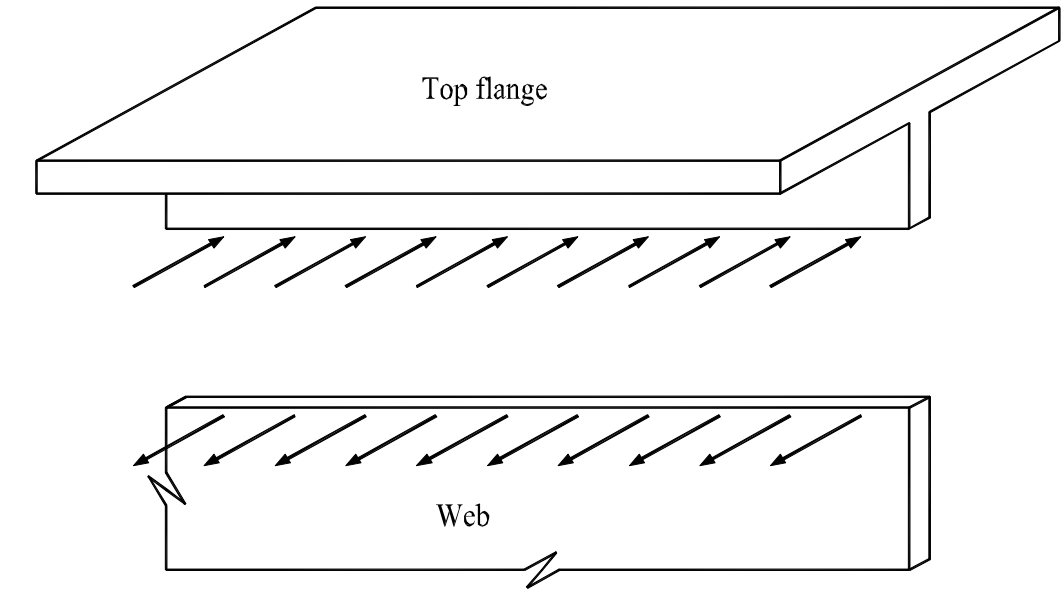

(b) Lateral force (*SF5*) transferred between web and top flange (positive sign)

Figure 3.21 Moment and force transferred between web and top flange

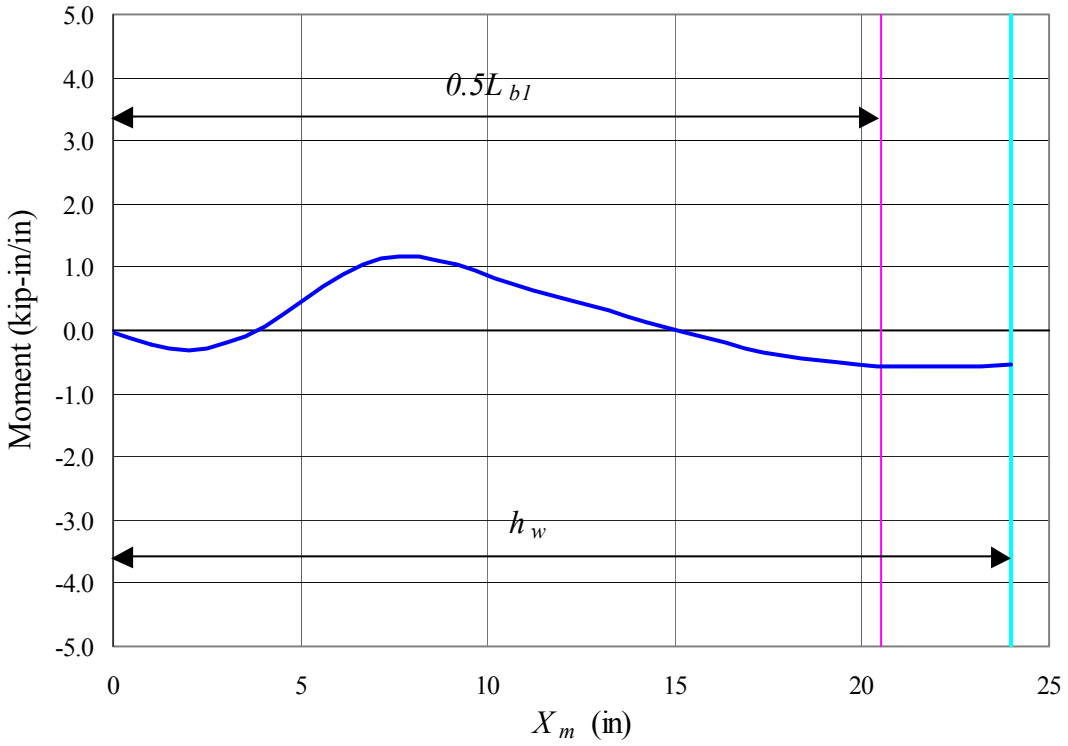

Figure 3.22 Moment (*SM2*) transferred between web and top flange (Specimen 1)

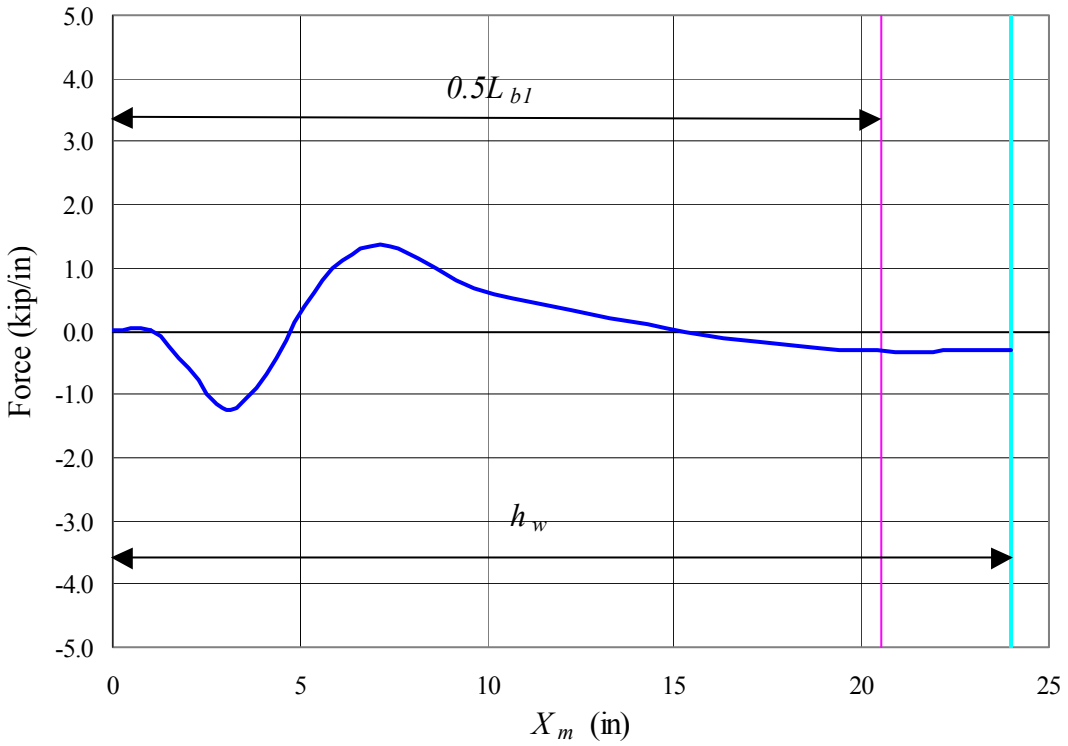

Figure 3.23 Lateral force (*SF5*) transferred between web and top flange (Specimen 1)

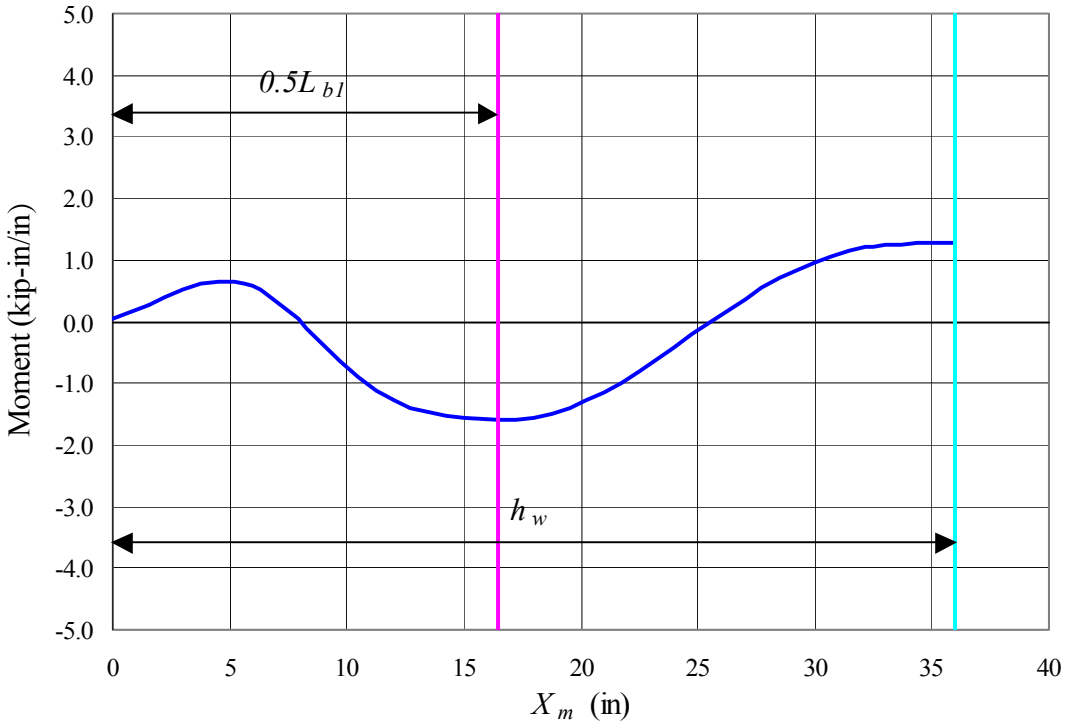

Figure 3.24 Moment (*SM2*) transferred between web and top flange (Specimen 2)

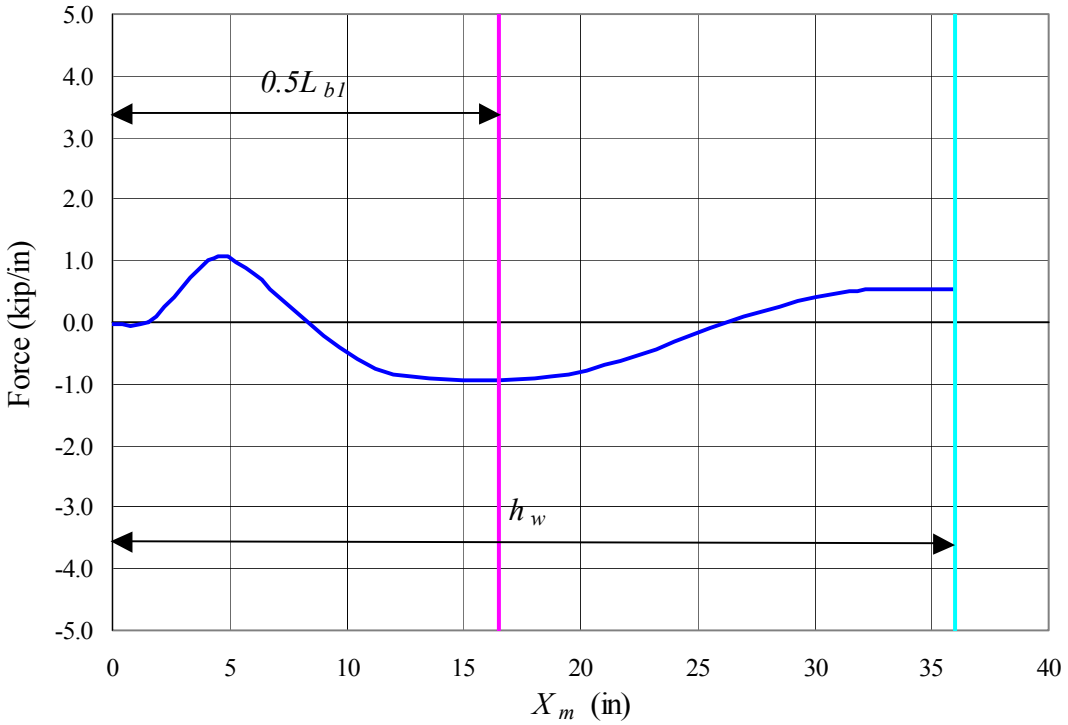

Figure 3.25 Lateral force (*SF5*) transferred between web and top flange (Specimen 2)

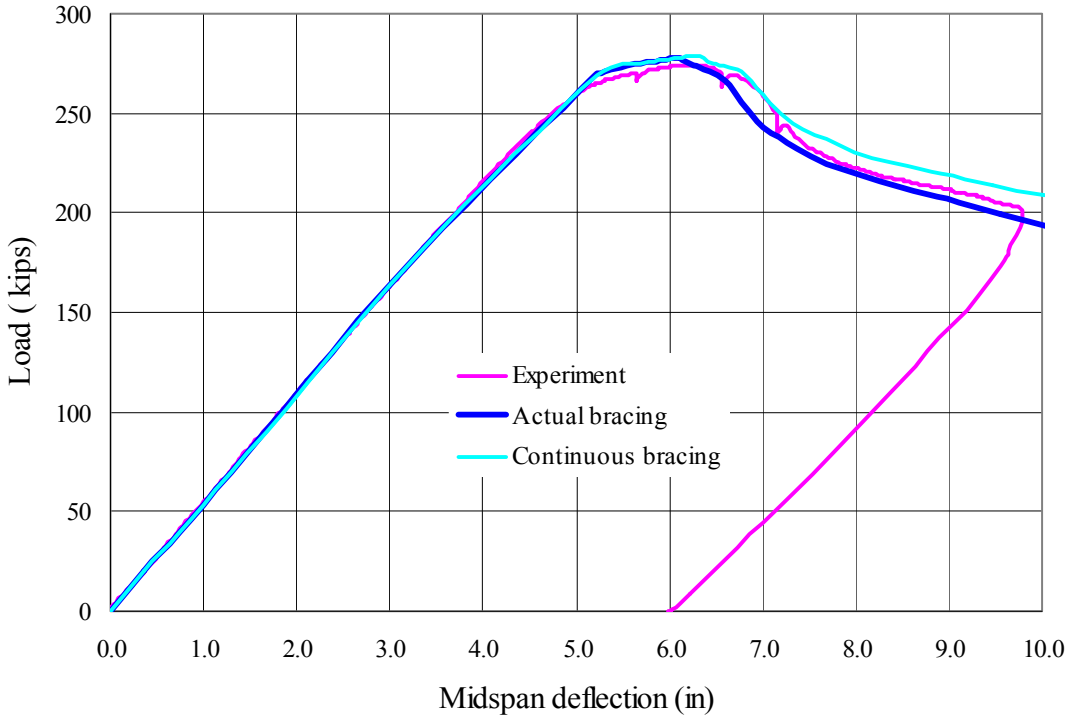

Figure 3.26 Effect of continuous bracing of the top flange (Specimen 1)

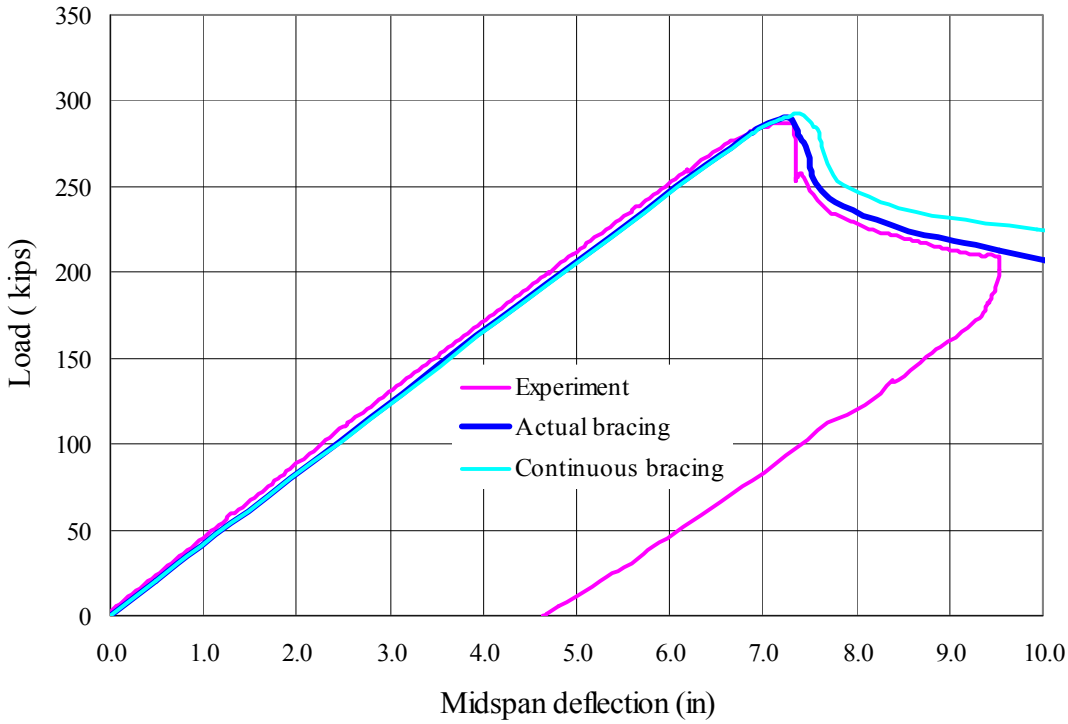

Figure 3.27 Effect of continuous bracing of the top flange (Specimen 2)

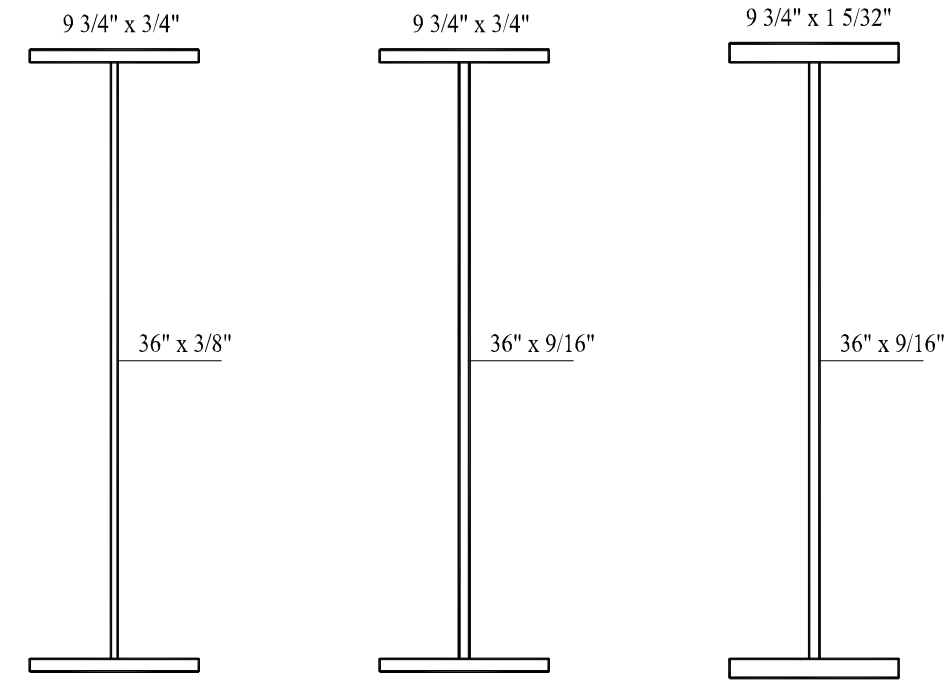

(a) Revised Specimen 2 models

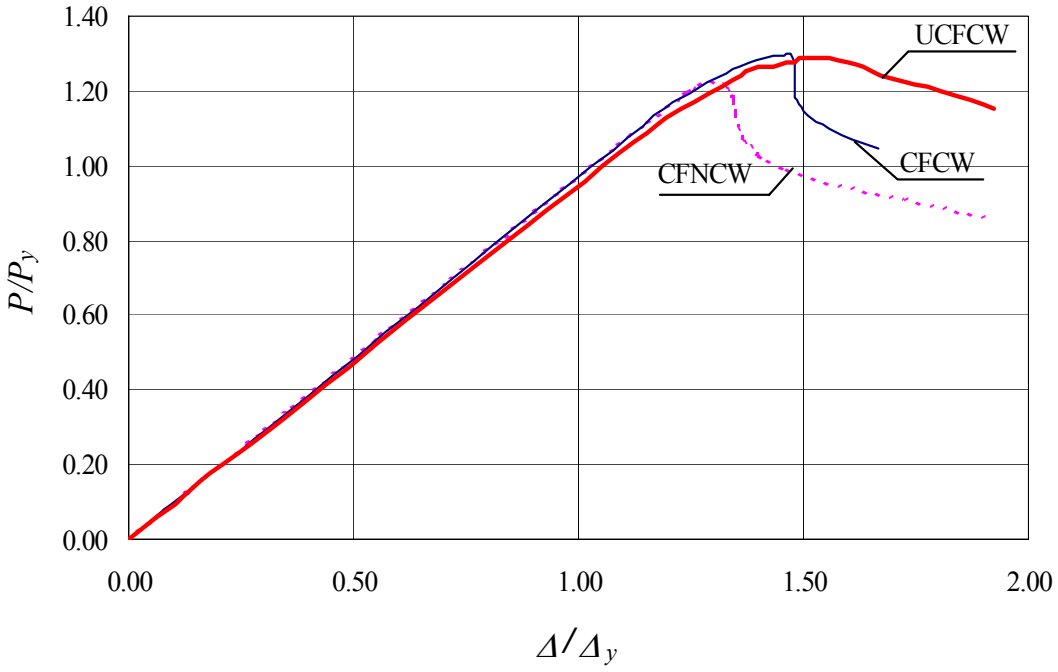

(b) Normalized load versus midspan vertical deflection

Figure 3.28 Effect of flange and web slenderness on Specimen 2 models ($h_w/b_f = 3.69$)
(1" = 1 in and 1' = 1 foot)

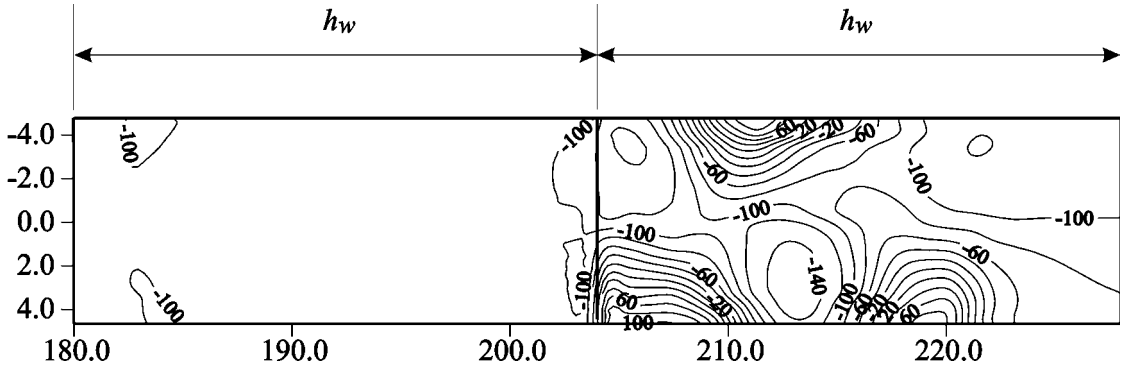

(a) Normal stress σ_{11} (ksi)

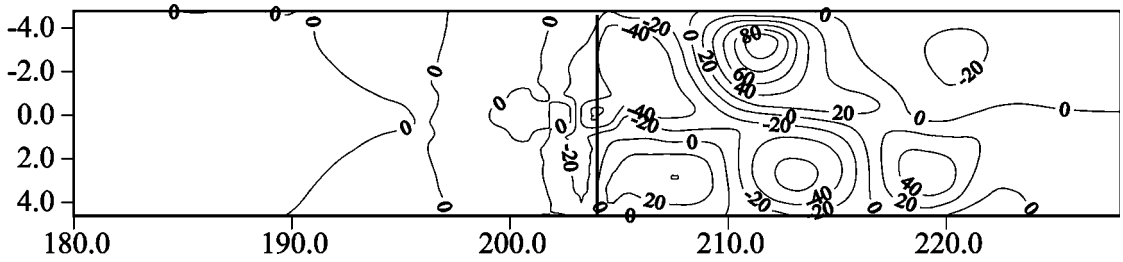

(b) Normal stress σ_{22} (ksi)

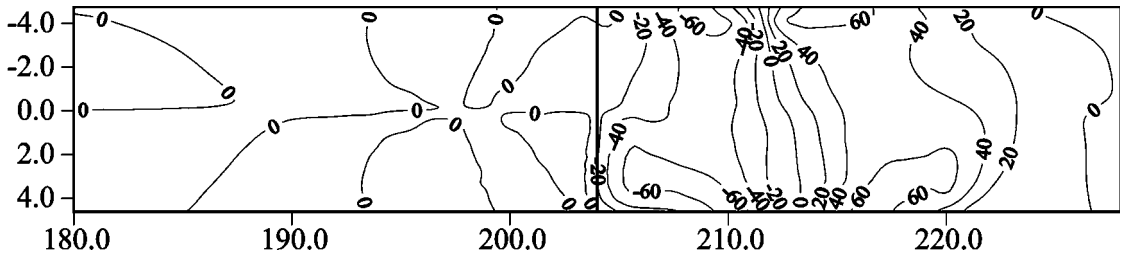

(c) Shear stress σ_{12} (ksi)

Figure 3.29 Top flange, upper surface, stress contours at 90% P_u-post peak (Specimen 1)

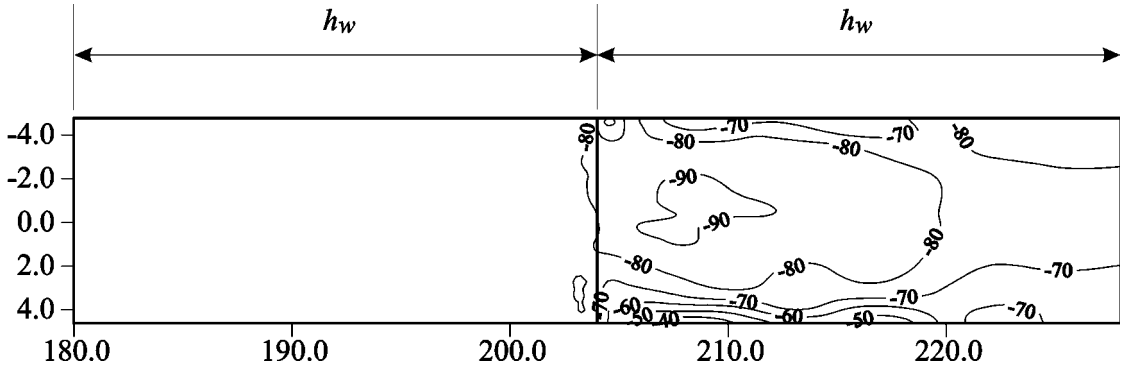

(a) Normal force *SF1* (kip/in)

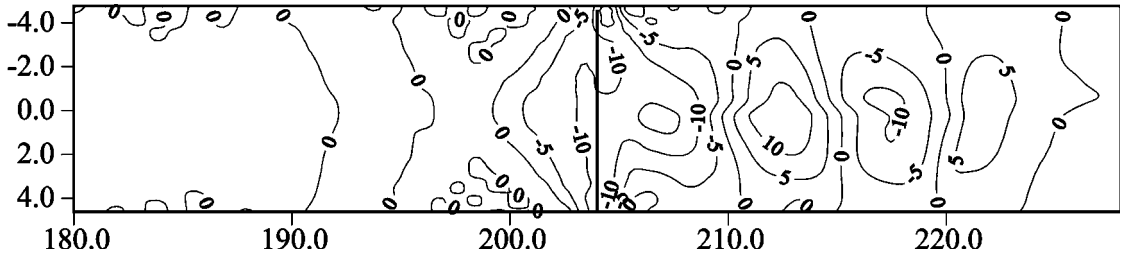

(b) Normal force *SF2* (kip/in)

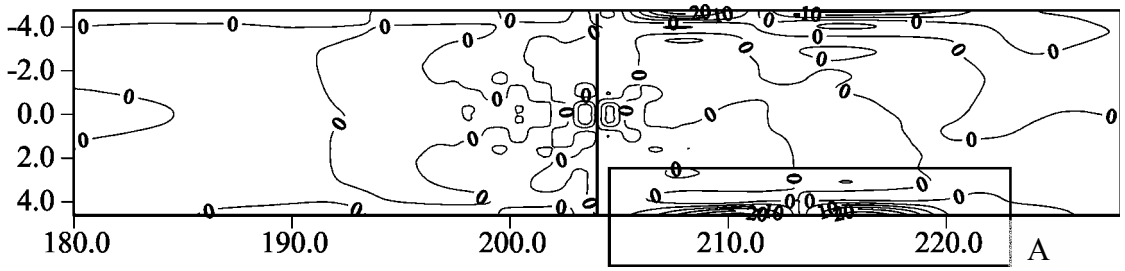

(c) Transverse force *SF4* (kip/in)

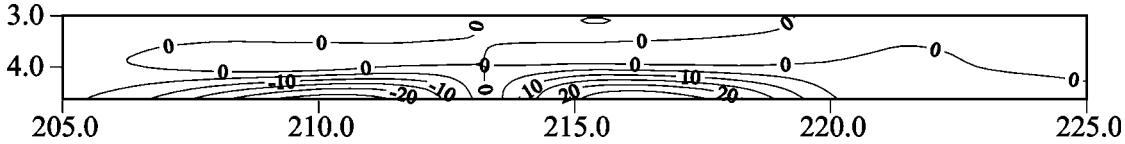

(d) Detail A

Figure 3.30 Top flange force contours at 90% P_u-post peak (Specimen 1)

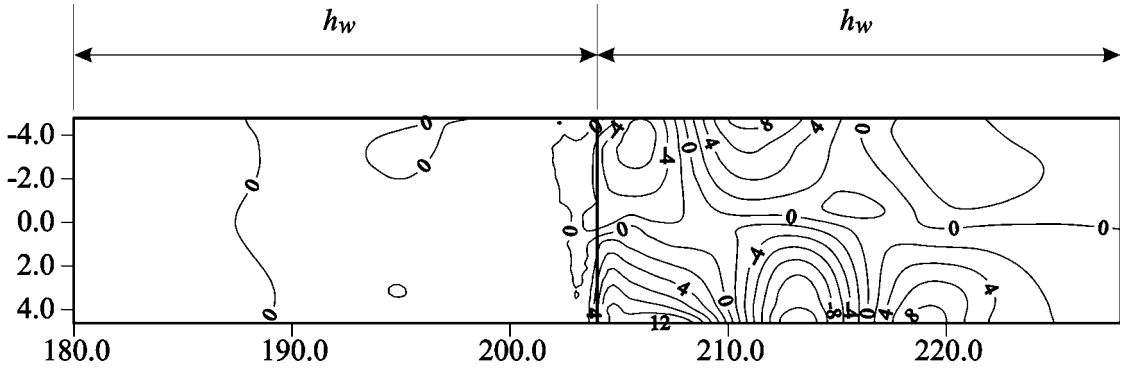

(a) Moment *SM1* (kip-in/in)

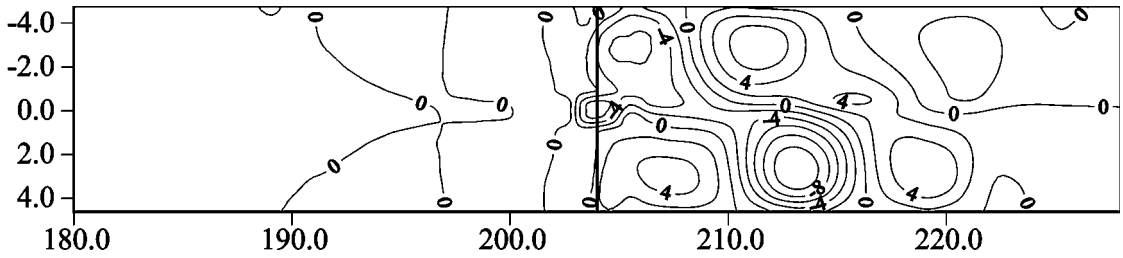

(b) Moment *SM2* (kip-in/in)

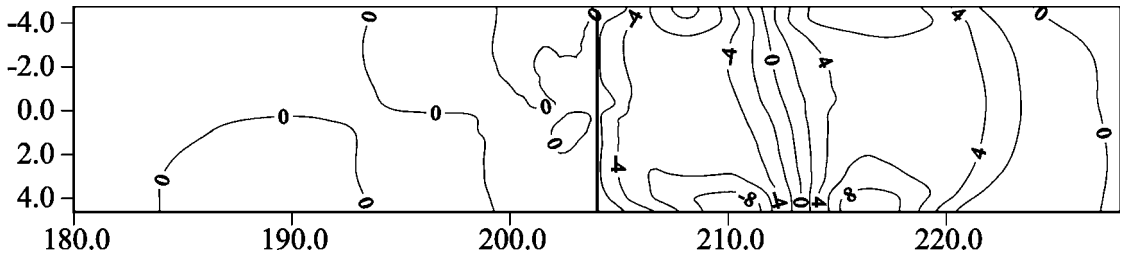

(c) Moment *SM3* (kip-in/in)

Figure 3.31 Top flange moment contours at 90% P_u-post peak (Specimen 1)

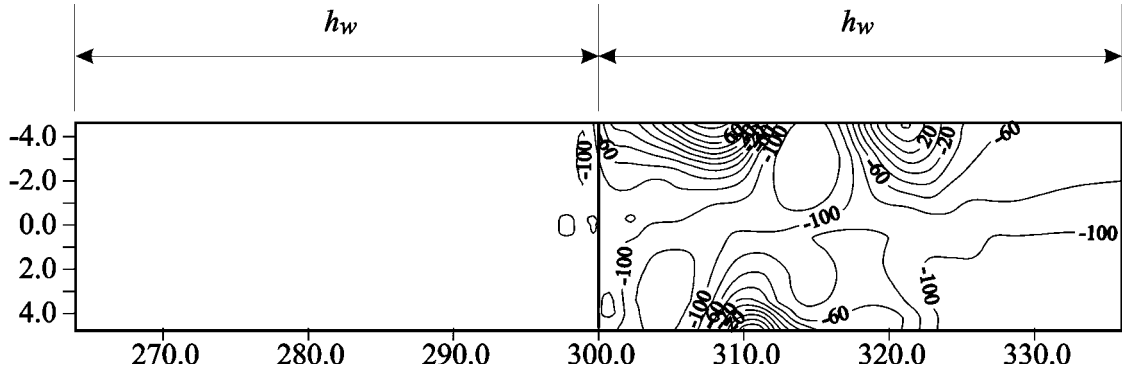

(a) Normal stress σ_{11} (ksi)

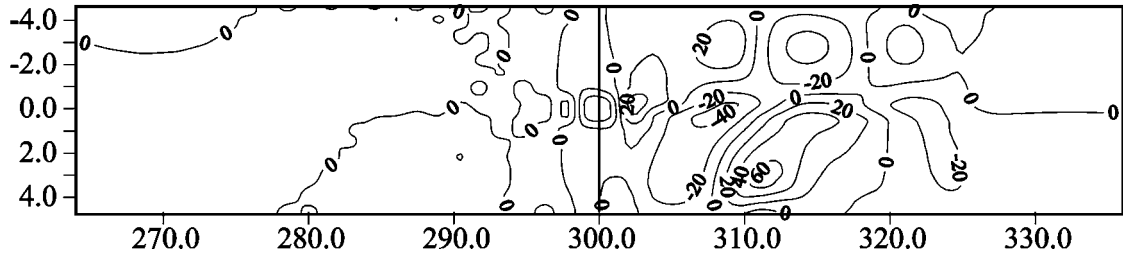

(b) Normal stress σ_{22} (ksi)

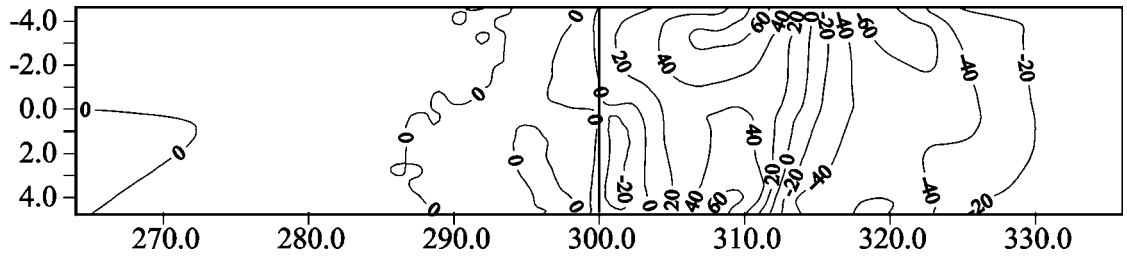

(c) Shear stress σ_{12} (ksi)

Figure 3.32 Top flange, upper surface, stress contours at 90% P_u-post peak (Specimen 2)

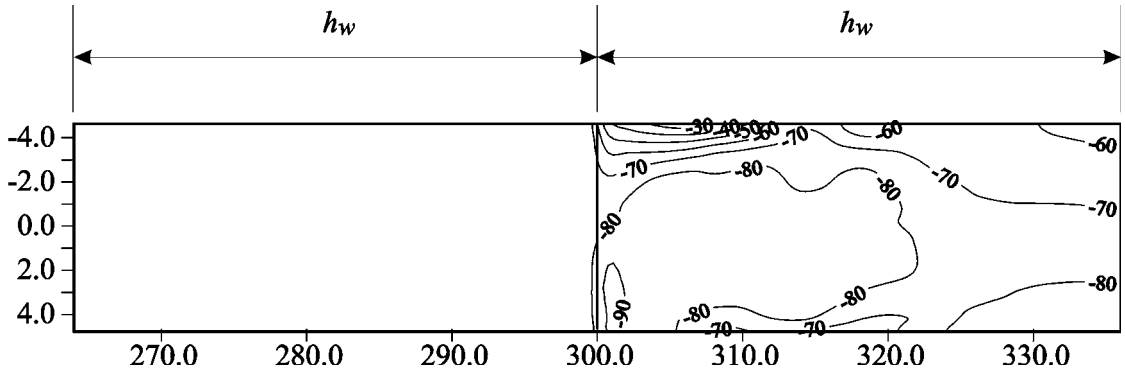

(a) Normal force *SF1* (kip/in)

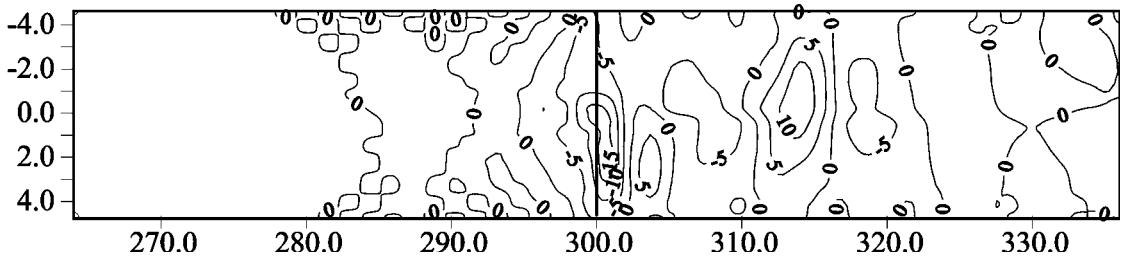

(b) Normal force *SF2* (kip/in)

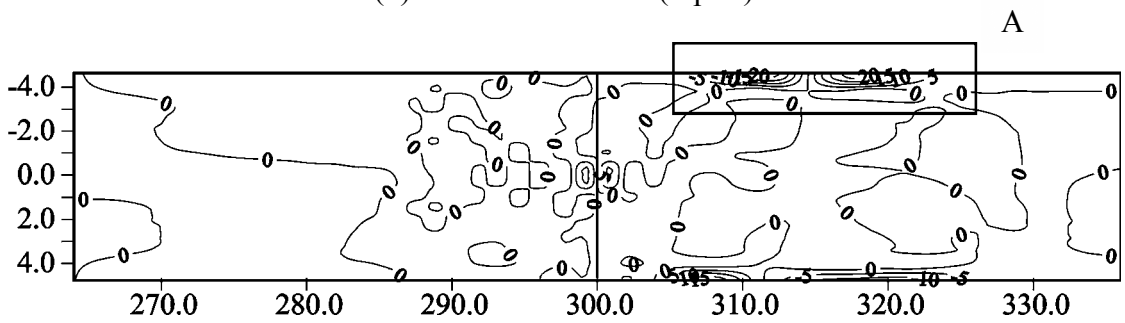

(c) Transverse force *SF4* (kip/in)

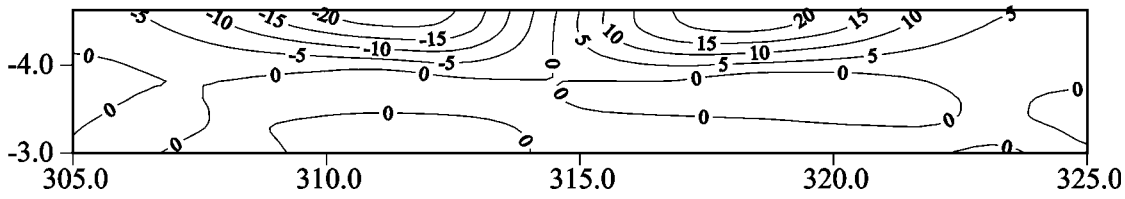

(d) Detail A

Figure 3.33 Top flange force contours at 90% P_u-post peak (Specimen 2)

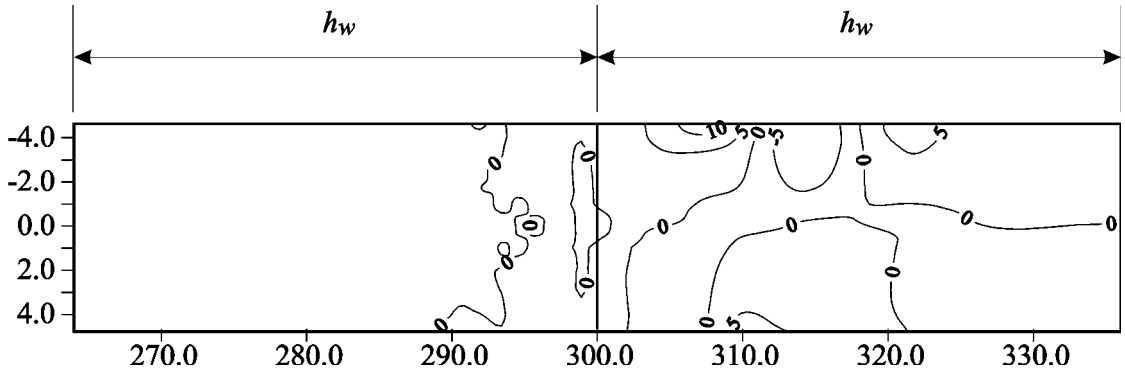

(a) Moment *SM1* (kip-in/in)

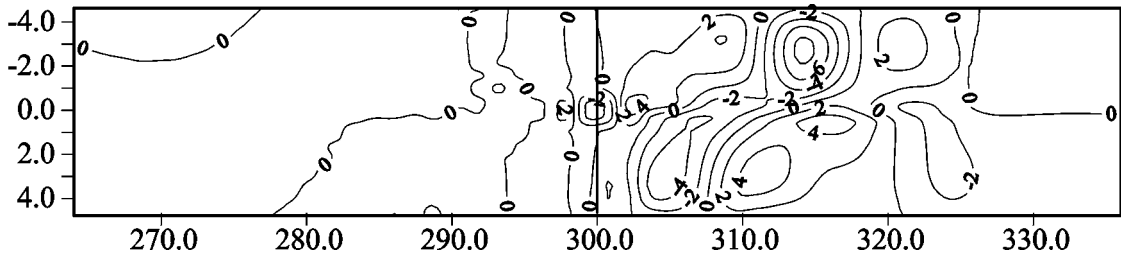

(b) Moment *SM2* (kip-in/in)

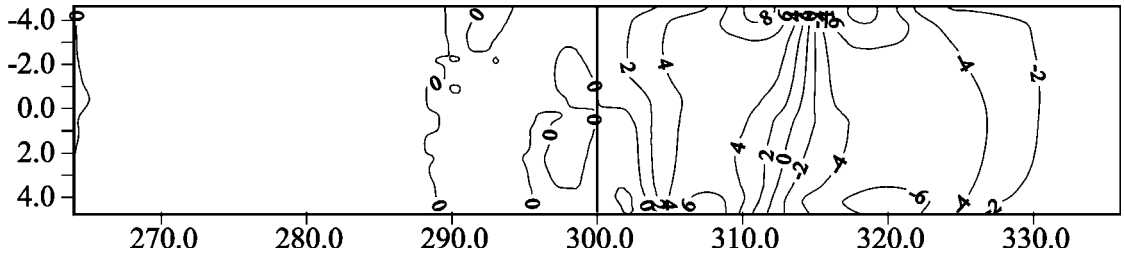

(c) Moment *SM3* (kip-in/in)

Figure 3.34 Top flange moment contours at 90% P_u-post peak (Specimen 2)

CHAPTER 4 Experimental Specimens and Instrumentation

4.1 Introduction

The design and instrumentation of the experimental specimens and the experimental test setup are described in this chapter. Three main parameters play an important role in the design of the experimental specimens. These parameters are the material properties, plate thickness, web height, and flange width. To minimize the discrepancy between the designed and fabricated experimental specimens, the material properties and plate thickness were determined prior to design and fabrication.

The material properties were determined from tensile coupons. The tensile coupons were cut from the plates to be used in fabricating the experimental specimens. The plate thickness was carefully measured for each tensile coupon after removing mill scale.

From the finite element simulation results described in Chapter 3, the main geometric parameters influencing the strength and ductility of the experimental specimens were determined. Guided by the actual material properties, actual plate thickness, and this knowledge of the main geometric parameters, the selection of the experimental specimens was performed. The possibility of making comparisons with previously tested specimens was also considered.

After selecting the specimen geometry, a detailed design of the specimens was performed following the provisions of the 2001 AASHTO LRFD specifications [AASHTO 2001]. The detailed design includes calculating the nominal flexural resistance, the lateral brace spacing, and the nominal shear resistance. A set of detailed drawings for fabrication was prepared.

After the fabricated specimens were delivered to the ATLSS Center, located at Lehigh University, the actual specimen geometry, geometric imperfections, and residual stresses were measured. The finite element study on the effect of imperfection location on the ductility, described in Chapter 3, reveals that as the imperfect region is made closer to the plastic hinge region, the ductility decreases. Based on this study, a distance of twice the web height on each side of the midspan was considered to represent the region at which web imperfections could have a prominent effect on the ductility, and the web geometric imperfections were measured in this region. The residual stresses were measured using a hole-drilling method in accordance with ASTM Standard Test Method E837 [ASTM 1997].

4.2 Material Properties

4.2.1 Experimental Specimen Plate Steel

On the basis of extensive laboratory studies, researchers at the ATLSS Center have developed HPS-100W, a 100 ksi grade of Cu-Ni steel with considerably

enhanced properties for infrastructure applications, such as bridges [Gross and Stout 2001]. A 165-ton full-scale heat was melted at the Coatesville plant of Bethlehem/Lukens Plate, now known as ISG Plate. The 165-ton full-scale heat was teemed (bottom-poured) into ingot molds, stripped, and slabbed. At the Burns Harbor, Coatesville, and Conshohocken plants of Bethlehem/Lukens Plate, the slabs were rolled to 1 in (25.4 mm), 3/4 in (19 mm), 3/8 in (10 mm), and 1/4 in (6 mm) [Gross and Stout 2001].

4.2.2 Tensile Coupon Specimens

The HPS-100W plates were shipped to the ATLSS Center where 8-inch gage length tensile coupon specimens were tested. The coupons were prepared and tested in accordance with ASTM E8 Standard Test Methods and Definitions for Mechanical Testing of Steel Products [ASTM 2001]. The tensile coupon dimensions and locations in the plates are shown in Figure 4.1 and Figure 4.2, respectively.

During the finite element simulation of Specimen 5, discussed in Chapter 7, the flexural strength predicted using finite element simulation was higher than the experimental results by almost 4%. It was thought that this difference could be attributed to a difference in the material properties. As a result, three tensile coupon specimens were cut from Specimen 5 after testing. The location of these tensile coupon specimens is shown in Figure 4.3. Tensile coupon Specimen E5-1 is shown in Figure 4.4.

4.2.3 Tensile Coupon Test Procedures

The tensile coupons were tested in a 600 kips (2670 kN) SATEC Universal Testing Machine. The mill scale was removed by grinding prior to dimension measurement. The width and thickness were measured at four locations along the 8-inch gage length. During the tension tests, longitudinal and transverse strains were measured using a pair of strain gages attached to the coupon as shown in Figure 4.1. In addition to the strain gages, two LVDTs were mounted on the tensile coupon to measure the longitudinal elongation of the 8-inch gage length. The load, strain gage, and LVDT data were recorded at two second intervals using a data acquisition system.

Each tensile test was performed in two stages. The first stage was primarily to accurately determine the Young's modulus and Poisson's ratio of the steel. In the second stage, a full stress-strain curve was obtained. During the first stage, the loading rate was 10 ksi/min (69 MPa/min) up to 50 ksi (345 MPa), which is roughly half the yield strength of the steel. Upon reaching this stress level, the tensile coupon was unloaded till the applied load reached zero. In the first stage, a gain of 1000 was used on the strain gage signal conditioners, which resulted in a resolution of 2.4 microstrain. For the second stage, the gain was set to 100, which resulted in a resolution of 24 microstrain. The loading rate for the second stage was 10 ksi/min (69 MPa/min) up to 50 ksi (345 MPa), and then a loading rate of 0.05 in/min was maintained until the test ended.

4.2.4 Tensile Coupon Properties

From the first stage of the tensile coupon tests, Young's modulus, E, was determined from the slope of the plot of the normal stress, σ_{11}, versus the average normal strain, ε_{11}, from the gage readings. The Poisson's ratio, ν, was determined from the slope of the plot of the normal stress, σ_{11}, and the average normal strain, ε_{22}, which equals $-E/\nu$. Figure 4.5 shows an example plot for calculating the material constants, E and ν, from tensile coupon Specimen E1-2. The results for E and ν are given in Table 4.1. Table 4.1 also shows the results of the second stage of the tensile coupon tests.

Three static yield stress, σ_{ys}, readings were obtained during the second stage of tensile coupon test, by holding the displacement constant till the load stabilized. For each reading, it took about two minutes to stabilize the load. An average value of the three readings is reported in Table 5.1. The yield stress, σ_y, was obtained by the standard 0.2% offset method, and the corresponding yield strain, ε_y, was recorded. The strain hardening modulus, E_{st}, was determined as the slope of stress-strain curve at which the stress exceeds the 0.2% yield stress by 0.5 ksi (3.5 MPa), and the corresponding strain, ε_{st}, was determined. The ultimate strength, σ_u, was calculated by dividing the maximum load by the original cross-sectional area of the coupon, and the corresponding strain, ε_u, was also determined. The yield ratio, YR, was determined by dividing the yield stress by the ultimate strength. The final strain, ε_f, was also recorded. The ductility ratio is determined by dividing ε_u by ε_y.

The tensile coupon test results are summarized in Table 4.1. For each plate thickness, the results were averaged and the average properties are reported in Table 4.2. Stress-strain curves for web plates are shown in Figure 4.6, while those for flange plates are shown in Figure 4.7.

4.2.5 Stress-Strain Model

A stress-strain model, as shown in Figure 4.8, is proposed to fit the tensile coupon data. To define this model, Young's modulus, E, and the stress and strain of six points, A through F, have to be determined. Point A marks the end of the linear elastic region. The stress at this point is called σ_{yp}, proportional yield stress. Point C marks the 0.2% offset stress and strain. Point B is selected at a stress close to the average stress for points A and C. Point D marks the start of strain hardening. Point F marks the ultimate stress. Point E is selected at a stress close to the average stress for points D and F. Young's modulus and the stress and strain values for the six points, A through F are reported in Table 4.3. The results were averaged and the average properties are reported in Table 4.4

The stress strain model is similar to that used by Green [2000] with the following exceptions: a curve was used to fit the transition zone between points A and C and the transition zone between points D and F was fitted by a curve passing

through points D, E, and F using the average values at these points. The stress strain model is linear up to point A. A transition zone between points A and C is defined by:

$$y_t = a_t \, x_t^n \tag{4.1}$$

where the origin is at point C. Points A and B are then used to calculate a_t and n. Similarly, the transition zone between points D and F is defined by:

$$y_u = a_u \, x_u^m \tag{4.2}$$

where the origin is at point F. Points D and E are then used to calculate a_u and m.

Figure 4.9 shows a fit of the stress-strain model to the measured data for six tensile coupons. On this figure, Points A through D are shown. A comparison between the measured stress-strain data and the stress-strain model for different plate thickness is shown in Figure 4.10 through Figure 4.13. It is important to note that in Figure 4.9, the measured stress strain data are those obtained from strain gages. However, in Figure 4.10 through Figure 4.13, the measured stress strain data are those obtained from the LVDTs.

4.3 Experimental Specimen Preliminary Selection

4.3.1 Cross Section and Span Length

Several different factors played an important role in selecting the dimensions of the experimental specimens, as follows:

1. Experimental specimen dimensions were limited by the available plate dimensions.
2. Experimental specimens should cover a wide practical range of flange and web slenderness values.
3. Experimental specimens should be comparable to previously tested specimens.
4. Experimental specimens should allow comparisons to show the effects of flange slenderness, web slenderness, and the ratio of specimen depth to flange width on the strength and ductility.

It was decided to examine five flange slenderness values, seven web slenderness values, two flange plate thickness values, and two web plate thickness values. The five normalized flange slenderness values are between the compact limit and 75% of the limit (i.e., 0.382 and 0.287), and the seven normalized web slenderness values are between 75% of compact limit and noncompact limit (i.e., 2.83 and 6.77). The selected normalized flange slenderness values, λ_f, (as defined in Section 2.4) are 0.382, 0.372, 0.334, 0.305, and 0.287. The selected normalized web slenderness values, λ_w, (as defined in Section 2.4) are 2.83, 3.76, 4.71, 5.25, 5.89, 6.48, and 6.77.

The two available flange-plate thickness are 0.759 in and 1.031 in (19 mm and 26 mm), while the two available web-plate thickness are 0.245 in and 0.374 in (6 mm and 10 mm).

A matrix of 4x35 is formed from these parameters as shown in Table 4.5. The four columns represent the possible combinations of flange and web plate thickness, while the 35 rows represent the possible combinations of web and flange slenderness. The elements shown in this matrix are the calculated web depth-to-flange width ratio, h_w/b_f. From this matrix, the cross section dimensions of the five experimental specimens, named Specimen 3 through Specimen 7, were selected.

After setting the dimensions of the experimental specimen cross section, the test span was chosen as a function of the section depth. The experimental specimens were designed to simulate the condition of negative flexure at an interior pier of a continuous-span bridge. The tests were planned as three point bending tests, with a single concentrated load at midspan of the specimen. The distance between the bearings of the experimental specimen simulates the region of negative flexure at an interior pier of a continuous span bridge. For a multi-span continuous girder subjected to uniformly distributed load, the inflection points near the piers theoretically occur at a distance of 0.21 L_{con} from the pier, where L_{con} is the span of the continuous girder. Consequently, the negative flexure region over the interior pier is equal to 0.42 L_{con}, and the experimental specimen span, L, equals 0.42 L_{con}.

The minimum depth-to-span ratio for constant depth continuous span bridge girders specified in the 2001 AASHTO LRFD specifications is 0.027. A value of 0.030 was selected for the experimental specimens, which results in a experimental specimen span, L, equal to 14 times the web depth.

4.3.2 Preliminary Geometry of Experimental specimens

Table 4.6 summarizes the flange and web slenderness of the experimental specimens based on the specified web height and flange width, and the actual thickness and material properties. It is important to note that accurately measuring the thickness and material properties of the plates used in fabricating the specimens, prior to fabrication, enabled the specimens to be made close to the desired flange and web slenderness combination. This procedure left only two parameters that would vary (within the fabrication tolerance), which are the actual web height and flange width.

4.4 Experimental Specimen Detailed Design

One of the objectives of this research is to examine the applicability of the provisions of the 2001 AASHTO LRFD specifications [AASHTO 2001] to I-girders fabricated from HPS-100W steel. Neglecting the 2001 AASHTO LRFD specifications limits on the use of high strength steel, five I-girders were designed using the 2001 AASHTO LRFD specifications. As noted before, the experimental specimens simulated the conditions of negative flexure at an interior pier of a continuous-span bridge.

4.4.1 Nominal Flexural Resistance

Except for Specimen 5, the experimental specimens have a compact flange and a non-compact web according to the 2001 AASHTO LRFD specifications [AASHTO 2001]. Specimen 5 has a compact flange and a compact web. Before calculating the flexural resistance of the experimental specimens, it was assumed that the compression flange brace spacing satisfied the requirements for compact sections. For these sections the flexural resistance can be calculated using the optional Q formula as per the 2001 AASHTO LRFD specifications [AASHTO 2001], as explained in Section 2.3.

When the Q formula was applied to the experimental specimens, M_p, was the predicted strength for all specimens except Specimen 6, as shown in Table 4.8. The predicted strength of Specimen 6 was 99% M_p. Note that the actual yield strengths of the flange and web, σ_{yf} and σ_{yw}, respectively, rather than the minimum specified yield strengths, F_{yc} and F_{yw}, were used in the calculations.

4.4.2 Lateral Brace Spacing

As noted previously, each specimen was tested as a simple beam in three point bending with one concentrated load applied at midspan. Lateral bracing was provided at the load point and at the bearings in addition to intermediate points. The locations of those intermediate bracing points were calculated to satisfy the 2001 AASHTO LRFD specifications [AASHTO 2001]. Since the optional Q formula was used to determine the flexural resistance of the specimens, the distance (unbraced length) to the first intermediate brace, on each side of the load point, was calculated using Equation 4.3.

$$L_{b1} \le \left[0.124 - 0.0759\left(\frac{M_l}{M_p}\right)\right]\left[\frac{r_y E}{\sigma_{yf}}\right] \tag{4.3}$$

where:

L_{b1} = First unbraced length measured from maximum moment location

r_y = Radius of gyration of the steel section with respect to the vertical axis

M_l = The lower moment at either end of the unbraced length

The remaining brace locations, L_{b2} and L_{b3}, were then designed such that the lateral-torsional resistance of each unbraced length was equal to the maximum moment required in the unbraced length when M_p is reached at midspan. The lateral brace spacing for all experimental specimens is shown in Figure 4.14. Table 4.7 summarizes the selected lateral brace spacing for all experimental specimens where:

$$L_p = 1.76 r_t \sqrt{\frac{E}{\sigma_{yf}}} \tag{4.4}$$

$$L_r = 4.44 r_t \sqrt{\frac{E}{\sigma_{yf}}} \tag{4.5}$$

where:

r_t = Radius of gyration about the vertical axis of a section comprised of the compression flange plus one-third of the depth of the web in compression

4.4.3 Nominal Shear Resistance

The nominal shear resistance was calculated for all specimens assuming an unstiffend web. However, the expected shear demand when M_p is reached at midspan exceeded this shear resistance for all specimens except Specimen 5. To satisfy the shear resistance requirement and avoid moment-shear interaction, transverse stiffeners were spaced so that the expected shear force, when M_p is reached at midspan, does not exceed 60% of the nominal shear resistance calculated using the 2001 AASHTO LRFD specifications [AASHTO 2001].

4.4.4 Preliminary Finite Element Simulations

Prior to fabrication of specimens, preliminary finite element simulations were performed to gain more insight into the behavior of each specimen. A modified finite element mesh was used for these analyses. A typical finite element mesh is shown in Figure 4.27. The modification over the mesh described in Chapter 3 was to extend the fine mesh, for both the flanges and web, to a distance roughly twice the web height from midspan. The boundary and loading conditions, element type, and brace model are the same as described in Chapter 3.

A true stress-natural plastic strain curve was calculated for use in the finite element simulation of each specimen. The true stress-natural plastic strain curve was based on the tensile coupon properties given in Table 4.3, without including the data from tensile coupons E5-1, E5-2, and E5-3. The procedure for converting the engineering stress-strain curve to a true stress- natural plastic strain curve was explained in detail in Chapter 3.

An initial imperfection with a sine wave in the local-x direction and cosine wave in the local-y direction was introduced to the web. The local-x and y coordinate system is shown in Figure 3.10. Equation 3.2 specifies the geometry of the imperfect region. This imperfection was introduced to the north of midspan. The imperfection amplitude, z_0, was taken as the maximum permitted by the AWS Structural Welding Code [1998] which states that for $h_w / t_w < 150$ the maximum imperfection amplitude, $z_0 = h_w / 115$. The residual stresses were not included in these preliminary analyses.

The flexural strength of the experimental specimens, calculated using the optional Q formula as per the 2001 AASHTO LRFD specifications [AASHTO 2001], was compared with that predicted by the finite element simulation. The comparison is shown in Table 4.8. The strength predicted by finite element simulation was less than that calculated using the optional Q formula by 3% for Specimens 4 and 6 and by 2% for Specimen 2. For the remaining specimens, the strength predicted by finite element

simulation was greater than or equal to that calculated using the optional Q formula as shown in Table 4.8.

Figure 4.15 through Figure 4.17 show that the flange slenderness, λ_f, has a predominant effect on the plastic rotation, θ_p. As λ_f decreases, θ_p considerably increases. Note that as λ_f changes, h_w/bf also changes.

Figure 4.18 and Figure 4.19 show the effect of web slenderness, λ_w, on θ_p. As λ_w decreases, θ_p slightly increases as shown in Figure 4.18. However, Figure 4.19 shows that the effect of h_w/bf overrides the effect of λ_w. Even though Specimen 6 has a more slender web, its plastic rotation, θ_p, is more than that of Specimen 2.

Figure 4.20 shows the effect of h_w/b_f on the strength and plastic rotation. As h_w/b_f is decreased, both the strength and θ_p considerably increase.

4.4.5 Specimen Fabrication

High Steel Structures, in Lancaster, Pennsylvania, fabricated the specimens from HPS-100W steel. All specimens, except Specimen 4, were fabricated from continuous web and flange plates. The plates were flame cut to the required width and length. Specimen 4 has a flange butt splice since the span was longer than the available plate size. The flange-to-web, stiffener-to-web, and stiffener-to-flange fillet welds were undermatched and made with semiautomatic submerged arc welding process, SAW, using Lincoln wire L61 with AXXX10 flux. The butt splice and filet weld metals were undermatched and had a minimum tensile strength of 70 ksi (485 MPa). All welding was performed in accordance with the ASW structural welding Code D1.1-98 [AWS 1998].

Specimen 3 and 4 were fabricated with flange plates cut from plate 04AA with a nominal thickness of 3/4 in, while Specimen 5, 6, and 7 were fabricated with flange plates cut from plate 400054 with a nominal thickness of 1 in. Specimen 3 and 4 were fabricated with web plates cut from plate 08AE with a nominal thickness of 1/4 in, while Specimen 5 was fabricated with web plates cut from plate 05AA with a nominal thickness of 3/8 in. Specimen 6 and 7 were fabricated with web plates cut from plate 05AB with a nominal thickness of 3/8 in.

Detailed drawings of Specimens 3 through 7 are shown in Figure 4.21 through Figure 4.25, respectively. The plate thickness shown on these figures is the nominal plate thickness, not the measured thickness. Each figure shows stiffener locations and dimensions, and weld location and size.

4.5 Fabricated Experimental Specimens

After the specimens had been fabricated, the dimensions of each specimen were measured and compared with the specified dimensions. As the imperfection amplitude and location greatly influence the specimen behavior, it was decided to measure the flange and web imperfections within a region two times the web height on

each side of the load stiffener. Residual stress measurements, for the flanges and web, were made using the hole-drilling method in accordance with ASTM Standard Test Method E837 [ASTM 1997].

4.5.1 Actual Specimen Geometry

After fabrication of the specimens, the actual lengths, web height, and flange widths, were measured and compared with those specified in the design. The maximum variation in dimensions was about 1/8 in. Table 4.6 summarizes the flange and web slenderness calculated from the actual dimensions and material properties of the experimental specimens. The procedure followed in selecting the experimental specimen minimized the differences between the specified and actual flange and web slenderness. A plot of the actual flange and web slenderness, along with the compact and non-compact limits (see Equations 2.13, 2.14, and 2.15), is shown in Figure 4.26.

4.5.2 Geometric Imperfection Measurements

Based on the finite element simulations of Specimen 1 and Specimen 2, described in Section 3.5, it was concluded that geometric imperfections have a detrimental effect on both the strength and ductility of steel I-girders. Two main parameters describe the imperfections: the location and the amplitude. If the imperfections are located within the expected plastic hinge region, it will have pronounced effect. While compression stresses magnify the imperfection amplitude, tensile stresses straighten the imperfect region. So, it is important to observe the imperfections present in the critical compression regions. A finite element study on the effect of imperfection location on ductility (described in Section 3.5) reveals that as the imperfect region is moved closer to the plastic hinge region, the ductility is decreased. From this study, a distance of roughly twice the web height on each side of the midspan represents the region where imperfections could have a prominent effect on the ductility. The outcome of this study is the basis for imperfection measurements for all experimental specimens.

To easily incorporate the imperfection measurements in the finite element model, the measurements were made over a mesh size with elements twice as large as that used in the finite element model. Imperfection measurements were made on the top (compression) flange and web. An area of the web centered on midspan, which has a length equal to roughly four times the web height and a width equal to the web height, was divided into this mesh. For the compression flange, an area with a length equal to roughly four times the web height was used with a width equal to the flange width. Details of the imperfection measurement mesh are shown in Figure 4.27. The imperfection measurements were performed using a 1485HP laser level from Spectra Precision as shown in Figure 4.28. The accuracy of the measurements was 1/64 in (0.4 mm).

The top flange imperfection amplitude was calculated with respect to a zero reference horizontal plane passing through the flange-web intersection. the web imperfection amplitude was calculated using two different references, one reference

with respect to plane through points A, B, and C as shown in Figure 4.29(a), and the other with respect to a line through the intersections with flanges as shown in Figure 4.29(b).

As mentioned above, the imperfection measurements were performed on a coarse mesh with element dimensions twice as large as those used in the finite element model. After calculating the imperfection amplitude at each node in the coarse mesh, interpolation was performed to map the imperfection amplitude to the finer mesh used in finite element model. Plots of imperfection amplitude for Specimens 3 through 7 are shown in Figure 4.30 through Figure 4.34, respectively. In these figures, the web imperfection amplitude was calculated with respect to the line through the intersections of the web with the flanges. Comparisons between the web imperfection amplitudes using the two different references for Specimens 3 through 7 are shown in Figure 4.35 through Figure 4.39, respectively. From these figures, it is clear that either reference is sufficient for describing the web imperfection amplitude, especially at regions of maximum imperfection amplitude even though the location of the maximum may be shifted. The maximum and minimum imperfection amplitudes of each specimen are shown in Table 4.9. In this table, the web imperfection amplitudes calculated using the two different reference methods are compared and good agreement is shown

4.5.3 Residual Stress Measurements

The hole-drilling method was used for measuring residual stresses [ASTM 1994]. This method involves drilling a small shallow hole in the specimen. The introduction of the hole relaxes the stresses at that location. A special strain gage rosette (062RE) from Measurements Group Inc. is used for the strain measurements. The design of this rosette has centering patterns for precisely positioning the boring tool at the center of the gage. The Measurements Group Inc. strain indicator Model P-3500 and switch-and-balance unit SB-10 were used to record the strains. The RS-200 Milling Guide, from Measurements Group Inc., was used for drilling the hole. The instrumentation used in residual stress measurements is shown in Figure 4.40.

The drilling was done in increments of 0.01 in up to a depth of 0.1 in. A strain gage rosette, type 062RE, was used, and strains in three directions were recorded for each drilling increment. H-DRILL [Schajer 2001], an interactive computer program, is used to calculate residual stresses from strain measurements made by the hole-drilling method.

With the experimental specimen instrumentation plan in mind (see Section 4.6.4), the locations for measuring residual stresses were selected to simulate the location of the set of strain rosettes on the top flange closest to the load stiffener at midspan. In order to avoid drilling holes at the locations of these strain rosettes, the locations for measuring residual stresses were moved to be at the same distance from the first intermediate stiffener. This location simulates the effect of the welded load stiffener on the distribution of residual stresses. The locations for measuring residual stresses in Specimen 7 are shown in Figure 4.41. The residual stress location is

marked as section 1-1 in Figure 4.42 through Figure 4.46 for Specimen 3 through Specimen 7, respectively. The residual stresses, σ_{11}, σ_{22}, and σ_{12} are reported in Table 4.10 through Table 4.14 for Specimens 3 through Specimen 7, respectively. Since the flange plates were flame cut to the required size, tensile residual stress was expected at the flange edges.

A simplified model for residual stress, σ_{11}, is proposed based, in part, on the measured residual stresses. In this model, as shown in Figure 4.47, the flange was divided to three regions, I, II, and III. The web was divided to two regions, I, II. The residual stress is given as a stress at the mid surface of the plate and is taken as the stress averaged through the thickness of the plate.

To completely define the residual stress for the flanges, the following six variables have to be determined: the widths of regions I, II, and III and the residual stress values in regions I, II, and III. As the residual stresses acting on the flange are self-equilibrating stresses, i.e., there is no net normal force resultant, equating the resultant tensile and compressive forces in the flange provides a constraint equation, which relates all these variables. In addition, the sum of the widths equals the flange width, b_f, which provides another constraint equation. With six variables and two constraint equations, the values of four variables have to be determined from the experimental data, or otherwise assumed in order to fully define the residual stresses in the flanges.

It is assumed that the residual stress at the junction between the flange and web is tension and equal to the yield stress, σ_y. In flange region I, the average value for the residual stress measured on the top surface is approximately $-0.2\sigma_y$ (i.e., compressive). As a result, the average value of $0.6\sigma_y$ is assumed in region I. The average measured residual stress in region II was $-0.25\sigma_y$, and this value is assumed for region II. The residual stress in region III is assumed to be $0.05\sigma_y$.

In selecting the width of each region, the finite element mesh was taken into consideration such that each group of elements in a region has the same residual stress. Therefore, the width of region II is assumed to be $5b_f/16$. Assigning this width to region II, the widths of region I and III were then determined from the two constraint equations.

For the web, the residual stress at the junction between the flange and web is assumed to be tension and equal to the yield stress, σ_y. This is the residual stress assumed in region I. The width of region I was selected with the finite element mesh in mind. The value of residual stress in region II was then calculated by equating the resultant tensile and compressive forces in the web. This value of $-0.09\sigma_y$ approximates the measured residual stresses in the web.

A comparison between the measured and idealized residual stresses for top flange is shown in Figure 4.48. This figure represents one half of the top flange, and

$z / (b_f/2) = 0$ represents web flange intersection. The measured residual stresses are from the upper surface of the top flange.

A comparison between the measured residual stresses and the residual stress model for the web is shown in Figure 4.49. For Specimen 7, the compression residual stresses measured at section 1-1 are less than those at section 2-2 and this may be attributed to the effect of the welded stiffener near section 1-1. For Specimen 4, high tensile residual stresses were observed in the web close to the welded stiffener. These high tensile residual stresses could be the result of welding the stiffener to the web. However, if the web had high tensile residual stresses through the thickness of the web plate, an increase in compression residual stresses in the top flange at that location should be observed, to maintain equilibrium. Increased compression residual stresses were not observed in the top flange at this section, so the tension web residual stresses observed for Specimen 4 were not considered in developing the residual stress model.

4.6 Test Setup

The specimens were tested as simple beams with one concentrated load applied at the midspan. Each specimen was supported on 5.75 in (146 mm) diameter steel cylindrical rollers resting on pedestals. The load was applied through a 600 kip (2669 kN) hydraulic actuator. To measure the applied load, a load cell was placed between the hydraulic actuator and a spherical bearing. A lateral bracing system was used to restrain the lateral movement of experimental specimens. An overall view and an elevation view of the test setup are shown in Figure 4.50 and Figure 4.51, respectively.

4.6.1 Bracing System

To provide lateral restraint to the experimental specimens, a bracing system was designed to accommodate different specimen configurations. Lateral bracing was provided to both compression and tension flanges. The design of the bracing system considered the fact that each specimen has different:

1. Web height and flange width
2. Lateral bracing locations
3. Lateral force and stiffness demand

The bracing system consists of vertical columns, W12x43, located at the required bracing points, on each side of the experimental specimen. To reduce the friction between the vertical columns and specimen flanges, a Teflon sheet was applied to both sides of the contact surface. The Teflon sheet attached to the vertical columns was long enough to accommodate the specimen deflection during testing. The vertical columns are supported at top and bottom on upper and lower longitudinal beams, B1 and B2 as shown in Figure 4.52. The upper longitudinal beam, B1 (W18x86), is supported on two frames, FR1 and FR2, as shown in Figure 4.53 and Figure 4.54. Beam B1 has an overhanging length of 42 in (1067 mm) to accommodate the brace point farthest from midspan needed for Specimen 6. Also, the overhanging length was selected to avoid clearance problem with another project (see Figure 4.50)

tested at the same time. The lower longitudinal beam, B2 (W18x55) is anchored to the lab floor each 60 in (1524 mm) intervals with an overhanging length of 42 in (1067 mm). Details of the bracing system are shown in Figure 4.52 through Figure 4.55. Overall views of frames FR1 and FR2 are shown in Figure 4.56 and Figure 4.57, respectively.

4.6.2 Loading System

From the preliminary finite element simulations of the experimental specimens, the maximum predicted applied load was less than 600 kips (2669 kN). Also, the expected maximum midspan displacement was about 12 in (305 mm). From these two main requirements, specifications for a new hydraulic actuator were developed. The hydraulic actuator was provided by Miller Fluid Power and customized such that the piston rod diameter would fit the narrowest specimen (Specimen 4). This customized hydraulic actuator has the following specifications:

1. 16 in (406 mm) bore diameter
2. 12 in (305 mm) stroke
3. 6.5 in (165 mm) piston rod diameter
4. 600 kip (2669 kN) maximum compressive load

The upper end of the hydraulic actuator was fixed to frame FR2, while the lower end was attached to one end of a 600 kip (2669 kN) load cell with a 3.5 in (89 mm) threaded rod. The other end of the load cell was attached to the convex plate of a spherical bearing with a 3.5 in (89 mm) threaded rod as shown in Figure 4.57. The spherical bearing was designed for a load capacity of 600 kips (2669 kN) and a rotational capacity of 0.08 radians. The spherical bearing was designed to fit within the flange width of the narrowest experimental specimen. The spherical bearing consists of a convex steel plate that slides on a concave steel plate with the same radius, with a lubricant applied between the convex and concave surfaces. The spherical bearing provided the following advantages:

1. The load was spread uniformly over the bottom of the bearing.
2. The torsional restraint of the compression flange at the load point was minimized.
3. Rotation which developed at the midspan due to unsymmetrical failure of a experimental specimen was accommodated.

4.6.3 Bearings

Based on preliminary finite element simulations of the experimental specimens, it was concluded that the maximum applied load would not exceed 600 kips (2669 kN). As a result, the end reaction would not exceed 300 kips (1334 kN). A cylindrical roller of 5.75 in (146 mm) in diameter and 10 in (254 mm) in length was used at each bearing. A base plate 12 in x 12 in x 3 in (305 mm x 305 mm x 76 mm)

was attached to a pedestal. A sole plate of the same dimensions was attached to the bottom flange of the experimental specimens.

4.6.4 Specimen Instrumentation

The preliminary finite element simulations of the experimental specimens provided information about local buckling modes and location. Guided with this information, strain gage locations were selected to capture the local buckling behavior of the experimental specimens. Three types of strain gages, from Measurements Group, Inc., were used:

1. 45^o rectangular rosette type (Model EP-08-250RA-120)
2. Two-element 90^o tee rosette type (Model EP-08-250TM-120)
3. Uniaxial gage type (Model EP-08-250BG-120)

The strain gages were high elongation gages intended for measuring large post-yield strains. The strain gages were bonded to the experimental specimens using CN adhesive (Cyanoacrylate) from Texas Measurements, Inc.

Typical strain gage locations for the top (compression) flange are shown in Figure 4.58. Locations for the bottom flange are shown in Figure 4.59. Web strain gage locations are shown in Figure 4.60. In these figures, strain gage locations are defined by distances a, b, c, and d, which are given in Table 4.15 for each specimen. Strain gages on the top flange and web of Specimen 4 are shown in Figure 4.61. A close-up view of the strain gages on the north side of the top flange is shown in Figure 4.62, and a close-up view of the strain gages at the junction between the web and top flange, on the southeast side, is shown in Figure 4.63. Strain gages on the upper surface of the top flange were clustered around the expected failure region to cover roughly one-half of the flange buckled wave. Strain gages located at the edges of the top flange were located at the integration points of elements used in the finite element model.

To measure normal and shear stresses developed during failure, a 45^o rectangular rosette was used for the strain gages on the upper surface of the top flange. Due to a limitation on the number of strain gage channels available for the data acquisition system, uniaxial strain gages were used for the gages on the lower surface of the top flange.

At the junction between web and top flange, a two-element 90^o tee rosette was used to measure the normal strain in the local-1 and local-2 directions. At nearby locations uniaxial strain gages were oriented to measure the strain in the local-2 direction. The purpose of the strain gages oriented in the local-2 direction is to monitor the web plate curvature due to the moment transferred between the web and top flange. The remaining strain gages on the web and bottom flange are uniaxial, oriented in the local-1 direction.

To monitor the global behavior of the specimens, rotations and displacements at selected key locations were recorded. Rotations were measured using AccuStar electronic rotation meters from Schaevitz Sensors. The output of the rotation meter

was amplified, resulting in a range of $\pm 10^{\circ}$, with a resolution of 0.005°. Vertical deflections of the specimens were measured using linear motion position sensors, Model 612, from Duncan Electronics, BEI Technologies, Inc. The range of these sensors is ± 6 in with resolution of 0.0060 in. Lateral displacements were measured using linear variable differential transformers (LVDTs), Model 2000 DC-E, from Schaevitz Sensors. The range of these sensors is ± 2 in with a resolution of 0.002 in. The locations of these sensors are shown in Figure 4.64 for a typical experimental specimen.

Vertical deflections were measured at the midspan of each specimen using two plastic slides, labeled PS_3 and PS_4. Also, vertical deflections were measured at the middle of each brace location. Lateral displacements of the top flange were measured at each brace location using two LVDTs, one on each side of the brace column. This arrangement permitted both lateral displacements and lateral rotations to be determined.

Two rotation meters were used at each end of the specimen. They were attached to the middle of the bearing. Also, two rotation meters were attached to the load stiffener to monitor the rotation of the midspan cross section.

Table 4.1 Tensile coupon properties

Plate ID	Specimen ID	Thickness (nominal) (in)	Thickness (actual) (in)	E (ksi)	ν	E_{st} (ksi)	σ_y (ksi)	σ_{ys} (ksi)	σ_u (ksi)	Yield ratio YR	ε_y (in/in)	ε_{st} (in/in)	ε_u (in/in)	Ductility ratio	ε_f (in/in)
08AE	E1-1	1/4	0.247	28900	N/A	90.00	123.47	118.50	127.70	0.97	0.00627	0.02800	0.0731	11.65	0.1307
08AE	E1-2	1/4	0.247	29100	0.281	87.50	127.54	123.60	130.51	0.98	0.00638	0.03164	0.0665	10.43	0.1192
08AE	E3-1	1/4	0.242	29200	N/A	103.30	122.26	118.00	127.41	0.96	0.00619	0.03327	0.0717	11.58	0.1243
05AB	E4-1	3/8	0.375	28400	0.276	122.00	116.23	115.20	123.47	0.94	0.00609	0.00668	0.0522	8.57	0.1303
05AB	E4-2	3/8	0.374	28000	N/A	135.20	115.09	N/A	122.43	0.94	0.00611	0.00659	0.0510	8.35	0.1082
05AB	E4-3	3/8	0.376	28500	0.282	123.50	117.01	115.00	124.48	0.94	0.00611	0.00685	0.0610	9.99	0.1111
05AA	E7-1	3/8	0.378	28300	0.272	134.90	119.08	N/A	124.48	0.96	0.00621	0.02095	0.0585	9.42	0.1190
05AA	E7-2	3/8	0.373	28800	N/A	126.40	116.45	112.50	121.24	0.96	0.00604	0.00704	0.0762	12.60	0.1448
05AA	E7-3	3/8	0.374	28900	0.281	111.00	115.14	111.70	120.84	0.95	0.00598	0.00967	0.0769	12.85	0.1429
05AB	E6-1	3/8	0.369	28200	0.282	158.80	107.88	107.70	118.55	0.91	0.00583	0.00630	0.0720	12.35	0.1428
04AA	E8-1	3/4	0.759	28800	N/A	134.50	112.54	108.90	121.72	0.92	0.00611	0.00710	0.0761	12.45	0.1690
04AA	E8-2	3/4	0.761	29200	0.283	154.50	115.05	111.00	122.54	0.94	0.00594	0.00691	0.0655	11.02	0.1633
04AA	E8-3	3/4	0.761	28900	0.2774	119.00	112.66	110.90	122.02	0.92	0.00590	0.00607	0.0796	13.49	0.1794
04AA	E9-1	3/4	0.755	28900	N/A	127.60	111.48	108.10	119.50	0.93	0.00586	0.00745	0.0751	12.83	0.1554
400054	E5-1	1.0	1.027	29801	N/A	199.65	112.16	N/A	122.49	0.92	0.00576	0.00615	0.0760	13.19	0.1756
400054	E5-2	1.0	1.027	29906	0.28	174.48	112.52	N/A	122.74	0.92	0.00576	0.00619	0.0808	14.02	0.1788
400054	E5-3	1.0	1.027	29950	0.28	164.66	112.95	N/A	123.00	0.92	0.00576	0.00616	0.0809	14.05	0.1872
400054	E10-1	1.0	1.033	29300	N/A	140.70	114.61	112.90	125.35	0.91	0.00591	0.00653	0.0756	12.78	0.1875
400054	E10-2	1.0	1.033	29000	0.267	133.30	114.26	112.10	124.50	0.92	0.00594	0.00658	0.0739	12.44	0.1797
400054	E10-3	1.0	1.033	29200	0.269	138.60	113.94	111.90	124.36	0.92	0.00590	0.00667	0.0780	13.22	0.1825
400054	E12-1	1.0	1.024	29200	N/A	136.60	113.93	111.90	123.42	0.92	0.00590	0.00665	0.0717	12.15	0.1854

Table 4.2 Average tensile coupon properties

Thickness (nominal) (in)	Thickness (actual) (in)	E (ksi)	ν	E_{st} (ksi)	σ_y (ksi)	σ_{ys} (ksi)	σ_u (ksi)	Yield ratio YR	ε_y (in/in)	ε_{st} (in/in)	ε_u (in/in)	Ductility ratio	ε_f (in/in)
1/4	0.245	29067	0.281	93.60	124.42	120.03	128.54	0.97	0.00628	0.03097	0.0704	11.22	0.1247
3/8 - O5AB	0.375	28300	0.279	126.90	116.11	115.10	123.46	0.94	0.00610	0.00671	0.0547	8.97	0.1165
3/8 - O5AA	0.375	28667	0.277	124.10	116.89	112.10	122.19	0.96	0.00608	0.01255	0.0705	11.62	0.1356
3/4	0.760	28967	0.28	136.00	113.42	110.27	122.09	0.93	0.00598	0.00669	0.0737	12.32	0.1706
1.0	1.030	29526	0.274	158.57	113.41	112.30	123.74	0.92	0.00584	0.00638	0.0775	13.28	0.1819

Table 4.3 Tensile coupon data used to develop stress-strain model

Specimen ID	E	Point A		Point B		Point C		Point D		Point E		Point F	
		ε	σ	ε	σ	ε	σ	ε	σ	ε	σ	ε	σ
	(ksi)	(in/in)	(ksi)	(in/in)	(ksi)	(in/in)	(ksi)	(in/in)	(ksi)	(in/in)	(ksi)	(in/in)	(ksi)
E1-1	28900	0.00427	123.47	———	———	0.00427	123.47	0.02800	123.47	0.04063	125.50	0.07310	127.70
E1-2	29100	0.00438	127.54	———	———	0.00438	127.54	0.03160	127.54	0.03908	129.00	0.06650	130.51
E3-1	29200	0.00419	122.26	———	———	0.00419	122.26	0.03327	122.26	0.03945	124.84	0.07170	127.41
E4-1	28400	0.00329	93.30	0.00391	104.77	0.00609	116.23	0.00668	116.23	0.01800	119.85	0.05220	123.47
E4-2	28000	0.00342	95.86	0.00403	105.48	0.00611	115.09	0.00659	115.09	0.01550	118.76	0.05100	122.43
E4-3	28500	0.00301	85.76	0.00369	101.39	0.00611	117.01	0.00685	117.01	0.01965	120.75	0.06100	124.48
E6-1	28200	0.00276	77.79	0.00330	92.95	0.00583	107.70	0.00630	107.70	0.01836	113.17	0.07200	118.55
E7-1	28300	0.00421	119.08	———	———	0.00421	119.08	0.01000	119.08	0.02844	121.78	0.05850	124.48
E7-2	28800	0.00404	116.45	———	———	0.00404	116.45	0.00704	116.45	0.03369	118.85	0.07620	121.24
E7-3	28900	0.00398	115.14	———	———	0.00398	115.14	0.00967	115.14	0.03223	117.99	0.07690	120.84
E8-1	28800	0.00347	99.99	0.00391	106.46	0.00611	112.54	0.00710	112.54	0.02455	117.13	0.07610	121.72
E8-2	29200	0.00350	100.53	0.00391	107.61	0.00594	115.05	0.00691	115.05	0.02446	118.80	0.06550	122.54
E8-3	28900	0.00345	99.56	0.00427	106.36	0.00590	112.66	0.00607	112.66	0.02454	117.34	0.07960	122.02
E9-1	28900	0.00344	99.56	0.00366	105.64	0.00586	111.48	0.00745	111.48	0.02803	115.48	0.07510	119.50
E5-1	29801	0.00278	83.04	0.00353	97.70	0.00576	112.16	0.00615	112.16	0.02172	117.32	0.07596	122.49
E5-2	29906	0.00285	85.25	0.00359	98.94	0.00576	112.52	0.00619	112.52	0.02239	117.64	0.08078	122.74
E5-3	29950	0.00261	78.20	0.00339	95.63	0.00576	112.95	0.00616	112.95	0.02227	117.97	0.08094	123.00
E10-1	29300	0.00265	77.50	0.00342	96.40	0.00591	114.62	0.00653	114.62	0.02197	119.99	0.07560	125.35
E10-2	29000	0.00263	76.36	0.00342	95.36	0.00594	114.26	0.00658	114.26	0.02238	119.38	0.07390	124.50
E10-3	29200	0.00263	76.88	0.00345	95.64	0.00590	113.94	0.00667	113.94	0.02177	119.15	0.07800	124.36

Table 4.4 Average tensile coupon data used to develop stress-strain model

Thickness nominal	E	Point A		Point B		Point C		Point D		Point E		Point F	
		ε	σ	ε	σ	ε	σ	ε	σ	ε	σ	ε	σ
(in)	(ksi)	(in/in)	(ksi)	(in/in)	(ksi)	(in/in)	(ksi)	(in/in)	(ksi)	(in/in)	(ksi)	(in/in)	(ksi)
1/4	29067	0.00428	124.42	———	———	0.00428	124.42	0.03096	124.42	0.03972	126.45	0.07043	128.54
3/8 - O5AB	28300	0.00324	91.64	0.00388	103.88	0.00610	116.11	0.00671	116.11	0.01772	119.79	0.05473	123.46
3/8 - O5AA	28667	0.00408	116.89	———	———	0.00408	116.89	0.00890	116.89	0.03145	119.54	0.07053	122.19
3/4	28967	0.00347	100.03	0.00403	106.81	0.00598	113.42	0.00669	113.42	0.02452	117.76	0.07373	122.09
1.0	29526	0.00269	79.54	0.00347	96.61	0.00584	113.41	0.00638	113.41	0.02208	118.58	0.07753	123.74

Table 4.5 Experimental specimen selection

λ_w	λ_f	h_w/b_f			
		A	B	C	D
2.83	0.382	1.14	0.84	1.81	1.34
	0.372	1.17	0.87	1.86	1.37
	0.334	1.31	0.96	2.07	1.53
	0.305	1.43	1.06	2.26	1.67
	0.287	1.52	1.12	2.41	1.78
3.76	0.382	1.52	1.12	2.41	1.78
	0.372	1.56	1.15	2.47	1.83
	0.334	1.74	1.28	2.75	2.03
	0.305	1.90	1.41	3.01	2.23 (5)
	0.287	2.02	1.49	3.20	2.37
4.71	0.382	1.90	1.41	3.01	2.23
	0.372	1.95	1.44	3.09	2.29
	0.334	2.18	1.61	3.45	2.55
	0.305	2.38	1.76	3.77	2.79
	0.287	2.53	1.87	4.01	2.96
5.30	0.382	2.14 (3)	1.58	3.39	2.51
	0.372	2.20	1.62	3.48	2.57
	0.334	2.45	1.81	3.88	2.87
	0.305	2.68	1.98	4.25	3.14 (7)
	0.287	2.85	2.10	4.51	3.34
5.89	0.382	2.38	1.76	3.77	2.78
	0.372	2.44	1.80	3.87	2.86
	0.334	2.72	2.01	4.31	3.18
	0.305	2.98	2.20	4.72	3.49
	0.287	3.16	2.34	5.01	3.71
6.48	0.382	2.61	1.93	4.14	3.06
	0.372	2.69	1.98	4.26	3.14
	0.334	2.99	2.21	4.74	3.50
	0.305	3.27	2.42	5.19	3.84
	0.287	3.48	2.57	5.52	4.08
6.77	0.382	2.73	2.02	4.33	3.20 (6)
	0.372	2.81	2.07	4.45	3.29
	0.334	3.13	2.31	4.95	3.66
	0.305	3.42 (4)	2.53	5.43	4.01
	0.287	3.64	2.69	5.77	4.26

(3): Specimen 3, (4): Specimen 4, (5): Specimen 5, (6): Specimen 6, (7): Specimen 7
A - made from 1/4 in web plate and 3/4 in flange plate
B - made from 1/4 in web plate and 1 in flange plate
C - made from 3/8 in web plate and 3/4 in flange plate
D - made from 3/8 in web plate and 1 in flange plate

Table 4.6 Actual thickness, specified dimensions, and actual material properties

Specimen	t_f (in)	t_w (in)	b_f (in)	h_w (in)	h_w/b_f (in/in)	h_w/t_w (in/in)	$b_f/2t_f$ (in/in)	E_f (ksi)	σ_{yf} (ksi)	E_w (ksi)	σ_{yw} (ksi)	λ_f	λ_w
3	0.7588	0.2452	9.250	20.000	2.16	81.6	6.10	28950.00	112.93	29067.00	124.42	0.381	5.34
4	0.7588	0.2452	7.375	25.375	3.44	103.5	4.86	28950.00	112.93	29067.00	124.42	0.304	6.77
5	1.0313	0.3742	10.000	22.000	2.20	58.8	4.85	29175.00	114.19	28443.00	115.27	0.303	3.74
6	1.0313	0.3742	12.626	39.750	3.15	106.2	6.12	29175.00	114.19	28443.00	115.27	0.383	6.76
7	1.0313	0.3742	10.000	31.500	3.15	84.2	4.85	29175.00	114.19	28443.00	115.27	0.303	5.36

Table 4.7 Calculated flexural strength and lateral brace spacing

Specimen	M_p (kip-in)	M_n (kip-in)	M_n/M_p	L (in)	L_p (in)	L_r (in)	L_{b1} required (in)	L_{b1} (in)	$\frac{L_{b1}\text{ req.}}{L_{b1}}$	L_{b2} required (in)	L_{b2} (in)	$\frac{L_{b2}\text{ req.}}{L_{b2}}$	L_{b3} required (in)	L_{b3} (in)	$\frac{L_{b3}\text{ req.}}{L_{b3}}$
3	19510	19510	1.00	300	75.32	187.07	40.50	37.50	1.08	113.02	112.50	1.00	----	----	----
4	21430	21430	1.00	390	60.06	143.82	25.43	25.50	1.00	60.14	55.75	1.08	113.75	113.75	1.00
5	32340	32340	1.00	336	80.43	200.80	41.03	42.00	0.98	120.88	126.00	0.96	----	----	----
6	77670	76510	0.99	576	101.88	242.48	43.74	42.00	1.04	112.95	114.00	0.99	132.00	132.00	1.00
7	49010	49010	1.00	480	80.70	193.44	34.24	33.75	1.01	89.25	85.00	1.05	121.25	121.25	1.00

Table 4.8 Comparison between calculated and finite element simulations

Specimen	M_n/M_p (calculated)	M_n/M_p (finite element)
1 *	1.00	1.02
2 *	0.98	0.96
3	1.00	1.02
4	1.00	0.97
5	1.00	1.07
6	0.99	0.96
7	1.00	1.00

* Specimens previously tested by Sause and Fahnestock [2001]

Table 4.9 Flange and web imperfection amplitudes

Specimen	Flange imperfection		Web imperfection (reference to line)		Web imperfection (reference to plane)	
	max. (in)	min. (in)	max. (in)	min. (in)	max. (in)	min. (in)
3	0.11	-0.17	0.17	-0.01	0.14	-0.09
4	0.11	-0.11	0.29	-0.07	0.33	-0.10
5	0.04	-0.06	0.03	-0.04	0.09	-0.06
6	0.05	-0.06	0.32	0.00	0.30	-0.05
7	0.08	-0.11	0.01	-0.14	0.09	-0.14

Table 4.10 Residual stresses for Specimen 3

Location	Residual stresses (ksi)		
	σ_{11}	σ_{22}	σ_{12}
A	-13.3	-10.0	-7.2
B	-28.9	-18.9	-4.0
C	-31.5	-21.7	-3.0
D	-9.2	5.6	-0.7

A through D: Top flange upper surface

Table 4.11 Residual stresses for Specimen 4

Location	Residual stresses (ksi)		
	σ_{11}	σ_{22}	σ_{12}
A	51.6	5.6	8.2
B	-32.1	-18.5	-1.7
C	-28.1	-5.2	0.30
D	-32.7	-11.4	-2.9
E	-25.9	3.4	2.0
F	-11.5	28.0	-2.6
G	-20.7	-8.6	0.1
H	10.6	1.4	-0.8
A'	-10.9	-5.3	4.6
B'	-24.5	-11.9	0.6
C'	-18.7	-8.4	3.0
G'	-21.0	-13.7	-1.5
H'	-17.9	-5.2	-3.4
I'	-1.6	-7.2	-0.1
J'	-24.7	-6.0	-2.4
K'	-2.3	16.6	-0.5
L'	-6.3	-3.5	-1.5

A through H: Top flange upper surface
A' through H': Top flange lower surface
I' through L': Bottom flange lower surface

Table 4.11 Residual stresses for Specimen 4 (continued)

Location	Residual stresses (ksi)		
	σ_{11}	σ_{22}	σ_{12}
O	1.8	-13.3	24.1
P	23.7	-12.0	13.3
Q	19.7	-12.0	6.7
R	21.8	-6.1	1.3
S	22.5	-8.6	-1.2
T	19.8	-7.9	-1.1
V	19.9	-10.1	-1.7
W	3.4	-13.5	-1.1
X	1.2	-6.0	3.0
O'	3.5	-2.4	-13.9
P'	20.1	-4.8	-15.8
Q'	16.6	-13.9	-11.2
R'	13.0	-10.6	-5.4
S'	9.2	-13.1	-5.4
T'	15.7	-10.2	-2.8
V'	15.6	-10.7	-2.7
W'	3.7	4.8	-0.7
X'	-8.5	4.1	1.1

O through X: Web west side
O' through X': Web east side

Table 4.12 Residual stresses for Specimen 5

Location	Residual stresses (ksi)		
	σ_{11}	σ_{22}	σ_{12}
A	-11.2	0.9	0.5
B	-35.4	-22.4	-1.7
C	-33.1	-25.4	-1.3
D	-25.2	-0.2	-0.2

A through D: Top flange upper surface

Table 4.13 Residual stresses for Specimen 6

Location	Residual stresses (ksi)		
	σ_{11}	σ_{22}	σ_{12}
A	-27.5	-5.3	1.1
B	-37.5	-26.0	-0.9
C	-34.9	-24.7	-2.0
D	-21.4	9.3	-0.7

A through D: Top flange upper surface

Table 4.14 Residual stresses for Specimen 7

Location	Residual stresses (ksi)		
	σ_{11}	σ_{22}	σ_{12}
A	-27.6	-8.0	-3.3
B	-33.5	-27.7	-1.0
C	-30.4	-22.4	2.7
D	-24.9	-0.2	0.0
A'	-5.7	3.1	7.7
B'	-25.6	-16.1	1.1
C'	NA	NA	NA

A through D: Top flange upper surface
A' through C': Top flange lower surface

Table 4.14 Residual stresses for Specimen 7 (continued)

Location	Residual stresses (ksi)		
	σ_{11}	σ_{22}	σ_{12}
E	-5.5	-8.4	-14.5
F	-4.2	-19.1	-3.2
G	8.5	-8.3	1.0
H	6.9	-0.6	-2.5
I	-4.8	-1.9	-1.5
J	-17.3	-6.8	-0.5
K	2.2	-2.9	0.8
E'	-12.3	-16.3	-13.7
F'	0.6	-14.2	-0.8
G'	-5.0	-17.8	1.1
H'	-11.7	-10.7	-2.1
I'	-12.4	-17.8	-1.7
J'	-3.7	-11.4	-0.2
K'	-8.8	-6.3	-1.1

E through K: Web west side
E' through K': Web east side

Table 4.15 Strain gage locations

Specimen	a (in)	b (in)	c (in)	d (in)
3	4 33/64	2 22/64	3 63/64	4 40/64
4	4 56/64	2 2/64	2 57/64	6 22/64
5	5 4/64	2 40/64	4 18/64	5 10/64
6	7 12/64	3	5 25/64	9 32/64
7	6	2 32/64	4 18/64	7 28/64

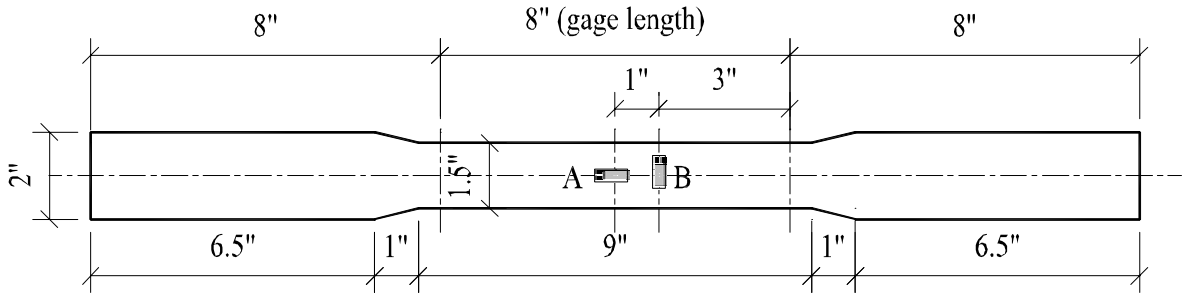

Figure 4.1 Tensile coupon dimensions
(1" = 1 in and 1' = 1 foot)

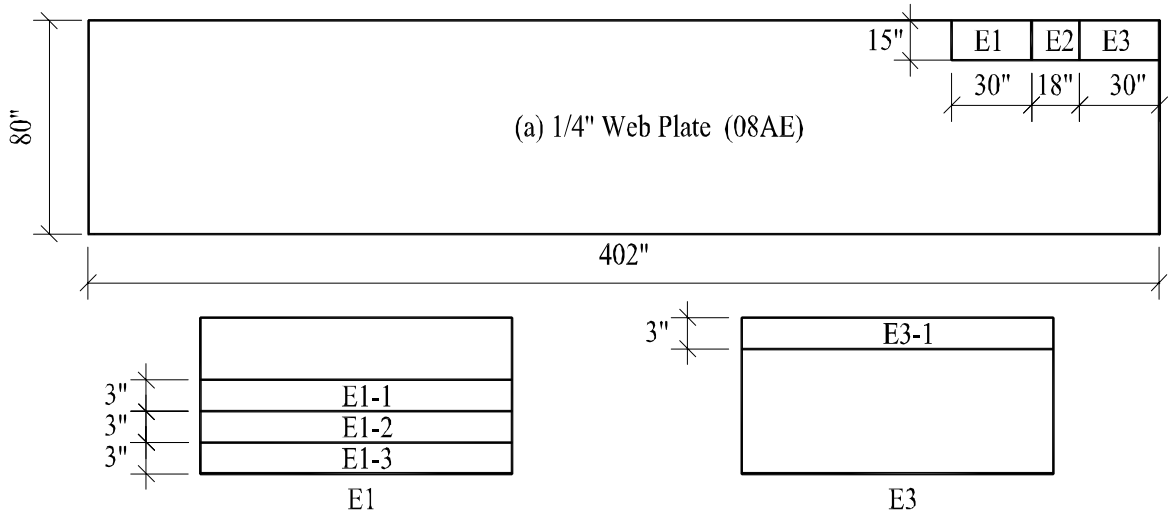

Figure 4.2 Tensile coupon locations
(1" = 1 in and 1' = 1 foot)

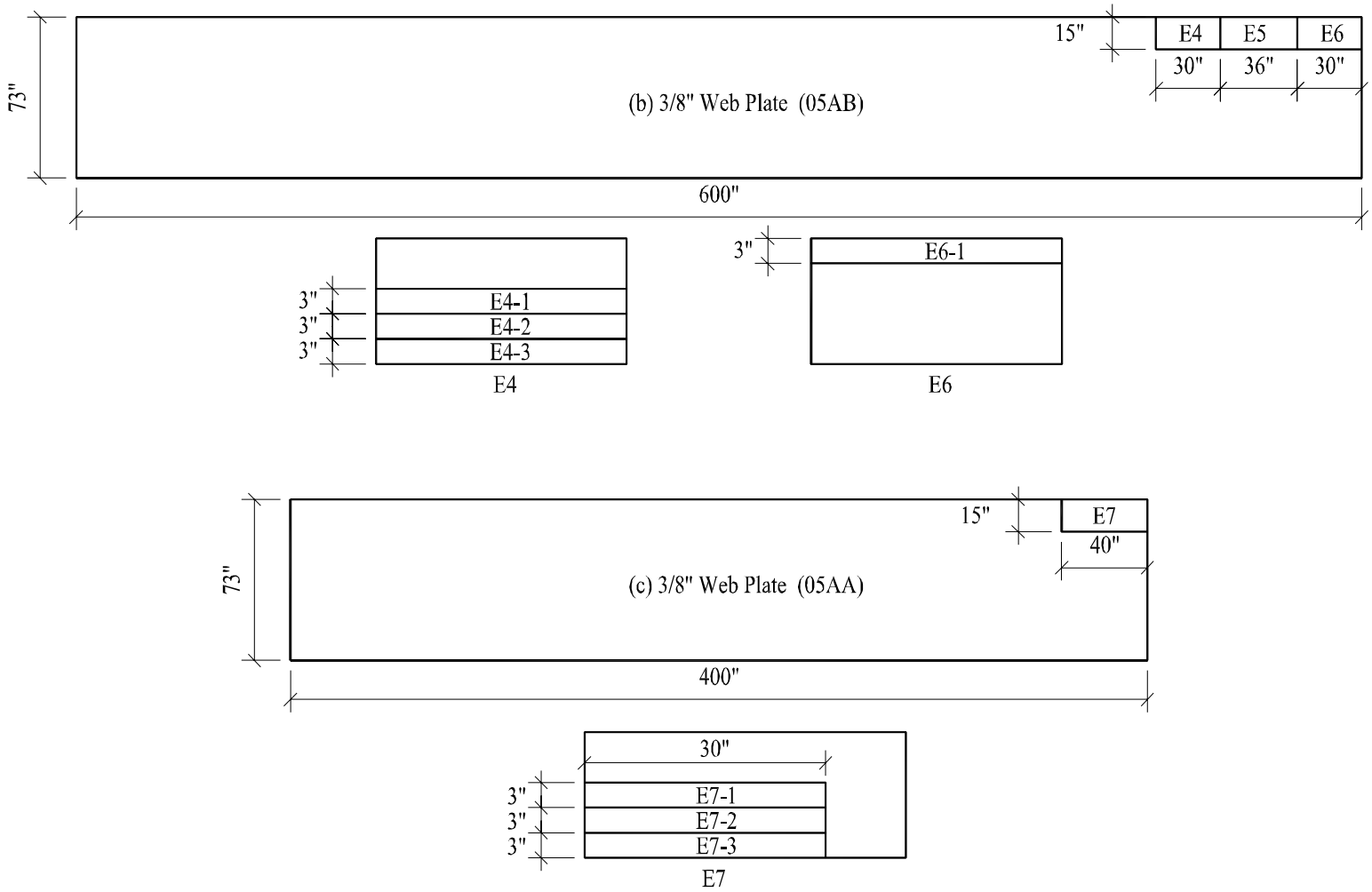

Figure 4.2 Tensile coupon locations (continued)
(1" = 1 in and 1' = 1 foot)

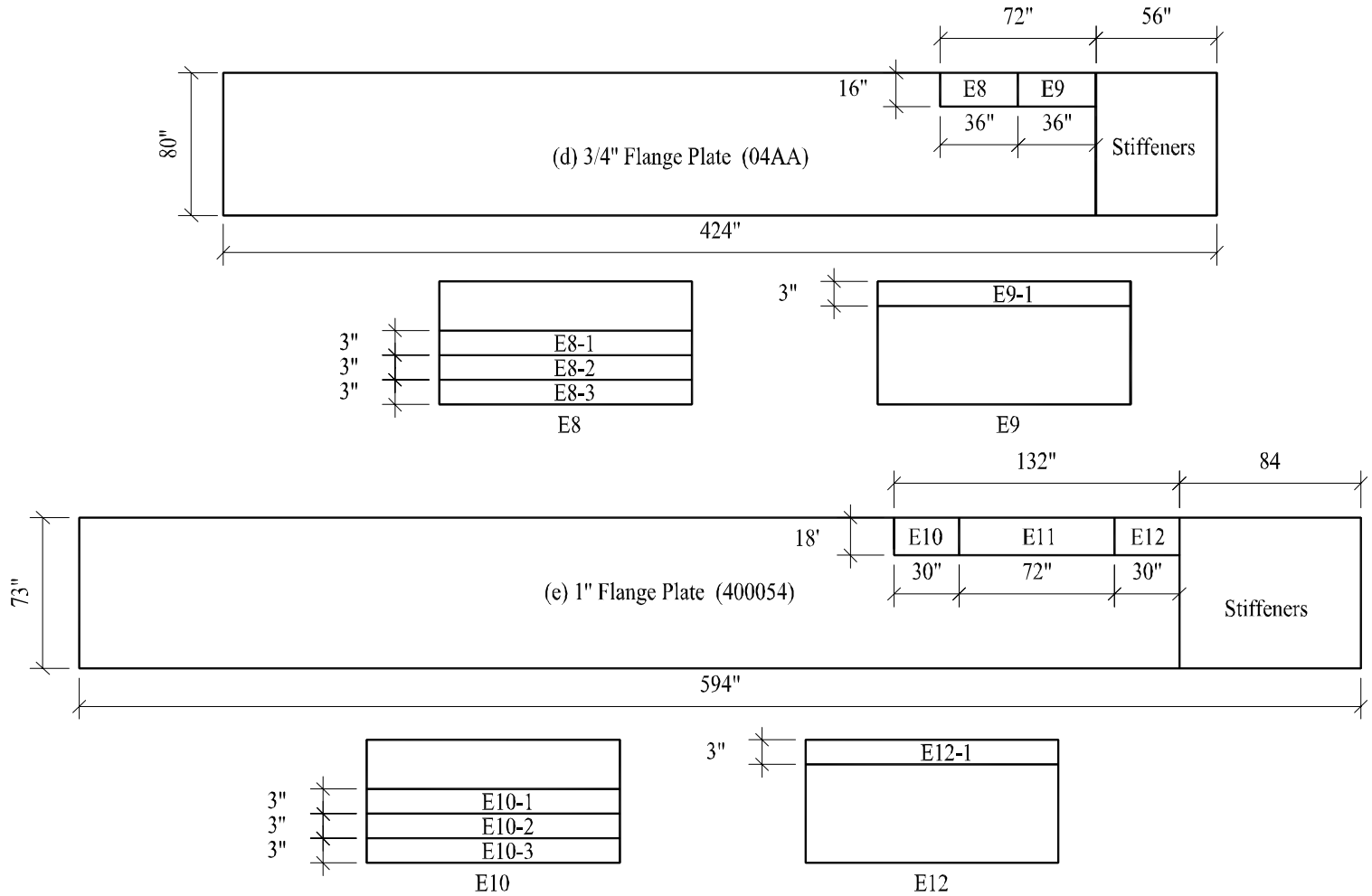

Figure 4.2 Tensile coupon locations (continued)
(1" = 1 in and 1' = 1 foot)

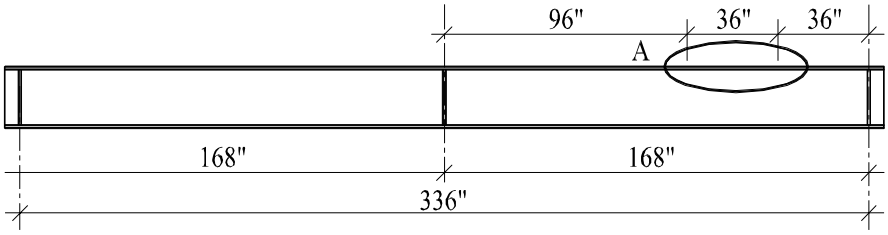

(a) Tensile coupon location

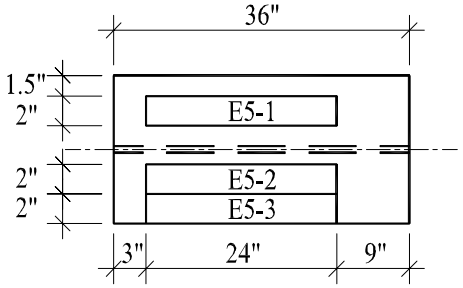

(b) Tensile coupon locations across the top flange

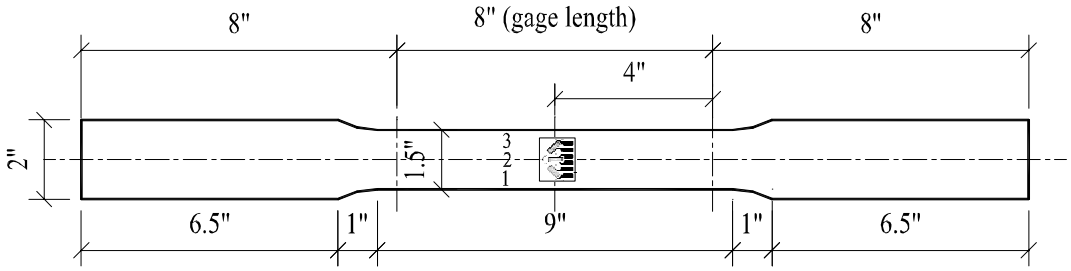

(c) Tensile coupon dimensions

Figure 4.3 Tensile coupons cut from Specimen 5
(1" = 1 in and 1' = 1 foot)

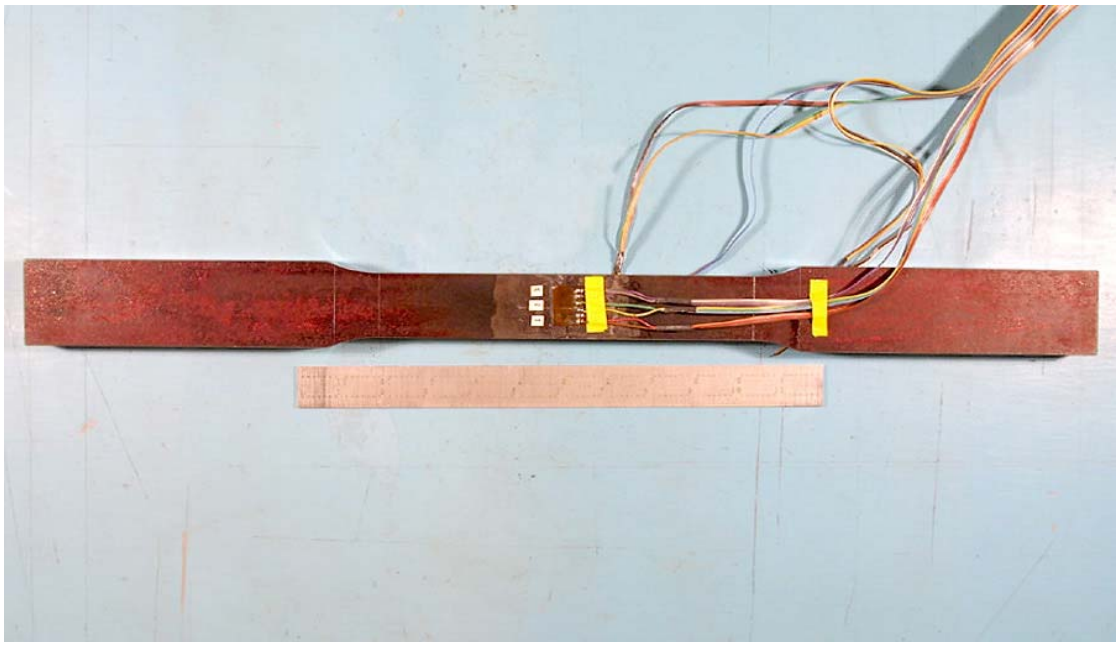

(a) Tensile coupon layout

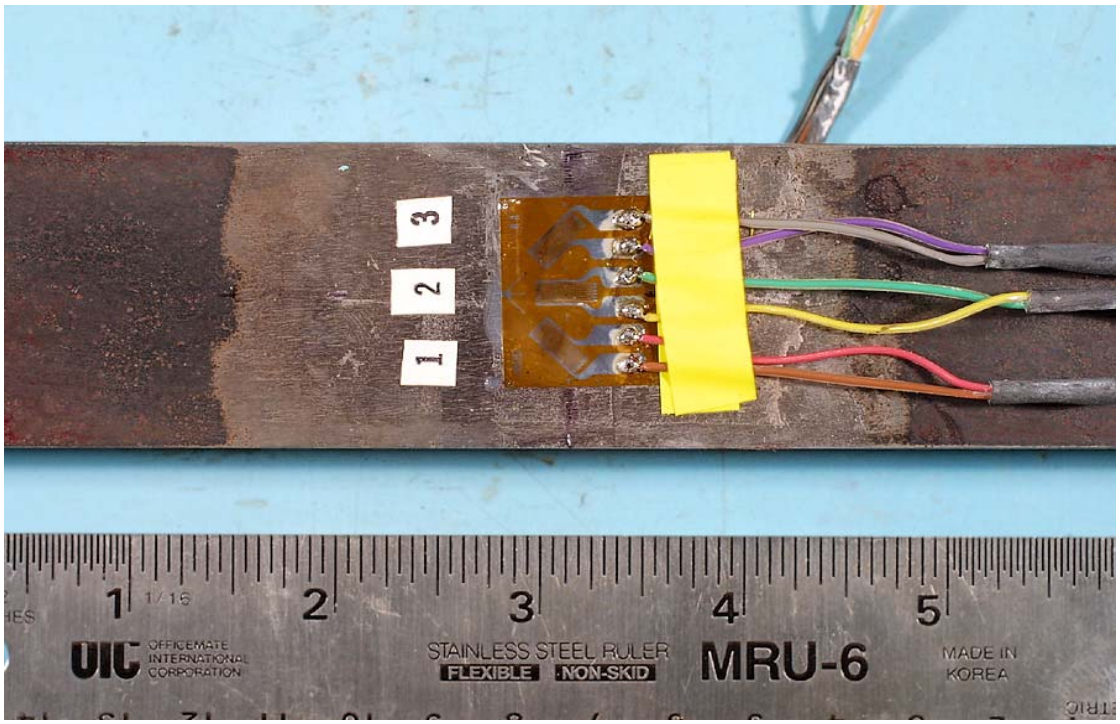

(b) Details at the middle of the tensile coupon

Figure 4.4 Tensile coupon Specimen E5-1

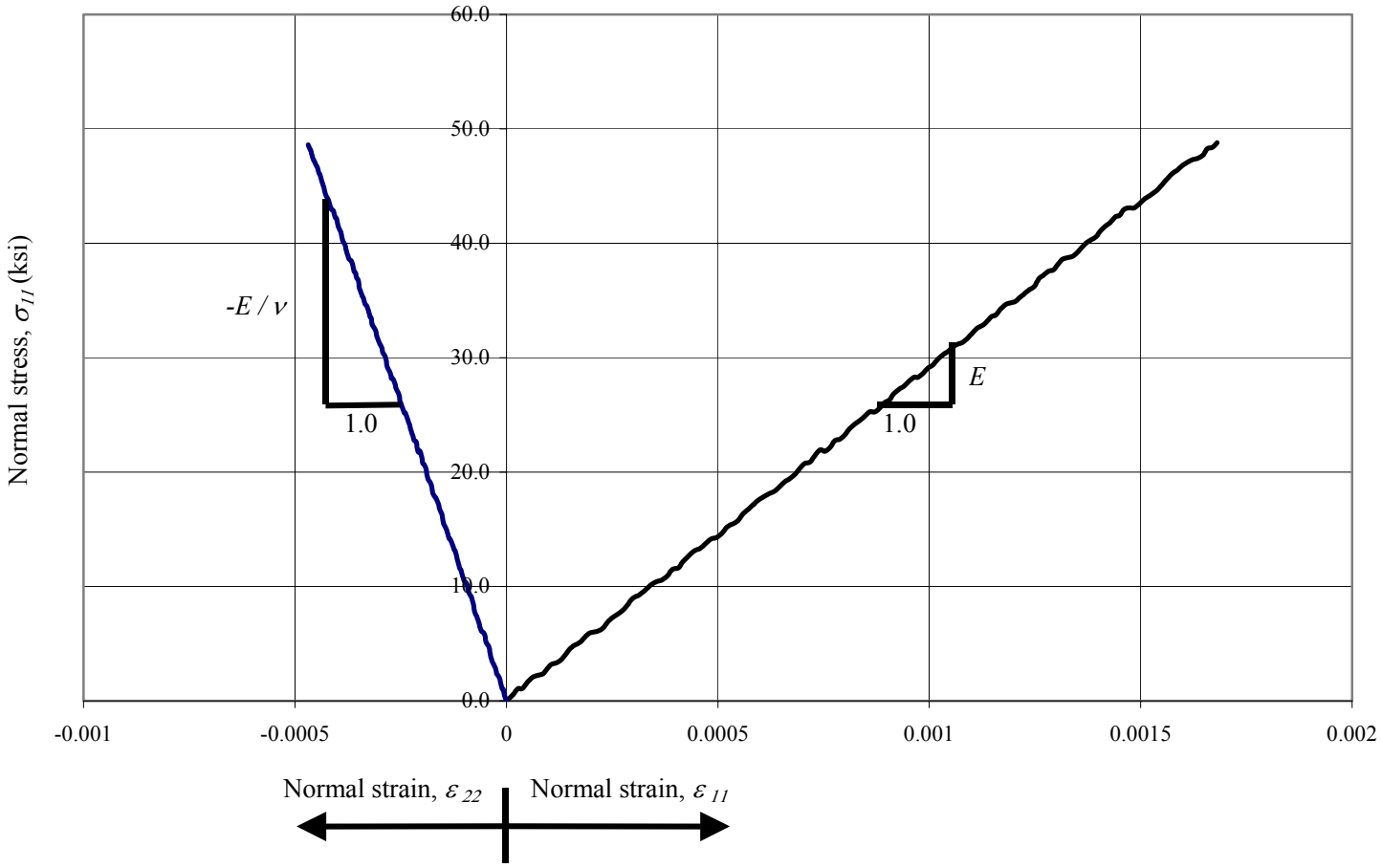

Figure 4.5 Material constants from tensile coupon test (Specimen E1-2)

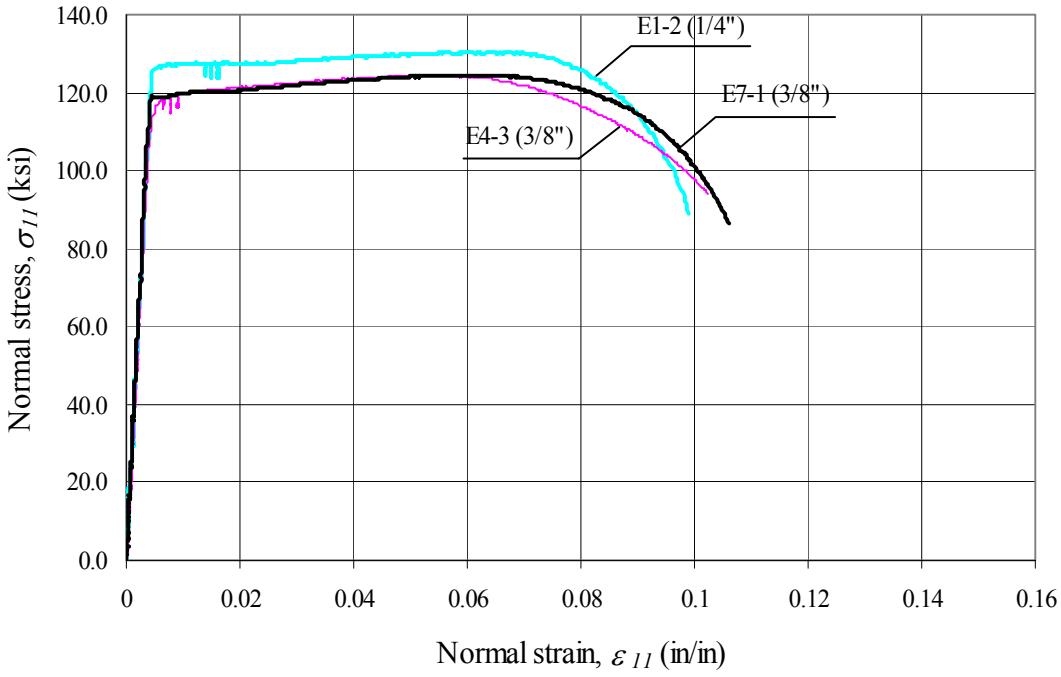

Figure 4.6 Stress versus strain for HPS-100W steel web plates

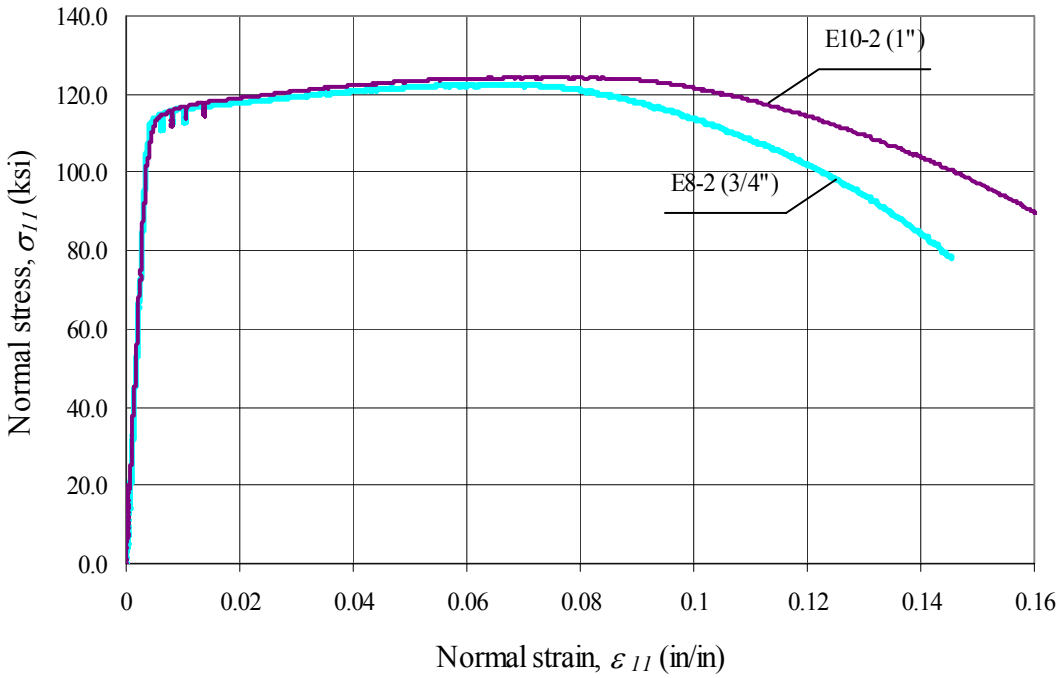

Figure 4.7 Stress versus strain for HPS-100W steel flange plates

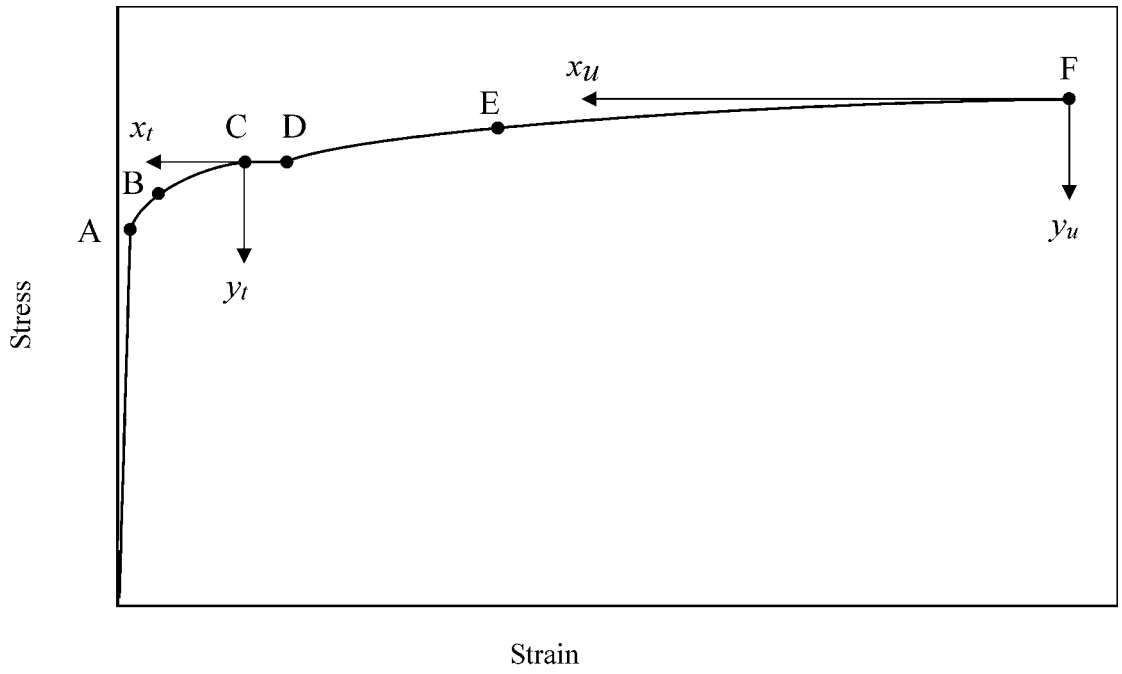

Figure 4.8 Stress-strain model

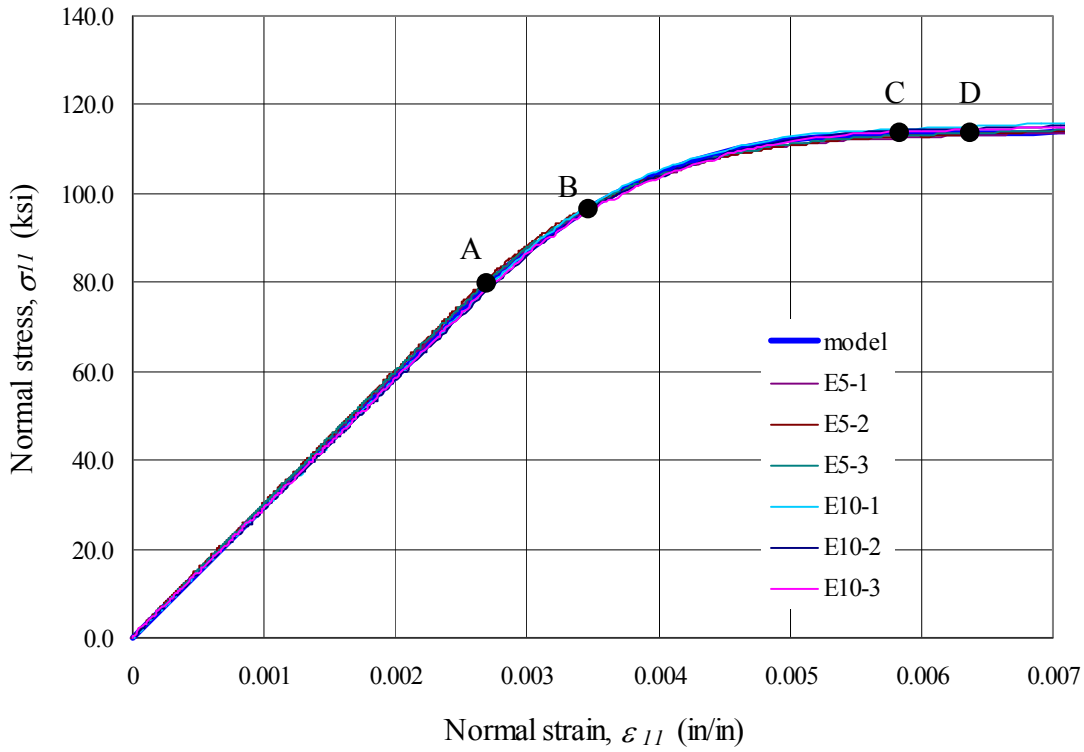

Figure 4.9 Measured and model for stress versus strain of 1 in flange plate (showing the points used in developing the model)

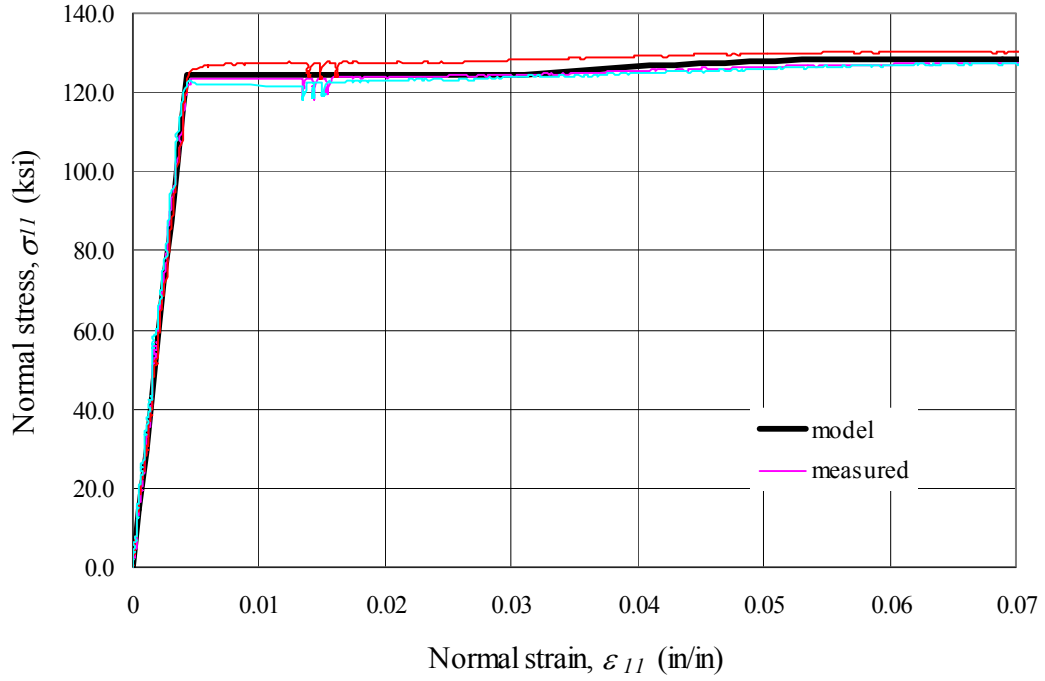

Figure 4.10 Measured and model for stress versus strain of 1/4 in web plate

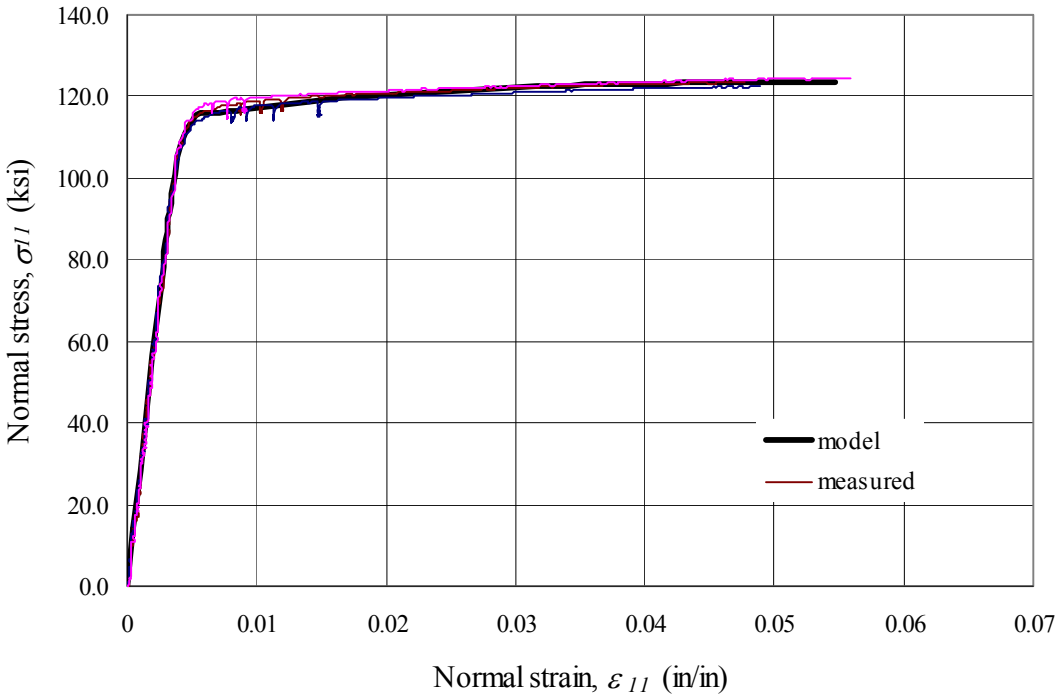

Figure 4.11 Measured and model for stress versus strain of 3/8 in web plate

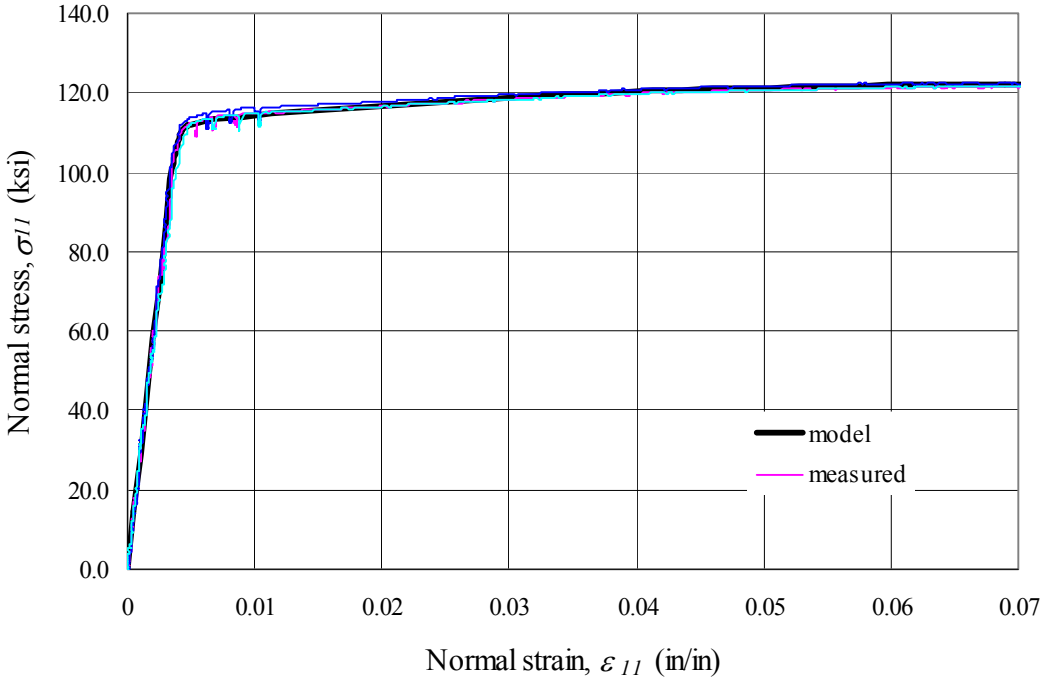

Figure 4.12 Measured and model for stress versus strain of 3/4 in flange plate

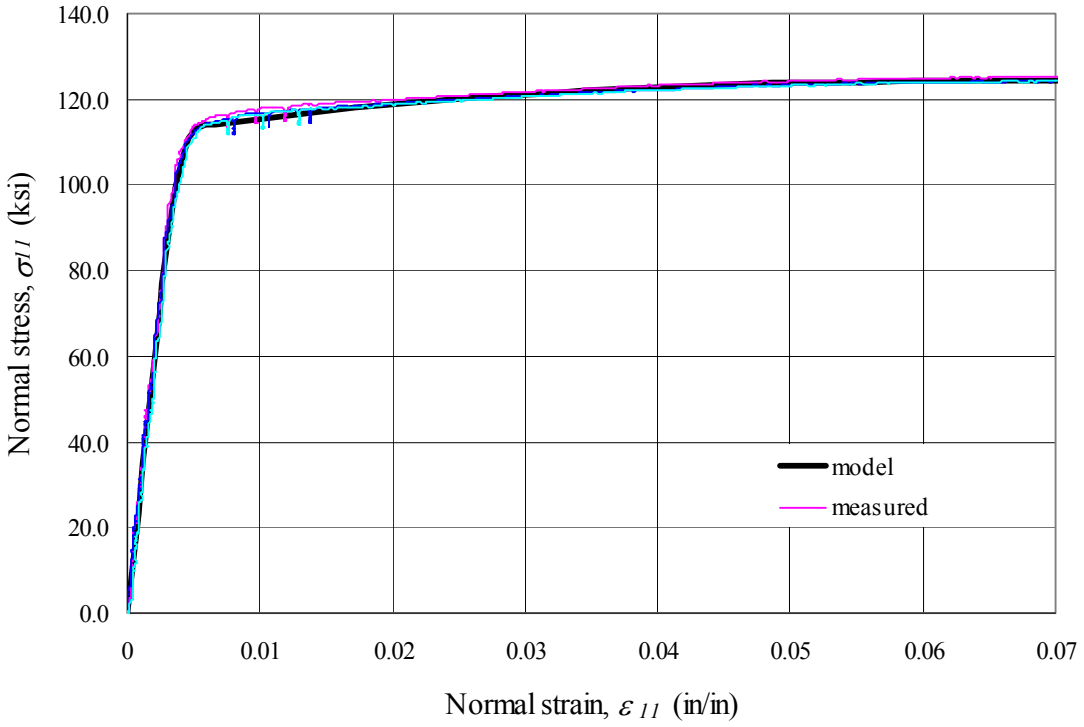

Figure 4.13 Measured and model for stress versus strain of 1 in flange plate

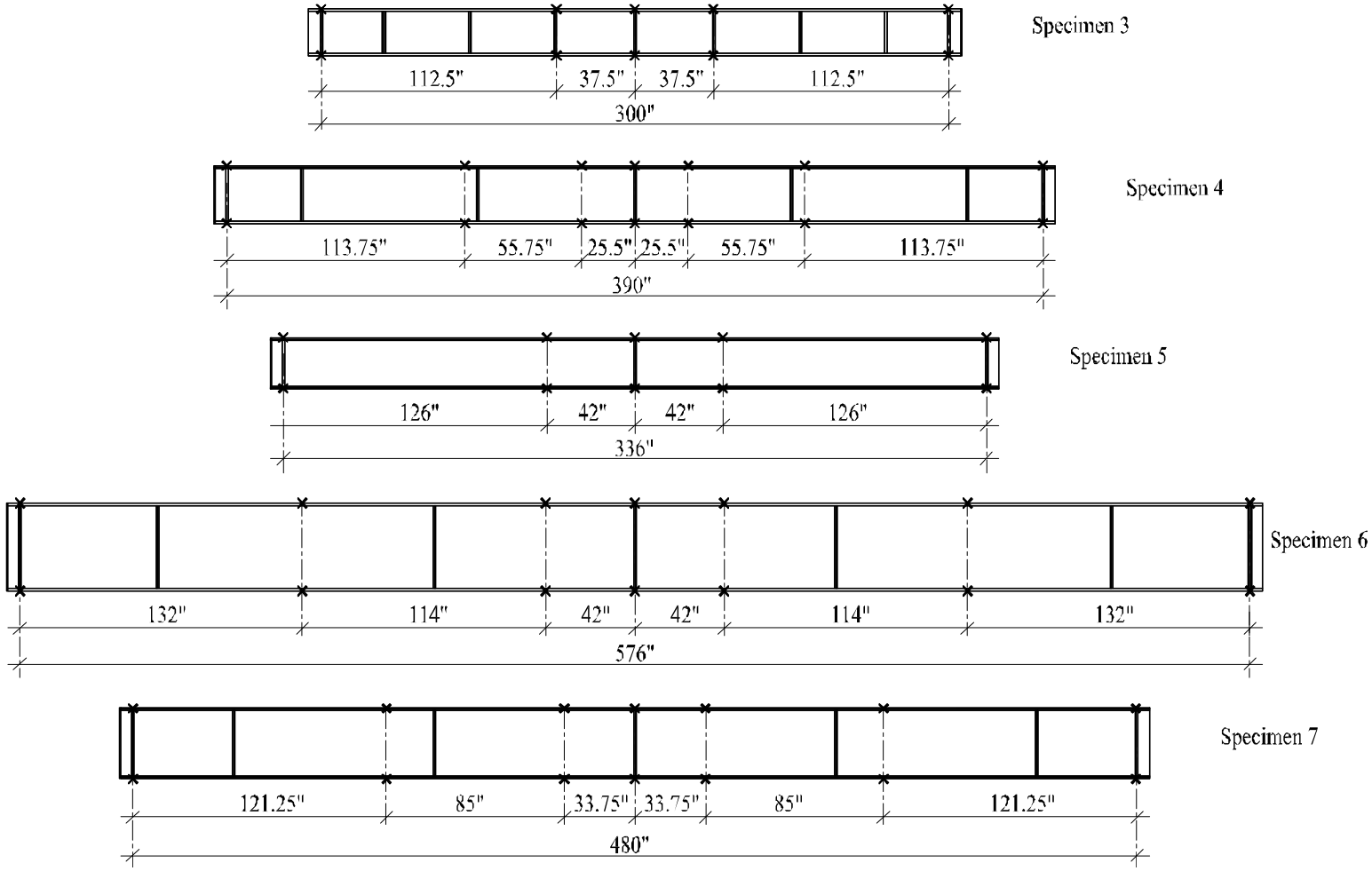

Figure 4.14 Lateral brace locations for experimental specimens
(1" = 1 in and 1' = 1 foot)

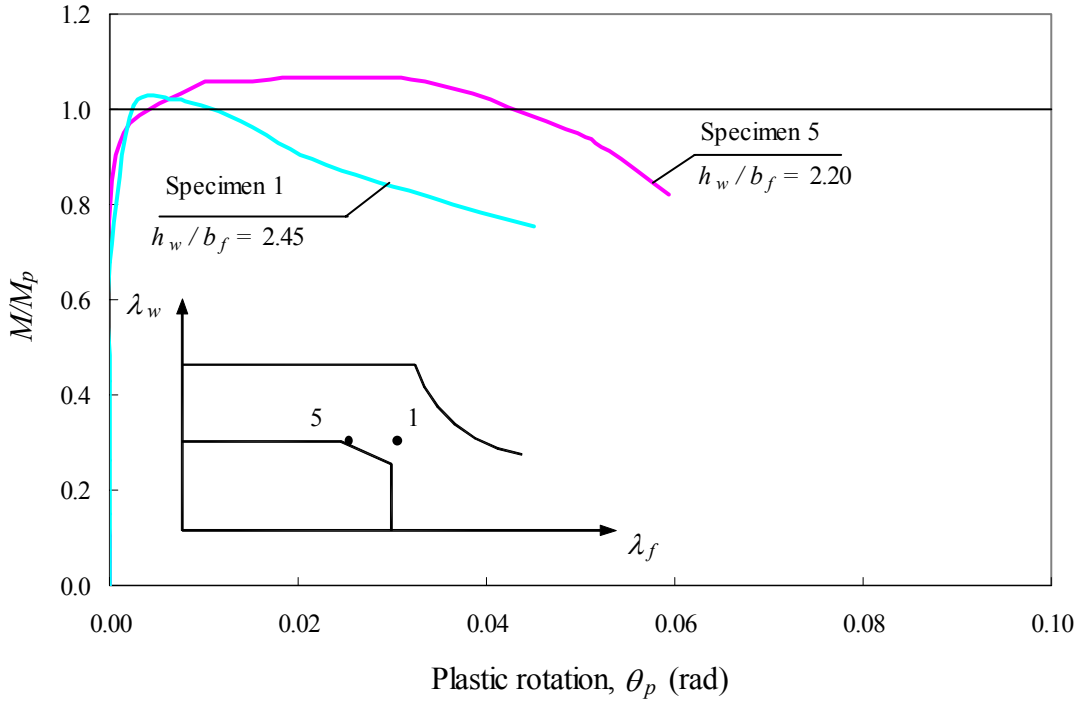

Figure 4.15 Comparison of Specimen 1 and Specimen 5

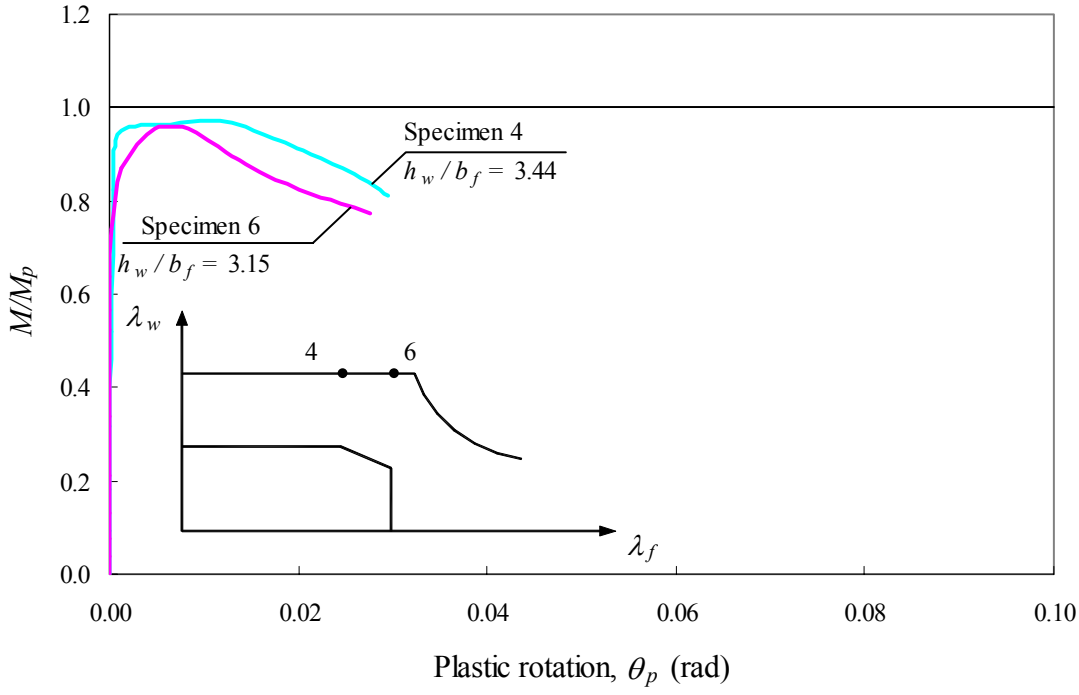

Figure 4.16 Comparison of Specimen 4 and Specimen 6

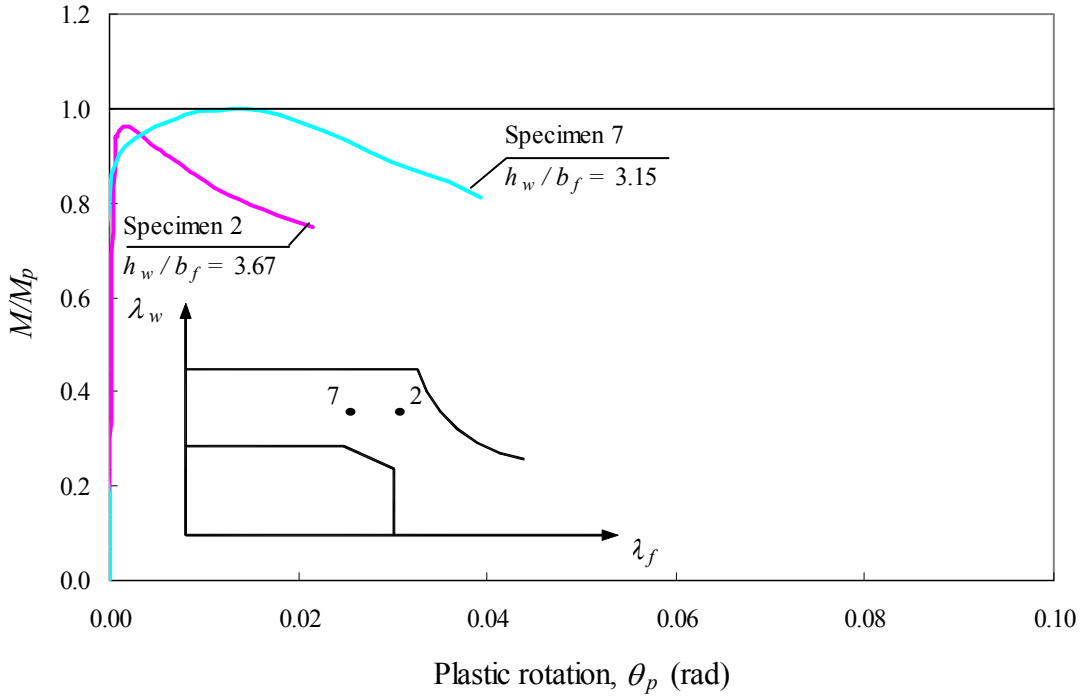

Figure 4.17 Comparison of Specimen 2 and Specimen 7

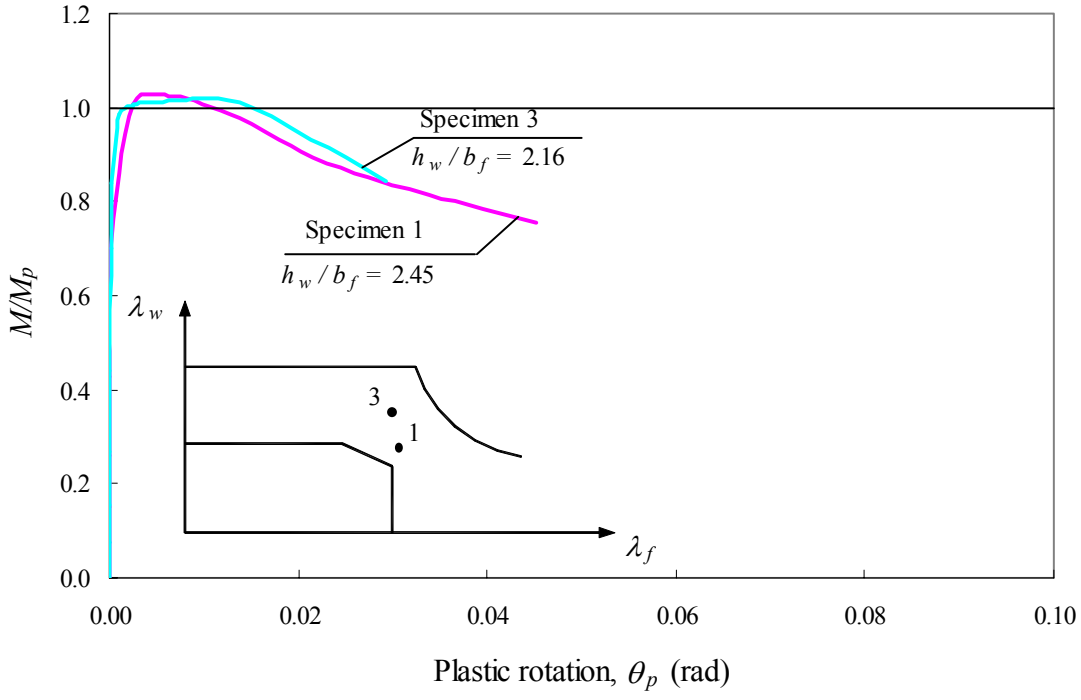

Figure 4.18 Comparison of Specimen 1 and Specimen 3

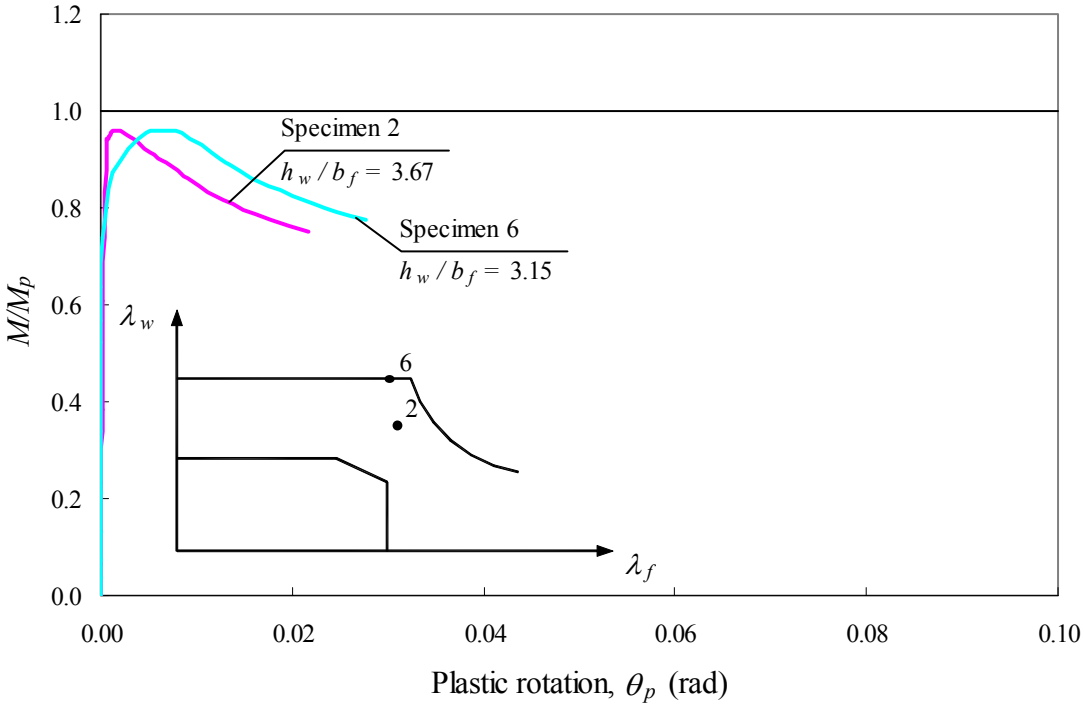

Figure 4.19 Comparison of Specimen 2 and Specimen 6

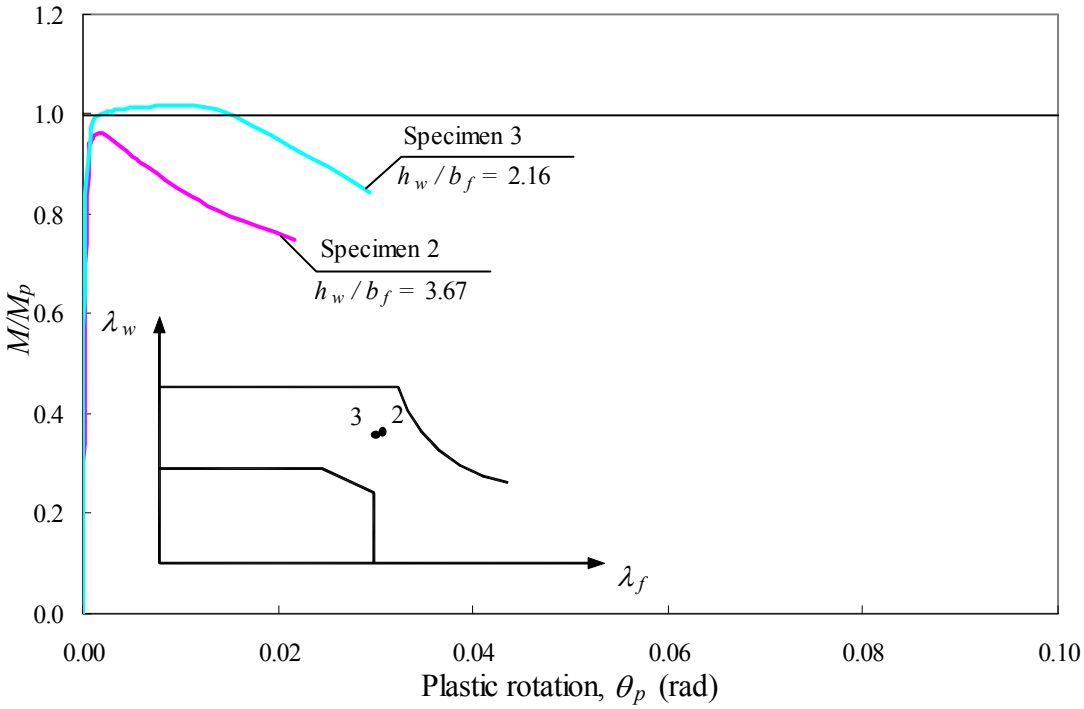

Figure 4.20 Comparison of Specimen 2 and Specimen 3

Specimen 3

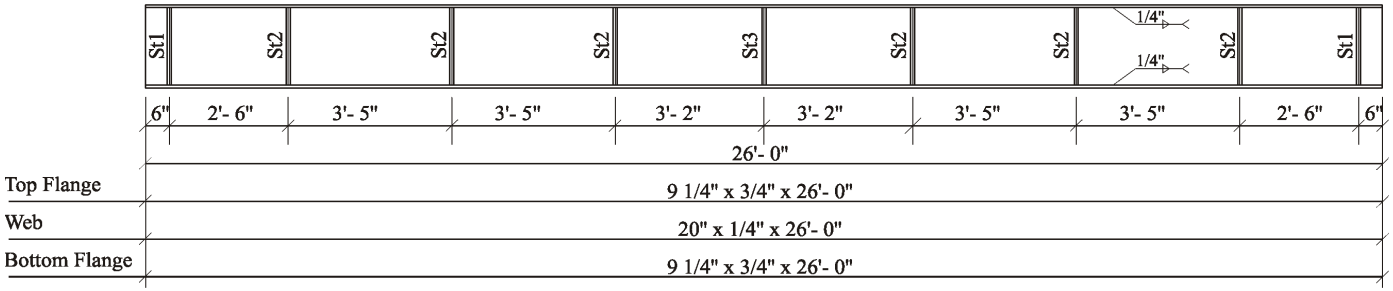

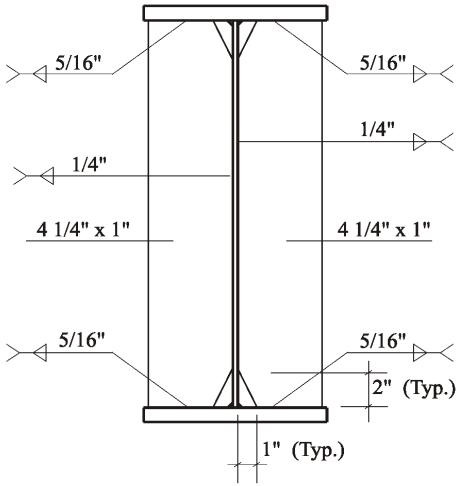

Bearing Stiffener St1

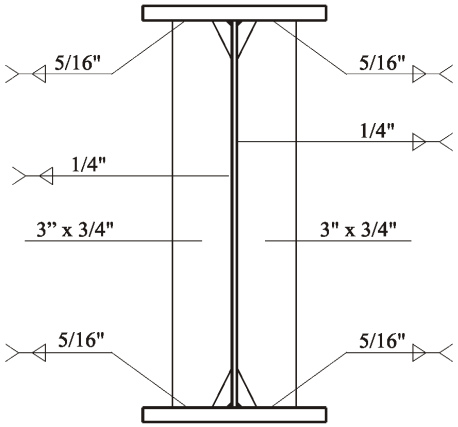

Intermediate Stiffener St2

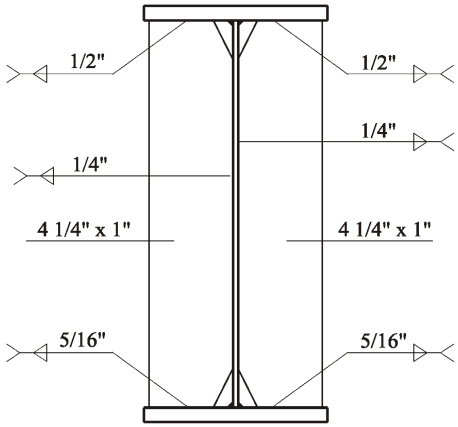

Load Stiffener St3

Figure 4.21 Experimental specimen 3
(1" = 1 in and 1' = 1 foot)

Specimen 4

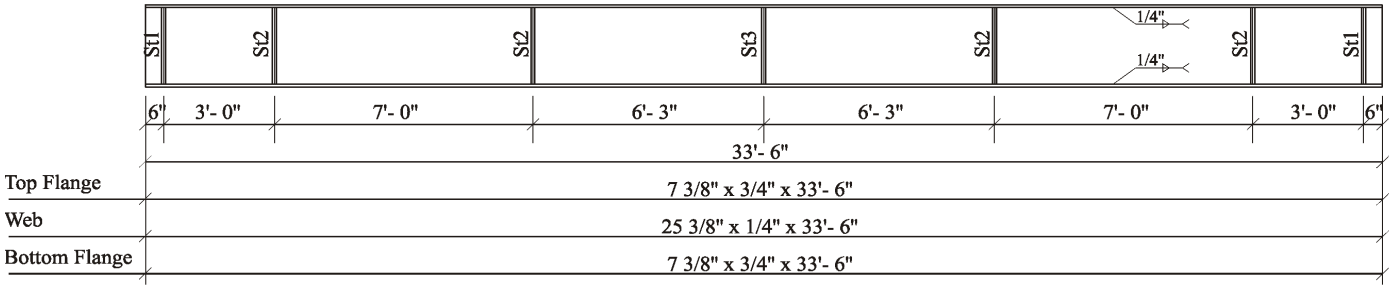

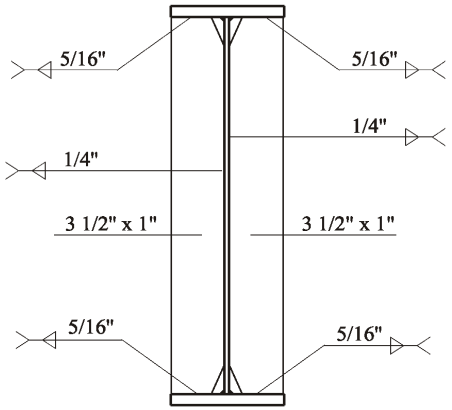

Bearing Stiffener St1

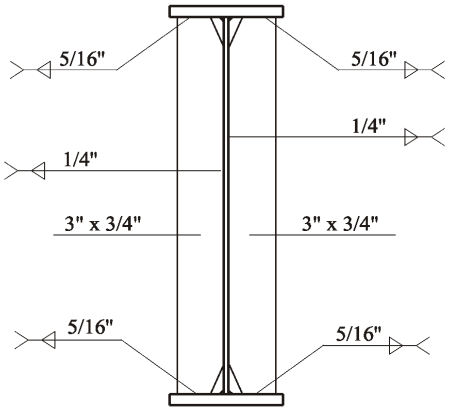

Intermediate Stiffener St2

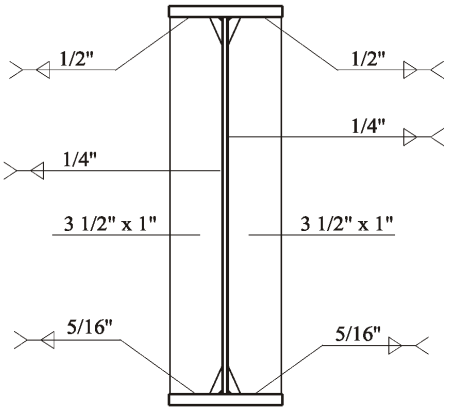

Load Stiffener St3

Figure 4.22 Experimental specimen 4
(1" = 1 in and 1' = 1 foot)

Specimen 5

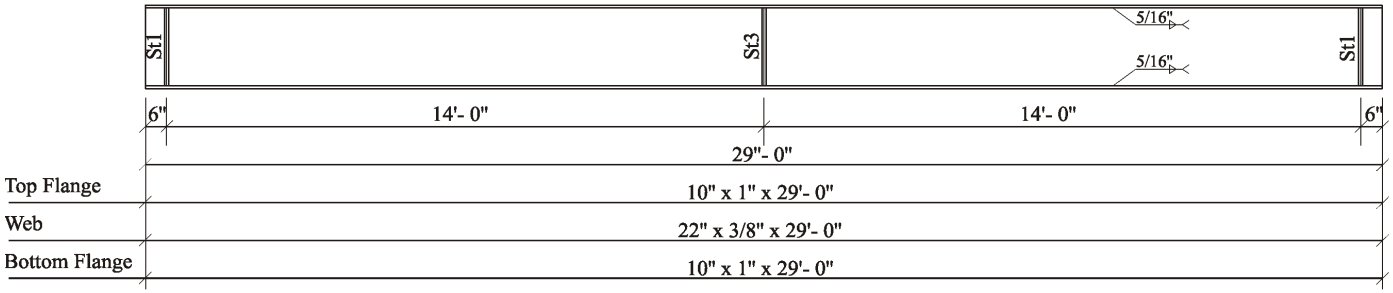

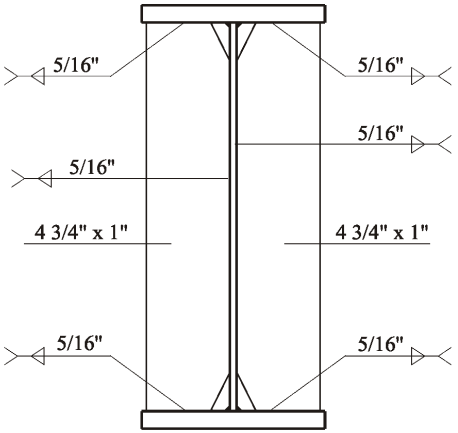

Bearing Stiffener St1

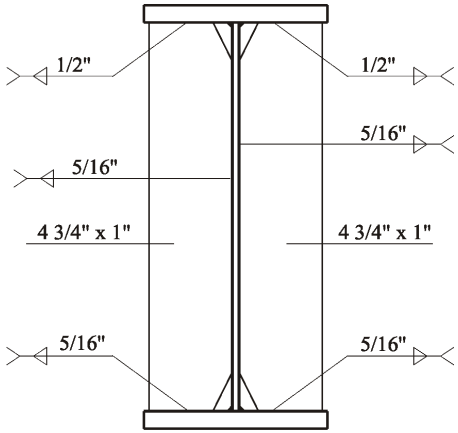

Load Stiffener St3

Figure 4.23 Experimental specimen 5
(1" = 1 in and 1' = 1 foot)

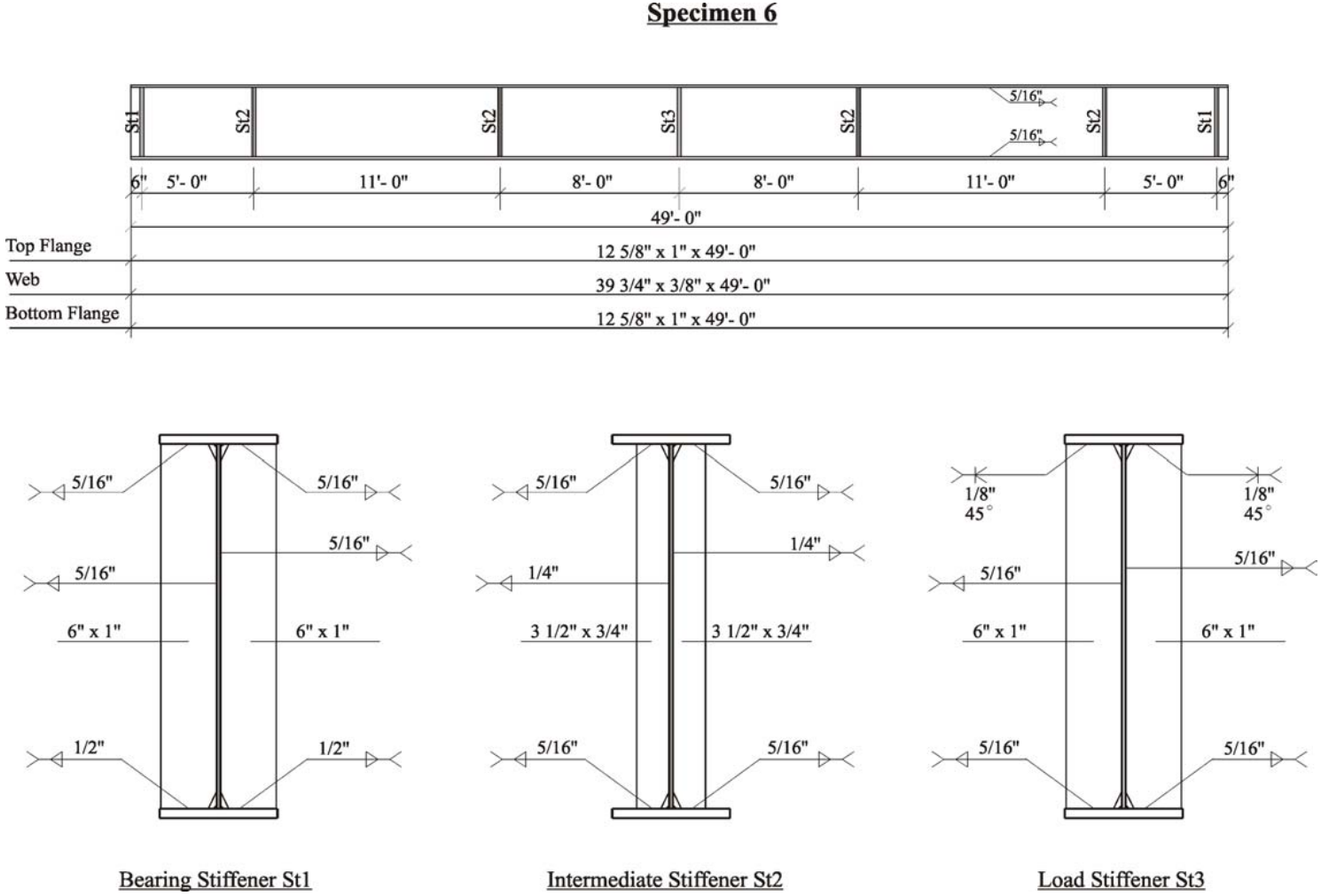

Figure 4.24 Experimental specimen 6
(1" = 1 in and 1' = 1 foot)

Specimen 7

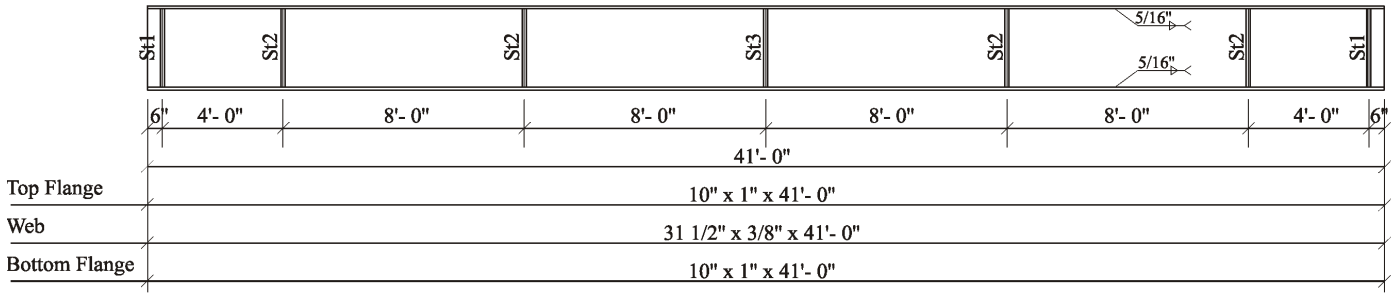

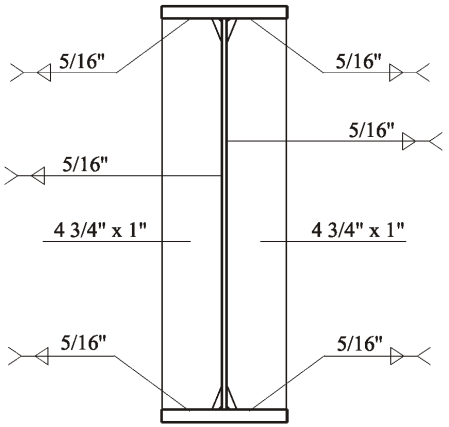

Bearing Stiffener St1

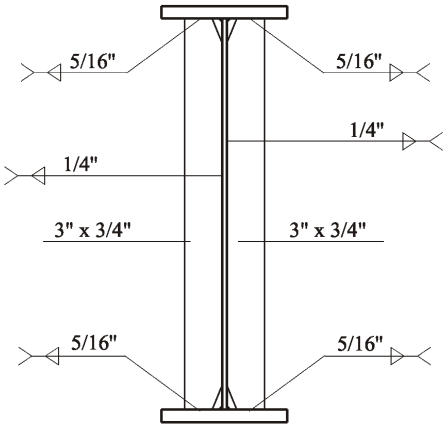

Intermediate Stiffener St2

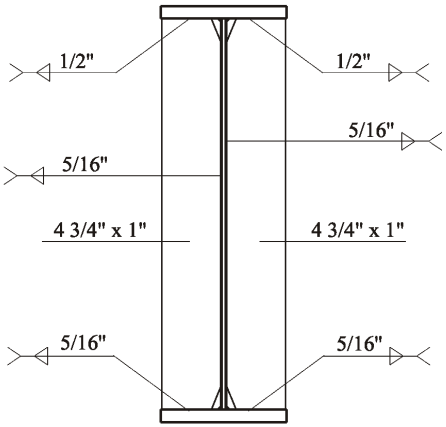

Load Stiffener St3

Figure 4.25 Experimental specimen 7
(1" = 1 in and 1' = 1 foot)

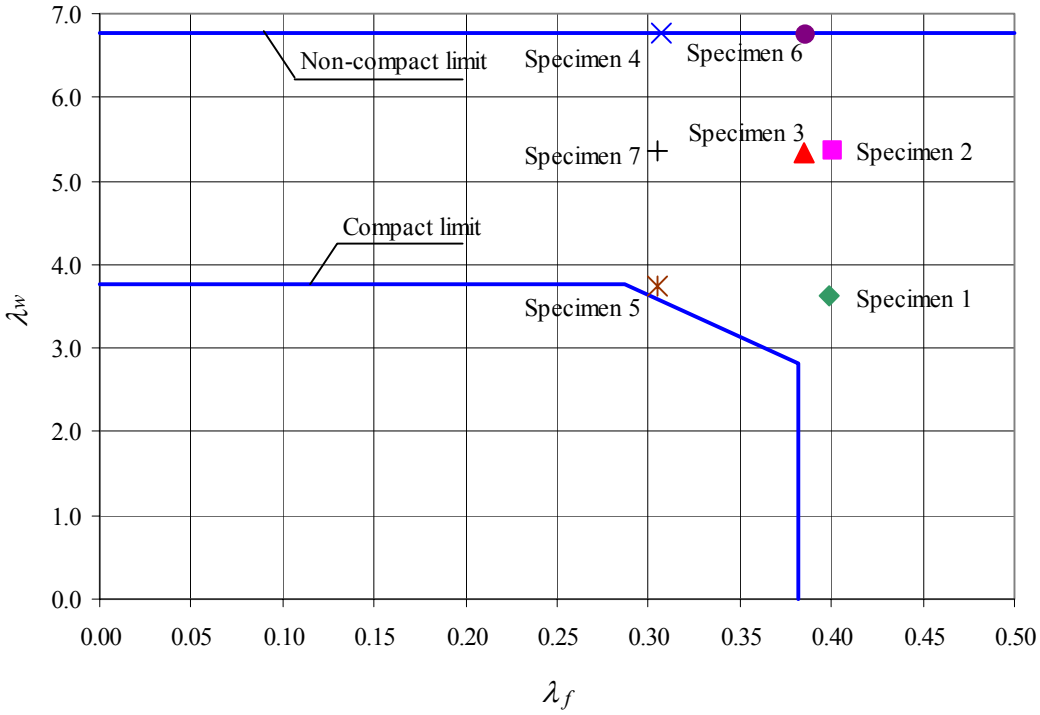

Figure 4.26 Actual flange and web slenderness

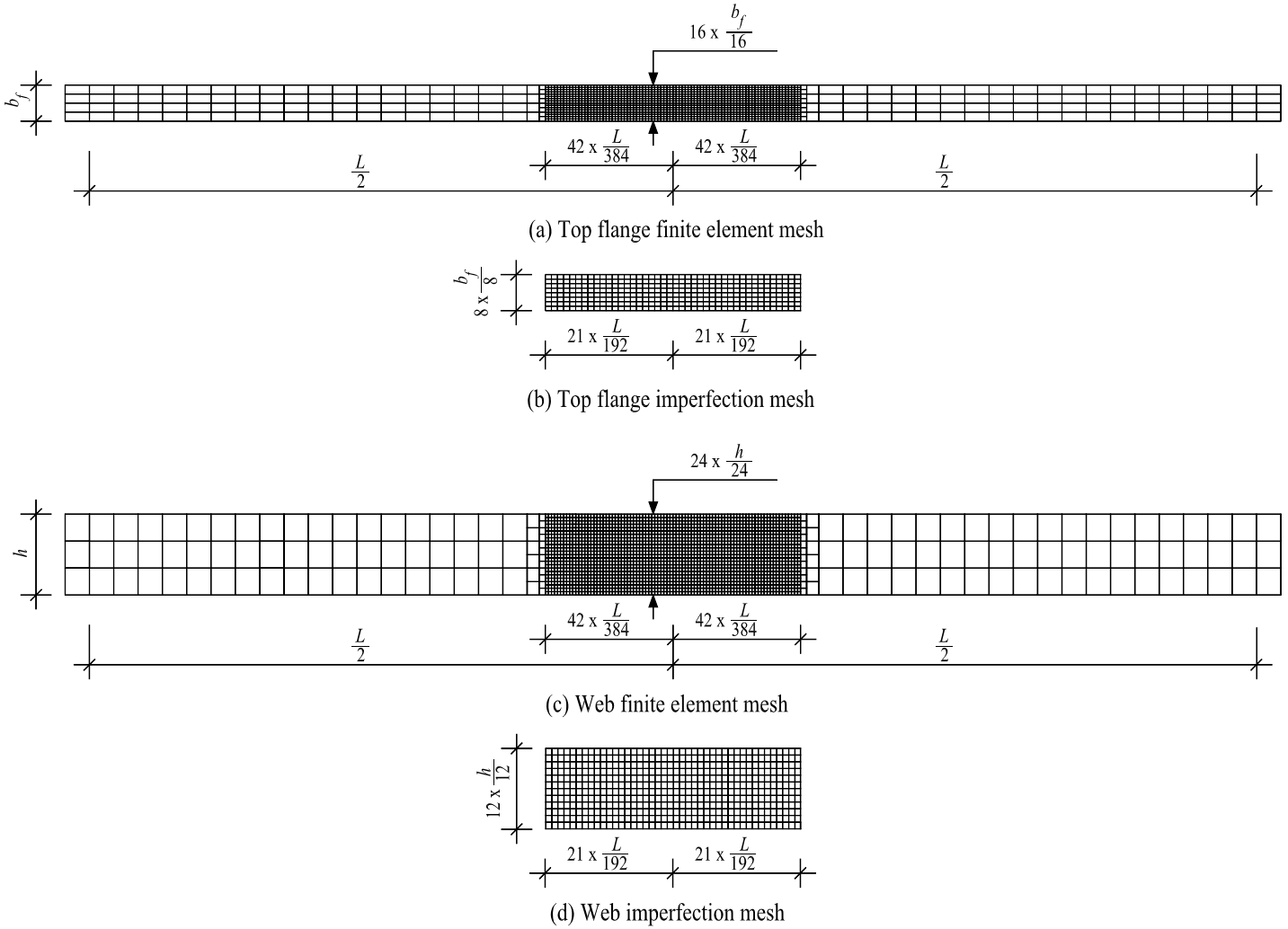

Figure 4.27 Imperfection measurement locations with reference to finite element mesh

Figure 4.28 Flange imperfection measurements using 1485HP laser level

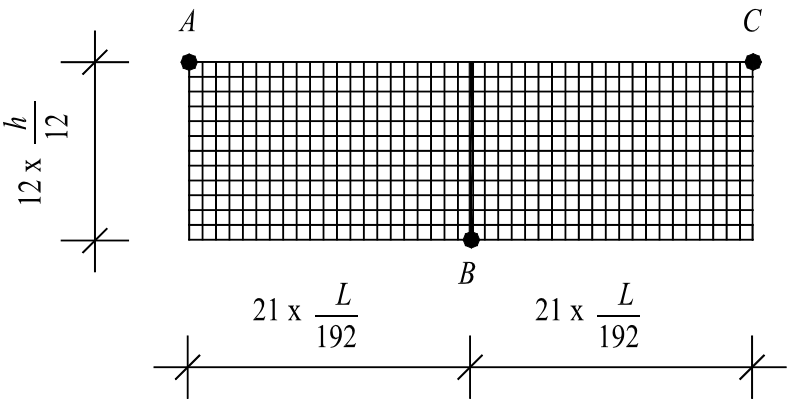

(a) Web imperfection amplitude with reference to plane through points A, B, and C

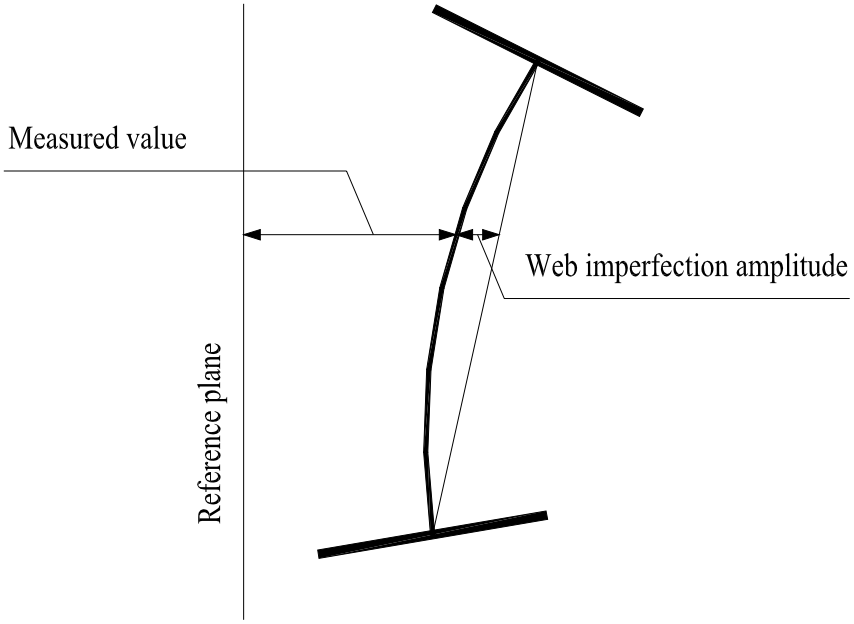

(b) Web imperfection amplitude with reference to line through intersection with flanges

Figure 4.29 Different web imperfection amplitude definitions

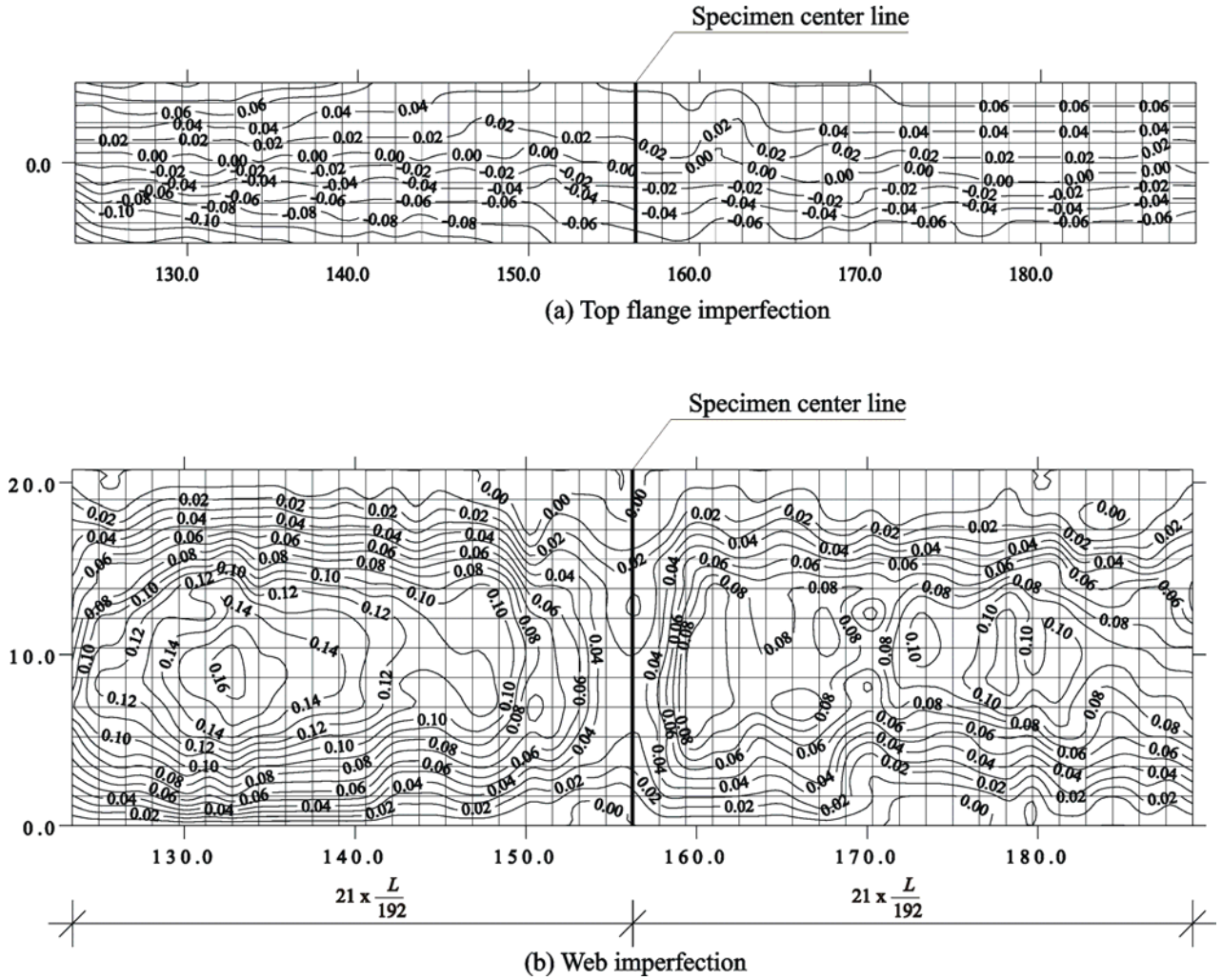

Figure 4.30 Specimen 3 top flange and web imperfections

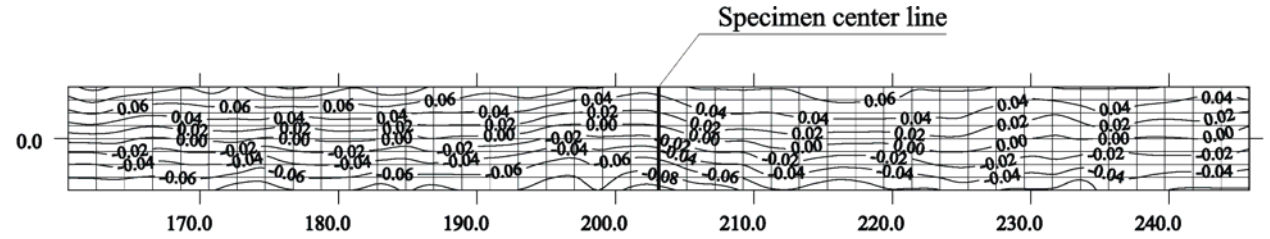

(a) Top flange imperfection

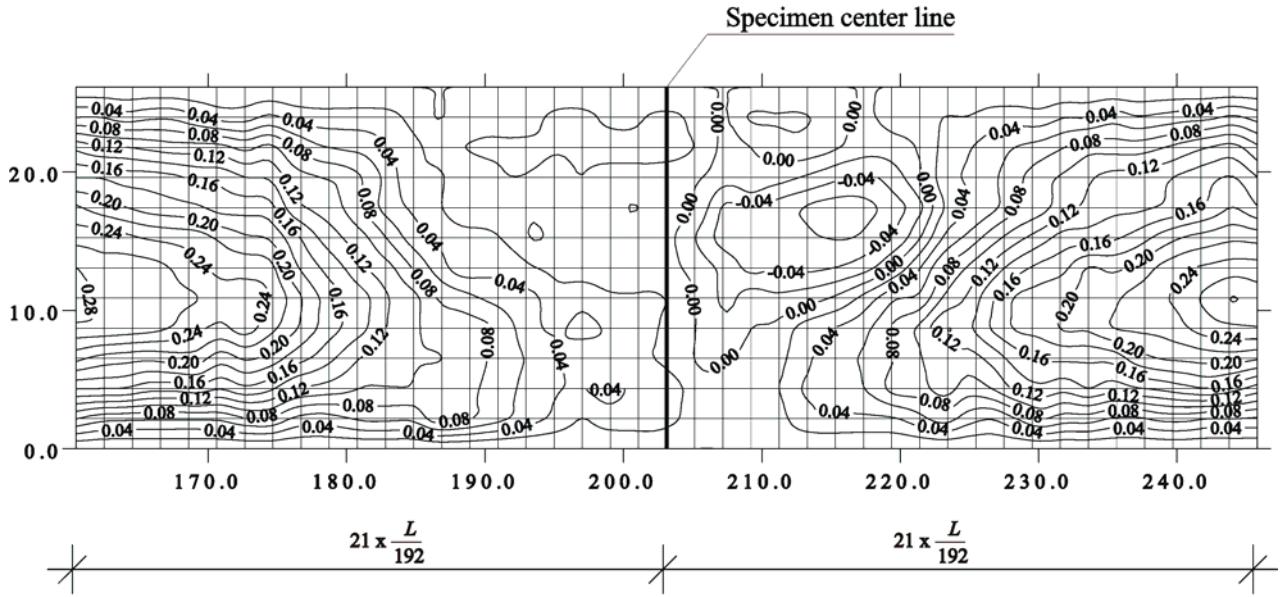

(b) Web imperfection

Figure 4.31 Specimen 4 top flange and web imperfections

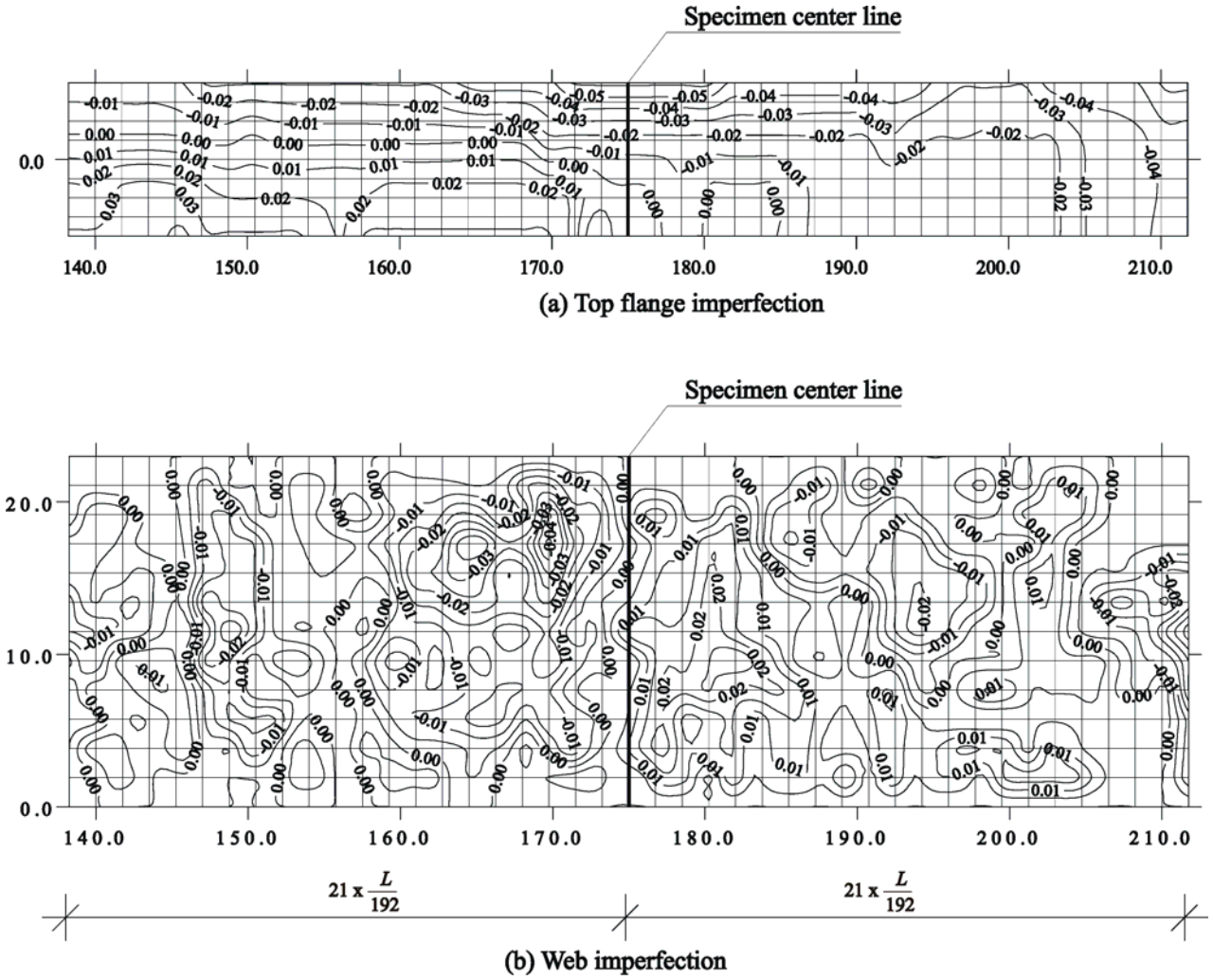

Figure 4.32 Specimen 5 top flange and web imperfections

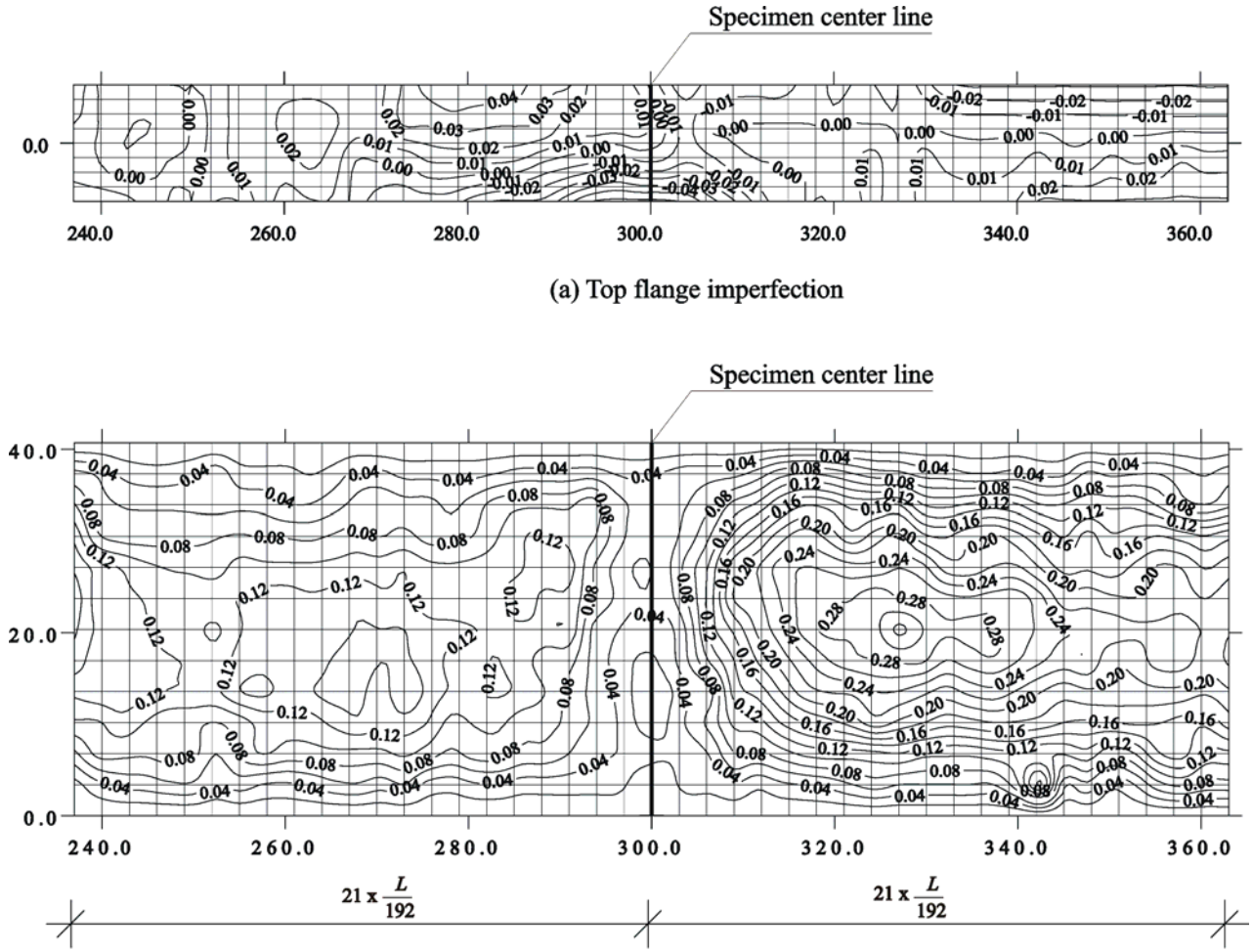

Figure 4.33 Specimen 6 top flange and web imperfections

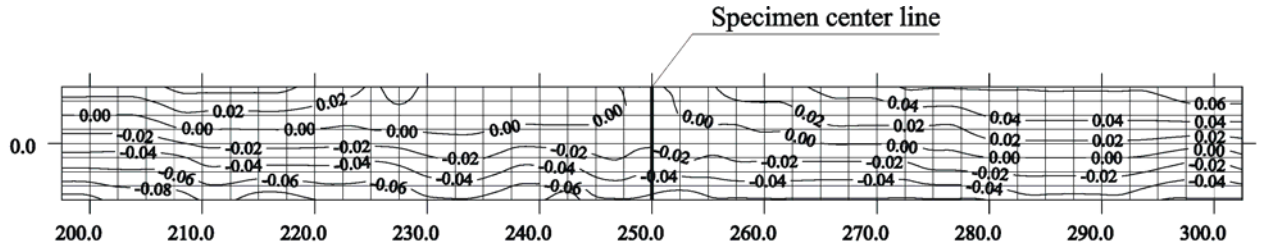

(a) Top flange imperfection

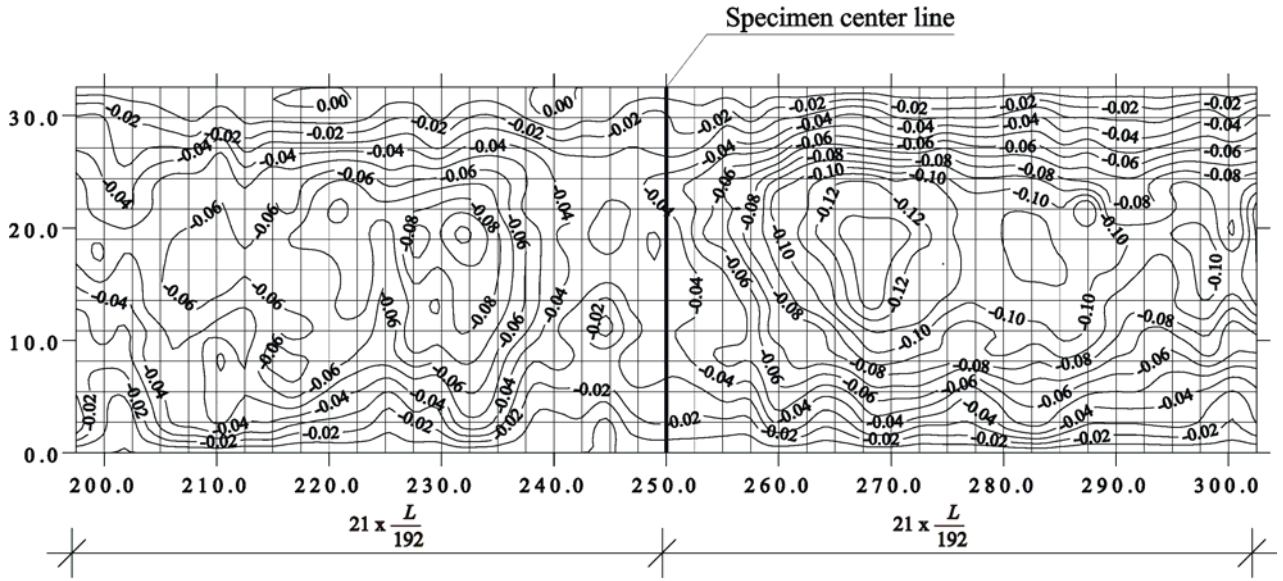

(b) Web imperfection

Figure 4.34 Specimen 7 top flange and web imperfections

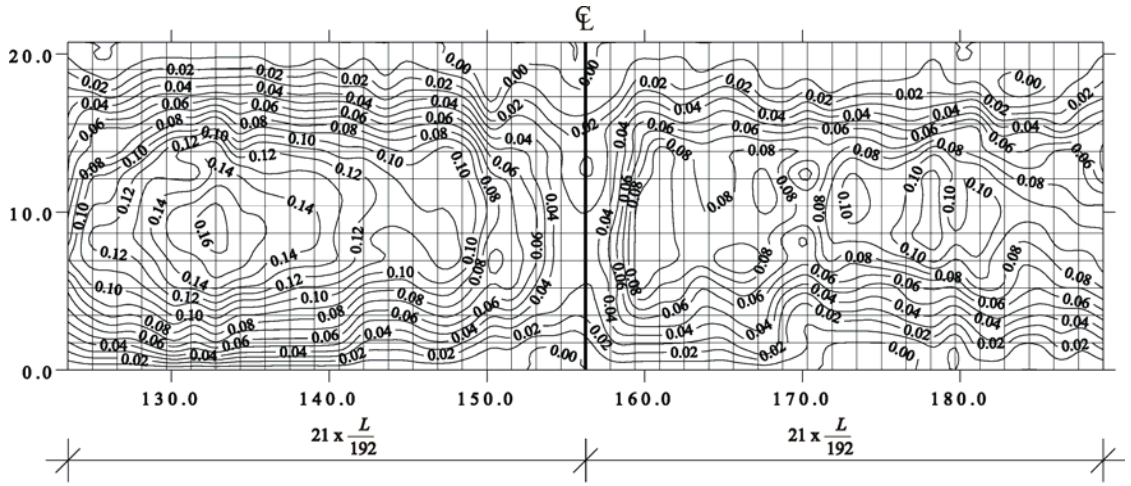

(a) Contour of web imperfection amplitude with reference to line through intersection with flanges

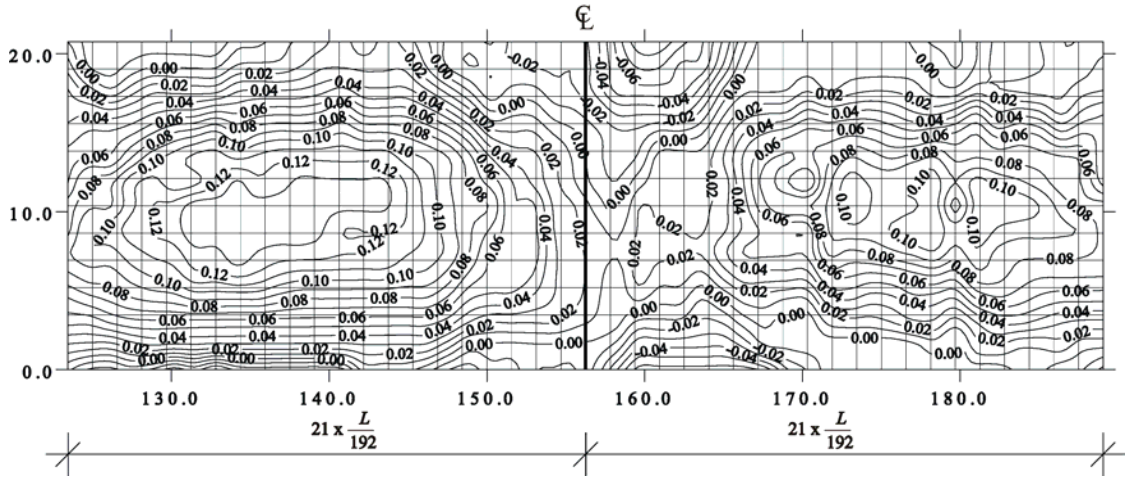

(b) Contour of web imperfection amplitude with reference to plane through points A, B, and C

Figure 4.35 Comparison of web imperfection amplitude using different reference definitions (Specimen 3)

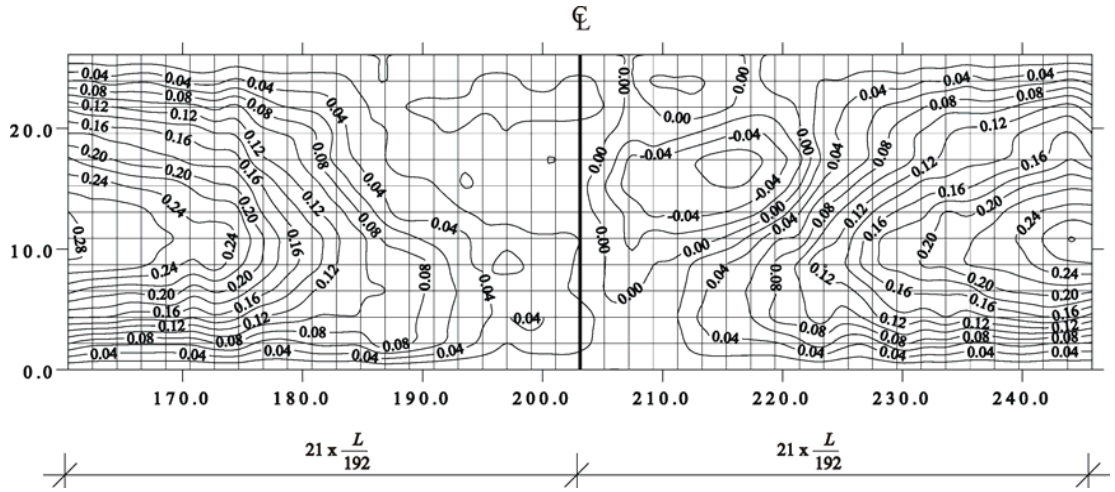

(a) Contour of web imperfection amplitude with reference to line through intersection with flanges

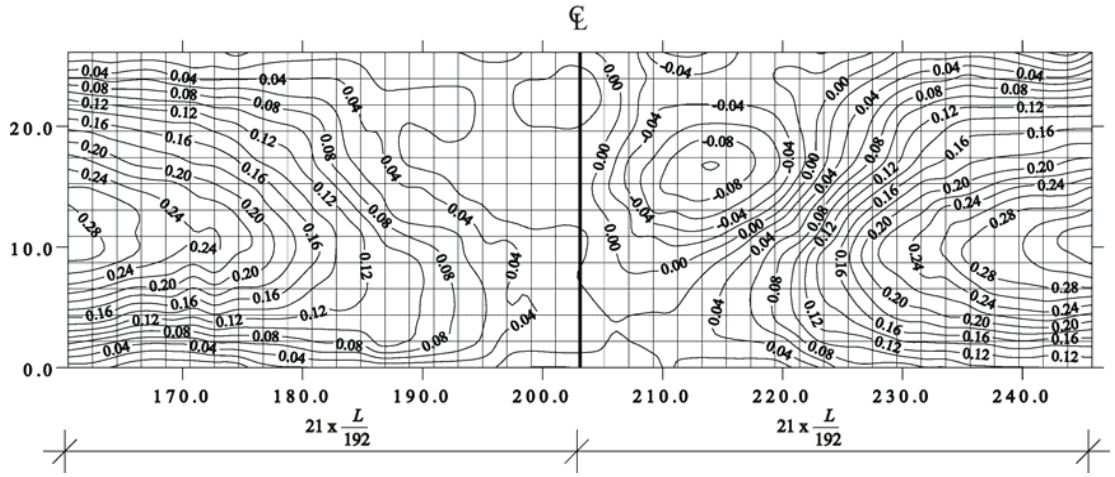

(b) Contour of web imperfection amplitude with reference to plane through points A, B, and C

Figure 4.36 Comparison of web imperfection amplitude using different reference definitions (Specimen 4)

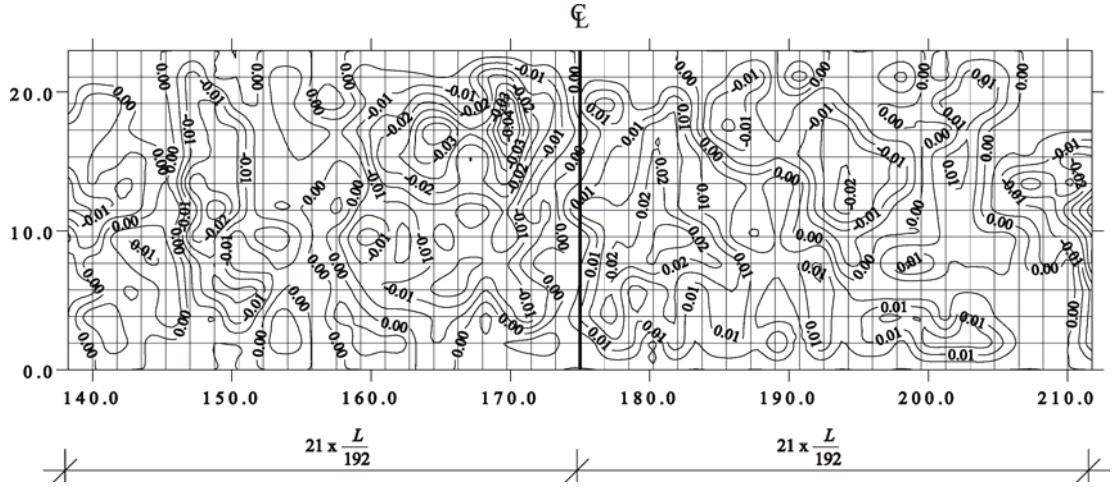

(a) Contour of web imperfection amplitude with reference to line through intersection with flanges

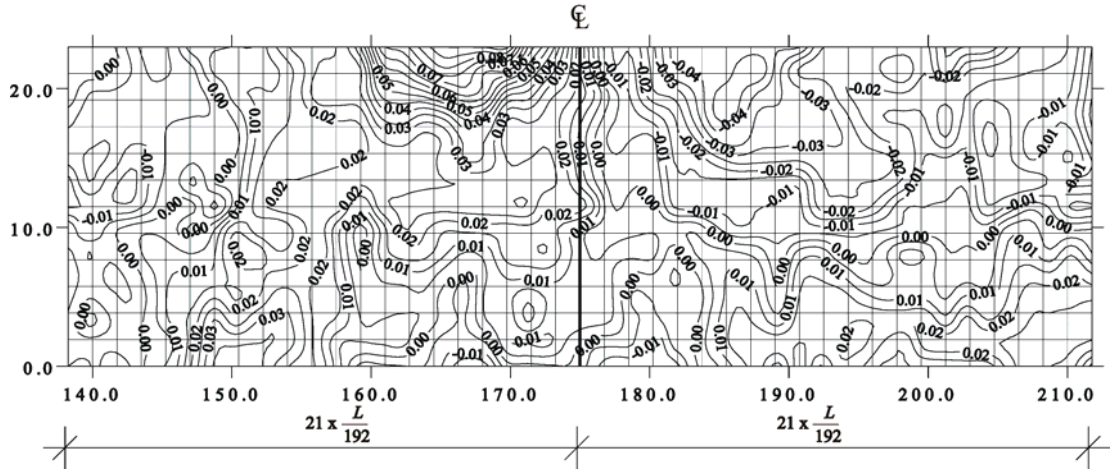

(b) Contour of web imperfection amplitude with reference to plane through points A, B, and C

Figure 4.37 Comparison of web imperfection amplitude using different reference definitions (Specimen 5)

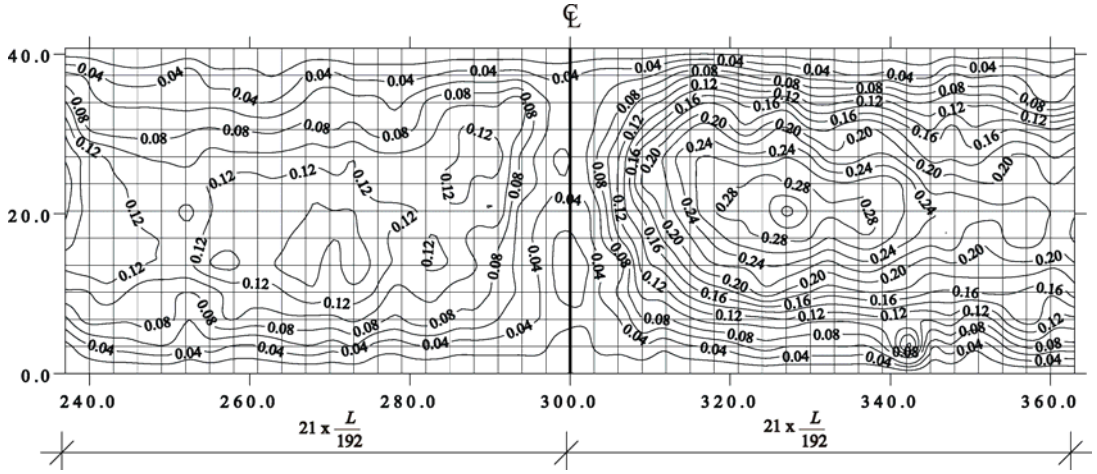

(a) Contour of web imperfection amplitude with reference to line through intersection with flanges

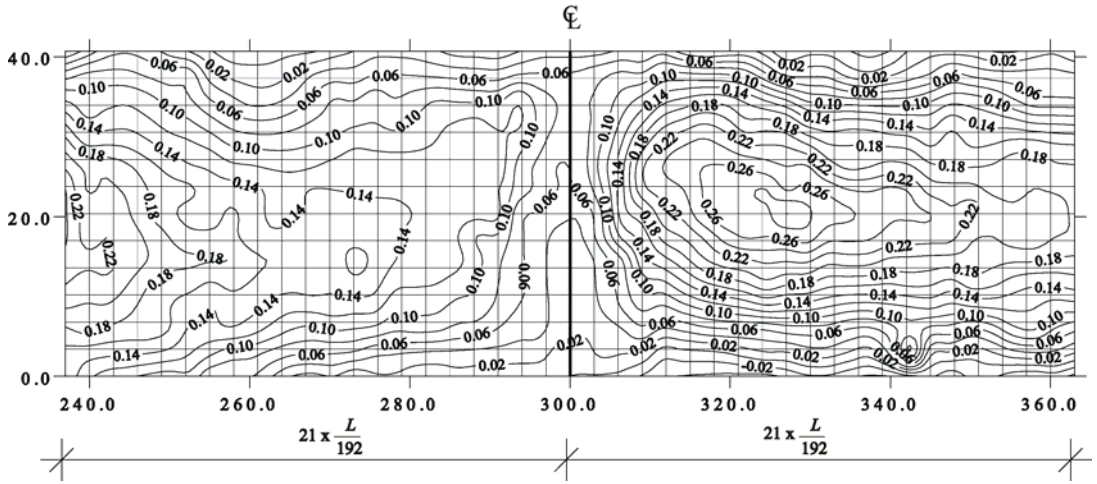

(b) Contour of web imperfection amplitude with reference to plane through points A, B, and C

Figure 4.38 Comparison of web imperfection amplitude using different reference definitions (Specimen 6)

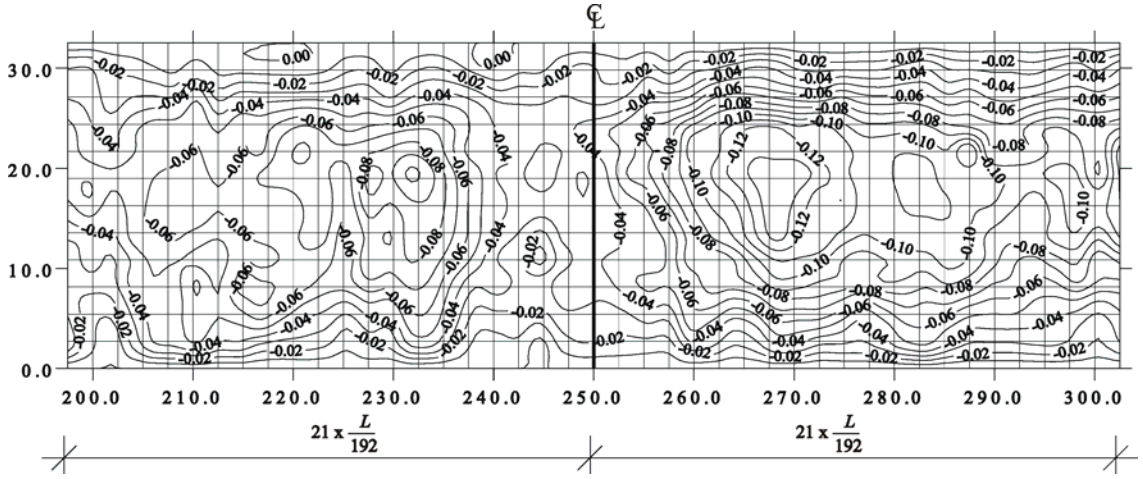

(a) Contour of web imperfection amplitude with reference to line through intersection with flanges

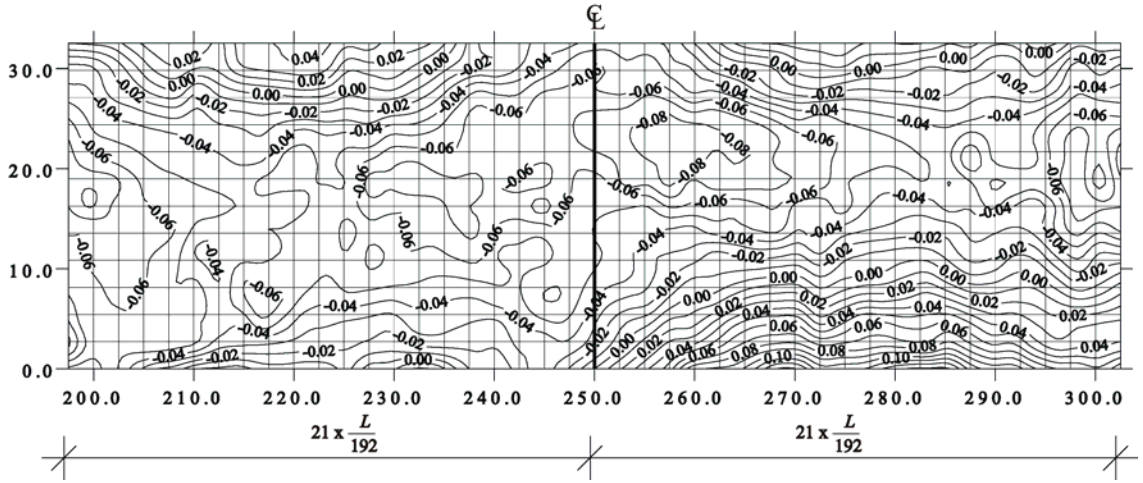

(b) Contour of web imperfection amplitude with reference to plane through points A, B, and C

Figure 4.39 Comparison of web imperfection amplitude using different reference definitions (Specimen 7)

(a) Residual stress measurements using hole-drilling method

(b) Strain indicator and RS-200 Milling Guide
Figure 4.40 Residual stress measurements

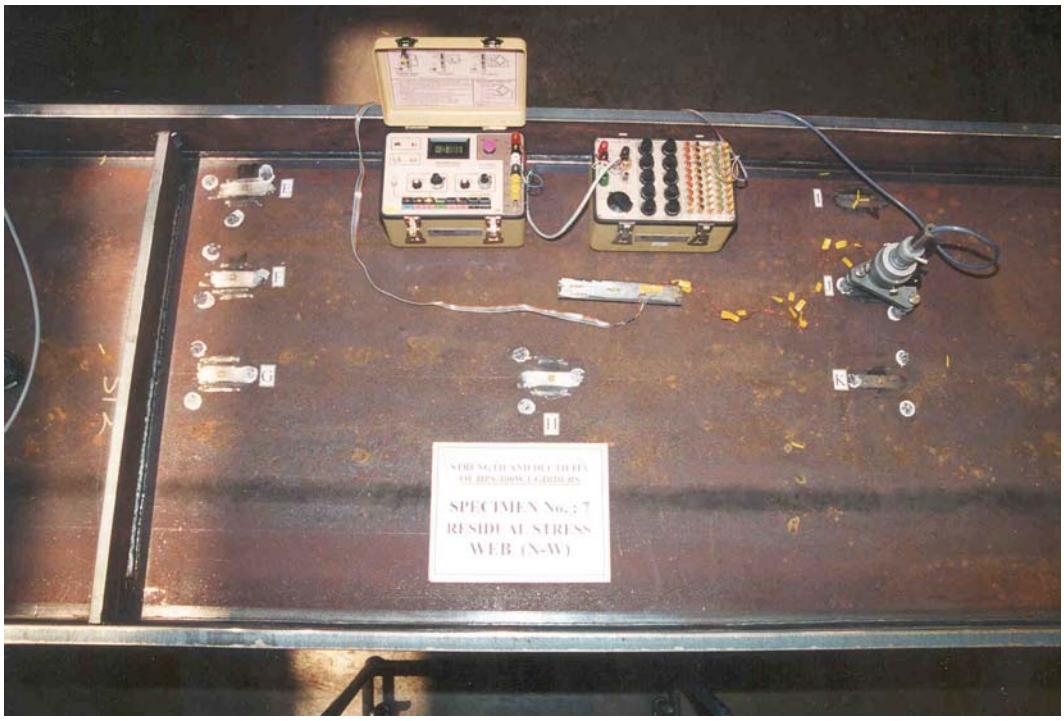

(a) Web

(b) Top flange

Figure 4.41 Locations for measuring residual stresses (Specimen 7)

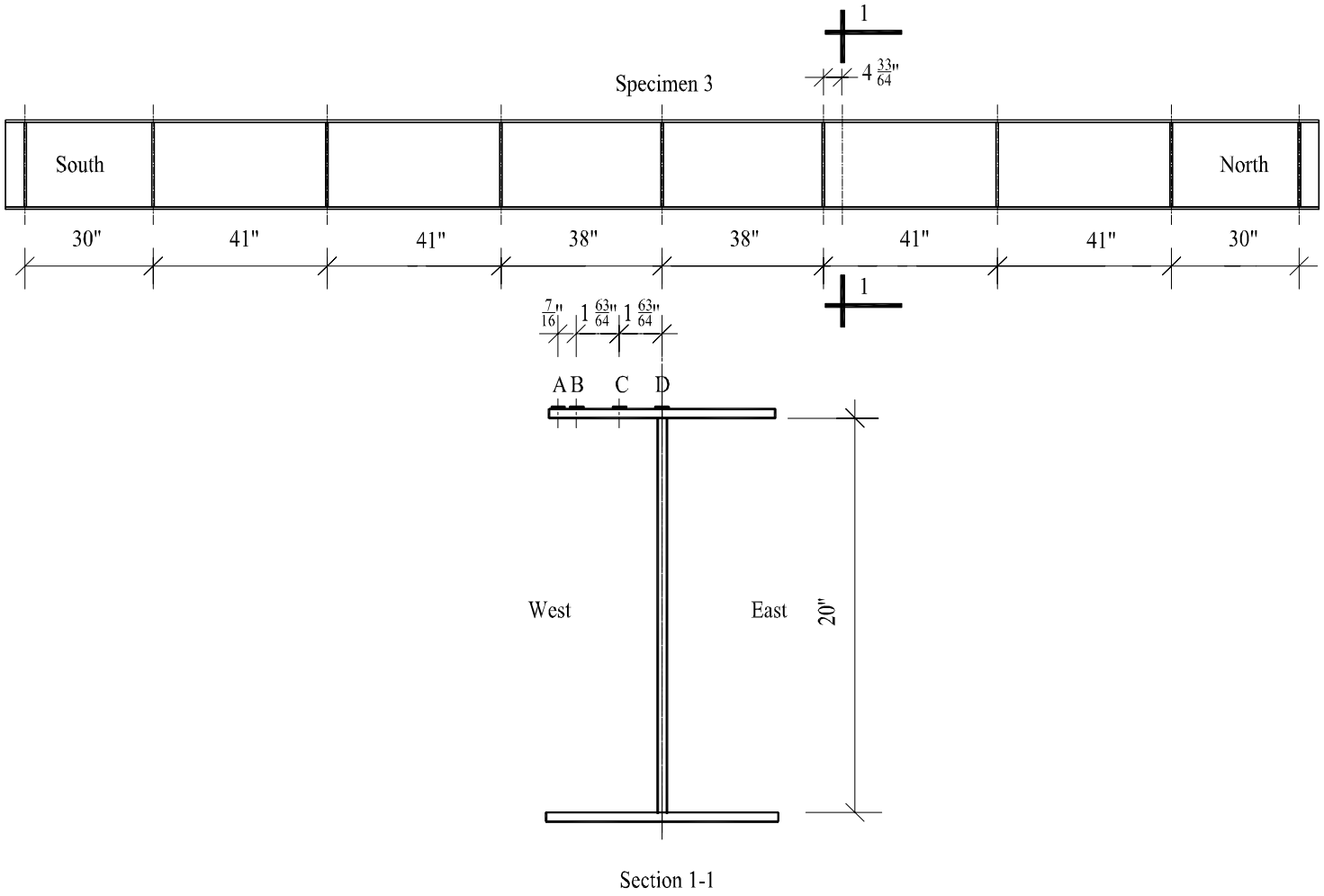

Figure 4.42 Locations of residual strain gages for Specimen 3
(1" = 1 in and 1' = 1 foot)

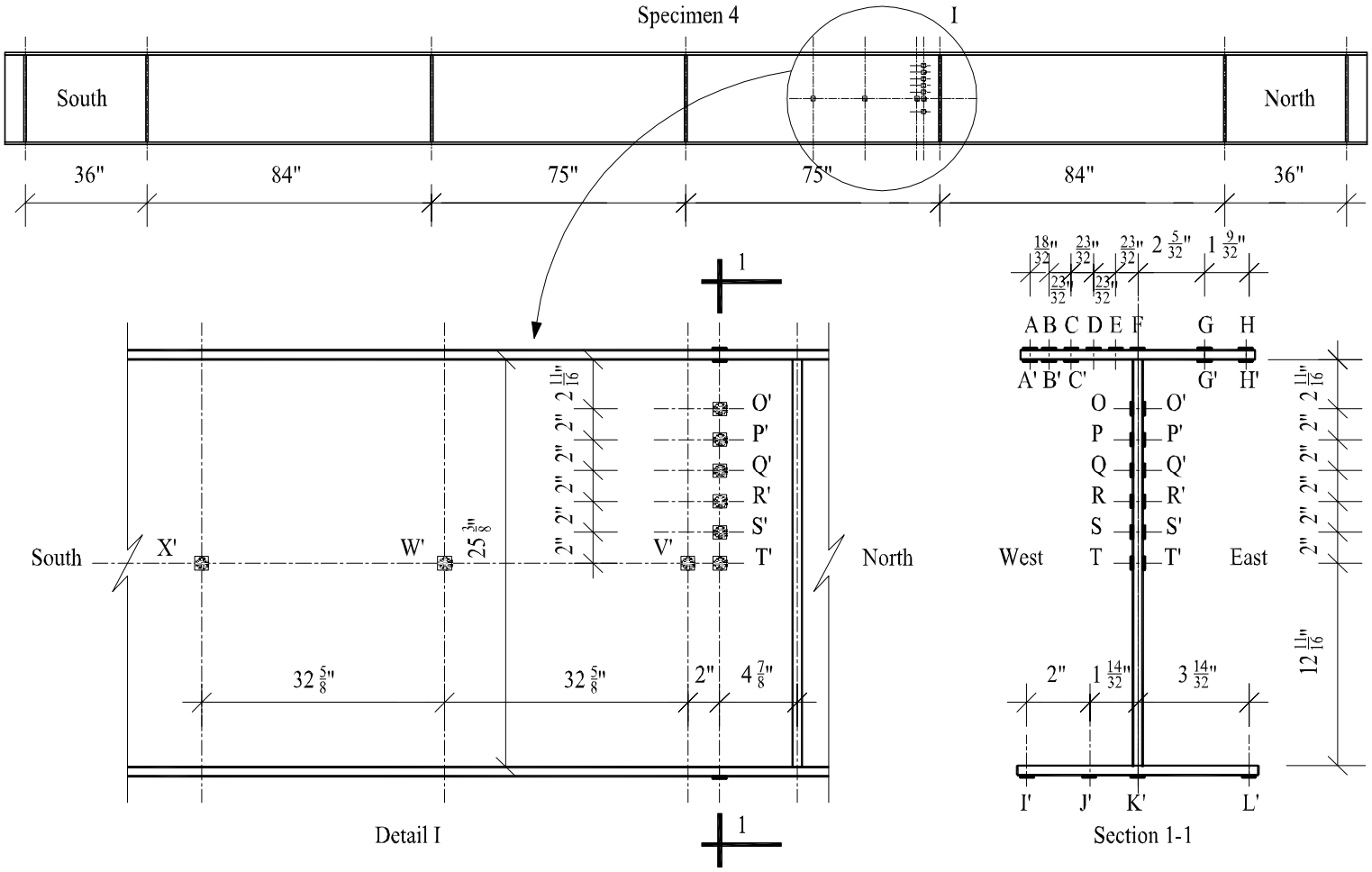

Figure 4.43 Locations of residual strain gages for Specimen 4
(1" = 1 in and 1' = 1 foot)

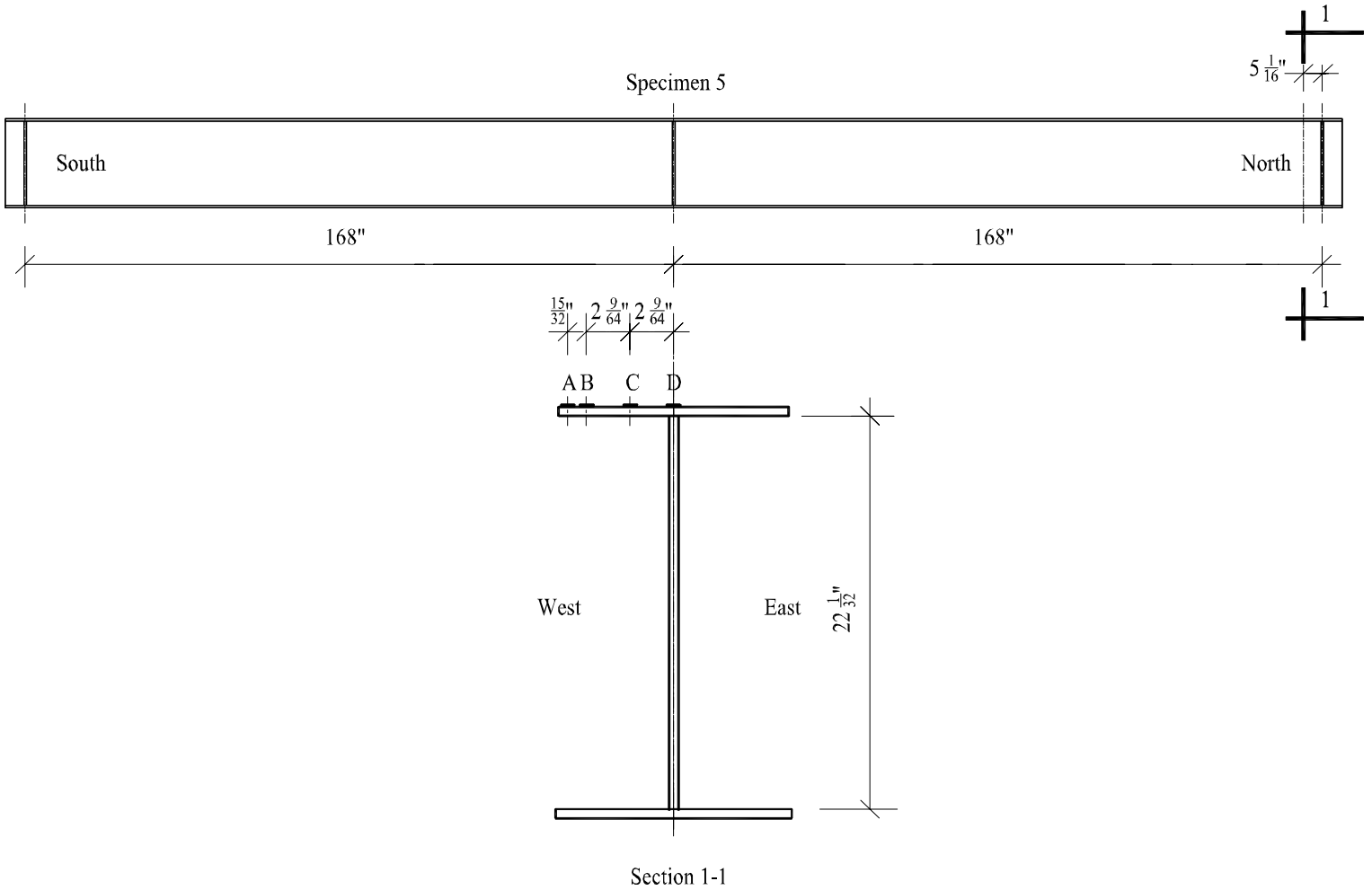

Figure 4.44 Locations of residual strain gages for Specimen 5
(1" = 1 in and 1' = 1 foot)

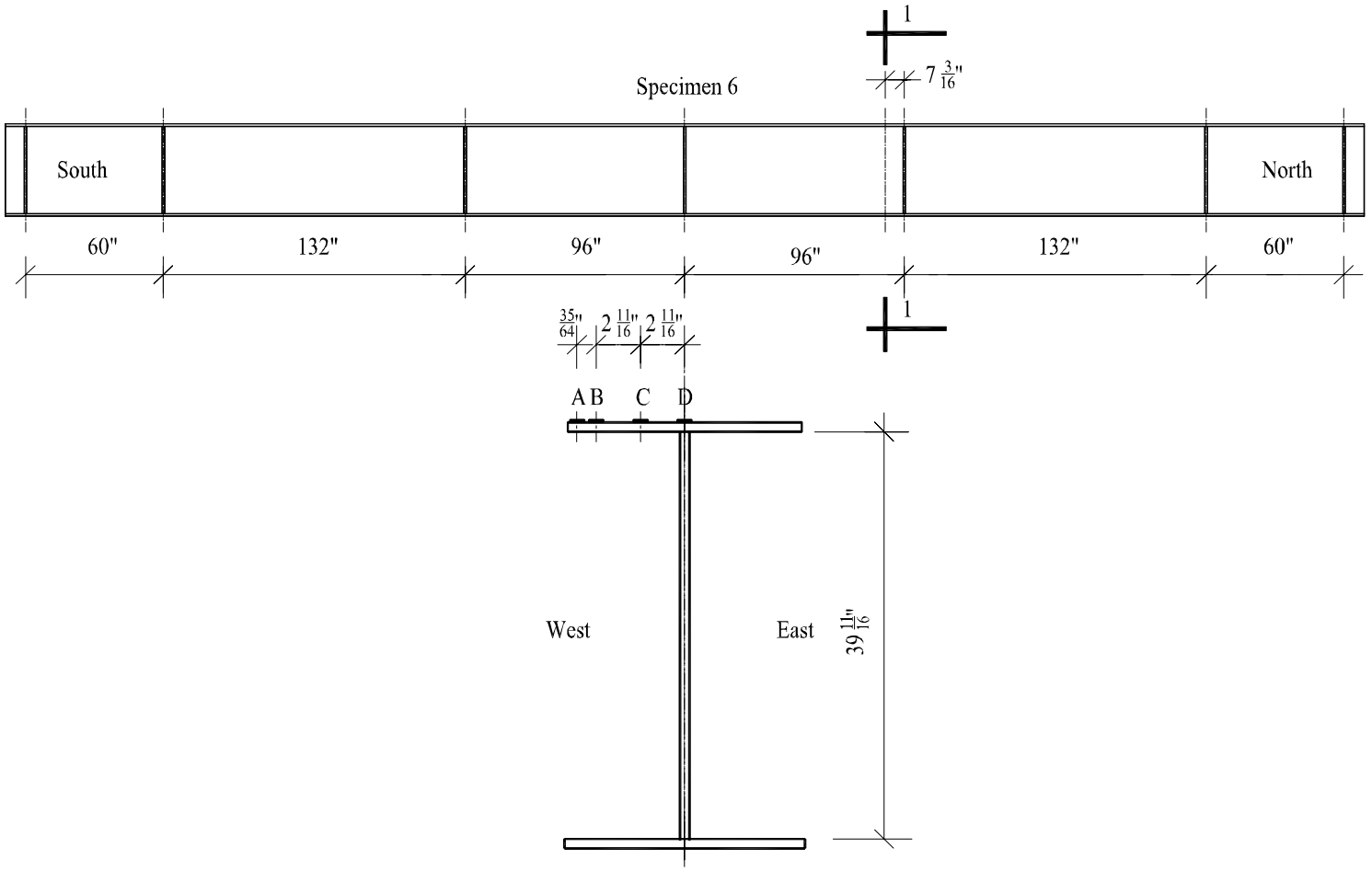

Section 1-1

Figure 4.45 Locations of residual strain gages for Specimen 6
(1" = 1 in and 1' = 1 foot)

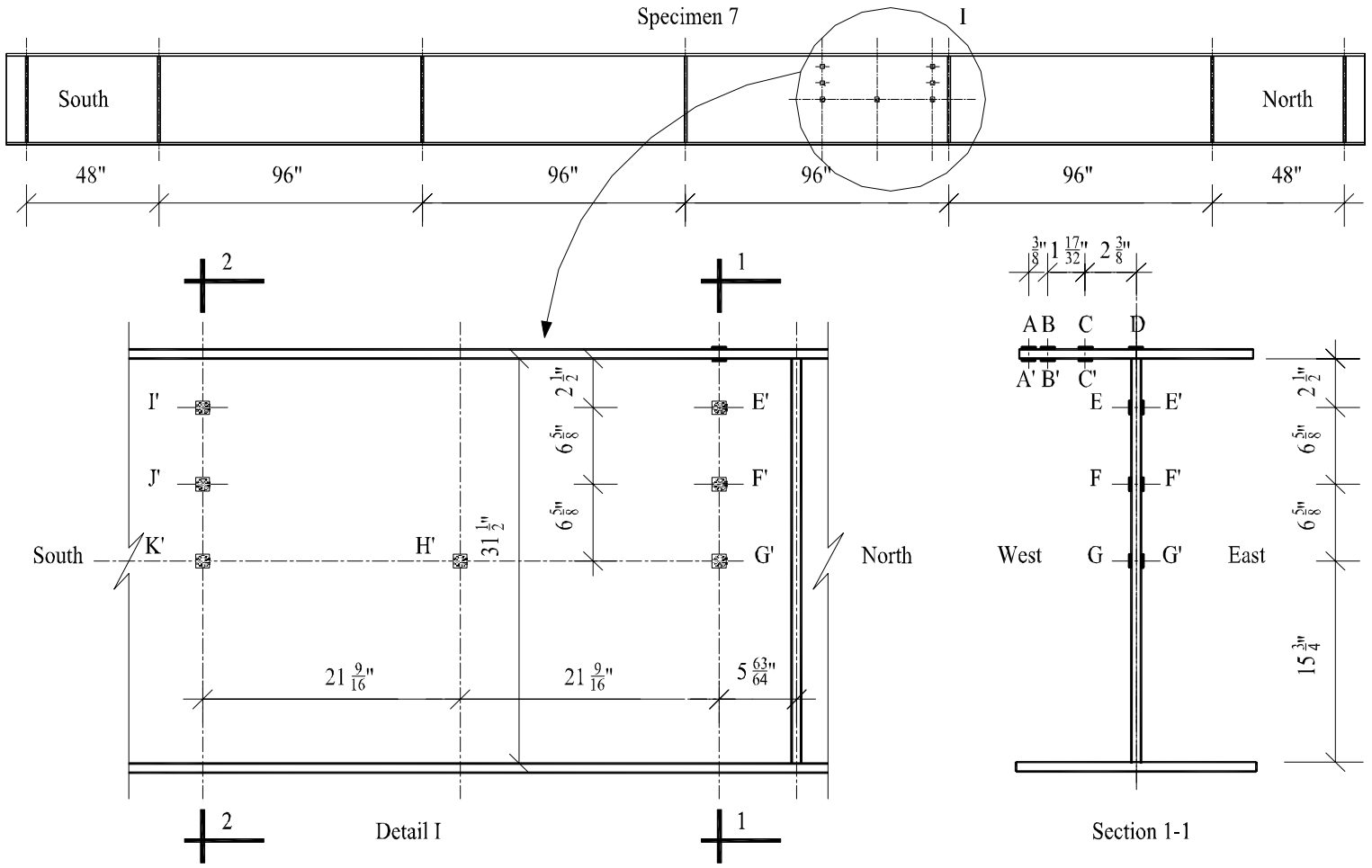

Figure 4.46 Locations of residual strain gages for Specimen 7
(1" = 1 in and 1' = 1 foot)

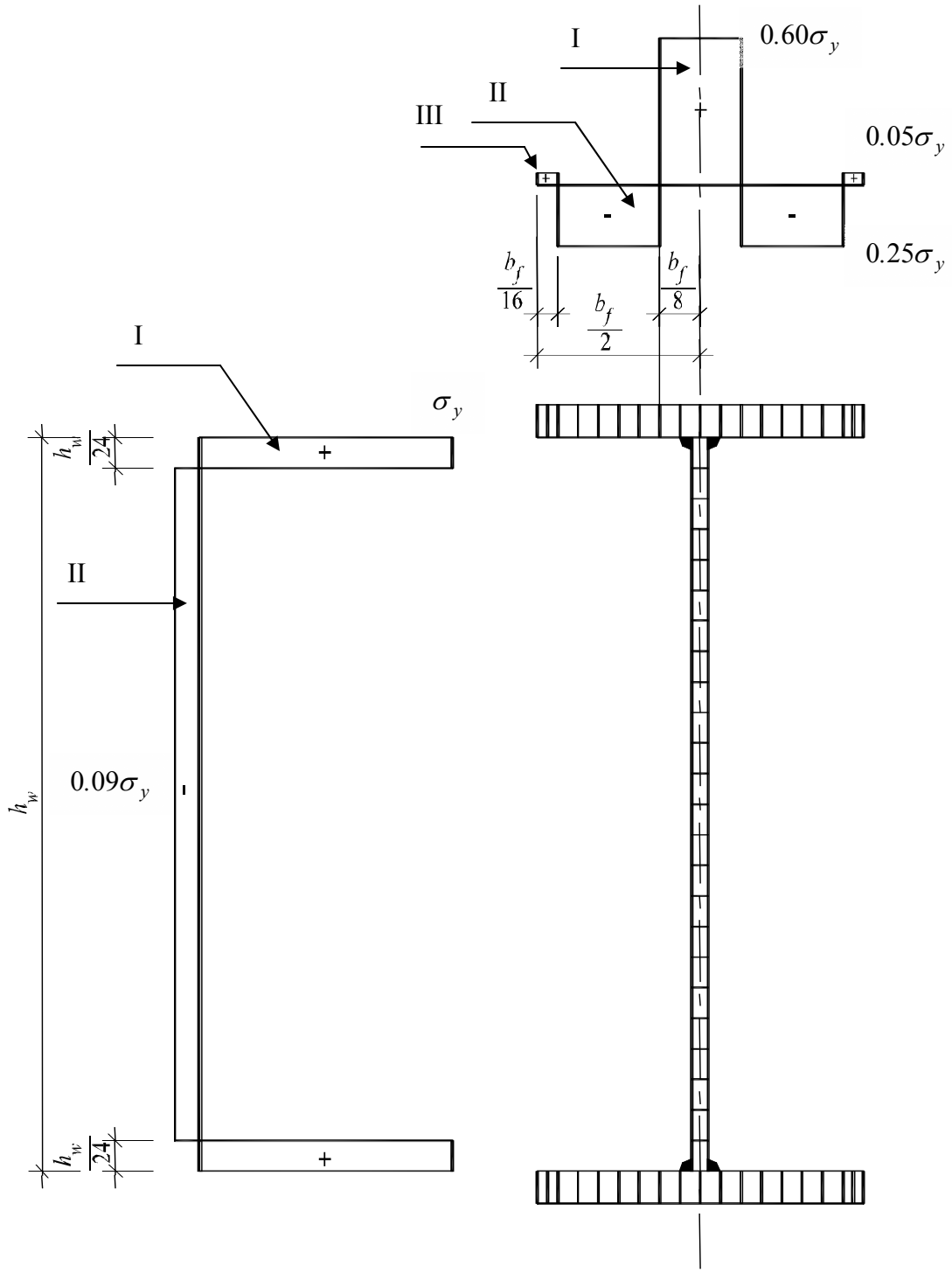

Figure 4.47 Residual stress model

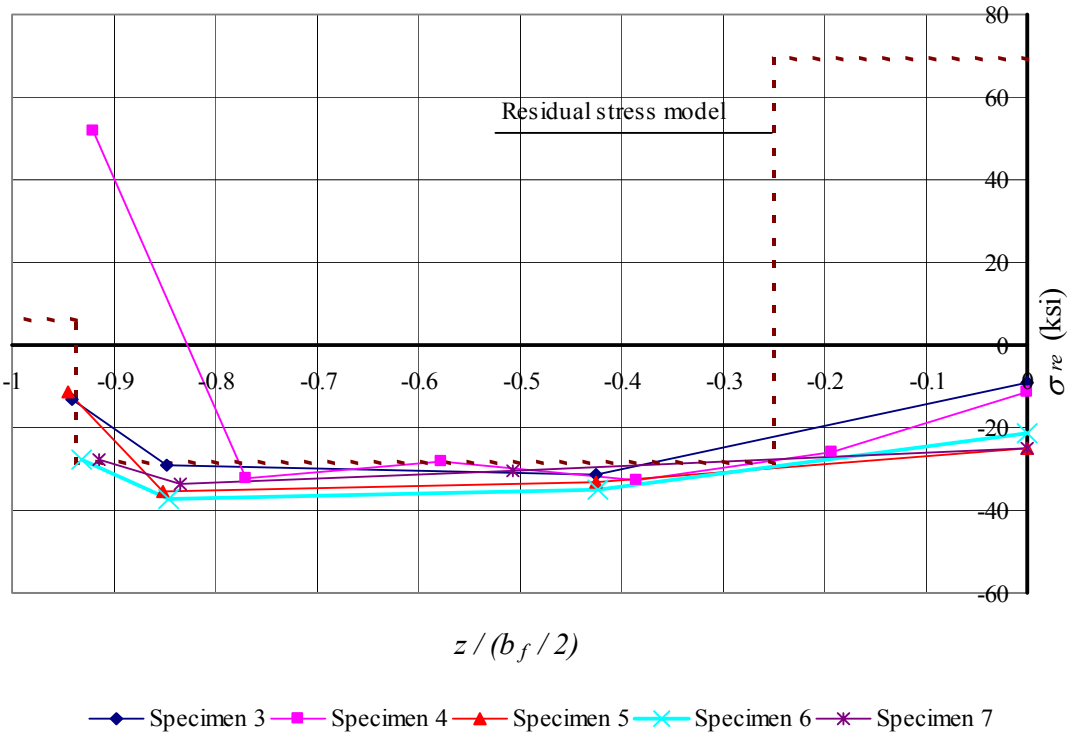

Figure 4.48 Measured and residual stress model (top flange)

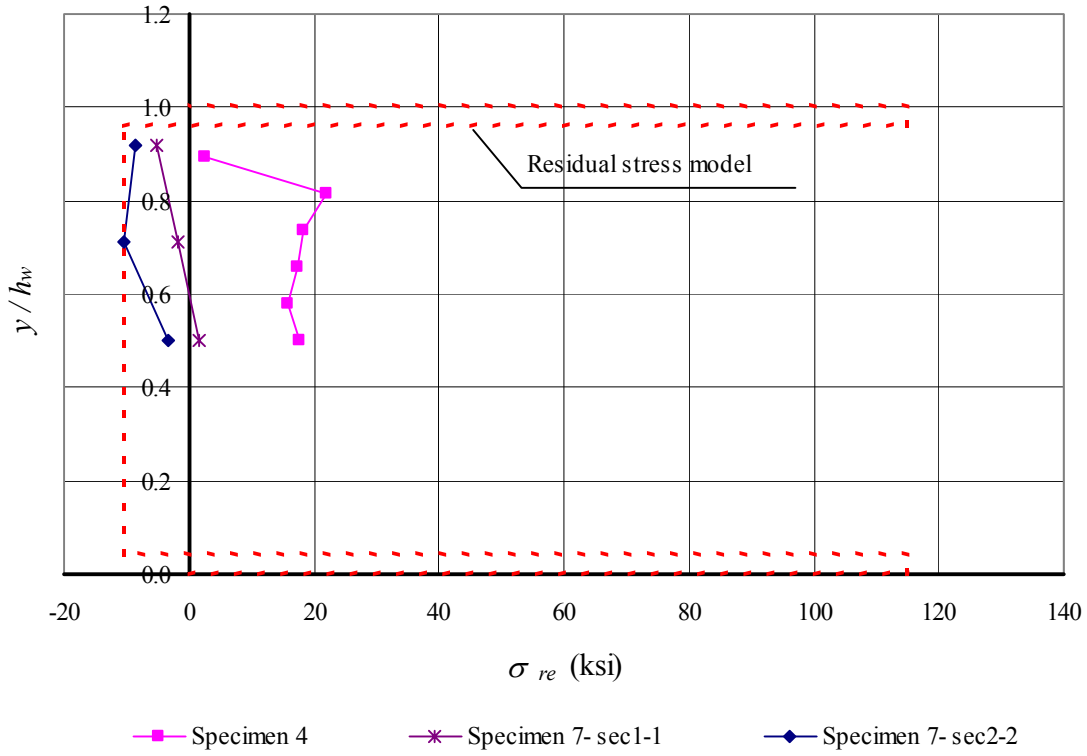

Figure 4.49 Measured and residual stress model (web)

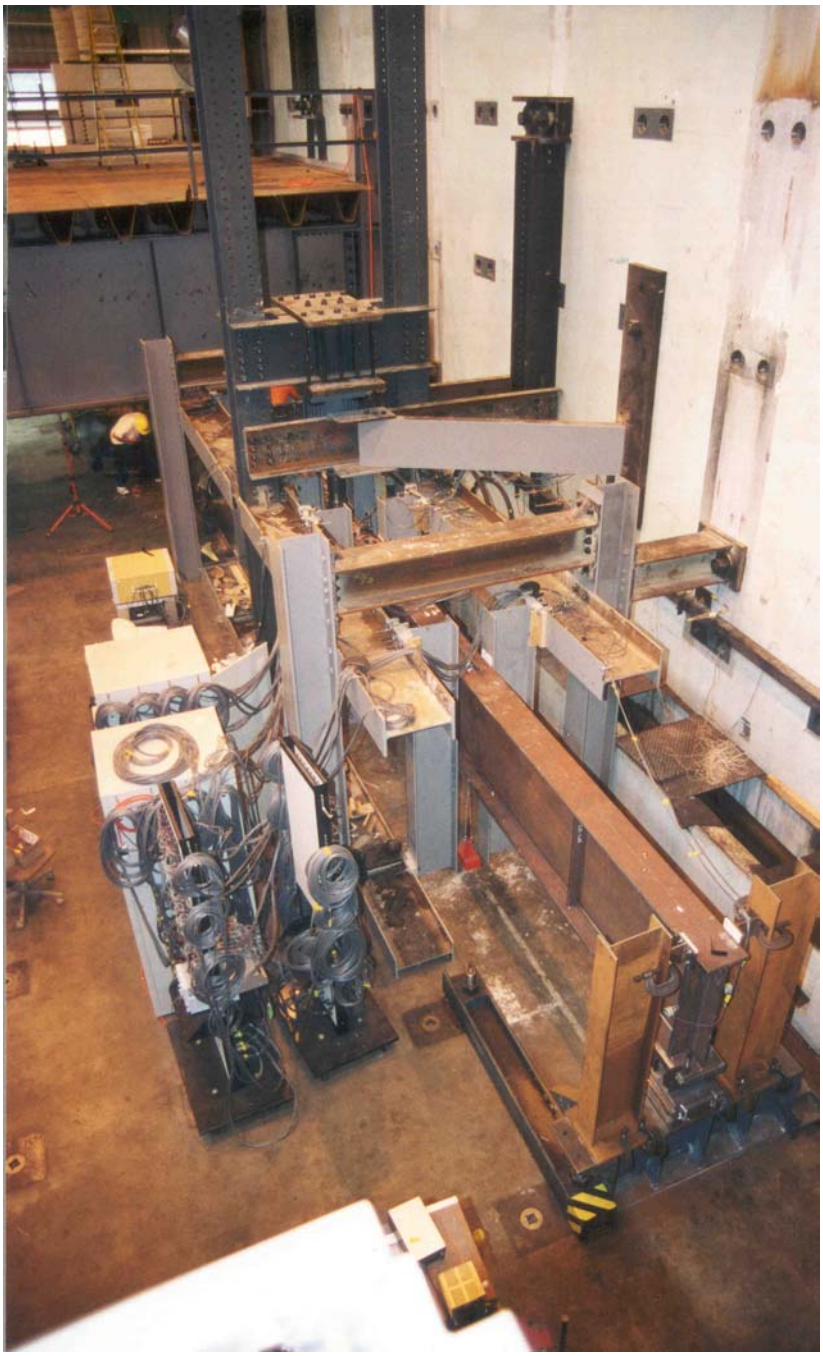

Figure 4.50 Overall view of test setup

Figure 4.51 Elevation view of test setup

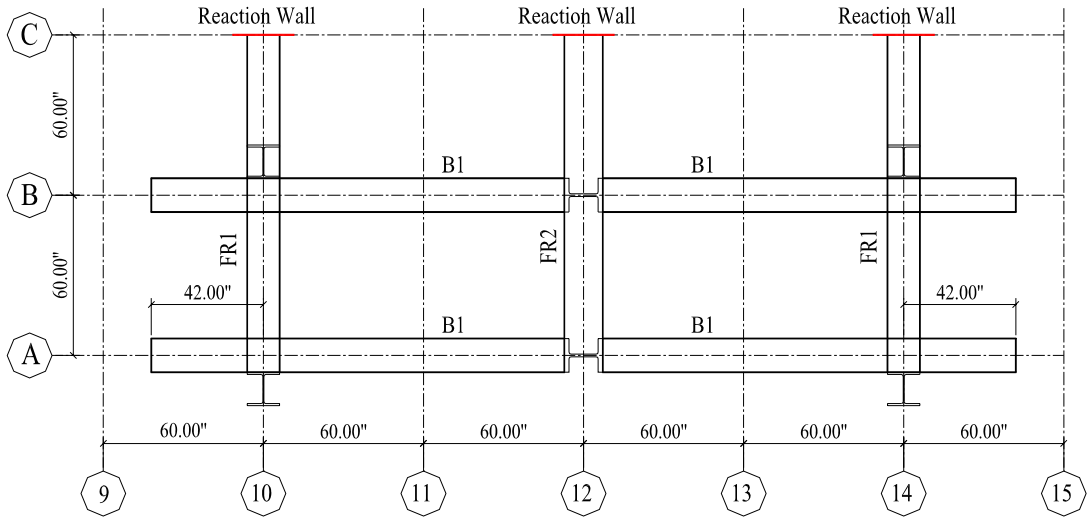

(a) Plan view at level of beam B1

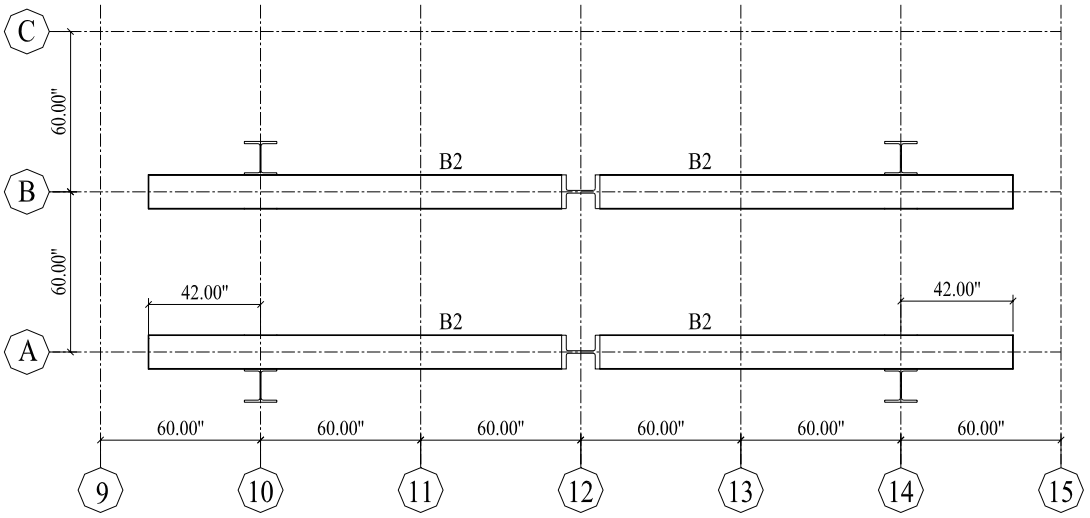

(b) Plan view at level of beam B2

Figure 4.52 Plan view of test setup at different levels
(1" = 1 in and 1' = 1 foot)

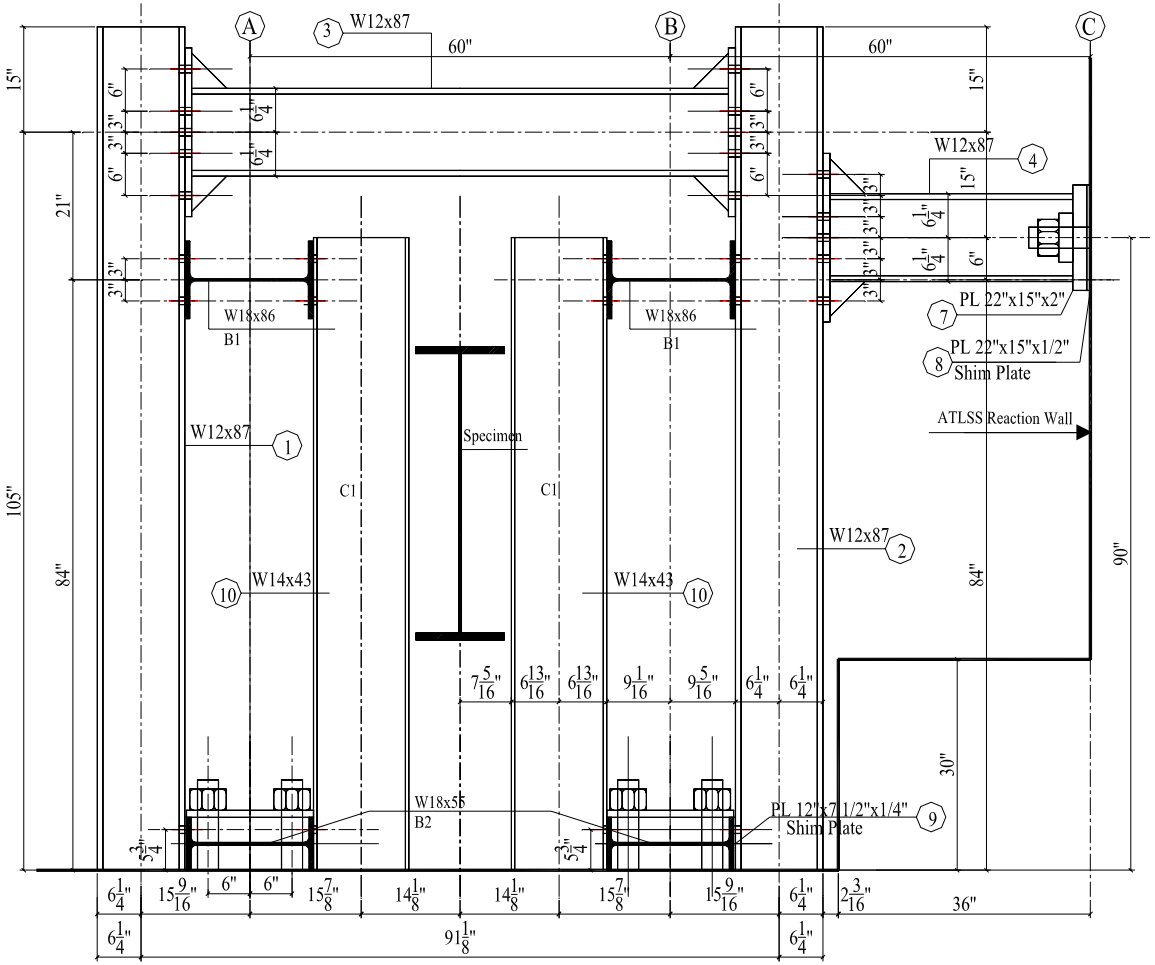

Figure 4.53 Frame FR1
(1" = 1 in and 1' = 1 foot)

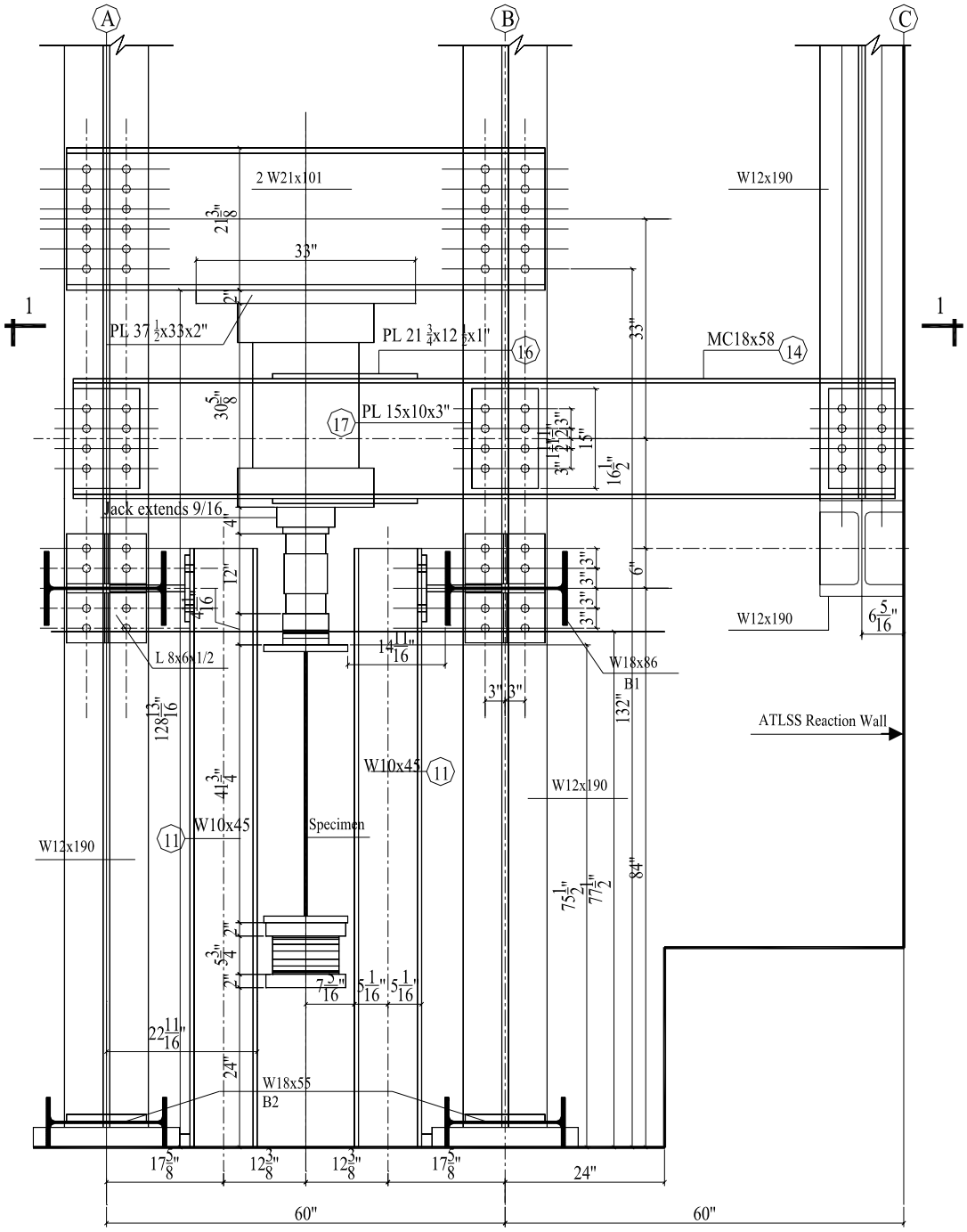

Figure 4.54 Frame FR2
(1" = 1 in and 1' = 1 foot)

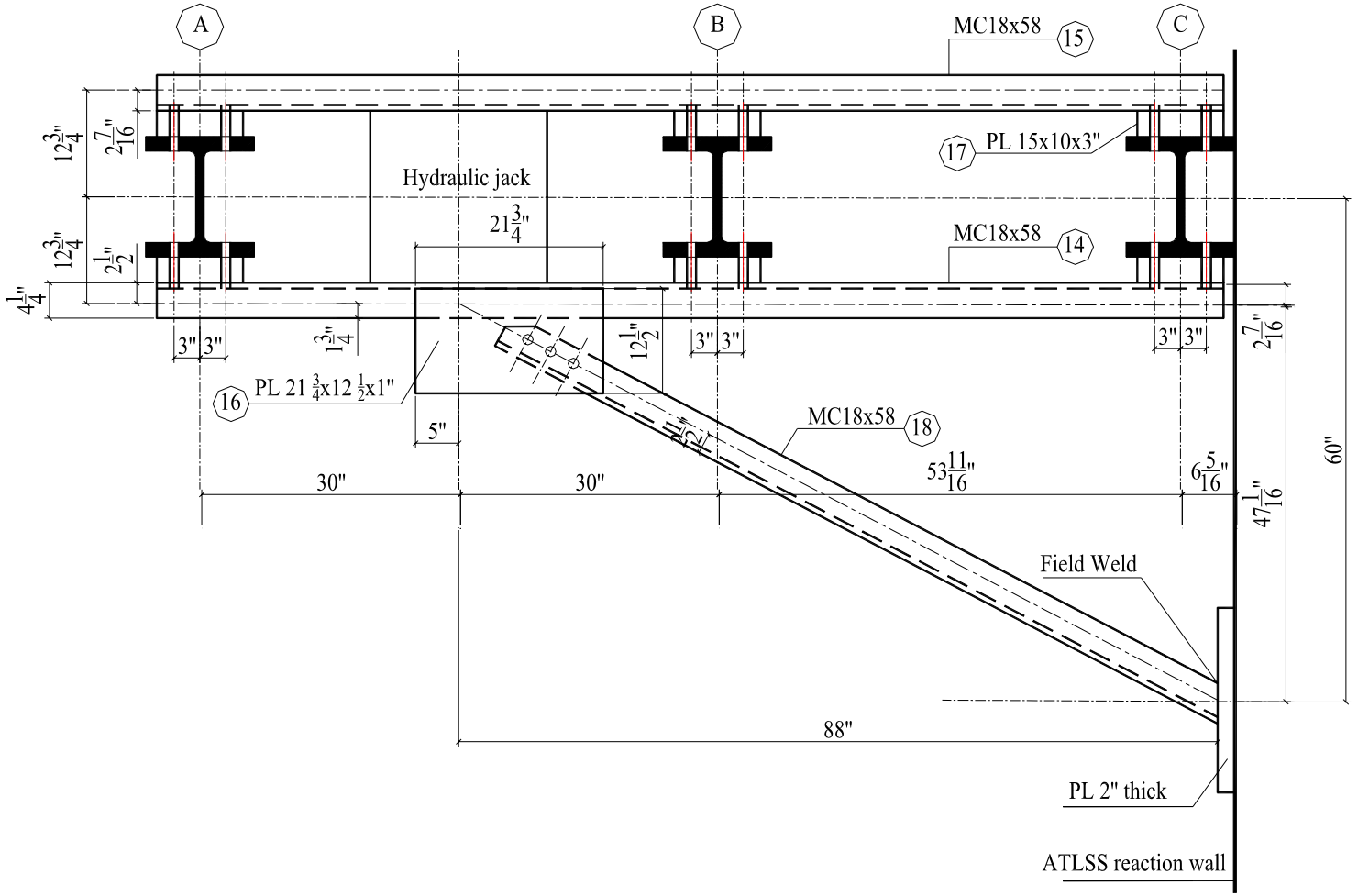

Figure 4.55 Detail of section 1-1 (see Figure 4.54)
(1" = 1 in and 1' = 1 foot)

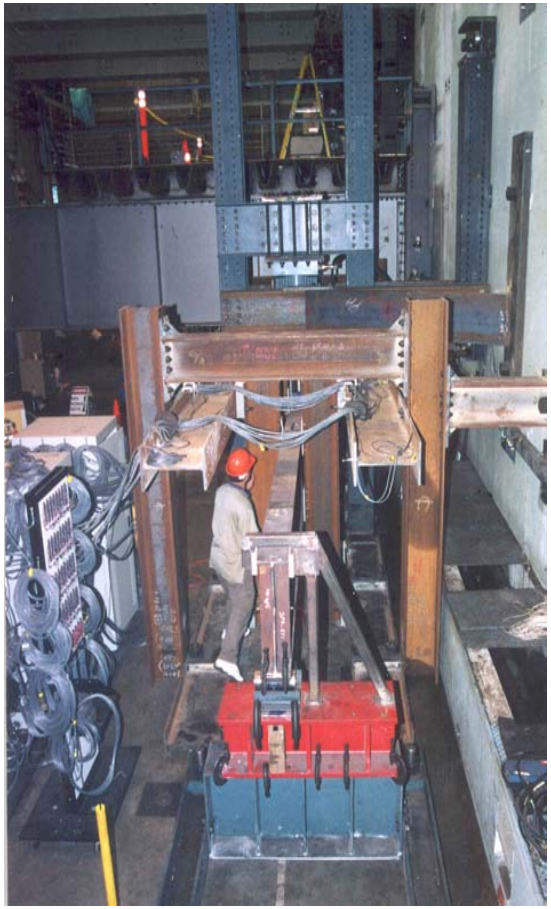

(a) Frame FR1

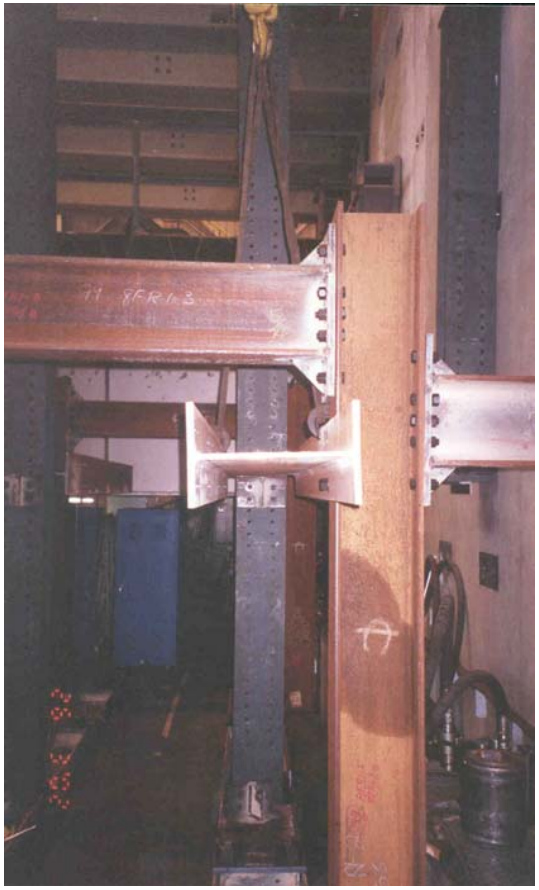

(b) Closeup view of frame FR1

Figure 4.56 Overall view of frame FR1

(a) Frame FR2 during construction

(b) Frame FR2 after construction

Figure 4.57 Overall view of frame FR2 during and after construction

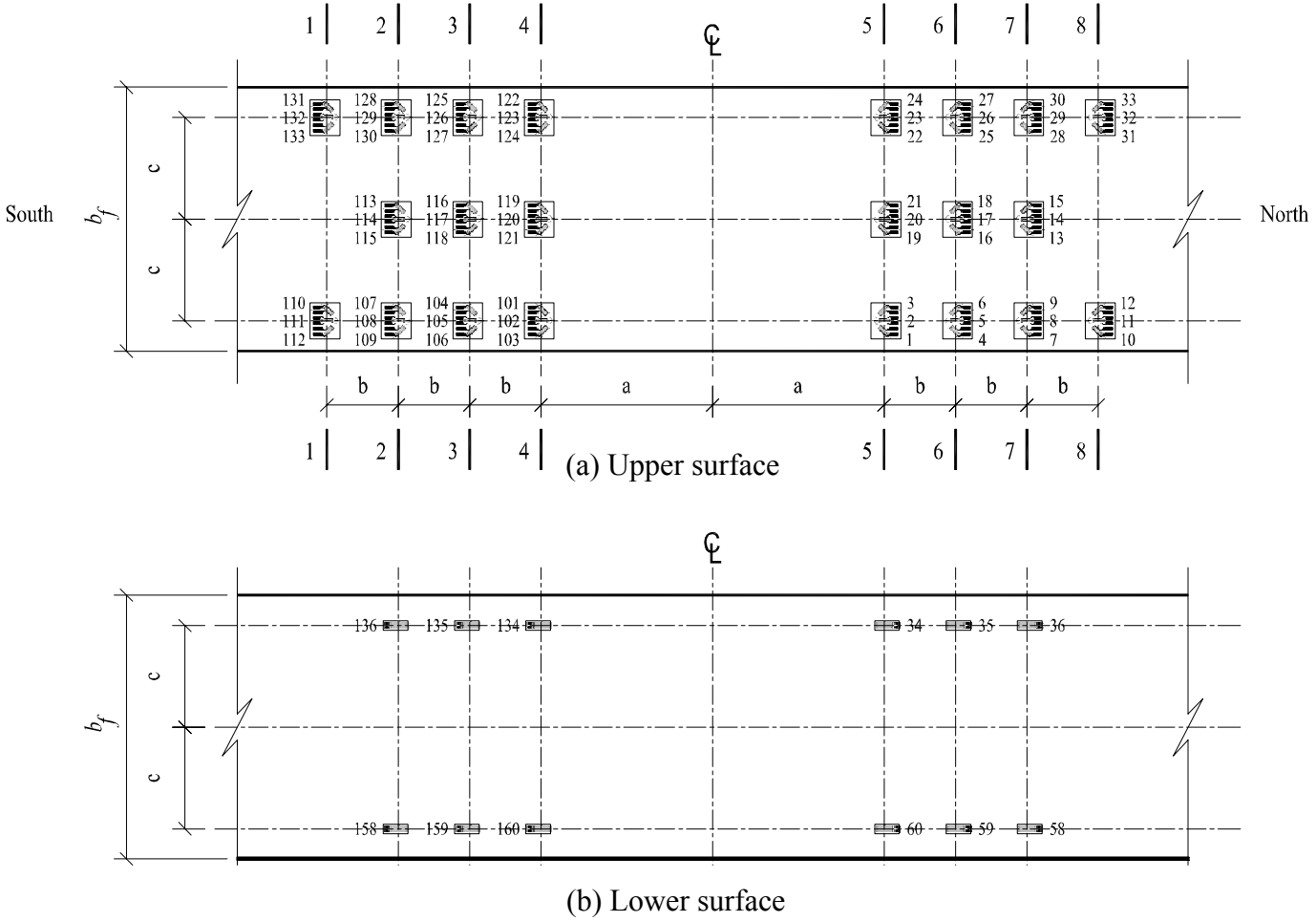

Figure 4.58 Top flange strain gage locations

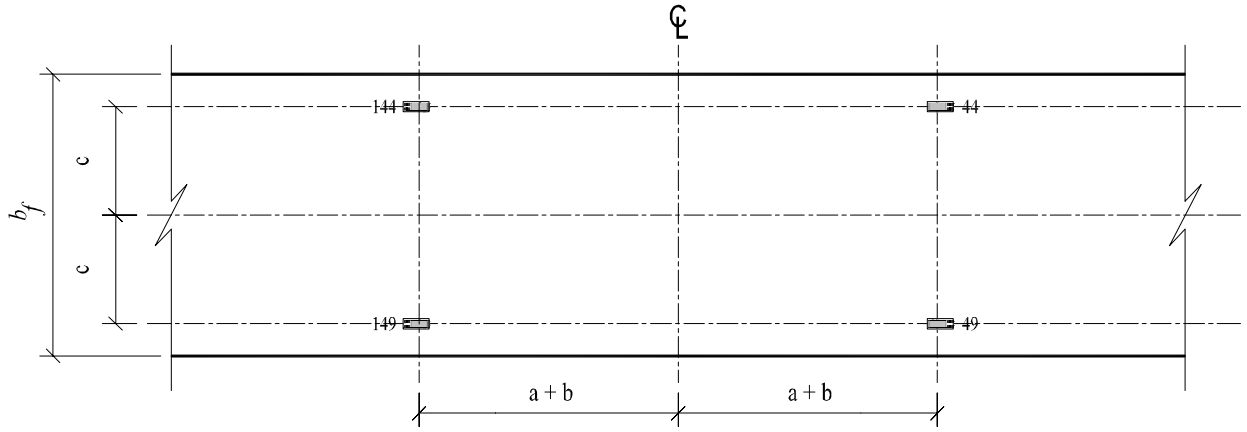

(a) Upper surface

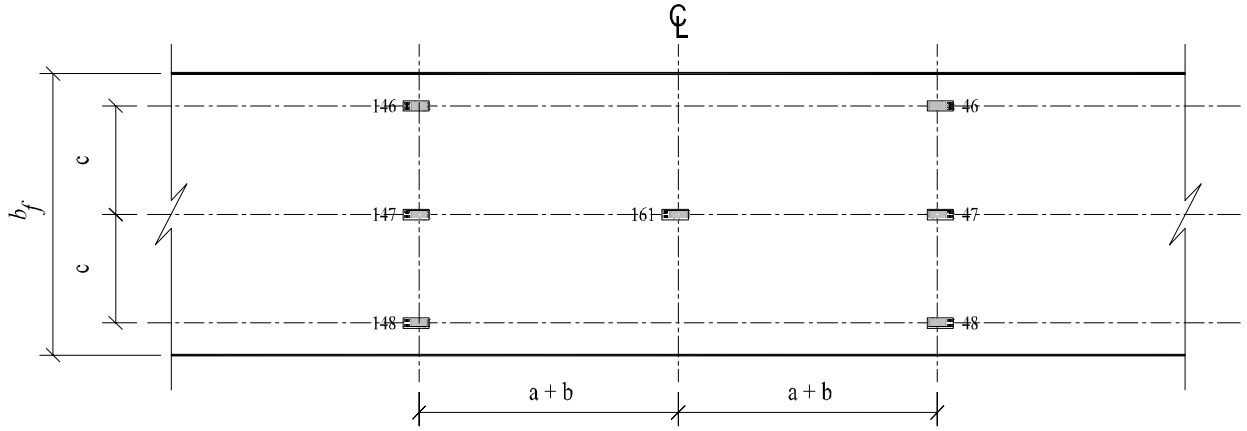

(b) Lower surface

Figure 4.59 Bottom flange strain gage locations

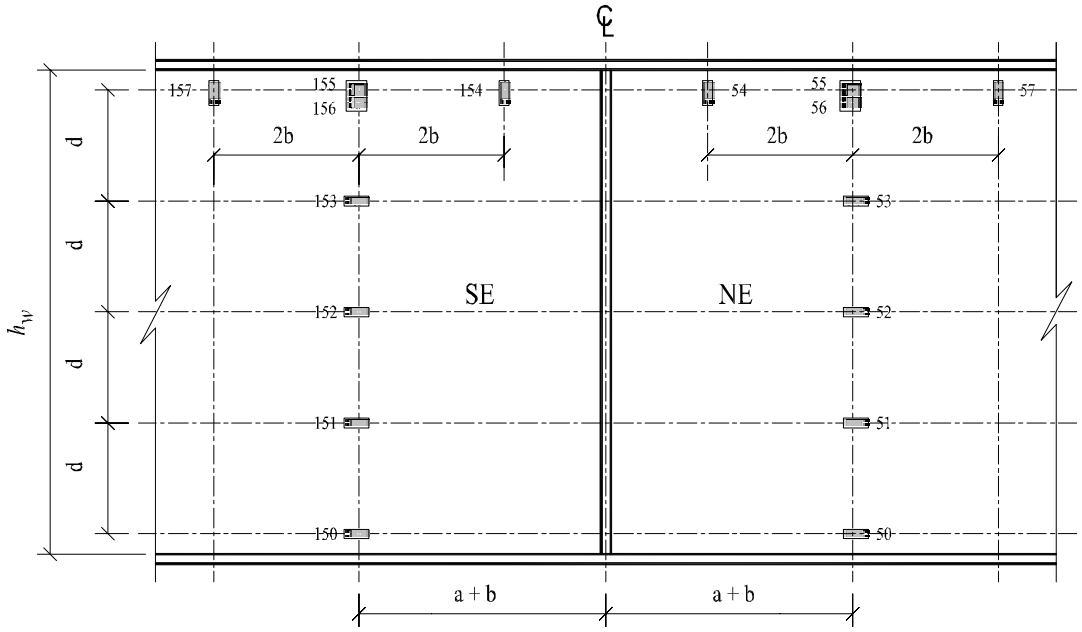

(a) East side

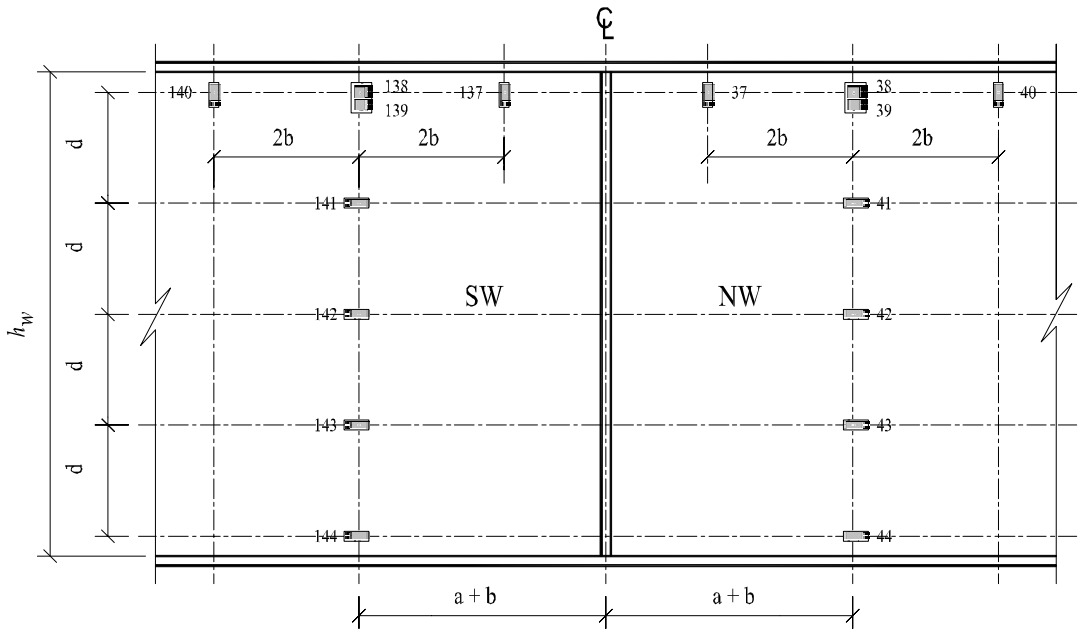

(b) West side

Figure 4.60 Web strain gage locations

(a) Strain gages on top flange (upper surface)

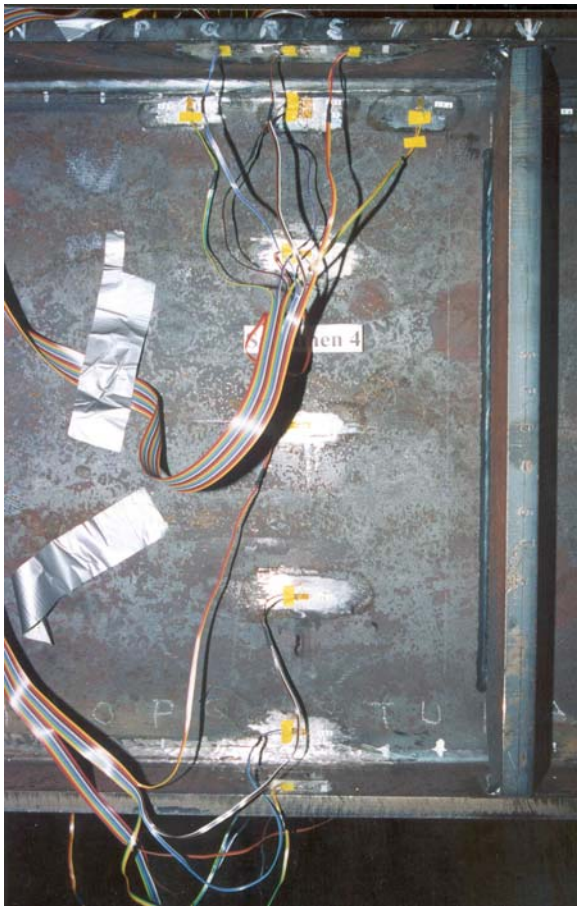

(b) Strain gages on web (south east side)

Figure 4.61 Strain gages for Specimen 4

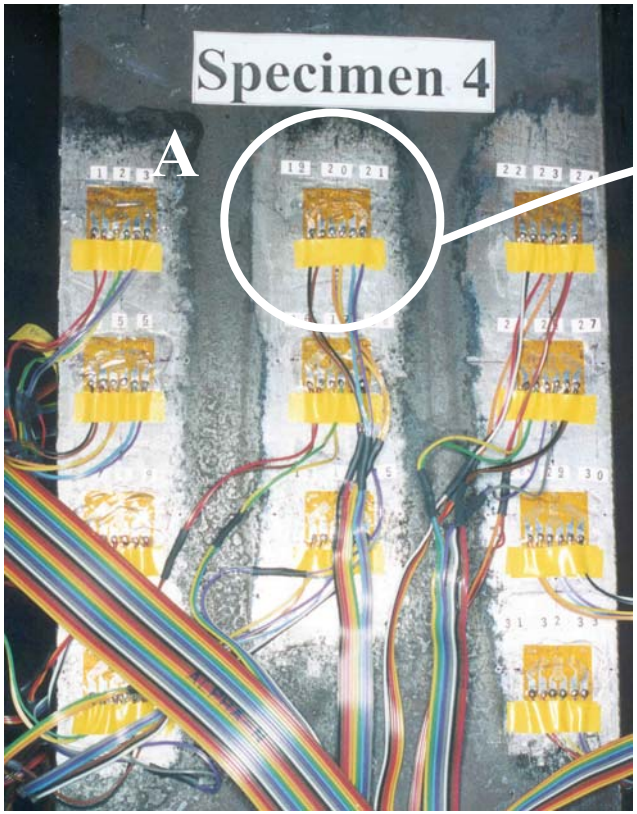

(a) Strain gages on top flange (upper surface)

(b) Detail A

Figure 4.62 Detail of strain gages on the north side of top flange (Specimen 4)

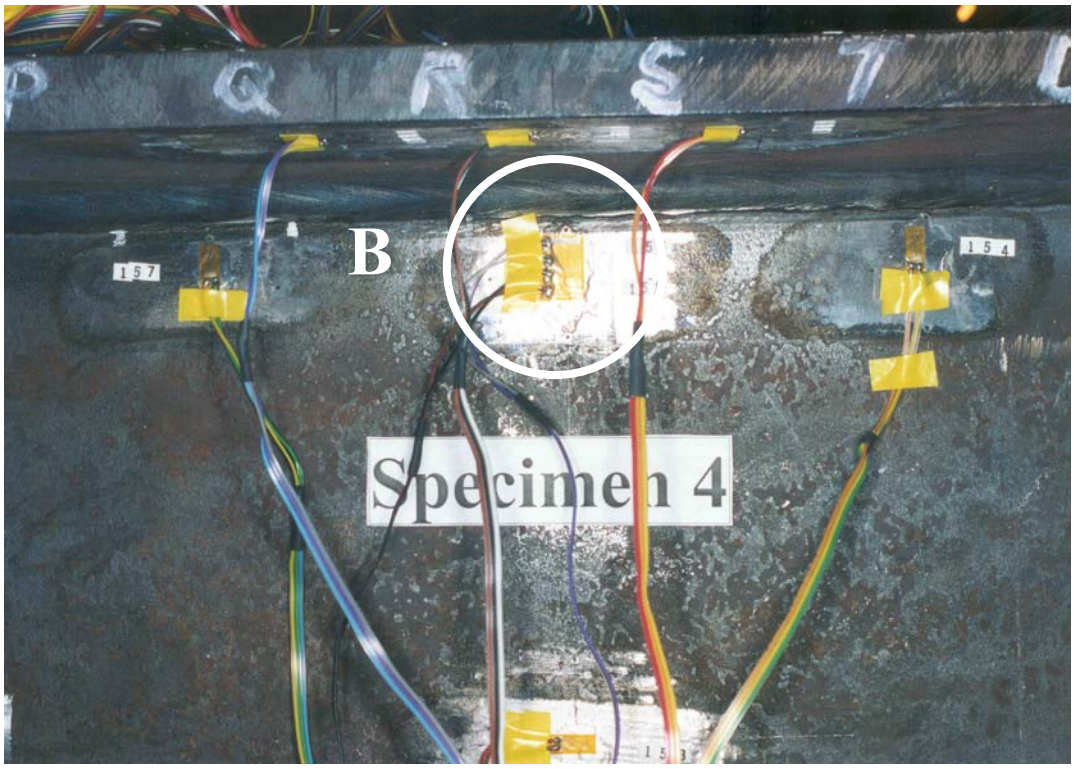

(a) Strain gages at the junction between web and top flange

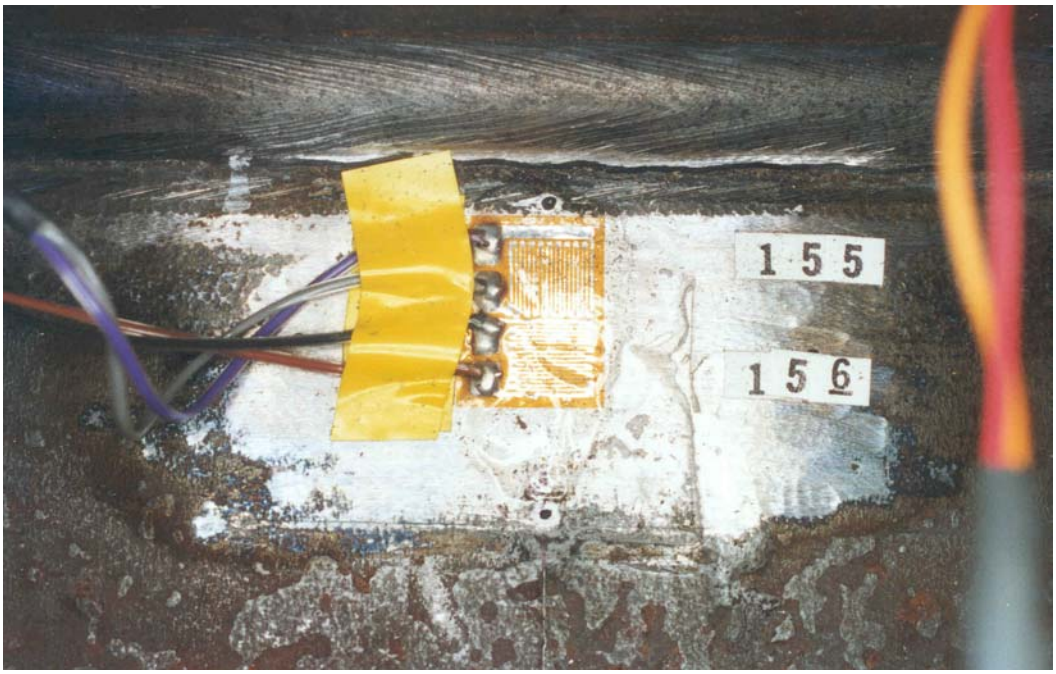

(b) Detail B

Figure 4.63 Strain gages at the junction between web and top flange (Specimen 4)

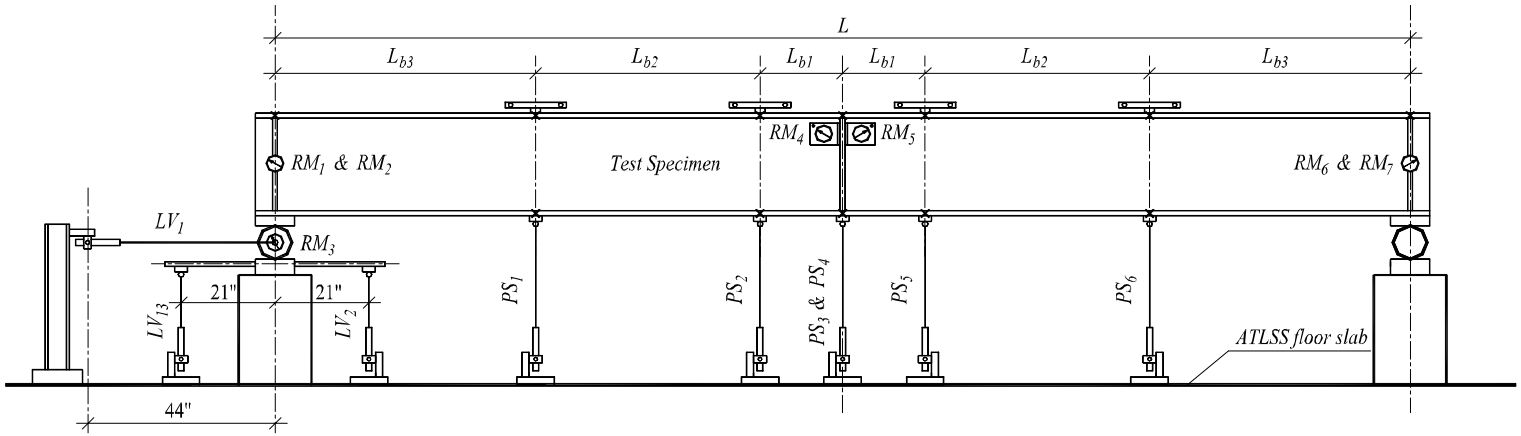

(a) Elevation view

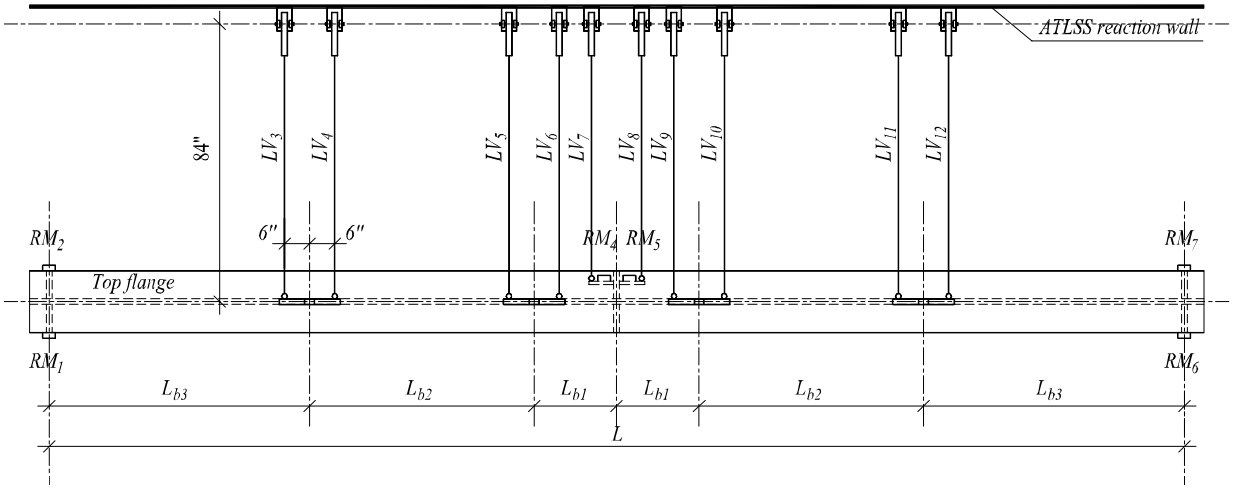

(b) Plan view

Figure 4.64 Specimen instrumentation

CHAPTER 5 Experimental Results

5.1 Introduction

In this chapter the experimental results for each specimen are presented, along with a discussion of key stages during loading and unloading. The global behavior of the specimens is presented through plots of midspan vertical deflection versus load and average end rotation versus midspan moment. The local behavior of the web and flanges of each specimen is studied and presented in terms of measured strain and curvature. The lateral distortion of the top (compression) flange is presented in terms of curvature. The inelastic behavior of the compression flange is studied using normal and shear strains recorded by strain rosettes attached to the top surface of the compression flange. These measured strains, along with the measured residual strains, are used to estimate the strain history which is then converted to stress history using a computer program based on incremental plasticity. The start of yielding on the compression flange surface is detected using Von Mises yield criterion. After yielding, an algorithm, based on plasticity theory (see Appendix A) is used to convert strains into stresses.

5.2 Specimen 3

According to the 2001 AASHTO LRFD specifications [AASHTO 2001], Specimen 3 has a noncompact section with a compact flange and a noncompact web. The compression flange brace spacing satisfies the AASHTO LRFD requirements for compact sections. The ultimate flexural strength of this specimen is expected to be the plastic moment capacity of the section, M_p, based on the optional Q formula for flexural resistance (Equation 2.16).

5.2.1 Test Procedure

The test procedure was composed of two steps: (1) two initial cycles, in each cycle the specimen was loaded to 100 kips (445 kN) and then unloaded, and (2) loading to failure.

The purpose of the initial cycles was to properly seat the test specimen and check the instrumentation. These two cycles were performed under displacement control with a displacement of 0.20 in per minute (5.08 mm per minute). At a midspan vertical deflection of 1.50 in (38 mm), the applied load was 117 kips (520.0 kN) and thus the corresponding loading rate was 15.6 kips per minute (69.0 kN per minute). This midspan vertical deflection corresponds to a strain of 0.00184 in/in at the middle

of the bottom (tension) flange (strain gage SG-161). The data were recorded at 1.0 second intervals.

After checking the results of the first two cycles, the specimen was loaded to failure under displacement control. The loading rate was 0.10 in per minute (2.54 mm per minute) until 5.5 in (139.7 mm) midspan vertical deflection was reached. Then the specimen was unloaded at a rate of 0.4 in per minute (10.2 mm per minute). This unloading was intended to verify that, if the specimen is unloaded elastically after the peak load is reached and then reloaded, it will reload elastically to the load at which it was unloaded. After the specimen was unloaded it was loaded again at a rate of 0.4 in per minute (10.2 mm per minute) until reaching 5.5 in (139.7 mm) midspan vertical deflection again. The loading rate was then changed to 0.10 in per minute (2.54 mm per minute) until 6.3 in (160.0 mm) midspan vertical deflection was reached. At this deflection the applied load was 167 kips (743.0 kN) which is 63% of the ultimate load, P_u. The specimen was then unloaded to end the test. The data were recorded at 2.0 second intervals through out the test.

5.2.2 Global Behavior

The theoretical plastic moment, M_p, was calculated based on the dimensions and yield stresses, and found to be 1638 kip-ft (2222 kN-m), corresponding to a theoretical plastic load, P_p, equal to 262 kips (1165 kN). The theoretical yield moment (based on σ_y and with residual stresses and web and flange distortion neglected), M_y, is equal to 1482 kip-ft (2011 kN-m), corresponding to a theoretical yield load, P_y, equal to 237 kips (1054 kN). In calculating M_y (and P_y) the yield stress is taken as σ_y (the 0.2% strain offset yield stress). Also, residual stresses, and web and flange distortion are neglected.

Plots of load versus midspan vertical deflection and midspan moment versus average end rotation are shown in Figure 5.1 and Figure 5.2, respectively. On these plots, a circle marks the ultimate load or moment, a rhombus marks 90% of the ultimate value on the loading branch, and a triangle marks 90% of the ultimate value on the unloading branch. Those symbols are used throughout this chapter to indicate these states for each specimen. Specimen 3 reached an ultimate load, P_u, of 262 kips (1165 kN), corresponding to an ultimate midspan moment, M_u, of 1638 kip-ft (2222 kN-m). M_u corresponds to 100% of M_p, which was the predicted moment capacity according to the 2001 AASHTO LRFD specifications [AASHTO 2001].

A photograph of Specimen 3 during testing is shown in Figure 5.3, and a photograph after testing is shown in Figure 5.4.

5.2.3 Yielding of Flange Extreme Fiber

The yield load, P_y, which equals 237 kips (1054 kN), is the load at which, theoretically, the extreme fiber of the flanges reaches σ_y (σ_y = 113 ksi (779 MPa)). The corresponding theoretical deflection is 2.70 in (69 mm). The theoretical stiffness (including both flexural and shear deformation) is compared with the stiffness from the experiment in Figure 5.5. In this figure, Point A corresponds to the theoretical yield deflection and point B is the experimental deflection corresponding to the theoretical yield load. It is clear that the specimen softens earlier in the experiment and this can be attributed to the following:

1. The yield stress, σ_y, used to calculate the theoretical yield load corresponds to the 0.2 % offset strain.
2. The presence of residual stresses.
3. Web and flange distortion, as described below.

The load versus strain for strain gage SG-161, at the middle of the lower surface of the tension flange, is plotted in Figure 5.6. On this plot, point B corresponds to the strain at the theoretical yield load. The strain at point B is 0.00602 in/in. Also on this plot, the strain at the ultimate load, 0.02 in/in, is marked with a circle.

5.2.4 Web Distortion

Due to the initial web geometric imperfections (out-of-flatness), bending of web plate is observed immediately after load is applied. Figure 5.7 shows strain separation, which is an indication of plate bending, at the location of strain gages SG-142 and SG-152. These strain gages are located at the mid height of the web. It is important to note that the web plate bending at this location is the result of amplifications of imperfections in the adjacent compression region of the web.

A plot of strains recorded by strain gages SG-144 and SG-150 is shown in Figure 5.8. These strain gages are located in the tension region of the web plate, where an initial imperfection will tend to decrease due to the normal tensile stress (in the local-1 direction). It is obvious that at this location, even further into the unloading stage, there is very little difference between these measured strains, and thus there is no significant web plate bending.

To monitor the moments, *SM2*, transferred between the web and compression flange, strain gages (oriented in the global-y direction) where attached to the web as close as possible to the web-flange intersection (as shown in Figure 5.9). The effect of these moments is to disturb the compression flange and increase its instability.

Strain gages located south of midspan are shown in Figure 5.9. The web plate curvature calculated from the strain gages attached at the web-flange intersection is shown in Figure 5.10 and Figure 5.11. This curvature is calculated by subtracting the strain on the east side from that at the west side, and dividing the result by the web thickness. Prior to reaching the ultimate load, these curvatures match with the schematic isometric diagram, shown in Figure 5.9, of the moments transferred between the web and compression flange. These moments act as twisting moments on the compression flange and increase its instability.

5.2.5 Lateral Distortion of Compression Flange

The occurrence of lateral distortion of the compression flange was determined by monitoring the average strain at the flange tips. This average strain is the average of strains measured by the gages on the upper and lower surfaces of the compression flange. Any difference between the average strains at the two flange tips signals the occurrence of lateral bending. The lateral curvature of the compression flange, ϕ_l, is calculated by subtracting the average strain at the east flange tip from that at the west flange tip and dividing the result by the distance between the east and west flange tip gages. A photograph of the lateral distortion of the compression flange, after testing, is shown in Figure 5.12. Plots of ϕ_l at sections 2, 4, and 5 are shown in Figure 5.13 through Figure 5.15, respectively. The locations of these sections are shown in Figure 4.58. In the following discussion, the following symbols will be used:

σ_{yp} = Proportional yield stress, at the end of the elastic range ($\sigma_{yp} = 100$ ksi (690 MPa))
P_{yp} = Proportional yield load, calculated when the extreme fiber of the flange reaches σ_{yp}, assuming no lateral curvature or other flange or web distortion
P_u = Ultimate load
ϕ_{lyp} = Lateral curvature of the flange when the stress at the flange tips reach σ_{yp} assuming no flange axial force
ϕ_l = Lateral flange curvature

At section 2, Figure 5.13, no noticeable lateral curvature occurs up to P_{yp}, 212.0 kips (943.0 kN). At a load equal to 90% P_u, 236 kips (1050 kN), ϕ_l is 4.0 x 10^{-5} in^{-1} (1.56 x 10^{-6} mm^{-1}). This curvature is equivalent to 5.4% ϕ_{lyp}.

At section 4 (Figure 5.14), up to a load of 165.0 kips (434.0 kN) ϕ_l is 2.80 x 10^{-5} in^{-1} (1.10 x 10^{-6} mm^{-1}), 3.8% ϕ_{lyp}. At a load equal to 90% P_u, ϕ_l is 2.1 x 10^{-4} in^{-1} (8.3 x 10^{-7} mm^{-1}). This curvature is equivalent to 28% ϕ_{lyp}.

At section 5 (Figure 5.15), up to a load of 182.0 kips (810.0 kN) ϕ_l is 2.3 x 10^{-5} in^{-1} (9.1 x 10^{-7} mm^{-1}), which equals 3.1% ϕ_{lyp}. The lateral curvature reverses

at a load equal to 84% P_u. At this load, ϕ_l is 3.3 x 10^{-5} in^{-1} (1.3 x 10^{-6} mm^{-1}). At P_u, ϕ_l reaches –3.2 x 10^{-4} in^{-1} (-1.3 x 10^{-5} mm^{-1}), which equals 43 % ϕ_{lyp}

Note that sections 2 and 4 are located to the south of midspan at which distortion occurs, while section 5 is located to the north of midspan at which no noticeable distortion occurs. From 90% P_u up to P_u, the specimen bends laterally in the same direction at sections 2 and 4. However, it bends in the opposite direction at section 5.

5.2.6 Plate Distortion of Compression Flange

The occurrence of plate distortion of the compression flange was determined by monitoring the strains at the upper and lower surfaces of the flange. Any difference between these strains signals the occurrence of flange plate bending. The flange plate curvature, ϕ_{fp}, is calculated by subtracting the strain at the upper surface from that at the lower surface and dividing the result by the flange thickness. Plots of ϕ_{fp} at sections 2-West, 3-West, 4-West, and 4-East are shown in Figure 5.16 through Figure 5.19, respectively.

At section 2-West (Figure 5.16) ϕ_{fp} was 1.2 x 10^{-4} in^{-1} (4.7 x 10^{-6} mm^{-1}) at P_{yp}. If no flange plate distortion occurs, this curvature should equal the beam curvature ϕ_b, which is 3.1 x 10^{-4} in^{-1} (1.2 x 10^{-5} mm^{-1}) at P_{yp}. Flange plate distortion at section 2-West has produced opposite curvature, and as a result, ϕ_{fp} is only 38% ϕ_b at P_{yp}. After that, ϕ_{fp} grows more rapidly to reach 8.2 x 10^{-4} in^{-1} (3.2 x 10^{-5} mm^{-1}) at a load equal to 97% P_u. At this load level, ϕ_{fp} reverses direction, reaching a curvature of –6.0 x 10^{-3} in^{-1} (-2.4 x 10^{-4} mm^{-1}) at P_u.

At section 3-West (Figure 5.17) ϕ_{fp} almost coincides with ϕ_b up to a load of 100.0 kips (444.8 kN). After that, ϕ_{fp} remains roughly constant, with a value of 1.1 x 10^{-4} in^{-1} (4.3 x 10^{-6} mm^{-1}), up to a load of 180.0 kips (801.0 kN). At that load level, the direction of ϕ_{fp} reverses, decreasing to 6.7 x 10^{-5} in^{-1} (2.6 x 10^{-6} mm^{-1}) at 90% P_u. At P_u, ϕ_{fp} is –9.3 x 10^{-3} in^{-1} (-3.7 x 10^{-4} mm^{-1}).

At section 4-West (Figure 5.18) ϕ_{fp} was 3.1 x 10^{-4} in^{-1} (1.2 x 10^{-5} mm^{-1}) at a load of 149.0 kips (663 kN), which is higher than ϕ_b by 39%. After that, ϕ_{fp} remains nearly constant up to a load of 187.0 kips (832.0 kN). At that load level, the direction of ϕ_{fp} reverses, decreasing to 7.7 x 10^{-5} in^{-1} (3.0 x 10^{-6} mm^{-1}) at 90% P_u. Then, ϕ_{fp} reverses again reaching 6.2 x 10^{-3} in^{-1} (2.4 x 10^{-4} mm^{-1}) at P_u. Shortly after reaching P_u, ϕ_{fp} reverses, yet again, reaching 2.6 x 10^{-3} in^{-1} (1.0 x 10^{-4} mm^{-1}) at 90% P_u-post peak.

At section 4-East (Figure 5.19) ϕ_{fp} follows ϕ_b up to 125.0 kips (556.0 kN), after which it grows rapidly to reach 1.7 x 10^{-3} in^{-1} (6.7 x 10^{-5} mm^{-1}) at 90% P_u. It continues to grow and reaches 4.6 x 10^{-2} in^{-1} (1.8 x 10^{-3} mm^{-1}) at P_u.

By comparing ϕ_{fp} at P_u for sections 2-West, 3-West, 4-West, and 4-East, it is clear that sections 2-West and 4-West have the same magnitude of curvature, but with opposite direction. The largest value of curvature occurs at section 4-East followed by sections 2-West and 4-West. The smallest value of curvature of these sections occurred at section 3-West.

5.2.7 Inelastic Stress State in Compression Flange

The upper surface of the compression flange is subjected to plane-stress conditions. The plane-stress plasticity algorithm, described in Appendix A, was used to estimate the stress conditions. For the plane-stress Von Mises yield criterion, the yield function, f, for a hardening material can be expressed as follows:

$$f = \sigma^2_{11} + \sigma^2_{22} - \sigma_{11}\,\sigma_{22} + 3\,\sigma^2_{12} - \sigma^2_{y}(\varepsilon_{ps}) \tag{5.1}$$

$$f = \sigma^2_{e} - \sigma^2_{y}(\varepsilon_{ps}) \tag{5.2}$$

$$\sigma_e = \sqrt{\sigma^2_{11} + \sigma^2_{22} - \sigma_{11}\,\sigma_{22} + 3\,\sigma^2_{12}} \tag{5.3}$$

where:

σ_e = Effective stress
ε_{ps} = Equivalent plastic strain
$\sigma_y(\varepsilon_{ps})$ = Yield stress as a function of the equivalent plastic strain

The total strain at each strain gage location is calculated by adding residual strain (the normal or shear strain) to the strain recorded during the test.

To facilitate the comparison of the stress terms in Equations 5.1 and 5.2, all terms are normalized by σ^2_{yp}. At yielding and during subsequent hardening f must be zero, which allows Equations 5.1 and 5.2 to be written in normalized form as follows:

$$\left(\frac{\sigma_{11}}{\sigma_{yp}}\right)^2 + \left(\frac{\sigma_{22}}{\sigma_{yp}}\right)^2 + \left(\frac{-\sigma_{11}\,\sigma_{22}}{\sigma_{yp}{}^2}\right) + \left(\frac{\sqrt{3}\sigma_{12}}{\sigma_{yp}}\right)^2 = \left(\frac{\sigma_y(\varepsilon_{ps})}{\sigma_{yp}}\right)^2 \tag{5.4}$$

$$\left(\frac{\sigma_e}{\sigma_{yp}}\right)^2 = \left(\frac{\sigma_y(\varepsilon_{ps})}{\sigma_{yp}}\right)^2 \tag{5.5}$$

The normalized terms in Equations 5.4 and 5.5 can be plotted on a single plot, versus ε_{ps}, and compared. The left hand side of Equations 5.4 and 5.5 represents the current state of stress, while the right hand side represents the strength of the material. Note that ($-\sigma_{11}\ \sigma_{22}/\sigma^2_{yp}$) has a negative sign, which leads to an apparent increase in the strength of the material if both normal stresses, σ_{11} and σ_{22}, have the same sign. Comparing $(\sigma_e/\sigma_{yp})^2$ versus ε_{ps} and $(\sigma_y(\varepsilon_{ps})/\sigma_{yp})^2$ versus ε_{ps} shows when yielding occurs and if the yield condition is maintained. If $(\sigma_e/\sigma_{yp})^2$ is less than $(\sigma_y(\varepsilon_{ps})/\sigma_{yp})^2$, the material is elastic.

5.2.8 State of Stress at Different Flange Locations

To study the effect of different stress components on the behavior of the compression flange and hence on the global behavior, four locations on the top surface of the compression flange were selected to illustrate the different states of stress that occur.

Section 2-West, as shown in Figure 4.58, is located to the south of midspan. At this location, significant distortion of Specimen 3 occurs. The residual stresses at this location are given in Table 4.10. Yielding at this location starts when the load reaches 73.3% P_u. According to the yield criterion, yielding initiates when σ_e equals σ_{yp} ($\sigma_{yp} = 100$ ksi (690 MPa)). Yield initiation is represented by a square. The presence of a compression residual normal stress, σ_{22}, has the effect of increasing the normal stress, σ_{11}, above $\sigma_y(\varepsilon_{ps})$ as shown in Figure 5.20. In this figure three vertical lines were drawn at ε_{ps} correspond to 90% P_u, P_u, and 90% P_u-post peak. In Figure 5.20, σ_{11} is multiplied by a negative sign so it can be compared with $\sigma_y(\varepsilon_{ps})$. At this location yielding continues without elastic unloading, as shown in Figure 5.20, where σ_e coincides with $\sigma_y(\varepsilon_{ps})$. At 90% P_u, σ_{11} is -120 ksi (-827 MPa), $\sigma_y(\varepsilon_{ps})$ is 112 ksi (772 MPa), σ_{22} is -19 ksi (-131 MPa), and σ_{12} is almost zero.

The contribution of each stress term in Equation 5.4, through out the loading history, is shown in Figure 5.21. At P_u, $(\sigma_{11}/\sigma_{yp})^2$ is 0.75, $(\sigma_{22}/\sigma_{yp})^2$ is almost zero, ($-\sigma_{11}\ \sigma_{22}/\sigma^2_{yp}$) is -0.03, and $(\sqrt{3}\sigma_{12}/\sigma_{yp})^2$ is 0.60. The sum of these four terms equals 1.32, which is equal to $(\sigma_y(\varepsilon_{ps})/\sigma_{yp})^2$ at this location when the load equals P_u. This equality shows this location is yielding. From these numbers, it is clear that the stresses causing yielding are σ_{11} and σ_{12}. Also, the main reason that σ_{11} is less than $\sigma_y(\varepsilon_{ps})$ is the presence of the shear stress σ_{12}.

As shown in Figure 5.22, soon after 90% P_u, σ_{11} starts to decrease while σ_{12} starts to increase. As the load increases from 90% P_u to P_u, σ_{11} decreases by 28%,

while σ_{12} increases from almost zero to –44 ksi (-303 MPa). At P_u, σ_{22} is -3 ksi (-21 MPa) which means that the decrease in σ_{11} is mainly attributed to the increase in σ_{12}.

Yield surfaces, in the σ_{11}-σ_{12} plane, are plotted for different increments in Figure 5.23, neglecting the normal stress, σ_{22}. At each of these increments, the yield stress equals $\sigma_y(\varepsilon_{ps})$. However, due to the presence of the normal stress, σ_{22}, the stress is not confined to the yield surfaces in the σ_{11}-σ_{12} plane. When the yield surface is the initial yield surface, and at 90% P_u, the stress state lies outside the yield surface in the σ_{11}-σ_{12} plane due to the effects of a significant compression normal stress, σ_{22}. However, at P_u the stress state almost coincides with the yield surface in the σ_{11}-σ_{12} plane because σ_{22} is small. At 90% P_u-post peak, the stress state lies outside the yield surface in the σ_{11}-σ_{12} plane due to the presence of a significant tension normal stress, σ_{22}. At this load level, σ_{11} is 68 ksi (469 MPa) in tension. It is important to note that as σ_{11} reverses from compression to tension the state of stress remains on the yield surface. This is a result of the normal stress, σ_{22}, and the shear stress σ_{12}.

Figure 5.24 and Figure 5.25 show the applied load versus strain and the midspan vertical deflection versus strain, respectively. The start of yielding, at section 2-West occurs at a load equal to 71% P_u when the midspan vertical deflection equals 2.4 in (61 mm). At this load level, the normal strain ε_{11}, equals –0.0035 in/in, the normal strain ε_{22}, equals 0.0003 in/in, and the engineering shear strain γ_{12} equals 0.0002 in/in. At P_u, which corresponds to a midspan vertical deflection of 4.8 in (122 mm), ε_{11} becomes –0.0085 in/in, ε_{22} becomes 0.003 in/in, and γ_{12} equals –0.006 in/in.

Section 2-Mid, as shown in Figure 4.58, is located to the south of the midspan. At this location, significant flange distortion occurs. The residual stresses at this location are given in Table 4.10. Yielding at this location starts when the load reaches 75% P_u. Yielding continues without elastic unloading as shown in Figure 5.26, where σ_e coincides with $\sigma_y(\varepsilon_{ps})$.

The contribution of each stress term in Equation 5.4 is shown in Figure 5.27. At P_u, $(\sigma_{11}/\sigma_{yp})^2$ is 1.25, $(\sigma_{22}/\sigma_{yp})^2$ is 0.03, $(-\sigma_{11}\,\sigma_{22}/\sigma^2_{yp})$ is –0.19, and $(\sqrt{3}\sigma_{12}/\sigma_{yp})^2$ is 0.28. The sum of these four terms equals 1.37, which is equal to $(\sigma_y(\varepsilon_{ps})/\sigma_{yp})^2$ at this location when the load equals P_u. This equality shows this location is yielding. Also, it is clear that $(\sqrt{3}\sigma_{12}/\sigma_{yp})^2$ almost offsets $(-\sigma_{11}\,\sigma_{22}/\sigma^2_{yp})$.

As shown in Figure 5.28, between 90% P_u and P_u σ_{11} increases by 2%, while σ_{12} increases from –6 ksi (-41 MPa) to –30 ksi (-214 MPa). It is important to note that even with this large increase in σ_{12}, σ_{11} increases. The reason for this is the change in σ_{22} from 4 ksi (28 MPa) to -17 ksi (117 MPa). Between P_u and 90% P_u-post peak,

σ_{11} decreases by 20%, σ_{12} increases by 47%, and σ_{22} increases from –30 ksi (207) MPa) to –52 ksi (359 MPa).

Yield surfaces, in the σ_{11}-σ_{12} plane, are plotted for different increments in Figure 5.29. When the yield surface is the initial surface (σ_{yp}) and at 90% P_u, the stress state almost coincides with the yield surface in the σ_{11}-σ_{12} plane due to the presence of only a small tension normal stress, σ_{22}, However, at P_u and at 90% P_u-post peak, the stress state lies outside the yield surface in the σ_{11}-σ_{12} plane, as a result of a considerable compression normal stress, σ_{22}.

Figure 5.30 and Figure 5.31 show the applied load versus strain and the midspan vertical deflection versus strain, respectively. The start of yielding at this section 2-Mid occurs at a load equal to 75% P_u when the midspan vertical deflection equals 2.6 in (66 mm). At this load level, ε_{11} equals –0.0034 in/in, ε_{22} equals 0.0012 in/in, and γ_{12} equals –0.00014 in/in. At P_u, which corresponds to a midspan vertical deflection of 4.8 in (122 mm), ε_{11} becomes –0.017 in/in, ε_{22} becomes 0.006 in/in, and γ_{12} equals –0.01 in/in.

Section 2-East, as shown in Figure 4.58, is also located to the south of the midspan. The residual stresses at this location are given in Table 4.10. Yielding at this location starts when the load reaches 68% P_u. The presence of the compression residual normal stress, σ_{22}, has the effect of increasing the normal stress, σ_{11}, above $\sigma_y(\varepsilon_{ps})$ as shown in Figure 5.32. At this location yielding continues without elastic unloading as shown in Figure 5.32.

The contribution of each stress term in Equation 5.4, is shown in Figure 5.33. At P_u, $(\sigma_{11}/\sigma_{yp})^2$ is 0.13, $(\sigma_{22}/\sigma_{yp})^2$ is 0.22, $(-\sigma_{11}\sigma_{22}/\sigma^2_{yp})$ is 0.17, and $(\sqrt{3}\sigma_{12}/\sigma_{yp})^2$ is 0.82. The sum of these four terms equals 1.34, which is equal to $(\sigma_y(\varepsilon_{ps})/\sigma_{yp})^2$ at this location, showing that this location is yielding. From these numbers, it is clear that the reasons for the reduction in σ_{11}, which is far below σ_{yp}, is the presence of σ_{12} and the tension normal stress, σ_{22}.

As shown in Figure 5.34, soon after 90% P_u is reached, σ_{11} starts to decrease while σ_{12} starts to increase. Between 90% P_u and P_u σ_{11} decreases by 70%, while σ_{12} increases from almost zero to –52 ksi (-359 MPa) and σ_{22} also changes from -19 ksi (-131 MPa) to 46 ksi (317 MPa).

Yield surfaces, in the σ_{11}-σ_{12} plane, are plotted for different increments in Figure 5.35, neglecting the normal stress, σ_{22}. However, due to the presence of normal stress, σ_{22}, the stress is not confined to the yield surfaces in the σ_{11}-σ_{12} plane. At the start of yielding and at 90% P_u, the stress state lies outside the yield surface in

the σ_{11}-σ_{12} plane due to the presence of a significant compression normal stress, σ_{22}. However, at P_u the stress state lies inside the yield surface in the σ_{11}-σ_{12} plane, as a result of a large tension normal stress, σ_{22}. At 90% P_u–post peak, when σ_{11} is tension, the stress state lies outside the σ_{11}-σ_{12} plane due to the presence of a significant tension normal stress, σ_{22}. At this load level, the normal stress, σ_{11} equals 113 ksi (779 MPa) tension. It is important to note that even though the normal stress, σ_{11}, has reversed from compression to tension, the state of stress at this location is still on the yield surface. This is a result of the normal stress, σ_{22}, and shear stress, σ_{12}.

Figure 5.36 and Figure 5.37 show the applied load versus strain and the midspan vertical deflection versus strain, respectively. The start of yielding, at section 2-East, occurs at a load equal to 68% P_u, when the midspan vertical deflection equals 2.3 in (58 mm). At this load level, ε_{11}equals –0.0035 in/in, ε_{22} equals 0.0003 in/in, and γ_{12} equals 0.0003 in/in. At P_u, which corresponds to a midspan vertical deflection of 4.8 in (122 mm), ε_{11} becomes –0.007 in/in, ε_{22} becomes 0.0043 in/in, and γ_{12} equals –0.006 in/in.

Section 4-East, as shown in Figure 4.58, is located to the south of the midspan. The residual stresses at this location are given in Table 4.10. Yielding at this location starts when the load reaches 60% P_u. The presence of the compression residual normal stress, σ_{22}, has the effect of increasing the normal stress, σ_{11}, above $\sigma_y(\varepsilon_{ps})$ as shown in Figure 5.38. Yielding continues without elastic unloading as shown in Figure 5.38. At 90% P_u, σ_{11} is -121 ksi (-834 MPa), while $\sigma_y(\varepsilon_{ps})$ is 114 ksi (786 MPa). At this load level, σ_{22} is -16 ksi (-110 MPa) and σ_{12} is 1 ksi (7 MPa).

The contribution of each stress term in Equation 5.4, is shown in Figure 5.39. At P_u, $(\sigma_{11}/\sigma_{yp})^2$ is 1.50, $(\sigma_{22}/\sigma_{yp})^2$ is almost zero, $(-\sigma_{11}\sigma_{22}/\sigma^2_{yp})$ is -0.03, and $(\sqrt{3}\sigma_{12}/\sigma_{yp})^2$ is 0.02. The sum of these four terms equals 1.49, which is equal to $(\sigma_y(\varepsilon_{ps})/\sigma_{yp})^2$ at this location. This equality shows this location is on the yield surface. Also, it is clear that yielding is mainly attributed to σ_{11}.

As shown in Figure 5.40, σ_{11} continues to increase until P_u is reached. Between P_u and 90% P_u-post peak, there is almost no change in σ_{11}.

Figure 5.41 and Figure 5.42 show the applied load versus strain and the midspan vertical deflection versus strain, respectively. The start of yielding, at section 4-East, occurs at a load equal to 60% P_u when the midspan vertical deflection equals 2.0 in (51 mm). At this load level, ε_{11} equals –0.0035 in/in, ε_{22} equals 0.0004 in/in, and γ_{12} equals 0.0005 in/in. At P_u, which corresponds to a midspan vertical deflection

of 4.8 in (122 mm), ε_{11} becomes –0.046 in/in, ε_{22} becomes 0.02 in/in, and γ_{12} equals 0.005 in/in.

Section 8-West, as shown in Figure 4.58, is located to the north of the midspan. At this location, no significant distortion occurs. The residual stresses at this location are given in Table 4.10. Yielding at this location starts when the load reaches 72% P_u, and continues until P_u is reached. The presence of a compression residual normal stress, σ_{22}, has the effect of increasing the normal stress, σ_{11}, above $\sigma_y(\varepsilon_{ps})$ as shown in Figure 5.43. The contribution of each term in Equation 5.4 and 6.5 is plotted in Figure 5.44. At 90% P_u, σ_{11} is -120 ksi (827 MPa), while $\sigma_y(\varepsilon_{ps})$ is 112 ksi (772 MPa). At this load level, σ_{22} is -22 ksi (-152 MPa) and σ_{12} is 6 ksi (41 MPa) as shown in Figure 5.45. Soon after P_u is reached, elastic unloading occurs, as shown in Figure 5.43, where σ_e falls below $\sigma_y(\varepsilon_{ps})$. It is important to point out that elastic unloading at this location is governed by unloading at other critical locations in the distorted region.

Yield surfaces, in the σ_{11}-σ_{12} plane, are plotted for different increments in Figure 5.46, neglecting σ_{22}. However, due to the presence of normal stress, σ_{22}, the stress is not confined to the yield surfaces in the σ_{11}-σ_{12} plane. At the start of yielding, at 90% P_u, and at P_u the stress state lies outside the yield surfaces in the σ_{11}-σ_{12} plane due to the presence of a significant compression σ_{22}. However, at 90% P_u-post peak the stress state lies inside the yield surface in the σ_{11}-σ_{12} plane, as a result of elastic unloading.

Figure 5.47 and Figure 5.48 show plots of the applied load and the midspan vertical deflection versus strain, respectively. From Figure 5.47, it is clear that soon after P_u is reached, unloading occurs.

5.3 Specimen 4

According to the 2001 AASHTO LRFD specifications [AASHTO 2001], Specimen 4 has a noncompact section with an ultra compact flange and a noncompact web. The compression flange brace spacing satisfies the AASHTO LRFD requirements for compact sections. The ultimate flexural strength of this specimen is expected to be the plastic moment capacity of the section, M_p, based on the optional Q formula for flexural resistance (Equation 2.16).

5.3.1 Test Procedure

The test procedure was composed of two steps: (1) two initial cycles, in each cycle the specimen was loaded to 100 kips (445 kN) and then unloaded, and (2) loading to failure.

The initial two cycles were performed under displacement control with a displacement of 0.10 in per minute (2.54 mm per minute). At a midspan vertical deflection of 1.94 in (49 mm), the applied load was 100 kips (445 kN) and thus the corresponding loading rate was 5.15 kips per minute (22.9 kN per minute). This midspan vertical deflection corresponds to a strain of 0.002179 in/in at the middle of the tension flange (strain gage SG-161). The data were recorded at 1.0 second intervals.

After checking the results of the first two cycles, the specimen was loaded to failure under displacement control. The loading rate was 0.10 in per minute (2.54 mm per minute) until the applied load was 200 kips (890 kN), with data recorded at 2.0 second intervals. To capture unexpected unloading, as the maximum predicted load was approached, the displacement rate was reduced to 0.05 in per minute (1.27 mm per minute), with data recorded at 2.0 second intervals. Upon reaching the maximum load, the data were recorded at 0.5 second intervals while maintaining the same displacement rate of 0.05 in per minute (1.27 mm per minute).

5.3.2 Global Behavior

The theoretical plastic moment, M_p, was calculated based on the dimensions and yield stresses, and found to be 1829 kip-ft (2481 kN-m), corresponding to a theoretical plastic load, P_p, equal to 224 kips (997 kN). The theoretical yield moment, M_y, is equal to 1618 kip-ft (2195 kN-m), corresponding to a theoretical yield load, P_y, equal to 199 kips (886 kN). The assumptions made in calculating M_y (and P_y) are discussed in Section 5.3.3.

Plots of load versus midspan vertical deflection and midspan moment versus average end rotation are shown in Figure 5.49 and Figure 5.50, respectively. Specimen 4 reached an ultimate load, P_u, of 209 kips (928 kN), corresponding to an ultimate midspan moment, M_u, of 1695 kip-ft (2299 kN-m). M_u corresponds to 92.7% of M_p. M_p was the predicted moment capacity according to the 2001 AASHTO LRFD specifications [AASHTO 2001].

A photograph of Specimen 4 during testing is shown in Figure 5.51, and a photograph after testing is shown in Figure 5.52.

5.3.3 Yielding of Flange Extreme Fiber

The yield load, P_y, which equals 199 kips (886 kN), is the load at which, theoretically, the extreme fiber of the flanges reaches σ_y (σ_y = 113 ksi (779 MPa)). In calculating M_y (and P_y), residual stresses, and web and flange distortion were neglected. The corresponding theoretical deflection is 3.72 in (94 mm). The theoretical stiffness (including both flexural and shear deformation) is compared with the stiffness

from the experiment in Figure 5.53. In this figure, Point A corresponds to the theoretical yield deflection and point B is the experimental deflection corresponding to the theoretical yield load.

The load versus strain for strain gage SG-161, at the middle of the lower surface of the tension flange, is plotted in Figure 5.54. On this plot, point B corresponds to the strain at the theoretical yield load. The strain at point B is 0.00555 in/in. Also on this plot, the strain at the ultimate load, 0.01198 in/in, is marked with a circle.

5.3.4 Web Distortion

Due to the initial web geometric imperfections (out-of-flatness), bending of web plate is observed immediately after load is applied. Figure 5.55 shows strain separation, which is an indication of plate bending, at the location of strain gages SG-42 and SG-52. These strain gages are located at mid height of the web. The web plate bending at this location is the result of amplifications of imperfections in the adjacent compression region of the web.

A plot of strains recorded by strain gages SG-44 and SG-50 is shown in Figure 5.56. These strain gages are located in the tension region of the web plate, where an initial imperfection will tend to decrease due to the normal tensile stress (in the local-1 direction). At this location, even far into the unloading stage, there is essentially no difference between these measured strains, and thus there is no web plate bending.

To monitor the moments, *SM2*, transferred between the web and compression flange, strain gages (oriented in the global-y direction) where attached to the web as close as possible to the web-flange intersection (as shown in Figure 5.57). The effect of these moments is to disturb the compression flange and increase its instability.

Strain gages located north of midspan are shown in Figure 5.57. The web plate curvature calculated from the strain gages attached at the web-flange intersection is shown in Figure 5.58 and Figure 5.59. The moments, SM2, as shown Schematically in Figure 5.57(b) act as twisting moment on the compression flange and increase its instability.

5.3.5 Lateral Distortion of Compression Flange

The calculation of ϕ_l was discussed in Section 5.2.6. A photograph of the lateral distortion of the compression flange, after testing, is shown in Figure 5.60. Plots of ϕ_l at sections 2 and 5 are shown in Figure 5.61 and Figure 5.62, respectively. The locations of these sections are shown in Figure 4.58.

At section 2, Figure 5.61, no noticeable lateral curvature occurs up to a load of 184.0 kips (818.0 kN). At a load equal to 90% P_u, 187.7 kips (834.9 kN), ϕ_l is 5.0 x 10^{-5} in^{-1} (1.97 x 10^{-6} mm^{-1}). This curvature is equivalent to 5.3% ϕ_{lyp}.

At section 5 (Figure 5.62), ϕ_l is small up to a load of 107.5 kips (478.2 kN). At a load equal to 90% P_u, ϕ_l reaches 3.6 x 10^{-4} in^{-1} (1.42 x 10^{-5} mm^{-1}), which equals 38% ϕ_{lyp}.

Note that section 2 is located to the south of midspan at which no noticeable distortion occurs, while section 5 is located to the north of midspan at which distortion occurs.

5.3.6 Plate Distortion of Compression Flange

The calculation of ϕ_{fp} was discussed in Section 5.2.6. Plots of ϕ_{fp} at sections 5-East and 5-West are shown in Figure 5.63 and Figure 5.64, respectively.

At section 5-East (Figure 5.63) ϕ_{fp} was almost zero at P_{yp}. If no flange plate distortion occurs, this curvature should equal the beam curvature ϕ_b, which is 3.1 x 10^{-4} in^{-1} (1.2 x 10^{-5} mm^{-1}) at P_{yp}. Therefore, flange plate distortion at section 5-East has produced opposite curvature, and as a result the net curvature is almost zero. At a load equal to 90% P_u, ϕ_{fp} is 1.82 x 10^{-4} in^{-1} (7.2 x 10^{-6} mm^{-1}).

At section 5-West (Figure 5.64) ϕ_{fp} was almost zero at 90% P_u. It reaches 4.0 x 10^{-2} in^{-1} (1.6 x 10^{-3} mm^{-1}) at P_u.

Note that as the compression flange bends laterally at section 5, as shown in Figure 5.62, tensile bending stresses will develop on the east side, while compressive bending stresses will develop on the west side. As a result, the flange plate distortion, of the compression flange, at section 5-East will be less than the flange plate distortion at section 5-West, as shown in Figure 5.63 and Figure 5.64.

5.3.7 State of Stress at Different Flange Locations

To study the effect of different stress components on the behavior of the compression flange and hence on the global behavior, two locations on the top surface of the compression flange were selected to illustrate the different states of stress that occur.

Section 1-East, as shown in Figure 4.58, is located to the south of the midspan. At this location, no significant distortion occurs. The residual stresses at this location are given in Table 4.11. Yielding at this location starts when the load reaches 59% P_u, and continues until P_u is reached. According to the yield criterion, yielding initiates

when σ_e equals σ_{yp} ($\sigma_{yp} = 100$ ksi (690 MPa)). Yield initiation is represented by a square. The presence of a compression residual normal stress, σ_{22}, has the effect of increasing the normal stress, σ_{11}, above $\sigma_y(\varepsilon_{ps})$ as shown in Figure 5.65. The contribution of each term in Equation 5.4 and 5.5 is plotted in Figure 5.66. At 90% P_u, σ_{11} is -118 ksi (-814 MPa), while $\sigma_y(\varepsilon_{ps})$ is 114 ksi (786 MPa). At this load level, σ_{22} is -8 ksi (-55 MPa) and σ_{12} is 8 ksi (55 MPa) as shown in Figure 5.67. As soon as P_u is reached, elastic unloading occurs, as shown in Figure 5.65, where σ_e falls below $\sigma_y(\varepsilon_{ps})$. Note that the elastic unloading at this location is governed by unloading at other critical locations.

Yield surfaces, in the σ_{11}-σ_{12} plane, are plotted for different increments in Figure 5.68, neglecting σ_{22}. However, due to the presence of the normal stress, σ_{22}, the stress is not confined to the yield surfaces in the σ_{11}-σ_{12} plane. At the start of yielding and at 90% P_u, the stress state lies outside the yield surface in the σ_{11}-σ_{12} plane due to the presence of a significant compression stress, σ_{22}. At P_u, the stress state lies almost on the yield surface in the σ_{11}-σ_{12} plane due to the presence of a small compression stress, σ_{22}. However, at 90% P_u-post peak the stress state lies inside the σ_{11}-σ_{12} plane, as a result of elastic unloading.

Section 7-East, as shown in Figure 4.58, is located to the north of midspan. At this location, significant distortion of Specimen 4 occurs. The residual stresses at this location are given in Table 4.11. Yielding at this location starts when the load reaches 65.3% P_u. The presence of the compression residual normal stress, σ_{22}, has the effect of increasing the normal stress, σ_{11}, above $\sigma_y(\varepsilon_{ps})$ as shown in Figure 5.69. At this location yielding continues without elastic unloading, as shown in Figure 5.69, where σ_e coincides with $\sigma_y(\varepsilon_{ps})$. At 90% P_u, σ_{11} is -117 ksi (-807 MPa), $\sigma_y(\varepsilon_{ps})$ is 113 ksi (779 MPa), σ_{22} is -12 ksi (-83 MPa), and σ_{12} is -8 ksi (-55 MPa).

The contribution of each stress term in Equation 5.4, through out the loading history, is shown in Figure 5.70. At P_u, $(\sigma_{11}/\sigma_{yp})^2$ is 0.65, $(\sigma_{22}/\sigma_{yp})^2$ is almost zero, $(-\sigma_{11}\,\sigma_{22}/\sigma^2_{yp})$ is -0.02, and $(\sqrt{3}\sigma_{12}/\sigma_{yp})^2$ is 0.72. The sum of these four terms equals 1.35, which is equal to $(\sigma_y(\varepsilon_{ps})/\sigma_{yp})^2$ at this location when the load equals P_u. This equality shows this location is yielding. From these numbers, it is clear that the stresses causing yielding are σ_{11} and σ_{12}. Also, the main reason that σ_{11} is less than $\sigma_y(\varepsilon_{ps})$ is the presence of the shear stress σ_{12}.

As shown in Figure 5.71, shortly before 90% P_u, σ_{11} starts to decrease while σ_{12} starts to increase. As the load increases from 90% P_u to P_u, σ_{11} decreases by 32%, while σ_{12} increases from –8 ksi (-55 MPa) to –49 ksi (-338 MPa). At P_u, σ_{22} is

-2 ksi (-14 MPa) which means that the decrease in σ_{11} is mainly attributed to the increase in σ_{12}.

Yield surfaces, in the σ_{11}-σ_{12} plane, are plotted for different increments in Figure 5.23, neglecting the normal stress, σ_{22}. At each of these increments, the yield stress equals $\sigma_y(\varepsilon_{ps})$. When the yield surface is the initial yield surface, and at 90% P_u, the stress state lies outside the yield surface in the σ_{11}-σ_{12} plane due to the effects of a significant compression normal stress, σ_{22}. However, at P_u the stress state almost coincides with the yield surface in the σ_{11}-σ_{12} plane because σ_{22} is small. At 90% P_u-post peak, the stress state lies outside the yield surface in the σ_{11}-σ_{12} plane due to the presence of a significant tension normal stress, σ_{22}. At this load level, σ_{11} is 67 ksi (462 MPa) in tension. It is important to note that as σ_{11} reverses from compression to tension the state of stress remains on the yield surface. This is a result of the normal stress, σ_{22}, and shear stress σ_{12}.

5.4 Specimen 5

According to the 2001 AASHTO LRFD specifications [AASHTO 2001], Specimen 5 has a compact section with an ultra compact flange and a compact web. The compression flange brace spacing satisfies the AASHTO LRFD requirements for compact sections. The ultimate flexural strength of this specimen is expected to be the plastic moment capacity of the section, M_p, based on the optional Q formula for flexural resistance (Equation 2.16).

5.4.1 Test Procedure

The test procedure was composed of two steps: (1) two initial cycles, in each cycle the specimen was loaded to 201 kips (894 kN) and then unloaded, and (2) loading to failure.

The two initial cycles were performed under displacement control with a displacement of 0.20 in per minute (5.08 mm per minute). At a midspan vertical deflection of 2.0 in (51 mm), the applied load was 201 kips (894 kN), so the corresponding loading rate was 20.1 kips per minute (89.4 kN per minute). This midspan vertical deflection corresponds to a strain of 0.00258 in/in at the middle of the tension flange (strain gage SG-161). The data were recorded at 2.0 second intervals.

After checking the results of the first two cycles, the specimen was loaded to failure under displacement control. The loading rate was 0.20 in per minute (5.08 mm per minute) until the applied load was 304 kips (1352 kN), with data recorded at 2.0 second intervals. As the maximum predicted load was approached, the

displacement rate was reduced to 0.1 in per minute (2.54 mm per minute), with data recorded at 1.0 second intervals.

5.4.2 Global Behavior

The theoretical plastic moment, M_p, was calculated based on the dimensions and yield stresses, and found to be 2693 kip-ft (3653 kN-m), corresponding to a theoretical plastic load, P_p, equal to 385 kips (1713 kN). The theoretical yield moment, M_y, is equal to 2418 kip-ft (3280 kN-m), corresponding to a theoretical yield load, P_y, equal to 345 kips (1535 kN). The assumptions made in calculating M_y (and P_y) are discussed in Section 5.4.3.

Plots of load versus midspan vertical deflection and midspan moment versus average end rotation are shown in Figure 5.73 and Figure 5.74, respectively. Specimen 5 reached an ultimate load, P_u, of 384 kips (1708 kN), corresponding to an ultimate midspan moment, M_u, of 2688 kip-ft (3647 kN-m). M_u corresponds to 99.8% of M_p. M_p was the predicted moment capacity according to the 2001 AASHTO LRFD specifications [AASHTO 2001].

A photograph of Specimen 5 during testing is shown in Figure 5.75, and a photograph after testing is shown in Figure 5.76.

5.4.3 Yielding of Flange Extreme Fiber

At the yield load, P_y, of 345 kips (1535 kN), the theoretical extreme fiber stress is σ_y (σ_y = 113 ksi (779 MPa)). In calculating M_y (and P_y), residual stresses, and web and flange distortion were neglected. The corresponding theoretical deflection is 3.32 in (84 mm). The theoretical stiffness (including both flexural and shear deformation) is compared with the stiffness from the experiment in Figure 5.77. In this figure, Point A corresponds to the theoretical yield deflection and point B is the experimental deflection corresponding to the theoretical yield load.

The load versus strain for strain gage SG-161, at the middle of the lower surface of the tension flange, is plotted in Figure 5.78. On this plot, point B corresponds to the strain at the theoretical yield load. The strain at point B is 0.00524 in/in. Also on this plot, the strain at the ultimate load, 0.03349 in/in, is marked with a circle.

5.4.4 Web Distortion

Figure 5.79 shows the applied load versus strain at location of strain gages SG-41 and SG-53. These strain gages are located in the compression region above the mid

height of the web, as is shown in Figure 4.60. Note that the web plate bending at this location starts at 90% P_u.

A plot of strains recorded by strain gages SG-144 and SG-150 is shown in Figure 5.80. These strain gages are located in the tension region of the web. At this location, up to 90% P_u there is essentially no difference between these measured strains, and thus no web plate bending.

Strain gages located to monitor the moments, *SM2*, transferred between the web and compression flange north and south of midspan are shown in Figure 5.81. The web plate curvature calculated from the strain gages attached at the web-flange intersection is shown in Figure 5.82 through Figure 5.85. For this specimen, the web buckling was in a direction opposed to the compression flange buckling. In other words, the web buckling restrains the compression flange buckling.

5.4.5 Lateral Distortion of Compression Flange

The calculation of ϕ_l was discussed in Section 5.2.6. A photograph of the lateral distortion of the compression flange, after testing, is shown in Figure 5.86. Plots of ϕ_l at sections 4 and 6 are shown in Figure 5.87 and Figure 5.88, respectively. The locations of these sections are shown in Figure 4.58.

At section 4, Figure 5.87, no noticeable lateral curvature occurs up to a load of 250 kips (112 kN). At a load equal to 90% P_u, 346 kips (1539 kN), ϕ_l is -4.7×10^{-5} in^{-1} (-1.85×10^{-6} mm^{-1}). This curvature is equivalent to 0.1% ϕ_{lyp}. At P_u, ϕ_l reaches -7.7×10^{-4} in^{-1} (3.03×10^{-5} mm^{-1}), which equals 144 % ϕ_{lyp}.

At section 6 (Figure 5.88), ϕ_l is small up to a load of 380 kips (1690 kN). At P_u, ϕ_l reaches 3.2×10^{-3} in^{-1} (1.26×10^{-4} mm^{-1}).

5.4.6 Plate Distortion of Compression Flange

The calculation of ϕ_{fp} was discussed in Section 5.2.6. Plots of ϕ_{fp} at sections 4-East and 4-West are shown in Figure 5.89 and Figure 5.90, respectively.

At section 4-East (Figure 5.89) ϕ_{fp} was almost zero at P_{yp}, 242 kips (1076 kN). If no flange plate distortion occurs, this curvature should equal the beam curvature ϕ_b, which is 2.2×10^{-4} in^{-1} (8.7×10^{-6} mm^{-1}) at P_{yp}. Therefore, flange plate distortion at section 4-East has produced opposite curvature, and as a result the net curvature is almost zero. At a load equal to 90% P_u, ϕ_{fp} is 4.1×10^{-5} in^{-1} (1.6×10^{-6} mm^{-1}) and at P_u, ϕ_{fp} is 9.2×10^{-3} in^{-1} (3.6×10^{-4} mm^{-1}).

At section 4-West (Figure 5.90) ϕ_{fp} was small up to 90% P_u. It reaches 5.2 x 10^{-2} in^{-1} (2.1 x 10^{-3} mm^{-1}) at P_u.

Note that as the compression flange bends laterally at section 4, as shown in Figure 5.87, tensile bending stresses will develop on the east side, while compressive bending stresses will develop on the west side. As a result, the flange plate distortion, of the compression flange, at section 4-East will be less than the flange plate distortion at section 4-West, as shown in Figure 5.89 and Figure 5.90.

5.4.7 State of Stress at Different Flange Locations

Two locations on the top surface of the compression flange were selected to illustrate the different states of stress that occur.

Section 4-Mid, as shown in Figure 4.58, is located to the south of the midspan. The residual stresses at this location are given in Table 4.12. Yielding at this location starts when the load reaches 48% P_u. According to the yield criterion, yielding initiates when σ_e equals σ_{yp} ($\sigma_{yp} = 80$ ksi (552 MPa)). Yield initiation is represented by a square. The presence of a compression residual normal stress, σ_{22}, has the effect of increasing the normal stress, σ_{11}, above $\sigma_y(\varepsilon_{ps})$ as shown in Figure 5.91. The contribution of each term in Equation 5.4 and 5.5 is plotted in Figure 5.92. At P_u, σ_{11} is -126 ksi (-869 MPa), while $\sigma_y(\varepsilon_{ps})$ is 122 ksi (841 MPa). At this load level, σ_{22} is -13 ksi (-90 MPa) and σ_{12} is 10 ksi (69 MPa) as shown in Figure 5.93. At this location, yielding continues even after P_u is reached, as shown in Figure 5.91.

Yield surfaces, in the σ_{11}-σ_{12} plane, are plotted for different increments in Figure 5.94, neglecting σ_{22}. However, due to the presence of the normal stress, σ_{22}, the stress is not confined to the yield surfaces in the σ_{11}-σ_{12} plane. At the start of yielding and at 90% P_u, the stress state almost lies on the yield surface in the σ_{11}-σ_{12} plane due to the presence of a small compression stress, σ_{22}. At P_u, the stress state lies outside the yield surface in the σ_{11}-σ_{12} plane due to the presence of a significant compression stress, σ_{22}.

Section 6-East, as shown in Figure 4.58, is located to the north of midspan. The residual stresses at this location are given in Table 4.12. Yielding at this location starts when the load reaches 45% P_u. The presence of the tension normal stress, σ_{22}, has the effect of reducing the normal stress, σ_{11}, below $\sigma_y(\varepsilon_{ps})$ as shown in Figure 5.95. At this location yielding continues without elastic unloading, as shown in Figure 5.95, where σ_e coincides with $\sigma_y(\varepsilon_{ps})$. At P_u, σ_{11} is -57 ksi (-393 MPa), $\sigma_y(\varepsilon_{ps})$ is 118 ksi (814 MPa), σ_{22} is 72 ksi (496 MPa), and σ_{12} is 21 ksi (145 MPa).

The contribution of each stress term in Equation 5.4 is shown in Figure 5.96. At P_u, $(\sigma_{11}/\sigma_{yp})^2$ is 0.52, $(\sigma_{22}/\sigma_{yp})^2$ is 0.83, $(-\sigma_{11}\sigma_{22}/\sigma^2_{yp})$ is 0.66, and $(\sqrt{3}\sigma_{12}/\sigma_{yp})^2$ is 0.21. The sum of these four terms equals 2.22, which is equal to $(\sigma_y(\varepsilon_{ps})/\sigma_{yp})^2$ at this location when the load equals P_u. This equality shows this location is yielding. From these numbers, it is clear that the main reason that σ_{11} is less than $\sigma_y(\varepsilon_{ps})$ is the presence of a high tension normal stress, σ_{22} and the shear stress σ_{12}.

Yield surfaces, in the σ_{11}-σ_{12} plane, are plotted for different increments in Figure 5.98, neglecting the normal stress, σ_{22}. At 90% P_u, the stress state lies almost on the yield surface in the σ_{11}-σ_{12} plane due to a small compression normal stress, σ_{22}. However, at P_u, the stress state lies inside the yield surface in the σ_{11}-σ_{12} plane due to the presence of a significant tension normal stress, σ_{22}. At this load level, σ_{22} is 72 ksi (496 MPa) in tension.

5.5 Specimen 6

According to the 2001 AASHTO LRFD specifications [AASHTO 2001], Specimen 6 has a noncompact section with a compact flange and a noncompact web. The compression flange brace spacing satisfies the AASHTO LRFD requirements for compact sections. The ultimate flexural strength of this specimen is expected to be 99% of the plastic moment capacity of the section, 99% M_p, based on the optional Q formula for flexural resistance (Equation 2.16).

5.5.1 Test Procedure

The test procedure was composed of two steps: (1) two initial cycles, in each cycle the specimen was loaded to 200 kips (890 kN) and then unloaded, and (2) loading to failure.

The two initial cycles were performed under displacement control with a displacement of 0.20 in per minute (5.08 mm per minute). At a midspan vertical deflection of 2.31 in (59 mm), the applied load was 200 kips (890 kN), so the corresponding loading rate was 17.3 kips per minute (77 kN per minute). This midspan vertical deflection corresponds to a strain of 0.00181 in/in at the middle of the tension flange (strain gage SG-161). The data were recorded at 1.0 second intervals.

After checking the results of the first two cycles, the specimen was loaded to failure under displacement control. The loading rate was 0.20 in per minute (5.08 mm per minute) until the applied load was 400 kips (1779 kN) at which the midspan vertical deflection was 4.67 in (119 mm). Then the specimen was loaded at a rate of 0.1 in per minute (2.54 mm per minute) up to a midspan vertical deflection of 9.77 in (248 mm). At this deflection the applied load was 392 kips (1744 kN) which is

77% of the ultimate load, P_u. Then the specimen was unloaded to a midspan vertical deflection of 7.4 in (188 mm). This unloading intended to verify that if the specimen is unloaded elastically after the peak load was reached, and then reloaded, it will reload elastically to the same load at which it was unloaded. After the specimen was unloaded it was loaded again at a rate 0.1 in per minute (2.54 mm per minute) until 10.7 in (272 mm) midspan vertical deflection was reached. At this deflection the applied load was 206 kips (916 kN) which is 41% P_u. The specimen was then unloaded to end the test. The data were recorded at 1.0 second intervals through out the test.

5.5.2 Global Behavior

The theoretical plastic moment, M_p, was calculated based on the dimensions and yield stresses, and found to be 6476 kip-ft (8785 kN-m), corresponding to a theoretical plastic load, P_p, equal to 540 kips (2402 kN). The theoretical yield moment, M_y, is equal to 5800 kip-ft (7869 kN-m), corresponding to a theoretical yield load, P_y, equal to 483 kips (2148 kN). The assumptions behind M_y (and P_y) are discussed in Section 5.5.3.

Plots of load versus midspan vertical deflection and midspan moment versus average end rotation are shown in Figure 5.99 and Figure 5.100, respectively. On these plots, a circle marks the ultimate load or moment, a rhombus marks 90% of the ultimate value on the loading branch, and a triangle marks 90% of the ultimate value on the unloading branch. Those symbols are used throughout this chapter to indicate these points in each specimen. Specimen 6 reached an ultimate load, P_u, of 508 kips (2260 kN), corresponding to an ultimate midspan moment, M_u, of 6096 kip-ft (8270 kN-m). M_u corresponds to 94% M_p. 99% M_p was the predicted moment capacity according to the 2001 AASHTO LRFD specifications [AASHTO 2001].

A photograph of Specimen 6 during testing is shown in Figure 5.101, and a photograph after testing is shown in Figure 5.102.

5.5.3 Yielding of Flange Extreme Fiber

At the yield load, P_y, of 483 kips (2148 kN), the theoretical extreme fiber stress is σ_y (σ_y = 113 ksi (779 MPa)). In calculating M_y (and P_y), residual stresses, and web and flange distortion were neglected. The corresponding theoretical deflection is 5.51 in (140 mm). The theoretical stiffness (including both flexural and shear deformation) is compared with the stiffness from the experiment in Figure 5.103. In this figure, Point A corresponds to the theoretical yield deflection and point B is the experimental deflection corresponding to the theoretical yield load. It is clear that the specimen softens earlier in the experiment.

The load versus strain for strain gage SG-161, at the middle of the lower surface of the tension flange, is plotted in Figure 5.104. On this plot, point B corresponds to the strain at the theoretical yield load. The strain at point B is 0.0053 in/in. Also on this plot, the strain at the ultimate load, 0.0086 in/in, is marked with a circle.

5.5.4 Web Distortion

Due to the initial web geometric imperfections (out-of-flatness), bending of web plate is observed immediately after load is applied. Figure 5.105 shows strain separation, which is an indication of plate bending, at location of strain gages SG-41 and SG-53. These strain gages are located in the compression region above the mid height of the web as shown in Figure 4.60.

A plot of strains recorded by strain gages SG-144 and SG-150 is shown in Figure 5.106. These strain gages are located in the tension region of the web. At this location, even further into the unloading stage, there is essentially no difference between these measured strains, and thus no web plate bending.

Strain gages to monitor the moments, *SM2*, transferred between the web and compression flange, located north of midspan are shown in Figure 5.107. The web plate curvature calculated from the strain gages attached at the web-flange intersection is shown in Figure 5.108 through Figure 5.110. The corresponding moments transferred between web and compression flange act as twisting moment on the compression flange.

5.5.5 Lateral Distortion of Compression Flange

ϕ_l was calculated as described in Section 5.2.6. A photograph of the lateral distortion of the compression flange, after testing, is shown in Figure 5.111. Plots of ϕ_l at sections 4 and 6 are shown in Figure 5.112 and Figure 5.113, respectively. The locations of these sections are shown in Figure 4.58.

At section 4, Figure 5.112, at a load equal to 90% P_u, 458.0 kips (2037 kN), ϕ_l is -2.0 x 10^{-5} in^{-1} (-7.9 x 10^{-7} mm^{-1}). This curvature is equivalent to 4.7% ϕ_{lyp}. After that ϕ_l reverses to reach 2.5 x 10^{-4} in^{-1} (9.8 x 10^{-6} mm^{-1}) at P_u. This curvature equals 47% ϕ_{lyp}.

At section 6 (Figure 5.113), at a load equal to 90% P_u, ϕ_l is –6.6 x 10^{-5} in^{-1} (-2.6 x 10^{-6} mm^{-1}). This curvature is equivalent to 12% ϕ_{lyp}. At 97% P_u-post peak, ϕ_l is –1.0 x 10^{-3} in^{-1} (-3.9 x 10^{-5} mm^{-1}), after which ϕ_l reverses.

Note that sections 4 is located to the south of midspan where no visible flange plate distortion occurs, while section 6 is located to the north of midspan where flange plate distortion occurs. Up to 90% P_u, the compression flange bends laterally in the same direction at sections 4 and 6. However, after that load level, the flange lateral bending is in opposite directions at sections 4 and 6.

5.5.6 Plate Distortion of Compression Flange

ϕ_{fp} was calculated as described in Section 5.2.6. Plots of ϕ_{fp} at sections 4-East and 6-East are shown in Figure 5.114 and Figure 5.115, respectively.

At section 4-East (Figure 5.114) ϕ_{fp} was –8.0 x 10^{-4} in^{-1} (-3.1 x 10^{-5} mm^{-1}) at 90% P_u. At a load equal to 99% P_u-post peak, ϕ_{fp} reverses direction.

At section 6-East (Figure 5.115) ϕ_{fp} was –3.7 x 10^{-4} in^{-1} (-1.5 x 10^{-5} mm^{-1}) at 90% P_u. At P_u, ϕ_{fp} was –2.8 x 10^{-3} in^{-1} (-1.1 x 10^{-4} mm^{-1}).

5.5.7 State of Stress at Different Flange Locations

Two locations on the top surface of the compression flange were selected to illustrate the different states of stress that occur. Section 4-East, as shown in Figure 4.58, is located to the south of midspan. At this location, no significant distortion of Specimen 6 occurs. The residual stresses at this location are given in Table 4.13. Yielding at this location starts when the load reaches 44.7% P_u. According to the yield criterion, yielding initiates when σ_e equals σ_{yp} ($\sigma_{yp} = 80$ ksi (552 MPa)). Yield initiation is represented by a square. The presence of the compression residual normal stress, σ_{22}, has the effect of increasing the normal stress, σ_{11}, above $\sigma_y(\varepsilon_{ps})$ as shown in Figure 5.116. At this location yielding continues without elastic unloading, as shown in Figure 5.116, where σ_e coincides with $\sigma_y(\varepsilon_{ps})$. At 90% P_u, σ_{11} is -119 ksi (-821 MPa), $\sigma_y(\varepsilon_{ps})$ is 109 ksi (752 MPa), σ_{22} is -23 ksi (-159 MPa), and σ_{12} is 2 ksi (14 MPa).

The contribution of each stress term in Equation 5.4 is shown in Figure 5.117. At P_u, $(\sigma_{11}/\sigma_{yp})^2$ is 2.31, $(\sigma_{22}/\sigma_{yp})^2$ is 0.02, $(-\sigma_{11}\sigma_{22}/\sigma^2_{yp})$ is -0.22, and $(\sqrt{3}\sigma_{12}/\sigma_{yp})^2$ is almost zero. The sum of these four terms equals 2.11, which is equal to $(\sigma_y(\varepsilon_{ps})/\sigma_{yp})^2$ at this location when the load equals P_u. This equality shows this location is yielding. From these numbers, it is clear that the stress causing yielding is σ_{11}. Also, the main reason that σ_{11} is more than $\sigma_y(\varepsilon_{ps})$ is the presence of the compression normal stress σ_{22}.

As shown in Figure 5.118, at 90% P_u, P_u, and 90% P_u-post peak, σ_{11} remains almost constant while σ_{12} decreases. At P_u, σ_{11} is -121 ksi (-834 MPa), σ_{22} is -12 ksi (-83 MPa), σ_{12} is almost zero, and $\sigma_y(\varepsilon_{ps})$ is 116 ksi (800 MPa), which means that the increase in σ_{11} is mainly attributed to the presence of the compression normal stress σ_{22}.

Yield surfaces, in the σ_{11}-σ_{12} plane, are plotted for different increments in Figure 5.119, neglecting the normal stress, σ_{22}. At each of these increments, the yield stress equals $\sigma_y(\varepsilon_{ps})$. However, due to the presence of the normal stress, σ_{22}, the stress is not confined to the yield surfaces in the σ_{11}-σ_{12} plane. The stress state lies outside the yield surface in the σ_{11}-σ_{12} plane due to the effects of a significant compression normal stress, σ_{22}.

Section 6-West, as shown in Figure 4.58, is located to the north of midspan. At this location, significant distortion of Specimen 6 occurs. The residual stresses at this location are given in Table 4.13. Yielding at this location starts when the load reaches 45.6% P_u. The presence of the compression residual normal stress, σ_{22}, has the effect of increasing the normal stress, σ_{11}, above $\sigma_y(\varepsilon_{ps})$ as shown in Figure 5.120. At 90% P_u, σ_{11} is -121 ksi (-834 MPa), $\sigma_y(\varepsilon_{ps})$ is 111 ksi (765 MPa), σ_{22} is -25 ksi (-171 MPa), and σ_{12} is 5 ksi (34 MPa).

The contribution of each stress term in Equation 5.4 is shown in Figure 5.121. At 90% P_u, $(\sigma_{11} / \sigma_{yp})^2$ is 2.33, $(\sigma_{22} / \sigma_{yp})^2$ is 0.10, $(-\sigma_{11}\,\sigma_{22} / \sigma^2_{yp})$ is -0.48, and $(\sqrt{3}\sigma_{12} / \sigma_{yp})^2$ is 0.01. The sum of these four terms equals 1.96, which is equal to $(\sigma_y(\varepsilon_{ps}) / \sigma_{yp})^2$ at this location when the load equals 90% P_u. This equality shows this location is yielding. From these numbers, it is clear that the stress causing yielding is σ_{11}. Also, the main reason that σ_{11} is more than $\sigma_y(\varepsilon_{ps})$ is the presence of compression normal stress, σ_{22}.

As shown in Figure 5.122, At 90% P_u, σ_{11} is -121 ksi (-834 MPa), $\sigma_y(\varepsilon_{ps})$ is 111 ksi (765 MPa), σ_{22} is -25 ksi (-171 MPa), and σ_{12} is 5 ksi (34 MPa).

Yield surfaces, in the σ_{11}-σ_{12} plane, are plotted for different increments in Figure 5.23, neglecting the normal stress, σ_{22}. When the yield surface is the initial yield surface, and at 90% P_u, the stress state lies outside the yield surface in the σ_{11}-σ_{12} plane due to the effects of a significant compression normal stress, σ_{22}. However, at P_u the stress state almost coincides with the yield surface in the σ_{11}-σ_{12} plane because σ_{22} is small. At 90% P_u-post peak, the stress state lies outside the yield surface in the σ_{11}-σ_{12} plane due to the presence of tension normal stress, σ_{22}. At this load level, σ_{11} is 34 ksi (234 MPa) in tension, σ_{22} is 15 ksi (103 MPa) in tension, and

σ_{12} is 66 ksi (455 MPa). Note that as σ_{11} reverses from compression to tension the state of stress remains on the yield surface.

5.6 Specimen 7

According to the AASHTO LRFD specifications [AASHTO 2001], Specimen 7 has a noncompact section with a compact flange and a noncompact web. The compression flange brace spacing satisfies the AASHTO LRFD requirements for compact sections. The ultimate flexural strength of this specimen is expected to be the plastic moment capacity of the section, M_p, based on the optional Q formula for flexural resistance (Equation 2.16).

5.6.1 Test Procedure

The test procedure was composed of two steps: (1) two initial cycles, in each cycle the specimen was loaded to 165 kips (734 kN) and then unloaded, and (2) loading to failure.

The two initial cycles were performed under displacement control with a displacement of 0.10 in per minute (2.54 mm per minute). At a midspan vertical deflection of 2.18 in (55 mm), the applied load was 165 kips (734 kN), so the corresponding loading rate was 7.57 kips per minute (33.7 kN per minute). This midspan vertical deflection corresponds to a strain of 0.001762 in/in strain gage SG-147. The data were recorded at 1.0 second intervals.

After checking the results of the first two cycles, the specimen was loaded to failure under displacement control. The loading rate was 0.10 in per minute (2.54 mm per minute) during the entire whole test, with data recorded at 2.0 second intervals. Due to an error in pretest setup, the range of the load cell was exceeded at a midspan vertical deflection of 4.2 in (107 mm). At a midspan vertical deflection of 4.4 in (112 mm) the test was halted and the specimen unloaded. There was a residual displacement of 0.2 in (5 mm) at zero load as shown in Figure 5.124. The load cell was then adjusted and the test was restarted. The data were recorded at 1.0 second intervals while maintaining the displacement rate at 0.1 in per minute (2.54 mm per minute).

5.6.2 Global Behavior

The theoretical plastic moment, M_p, was calculated based on the dimensions and yield stresses, and found to be 4090 kip-ft (5549 kN-m), corresponding to a theoretical plastic load, P_p, equal to 409 kips (1819 kN). The theoretical yield moment, M_y, is equal to 3638 kip-ft (4936 kN-m), corresponding to a theoretical yield load, P_y,

equal to 364 kips (1619 kN). The assumptions made in calculating M_y (and P_y) are discussed in Section 5.6.3.

Plots of load versus midspan vertical deflection and midspan moment versus average end rotation are shown in Figure 5.125 and Figure 5.126, respectively. Specimen 7 reached an ultimate load, P_u, of 395 kips (1757 kN), corresponding to an ultimate midspan moment, M_u, of 3949 kip-ft (5357 kN-m). M_u corresponds to 96.5% M_p. M_p was the predicted moment capacity according to the 2001 AASHTO LRFD specifications [AASHTO 2001].

A photograph of Specimen 4 during testing is shown in Figure 5.127, and a photograph after testing is shown in Figure 5.128.

5.6.3 Yielding of Flange Extreme Fiber

At the yield load, P_y, of 364 kips (1619 kN), the theoretical extreme fiber stress is σ_y (σ_y = 113 ksi (779 MPa)). In calculating M_y (and P_y), residual stresses, and web and flange distortion were neglected. The corresponding theoretical deflection is 4.73 in (120 mm). The theoretical stiffness (including both flexural and shear deformation) is compared with the stiffness from the experiment in Figure 5.129. In this figure, Point A corresponds to the theoretical yield deflection and point B is the experimental deflection corresponding to P_y. The two points almost coincide. Note that due to inelastic deformation from the test that was halted, due to an error in pretest setup, as explained in Section 5.6.1, the elastic range region for Specimen 7 appears to be larger than that of the other specimens.

The strain versus load for strain gage SG-147, at the lower surface of the tension flange, is plotted in Figure 5.130. On this plot, point B corresponds to the strain at the theoretical yield load. The strain at point B is 0.00408 in/in. Also, on this plot the strain at the ultimate load, 0.00777 in/in, is marked with a circle.

5.6.4 Web Distortion

A plot of strains recorded by strain gages SG-141 and SG-153 is shown in Figure 5.131. These strain gages are located in the compression region above the mid height of the web as shown in Figure 4.60. Due to small initial web geometric imperfections (out-of-flatness), there is a small difference between the strains recorded by the two strain gages up to 90% P_u. After that the difference between the strains recorded by the two strain gages grows due to the buckling of the web plate.

A plot of strains recorded by strain gages SG-144 and SG-150 is shown in Figure 5.132. These strain gages are located in the tension region of the web plate.

There is essentially no difference between these measured strains, and thus no web plate bending.

Strain gages to monitor the moments, *SM2*, transferred between the web and compression flange located south of midspan are shown in Figure 5.133. The web plate curvature calculated from the strain gages attached at the web-flange intersection is shown in Figure 5.134 through Figure 5.136.

5.6.5 Lateral Distortion of Compression Flange

ϕ_l was calculated as described in Section 5.2.6. A photograph of the lateral distortion of the compression flange, after testing, is shown in Figure 5.137. Plots of ϕ_l at sections 2 and 4 are shown in Figure 5.138 and Figure 5.139, respectively. The locations of these sections are shown in Figure 4.58.

At section 2 (Figure 5.138), no noticeable lateral curvature occurs up to a load equal to 90% P_u, 356 kips (1583 kN). After that, ϕ_l rapidly increases to reach –1.6 x 10^{-3} in^{-1} (-6.3 x 10^{-5} mm^{-1}). This curvature is equivalent to 299% ϕ_{lyp}.

At section 4 (Figure 5.139), no noticeable lateral curvature occurs up to a load equal to 90% P_u. At a load equal to 98% P_u, ϕ_l reverses direction to reach –3.5 x 10^{-4} in^{-1} (-1.38 x 10^{-5} mm^{-1}) at P_u. At a load equal to 98% P_u-post peak, ϕ_l reverses direction again.

5.6.6 Plate Distortion of Compression Flange

The calculation of ϕ_{fp} was described in Section 5.2.6. Plots of ϕ_{fp} at sections 2-West and 4-West are shown in Figure 5.140 and Figure 5.141, respectively. At section 2-West (Figure 5.140) ϕ_{fp} was almost zero at 90% P_u. It reaches 2.7 x 10^{-3} in^{-1} (1.06 x 10^{-4} mm^{-1}) at P_u. At section 4-West (Figure 5.141) ϕ_{fp} was almost zero at 90% P_u. It reaches –1.5 x 10^{-3} in^{-1} (-5.9 x 10^{-5} mm^{-1}) at P_u.

Note that as the compression flange bends laterally at section 2, as shown in Figure 5.138, tensile bending stresses will develop on the east side, while compressive bending stresses will develop on the west side. As a result, the flange plate distortion, of the compression flange, at section 2-West will increase.

5.6.7 State of Stress at Different Flange Locations

Two locations on the top surface of the compression flange were selected to illustrate the different states of stresses, which occur. Section 2-West, as shown in Figure 4.58, is located to the south of midspan. At this location, significant distortion occurs. The residual stresses at this location are given in Table 4.14. Note that the

possible changes in residual stresses due to the inelastic deformation that occured during the test that was halted due to an error in the pretest setup were not considered. Yielding at this location starts when the load reaches 50% P_u, and continues beyond 90% P_u-post peak. According to the yield criterion, yielding initiates when σ_e equals σ_{yp} ($\sigma_{yp} = 80$ ksi (552 MPa)). Yield initiation is represented by a square. The presence of a compression residual normal stress, σ_{22}, has the effect of increasing the normal stress, σ_{11}, above $\sigma_y(\varepsilon_{ps})$ as shown in Figure 5.142. The contribution of each term in Equation 5.4 is plotted in Figure 5.143. At 90% P_u, σ_{11} is -118 ksi (-814 MPa), while $\sigma_y(\varepsilon_{ps})$ is 107 ksi (738 MPa). At this load level, σ_{22} is -28 ksi (-193 MPa) and σ_{12} is 1 ksi (7 MPa) as shown in Figure 5.144.

Yield surfaces, in the σ_{11}-σ_{12} plane, are plotted for different increments in Figure 5.145, neglecting σ_{22}. However, due to the presence of the normal stress, σ_{22}, the stress is not confined to the yield surfaces in the σ_{11}-σ_{12} plane. At the start of yielding and at 90% P_u, the stress state lies outside the yield surfaces in the σ_{11}-σ_{12} plane due to the presence of a significant compression stress, σ_{22}. At P_u and 90% P_u-post peak, the stress state lies almost on the yield surface in the σ_{11}-σ_{12} plane due to the presence of a small compression stress, σ_{22}.

Section 4-West, as shown in Figure 4.58, is also located to the south of midspan. The residual stresses at this location are given in Table 4.14. Yielding at this location starts when the load reaches 46% P_u. The presence of the compression residual normal stress, σ_{22}, has the effect of increasing the normal stress, σ_{11}, above $\sigma_y(\varepsilon_{ps})$ as shown in Figure 5.146. The contribution of each stress term in Equation 5.4, is shown in Figure 5.147.

Elastic unloading occurs at a load equal to 99% P_u-post peak. Yielding starts again at 93% P_u-post peak. At this load level σ_{11} is 65 ksi (448 MPa), while $\sigma_y(\varepsilon_{ps})$ is 116 ksi (800 MPa), σ_{22} is -28 ksi (-193 MPa), and σ_{12} is –47 ksi (-324 MPa) as shown in Figure 5.148.

Yield surfaces, in the σ_{11}-σ_{12} plane, are plotted for different increments in Figure 5.149, neglecting the normal stress, σ_{22}. At the start of yielding, at 90% P_u, and at P_u, the stress state lies outside the yield surface in the σ_{11}-σ_{12} plane due to the presence of a significant compression normal stress, σ_{22}. However, at 90% P_u-post peak, the stress state lies almost on the yield surface in the σ_{11}-σ_{12} plane.

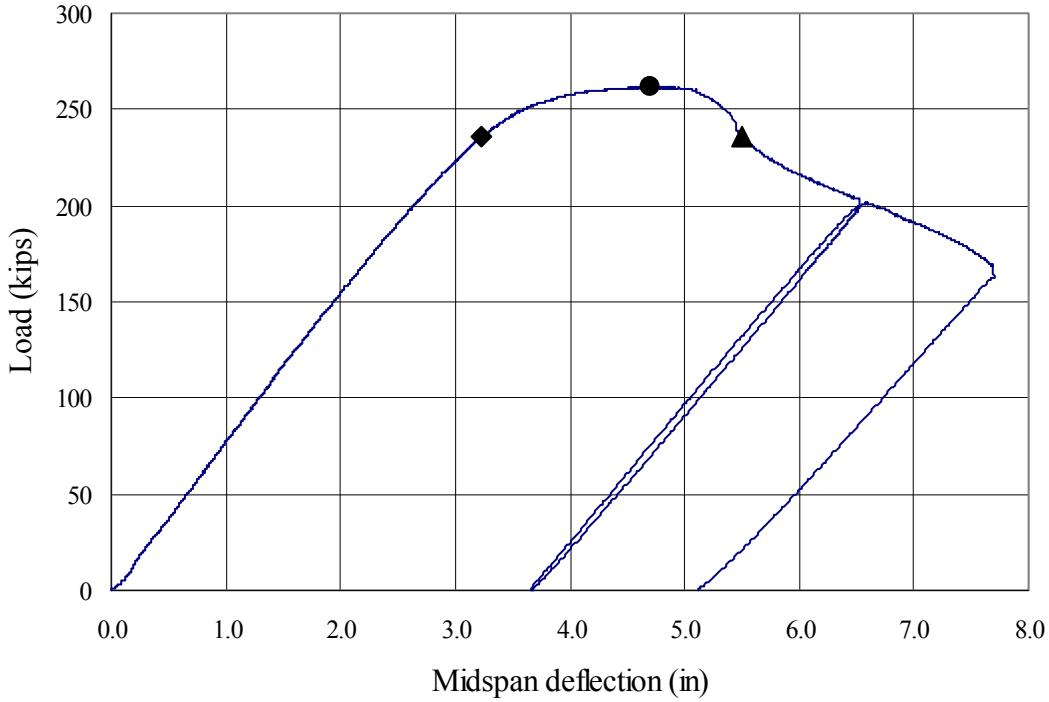

Figure 5.1 Load versus midspan vertical deflection (Specimen 3)

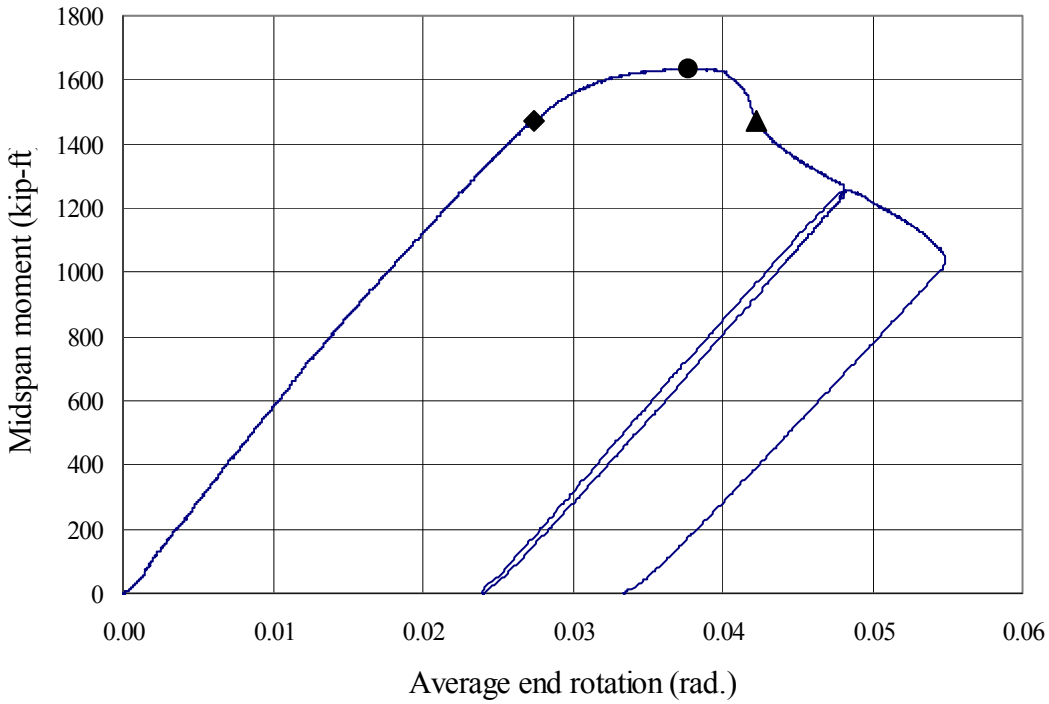

Figure 5.2 Midspan moment versus average end rotation (Specimen 3)

Figure 5.3 Specimen 3 during testing

Figure 5.4 Specimen 3 after testing

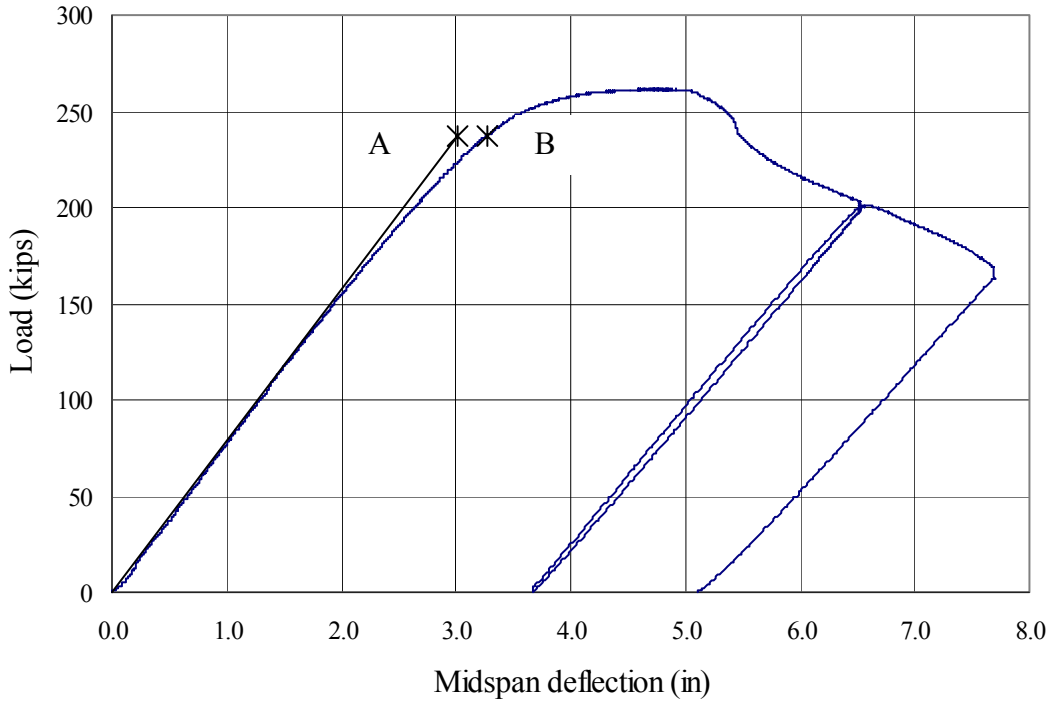

Figure 5.5 Load versus midspan vertical deflection (Specimen 3)

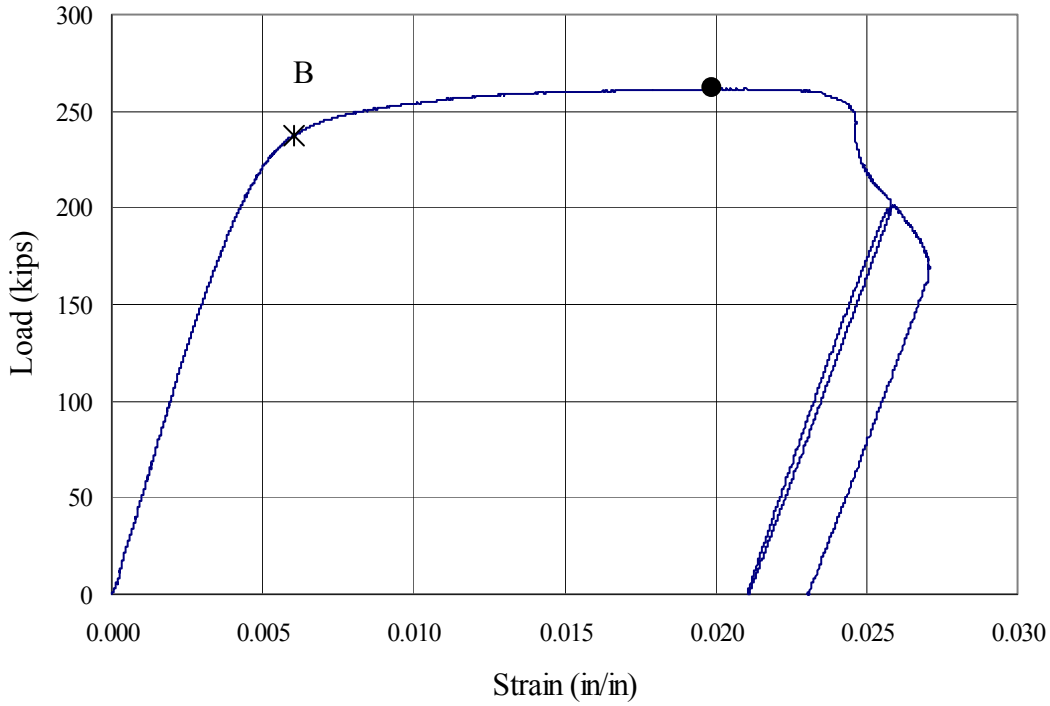

Figure 5.6 Load versus strain recorded by strain gage 161 (Specimen 3)

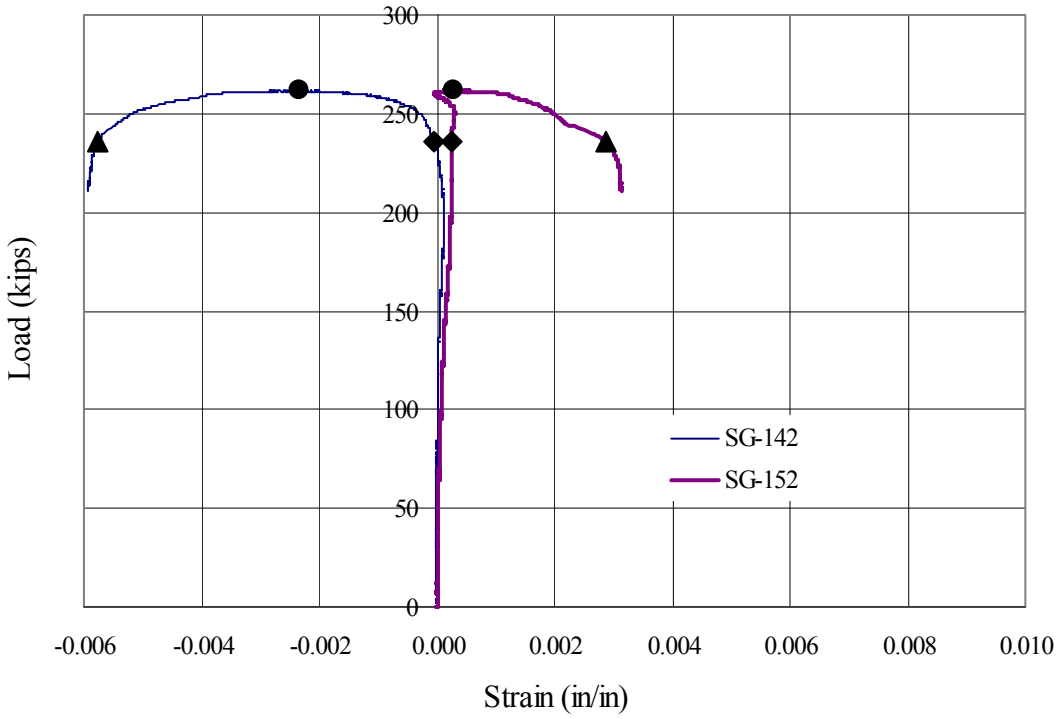

Figure 5.7 Effect of initial imperfection on web distortion (Specimen 3)

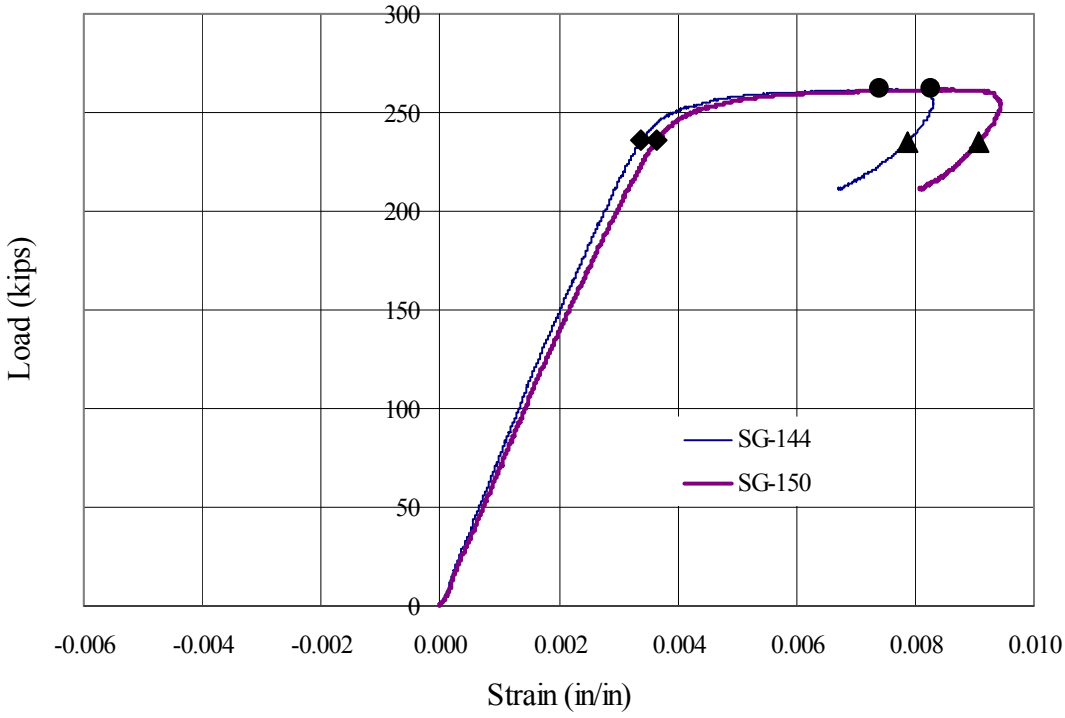

Figure 5.8 Load versus strain for strain gages SG-144 and SG-150 (Specimen 3)

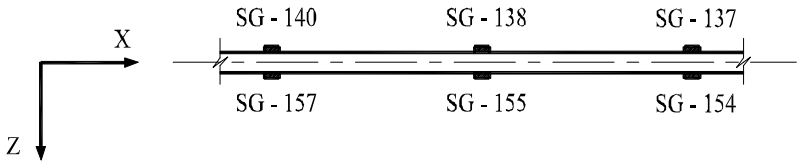

(a) Strain gages at web-flange intersection

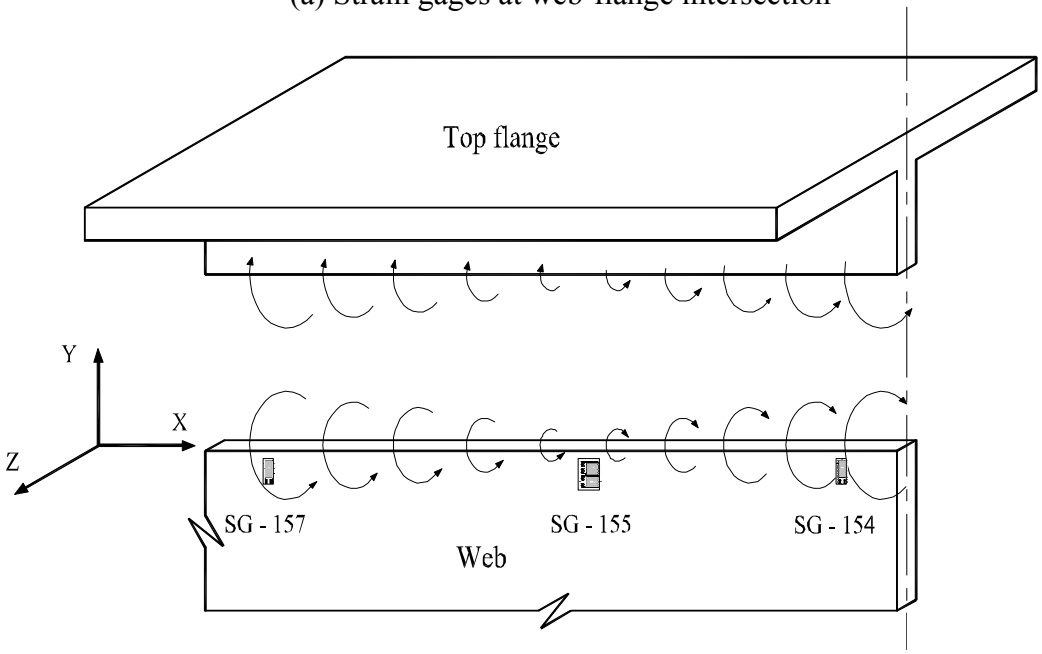

(b) Moment transfer at web-flange intersection

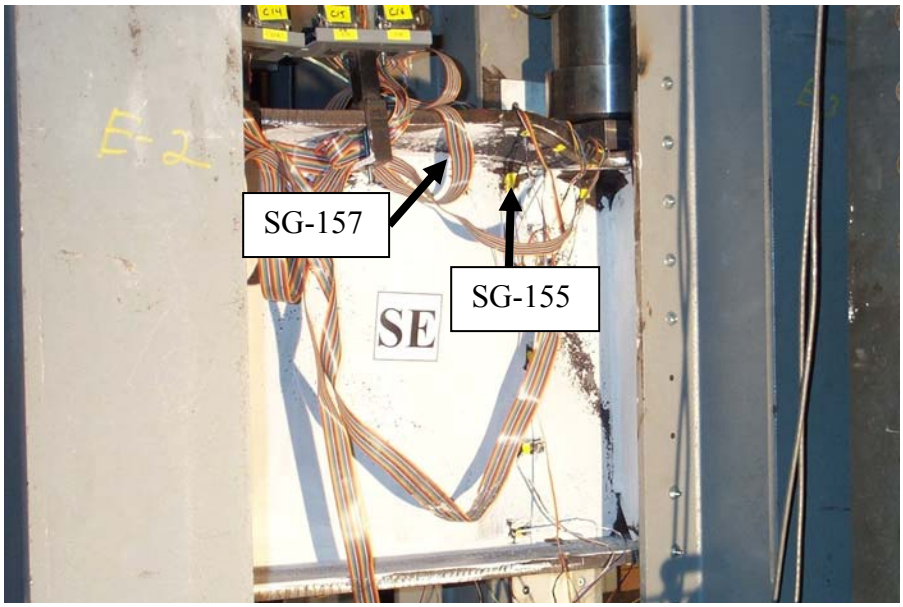

(b) Location of strain gages SG-155 and SG-157

Figure 5.9 Interaction between web and compression flange at the distorted region

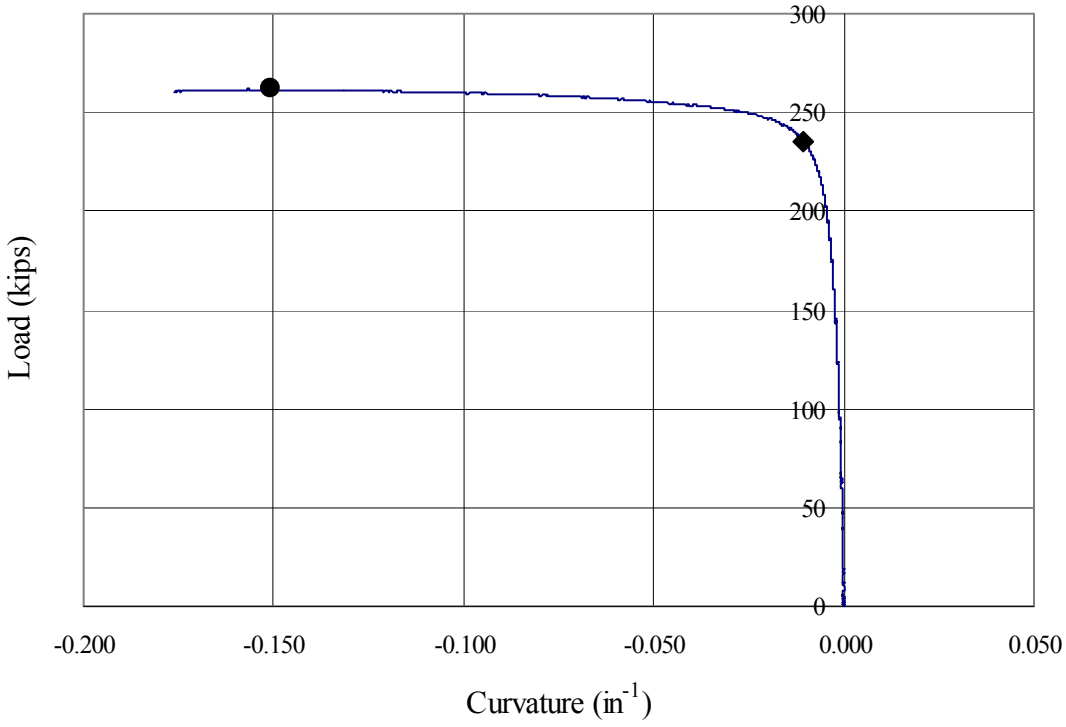

Figure 5.10 Load versus curvature at strain gages SG-138 and SG-155 (Specimen 3)

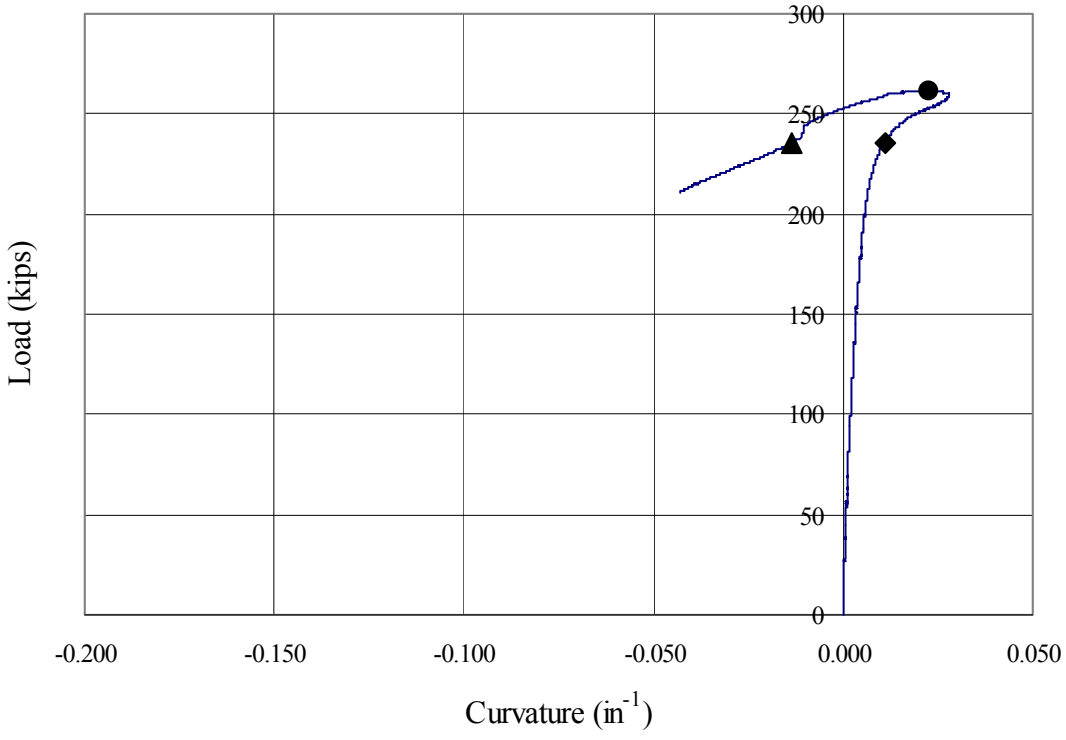

Figure 5.11 Load versus curvature at strain gages SG-140 and SG-157 (Specimen 3)

Figure 5.12 Lateral distortion of compression flange (Specimen 3)

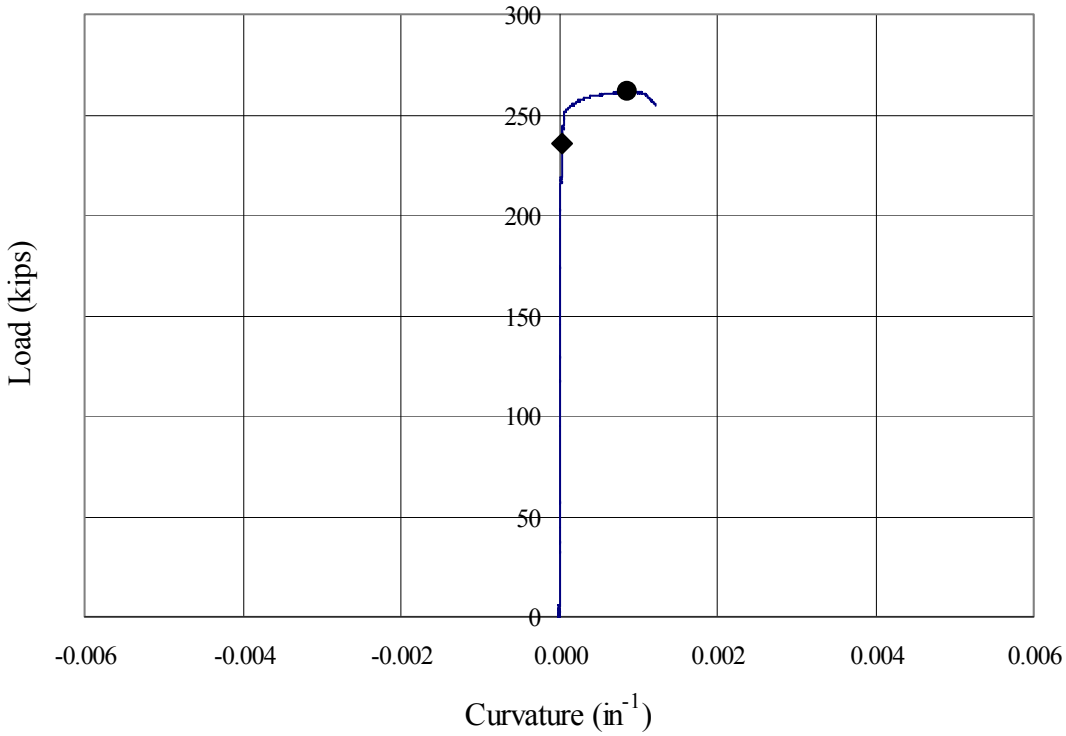

Figure 5.13 Load versus ϕ_l at section 2 (Specimen 3)

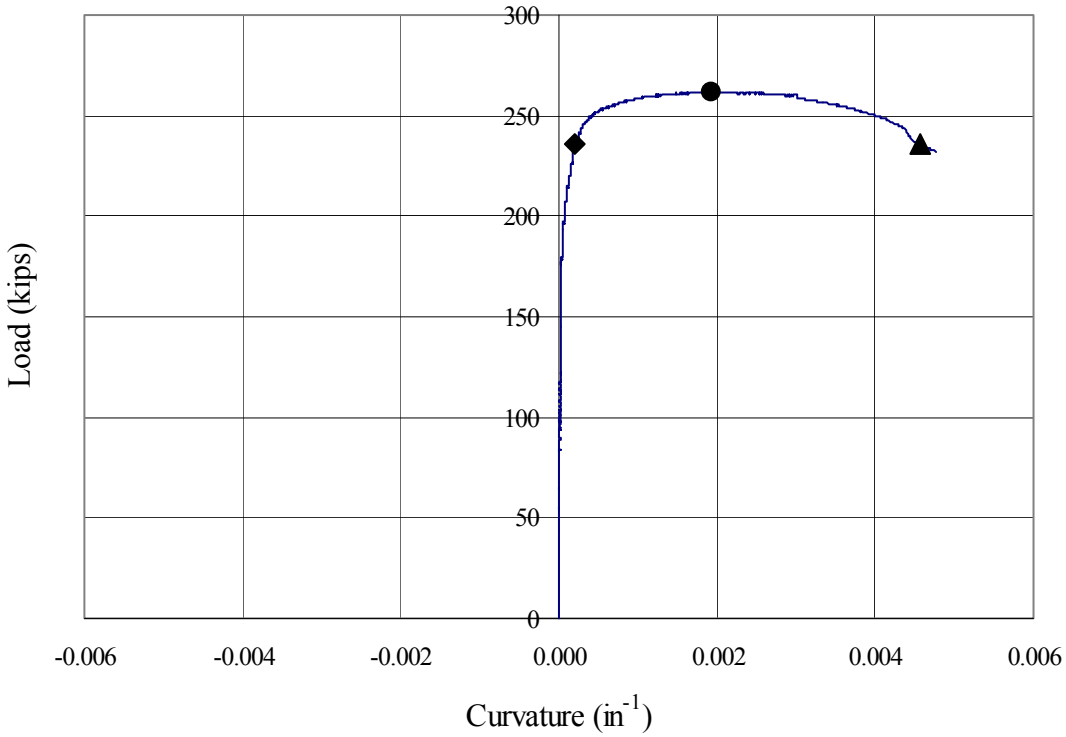

Figure 5.14 Load versus ϕ_l at section 4 (Specimen 3)

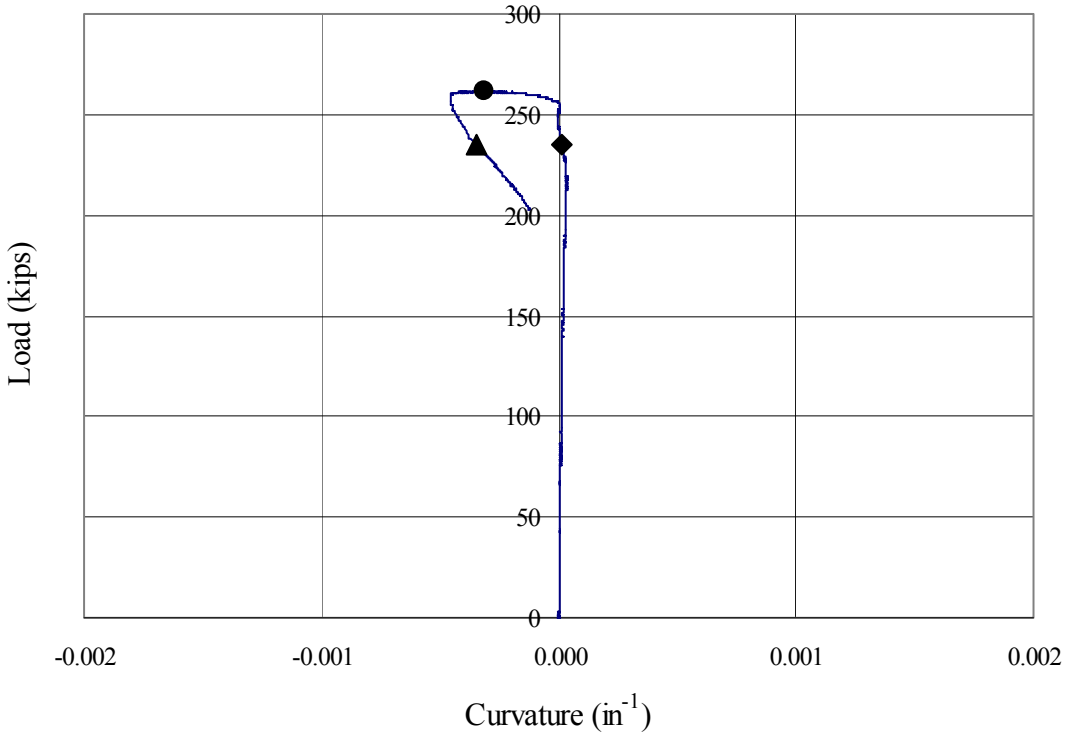

Figure 5.15 Load versus ϕ_l at section 5 (Specimen 3)

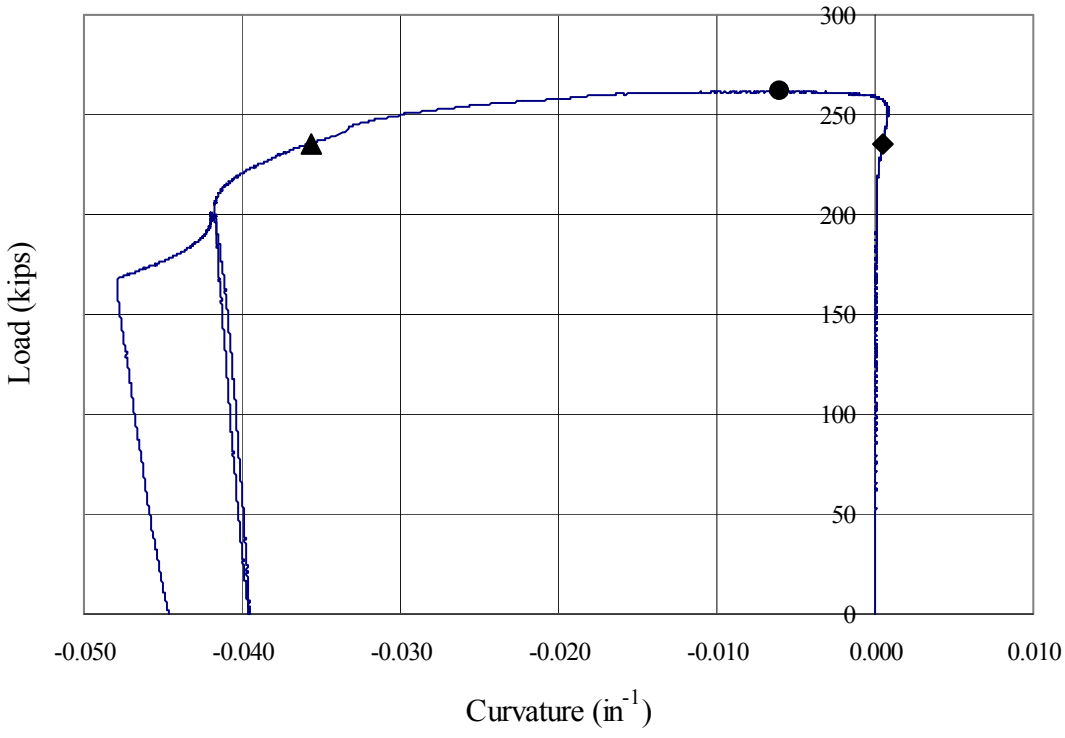

Figure 5.16 Load versus ϕ_{fp} at section 2-West (Specimen 3)

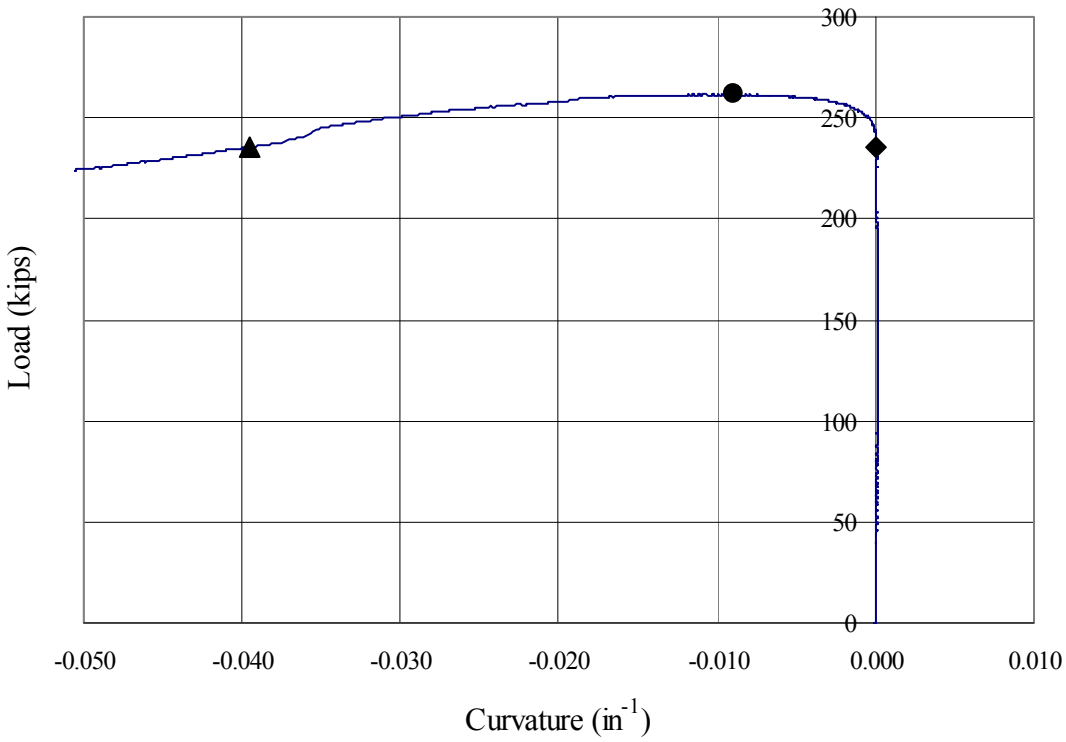

Figure 5.17 Load versus ϕ_{fp} at section 3-West (Specimen 3)

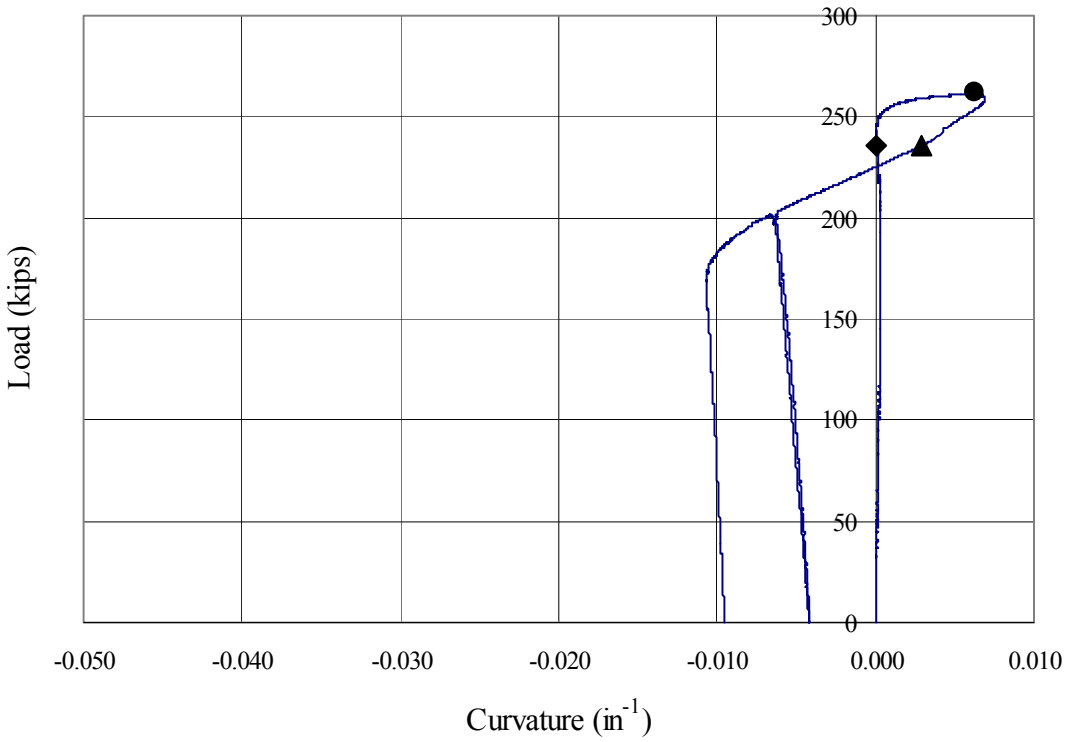

Figure 5.18 Load versus ϕ_{fp} at section 4-West (Specimen 3)

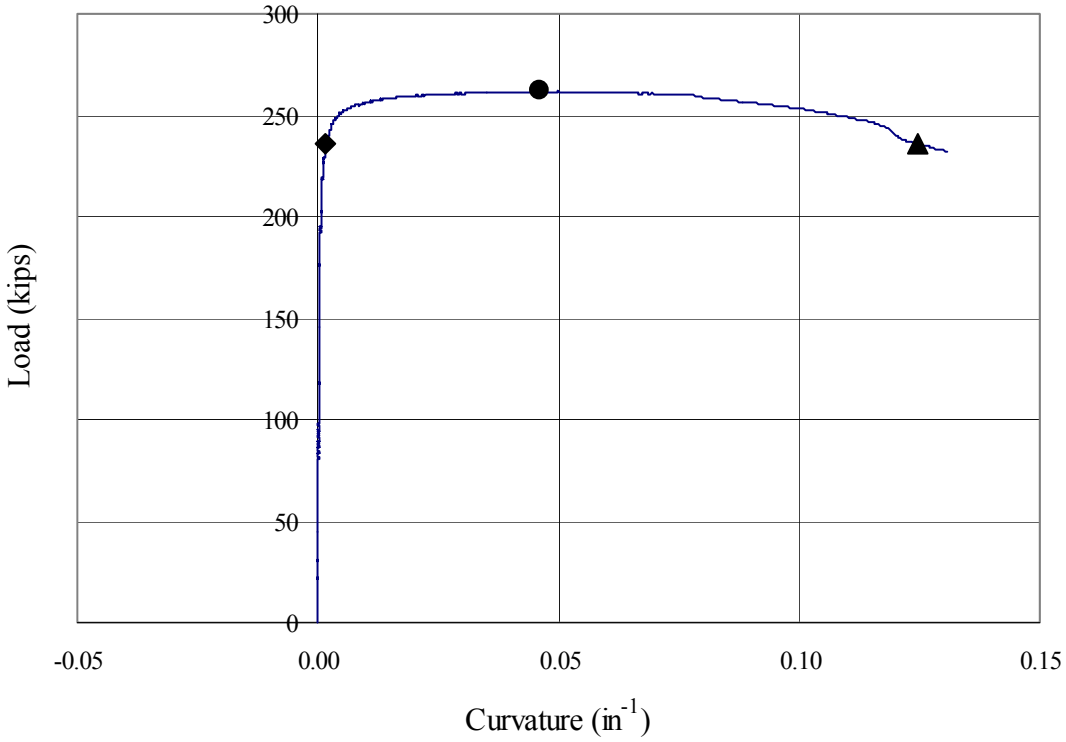

Figure 5.19 Load versus ϕ_{fp} at section 4-East (Specimen 3)

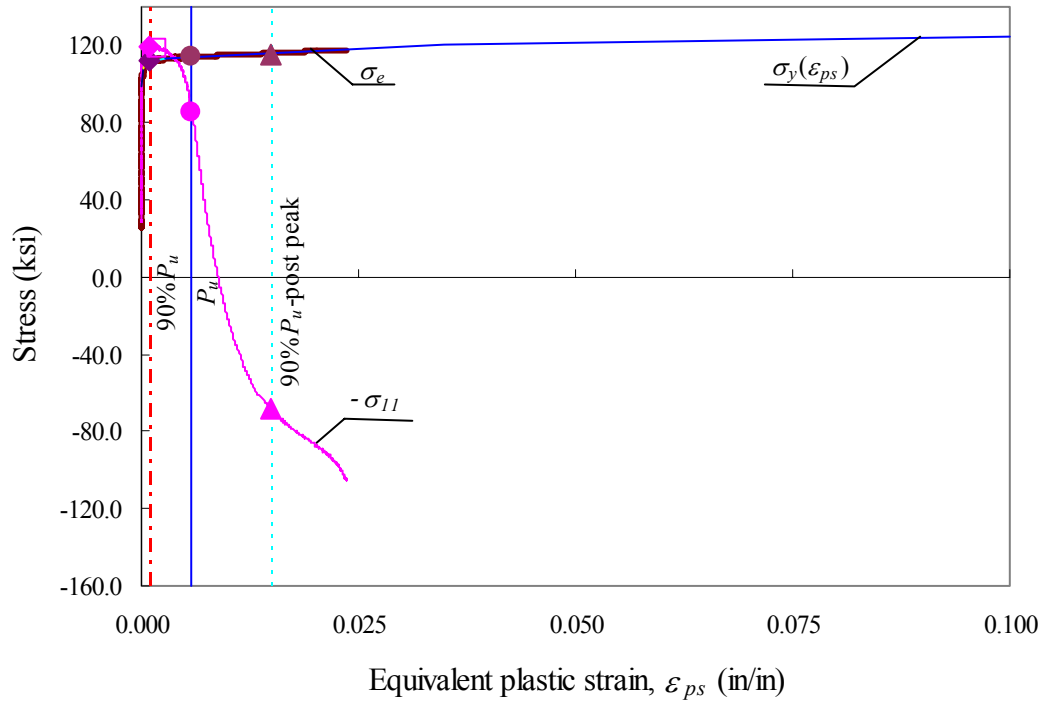

Figure 5.20 Stress versus equivalent plastic strain (section 2-West, Specimen 3)

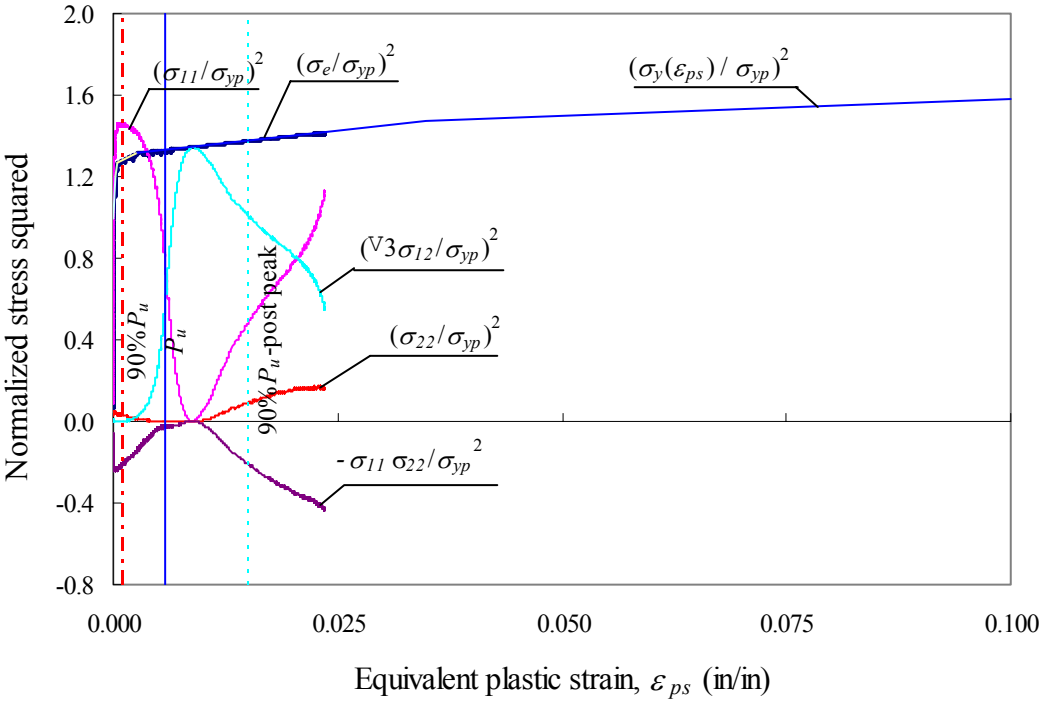

Figure 5.21 Contributions to effective stress (section 2-West, Specimen 3)

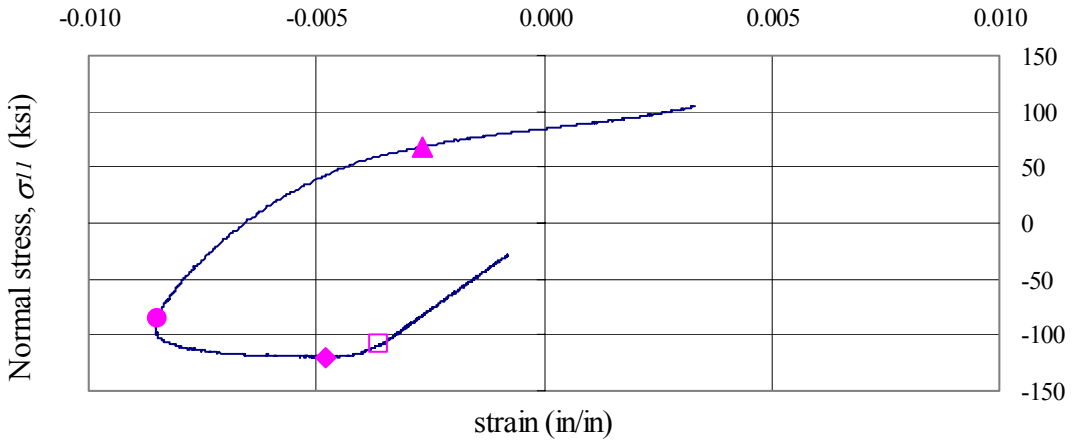

(a) Normal strain, ε_{11}

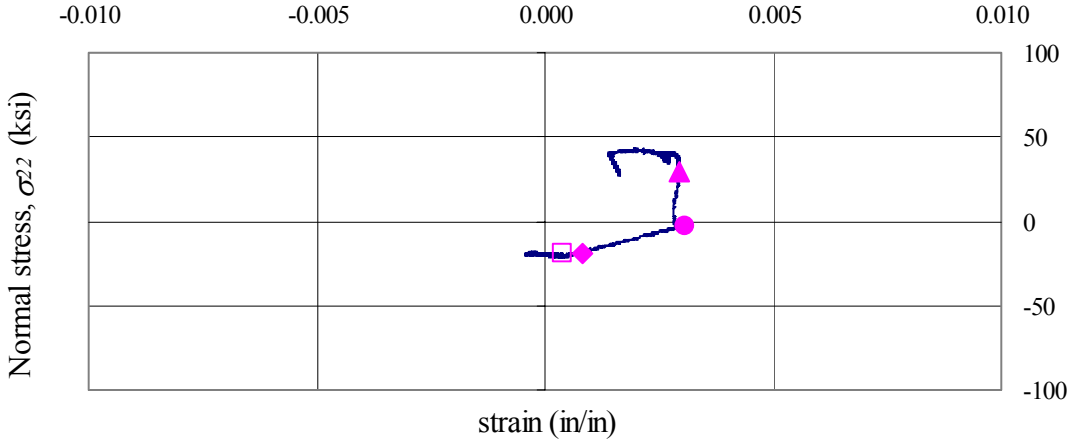

(b) Normal strain, ε_{22}

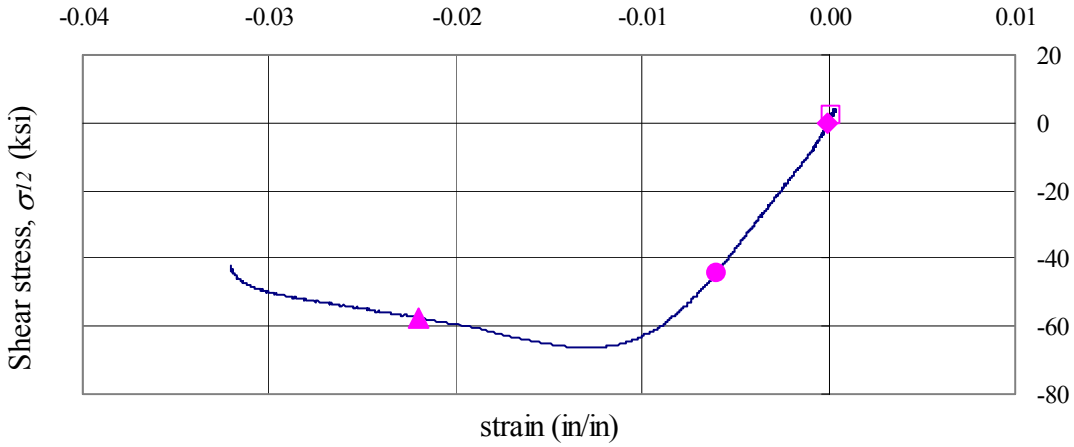

(c) Engineering shear strain, γ_{12}

Figure 5.22 Stress versus strain (section 2-West, Specimen 3)

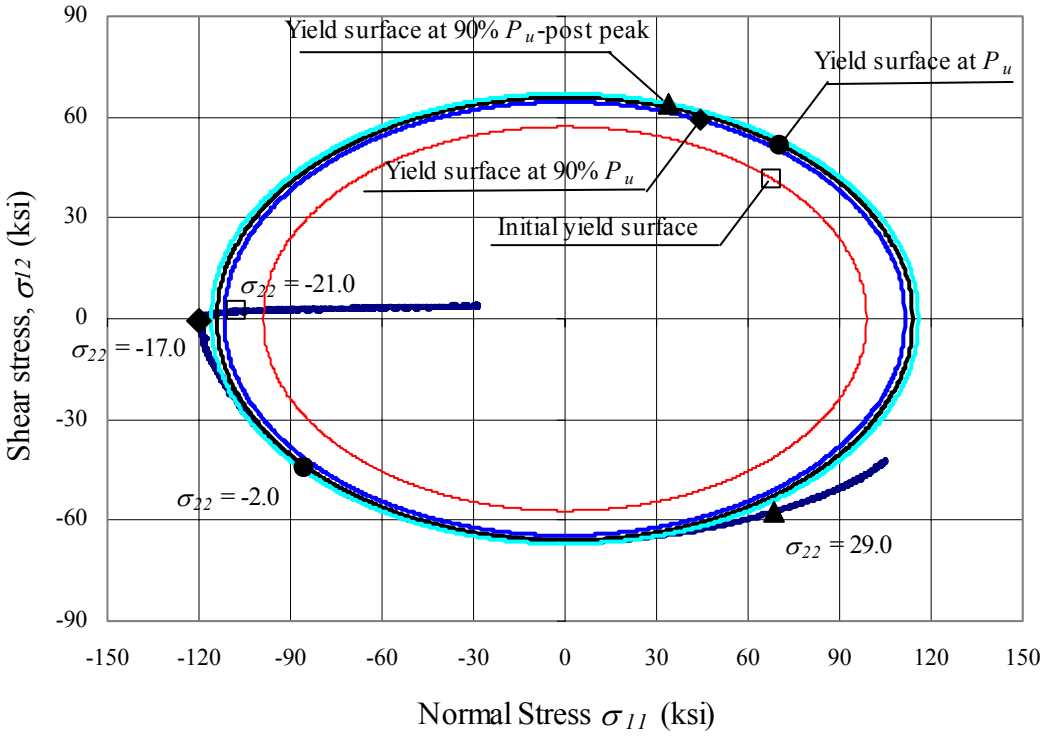

Figure 5.23Yield surface in σ_{11}- σ_{12} plane at different increments (section 2-West, Specimen 3)

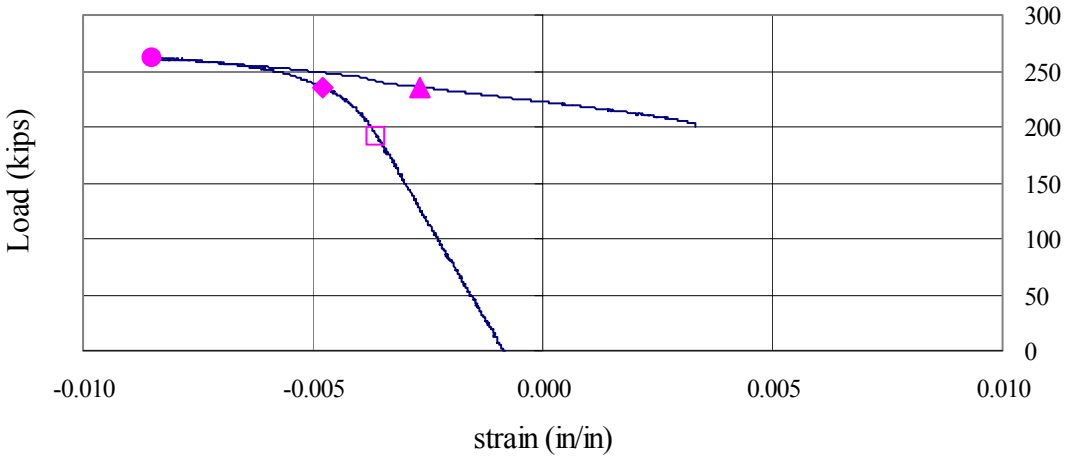

(a) Normal strain, ε_{11}

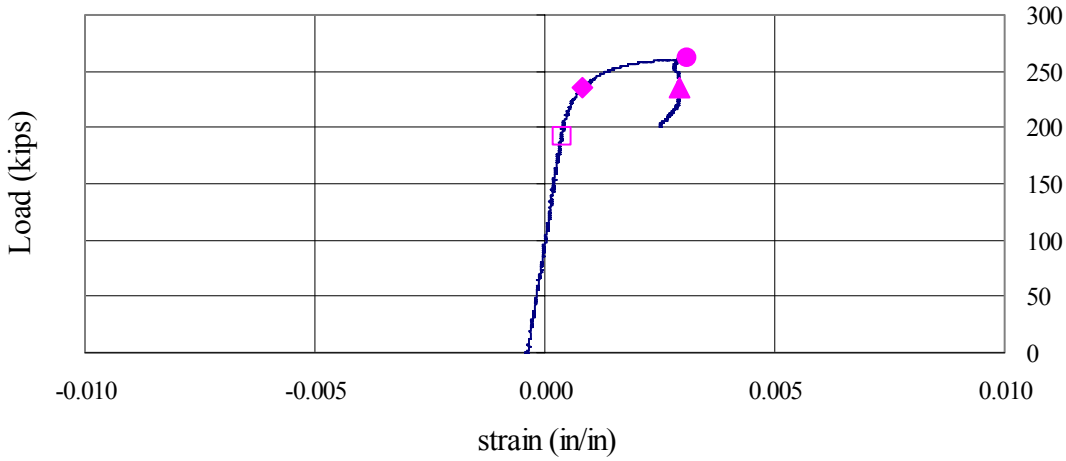

(b) Normal strain, ε_{22}

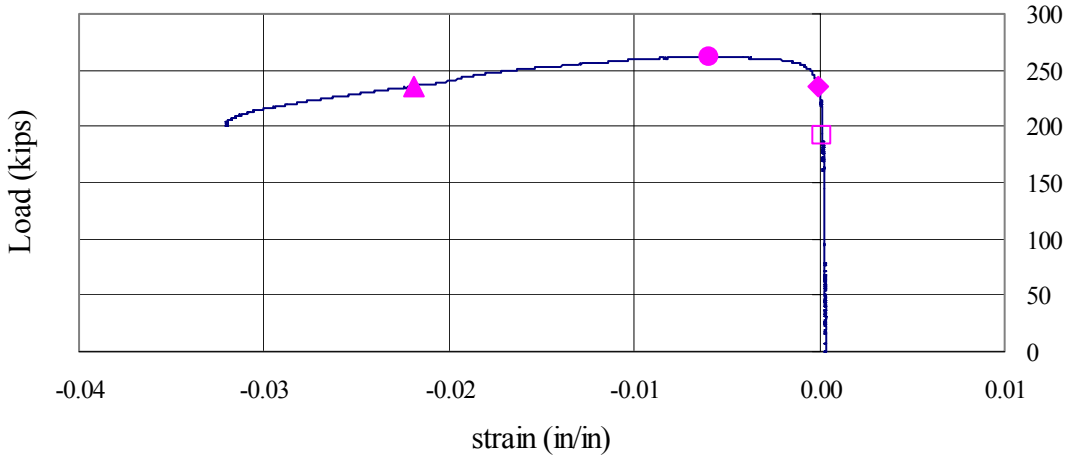

(c) Engineering shear strain, γ_{12}

Figure 5.24 Load versus strain (section 2-West, Specimen 3)

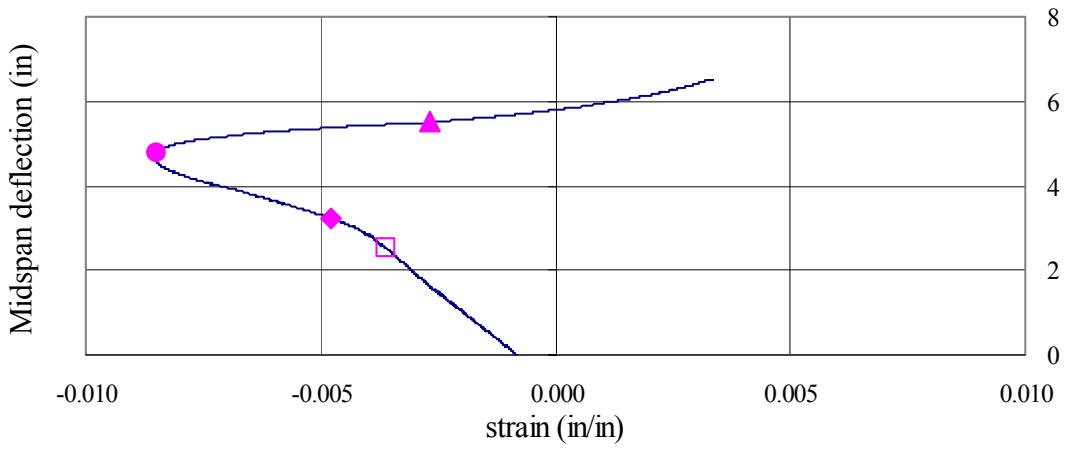

(a) Normal strain, ε_{11}

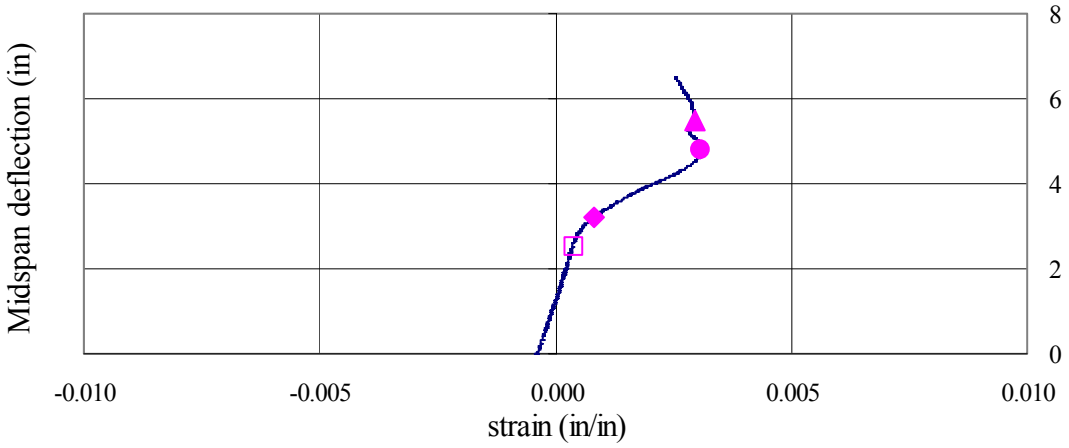

(b) Normal strain, ε_{22}

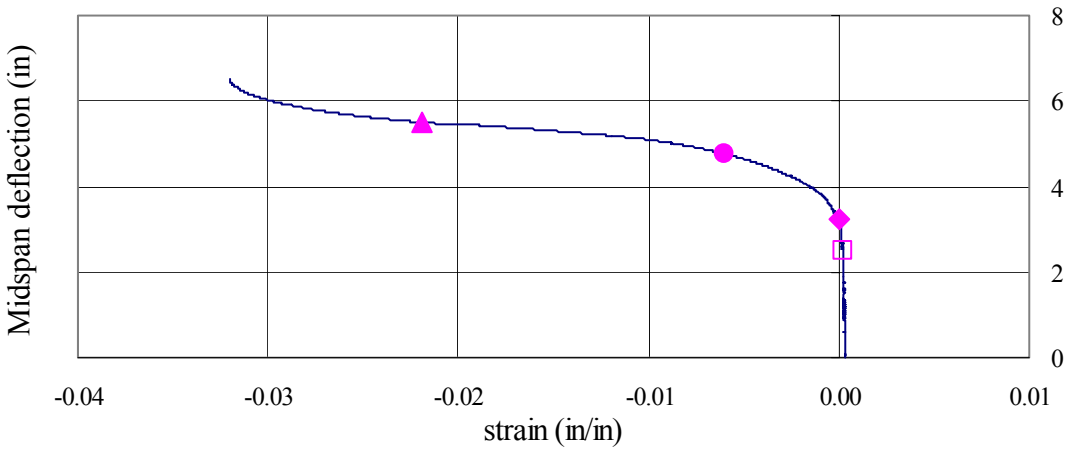

(c) Engineering shear strain, γ_{12}

Figure 5.25 Midspan vertical deflection versus strain (section 2-West, Specimen 3)

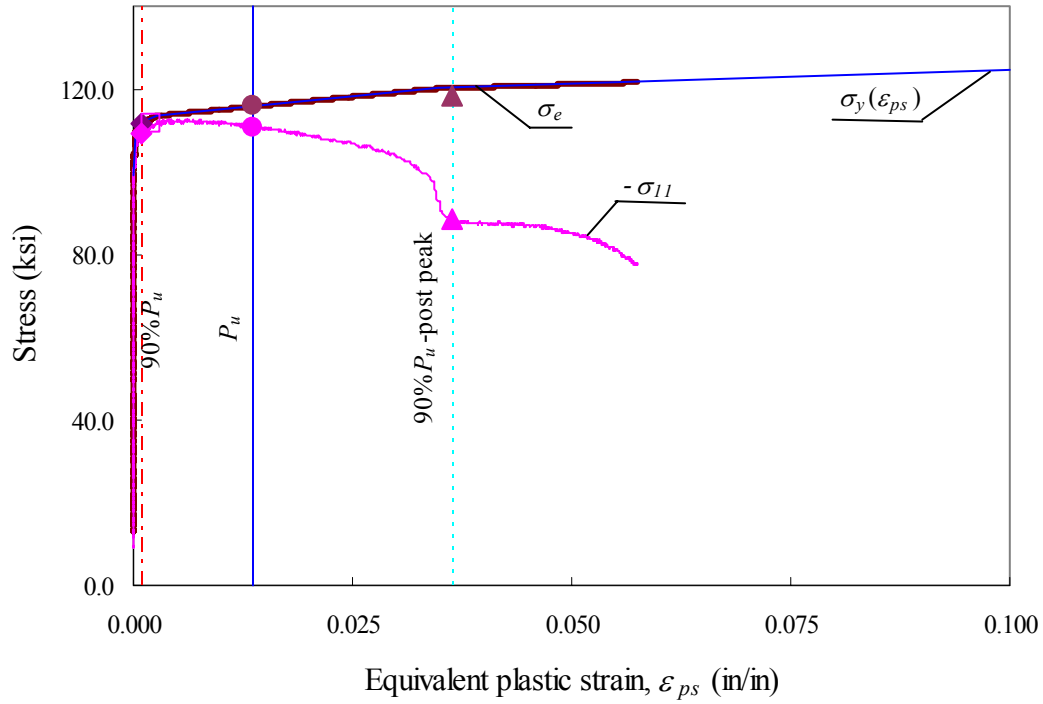

Figure 5.26 Stress versus equivalent plastic strain (section 2-Mid, Specimen 3)

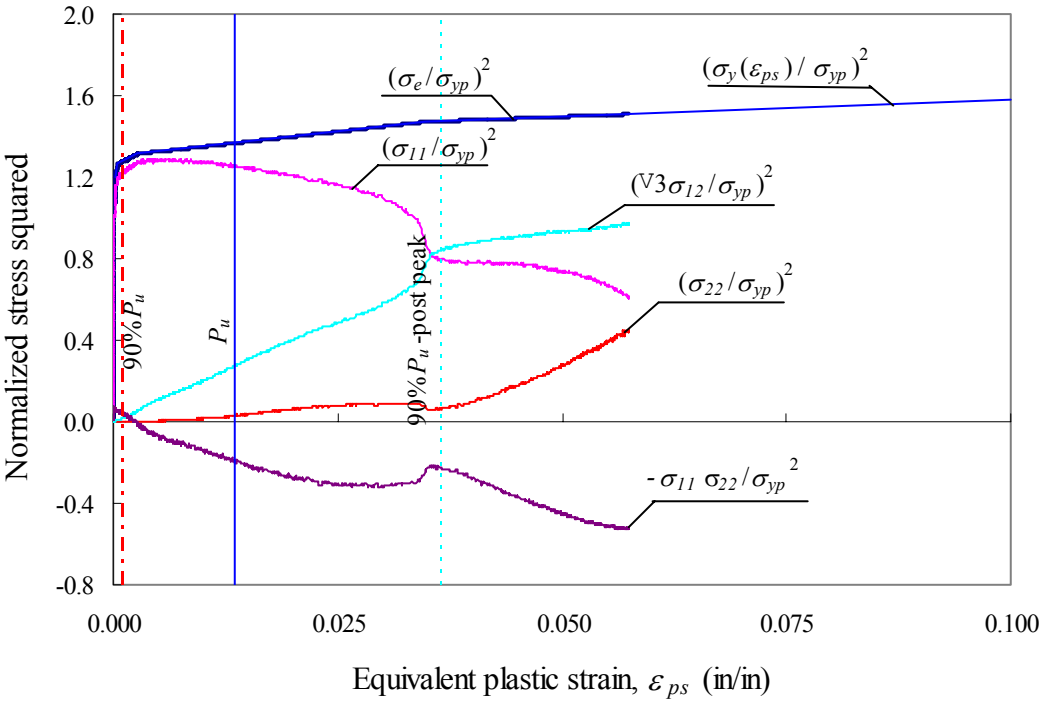

Figure 5.27 Contributions to effective stress (section 2-Mid, Specimen 3)

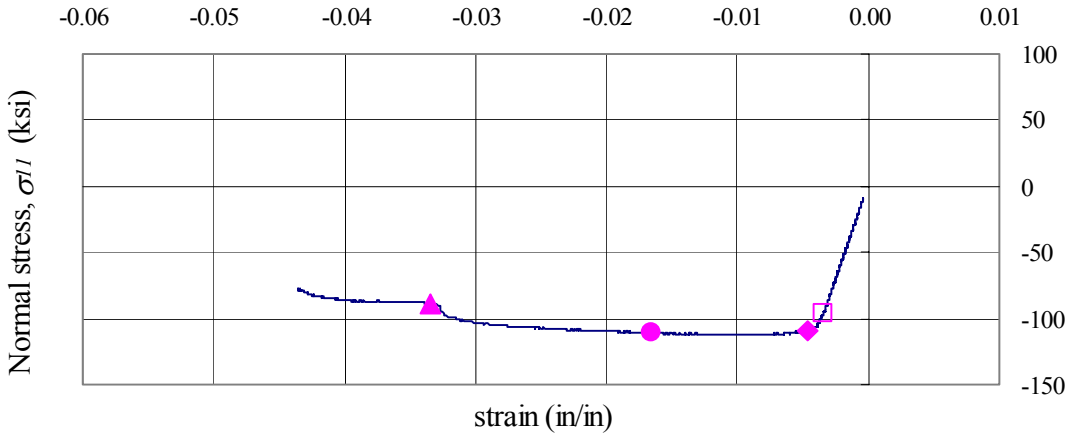

(a) Normal strain, ε_{11}

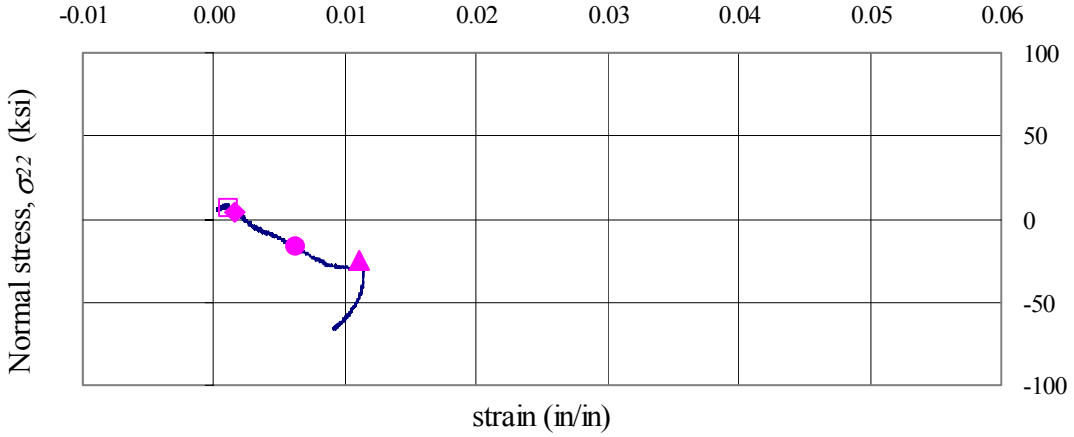

(b) Normal strain, ε_{22}

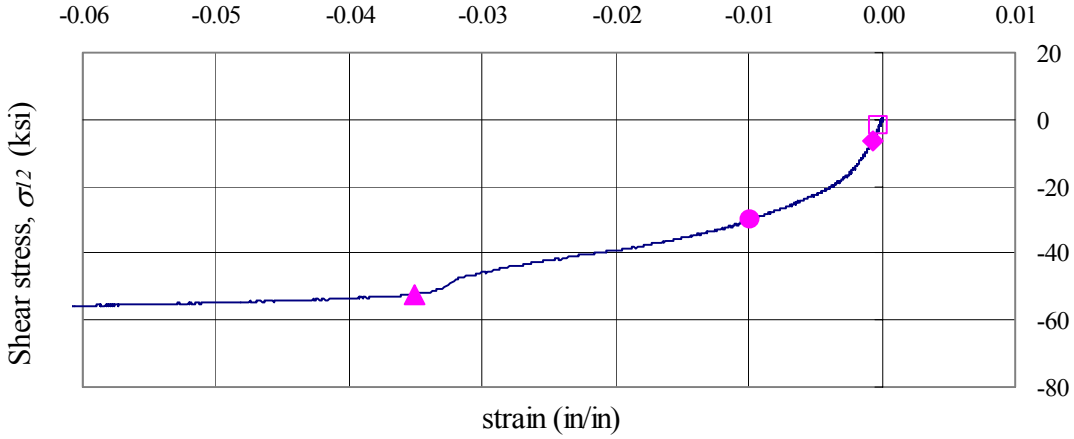

(c) Engineering shear strain, γ_{12}

Figure 5.28 Stress versus strain (section 2-Mid, Specimen 3)

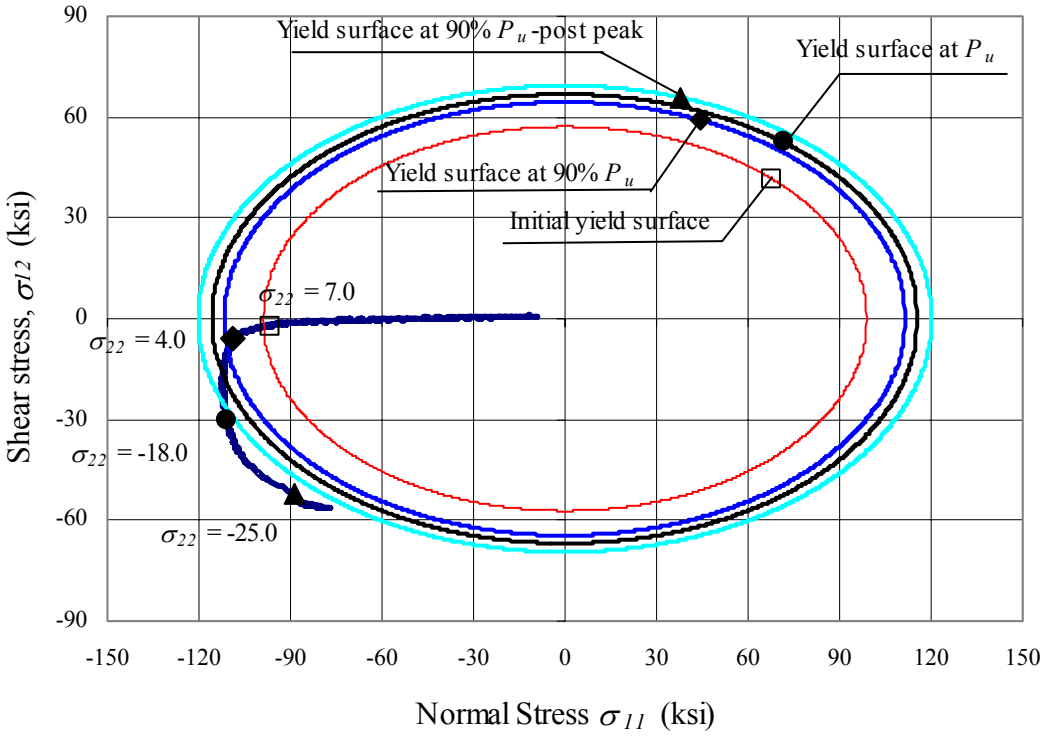

Figure 5.29 Yield surface in σ_{11}- σ_{12} plane at different increments (section 2-Mid, Specimen 3)

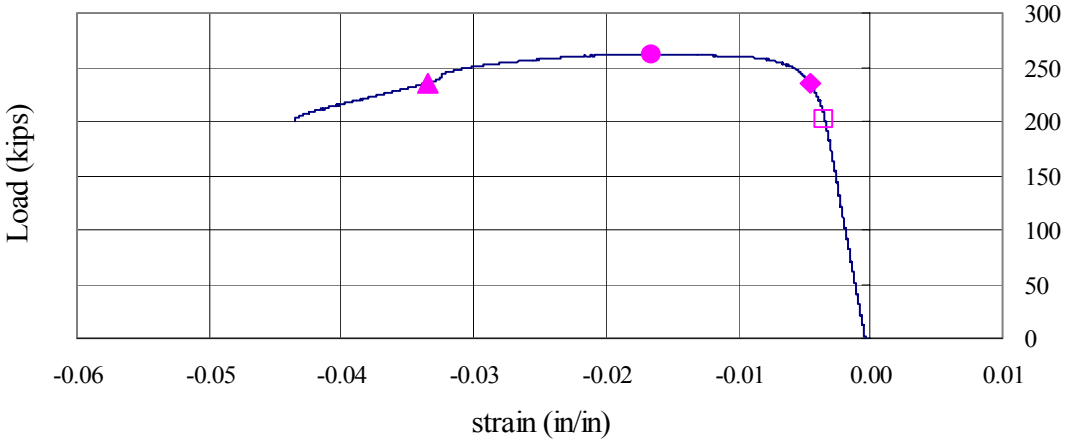

(a) Normal strain, ε_{11}

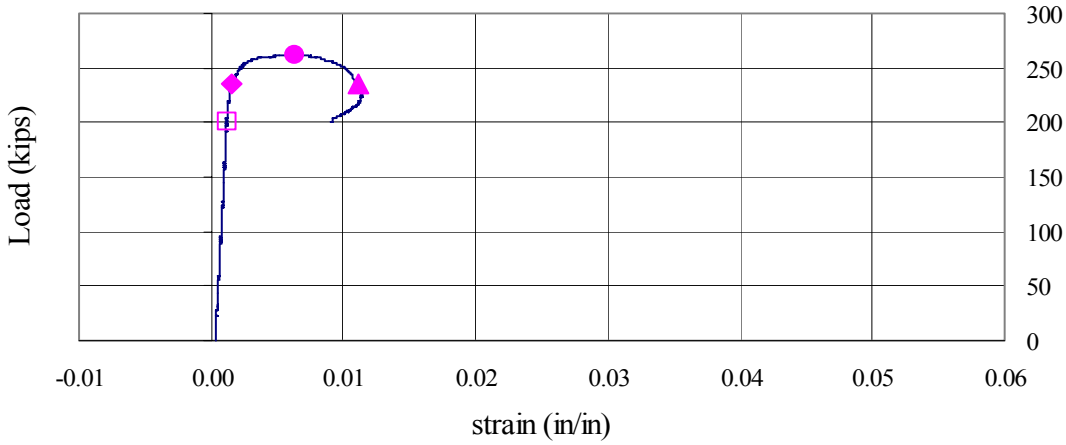

(b) Normal strain, ε_{22}

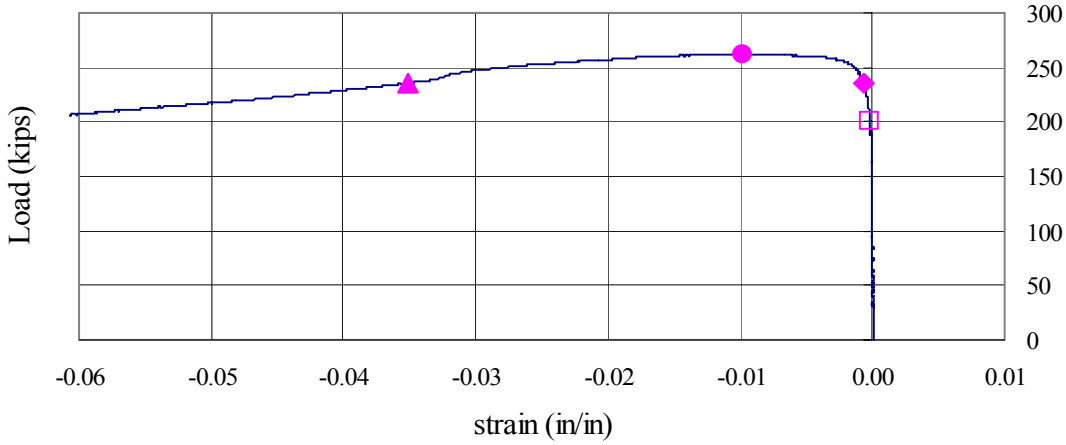

(c) Engineering shear strain, γ_{12}

Figure 5.30 Load versus strain (section 2-Mid, Specimen 3)

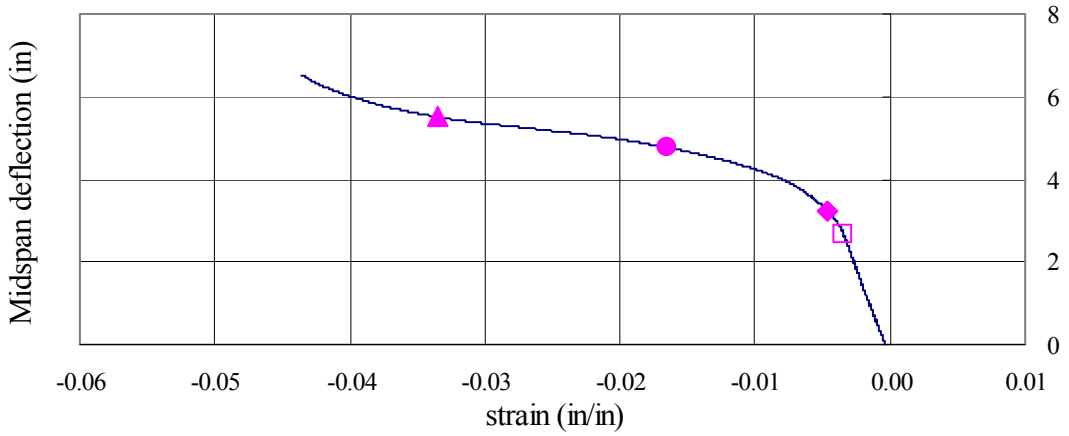

(a) Normal strain, ε_{11}

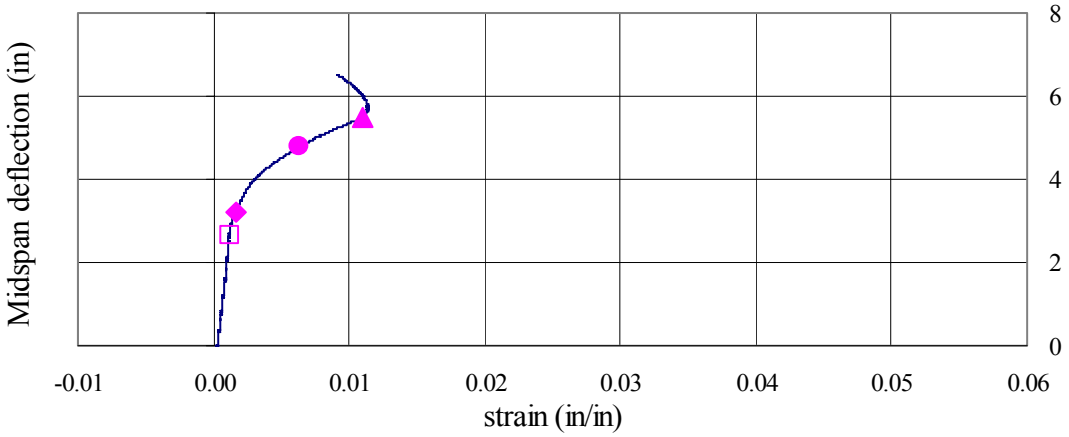

(b) Normal strain, ε_{22}

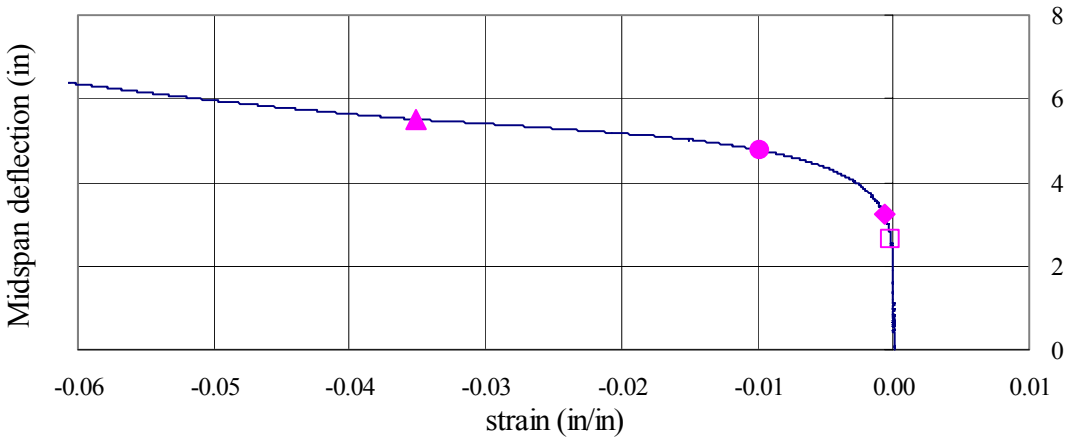

(c) Engineering shear strain, γ_{12}

Figure 5.31 Midspan vertical deflection versus strain (section 2-Mid, Specimen 3)

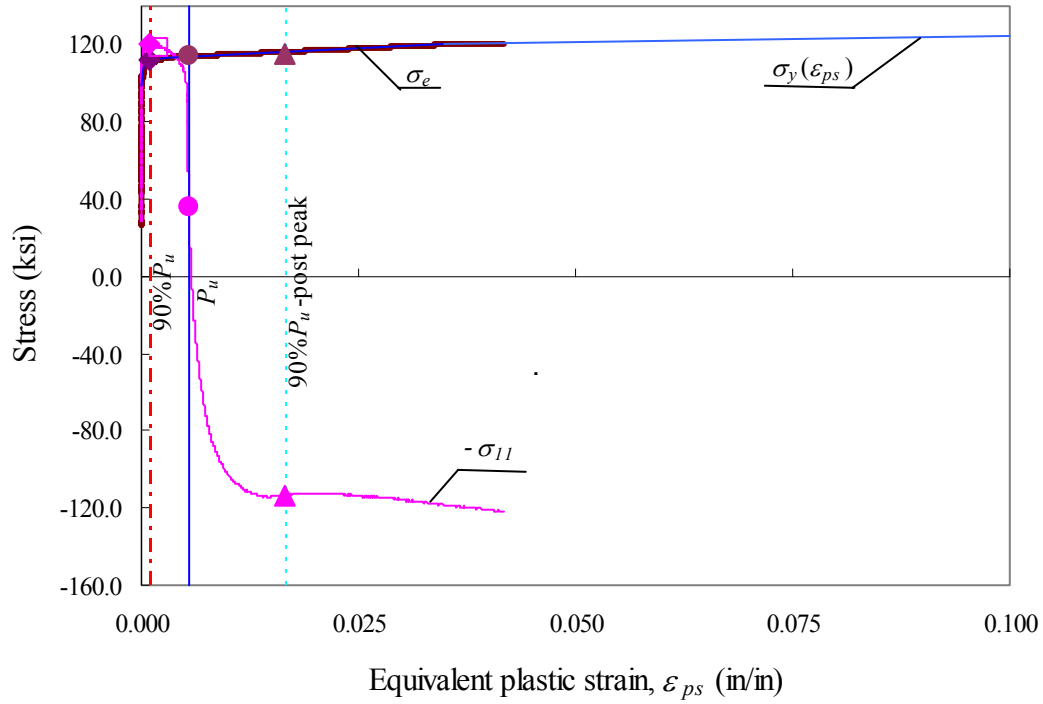

Figure 5.32 Stress versus equivalent plastic strain (section 2-East, Specimen 3)

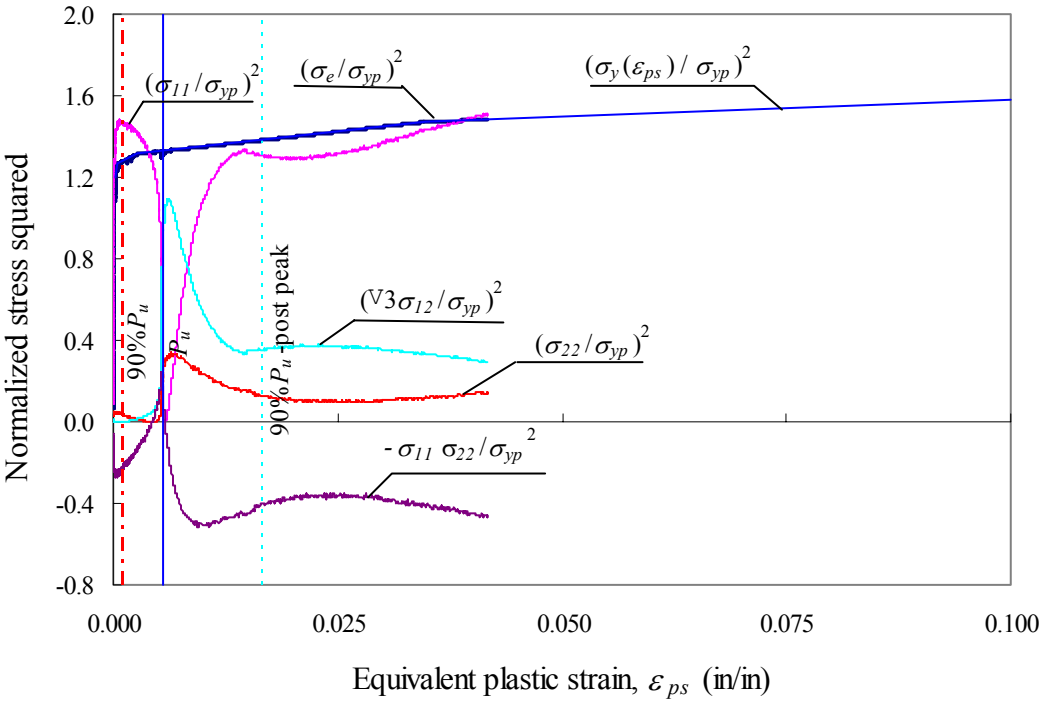

Figure 5.33 Contributions to effective stress (section 2-East, Specimen 3)

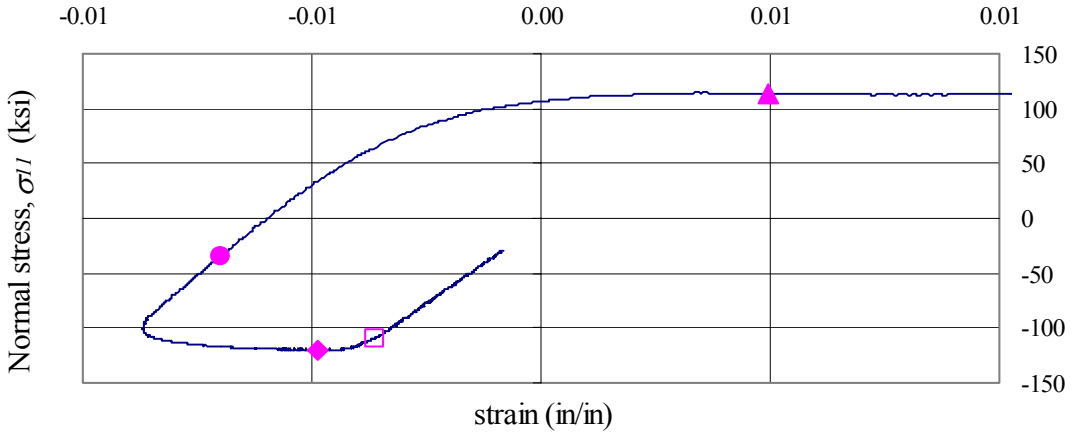

(a) Normal strain, ε_{11}

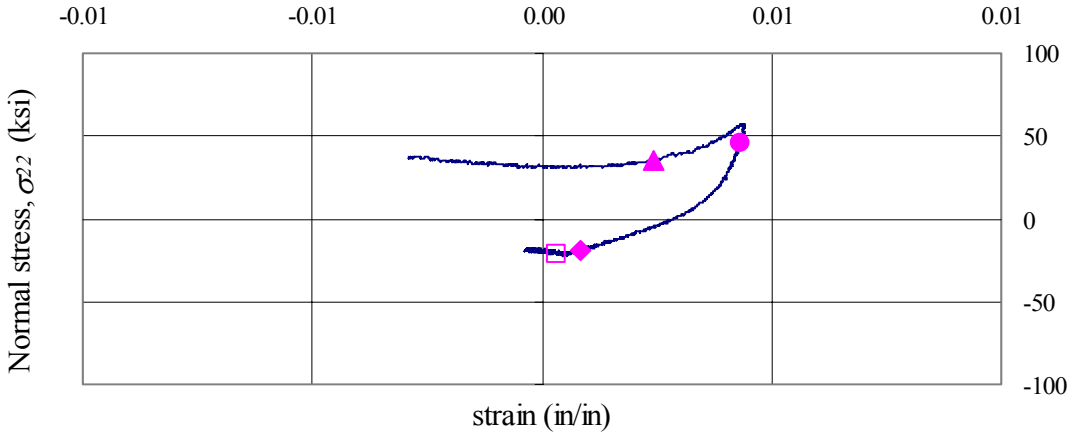

(b) Normal strain, ε_{22}

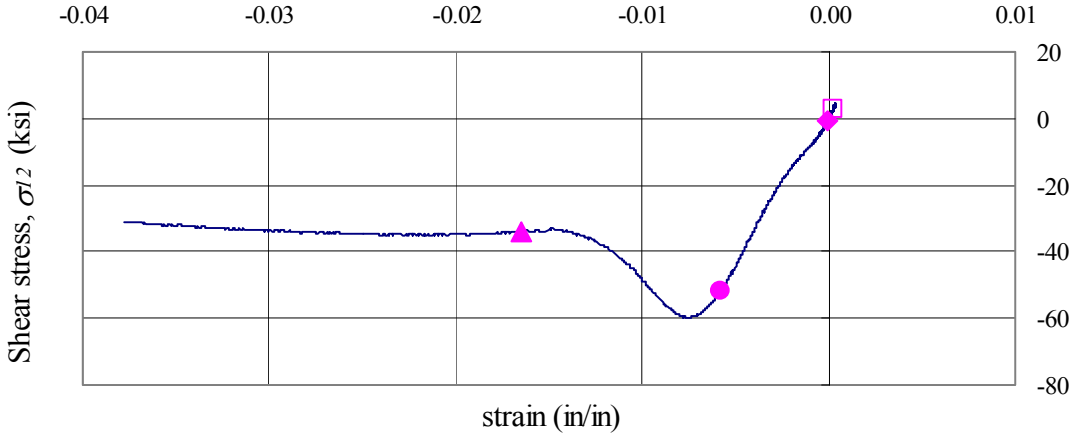

(c) Engineering shear strain, γ_{12}

Figure 5.34 Stress versus strain (section 2-East, Specimen 3)

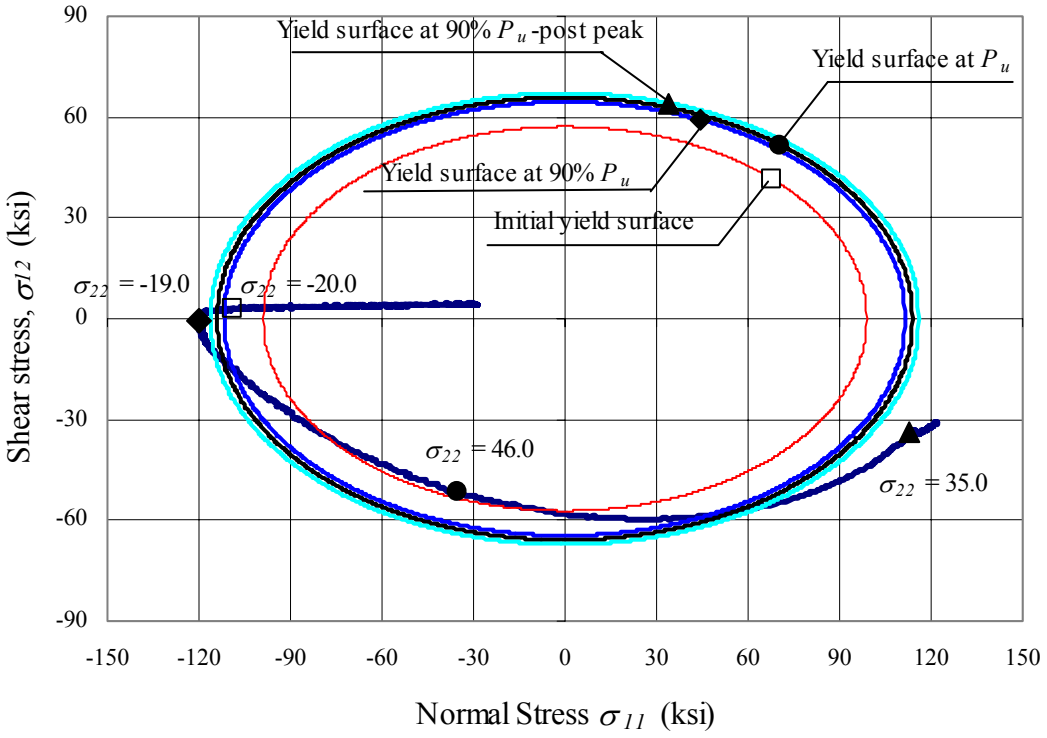

Figure 5.35 Yield surface in σ_{11}- σ_{12} plane at different increments (section 2-East, Specimen 3)

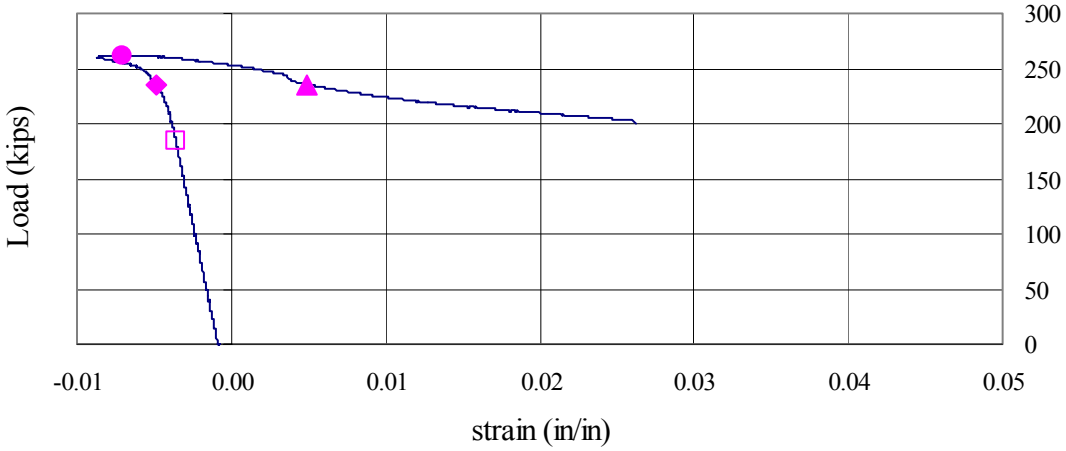

(a) Normal strain, ε_{11}

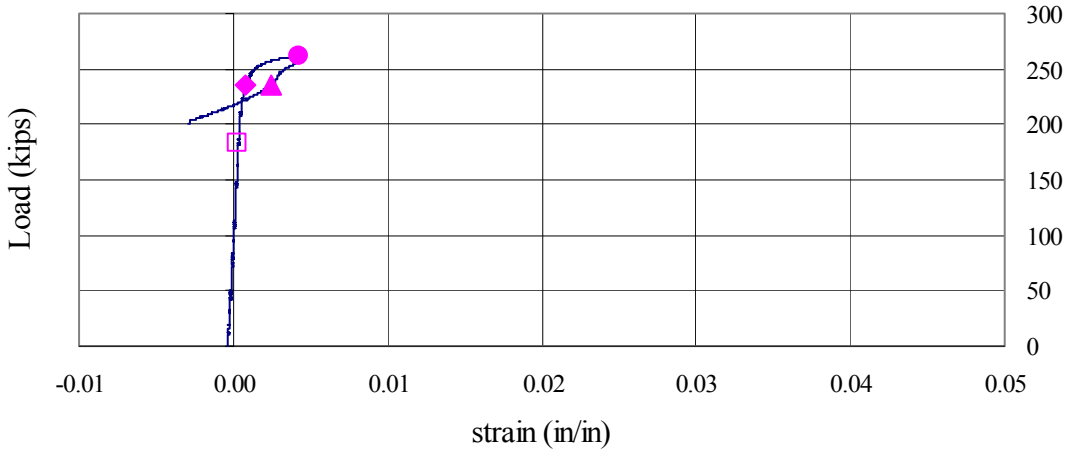

(b) Normal strain, ε_{22}

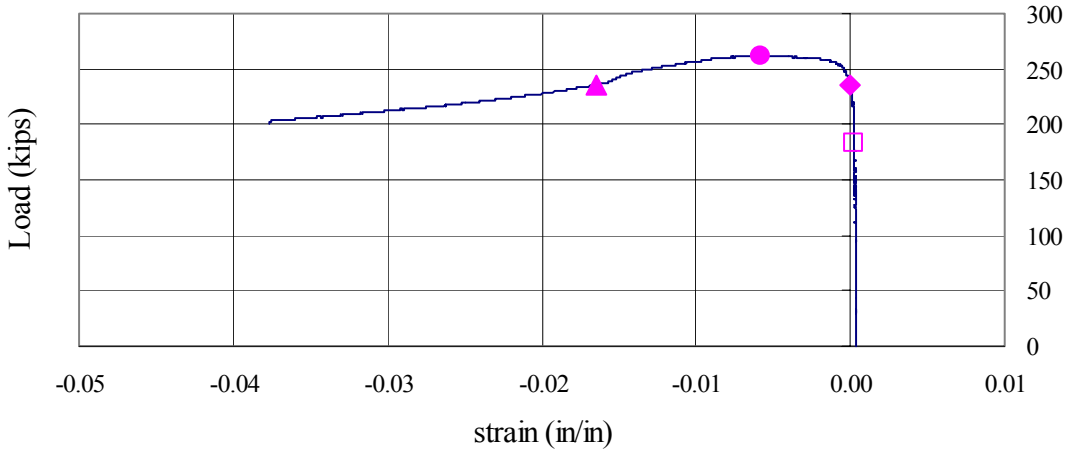

(c) Engineering shear strain, γ_{12}

Figure 5.36 Load versus strain (section 2-East, Specimen 3)

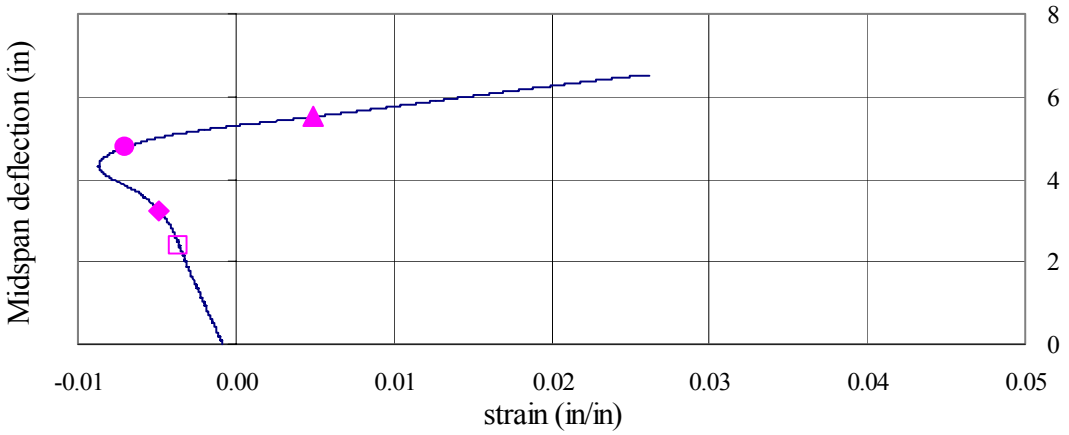

(a) Normal strain, ε_{11}

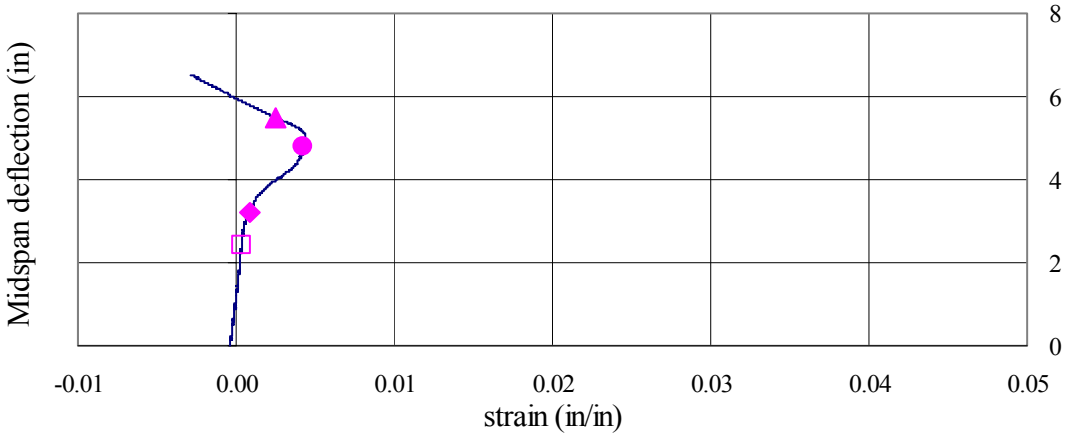

(b) Normal strain, ε_{22}

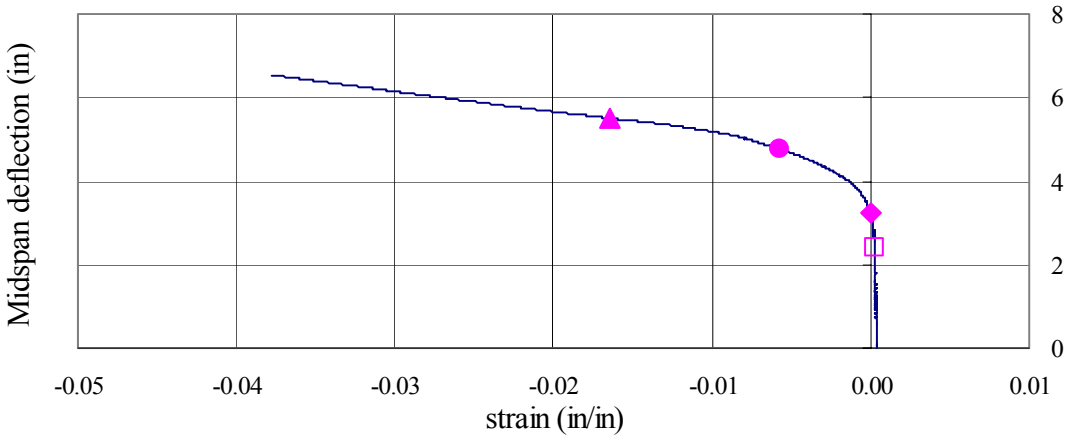

(c) Engineering shear strain, γ_{12}

Figure 5.37 Midspan vertical deflection versus strain (section 2-East, Specimen 3)

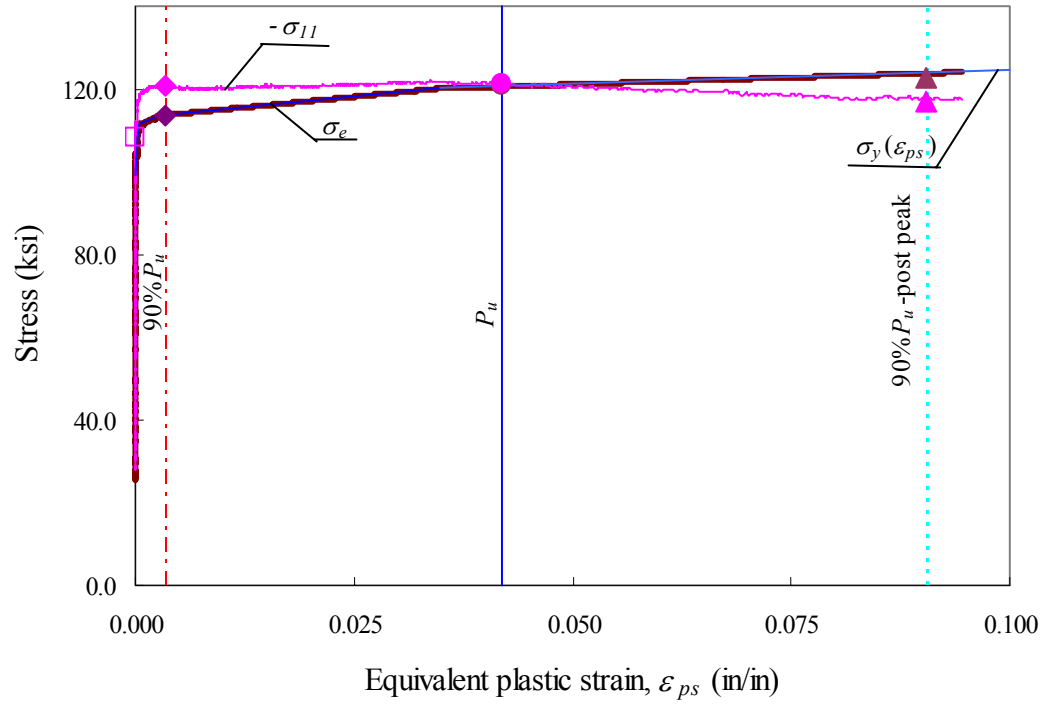

Figure 5.38 Stress versus equivalent plastic strain (section 4-East, Specimen 3)

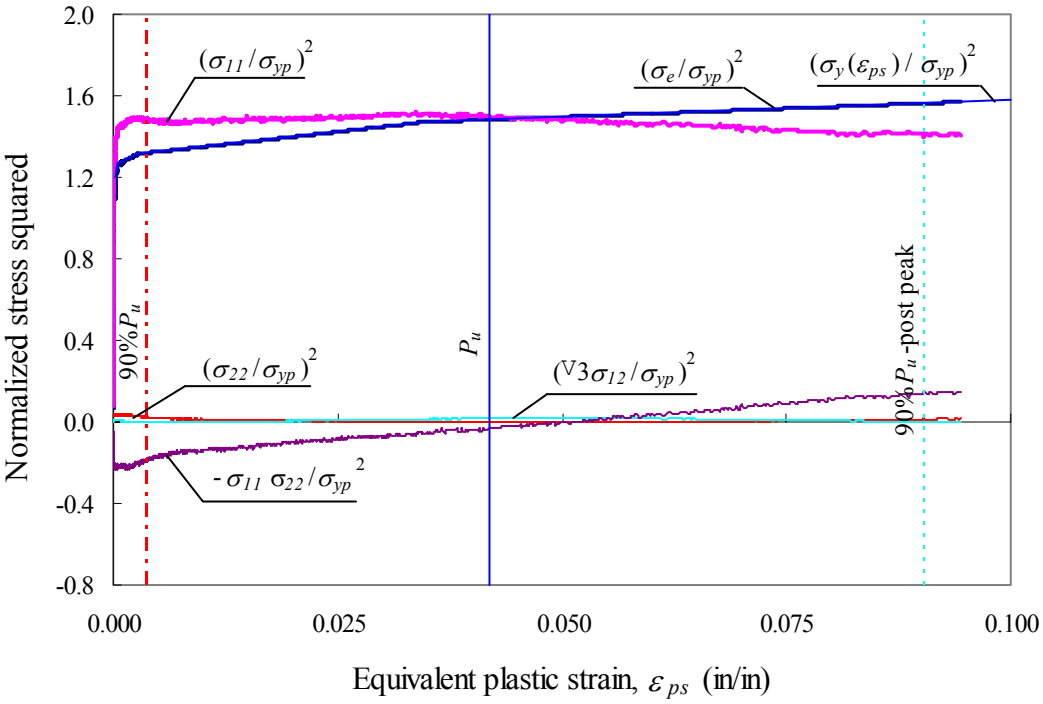

Figure 5.39 Contributions to effective stress (section 4-East, Specimen 3)

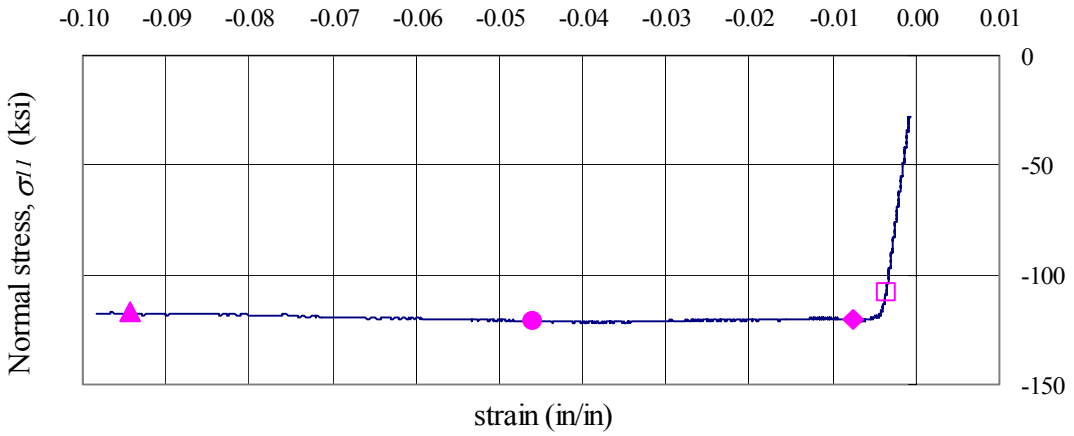

(a) Normal strain, ε_{11}

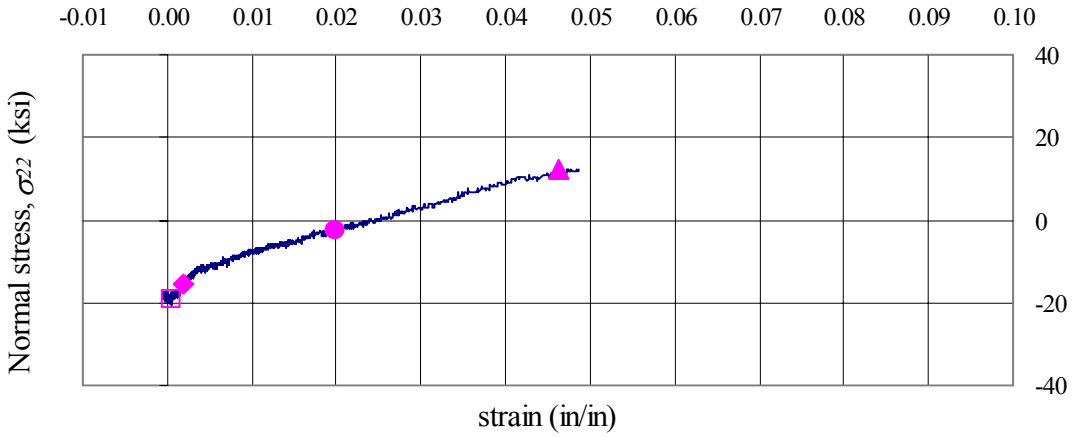

(b) Normal strain, ε_{22}

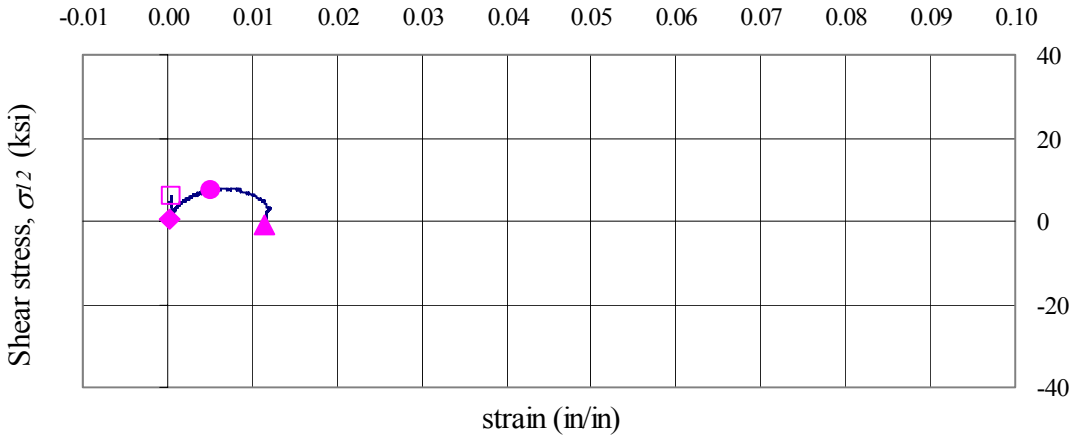

(c) Engineering shear strain, γ_{12}

Figure 5.40 Stress versus strain (section 4-East, Specimen 3)

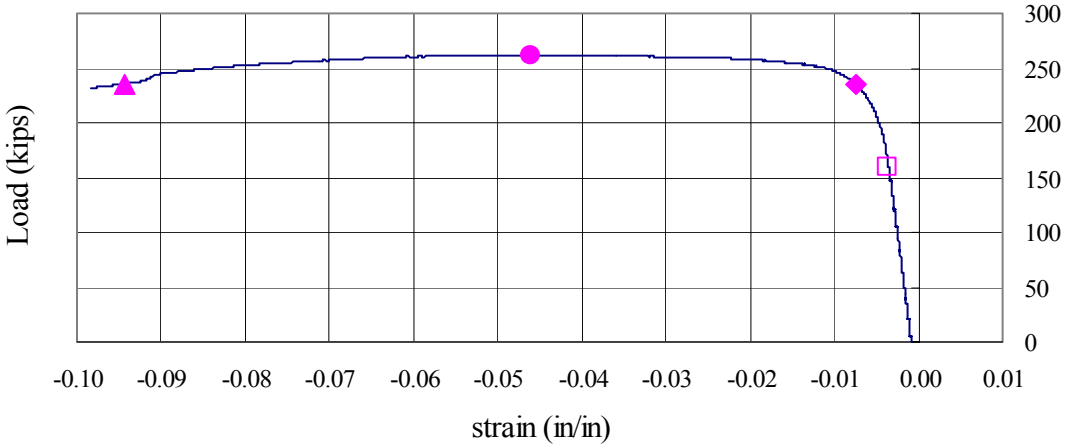

(a) Normal strain, ε_{11}

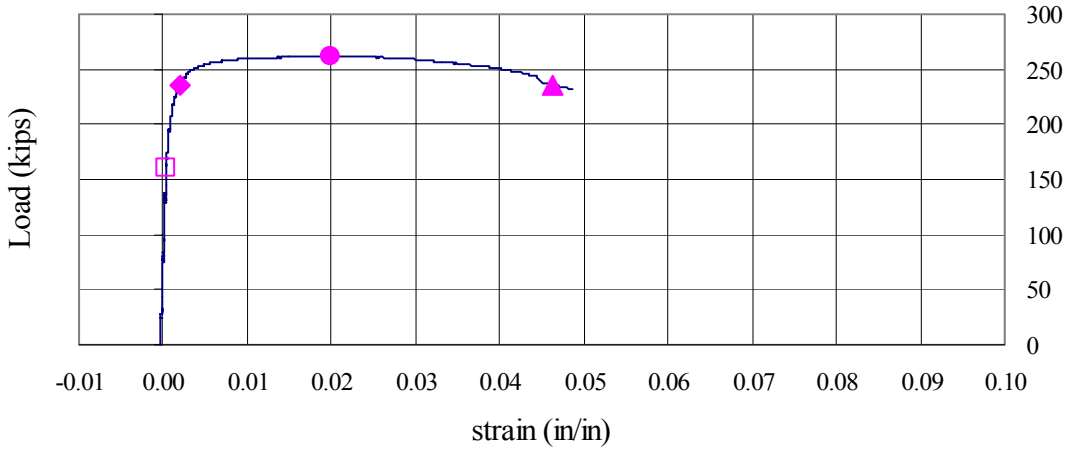

(b) Normal strain, ε_{22}

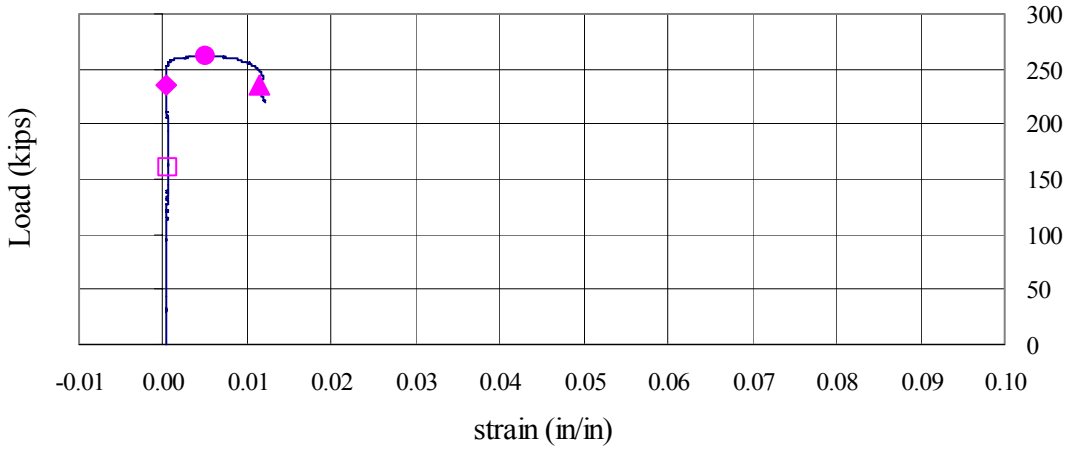

(c) Engineering shear strain, γ_{12}

Figure 5.41 Load versus strain (section 4-East, Specimen 3)

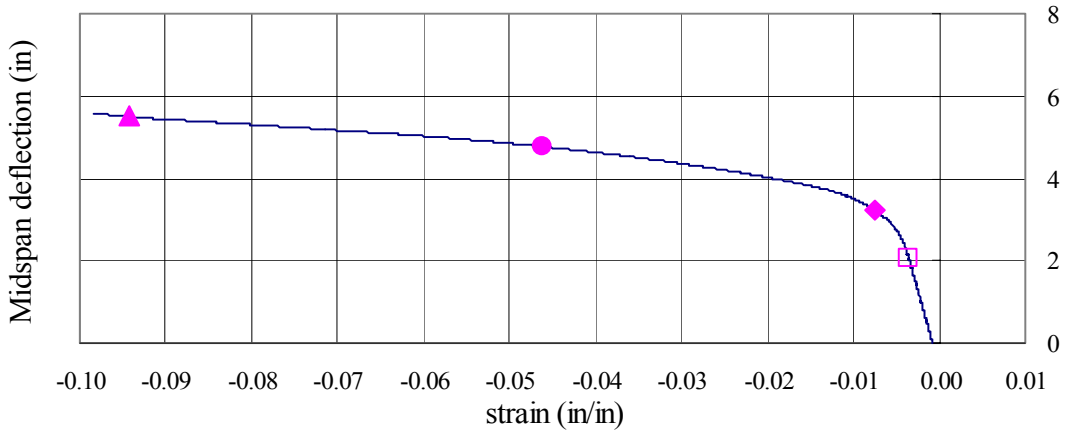

(a) Normal strain, ε_{11}

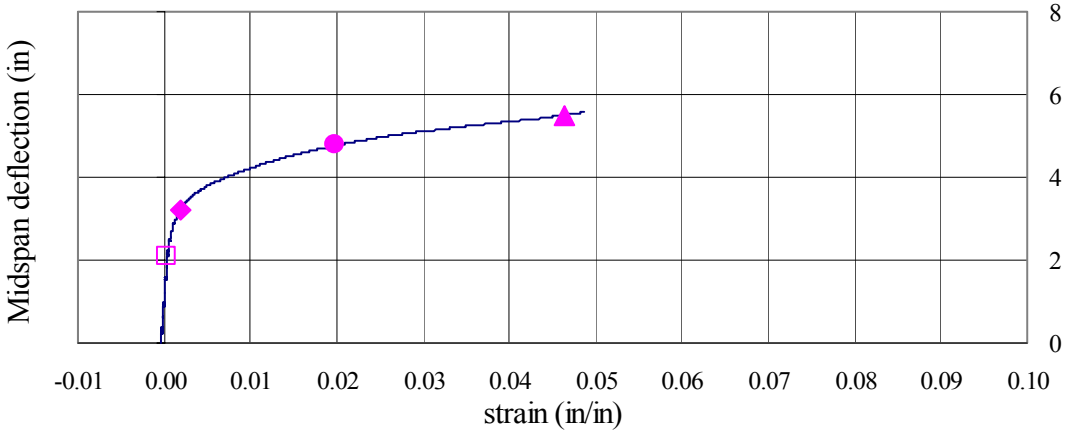

(b) Normal strain, ε_{22}

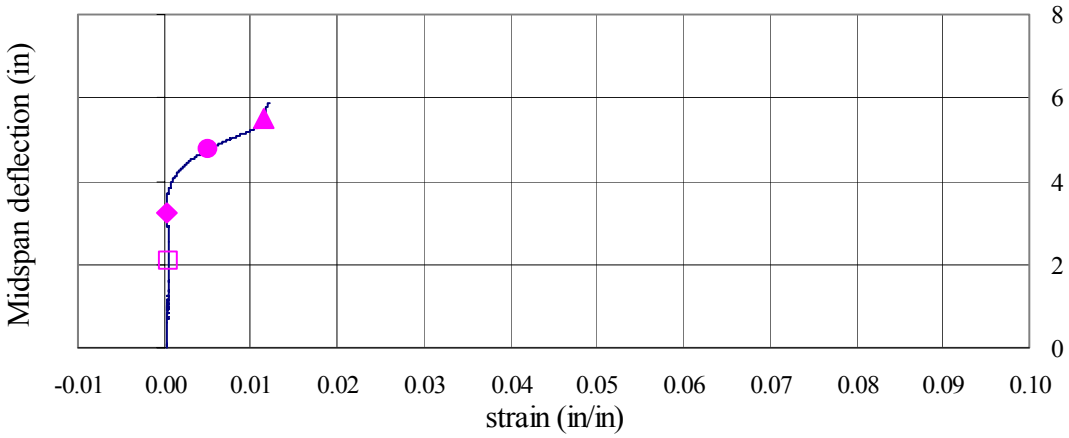

(c) Engineering shear strain, γ_{12}

Figure 5.42 Midspan vertical deflection versus strain (section 4-East, Specimen 3)

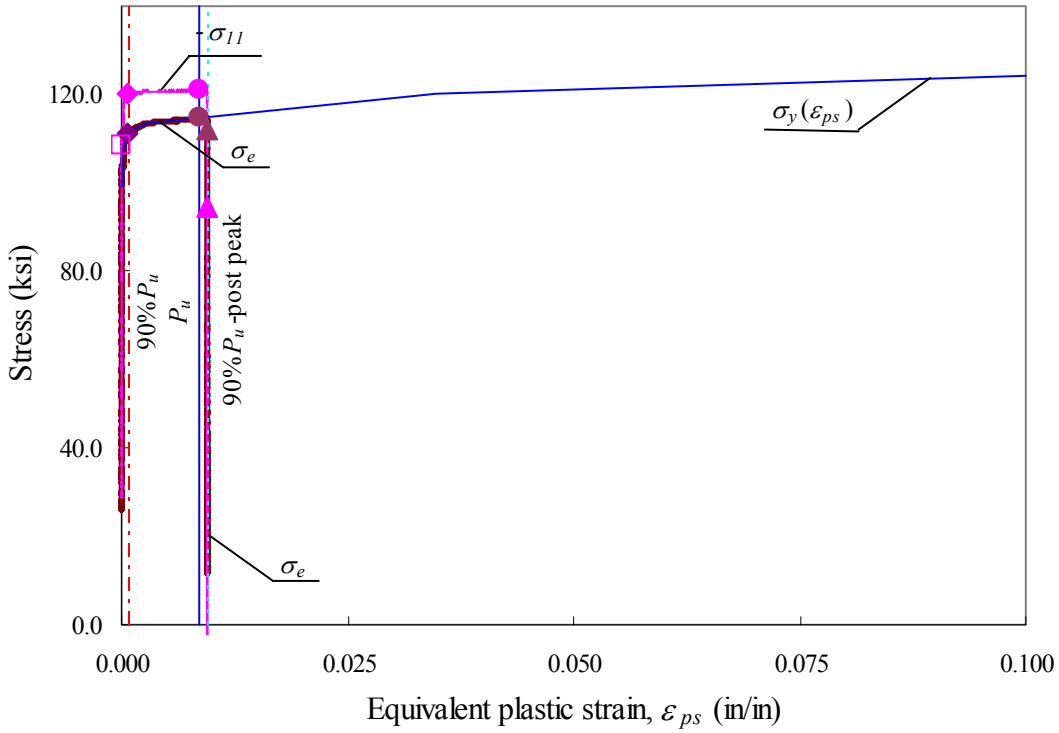

Figure 5.43 Stress versus equivalent plastic strain (section 8-West, Specimen 3)

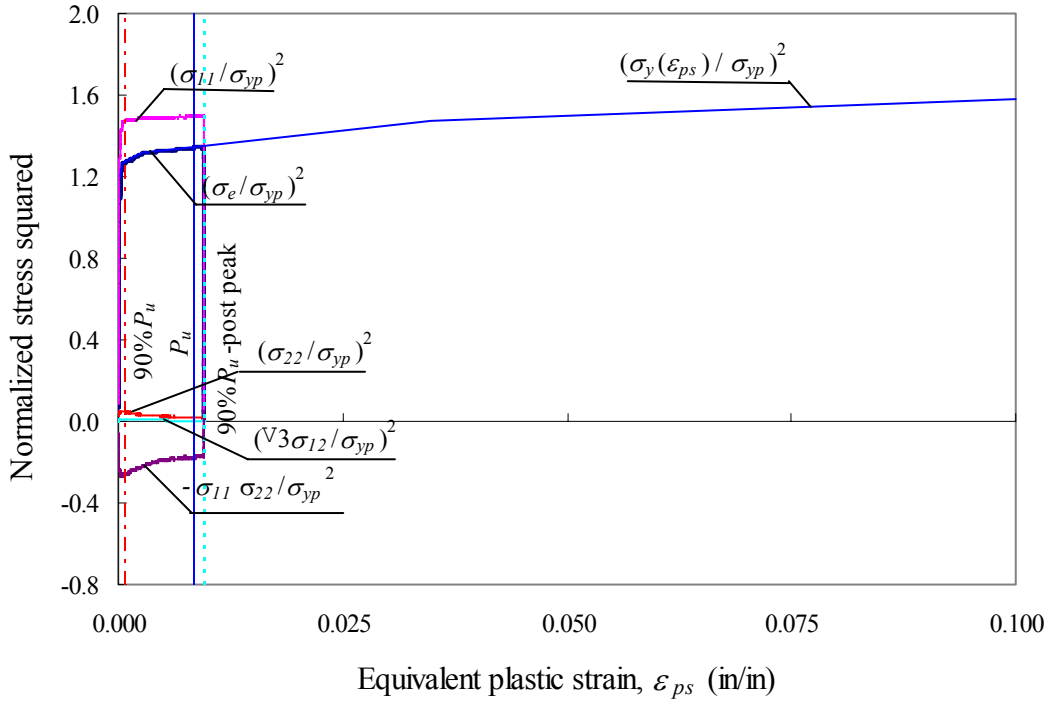

Figure 5.44 Contributions to effective stress (section 8-West, Specimen 3)

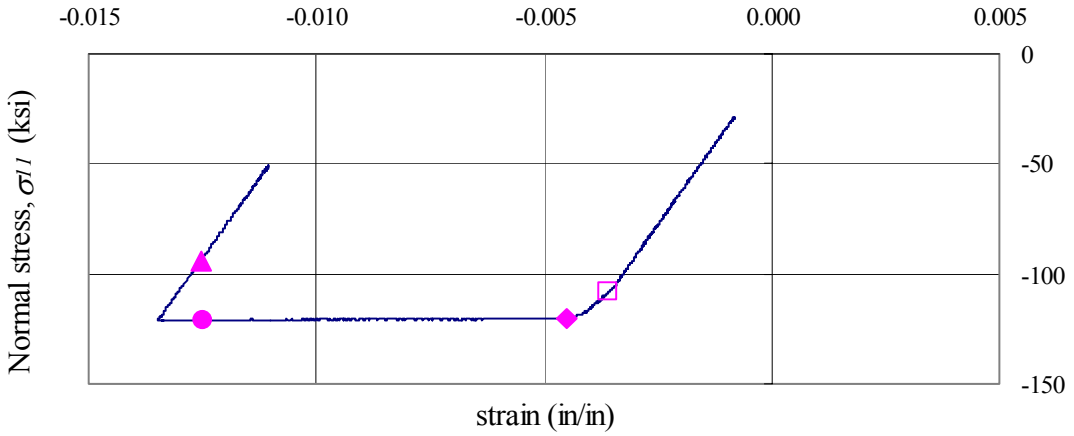

(a) Normal strain, ε_{11}

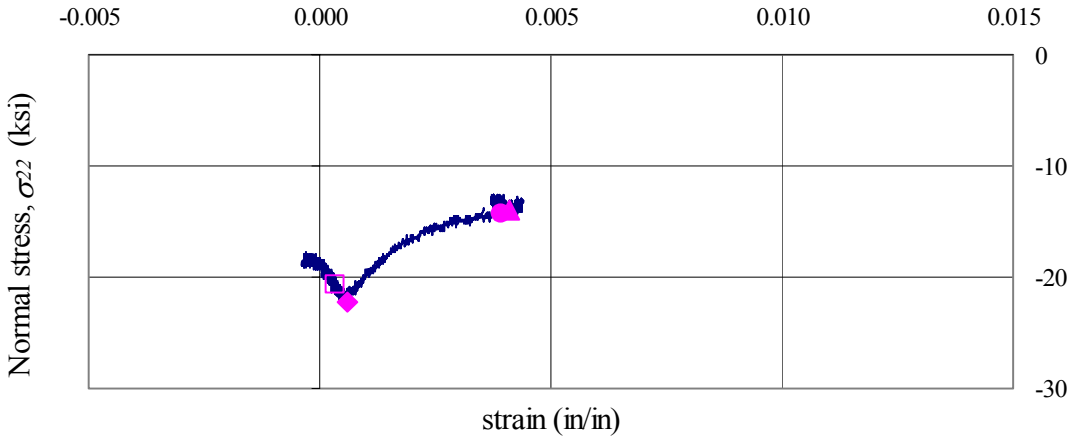

(b) Normal strain, ε_{22}

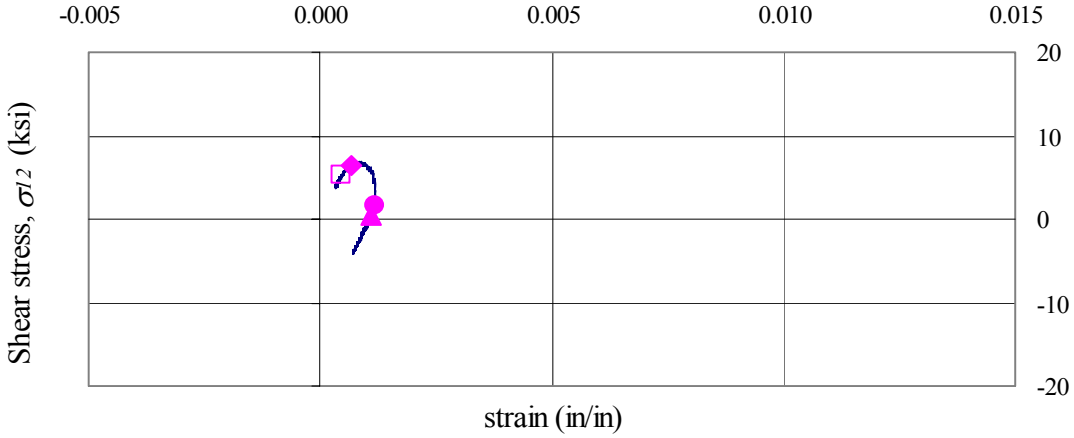

(c) Engineering shear strain, γ_{12}

Figure 5.45 Stress versus strain (section 8-West, Specimen 3)

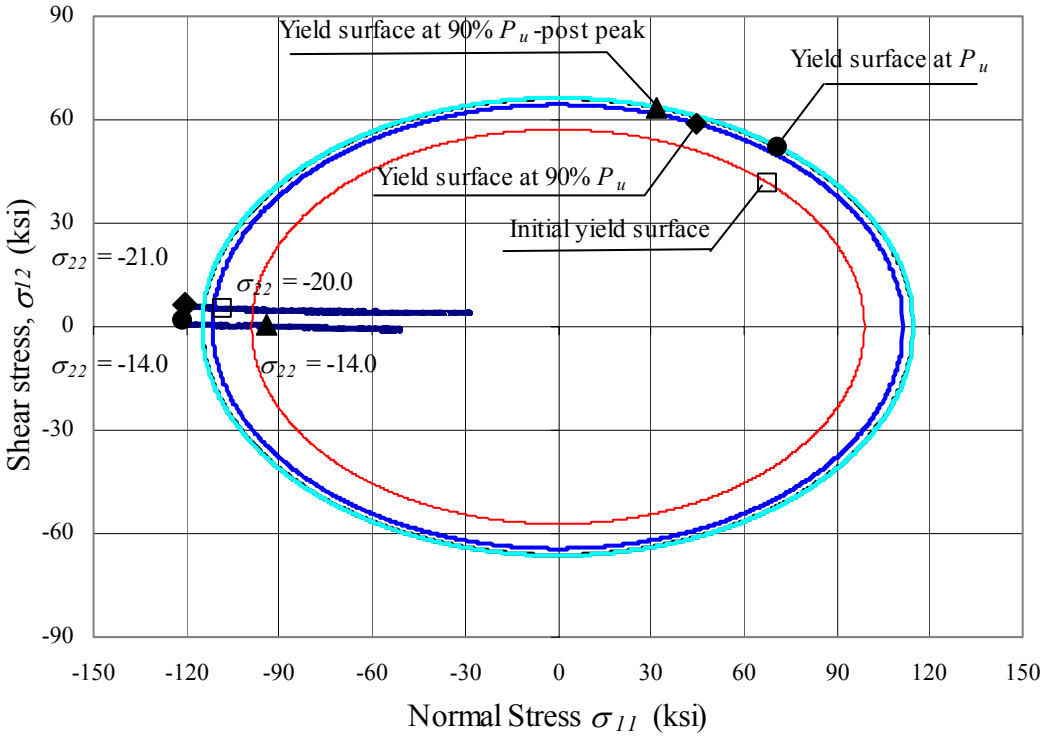

Figure 5.46 Yield surface in σ_{11}- σ_{12} plane at different increments (section 8-West, Specimen 3)

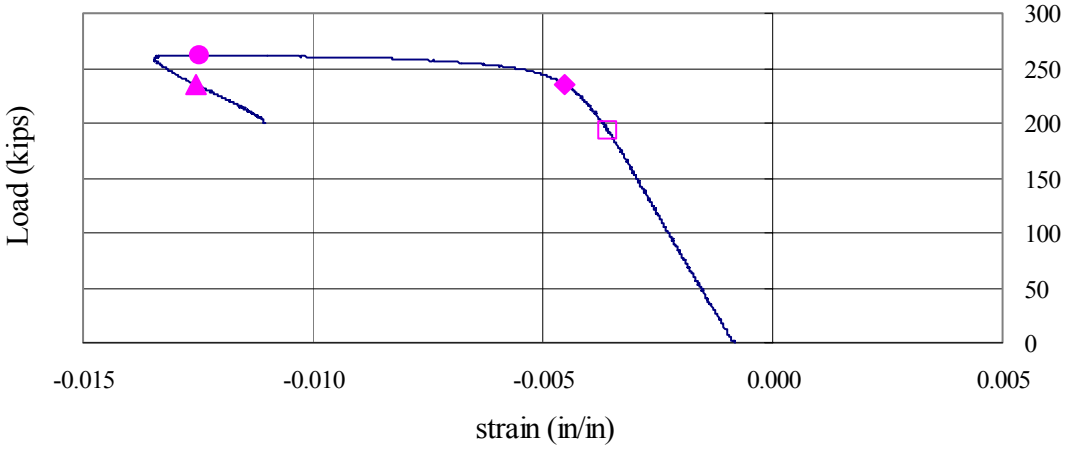

(a) Normal strain, ε_{11}

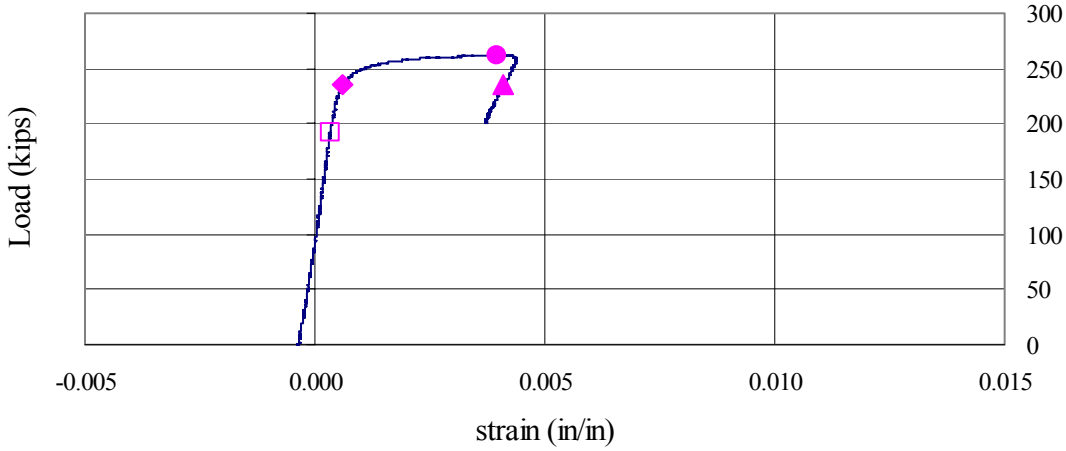

(b) Normal strain, ε_{22}

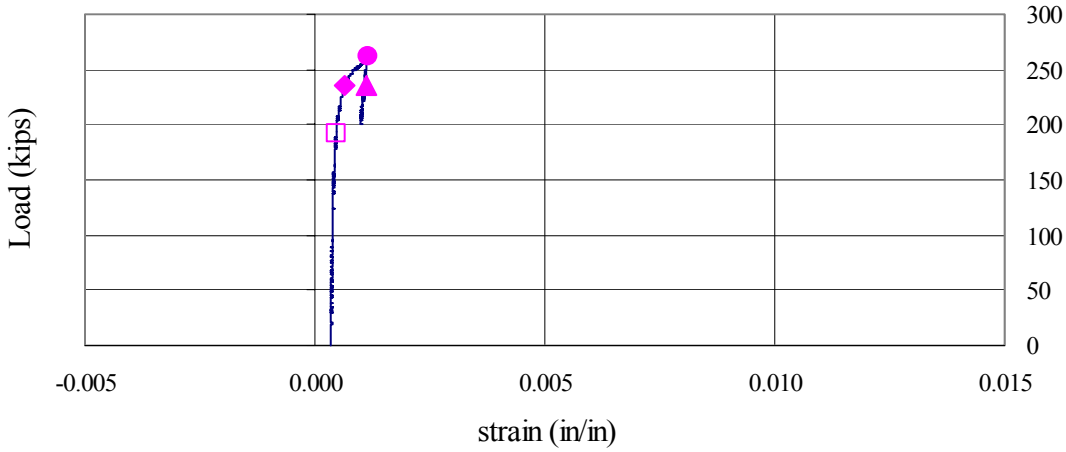

(c) Engineering shear strain, γ_{12}

Figure 5.47 Load versus strain (section 8-West, Specimen 3)

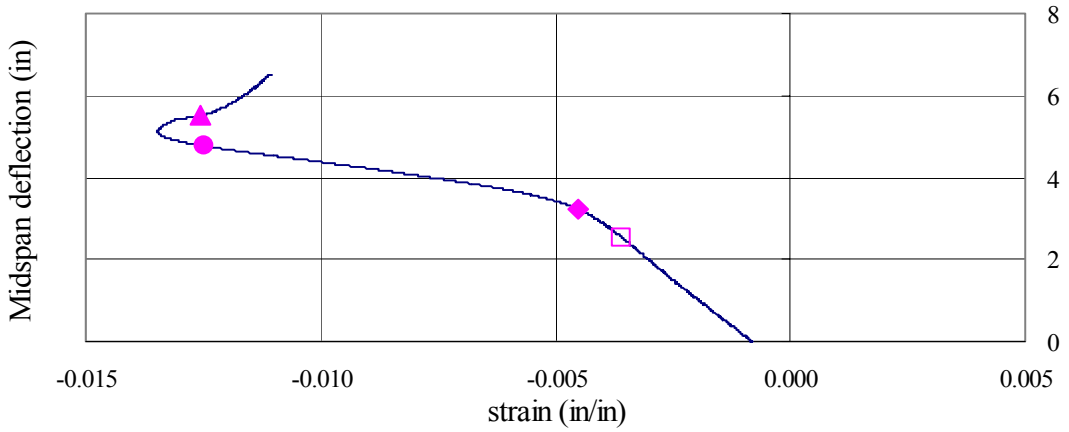

(a) Normal strain, ε_{11}

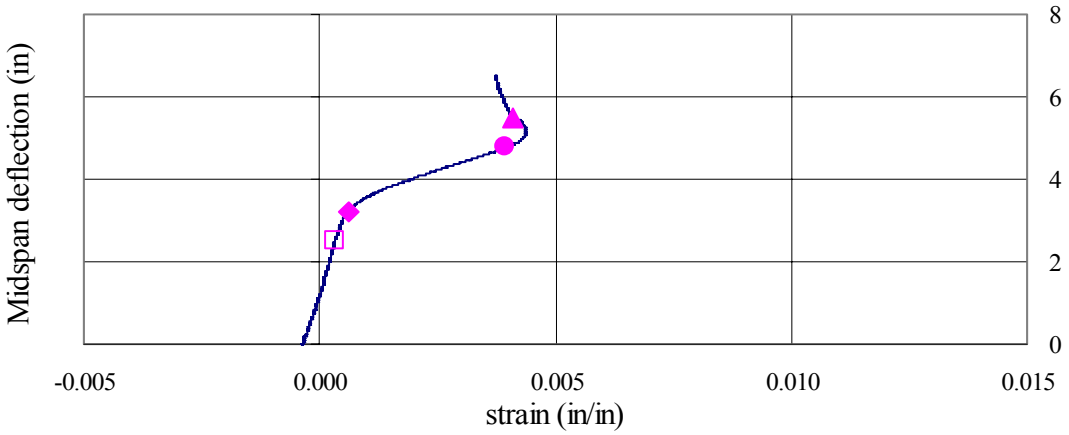

(b) Normal strain, ε_{22}

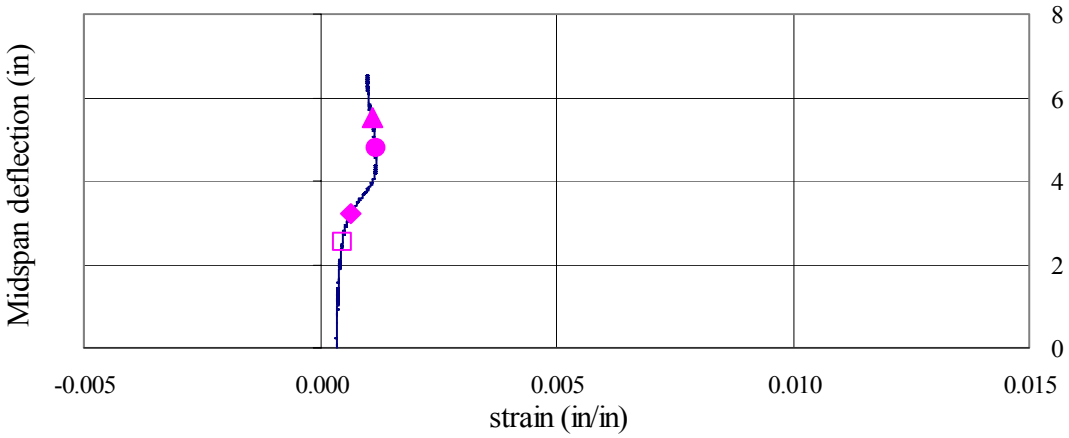

(c) Engineering shear strain, γ_{12}

Figure 5.48 Midspan vertical deflection versus strain (section 8-West, Specimen 3)

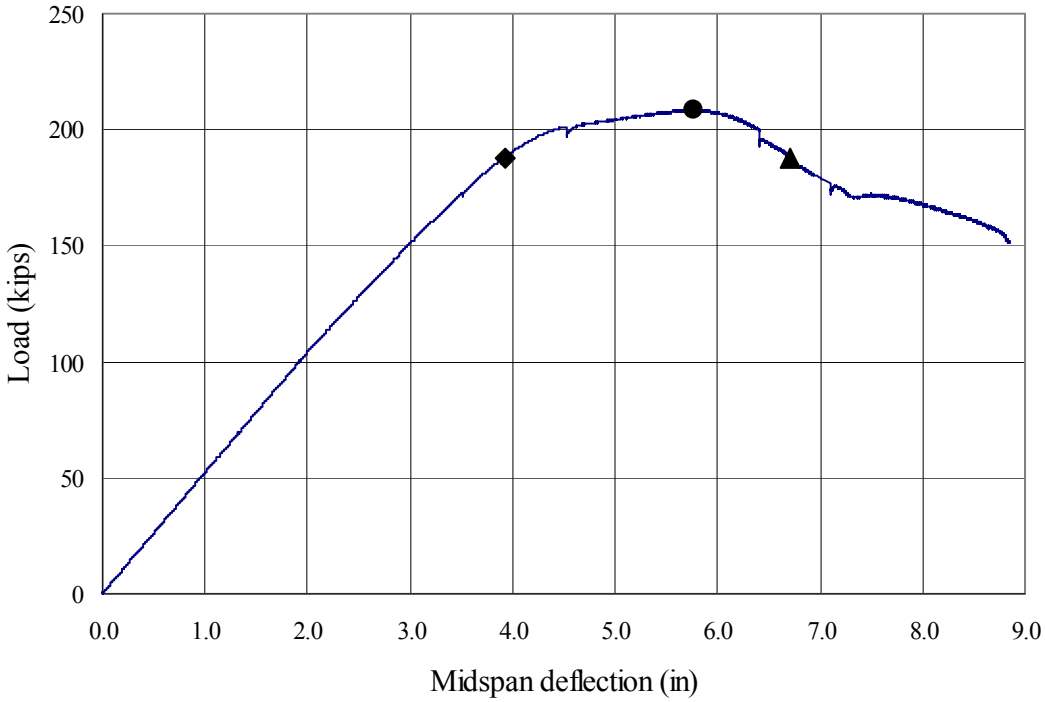

Figure 5.49 Load versus midspan vertical deflection (Specimen 4)

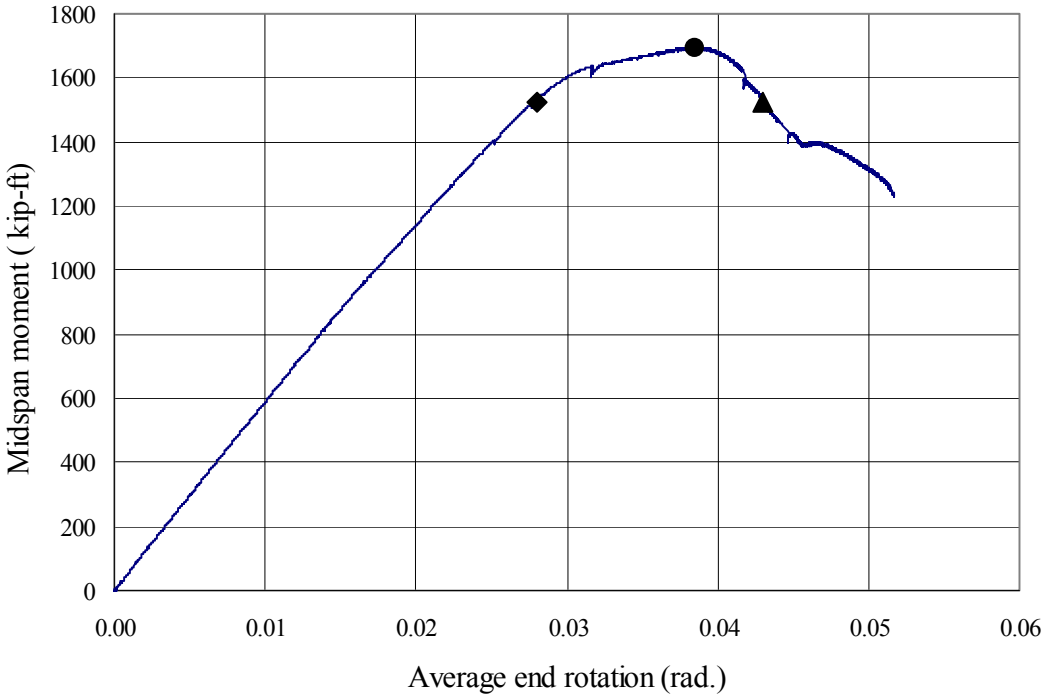

Figure 5.50 Midspan moment versus average end rotation (Specimen 4)

Figure 5.51 Specimen 4 during testing

Figure 5.52 Specimen 4 after testing

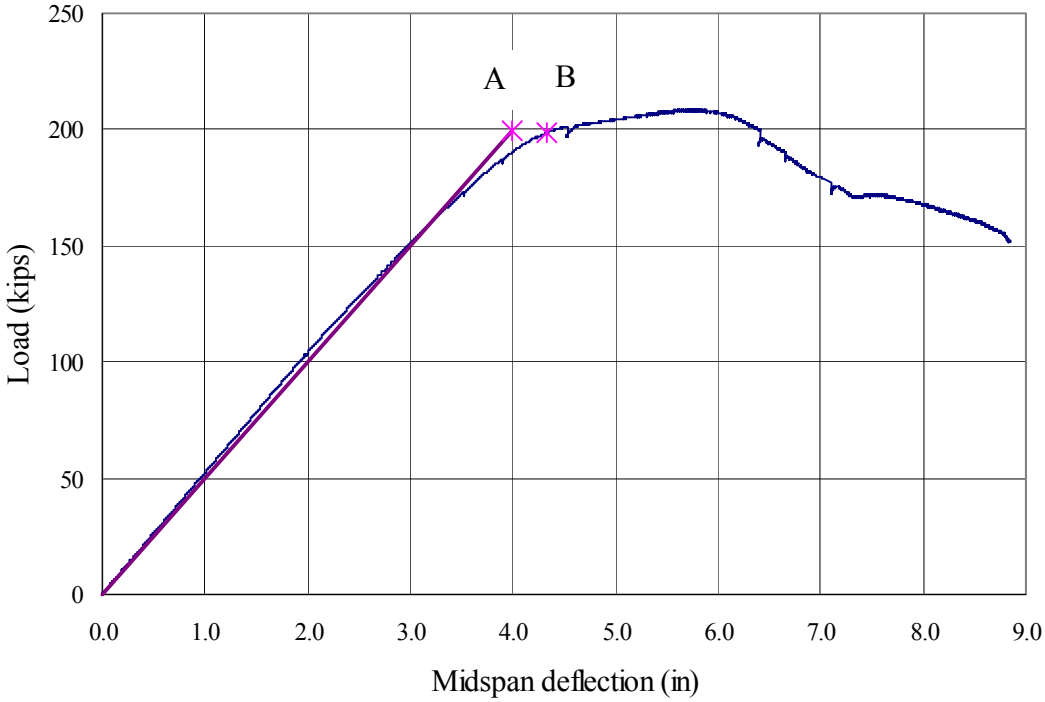

Figure 5.53 Load versus midspan vertical deflection (Specimen 4)

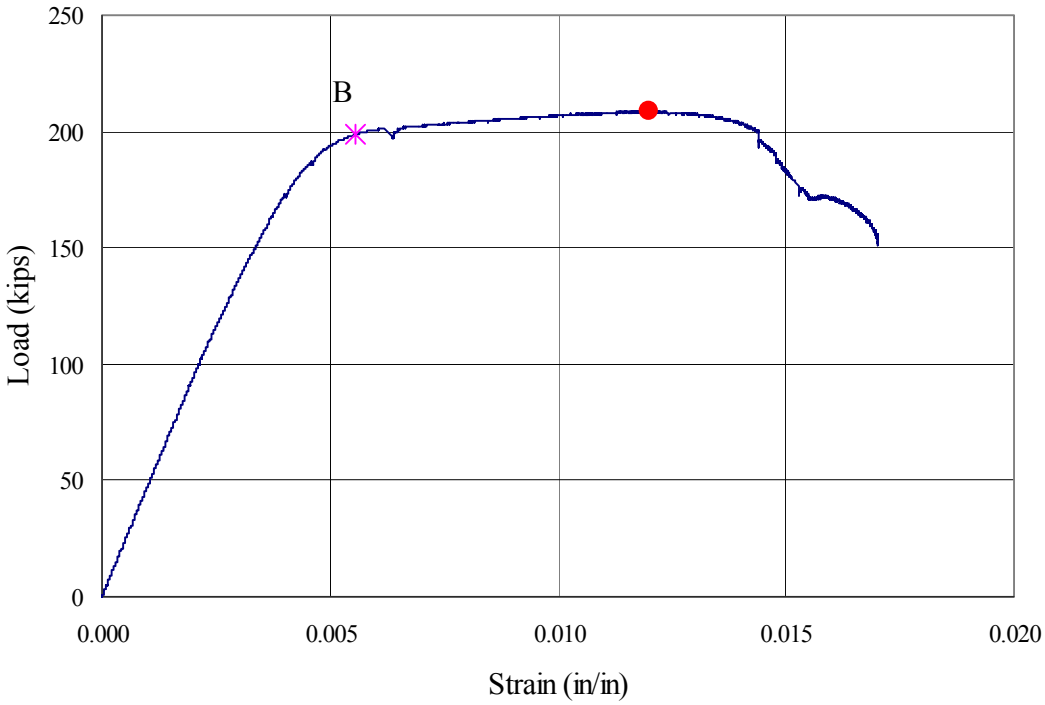

Figure 5.54 Load versus strain recorded by strain gage 161 (Specimen 4)

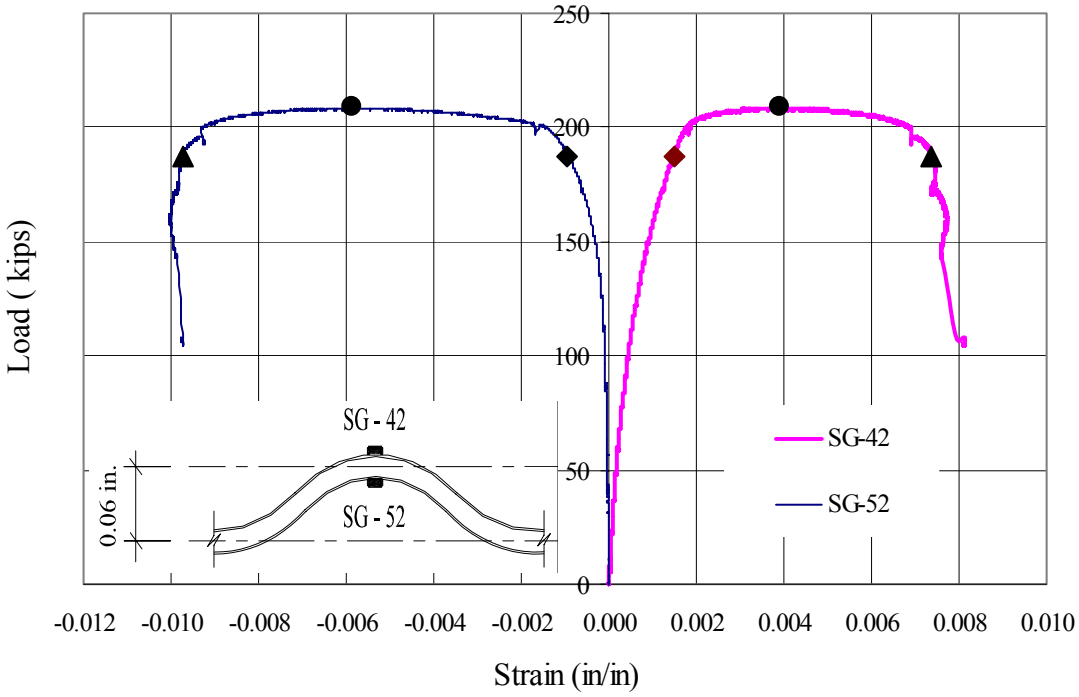

Figure 5.55 Effect of initial imperfection on web distortion (Specimen 4)

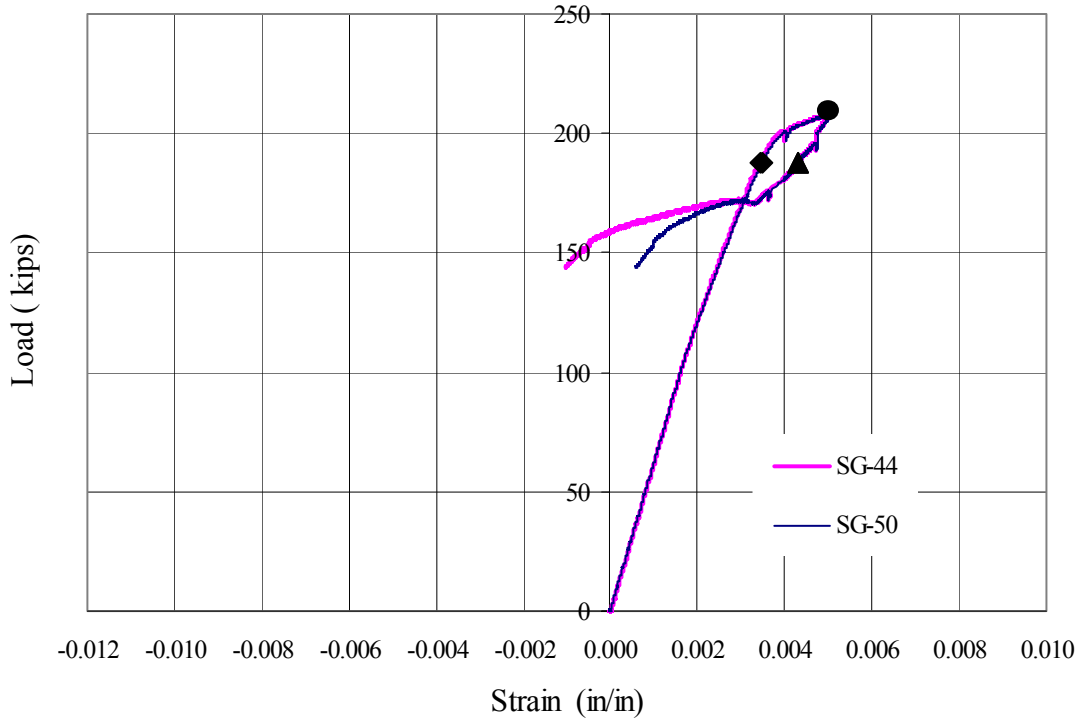

Figure 5.56 Load versus strain for strain gages SG-44 and SG-50 (Specimen 4)

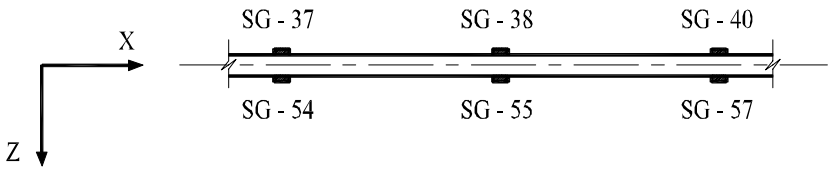

(a) Strain gages at web-flange intersection

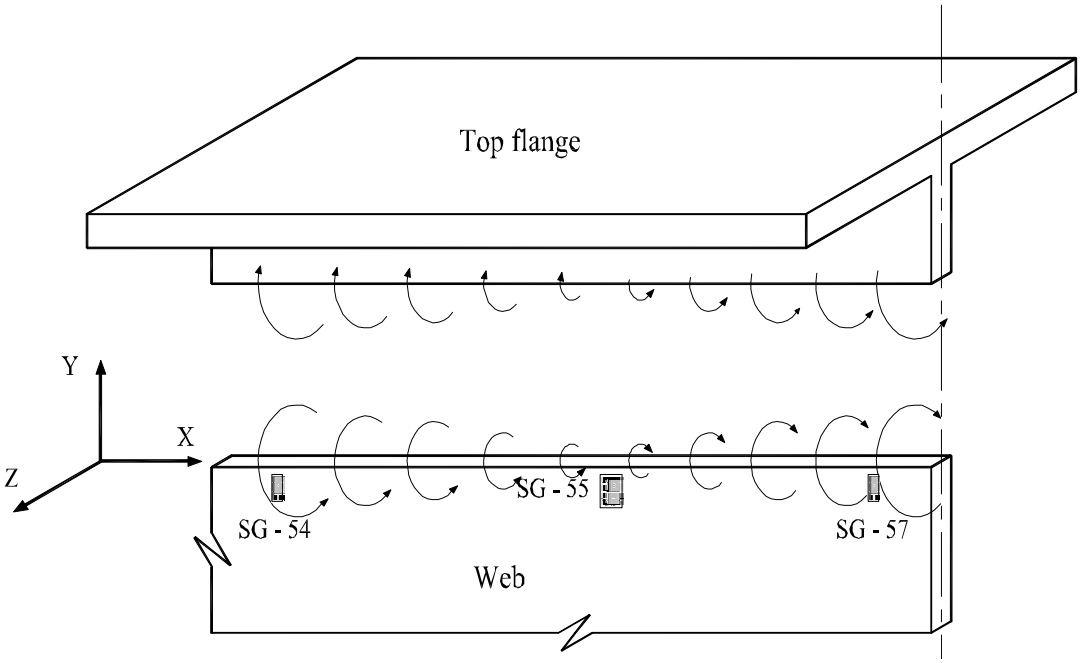

(b) Moment transfer at web-flange intersection

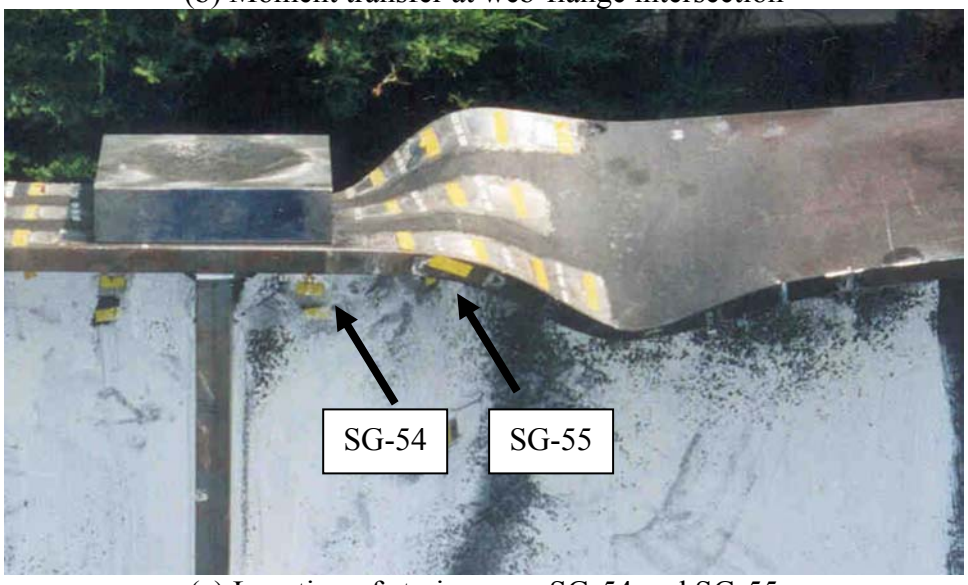

(c) Location of strain gages SG-54 and SG-55

Figure 5.57 Interaction between web and compression flange at the distorted region

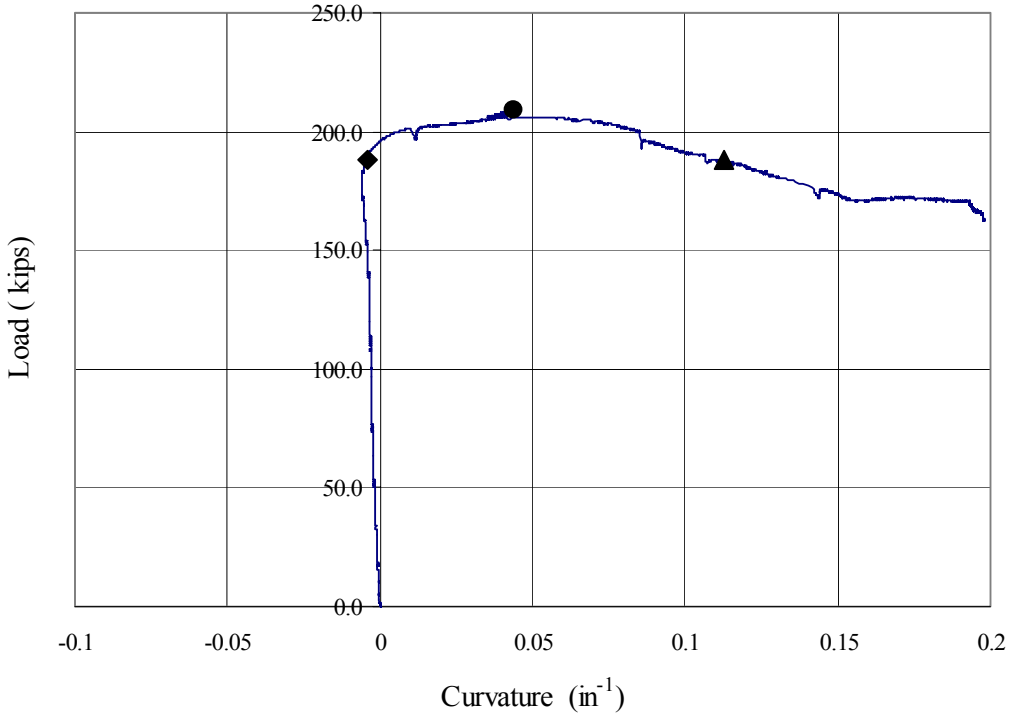

Figure 5.58 Load versus curvature at strain gages SG-38 and SG-55 (Specimen 4)

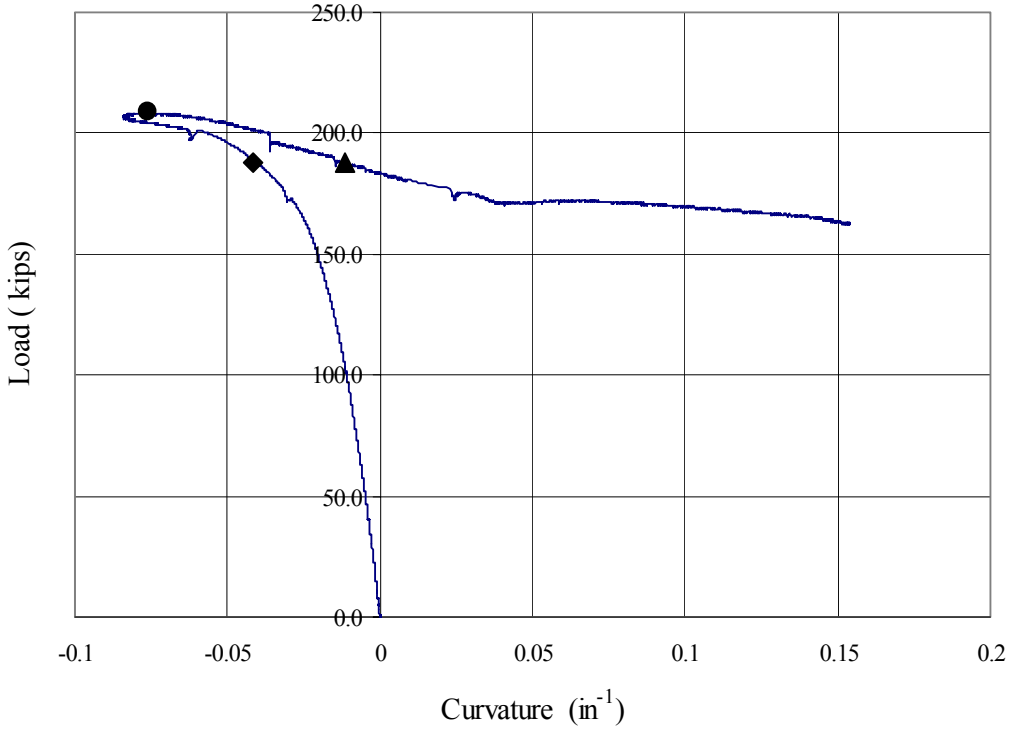

Figure 5.59 Load versus curvature at strain gages SG-40 and SG-57 (Specimen 4)

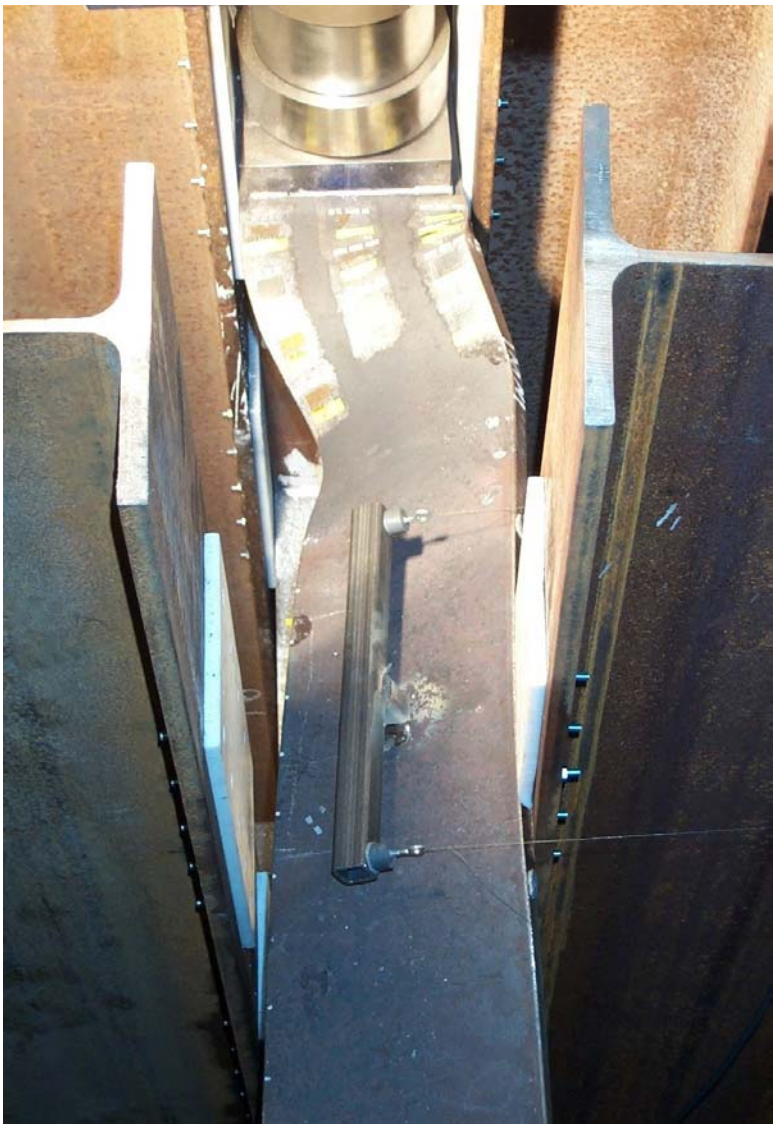

Figure 5.60 Lateral distortion of compression flange (Specimen 4)

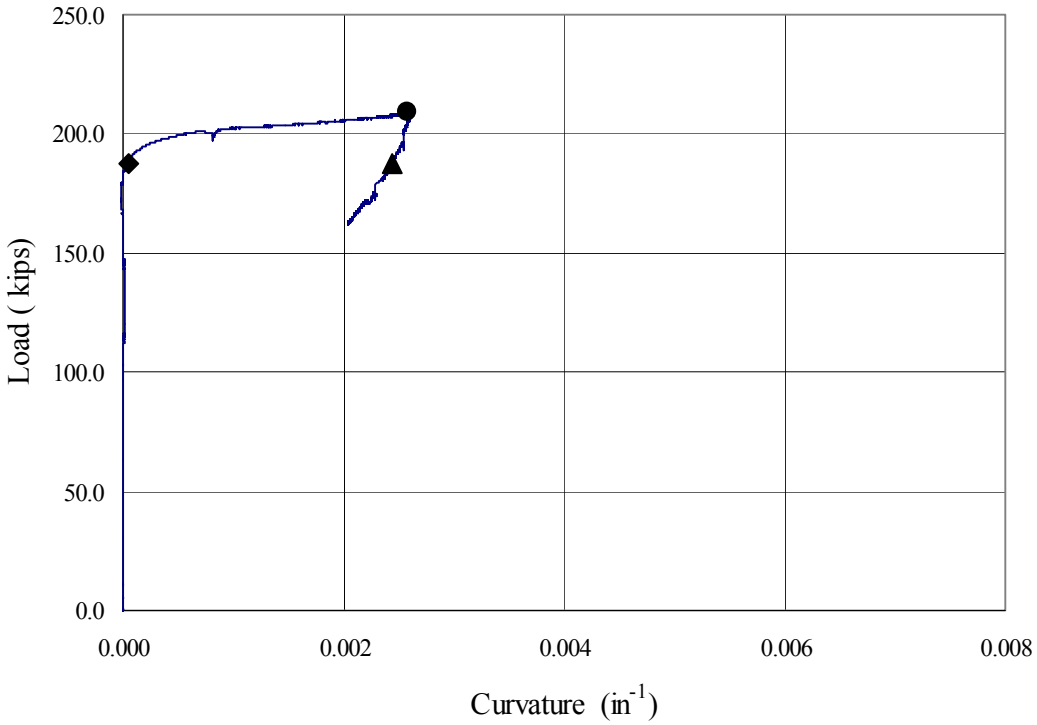

Figure 5.61 Load versus ϕ_l at section 2 (Specimen 4)

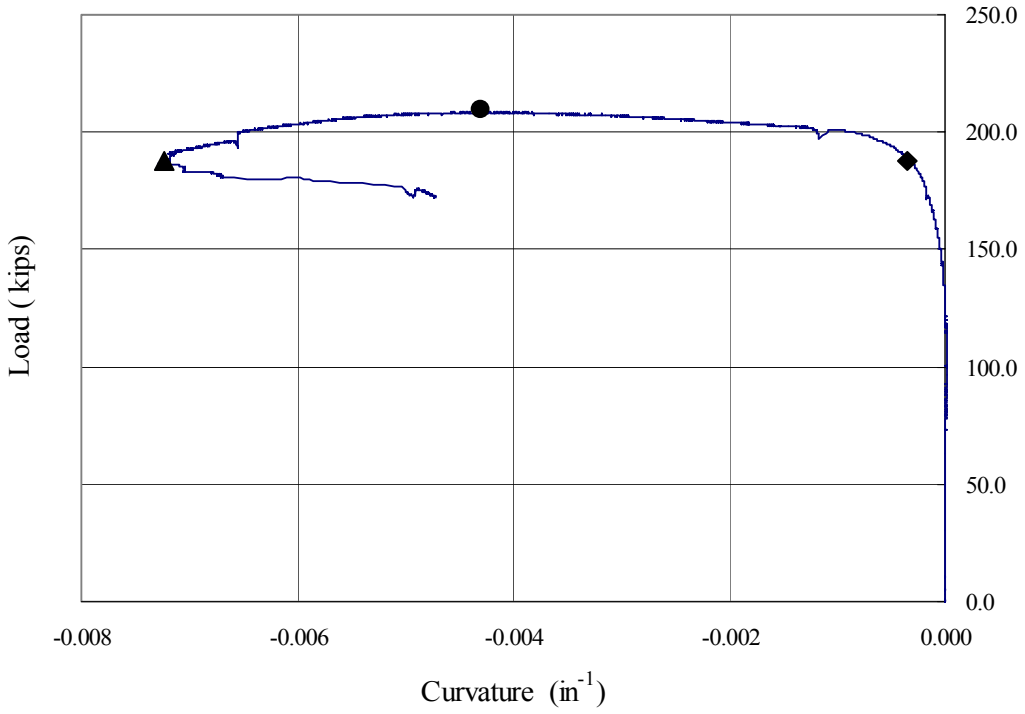

Figure 5.62 Load versus ϕ_l at section 5 (Specimen 4)

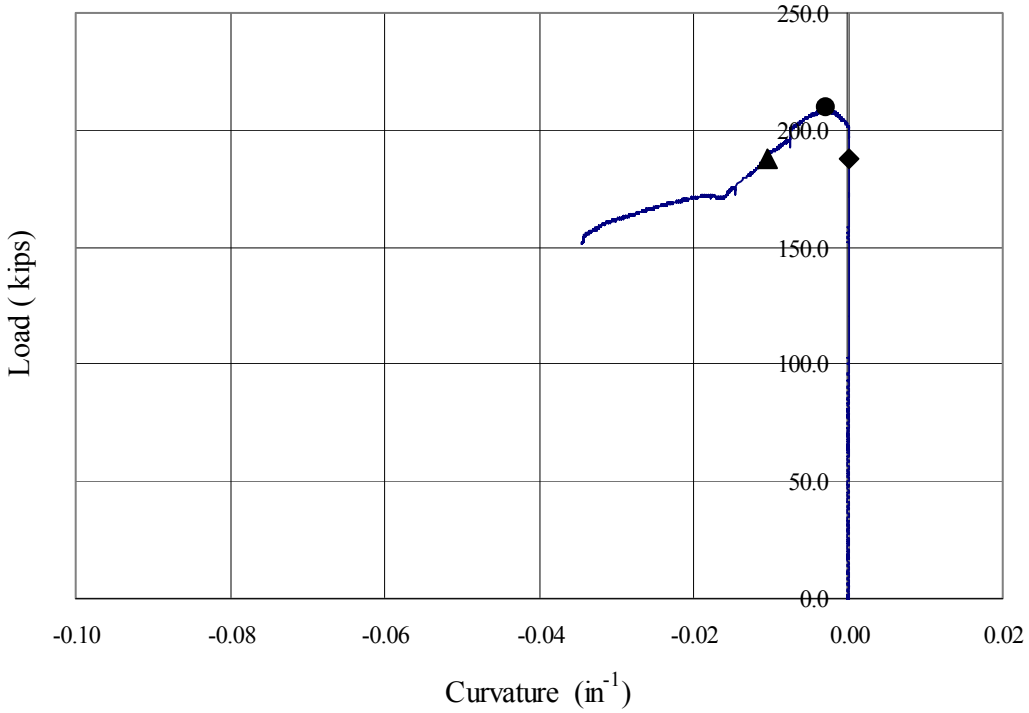

Figure 5.63 Load versus ϕ_{fp} at section 5-East (Specimen 4)

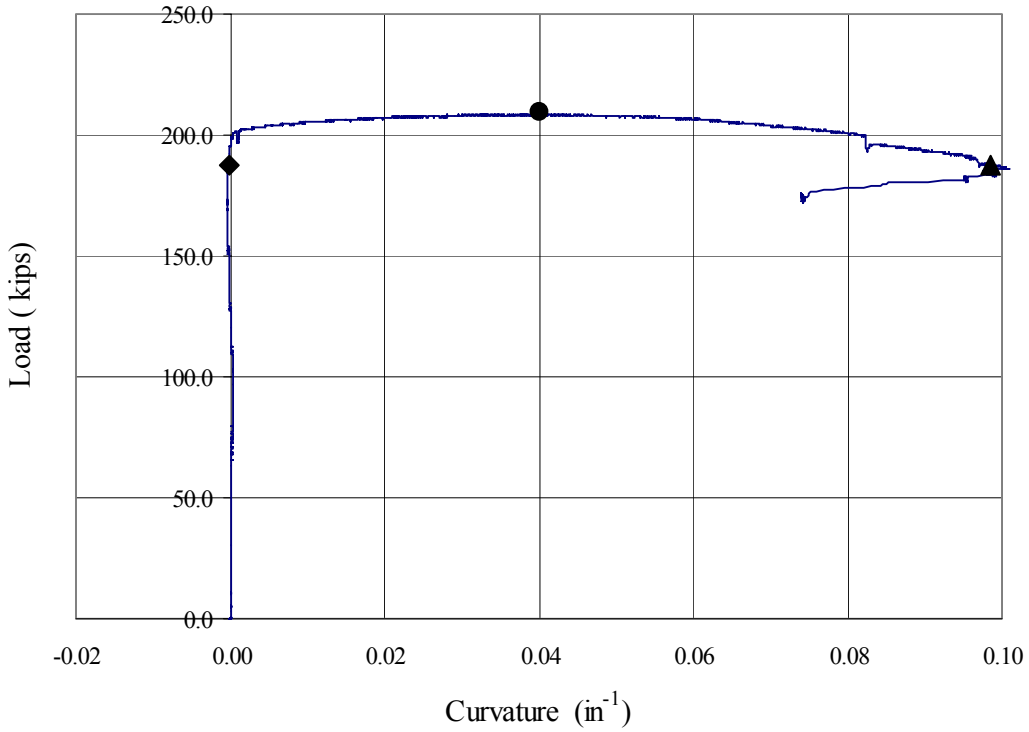

Figure 5.64 Load versus ϕ_{fp} at section 5-West (Specimen 4)

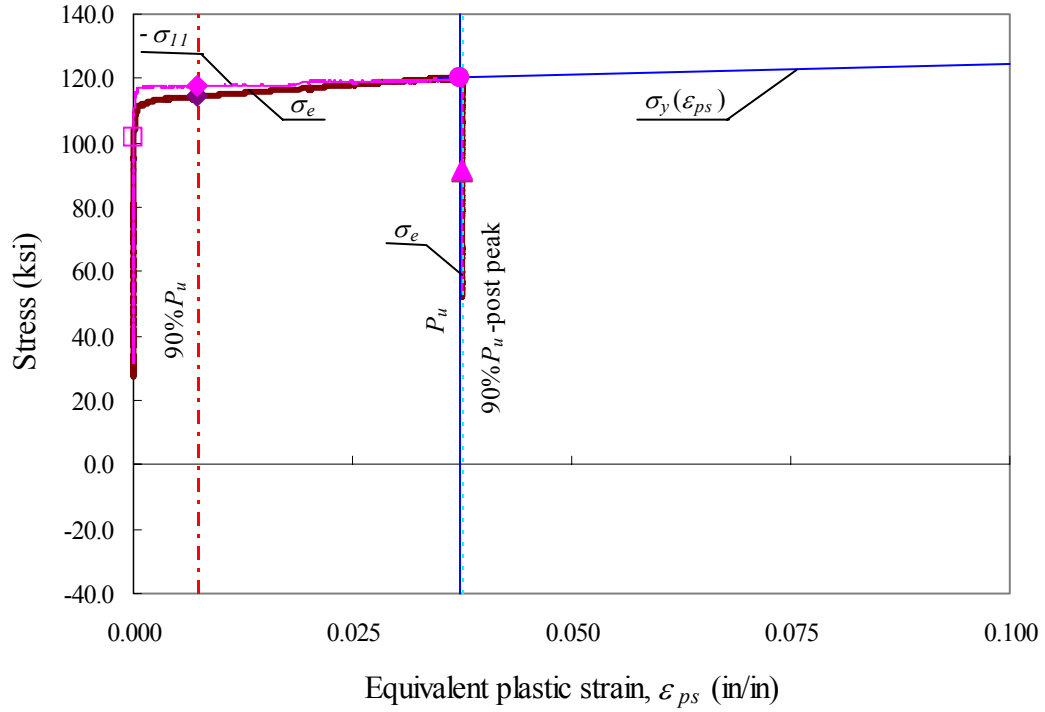

Figure 5.65 Stress versus equivalent plastic strain (section 1-East, Specimen 4)

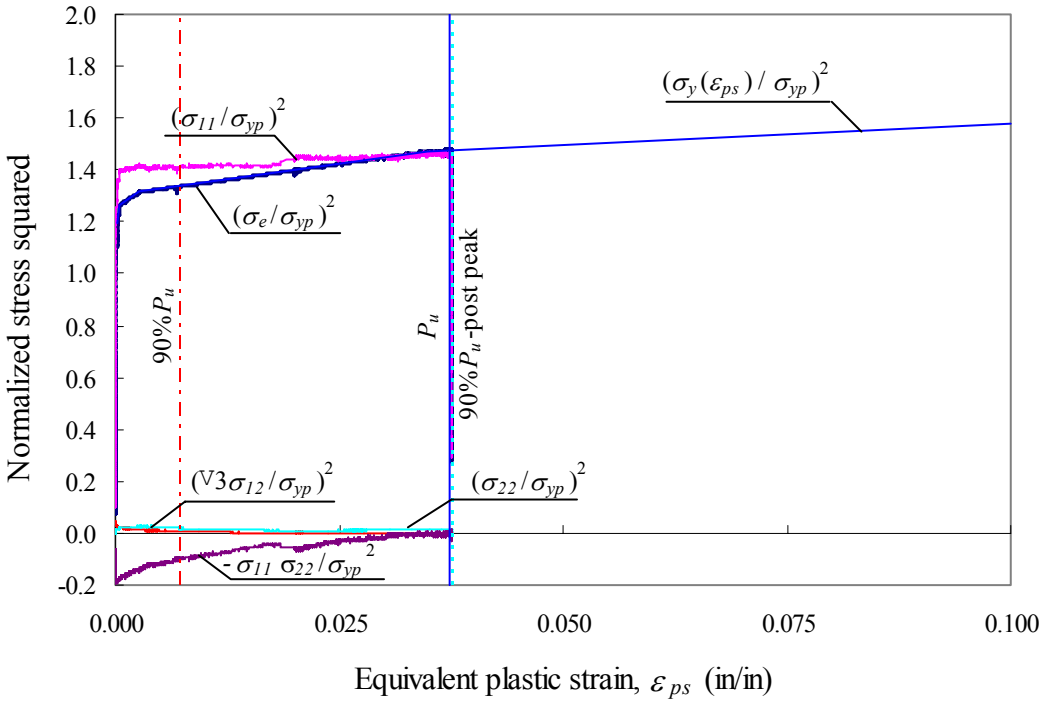

Figure 5.66 Contributions to effective stress (section 1-East, Specimen 4)

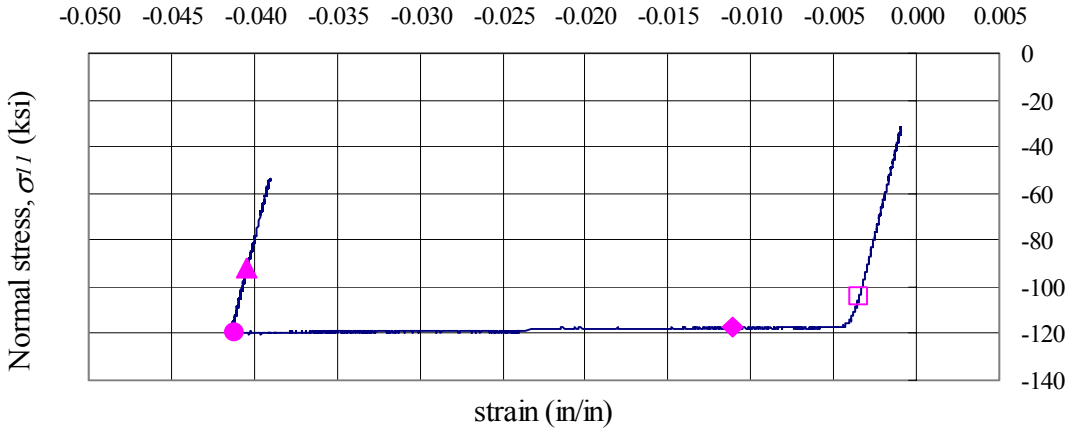

(a) Normal strain, ε_{11}

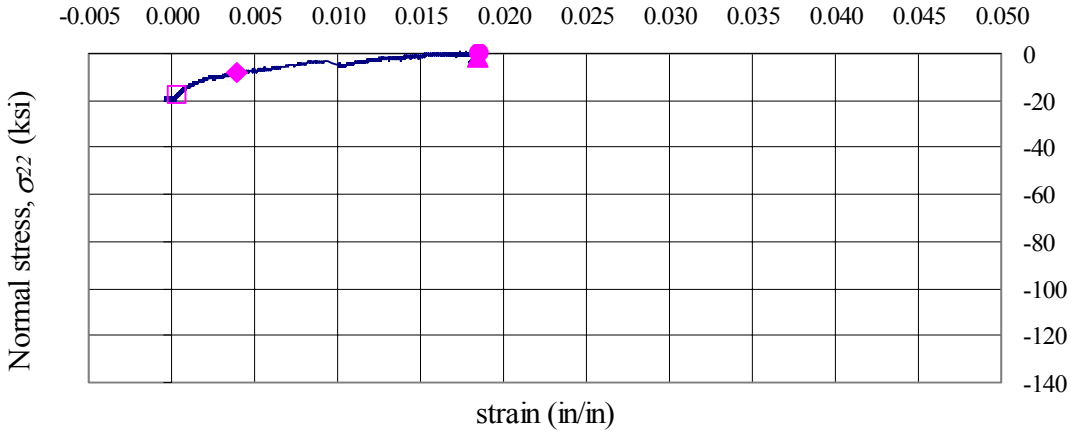

(a) Normal strain, ε_{22}

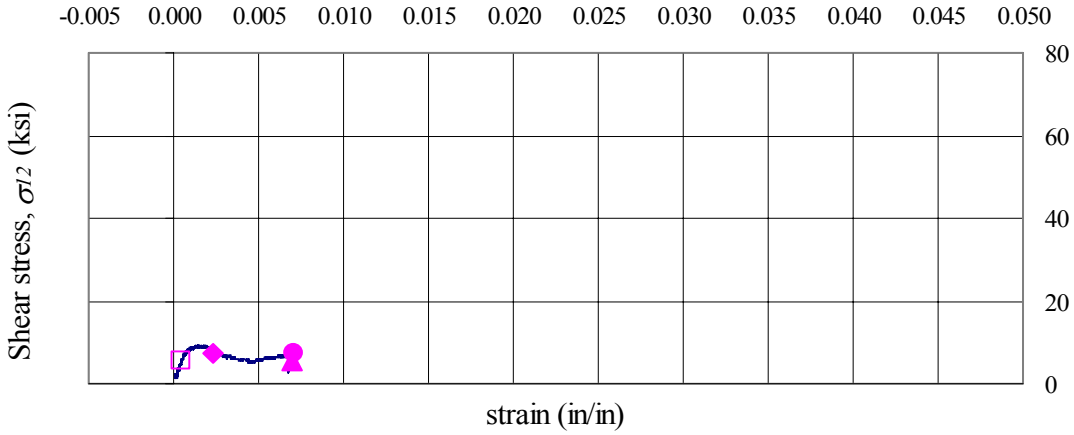

(c) Engineering shear strain, γ_{12}

Figure 5.67 Stress versus strain (section 1-East, Specimen 4)

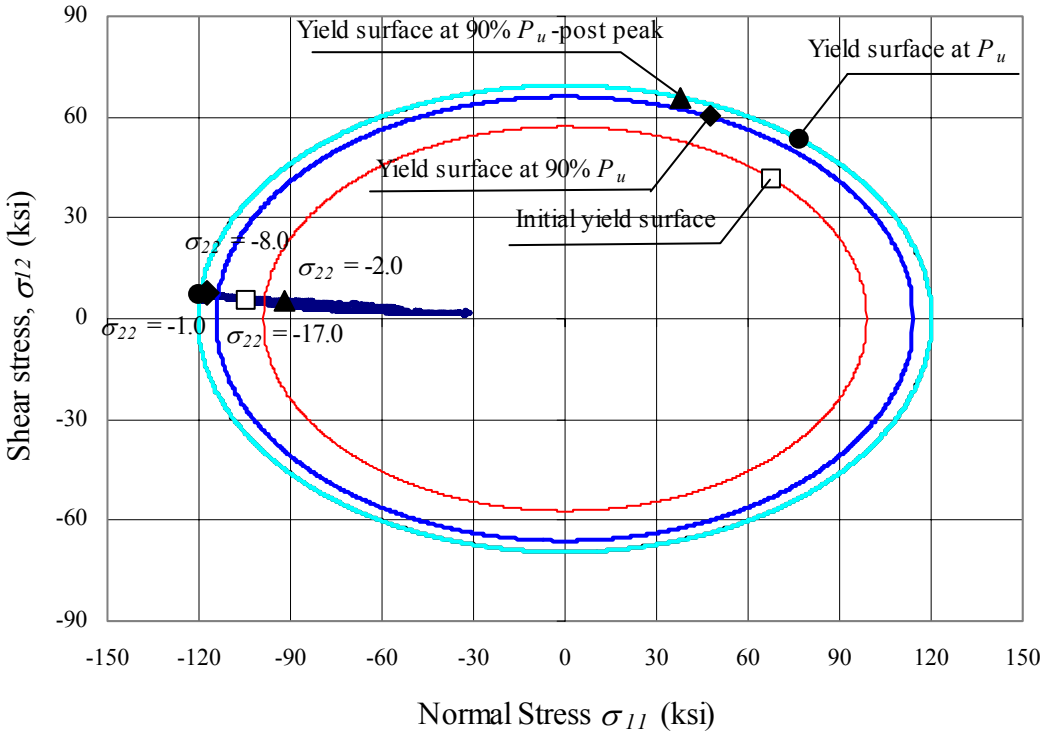

Figure 5.68 Yield surface in σ_{11}- σ_{12} plane at different increments (section 1-East, Specimen 4)

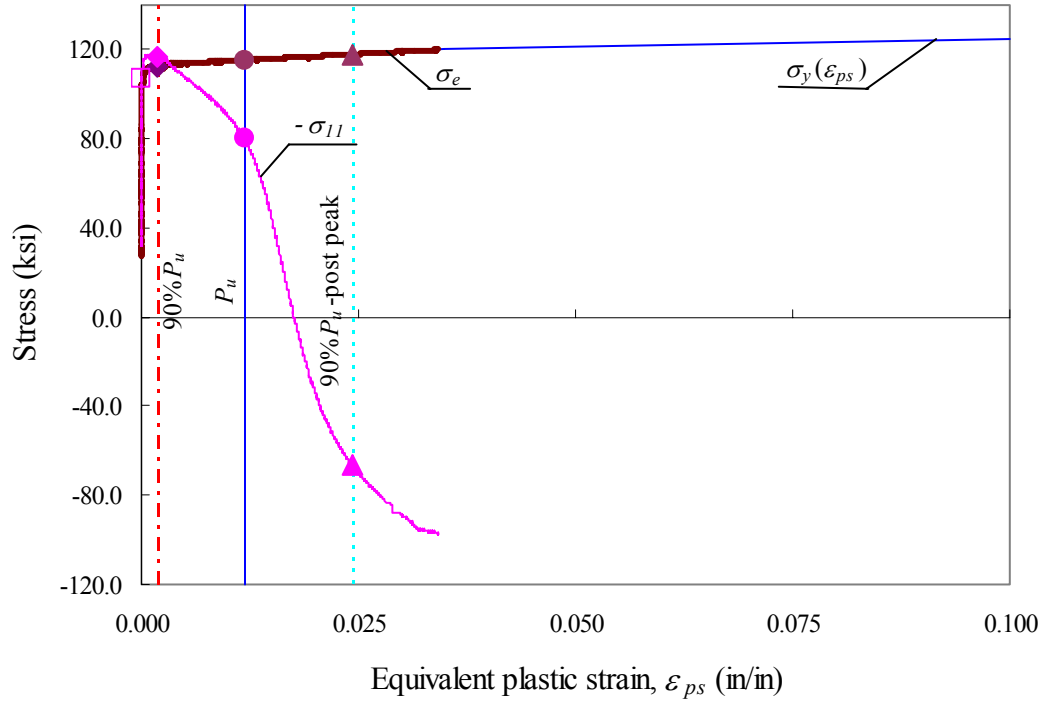

Figure 5.69 Stress versus equivalent plastic strain (section 7-East, Specimen 4)

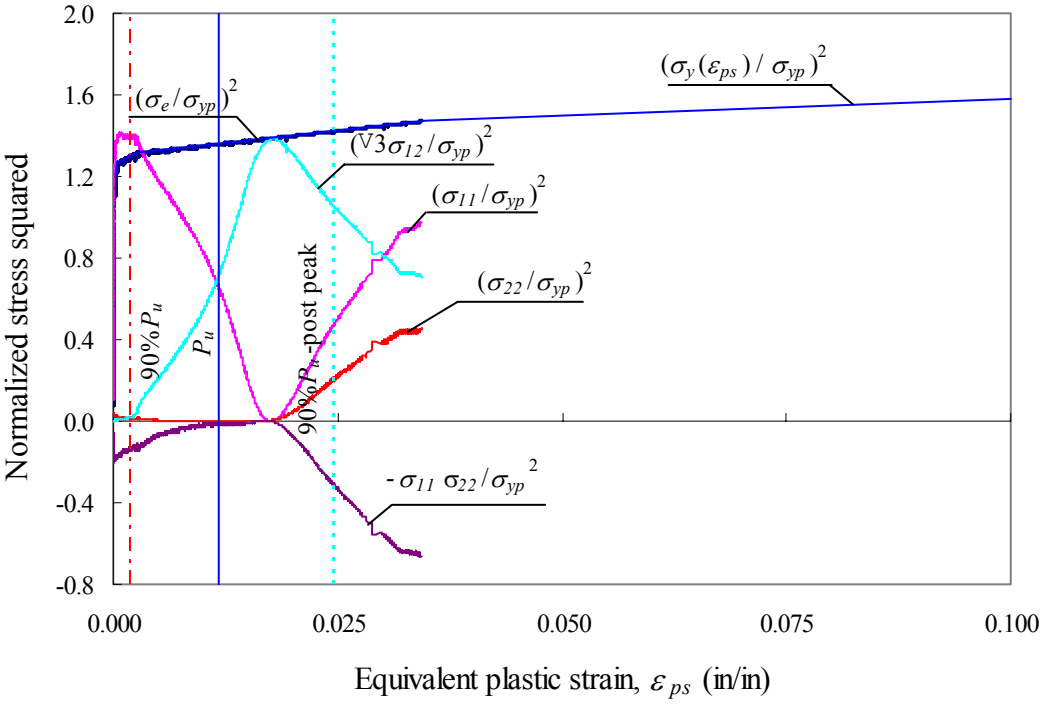

Figure 5.70 Contributions to effective stresses (section 7-East, Specimen 4)

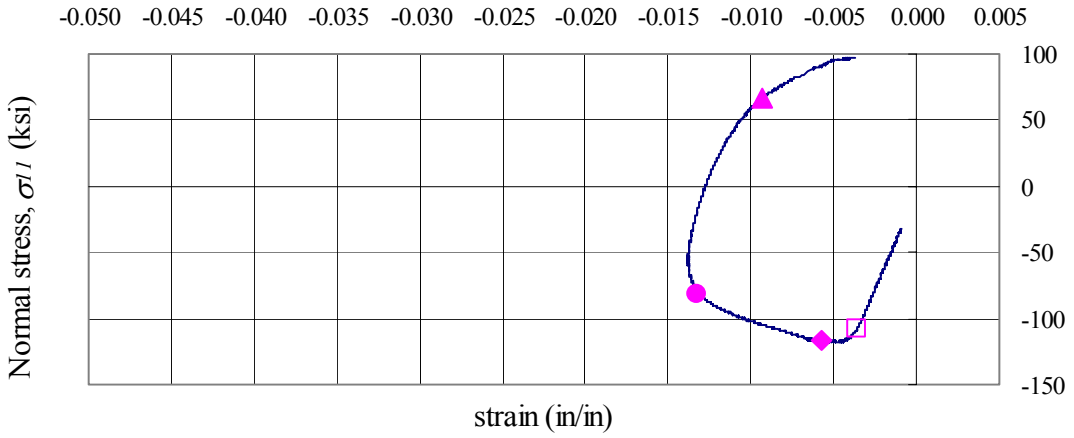

(a) Normal strain, ε_{11}

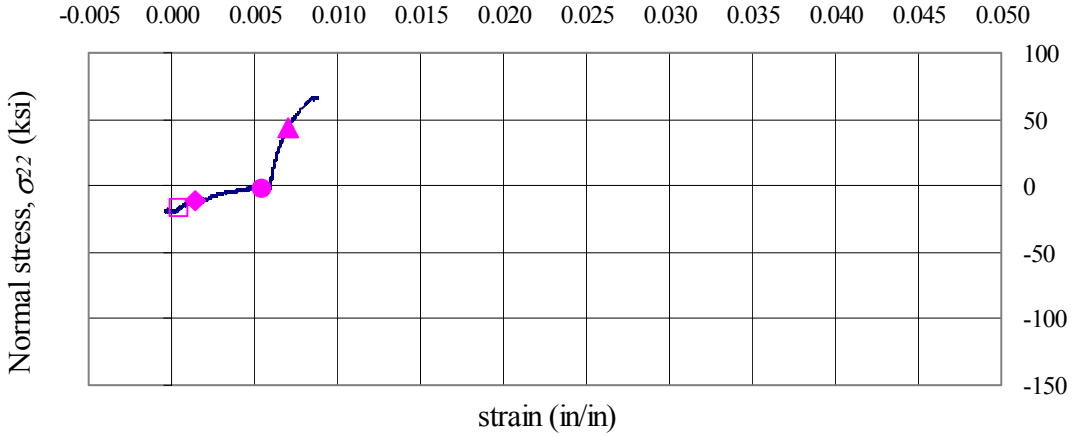

(b) Normal strain, ε_{22}

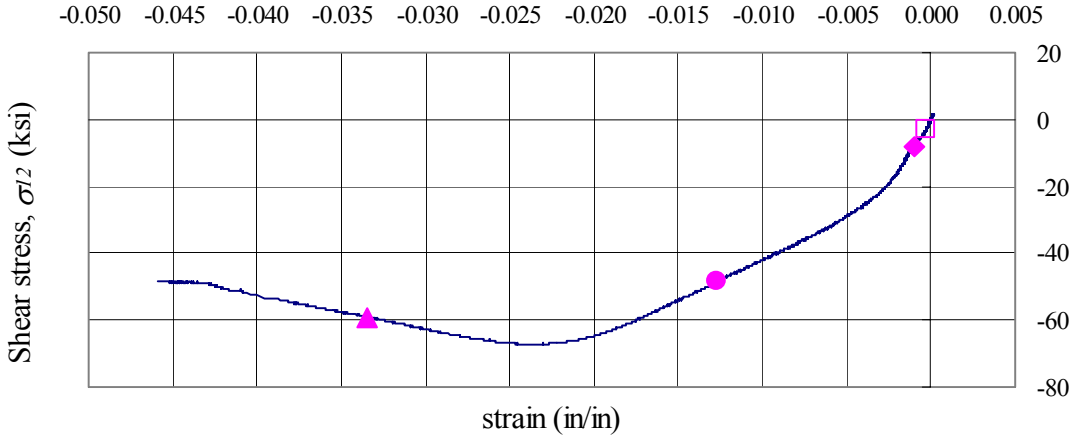

(c) Engineering shear strain, γ_{12}

Figure 5.71 Stress versus strain (section 7-East, Specimen 4)

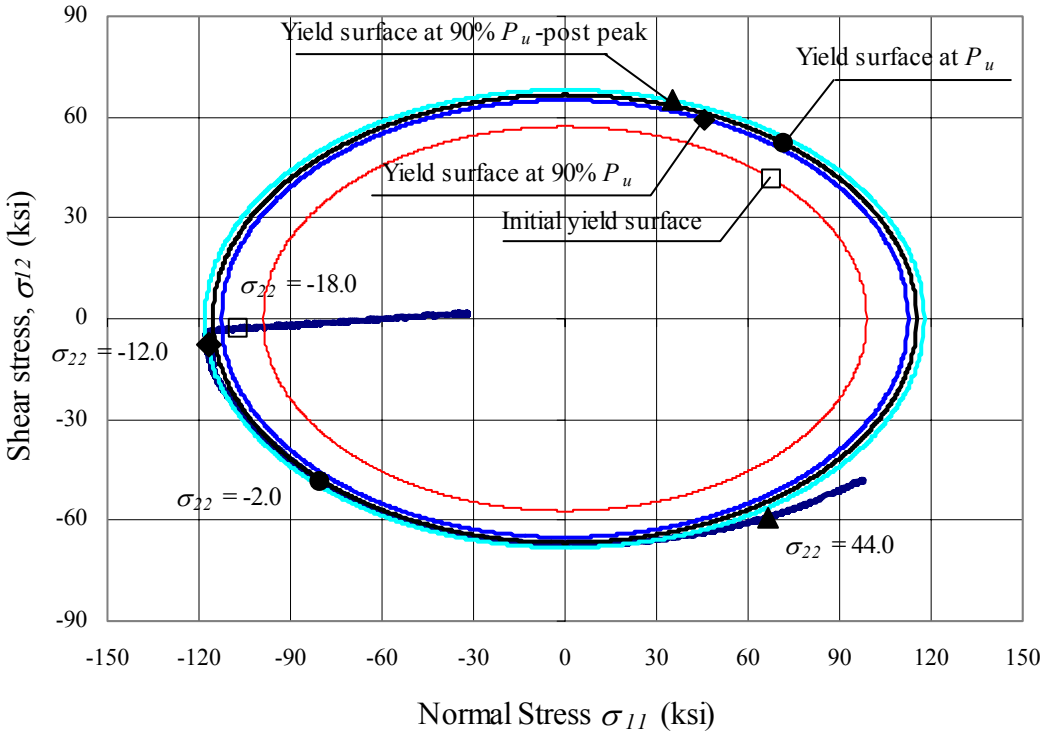

Figure 5.72 Yield surface in σ_{11}- σ_{12} plane at different increments (section 7-East, Specimen 4)

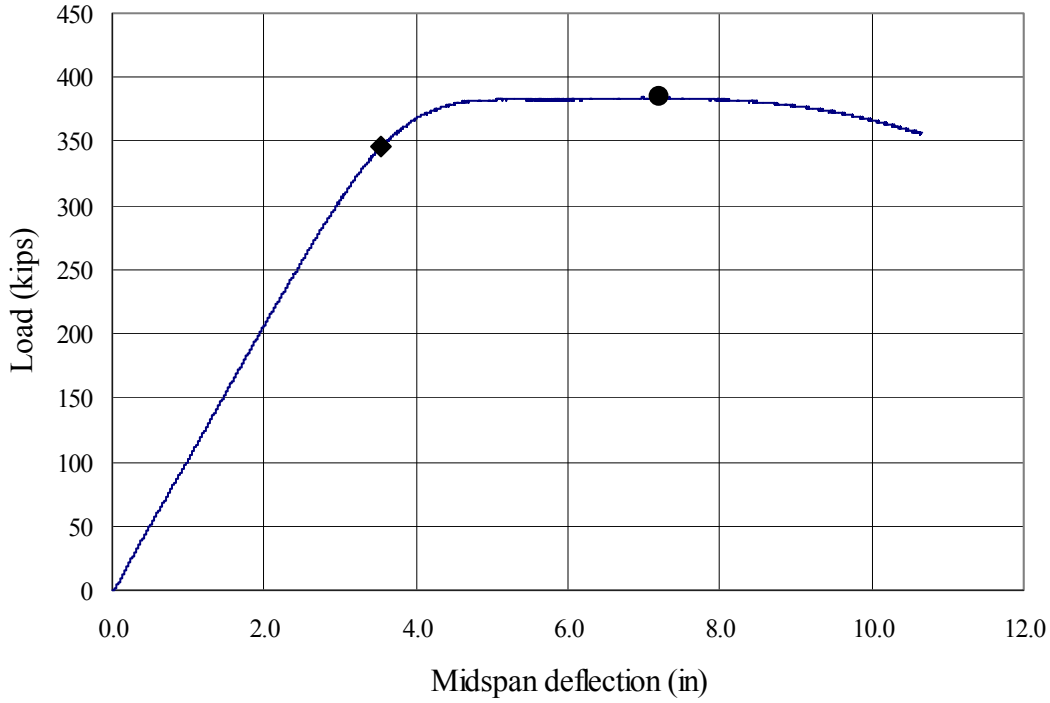

Figure 5.73 Load versus midspan vertical deflection (Specimen 5)

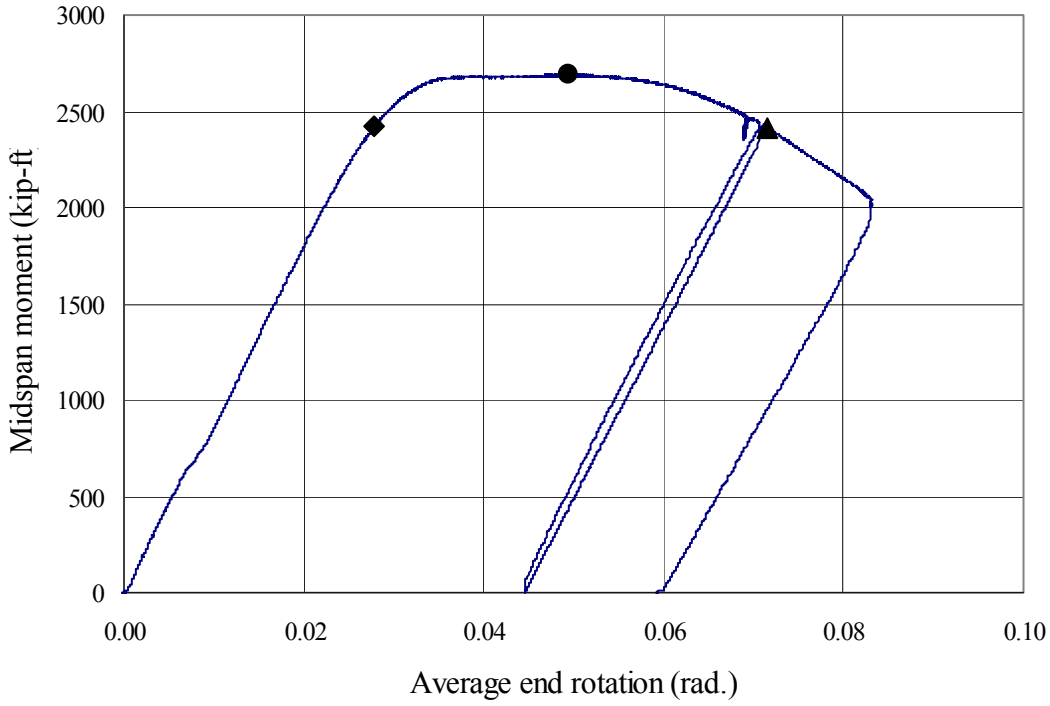

Figure 5.74 Midspan moment versus average end rotation (Specimen 5)

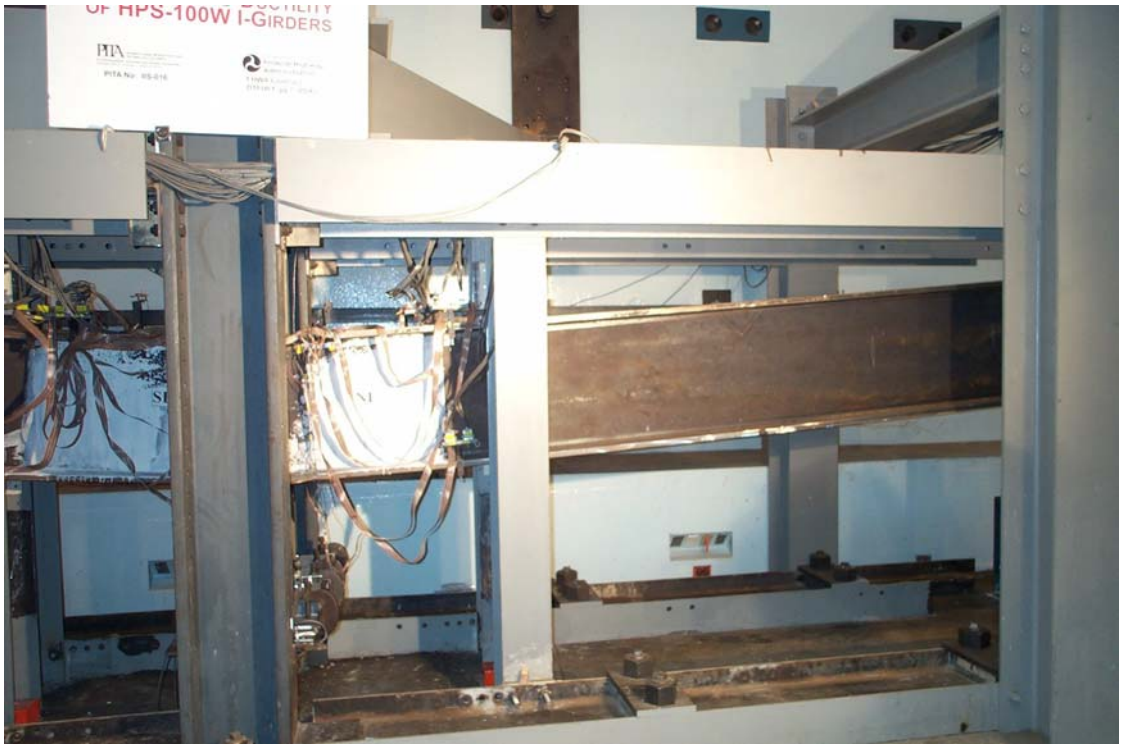

Figure 5.75 Specimen 5 during testing

Figure 5.76 Specimen 5 after testing

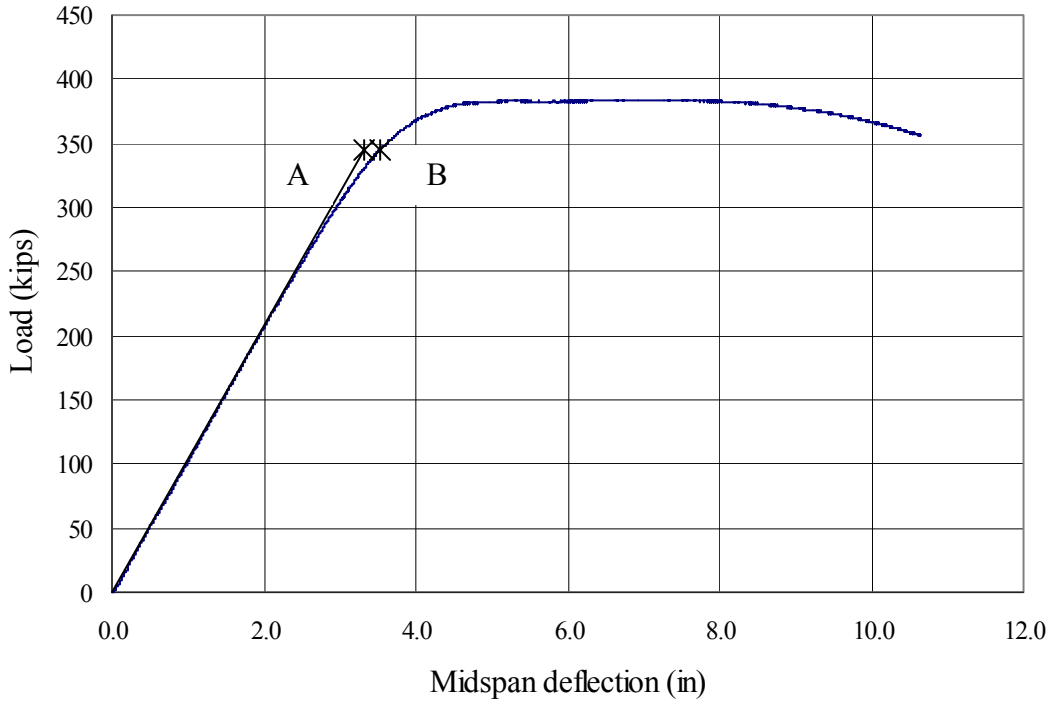

Figure 5.77 Load versus midspan vertical deflection (Specimen 5)

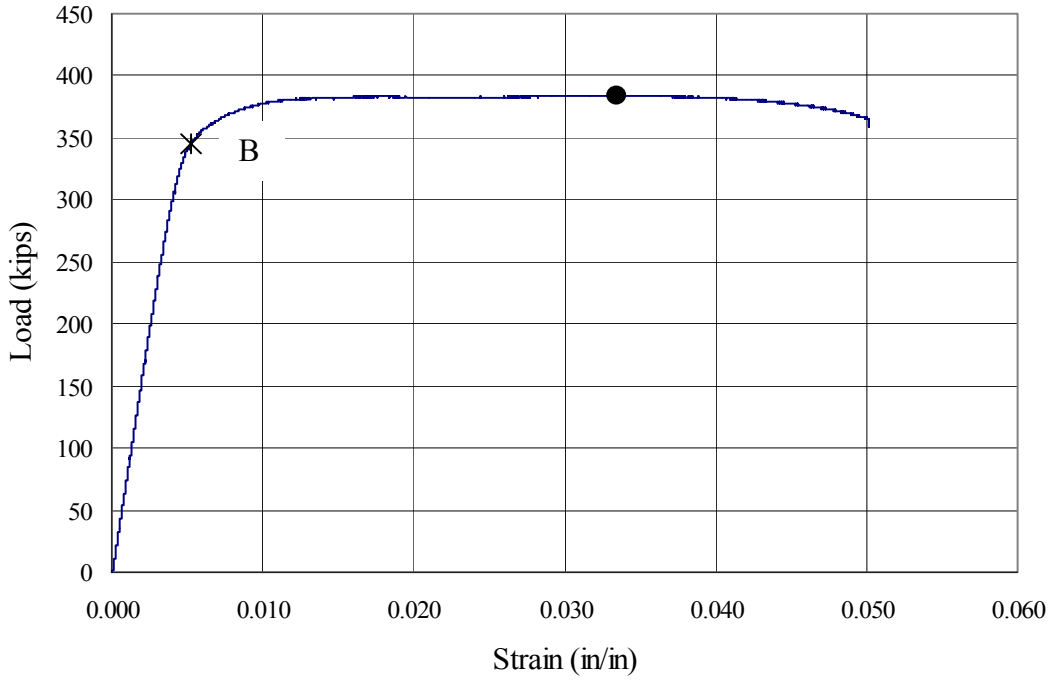

Figure 5.78 Load versus strain recorded by strain gage 161 (Specimen 5)

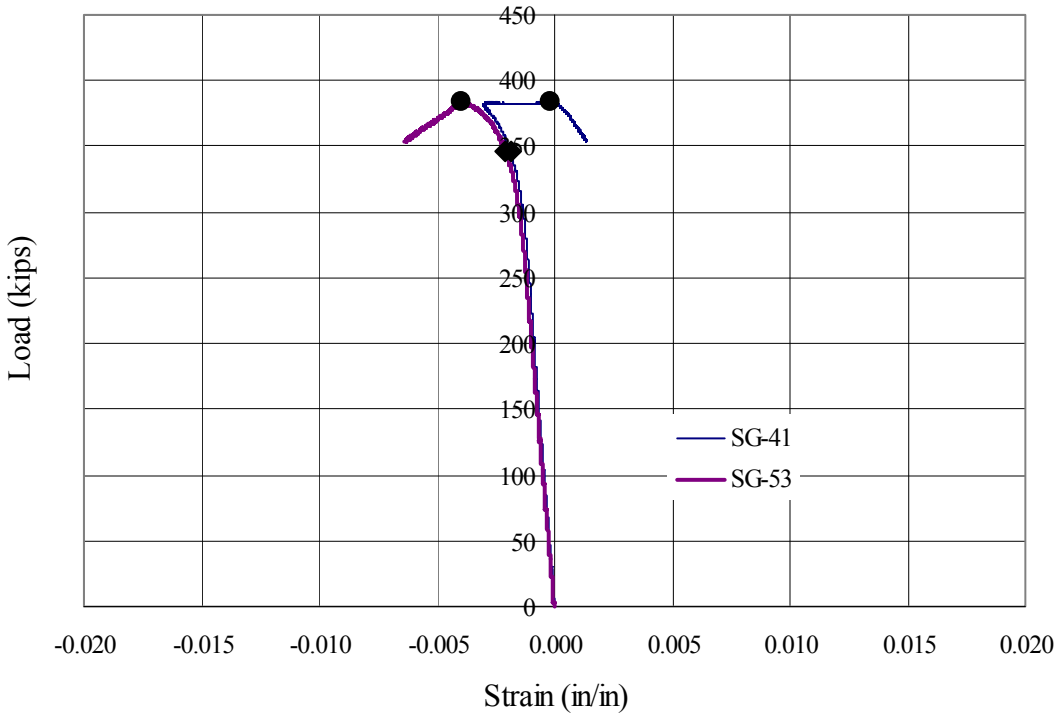

Figure 5.79 Effect of initial imperfection on web distortion (Specimen 5)

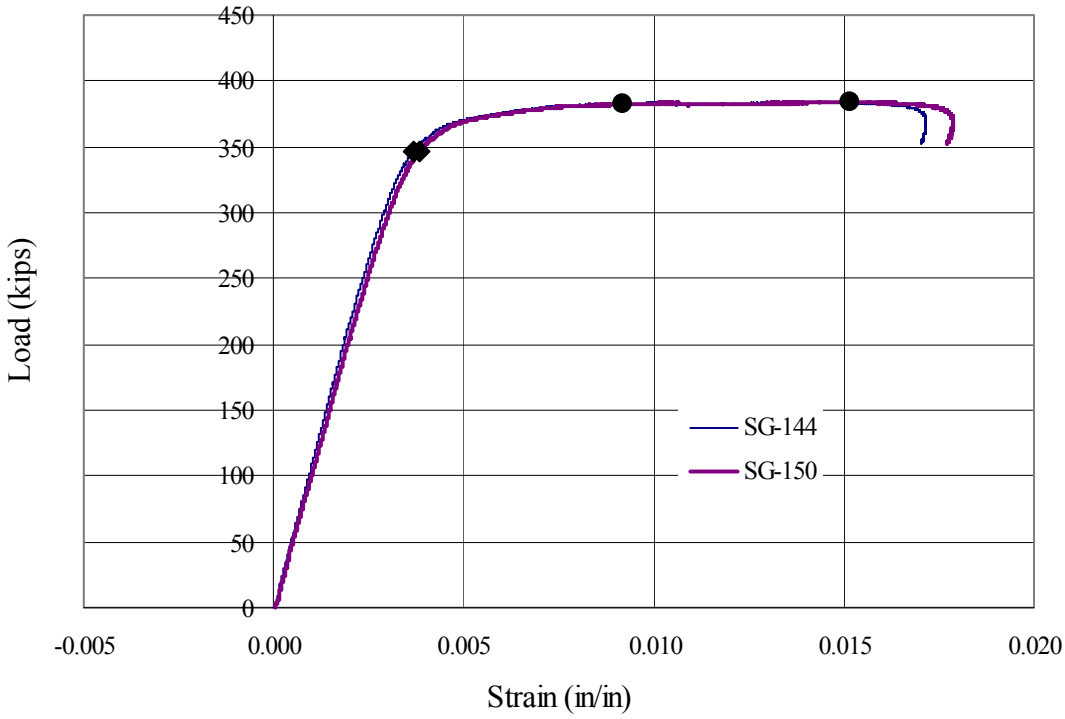

Figure 5.80 Load versus strain for strain gages SG-144 and SG-150 (Specimen 5)

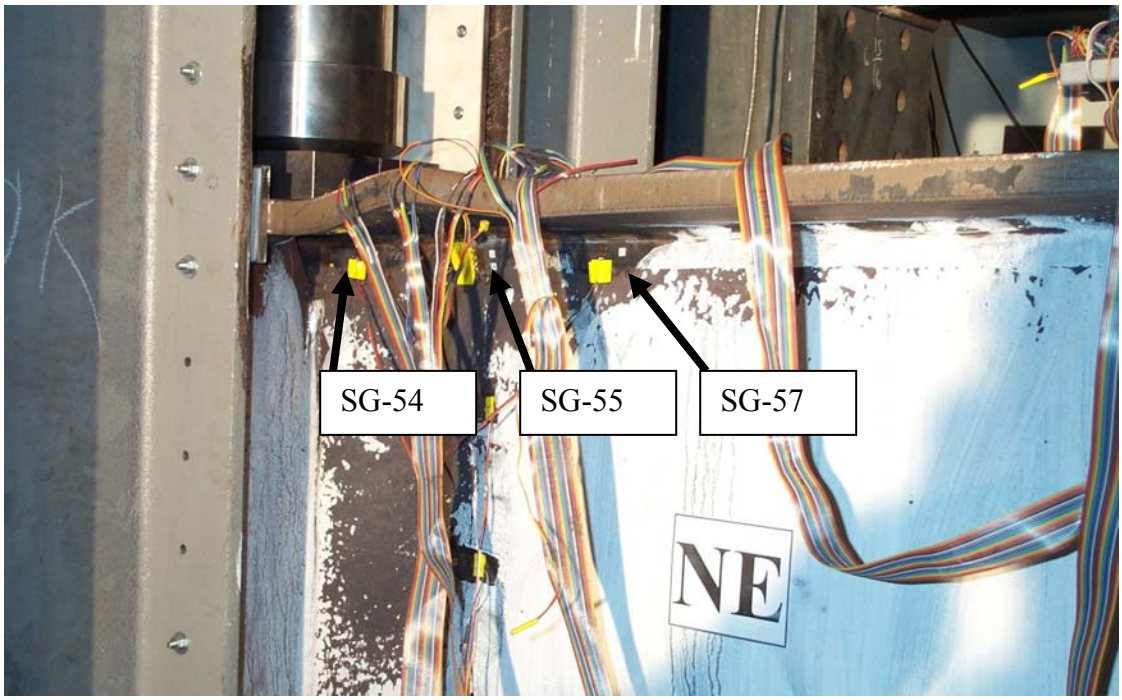

(a) Location of strain gages SG-54, SG-55 and SG-57

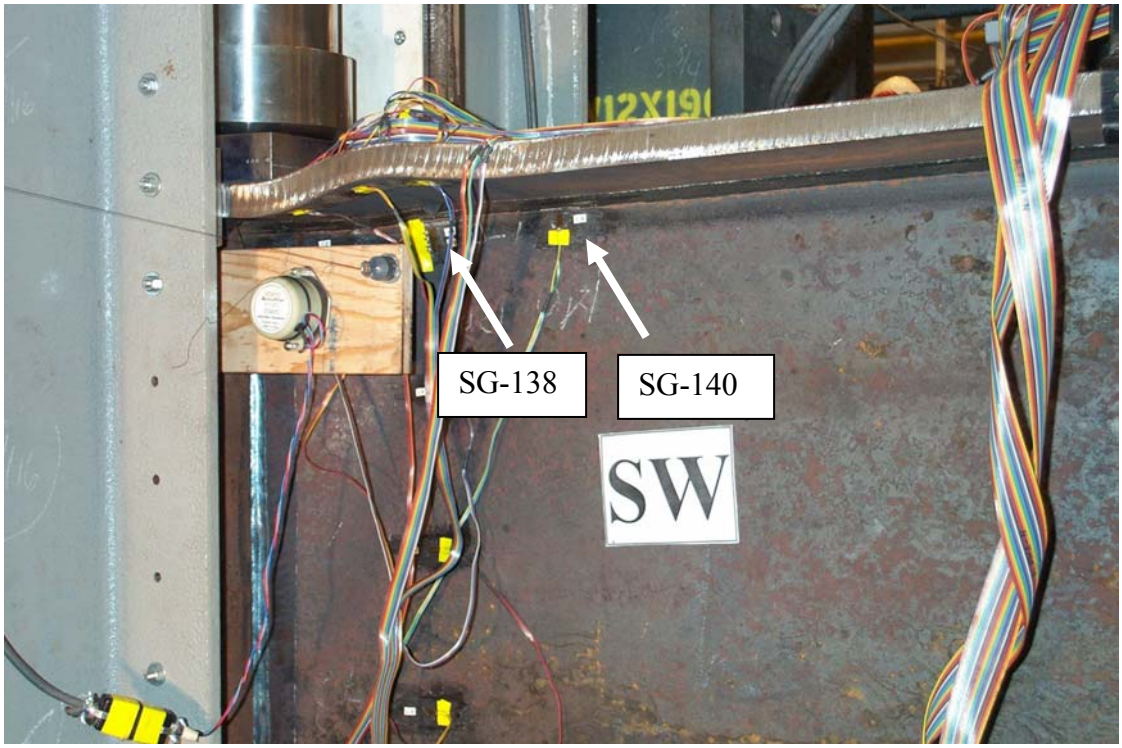

(b) Location of strain gages SG-138 and SG-140

Figure 5.81 Interaction between web and compression flange at the distorted region

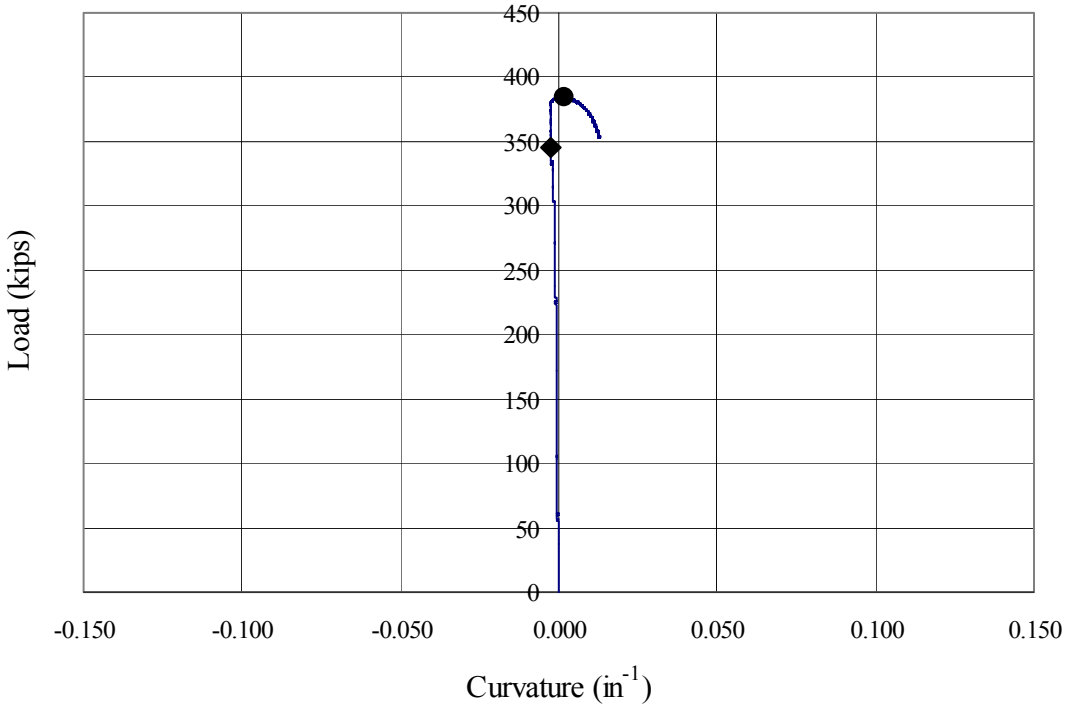

Figure 5.82 Load versus curvature at strain gages SG-37 and SG-54 (Specimen 5)

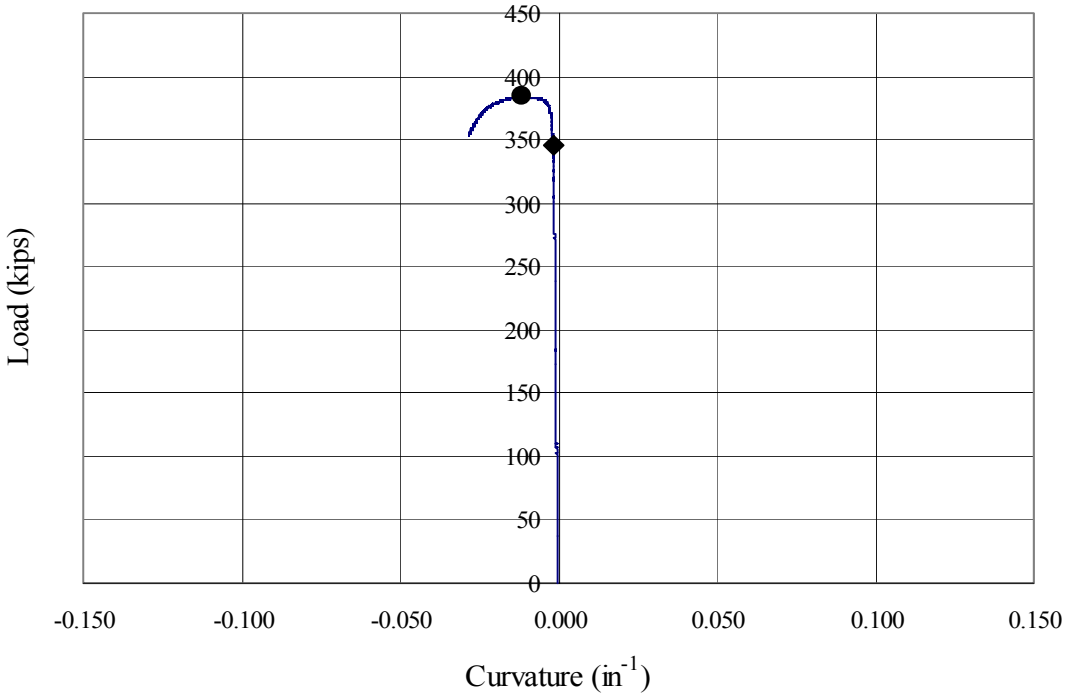

Figure 5.83 Load versus curvature at strain gages SG-137 and SG-154 (Specimen 5)

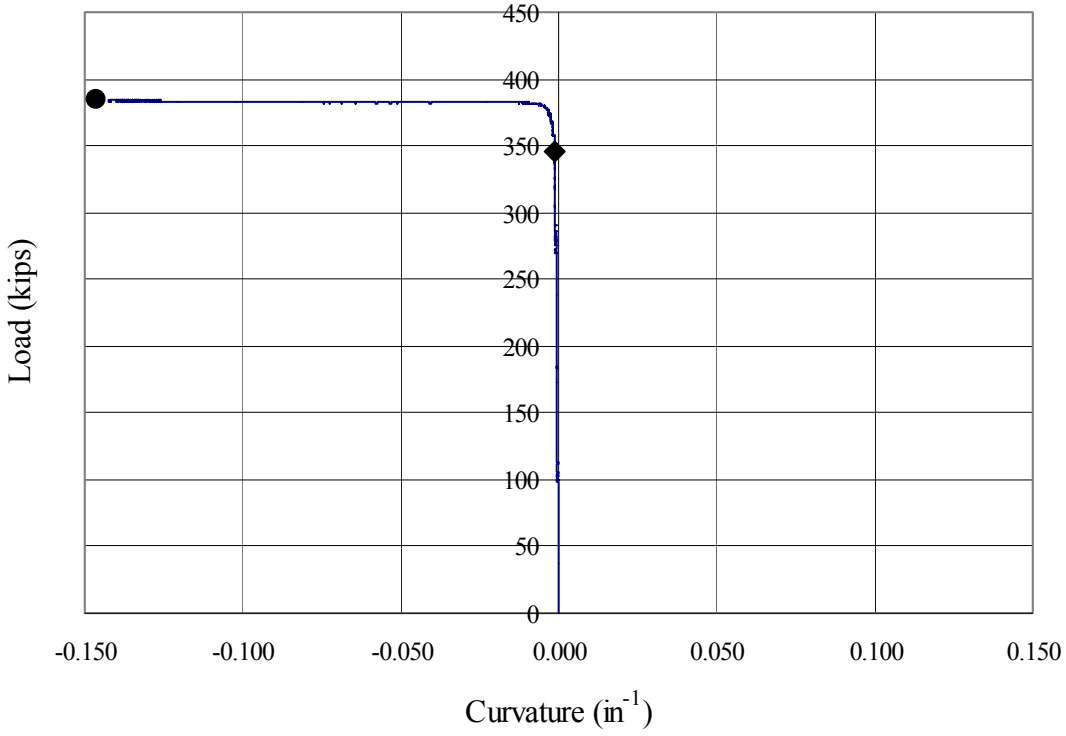

Figure 5.84 Load versus curvature at strain gages SG-38 and SG-55 (Specimen 5)

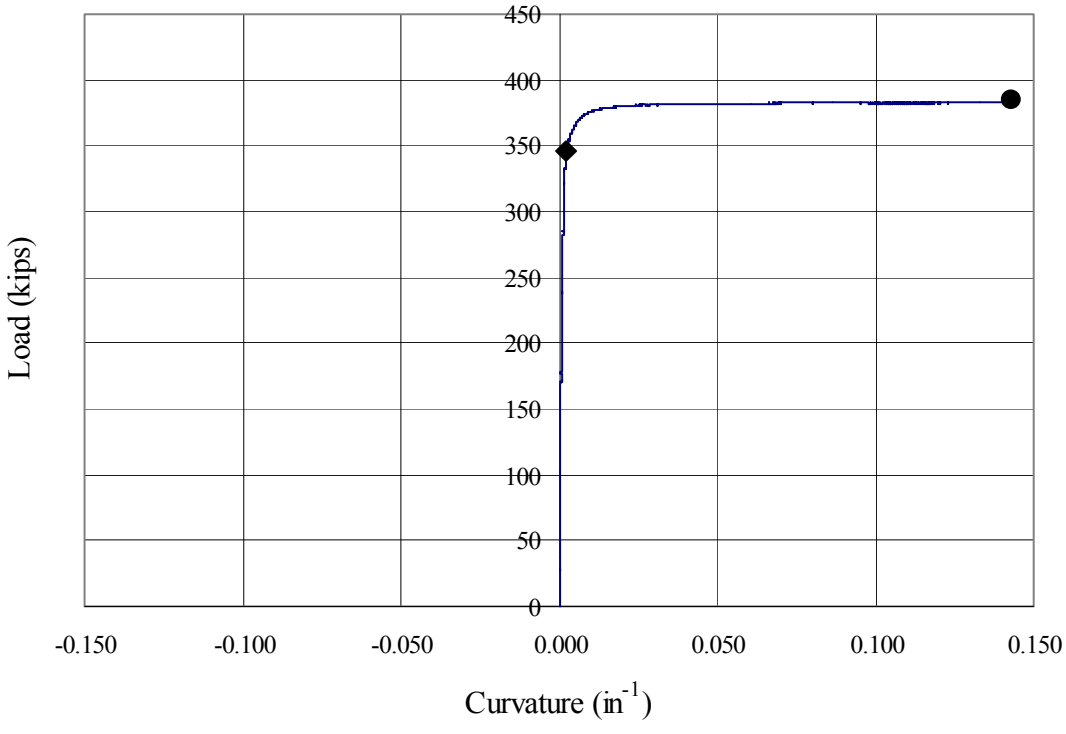

Figure 5.85 Load versus curvature at strain gages SG-138 and SG-155 (Specimen 5)

Figure 5.86 Lateral distortion of compression flange (Specimen 5)

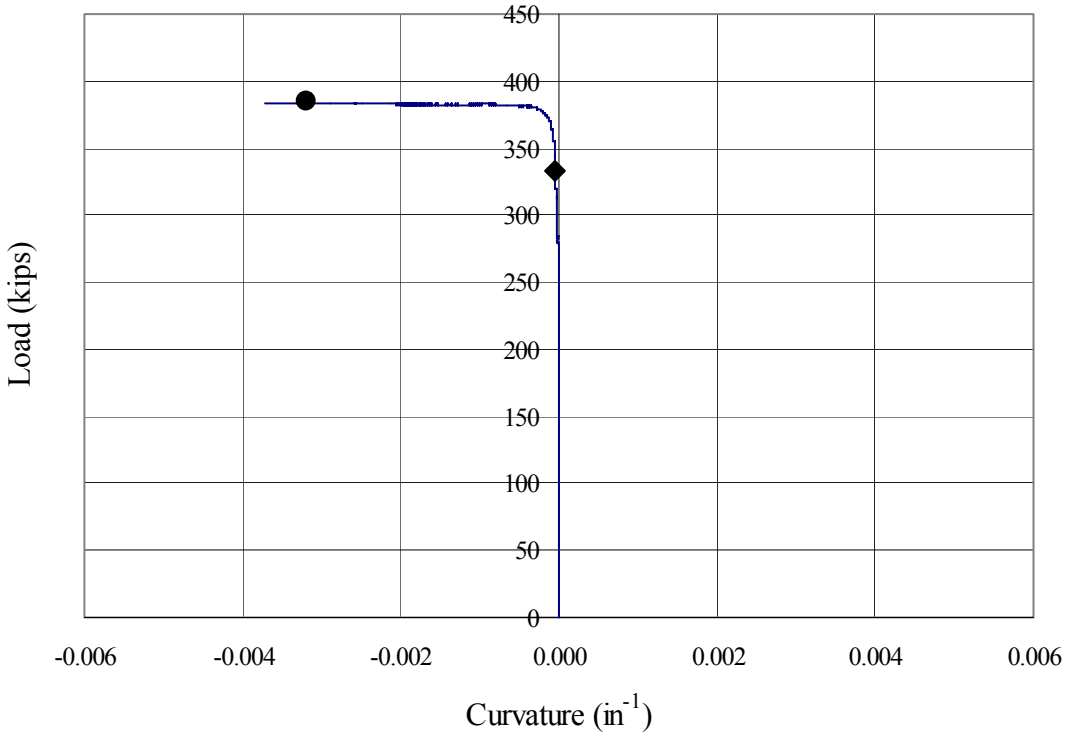

Figure 5.87 Load versus ϕ_l at section 4 (Specimen 5)

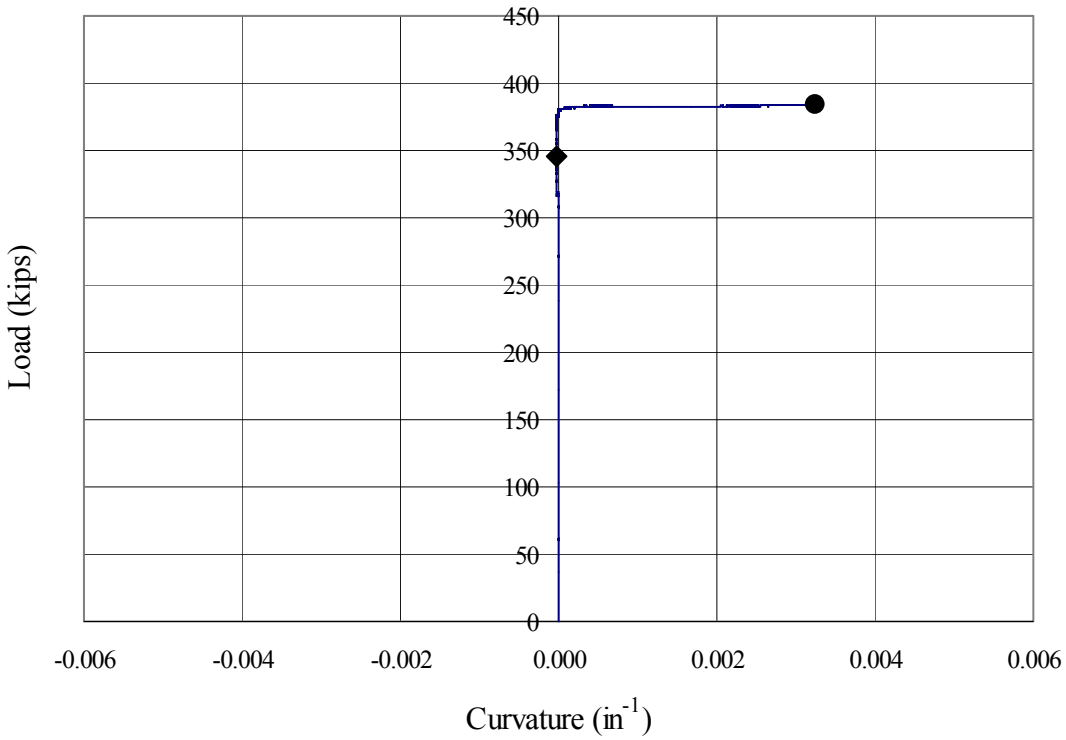

Figure 5.88 Load versus ϕ_l at section 6 (Specimen 5)

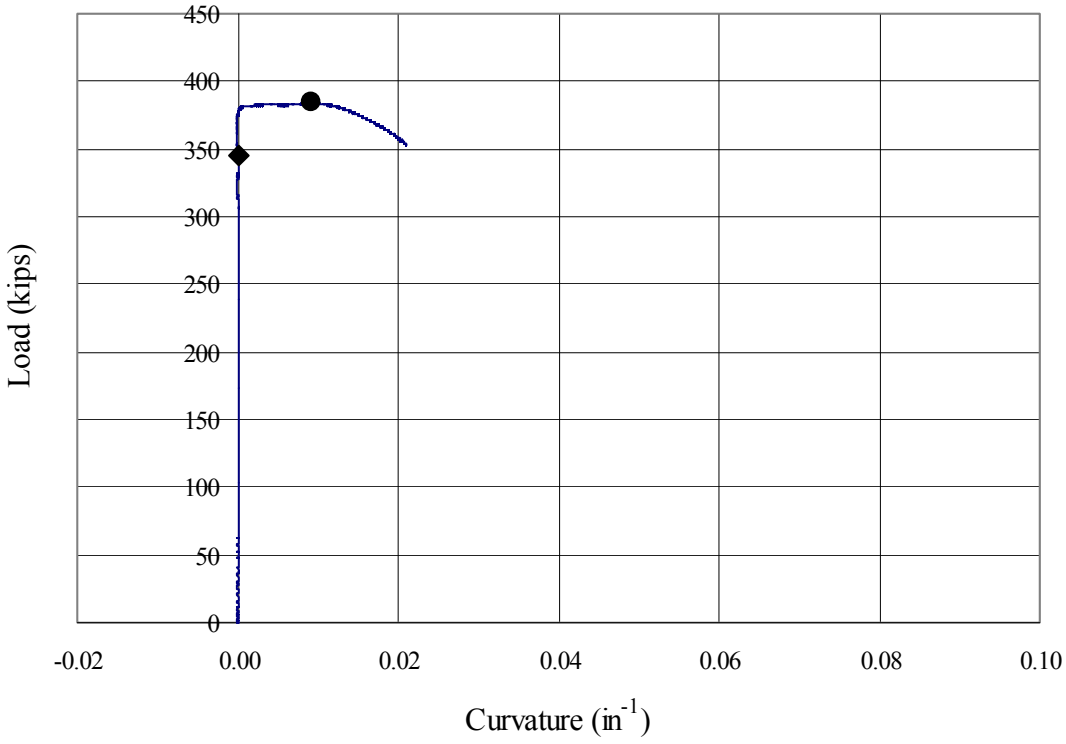

Figure 5.89 Load versus ϕ_{fp} at section 4-East (Specimen 5)

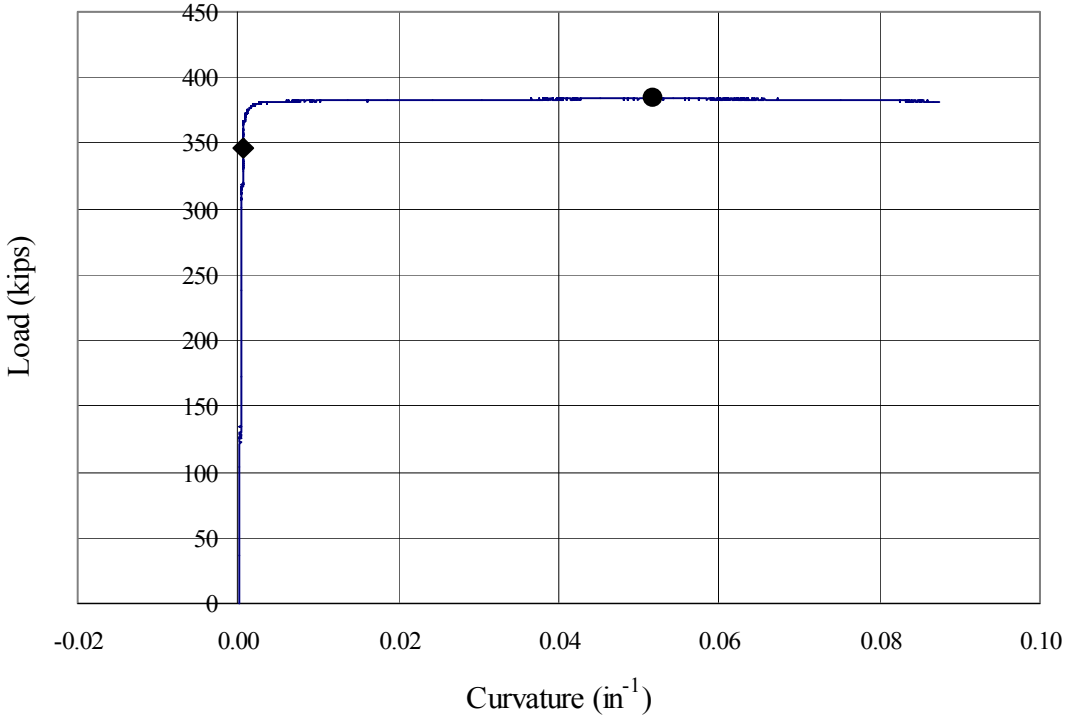

Figure 5.90 Load versus ϕ_{fp} at section 4-West (Specimen 5)

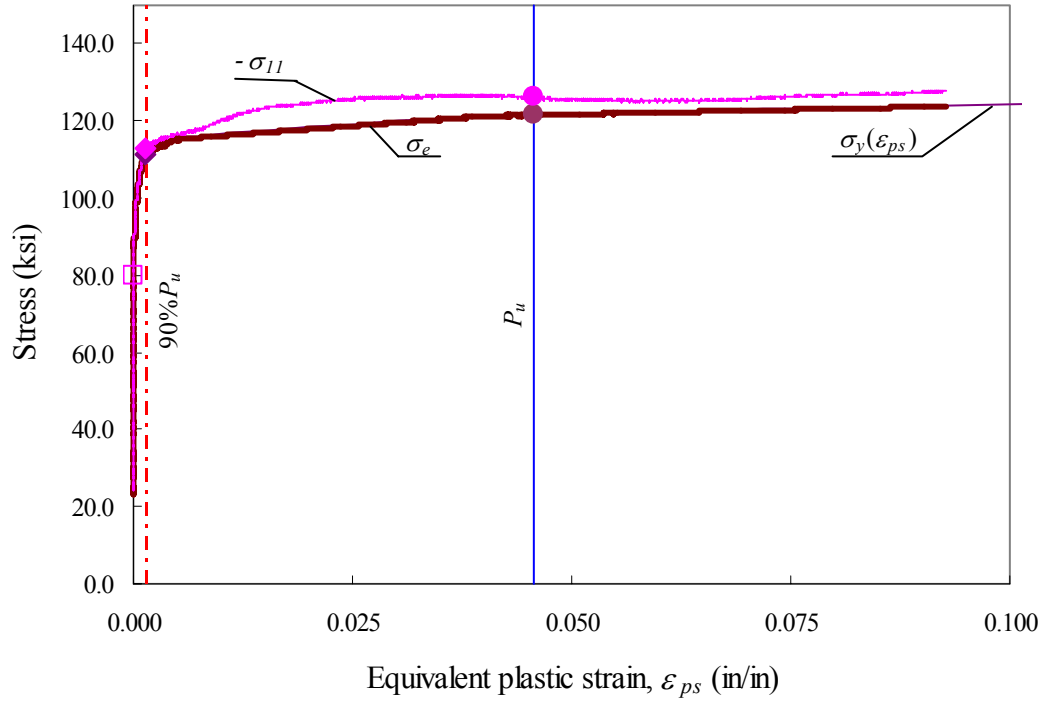

Figure 5.91 Stress versus equivalent plastic strain (section 4-Mid, Specimen 5)

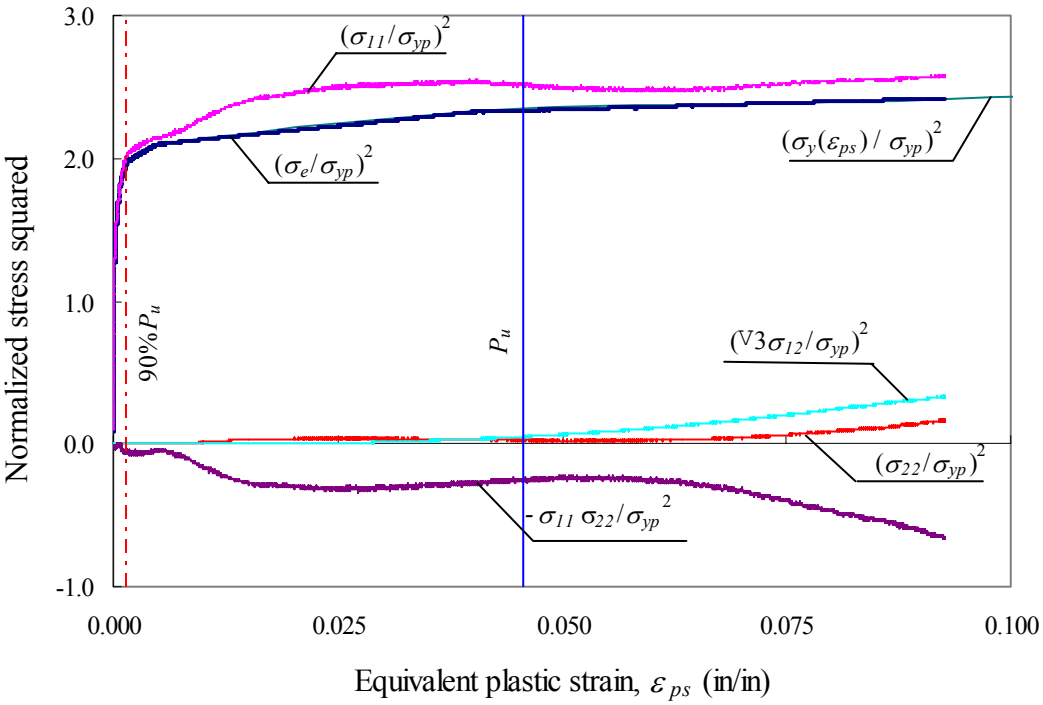

Figure 5.92 Contributions to effective stresses (section 4-Mid, Specimen 5)

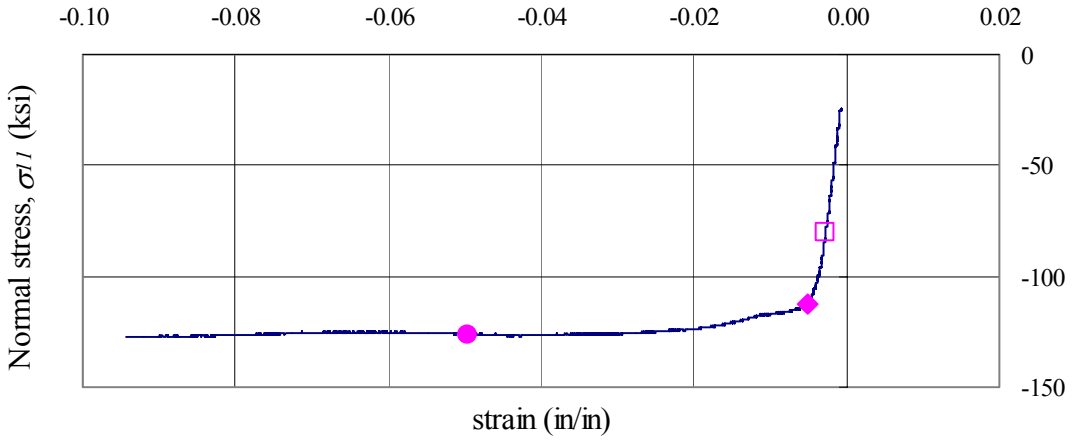

(a) Normal strain, ε_{11}

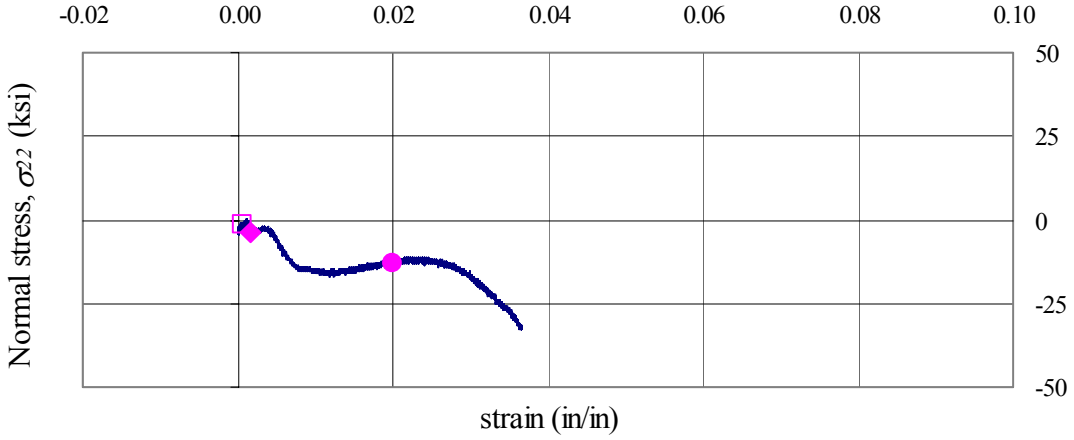

(b) Normal strain, ε_{22}

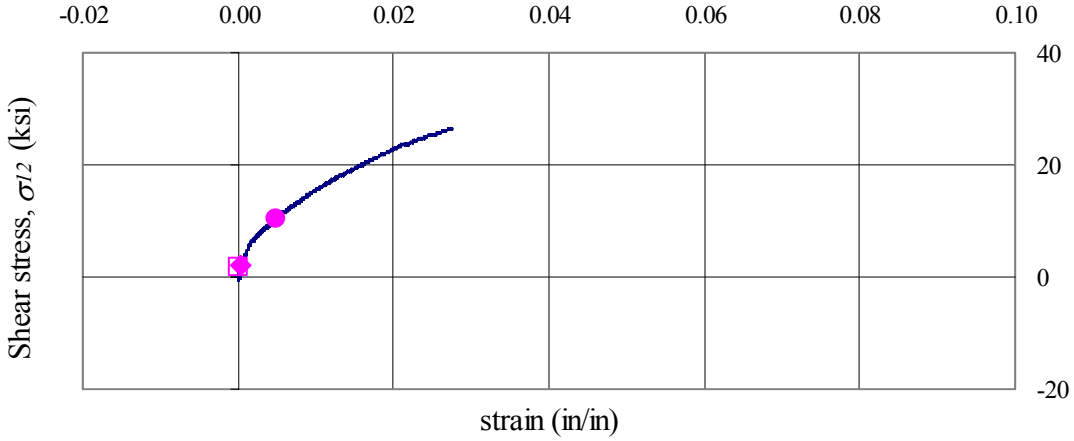

(c) Engineering shear strain, γ_{12}

Figure 5.93 Stress versus strain (section 4-Mid, Specimen 5)

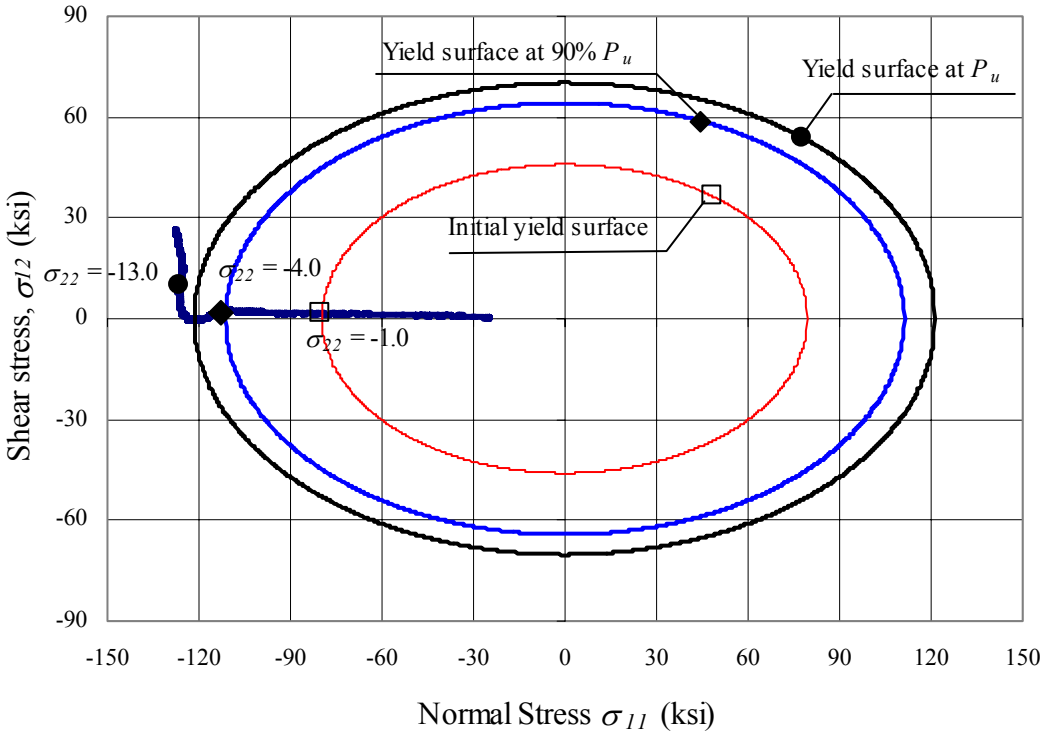

Figure 5.94 Yield surface in σ_{11}- σ_{12} plane at different increments (section 4-Mid, Specimen 5)

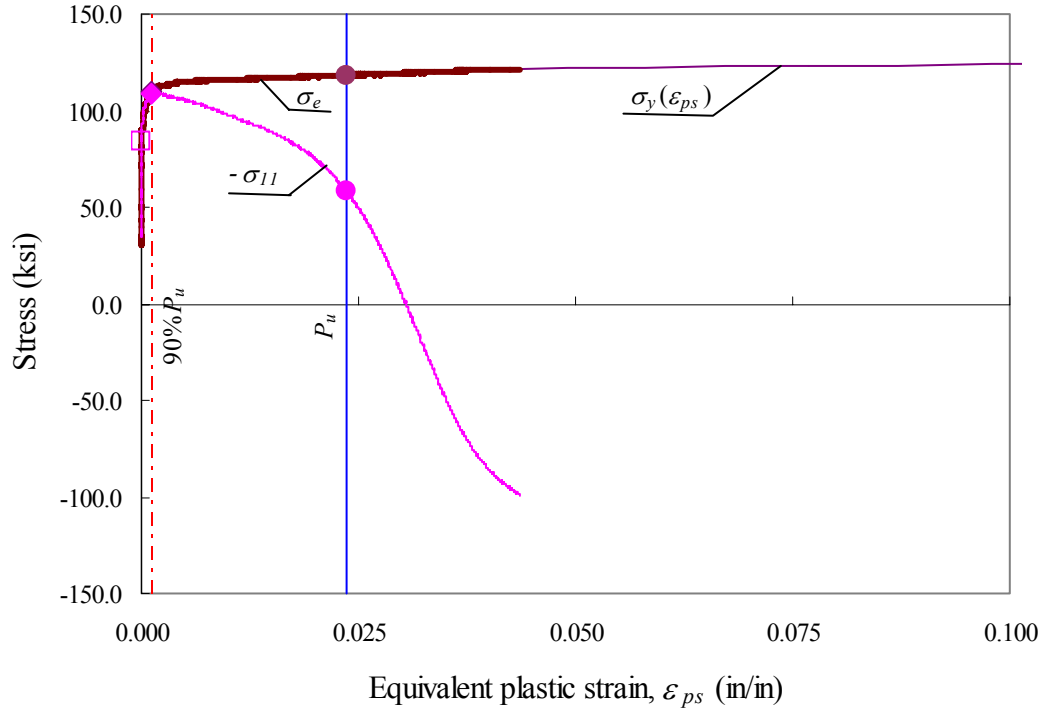

Figure 5.95 Stress versus equivalent plastic strain (section 6-East, Specimen 5)

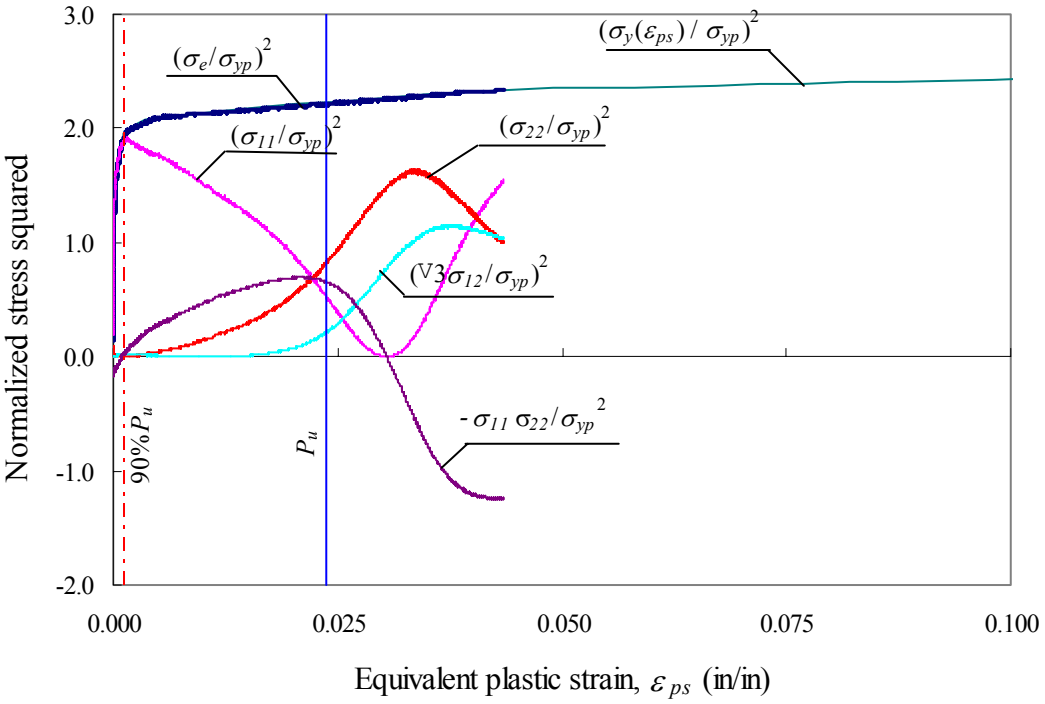

Figure 5.96 Contributions to effective stress (section 6-East, Specimen 5)

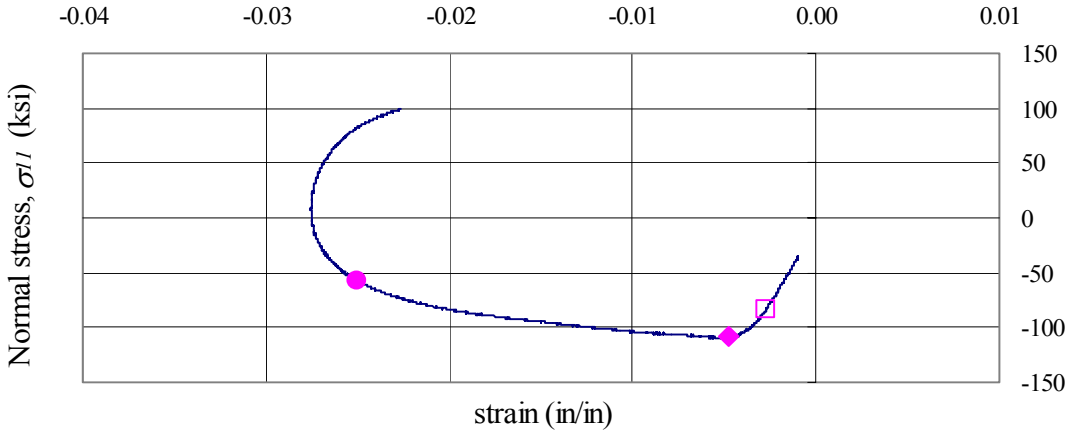

(a) Normal strain, ε_{11}

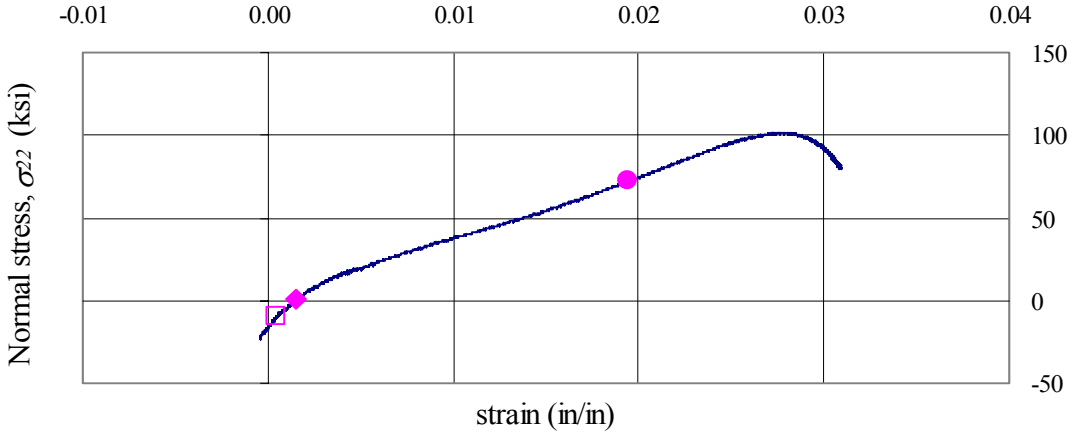

(b) Normal strain, ε_{22}

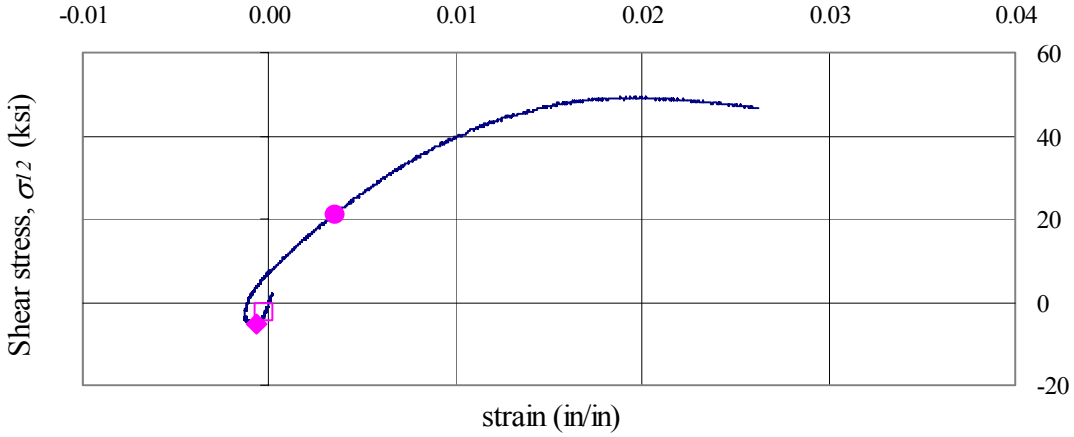

(c) Engineering shear strain, γ_{12}

Figure 5.97 Stress versus strain (section 6-East, Specimen 5)

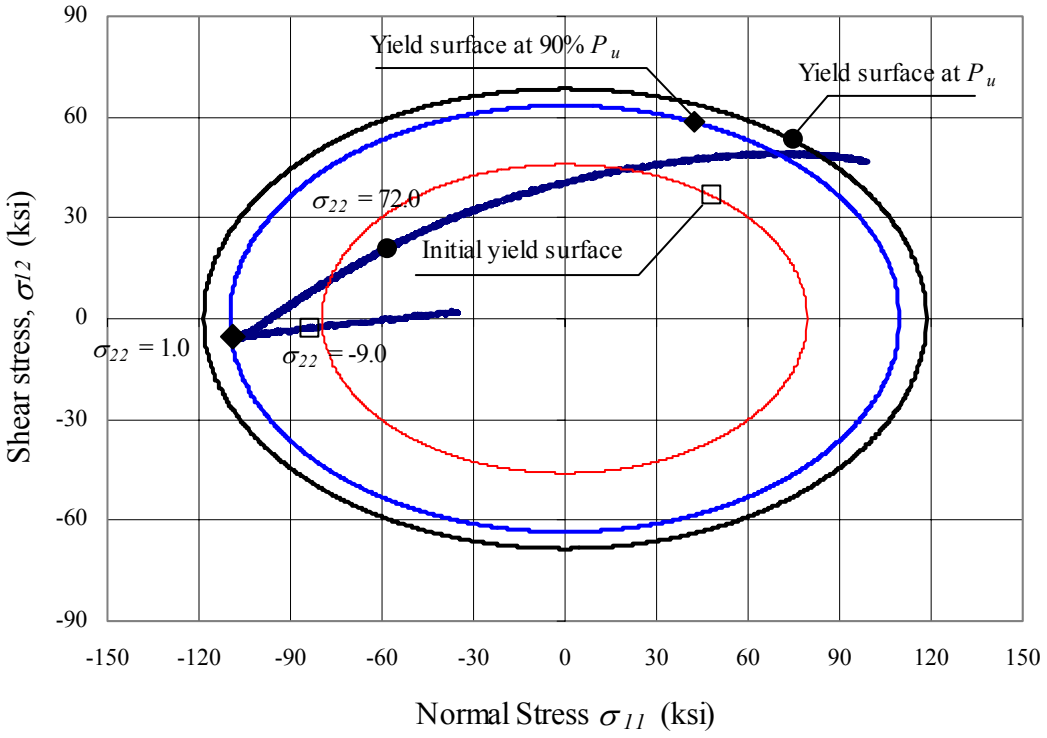

Figure 5.98 Yield surface in σ_{11}- σ_{12} plane at different increments (section 6-East, Specimen 5)

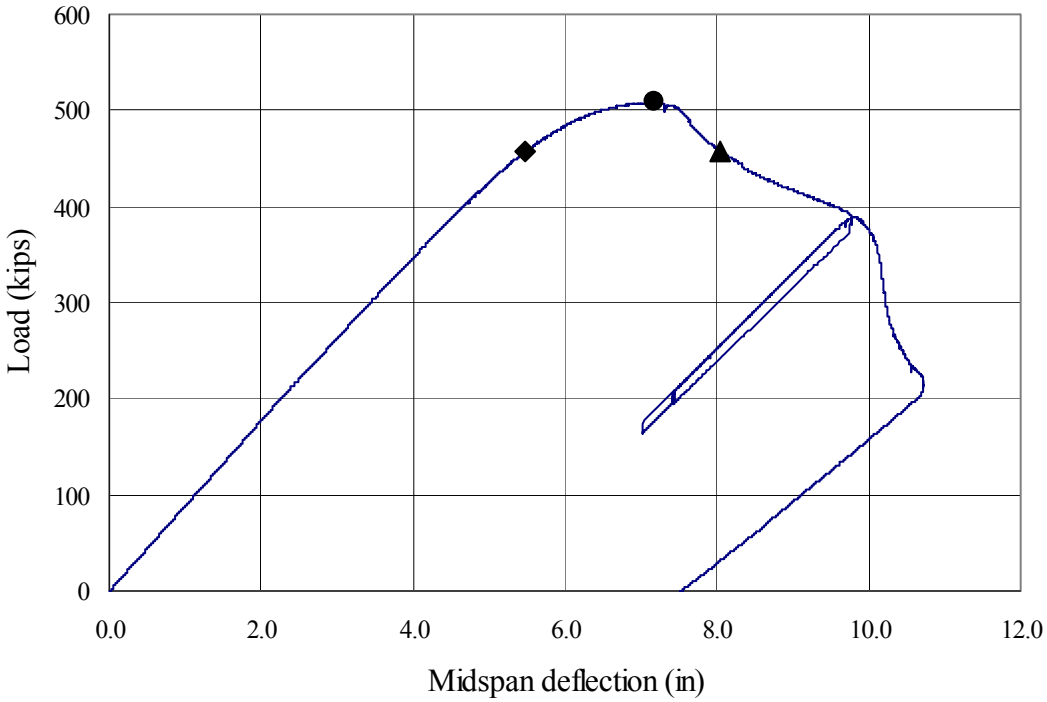

Figure 5.99 Load versus midspan vertical deflection (Specimen 6)

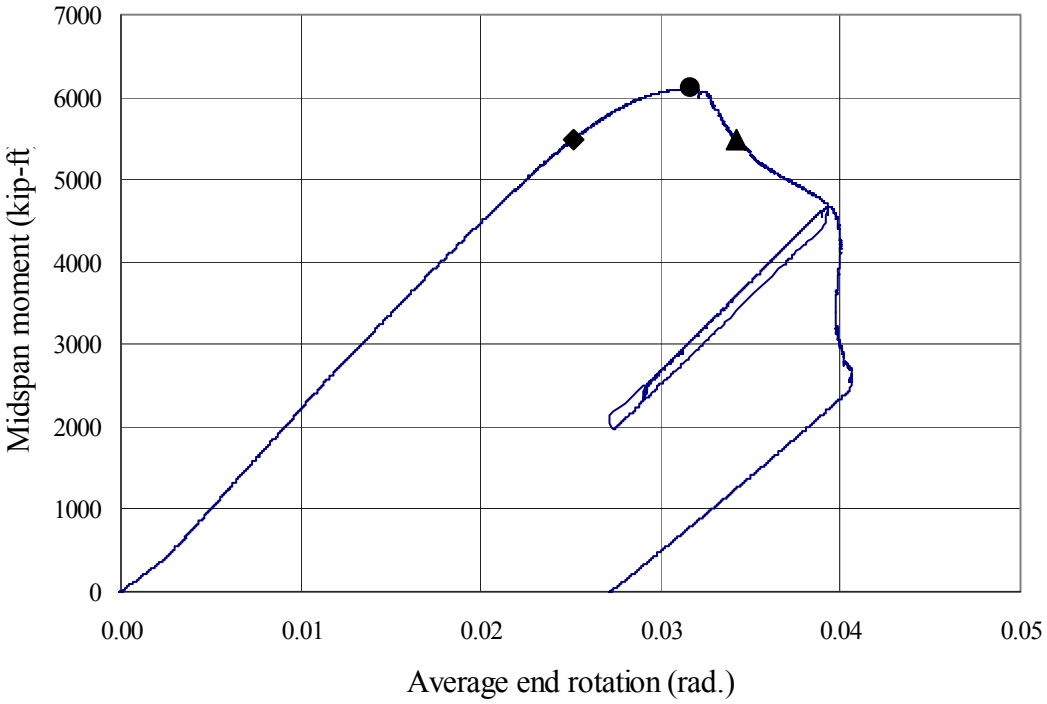

Figure 5.100 Midspan moment versus average end rotation (Specimen 6)

Figure 5.101 Specimen 6 during testing

Figure 5.102 Specimen 6 after testing

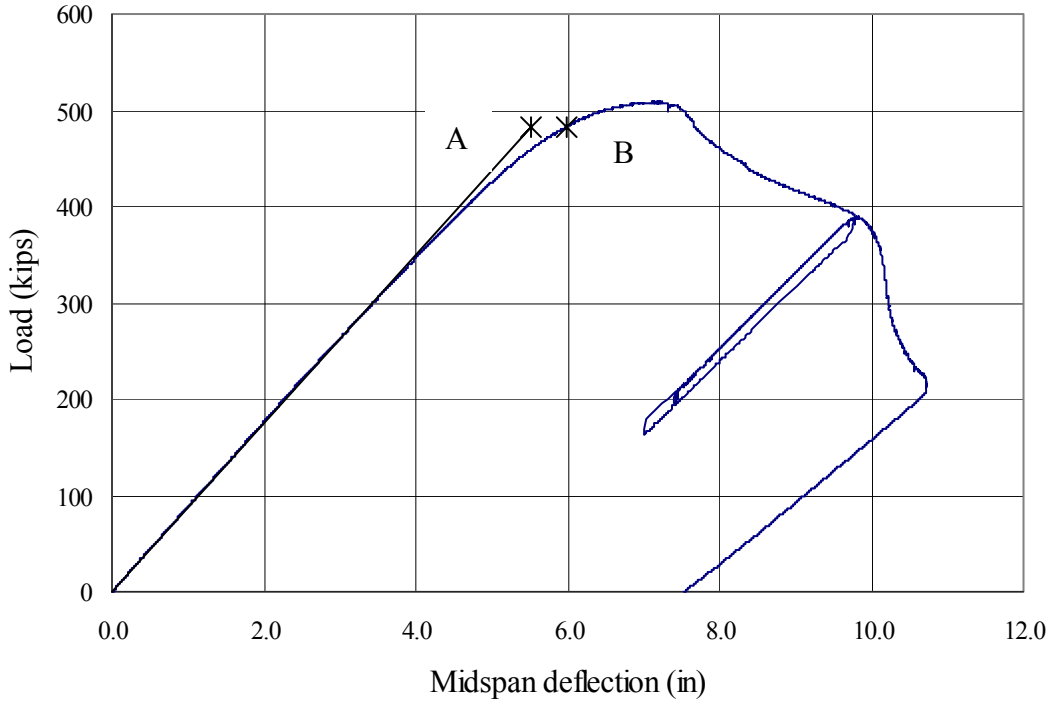

Figure 5.103 Load versus midspan vertical deflection (Specimen 6)

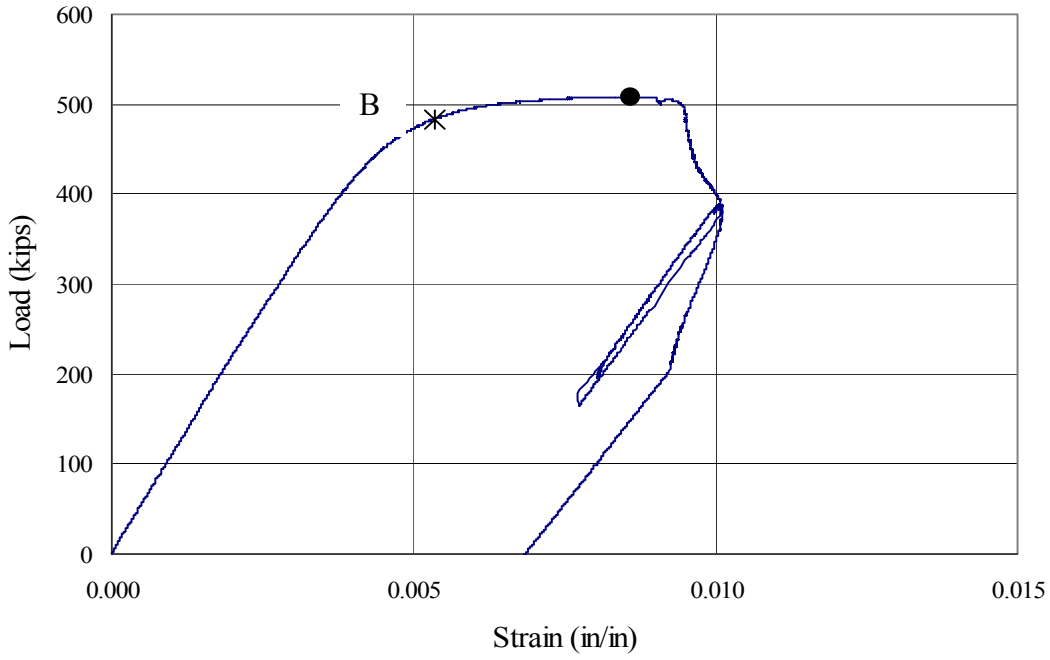

Figure 5.104 Load versus strain recorded by strain gage 161 (Specimen 6)

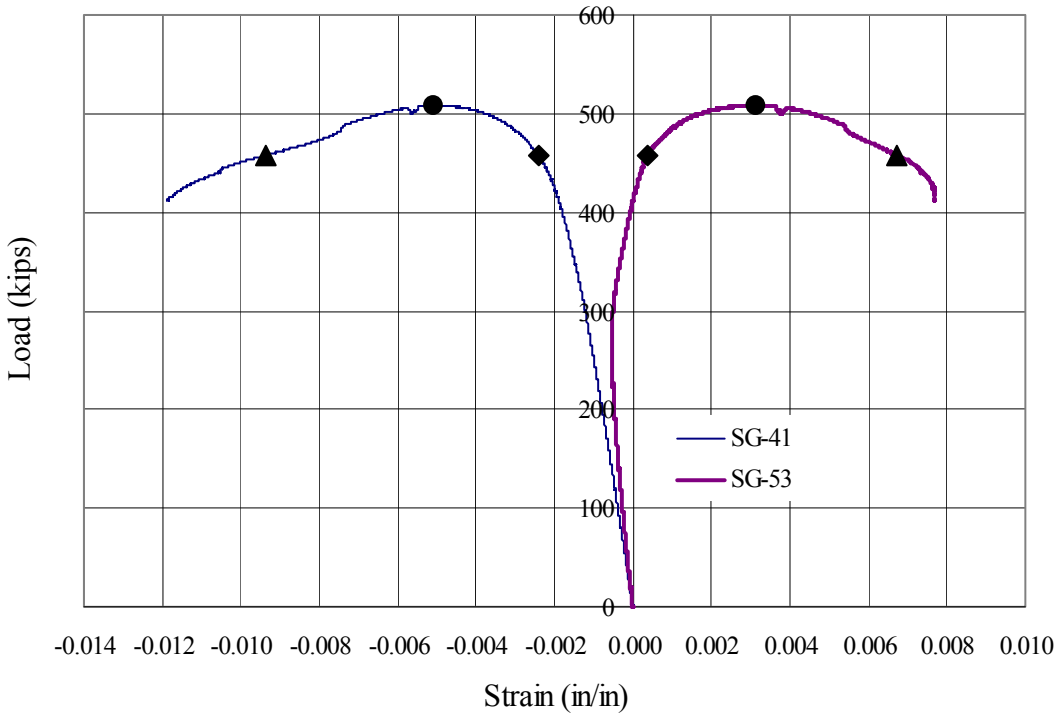

Figure 5.105 Effect of initial imperfection on web distortion (Specimen 6)

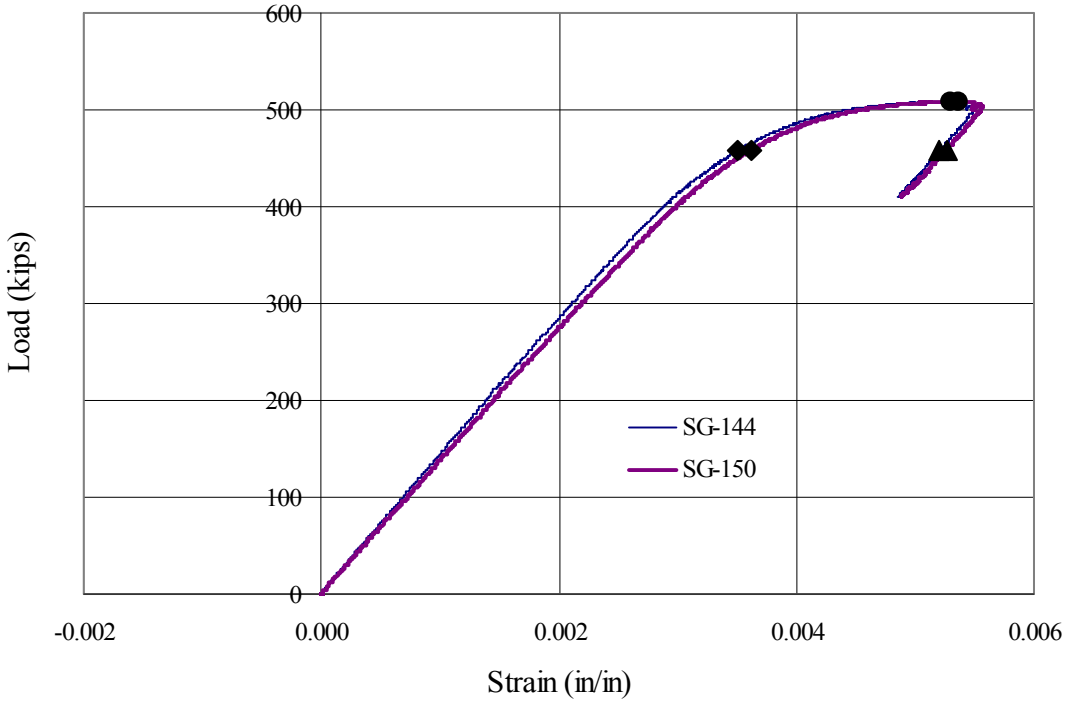

Figure 5.106 Load versus strain for strain gages SG-144 and SG-150 (Specimen 6)

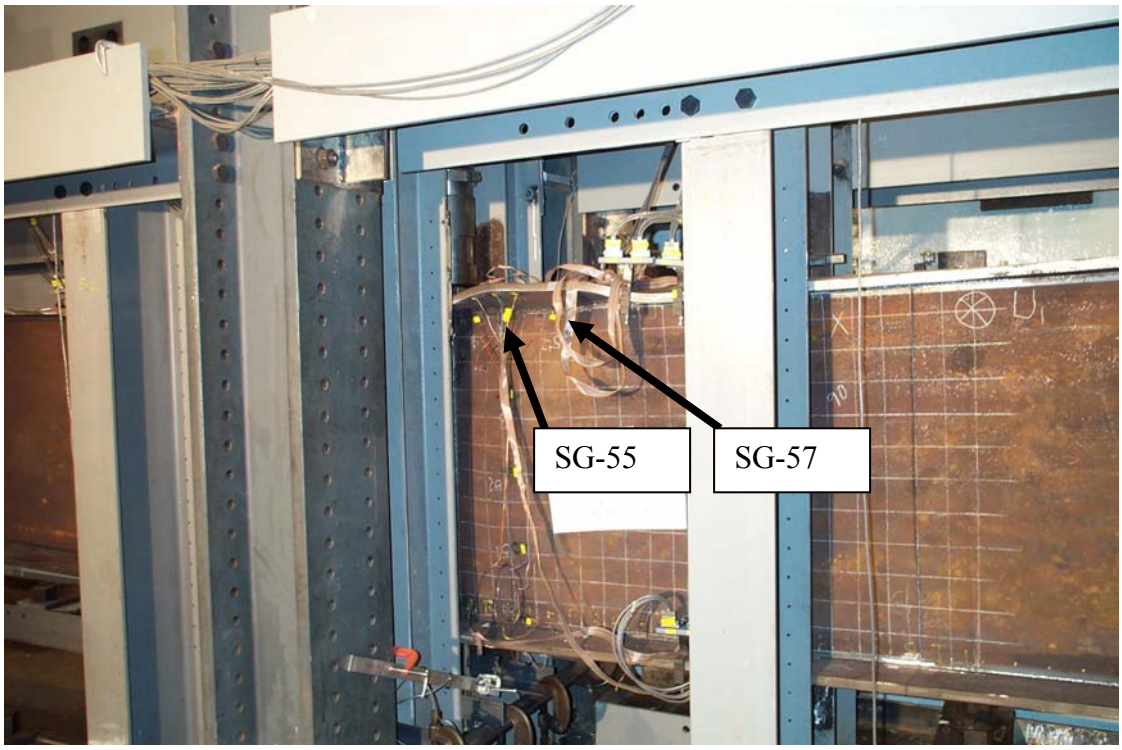

Figure 5.107 Interaction between web and compression flange at the distorted region

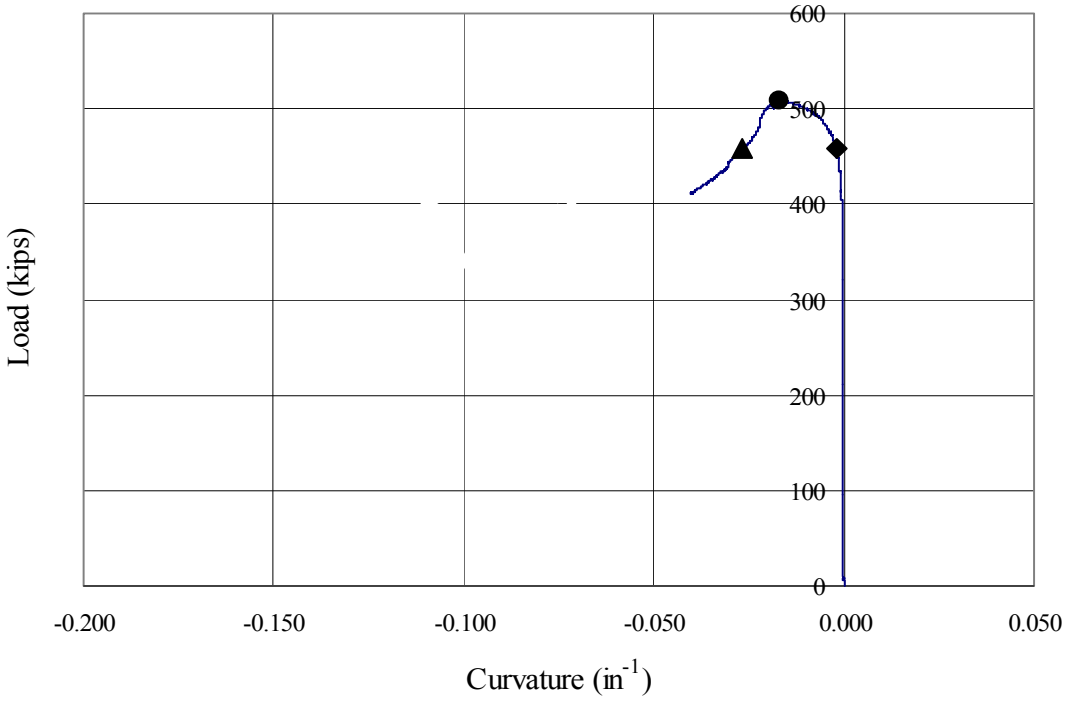

Figure 5.108 Load versus curvature at strain gages SG-37 and SG-54 (Specimen 6)

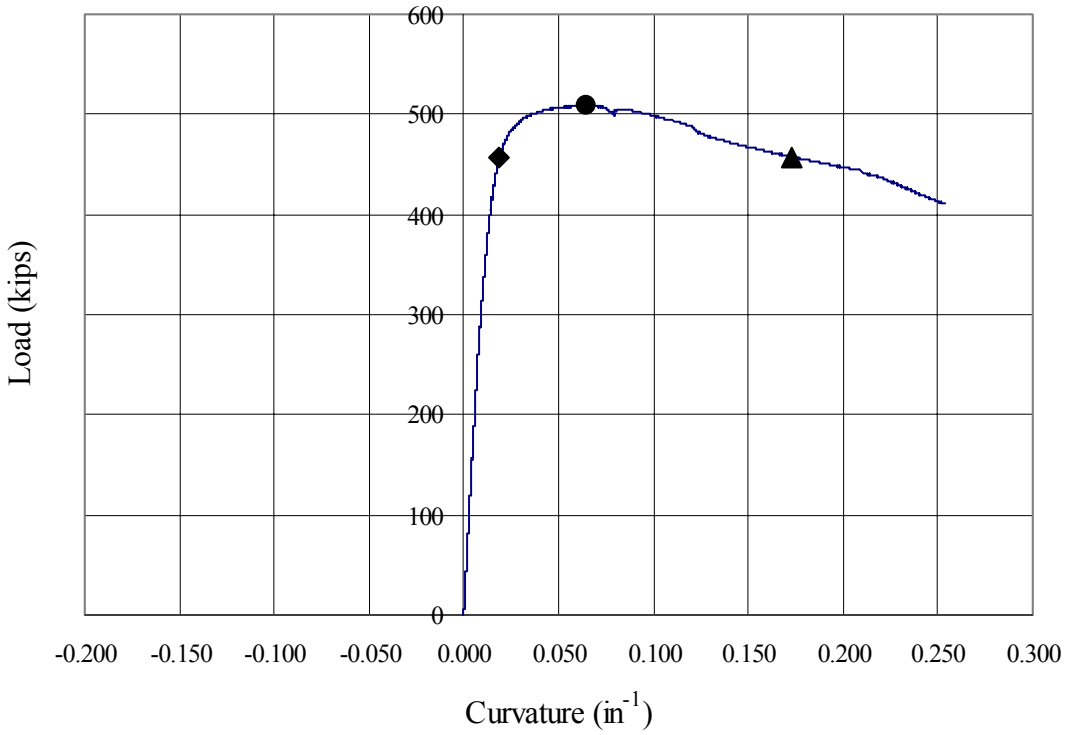

Figure 5.109 Load versus curvature at strain gages SG-38 and SG-55 (Specimen 6)

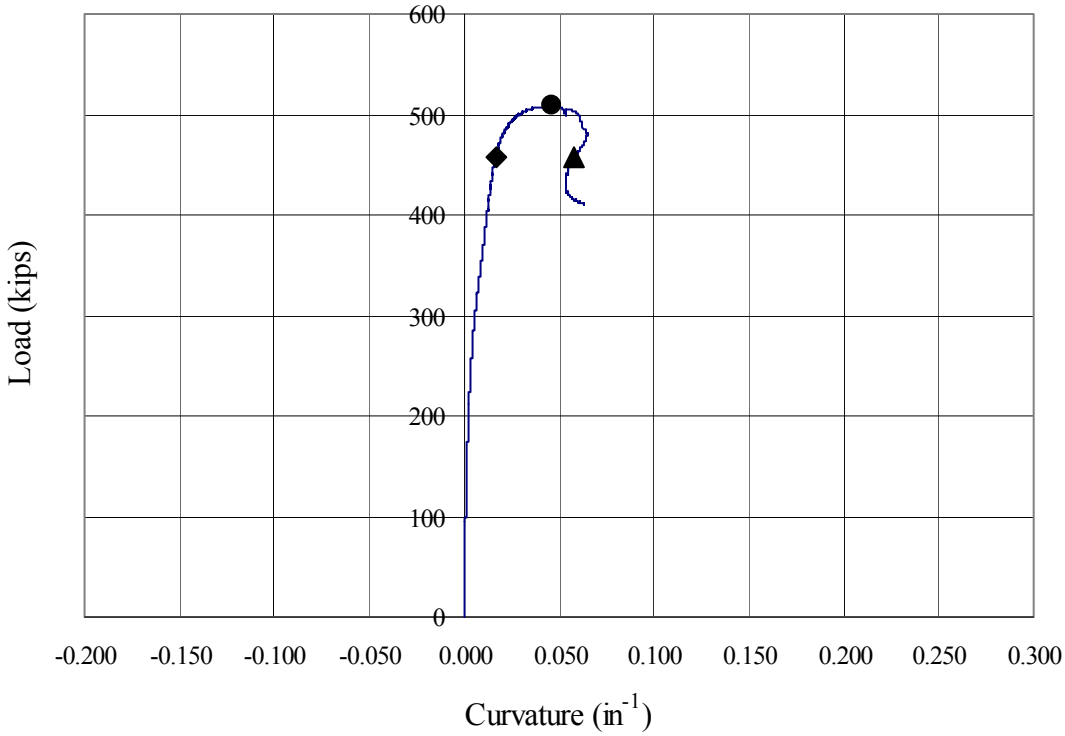

Figure 5.110 Load versus curvature at strain gages SG-40 and SG-57 (Specimen 6)

Figure 5.111 Lateral distortion of compression flange (Specimen 6)

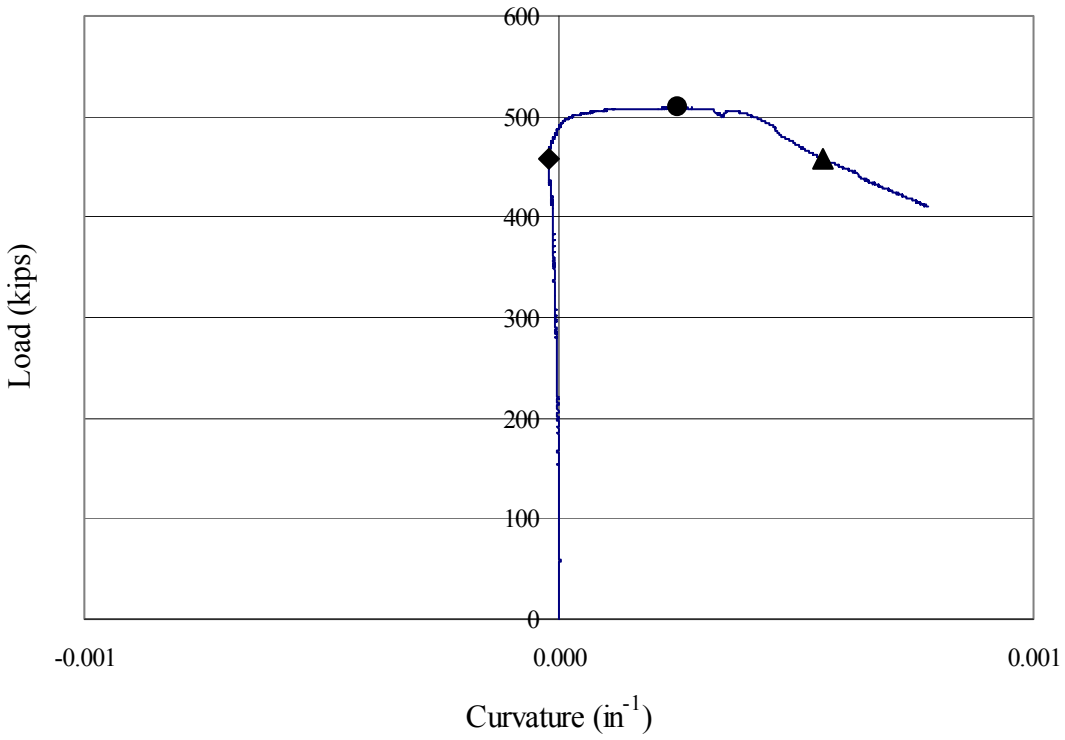

Figure 5.112 Load versus ϕ_l at section 4 (Specimen 6)

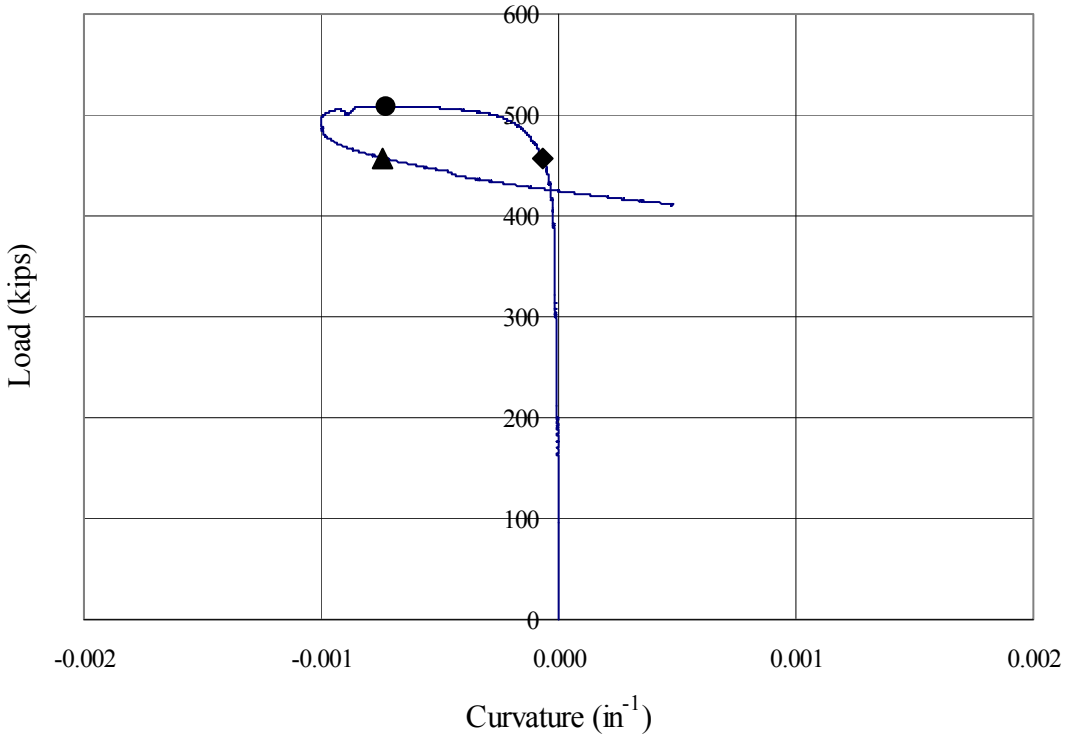

Figure 5.113 Load versus ϕ_l at section 6 (Specimen 6)

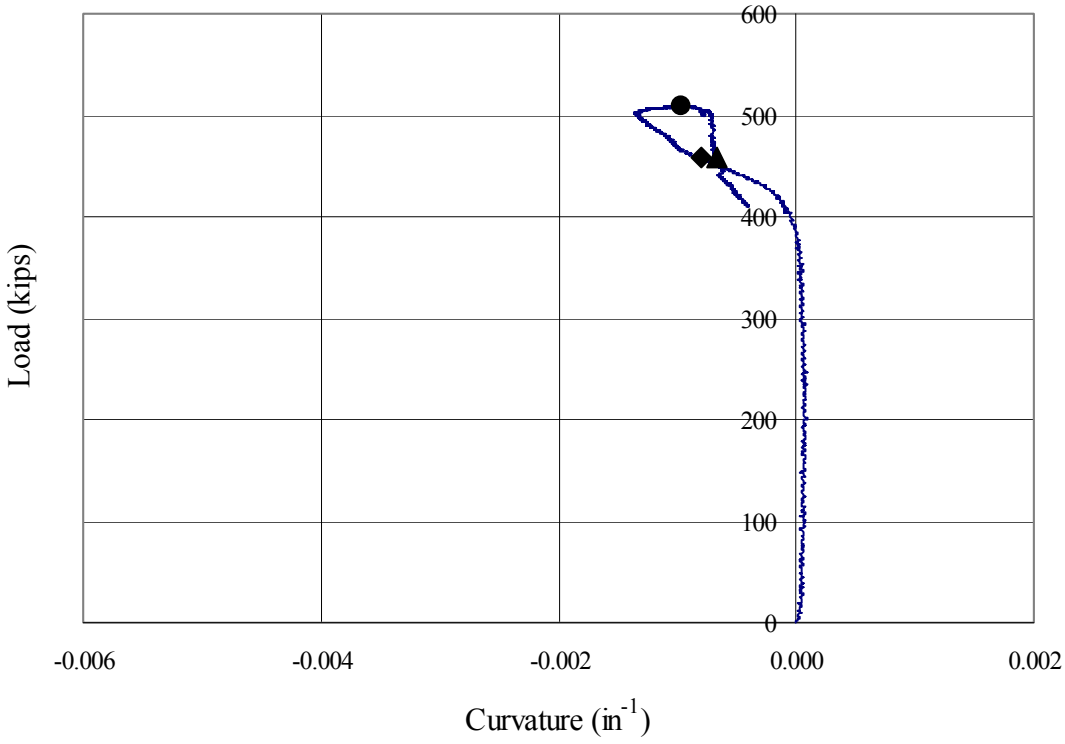

Figure 5.114 Load versus ϕ_{fp} at section 4-East (Specimen 6)

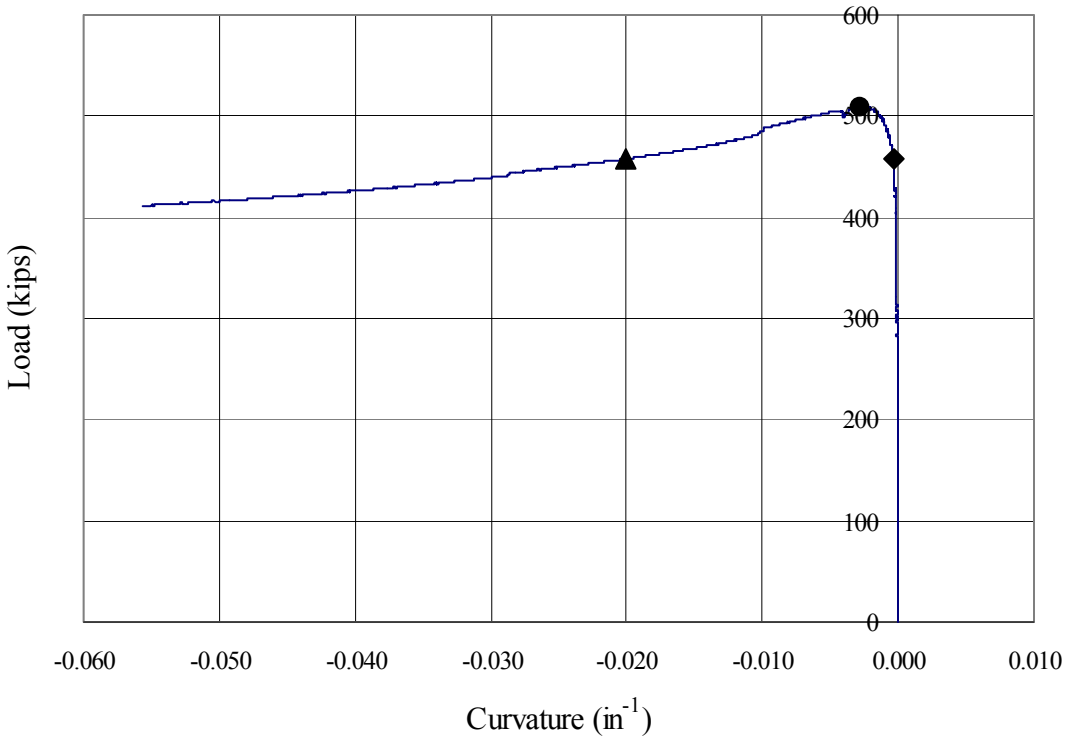

Figure 5.115 Load versus ϕ_{fp} at section 6-East (Specimen 6)

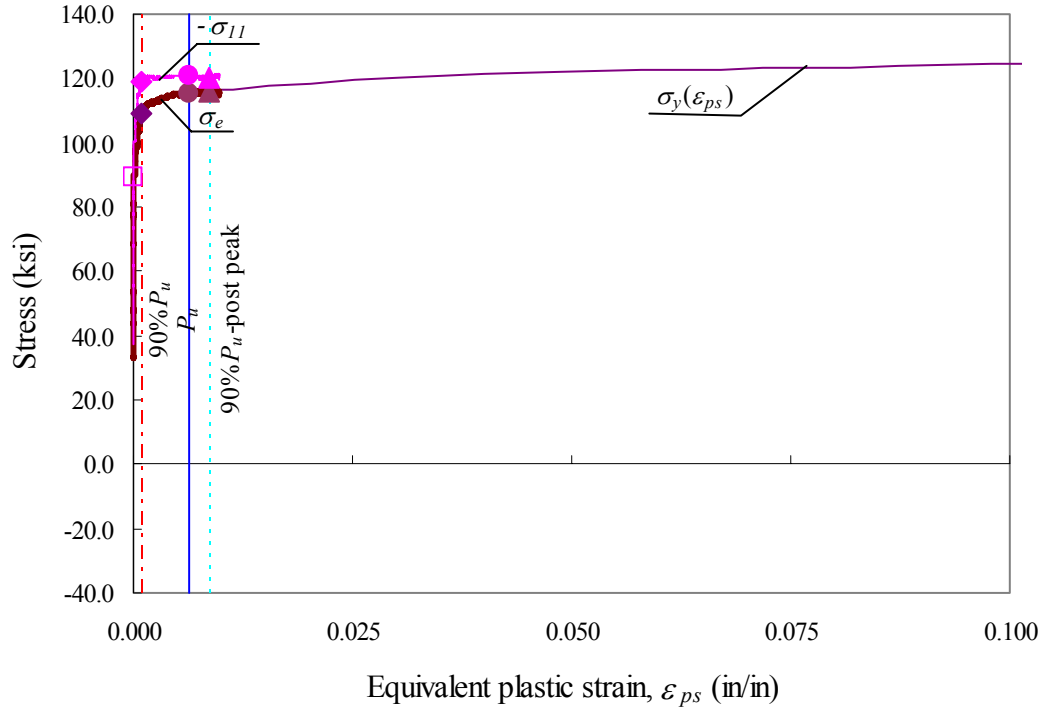

Figure 5.116 Stress versus equivalent plastic strain (section 4-East, Specimen 6)

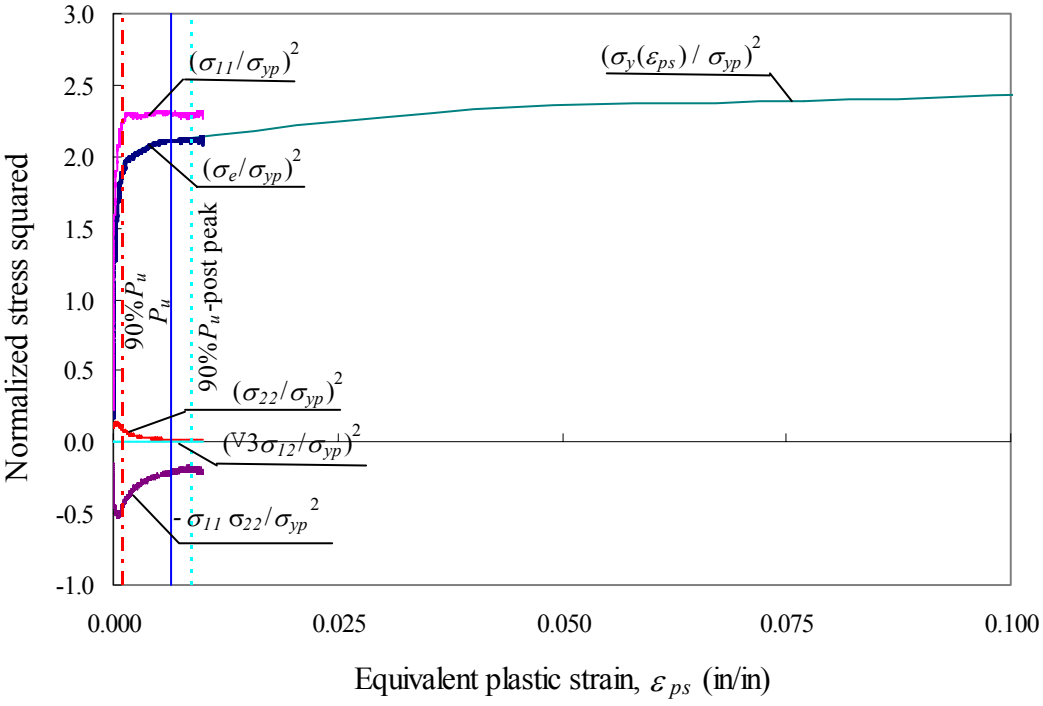

Figure 5.117 Contributions to effective stresses (section 4-East, Specimen 6)

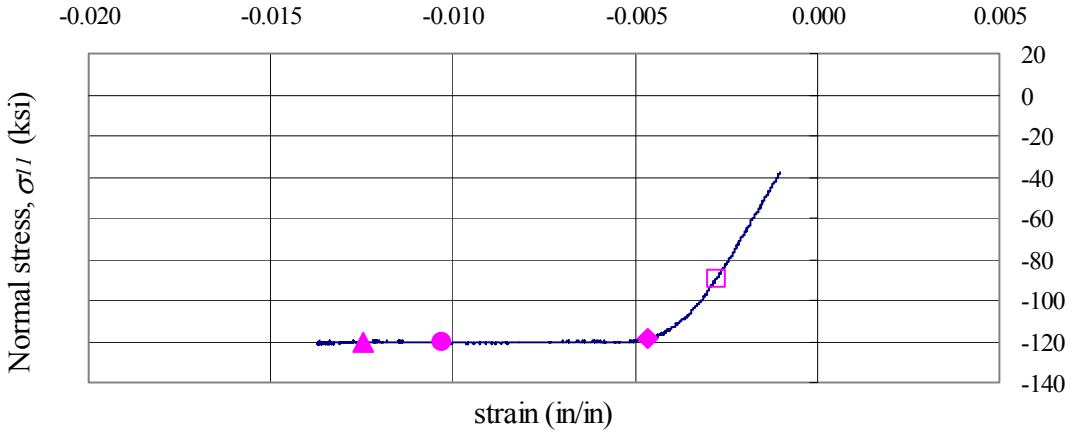

(a) Normal strain, ε_{11}

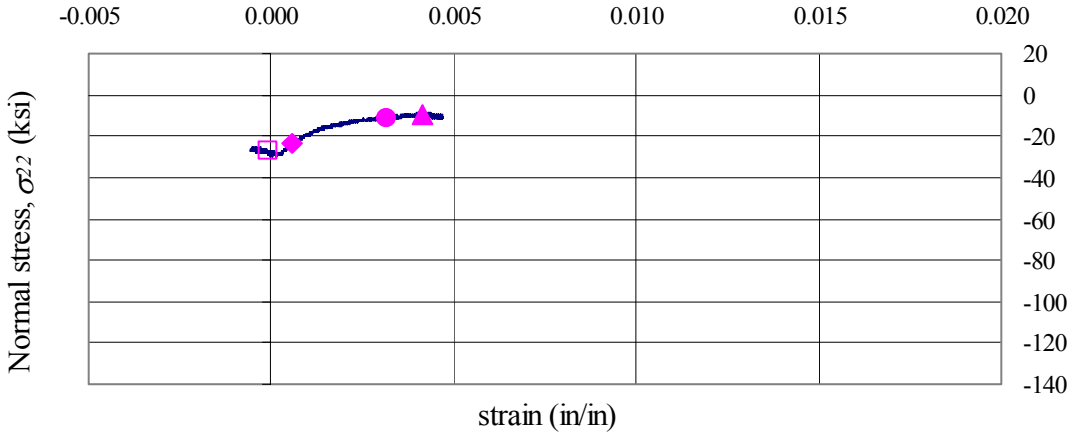

(b) Normal strain, ε_{22}

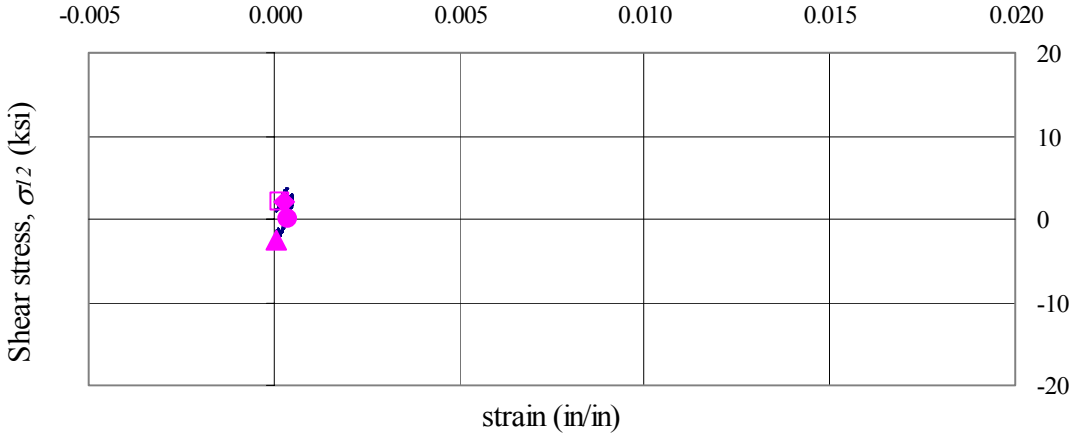

(c) Engineering shear strain, γ_{12}

Figure 5.118 Stress versus strain (section 4-East, Specimen 6)

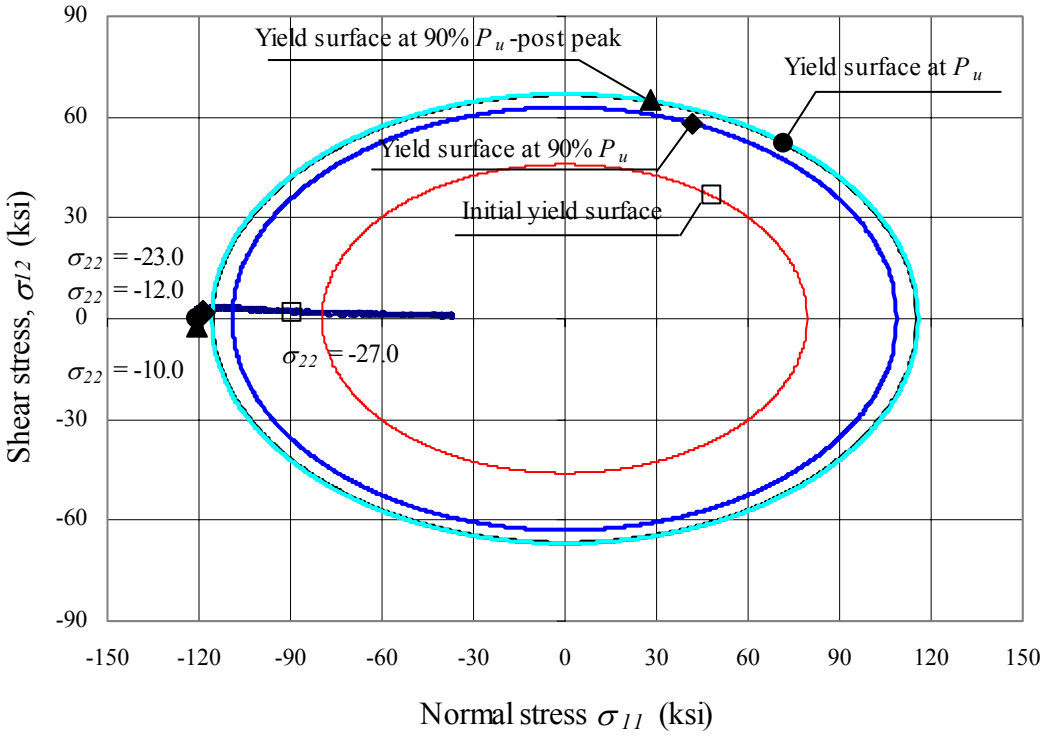

Figure 5.119 Yield surface in σ_{11}- σ_{12} plane at different increments (section 4-East, Specimen 6)

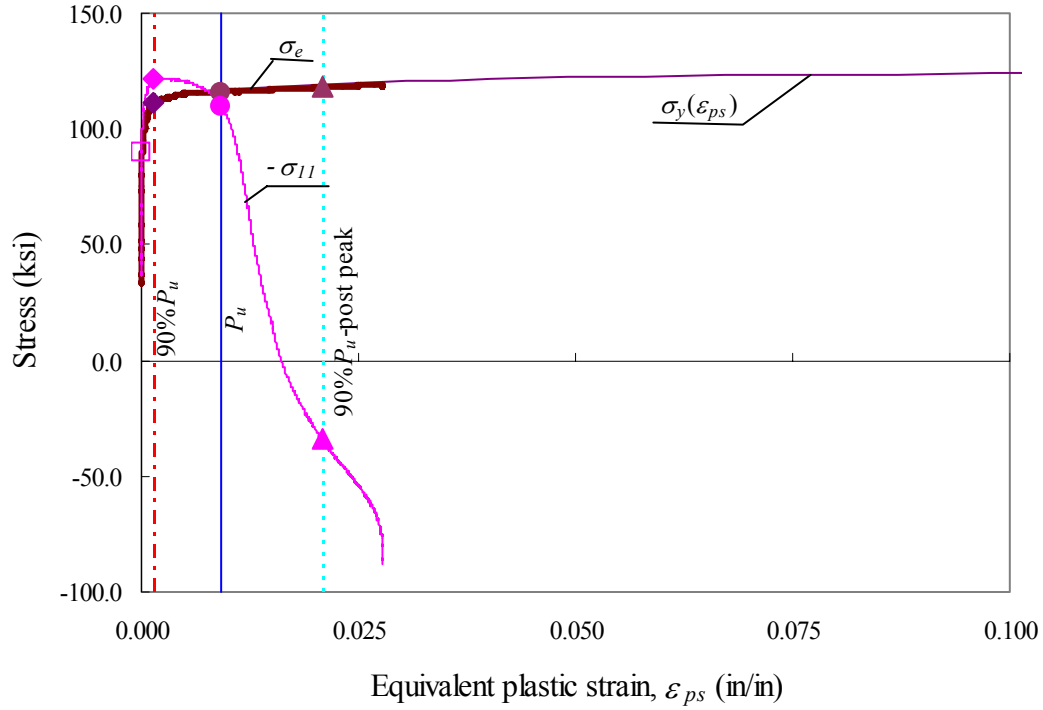

Figure 5.120 Stress versus equivalent plastic strain (section 6-West, Specimen 6)

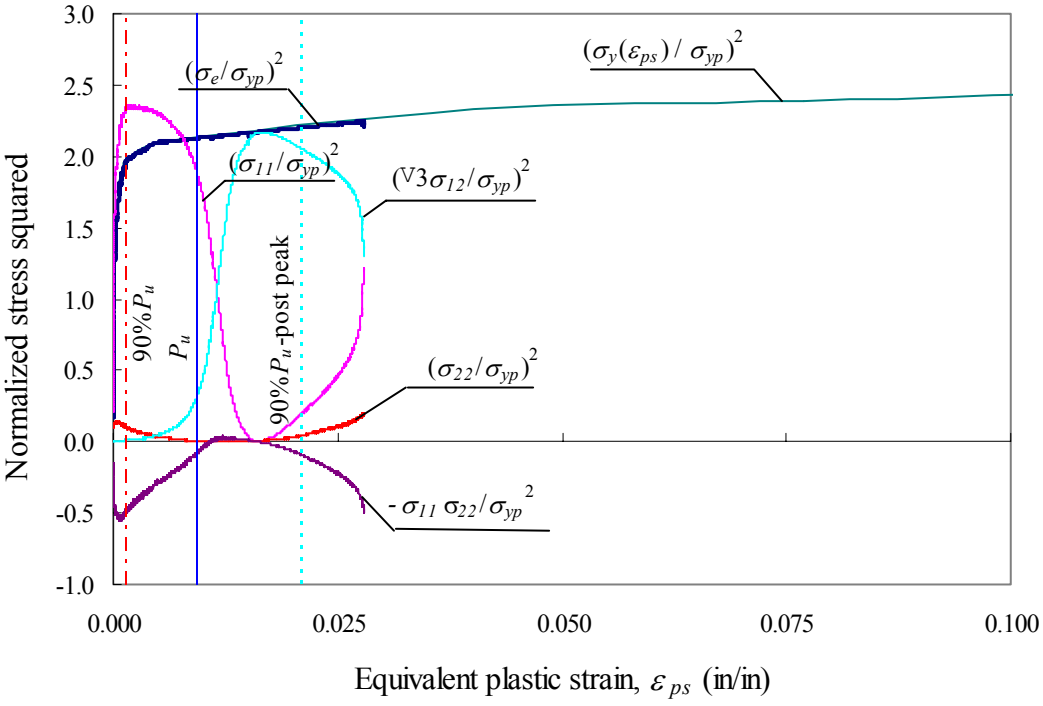

Figure 5.121 Contributions to effective stresses (section 6-West, Specimen 6)

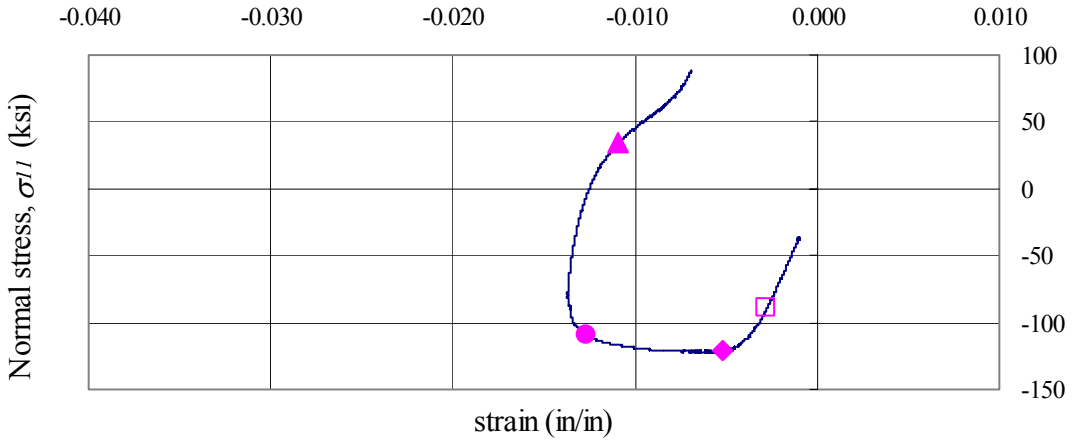

(a) Normal strain, ε_{11}

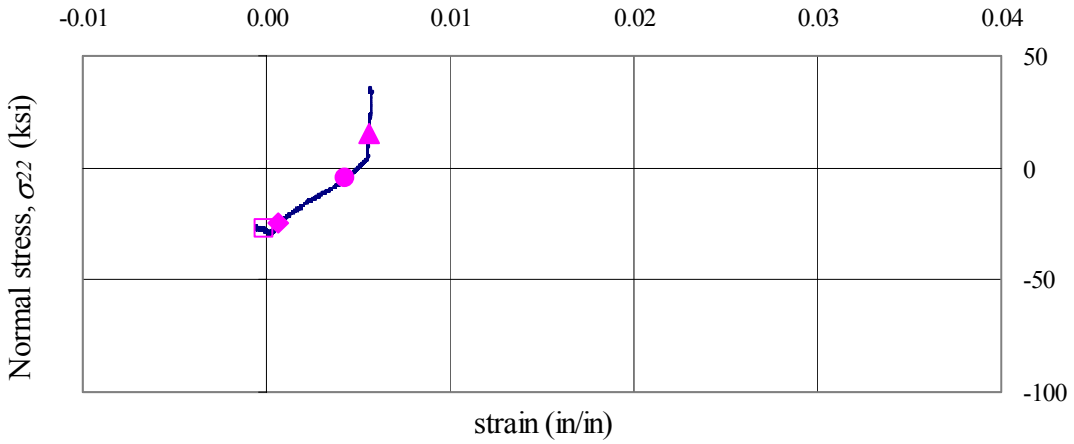

(b) Normal strain, ε_{22}

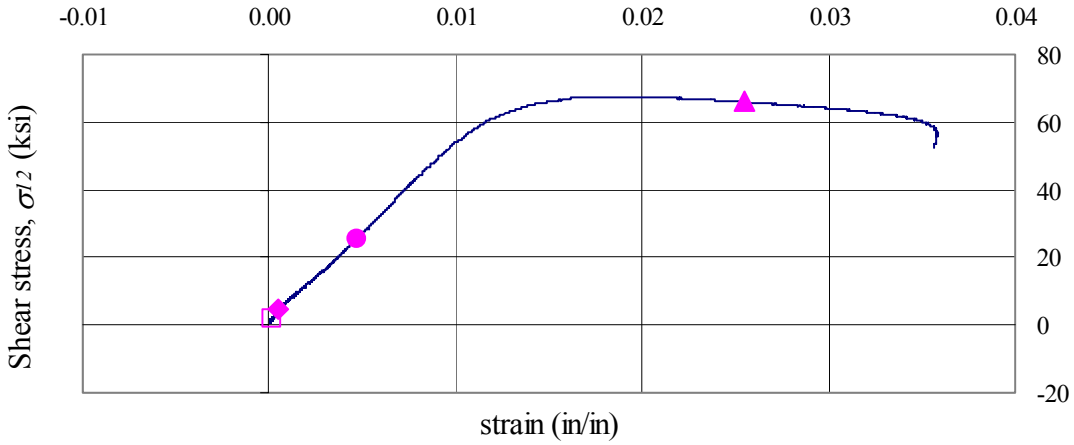

(c) Engineering shear strain, γ_{12}

Figure 5.122 Stress versus strain (section 6-West, Specimen 6)

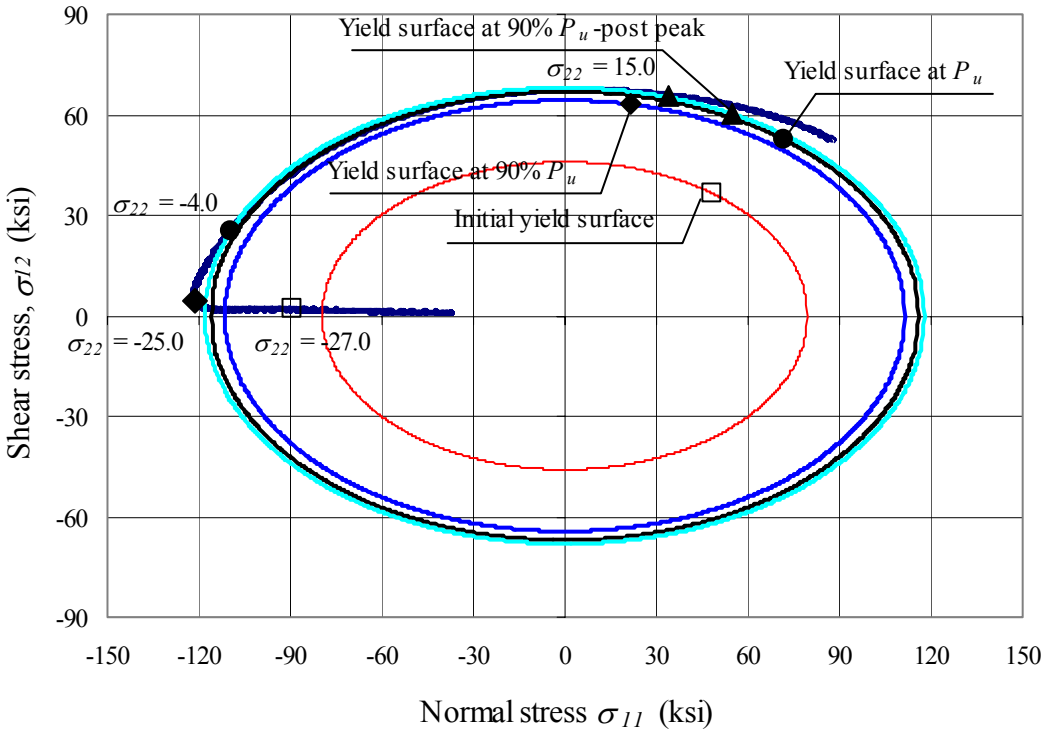

Figure 5.123 Yield surface in σ_{11}- σ_{12} plane at different increments (section 6-West, Specimen 6)

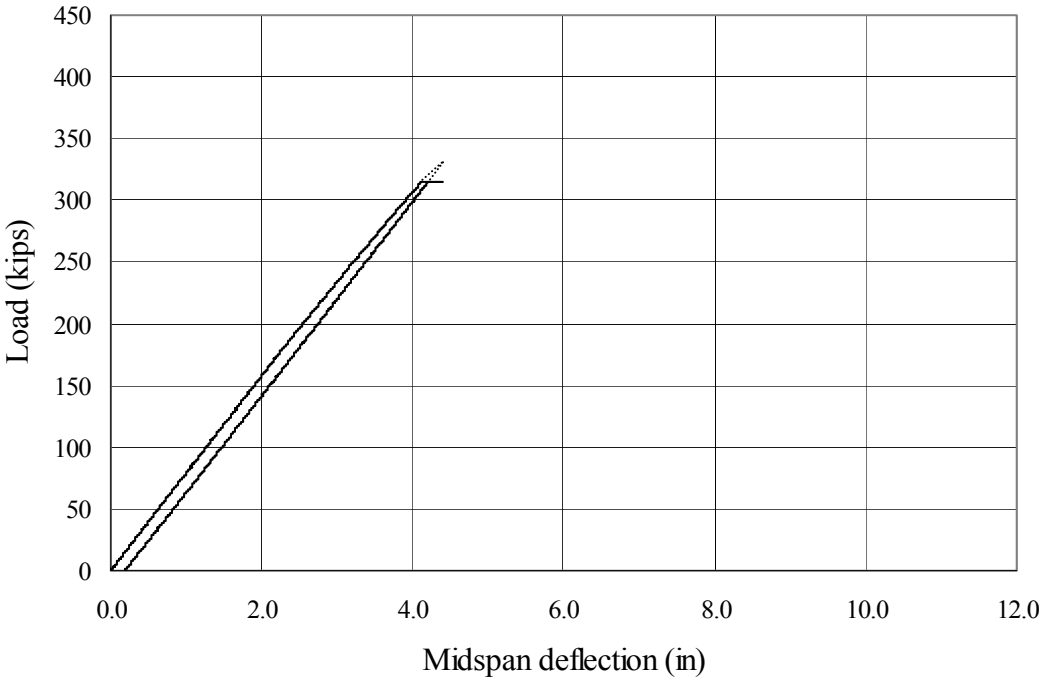

Figure 5.124 Load versus midspan vertical deflection showing the result from the test halted due to an error in the pretest setup (Specimen 7)

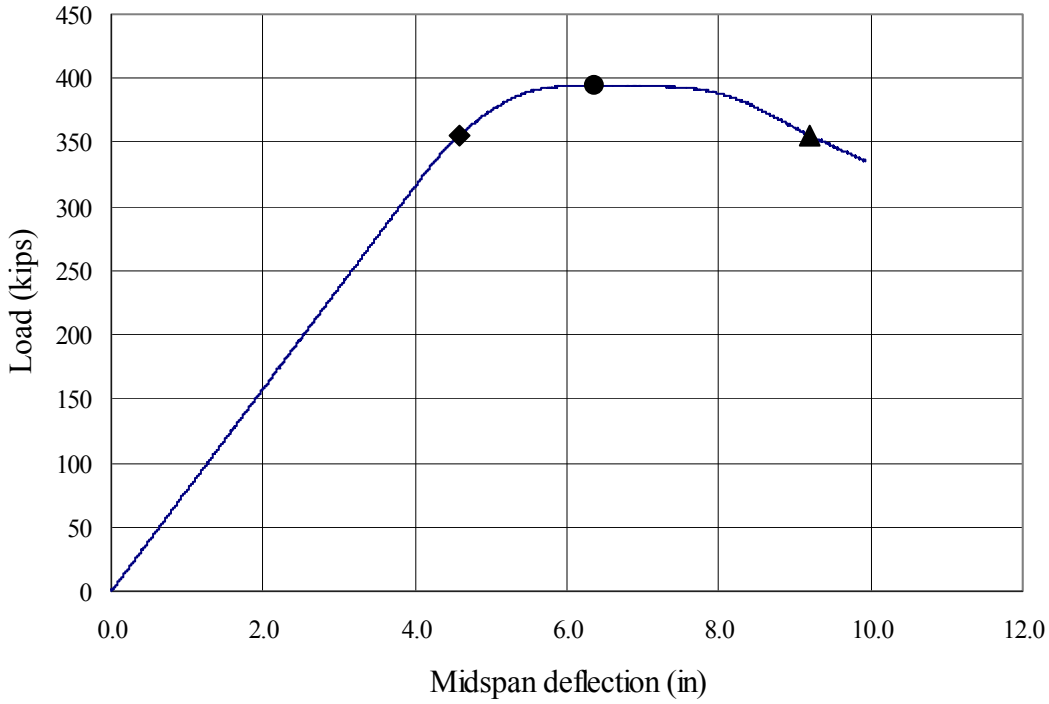

Figure 5.125 Load versus midspan vertical deflection (Specimen 7)

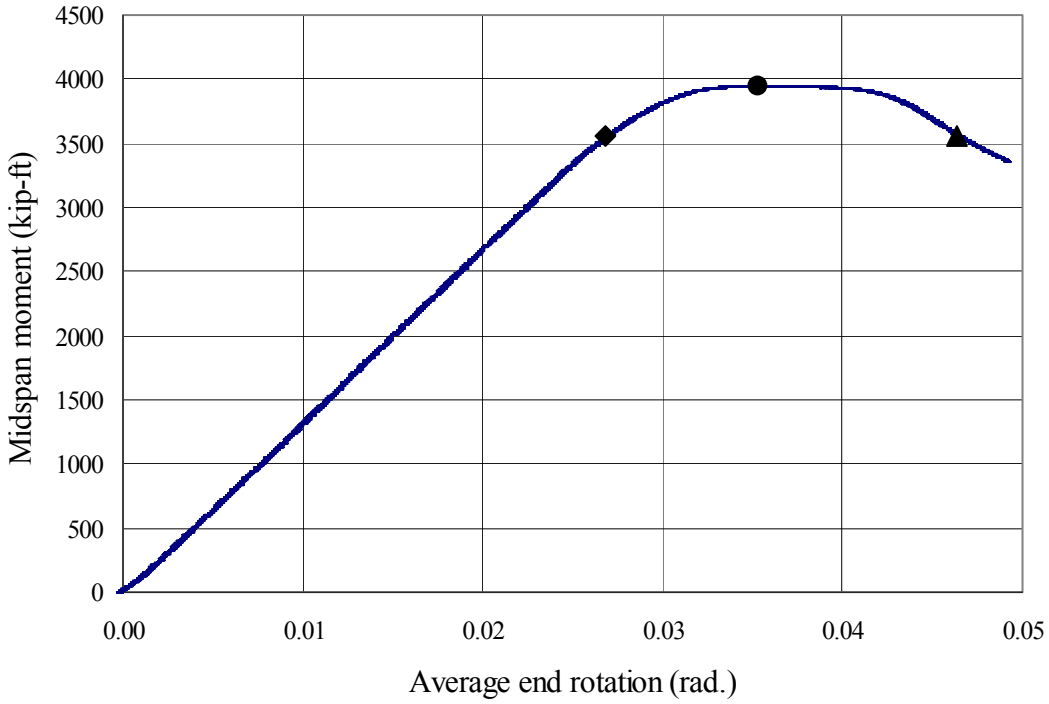

Figure 5.126 Midspan moment versus average end rotation (Specimen 7)

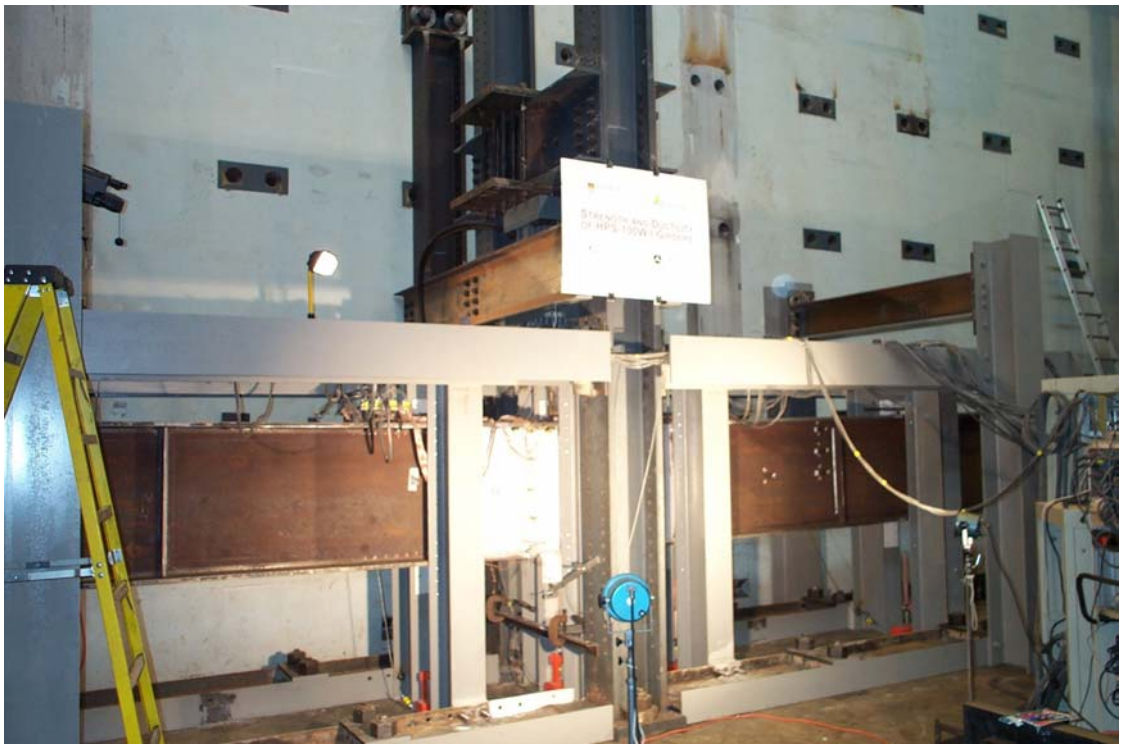

Figure 5.127 Specimen 7 during testing

Figure 5.128 Specimen 7 after testing

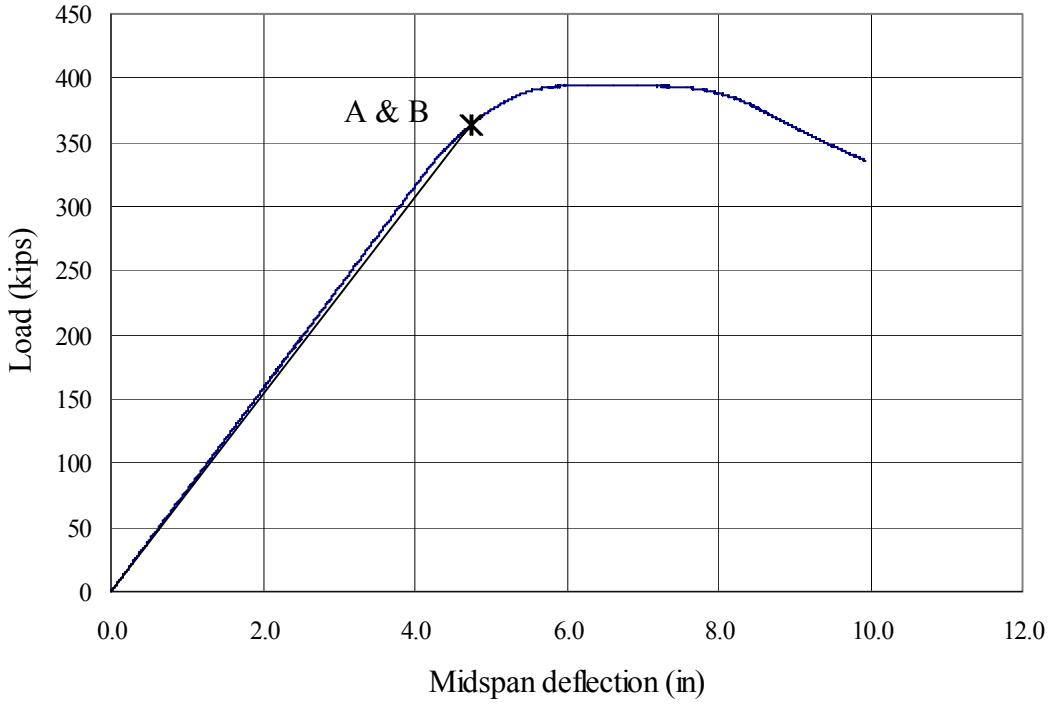

Figure 5.129 Load versus midspan vertical deflection (Specimen 7)

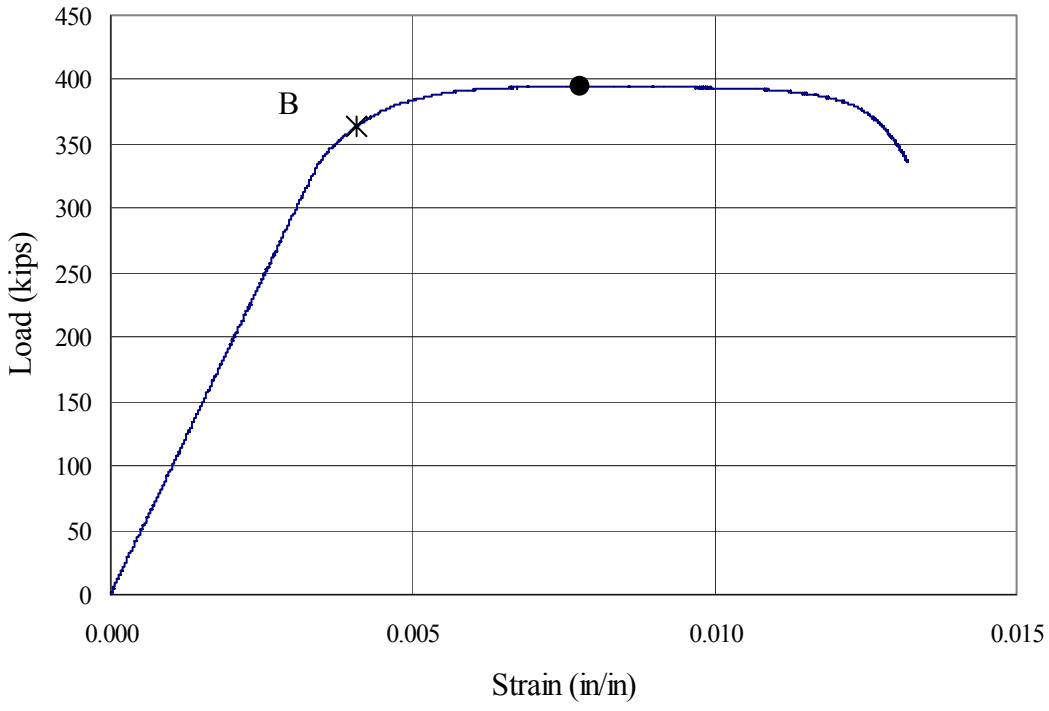

Figure 5.130 Load versus strain recorded by strain gage 147 (Specimen 7)

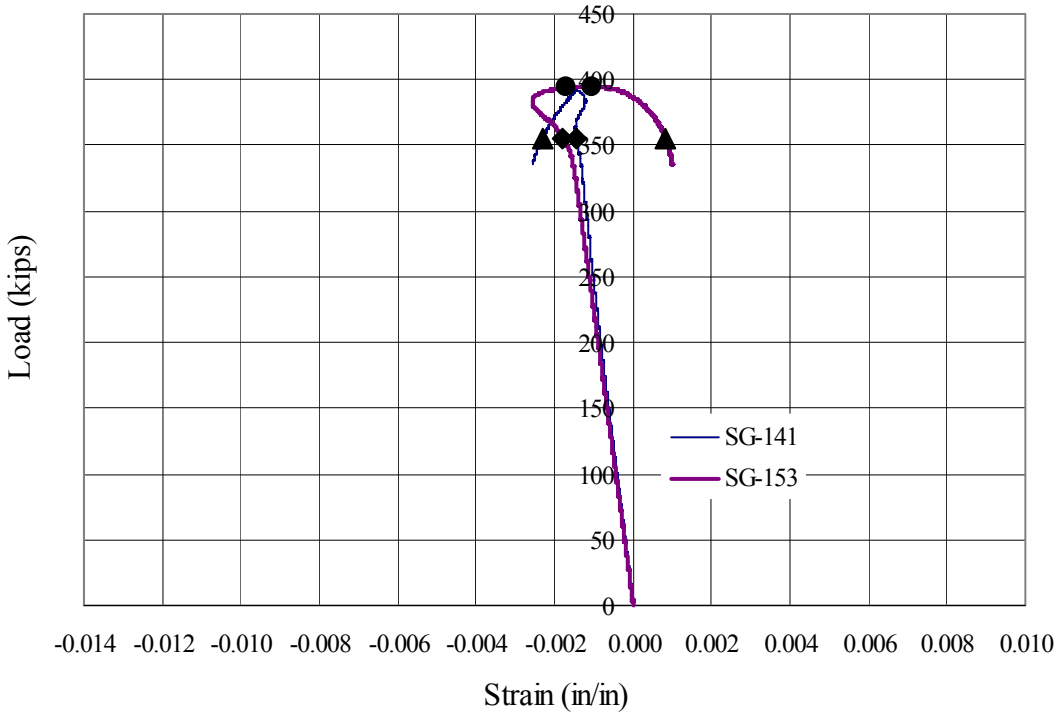

Figure 5.131 Effect of initial imperfection on web distortion (Specimen 7)

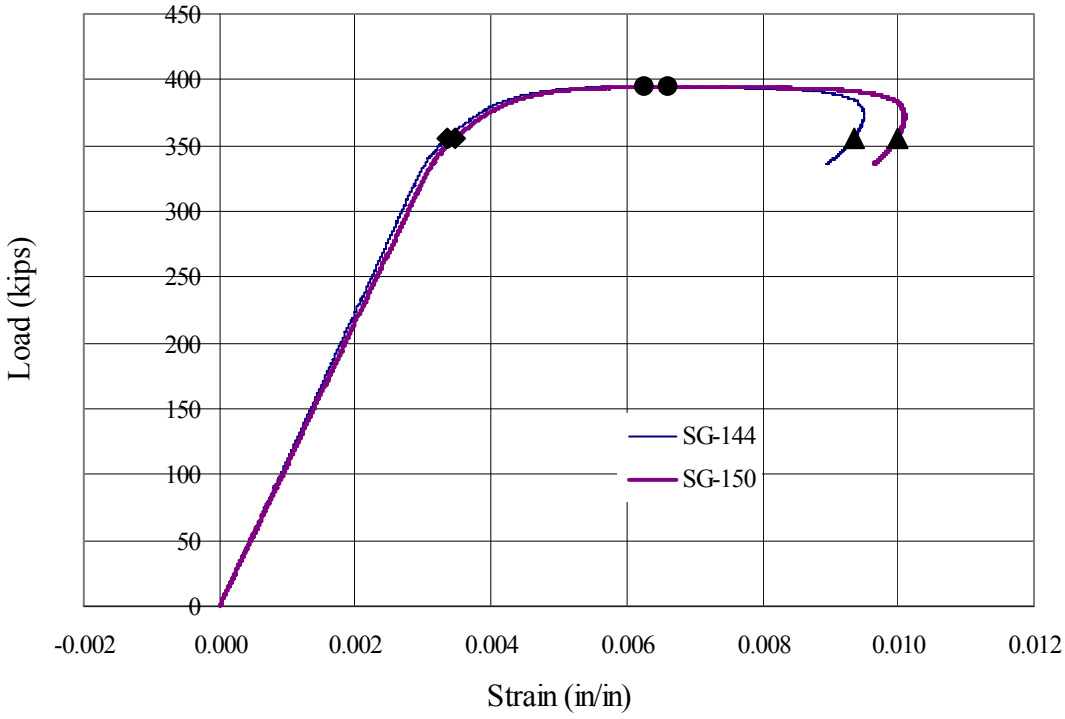

Figure 5.132 Load versus strain for strain gages SG-144 and SG-150 (Specimen 7)

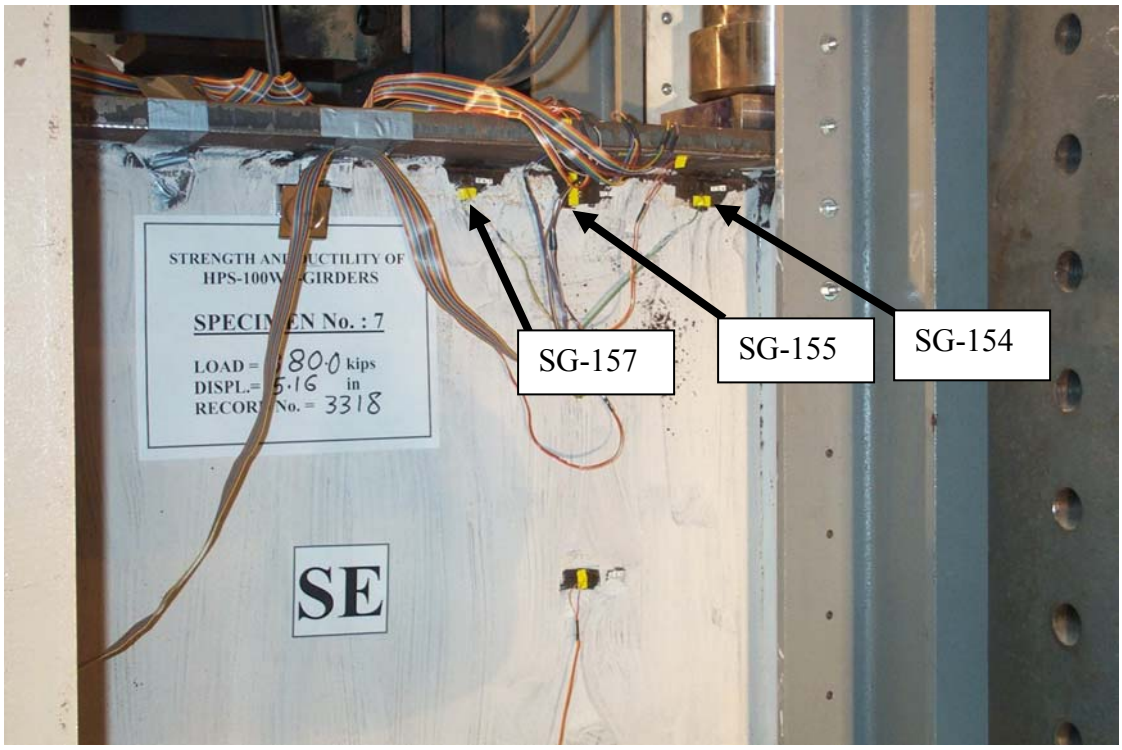

Figure 5.133 Interaction between web and compression flange at the distorted region

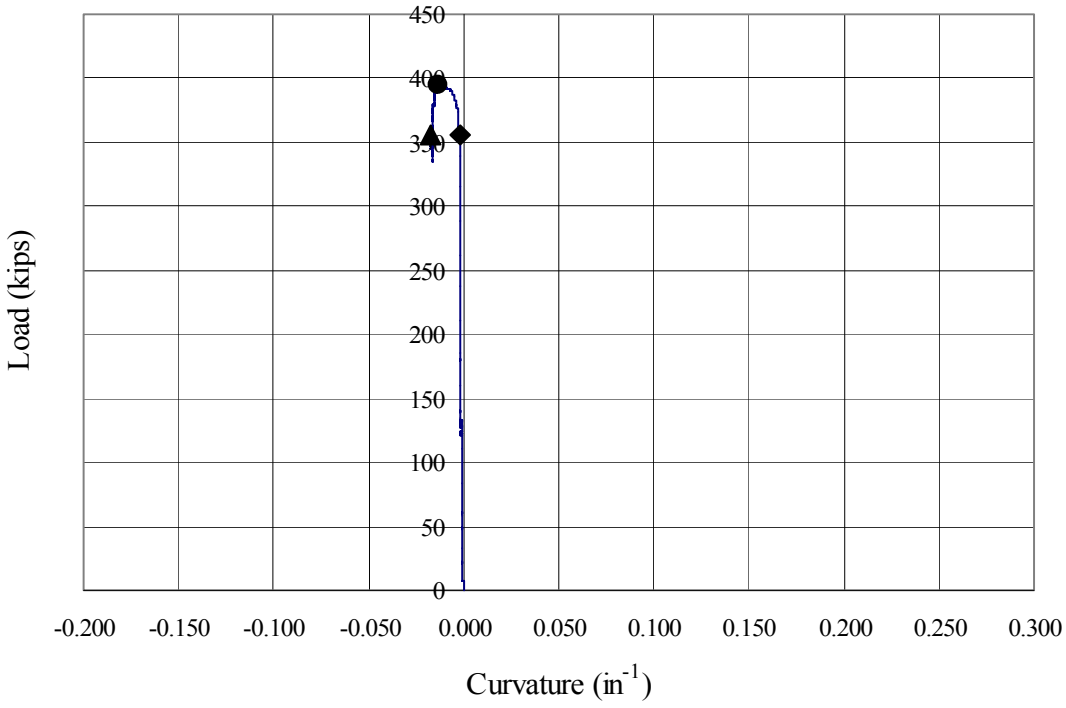

Figure 5.134 Load versus curvature at strain gages SG-137 and SG-154 (Specimen 7)

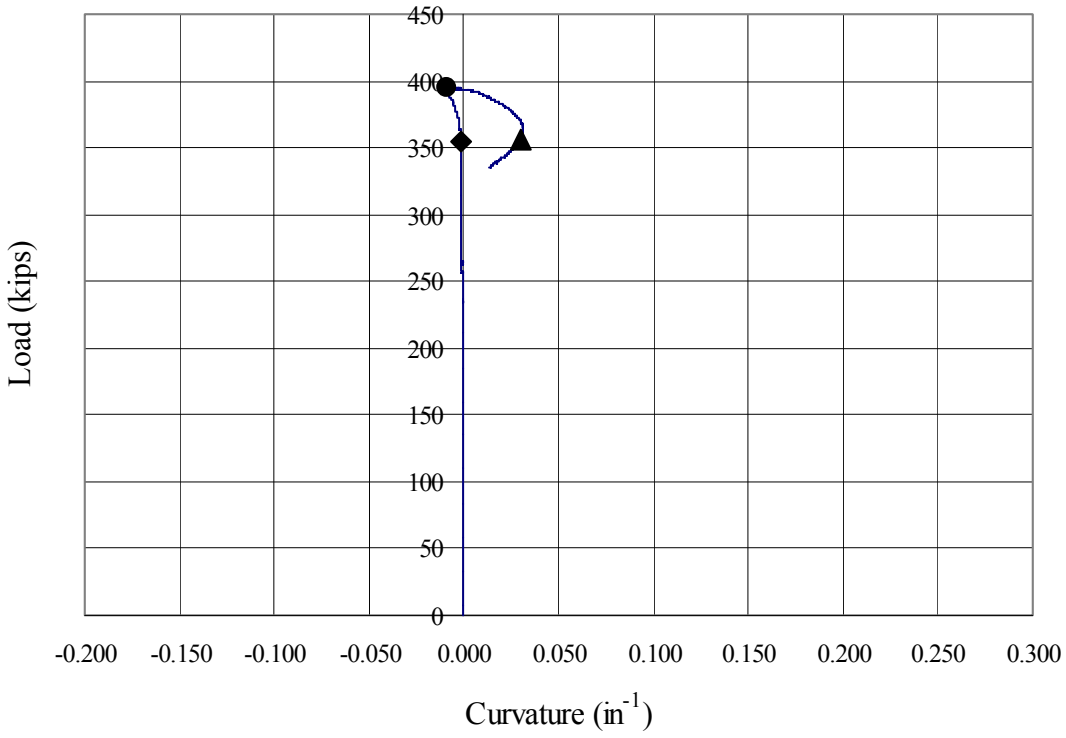

Figure 5.135 Load versus curvature at strain gages SG-138 and SG-155 (Specimen 7)

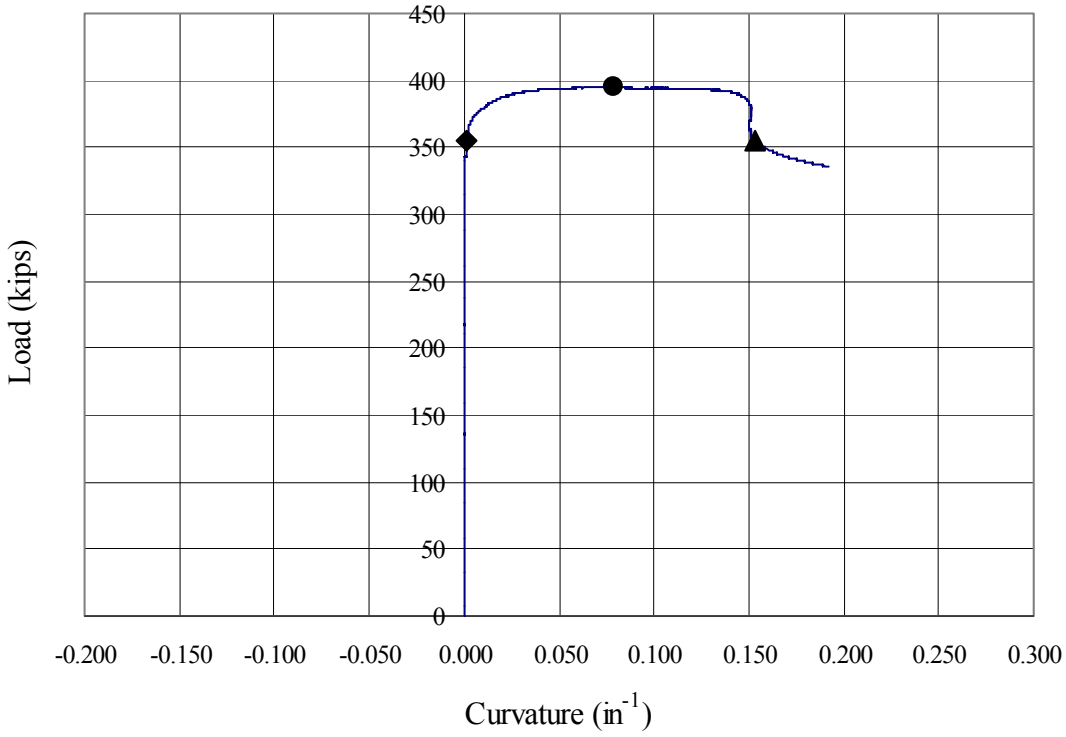

Figure 5.136 Load versus curvature at strain gages SG-140 and SG-157 (Specimen 7)

Figure 5.137 Lateral distortion of compression flange (Specimen 7)

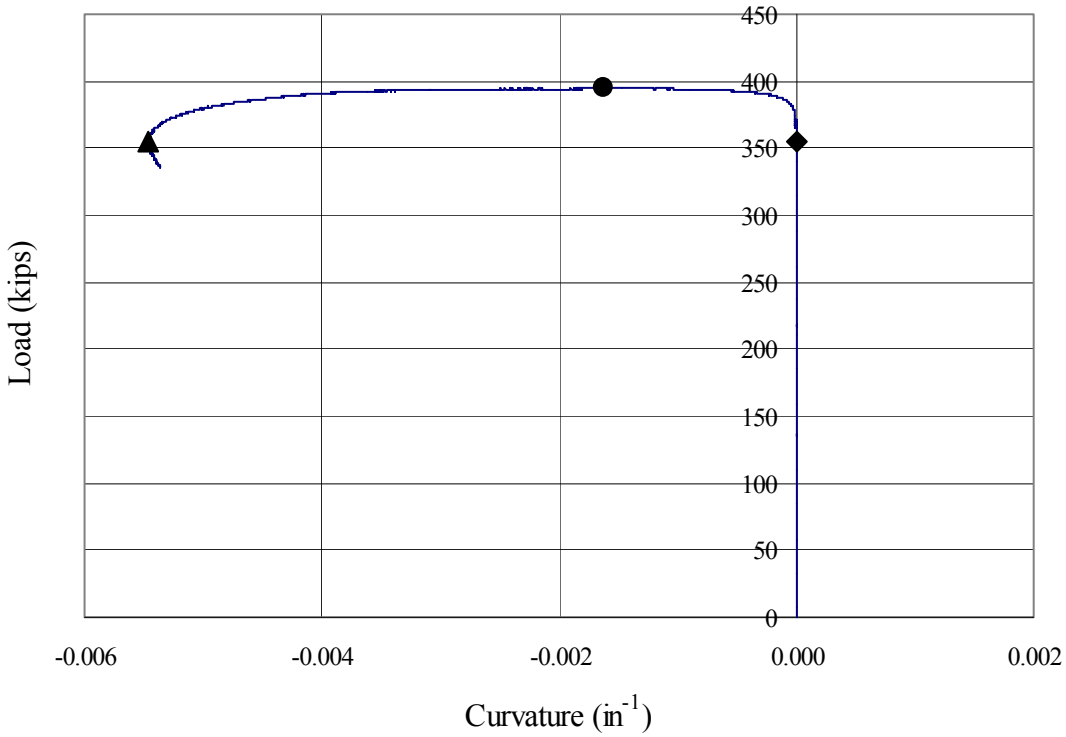

Figure 5.138 Load versus ϕ_l at section 2 (Specimen 7)

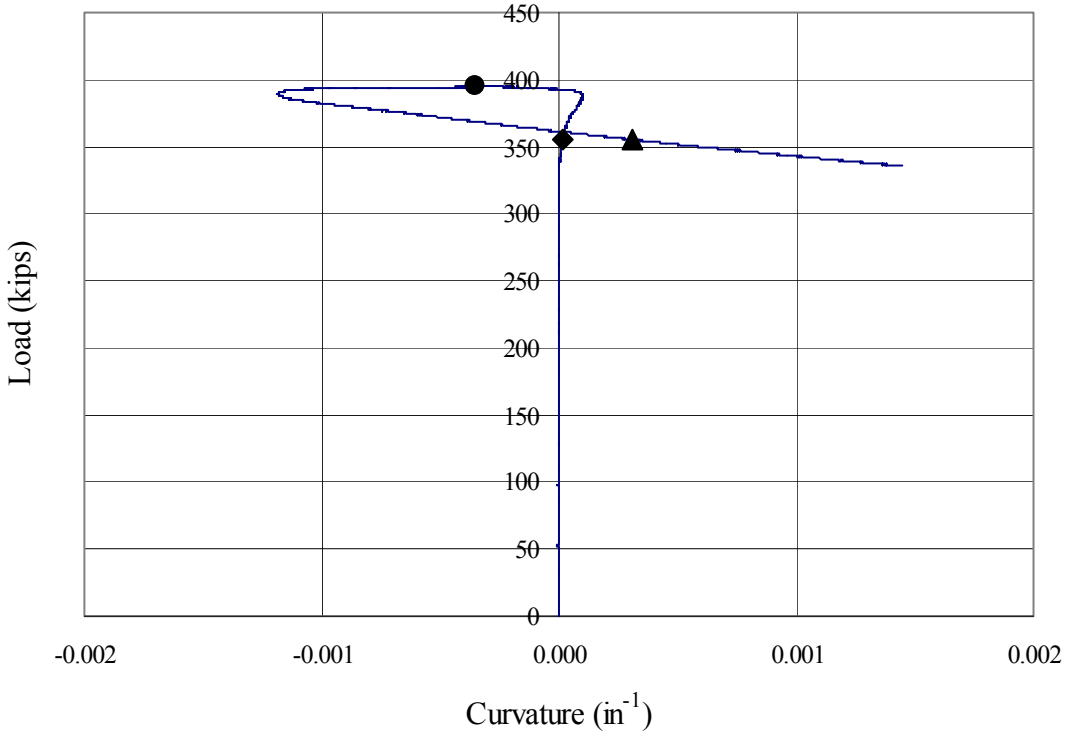

Figure 5.139 Load versus ϕ_l at section 4 (Specimen 7)

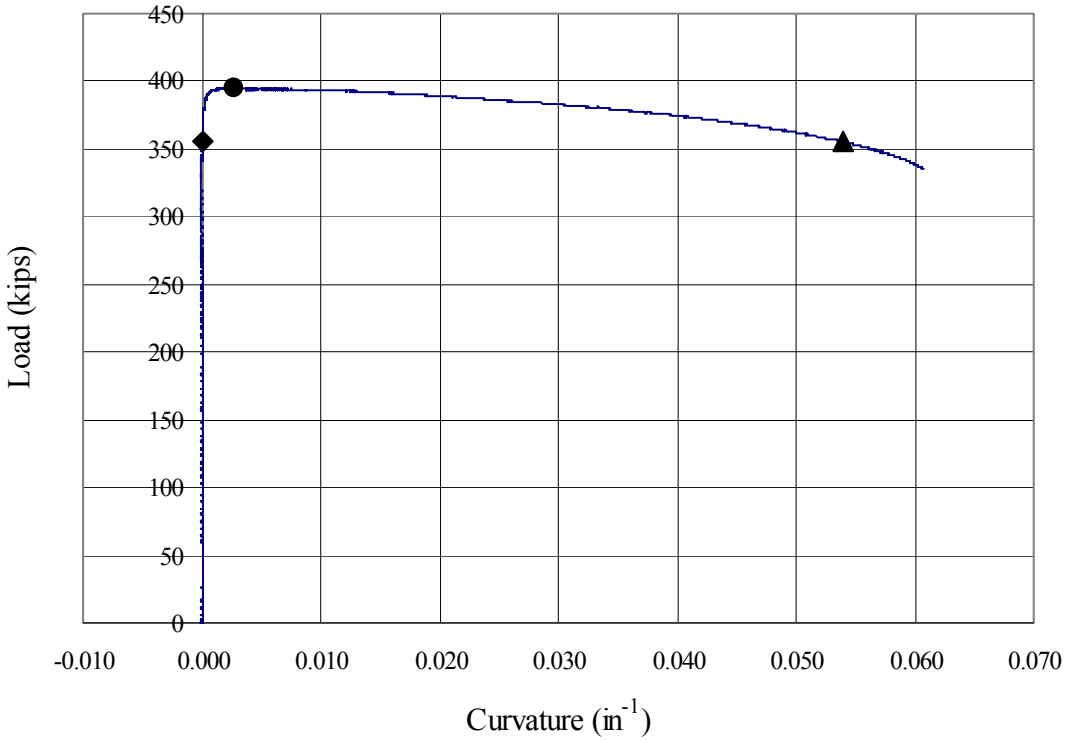

Figure 5.140 Load versus ϕ_{fp} at section 2-West (Specimen 7)

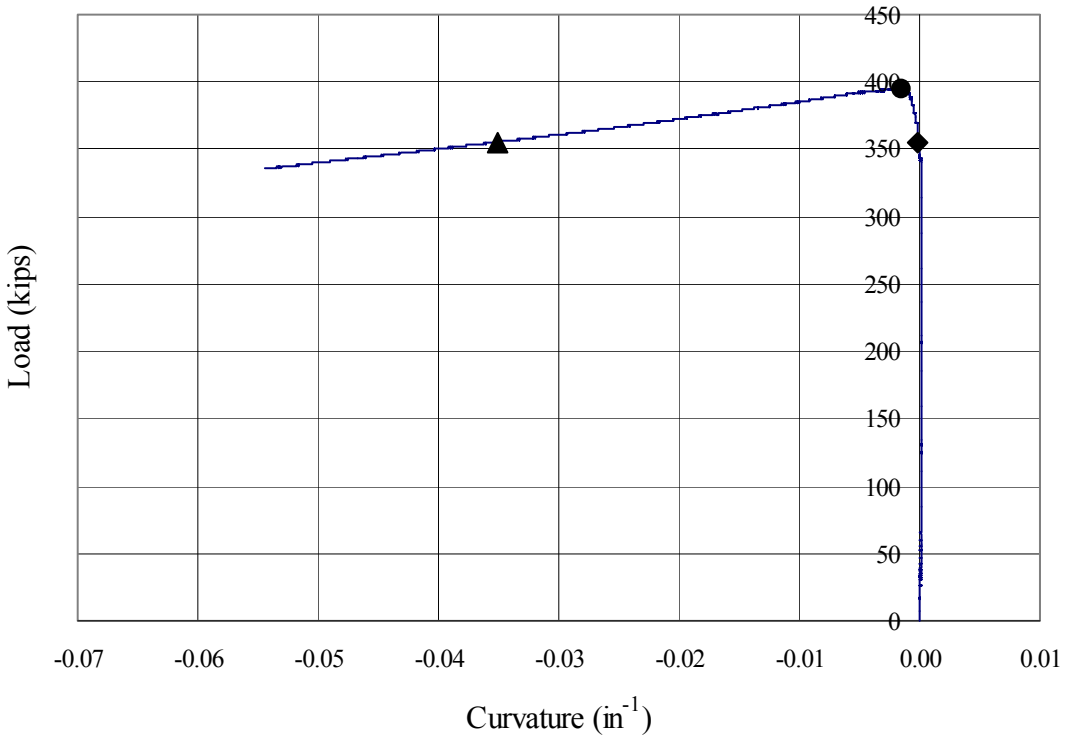

Figure 5.141 Load versus ϕ_{fp} at section 4-West (Specimen 7)

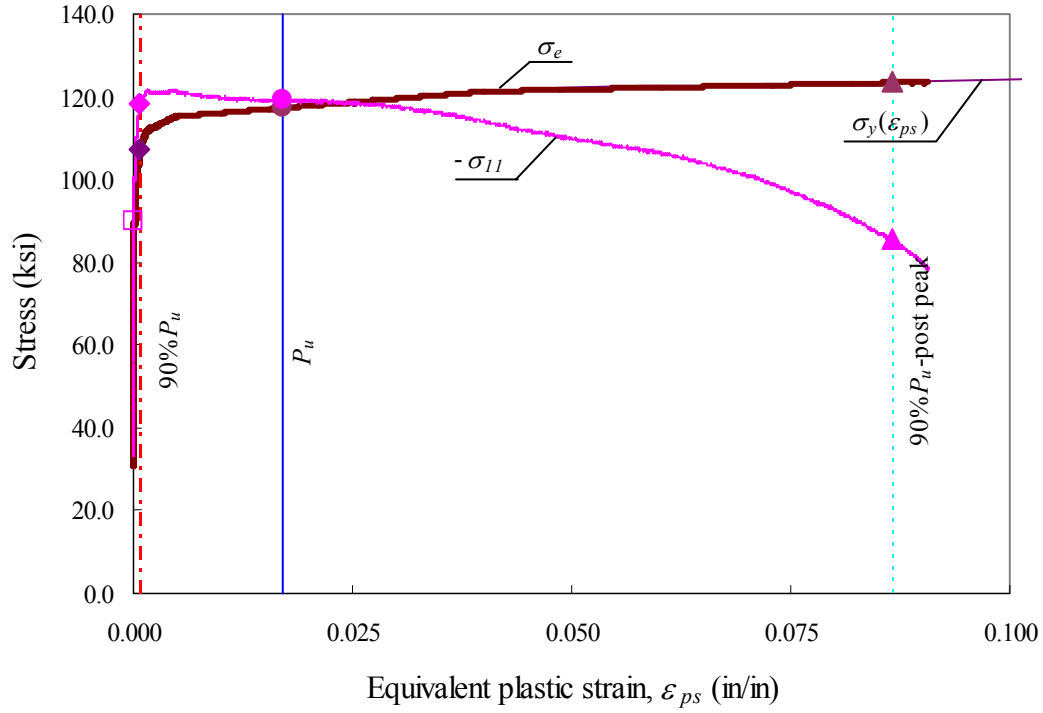

Figure 5.142 Stress versus equivalent plastic strain (section 2-West, Specimen 7)

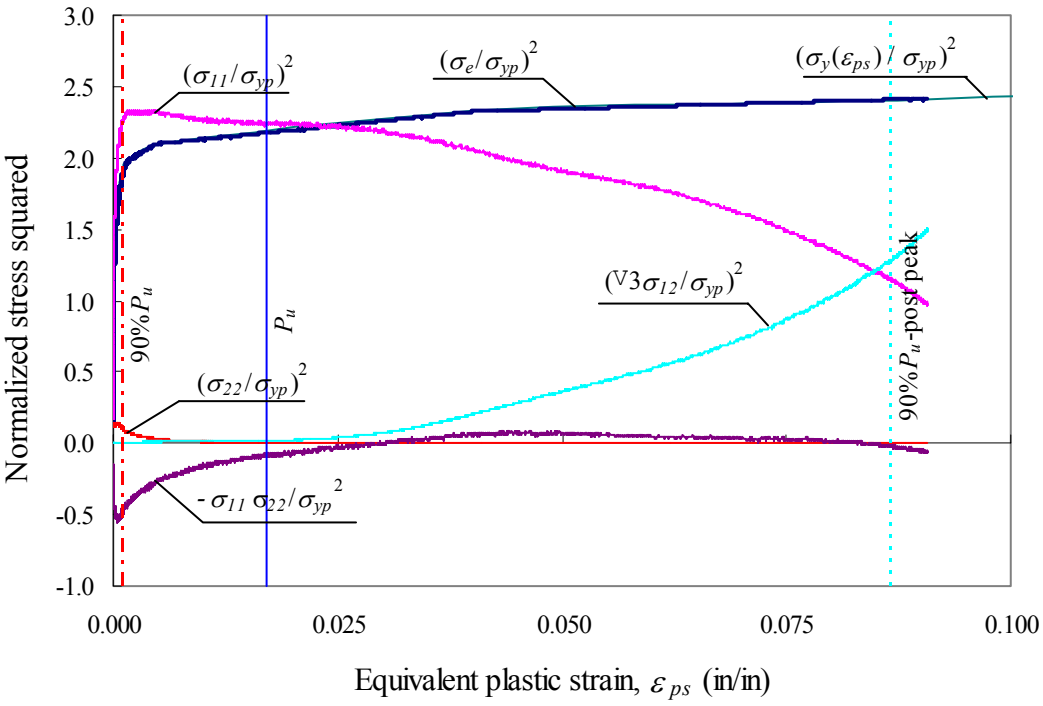

Figure 5.143 Contributions to effective stresses (section 2-West, Specimen 7)

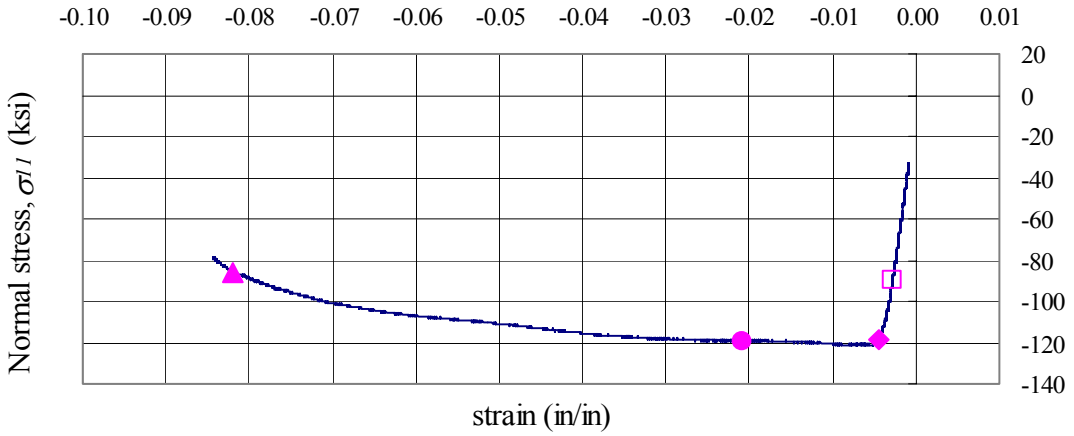

(a) Normal strain, ε_{11}

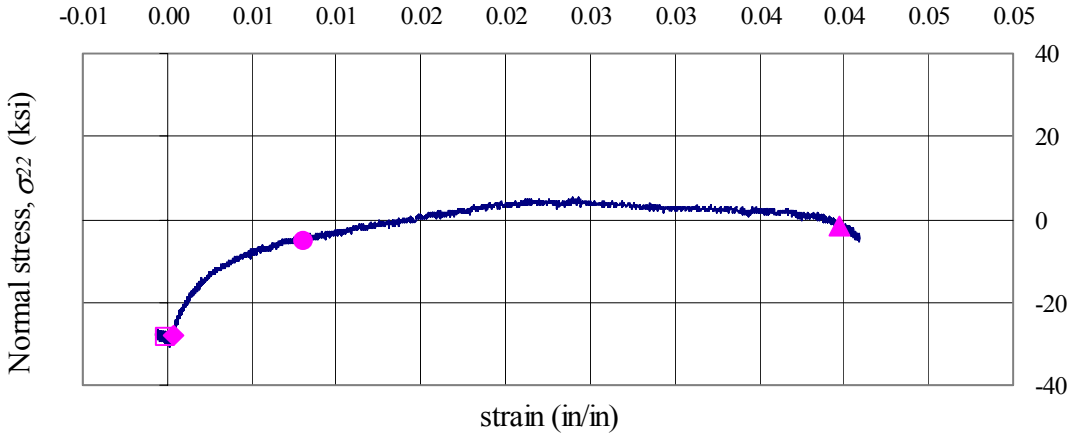

(b) Normal strain, ε_{22}

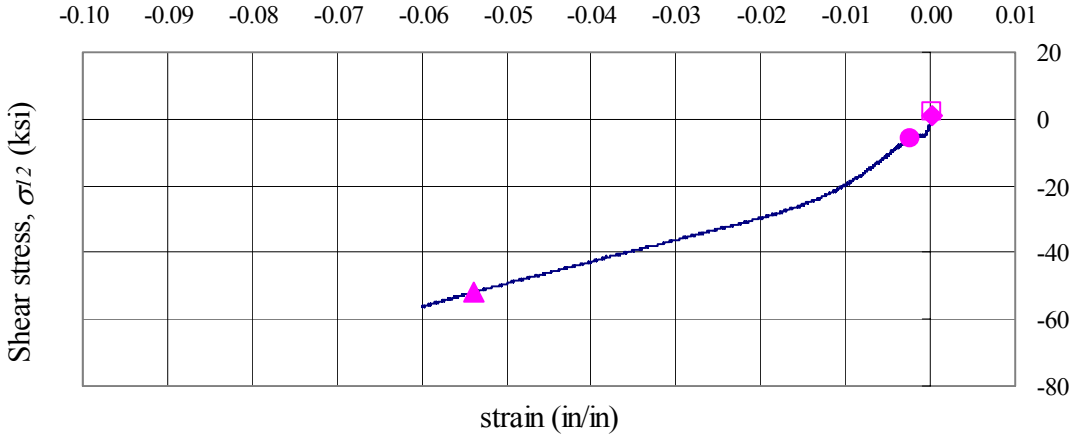

(c) Engineering shear strain, γ_{12}

Figure 5.144 Stress versus strain (section 2-West, Specimen 7)

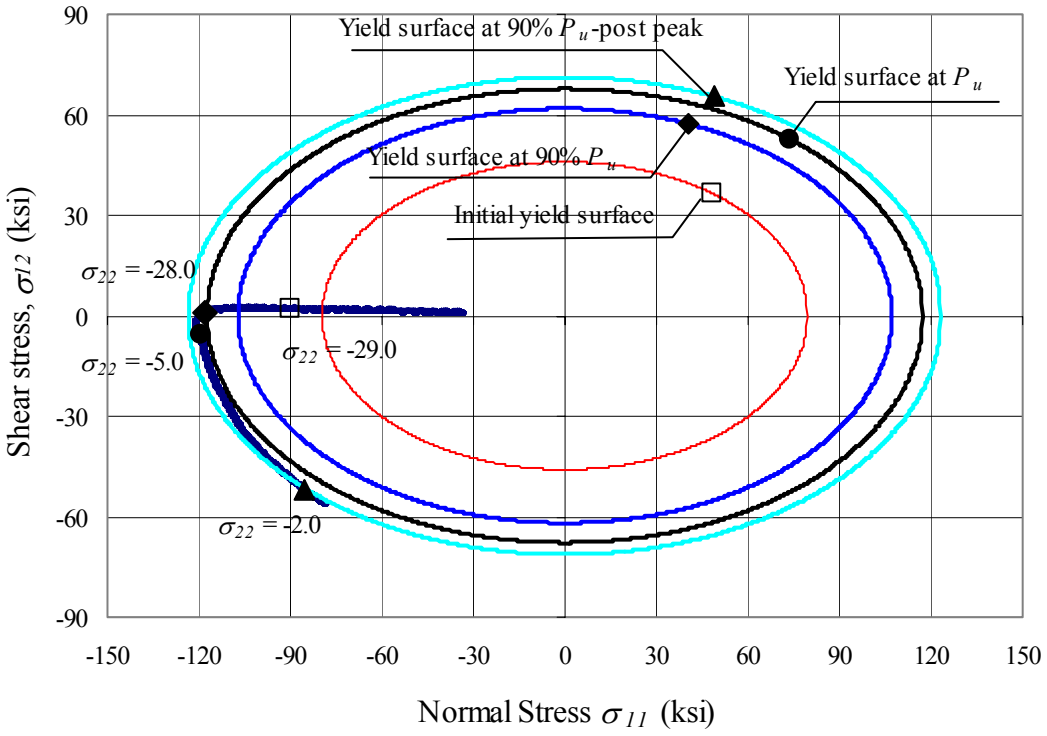

Figure 5.145 Yield surface in σ_{11}- σ_{12} plane at different increments (section 2-West, Specimen 7)

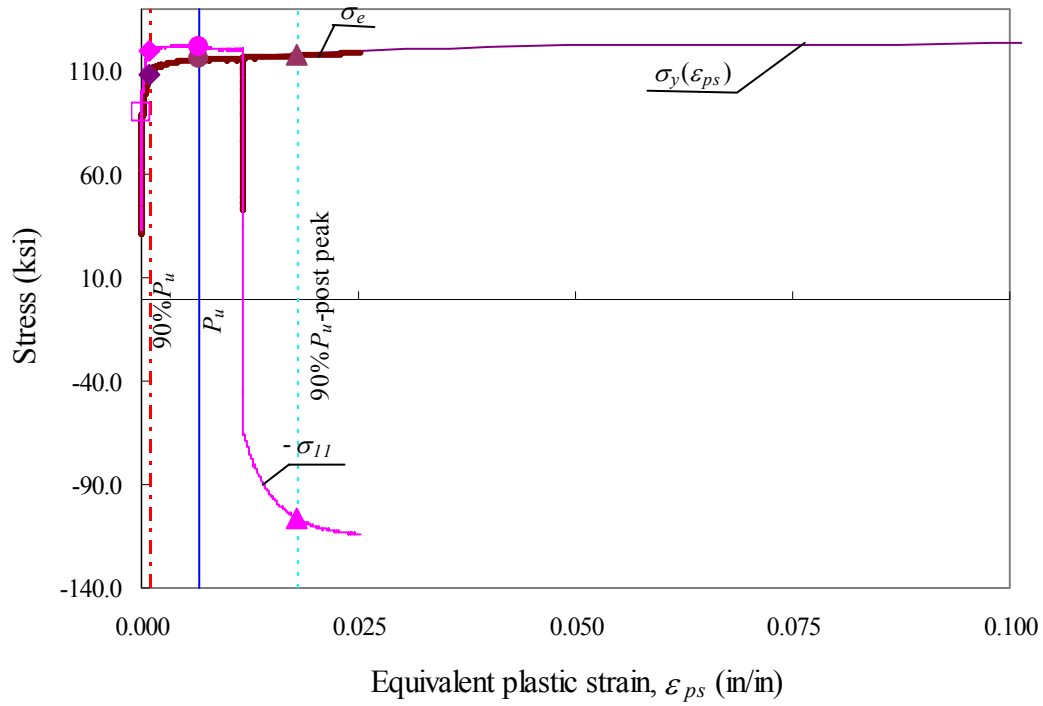

Figure 5.146 Stress versus equivalent plastic strain (section 4-West, Specimen 7)

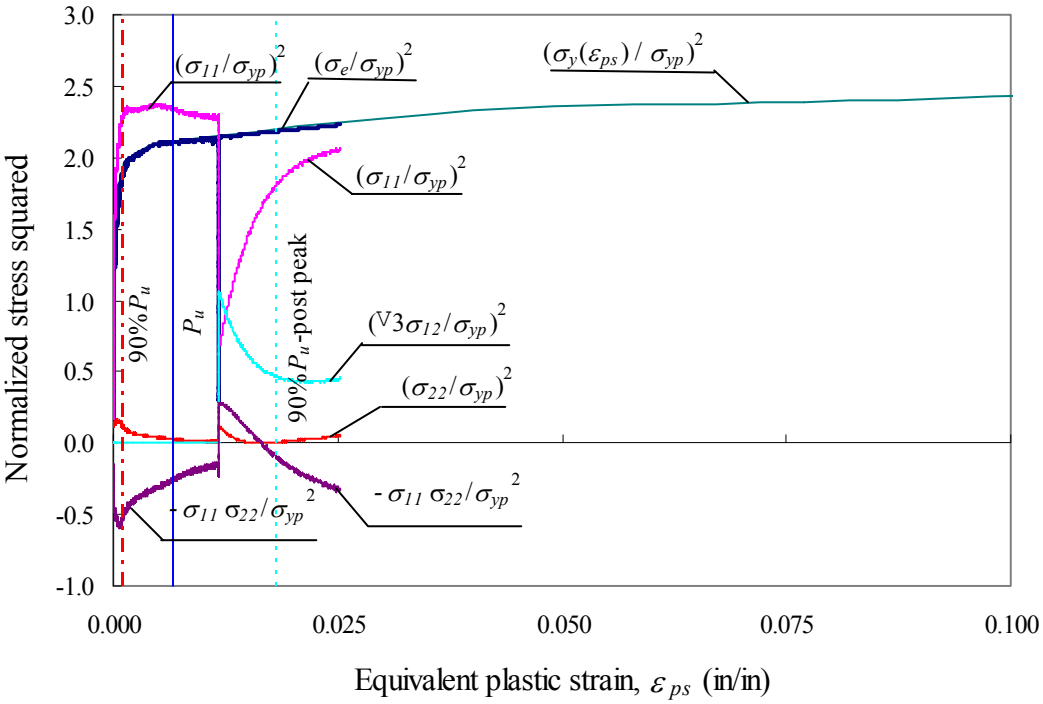

Figure 5.147 Contributions to effective stresses (section 4-West, Specimen 7)

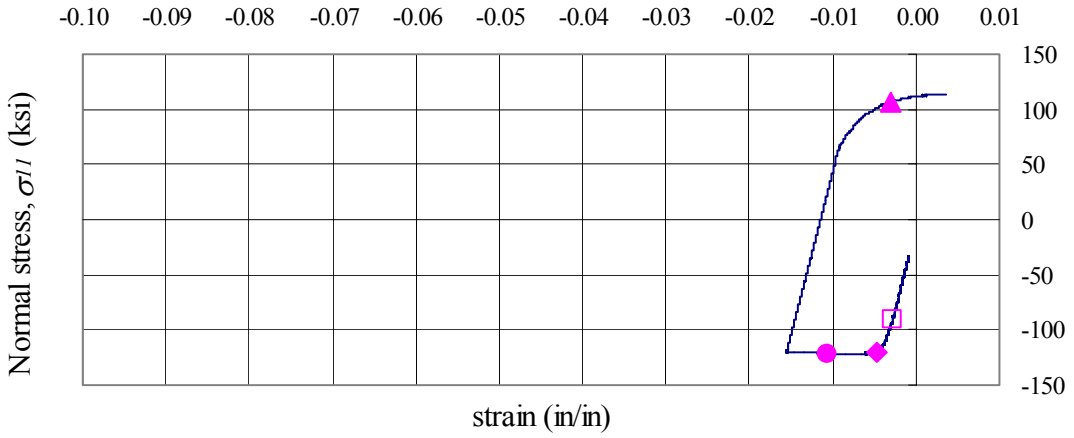

(a) Normal strain, ε_{11}

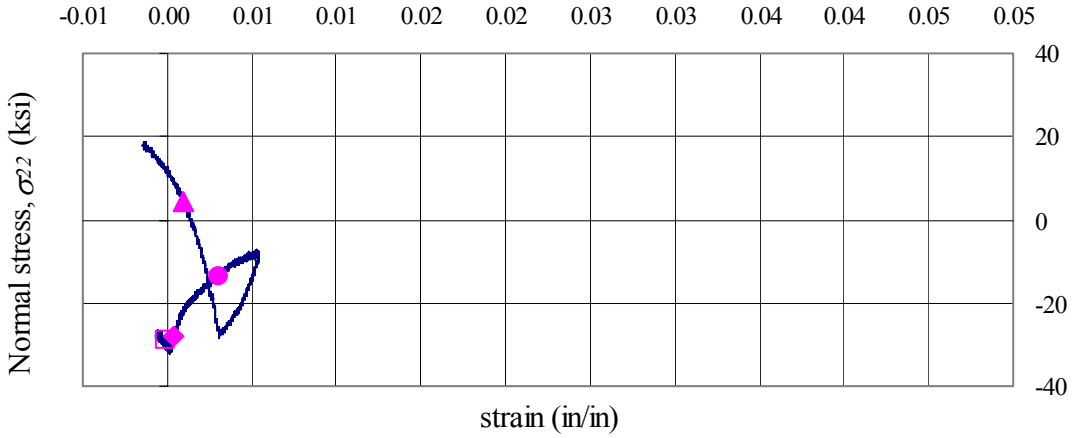

(b) Normal strain, ε_{22}

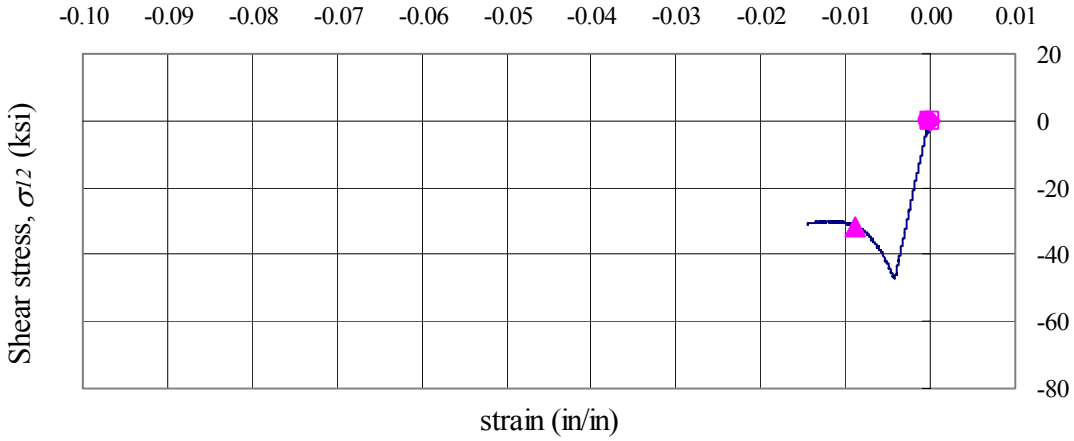

(c) Engineering shear strain, γ_{12}

Figure 5.148 Stress versus strain (section 4-West, Specimen 7)

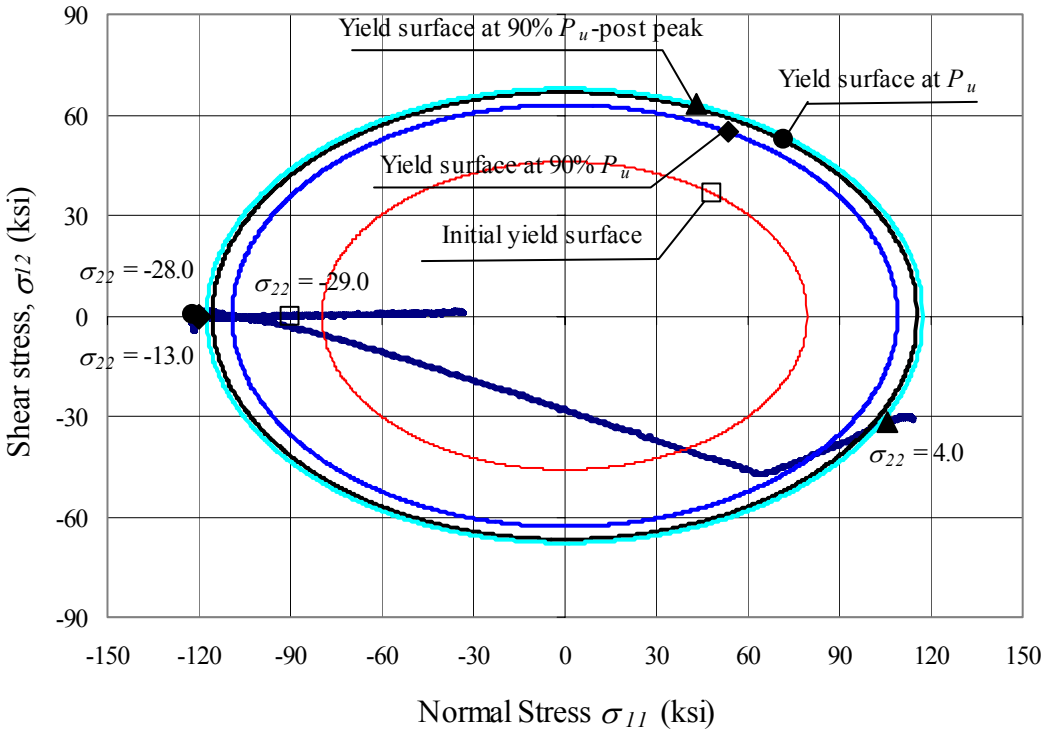

Figure 5.149 Yield surface in σ_{11}- σ_{12} plane at different increments (section 4-West, Specimen 7)

CHAPTER 6 Finite Element Simulations

6.1 Introduction

Finite element simulations of the experimentally tested specimens are presented in this chapter. Modifications to the finite element model presented in Section 3.3 are explained and the parameters varied in the model for each specimen are discussed. A comparison between the experimental results and the finite element simulation results is presented for each specimen. The comparison is presented in terms of load versus midspan vertical deflection and moment versus total end rotation, where the total end rotation is the sum of right and left end rotations.

To assess the contribution of the web and the flanges to the total moment carried by the specimen, the moment carried by the web, the moment carried by the flanges, and the total moment is plotted versus midspan vertical deflection.

Contour plots of stresses on the upper surface of the top flange are also presented, and the contours of the resultant normal forces, transverse shear force, and the resultant moments for the top flange are also presented. These contours are plotted for two increments, at P_u and 90% P_u-post peak.

6.2 Finite Element Model

The geometry of the finite element model used in the simulations is explained in detail in Section 3.3.3. However a minor enhancement was made to the model described in Section 3.3.3. This enhancement refined the mesh at the edges of the top flange. The refinement replaced the edge element by two elements in the direction of the flange width, leaving the flange element length along the specimen length unchanged. This refinement provided better transverse shear forces in the elements at the flange tips.

Lateral brace locations for each specimen are discussed in Section 4.4.2. The dimensions of each specimen are discussed in Section 4.5.1, and the geometric imperfections of the web and flanges are explained in Section 4.5.2. The residual stress model used in the finite element simulations is explained in Section 4.5.3. These residual stresses were incorporated in the finite element simulation as initial conditions.

The finite element simulation requires the stress-strain behavior of the steel to be input as true stress versus natural plastic strain. Plots of the true stress versus natural plastic strain curves used in the finite element simulations are shown in Figure

6.1 and Figure 6.2 for the web and flange plates, respectively. The true stress versus natural plastic strain was calculated from the stress-strain model described in Section 4.2.5, using the average tensile coupon data shown in Table 5.5, and the approach described in Section 3.3.2.

In some cases, the local buckling deflected shape of the finite element model did not closely resemble that from the experiment. In these cases, either removing the flange imperfection from the model or changing the reference used to specify the web imperfection resulted in better agreement of the local buckling shape. The difficulties in obtaining good agreement in the local buckling shape can be classified as follows:

1. Buckling occurred on the opposite side of the midspan in the finite element model compared to the experimental results.
2. Buckling deformations occurred either closer or farther away from the midspan compared to the experimental results.
3. The imperfection amplitude was too small, which led to convergence problems in the simulation.

It is important to note that these difficulties, in most cases, have only a local effect on the finite element simulation. However, they have little effect on the global behavior in terms of load versus midspan vertical deflection or midspan moment versus total rotation.

6.3 Specimen 3

6.3.1 Finite Element Simulation Results

Comparisons between the experimental results and the finite element simulation results are presented in Figure 6.3 and Figure 6.4. Load versus midspan vertical deflection is compared in Figure 6.3 and midspan moment versus total rotation is compared in Figure 6.4. The total rotation is the sum of the right and left end rotation. From these figures, it is clear that the finite element simulation accurately predicted the experimental specimen response. The ultimate load predicted by the finite element simulation is 266 kips (1183 kN), which is higher than the experimental ultimate load by 1%. This ultimate load corresponds to an ultimate midspan moment, M_u, of 1663 kip-ft (2256 kN-m). M_u, predicted by the finite element simulation, is 1% greater than M_p.

6.3.2 Moment Components

To show the contribution of the web and the flanges to carrying the applied moment and to show when the web and flanges start to unload, the moment carried by the web and flanges is plotted versus midspan vertical deflection, along with the total moment in Figure 6.5. The cross section at which these moments are calculated is the

section where the edge of the top flange has the steepest slope at 90% P_u-post peak. This section has the highest transverse shear force, *SF4*. For Specimen 3, this section is located at 5.08 in (129 mm) to the south of midspan.

The total moment at this critical section is calculated as follows. To calculate the moment carried by the flanges, the top flange force in the local-1 direction, *SF1*, is converted to the global direction. The moment of this force is calculated about the middle of bottom flange. The instantaneous coordinate of the middle of the bottom flange is subtracted from that of the top flange elements to calculate the flange moment arm of each top flange element. Multiplying the top flange global force by the moment arm and summing for all the top flange elements provides the moment carried by flanges. The moment carried by the web is determined by subtracting the flange moment from the total moment.

The total moment, M_t, the moment carried by the flanges, M_{fl}, and the moment carried by the web, M_w, are plotted in Figure 6.5. On this plot, vertical lines are plotted to show when the maximum moment is reached. M_w reached its maximum value, which was 17% M_t, at a midspan vertical deflection of 3.63 in (92 mm). The web starts to shed its moment to the flanges as soon it reaches its maximum moment. The flange contribution continues to increase after the web begins to unload.

M_t depends on the flange loading and the web unloading rates. For this specimen, even though after the web starts unloading, M_t continues to increase as a result of continuing flange loading. When the flange loading rate equals the web unloading rate, M_t reaches its maximum value, at a midspan vertical deflection of 4.63 in (118 mm). Note that the flange moment continues to increase even though M_t starts decreasing. M_{fl} reaches its maximum at midspan vertical deflection of 5.0 in (127 mm).

6.3.3 Moment and Force Transferred Between Web and Top Flange

As soon as the web starts to unload, the demands on the top flange increase because the web sheds moment, and also because twisting moment and lateral force are applied to the flange by the buckling web. The twisting moment disturbs the top flange and increases its torsional instability. The lateral force increases its lateral instability and produces lateral bending in the top flange. This lateral flange bending produces tension on one side of the flange and compression on the other side. The tension enhances the top flange torsional stability, while the compression increases its torsional instability.

The positive direction for moment, *SM2*, and lateral force, *SF5*, transferred between the web and top flange is shown in Figure 6.6. The moment and lateral force shown in Figure 6.7 and Figure 6.8, respectively, are the moment and force at the integration points of the web elements that are adjacent to the top flange. In these

figures the horizontal axis represent the normalized position, X/L, along the specimen length. For example, $X/L = 0.5$ represents the midspan of the specimen. The moment and lateral force develop as a result of web buckling deformation, and their largest values occur within a distance almost equal to the web height, h_w, north and south of midspan. Two vertical lines spaced at h_w/L on each side of the midspan are plotted in Figure 6.7 and Figure 6.8. As a reference to represent the distance to the first lateral brace on each side of midspan, L_{b1}, two vertical lines spaced at $0.5\ L_{b1}/L$ are plotted on these figures.

In Figure 6.7 and Figure 6.8, moment and lateral force are plotted for two increments, at P_u and at 90% P_u-post peak. Note that in the buckled region of the web the resultants of these moment and lateral force are consistent with the deformed shape shown (later) in Figure 6.15(a).

6.3.4 Contour Plots of Stresses and Resultant Forces and Moments

Contour plots of the stresses on the upper surface of the top flange, σ_{11}, σ_{22}, and σ_{12}, are shown in Figure 6.9 for an increment corresponding to P_u. The corresponding resultant normal forces, *SF1* and *SF2*, and transverse force, *SF4*, for the top flange are shown in Figure 6.10 and resultant moments, *SM1*, *SM2*, and *SM3,* for the top flange are shown in Figure 6.11.

Contour plots of the stresses on the upper surface of the top flange, σ_{11}, σ_{22}, and σ_{12}, are shown in Figure 6.12 for an increment corresponding to 90% P_u-post peak. The corresponding resultant normal forces, *SF1* and *SF2*, and transverse force, *SF4*, for the top flange are shown in Figure 6.13 and resultant moments, *SM1*, *SM2*, and *SM3,* for the top flange are shown in Figure 6.14.

The contour plot area represents an area with a width equal to b_f and a length equal to h_w on each side of midspan. By comparing the contour plots of normal force *SF1* for the increments corresponding to P_u and 90% P_u-post peak, one can find the area which has the largest reduction in *SF1*, as discussed below.

In Figure 6.9, it is important to note that σ_{11} reaches 130 ksi (896 MPa) in compression at P_u, which is 115% of σ_y. This increase in σ_{11} is a result of high compression strains due to bending deformation. Note that the shear stress σ_{12} at the location of maximum plate bending moment, *SM1*, is zero. As a result, the increase in σ_{11} over σ_y is due to plastic deformation, as represented by the input true stress-natural plastic strain behavior input to the finite element simulation and Von Mises yield function as expressed by Equation 5.1.

At 90% P_u-post peak, the normal force *SF1* is reduced near the edges of the buckled zone to the south of midspan as shown in Figure 6.13. The reduction in *SF1* at

the west flange tip, south of midspan, is attributed to flange plate bending, *SM1* and high transverse shear force, *SF4*. Note that the effect of flange plate bending occurs at the locations of maximum plate curvature, while the effect of transverse shear force occurs at the location of maximum slope at the flange tip. These two effects, occur at two different locations, but combine together to produce the reduction in *SF1* at the west flange tip, south of midspan. The reduction in *SF1* at the east flange tip, south of midspan, is attributed to flange plate bending, *SM1*, high transverse shear force, *SF4*, and lateral flange bending at the location closer to midspan, and lateral flange bending alone at the other location farther from midspan. As seen from the deflected shape in Figure 6.15, the lateral flange bending provides tension deformation at the east flange tip, south of midspan, is more pronounced.

6.3.5 Deflected Shape

A comparison between different buckling deflected shapes from using different initial imperfections in the finite element simulation is shown in Figure 6.15. In this figure, the deflected shape is plotted for increments corresponding to 90% P_u-post peak. For the simulation that produced deflected shape A, flange imperfections were not included in the finite element simulation (imperfection A), while flange imperfections were included in the finite element simulation that produced deflected shape B (imperfection B). Comparing these deflected shapes with the deflected shape from the experiment (after testing was completed), shown in Figure 6.15(c), it is clear that deflected shape A closely matches the experimental deflected shape.

Stress and strain histories, obtained from the finite element simulation, are plotted in Figure 6.16 for the initial imperfection cases, and compared with the experimental results. Note that in the finite element simulation, the residual stress corresponds to the residual stress model introduced in Chapter 4. This model accounts only for normal residual stress in the local-1 direction but does not account for the normal residual stress in the local-2 direction or the shear residual stress. On the other hand, the complete set of measured residual stresses were used as initial conditions to calculate the stress-strain histories from the experimental results. As shown in Figure 6.16 the stress-strain history from the simulation using initial imperfection A agrees well with the experimental results.

6.4 Specimen 4

6.4.1 Finite Element Simulation Results

Comparisons between the experimental results and the finite element simulation results are presented in Figure 6.17 and Figure 6.18 Load versus midspan vertical deflection is compared in Figure 6.17 and midspan moment versus total rotation in Figure 6.18. From these figures, it is clear that the finite element simulation accurately predicts the experimental specimen response. The ultimate load predicted

by the finite element simulation is 210.9 kips (938 kN), which is higher than the experimental ultimate load by 1%. This ultimate load corresponds to an ultimate midspan moment, M_u, of 1714 kip-ft (2325 kN-m). M_u, predicted by the finite element simulation, corresponds to 95% M_p.

6.4.2 Moment Components

The cross section at which these moments are calculated is the section where the edge of the top flange has the steepest slope at 90% P_u-post peak. For Specimen 4, this section is located at 6.60 in (168 mm) to the north of midspan.

The total moment, M_t, the moment carried by the flanges, M_{fl}, and the moment carried by web, M_w, are plotted in Figure 6.19. On this plot, vertical lines show the maximum moment. M_w reached its maximum value, which was 19% M_t at a midspan vertical deflection of 4.71 in (120 mm). The web starts to shed its moment to the flanges as soon it reaches its capacity.

M_t depends on the flange loading and the web unloading rates. For this specimen, even though after the web starts unloading, M_t continues to increase as a result of continuing flange loading. M_t reaches its maximum value at a midspan vertical deflection of 5.44 in (138 mm). Note that the flange moment continues to increase even though M_t starts decreasing. M_{fl} reaches its maximum value at a midspan vertical deflection of 5.81 in (148 mm).

6.4.3 Moment and Force Transferred Between Web and Top Flange

The moment and lateral force transferred between web and top flange shown in Figure 6.20 and Figure 6.21, respectively, are the moment and force at the integration points of the web elements that are adjacent to the top flange. In Figure 6.20 and Figure 6.21, the moment and lateral force are plotted for two increments, at P_u and at 90% P_u-post peak. The moment and lateral force develop as a result of web buckling deformation, and their largest values occur within a distance almost equal to the web height, h_w, north and south of midspan.

6.4.4 Deflected Shape

The deflected shape from the finite element simulation at 90% P_u-post peak, and deflected shape from the experiment (after testing was complete) are shown in Figure 6.22. The agreement between the deflected shape from the experiment and the deflected shape from the finite element simulation is not very good.

6.5 Specimen 5

6.5.1 Finite Element Simulation Results

Comparisons between the experimental results and the finite element simulation results are presented in Figure 6.23 and Figure 6.24 Load versus midspan vertical deflection is compared in Figure 6.23 and midspan moment versus total rotation in Figure 6.24. From these figures, it is clear that the finite element simulation slightly overestimates the experimental specimen strength. The ultimate load predicted by the finite element simulation is 400.7 kips (1782 kN), which is higher than the experimental ultimate load by 4.3%. This ultimate load corresponds to an ultimate midspan moment, M_u, of 2805 kip-ft (3805 kN-m). M_u, predicted by the finite element simulation, is 4.3% greater than M_p.

6.5.2 Moment Components

The cross section at which these moments are calculated is the section where the edge of the top flange has the steepest slope at 90% P_u-post peak. For Specimen 5, this section is located at 8.31 in (211 mm) to the north of midspan.

The total moment, M_t, the moment carried by the flanges, M_{fl}, and the moment carried by web, M_w, are plotted in Figure 6.25. On this plot, vertical lines show the maximum moment. M_w reached its maximum value, which was 19% M_t, at a midspan vertical deflection of 5.48 in (139 mm). M_t depends on the flange loading and the web unloading rates. For this specimen, both M_t and M_{fl} reach their maximum simultaneously at a midspan vertical deflection of 7.92 in (201 mm).

6.5.3 Moment and Force Transferred Between Web and Top Flange

In Figure 6.26 and Figure 6.27, the moment and lateral force transferred between the web and top flange are plotted for two increments, at P_u and 90% P_u-post peak. The moment and lateral force develop as a result of web buckling deformation.

6.5.4 Deflected Shape

The deflected shape from the finite element simulation, at 90% P_u-post peak, and the deflected shape from the experiment (after testing) are shown in Figure 6.28. Note the difference in orientation between the deflected shape plotted in Figure 6.28(a) and that in Figure 6.28(b). The agreement between the deflected shape from the experiment and the deflected shape from the finite element simulation is not very good.

6.6 Specimen 6

6.6.1 Finite Element Simulation Results

Comparisons between the experimental results and the finite element simulation results are presented in Figure 6.29 and Figure 6.30. Load versus midspan vertical deflection is compared in Figure 6.29 and midspan moment versus total rotation in Figure 6.30. From these figures, it is clear that the finite element simulation accurately predicts the experimental specimen response. The ultimate load predicted by the finite element simulation is 512 kips (2278 kN), which is higher than the experimental ultimate load by 1%. This ultimate load corresponds to an ultimate midspan moment, M_u, of 6144 kip-ft (8335 kN-m). M_u, predicted by the finite element simulation, corresponds to 95% M_p.

6.6.2 Moment Components

The cross section at which these moments are calculated is the section where the edge of the top flange has the steepest slope at 90% P_u-post peak. This section is located at 20.25 in (514 mm) to the north of midspan.

The total moment, M_t, the moment carried by the flanges, M_{fl}, and the moment carried by web, M_w, are plotted in Figure 6.31. M_w reached its maximum value, which was 19% M_t at a midspan vertical deflection of 6.76 in (172 mm). M_t depends on the flange loading and the web unloading rates. For this specimen, both M_t and M_{fl} reach their maximum values simultaneously, soon after the web reaches its maximum value, at a midspan vertical deflection of 7.14 in (181 mm).

6.6.3 Moment and Force Transferred Between Web and Top Flange

The moment and lateral force transferred between the web and top flange are shown in Figure 6.32 and Figure 6.33, for two increments, at P_u and 90% P_u-post peak.

It is clear that as h_w increases, the length over which these moment and lateral force increases. As the moment and lateral force twists and bends laterally the top flange, they act to disturb the top flange when the web buckles before the top flange.

6.6.4 Deflected Shape

The deflected shape from the finite element simulation, at 90% P_u-post peak, and the deflected shape from experiment (during testing) are shown in Figure 6.34. The agreement between the deflected shape from the experiment and the deflected shape from the finite element simulation is very good.

6.6.5 Stress-Strain History Comparisons

Comparisons between the stress-strain histories from the experiment and the finite element simulation at section 6-East and section 7-West are shown in Figure 6.35 and Figure 6.36, respectively. The strains from the experiment were converted to stresses using the plasticity program developed in Appendix A, of the present study. In Figure 6.35(a), the agreement between the results from the experiment and the finite element simulation is very good. However, the agreement is not very good in Figure 6.35(b). In Figure 6.35(c), the agreement is very good up to 90% P_u-post peak. In Figure 6.36(a) and (c), the agreement between the results from the experiment and the finite element simulation is very good. However, the agreement is not very good in Figure 6.36(b).

6.7 Specimen 7

6.7.1 Finite Element Simulation Results

Comparisons between the experimental results and the finite element simulation results are presented in Figure 6.37 and Figure 6.38. Load versus midspan vertical deflection is compared in Figure 6.37 and midspan moment versus total rotation in Figure 6.38. From these figures, it is clear that the finite element simulation accurately predicts the experimental specimen response. The ultimate load predicted by the finite element simulation is 405.6 kips (1804 kN), which is higher than the experimental ultimate load by 1%. This ultimate load corresponds to an ultimate midspan moment, M_u, of 4056 kip-ft (5503 kN-m). M_u, predicted by the finite element simulation, corresponds to 99% M_p.

6.7.2 Moment Components

The cross section at which these moments are calculated is the section where the edge of top flange has the steepest slope at 90% P_u-post peak. For Specimen 7, this section is located at 13.13 in (334 mm) to the south of midspan.

The total moment, M_t, the moment carried by the flanges, M_{fl}, and the moment carried by web, M_w, are plotted in Figure 6.39. On this plot, vertical lines show the maximum moment. M_w reached its maximum value, which was 21% M_t at a midspan vertical deflection of 5.78 in (147 mm).

M_t depends on the flange loading and the web unloading rates. For this specimen, even though after the web starts unloading, M_t continues to increase as a result of continuing flange loading. M_t reaches its maximum value at a midspan vertical deflection of 6.98 in (177 mm). Note that the flange moment continues to

increase even though M_t starts decreasing. M_{fl} reaches its maximum value at a midspan vertical deflection of 7.5 in (191 mm).

6.7.3 Moment and Force Transferred Between Web and Top Flange

The moment and lateral force transferred between the web and the top flange are shown in Figure 6.40 and Figure 6.41, respectively. The moment and lateral force develop as a result of web buckling deformation, and are largest within a distance almost equal to the web height, h_w.

6.7.4 Deflected Shape

The deflected shape from the finite element simulation, at 90% P_u-post peak, and the deflected shape from experiment (after testing) are shown in Figure 6.42. The agreement between the deflected shape from the experiment and the deflected shape from the finite element simulation is very good.

6.8 Summary

The results in this chapter suggest that by reducing h_w/b_f, for a given b_f, the length over which the forces and moment are transferred between the web and the compression flange will be reduced, as can be seen by comparing Figure 3.22 through 3.25, for Specimen 1 and Specimen 2. Note that the specimens with a smaller h_w/b_f, Specimen 1, Specimen 3, and Specimen 5, suffer less lateral flange bending than those with a larger h_w/b_f, Specimen 2, Specimen 4, Specimen 6, and Specimen 7. This can be seen by comparing the deflected shapes from the experiments.

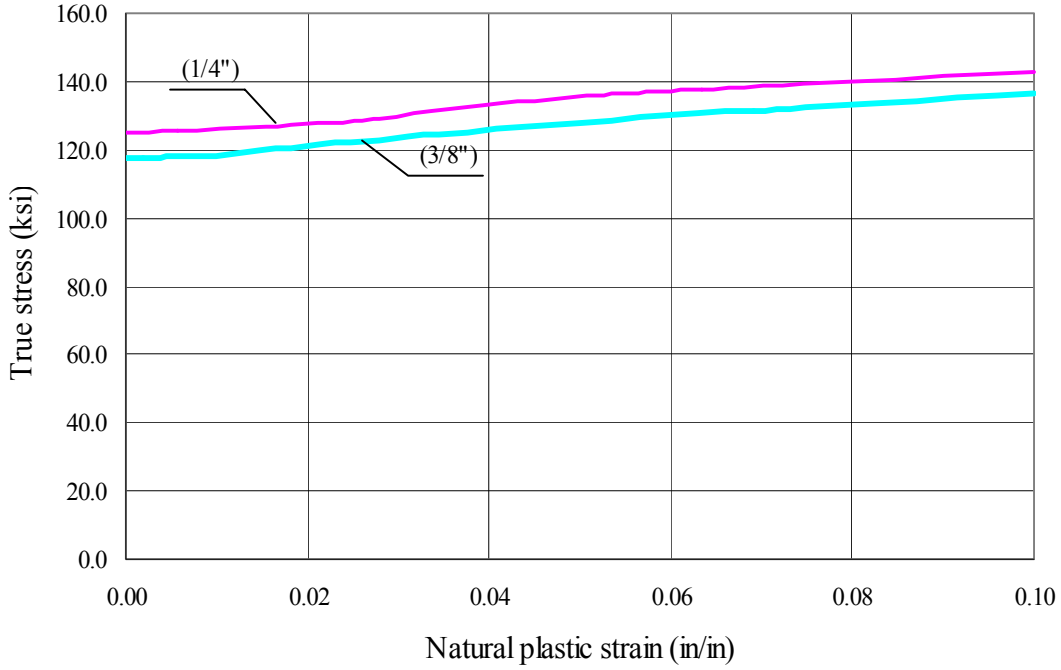

Figure 6.1 True stress versus natural plastic strain for web plates

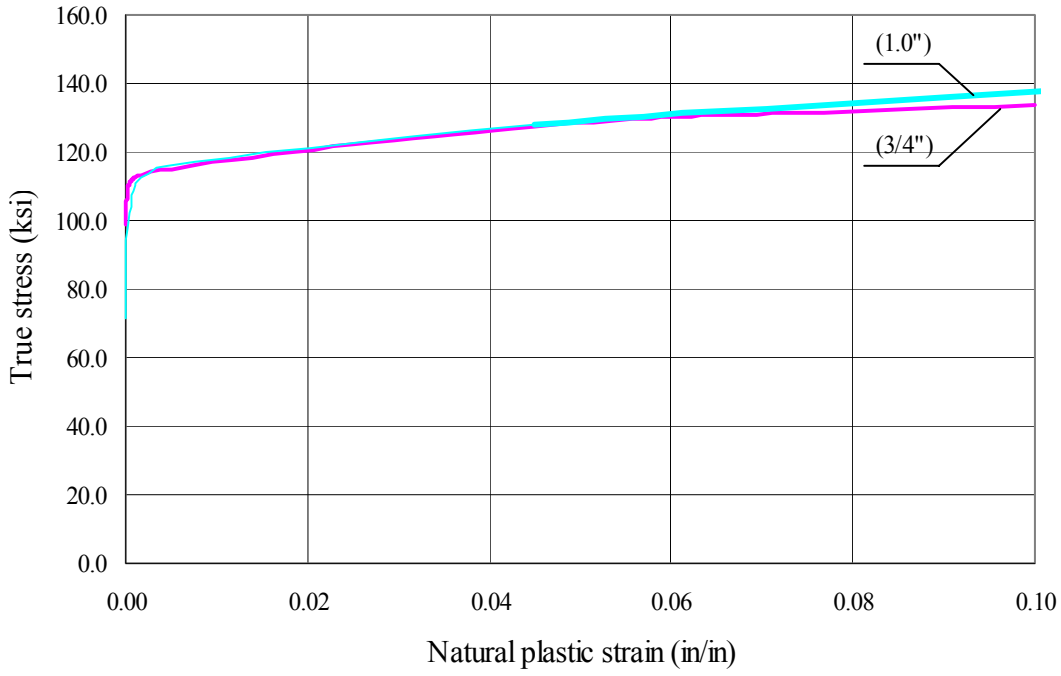

Figure 6.2 True stress versus natural plastic strain for flange plates

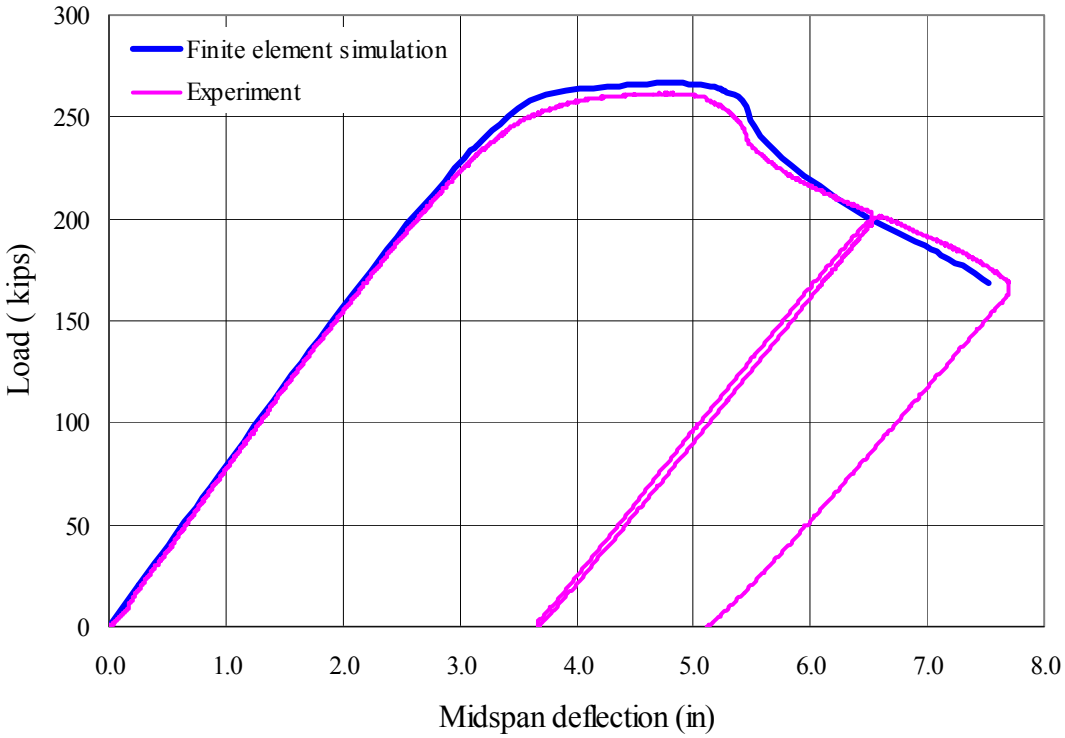

Figure 6.3 Load versus midspan vertical deflection (Specimen 3)

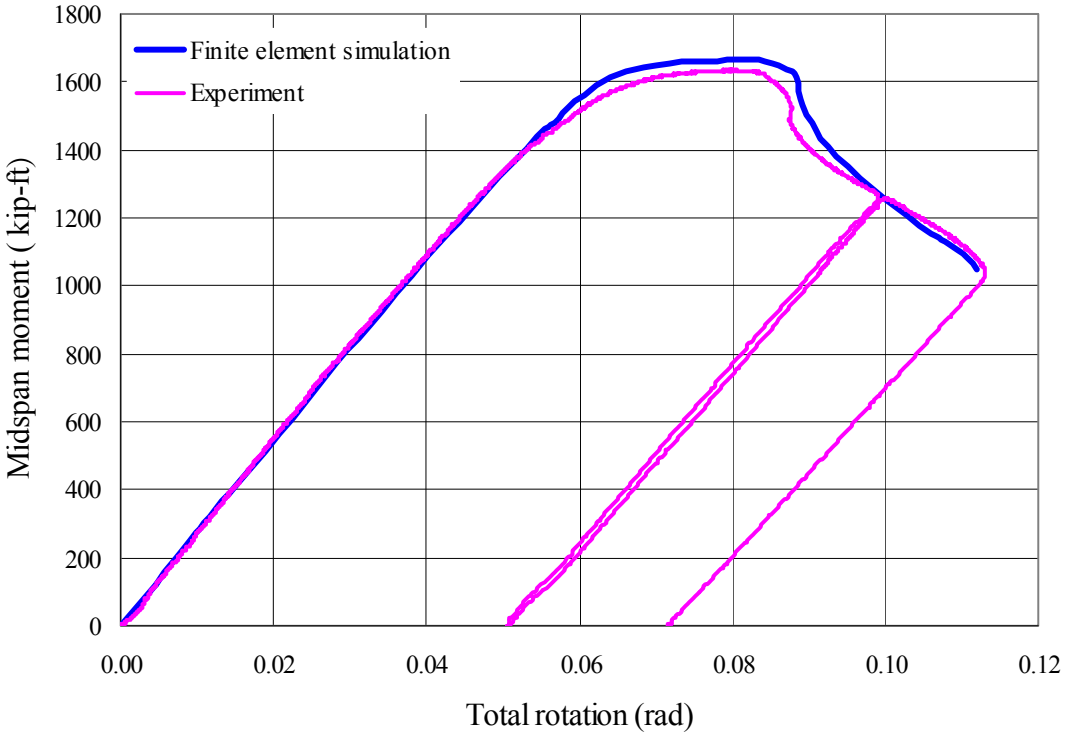

Figure 6.4 Midspan moment versus total rotation (Specimen 3)

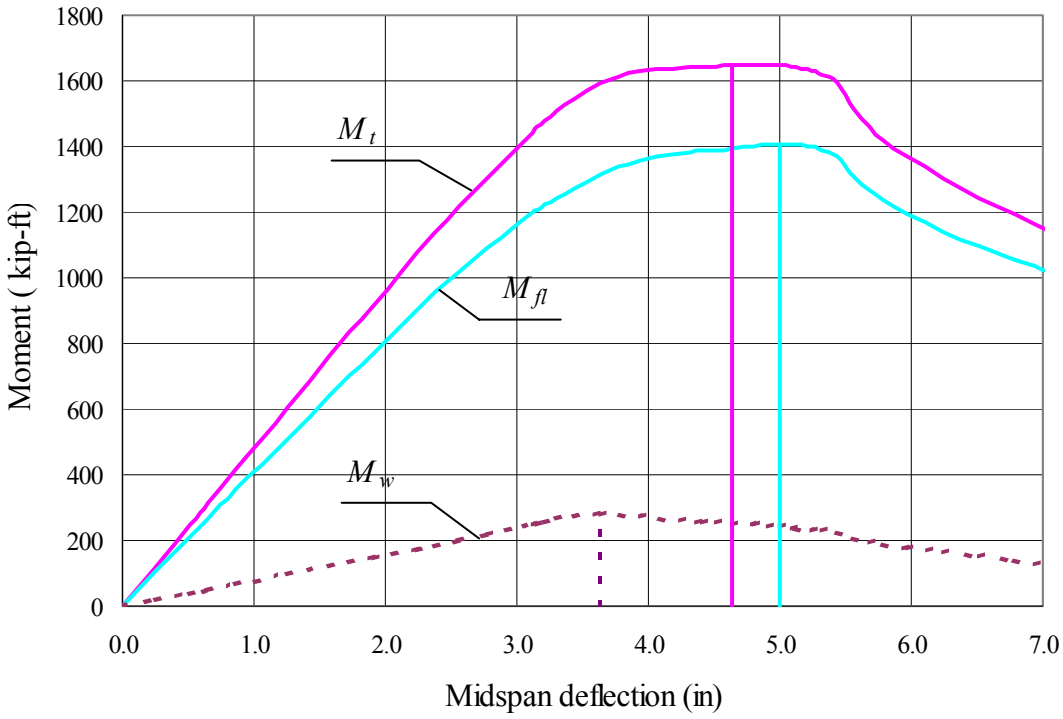

Figure 6.5 Moment components versus midspan vertical deflection (Specimen 3)

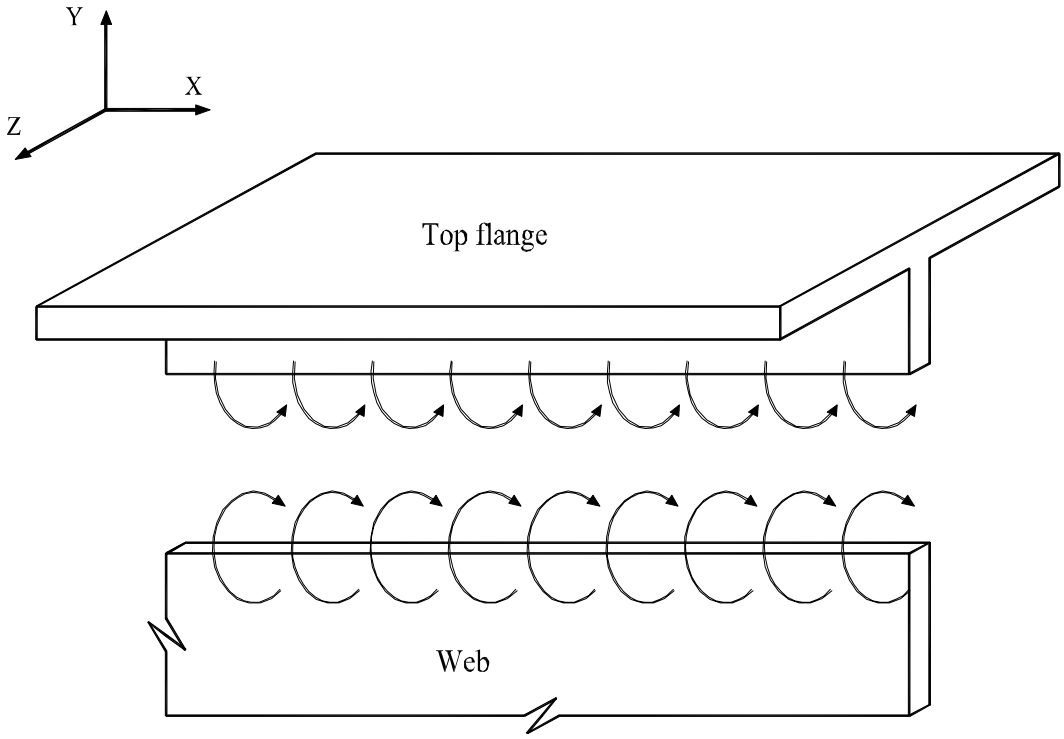

(a) Moment (*SM2*) transferred between web and top flange (positive sign)

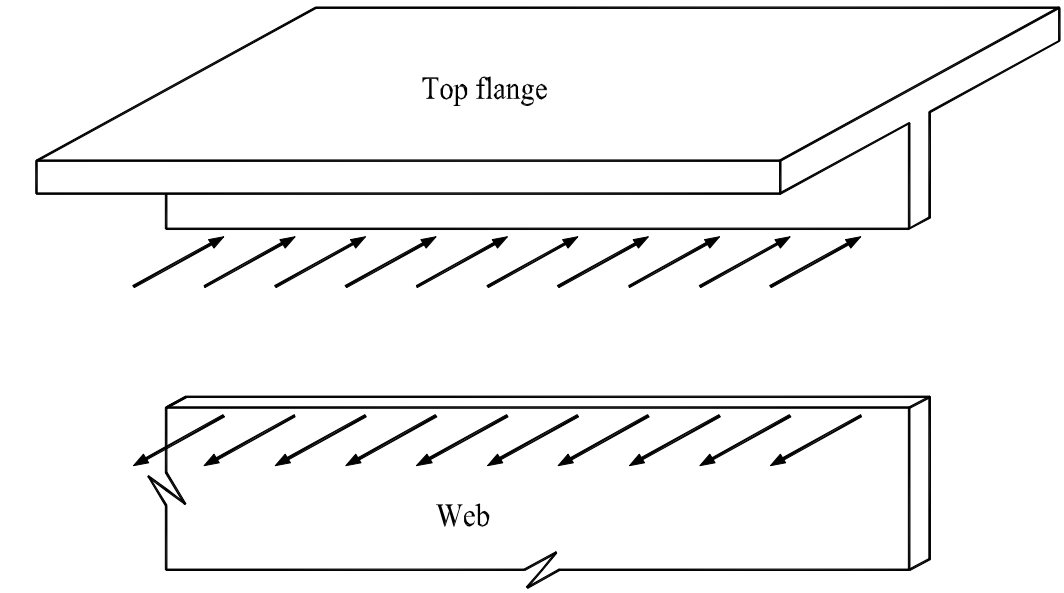

(b) Lateral force (*SF5*) transferred between web and top flange (positive sign)

Figure 6.6 Moment and lateral force transferred between web and top flange

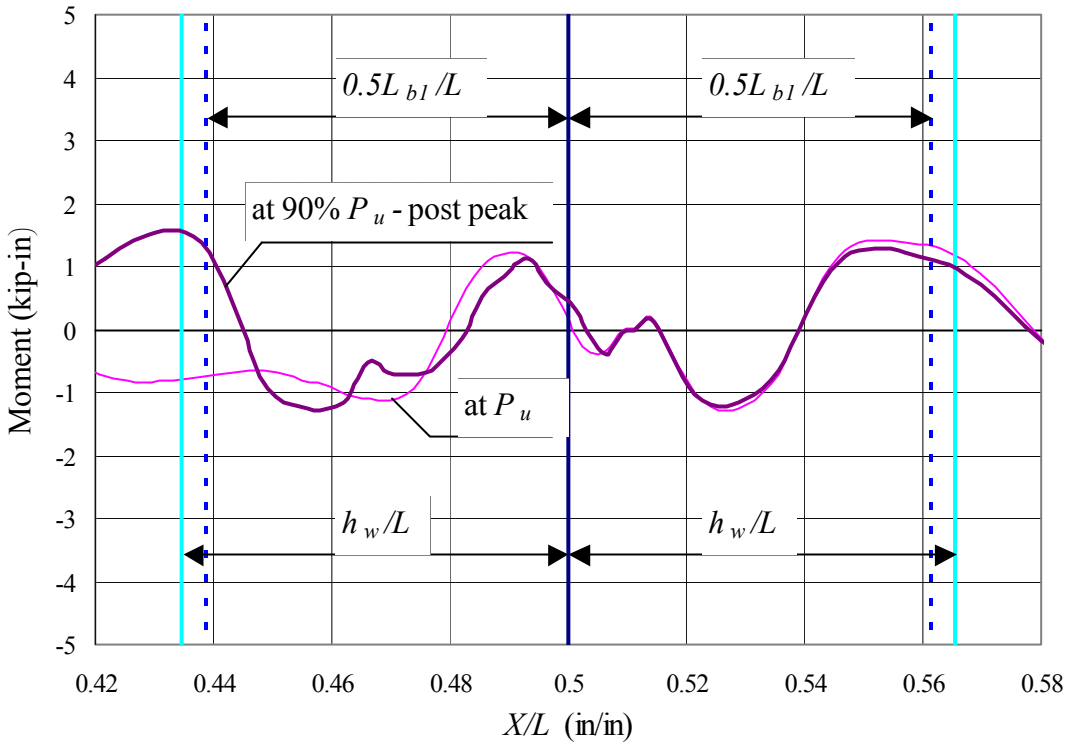

Figure 6.7 Moment (*SM2*) transferred between web and top flange (Specimen 3)

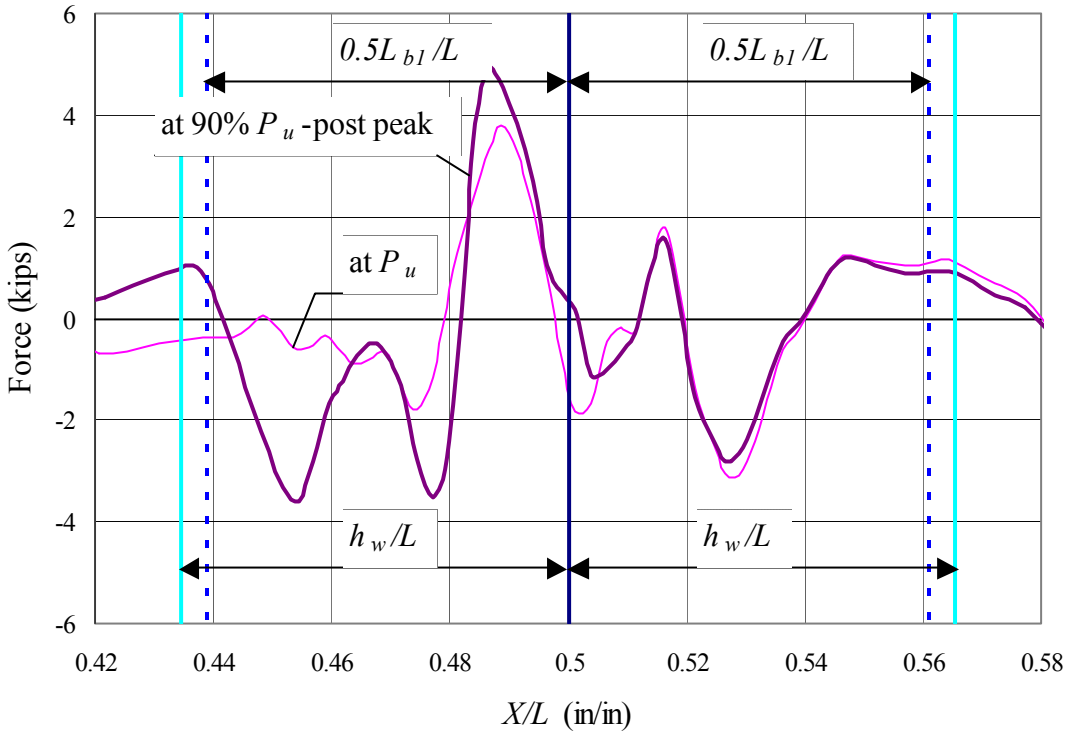

Figure 6.8 Lateral force (*SF5*) transferred between web and top flange (Specimen 3)

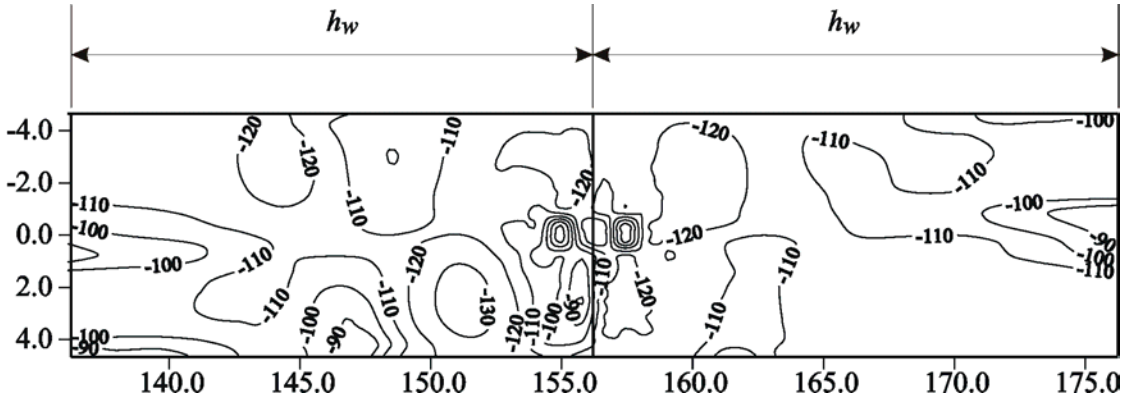

(a) Normal stress σ_{11} (ksi)

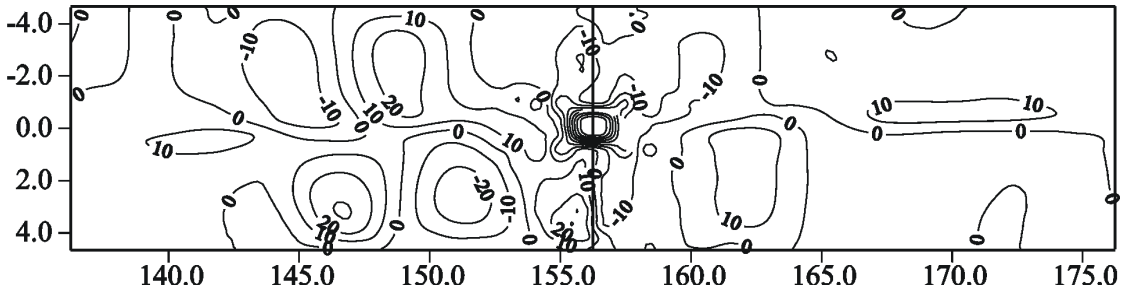

(b) Normal stress σ_{22} (ksi)

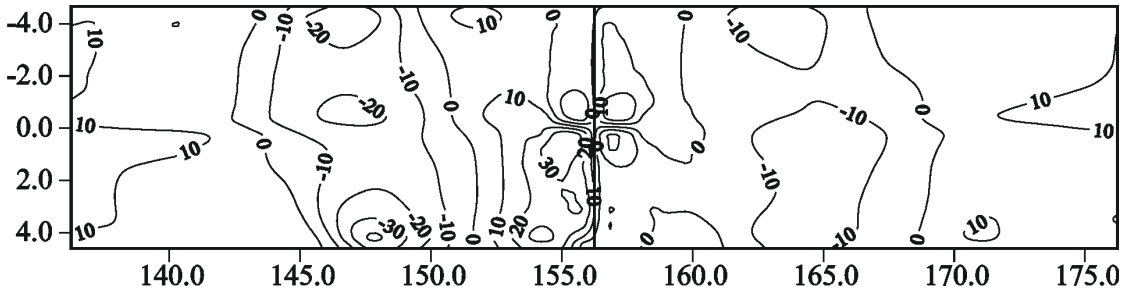

(c) Shear stress σ_{12} (ksi)

Figure 6.9 Top flange, upper surface, stress contours at P_u (Specimen 3)

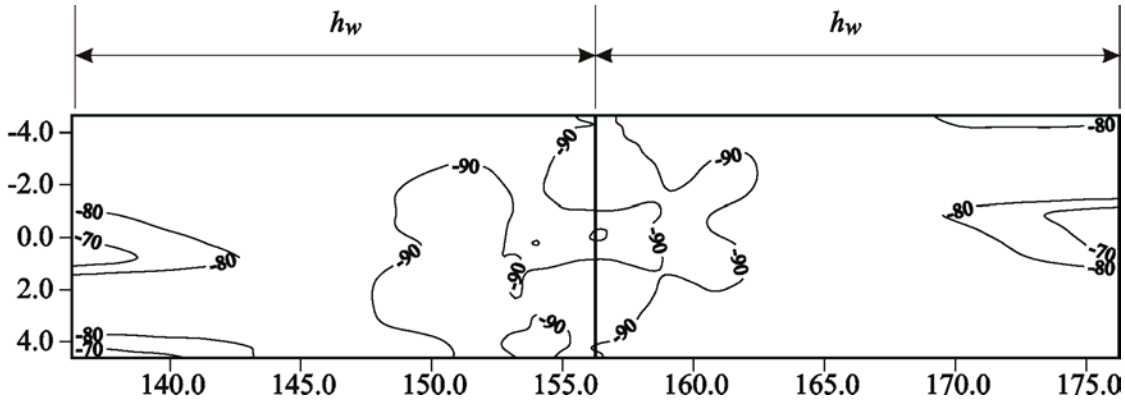

(a) Normal force *SF1* (kip/in)

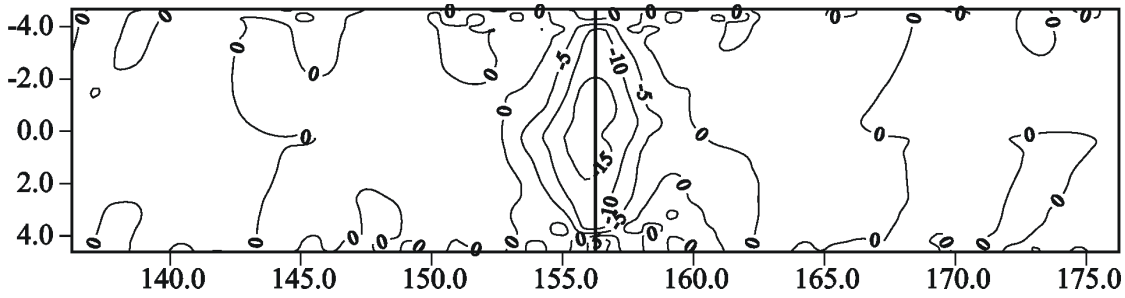

(b) Normal force *SF2* (kip/in)

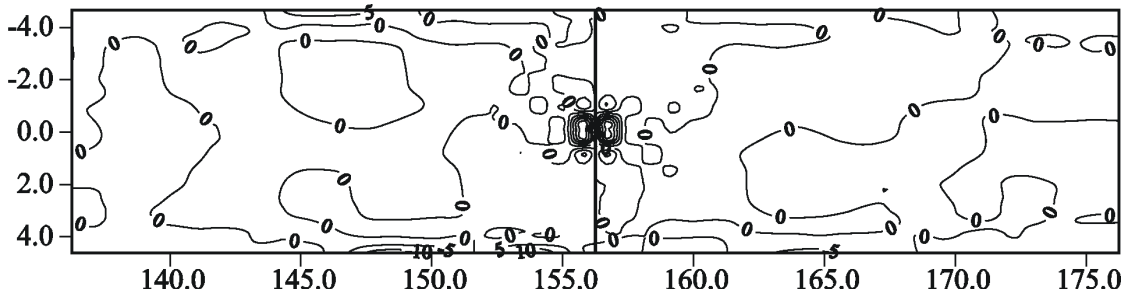

(c) Transverse force *SF4* (kip/in)

Figure 6.10 Top flange force contours at P_u (Specimen 3)

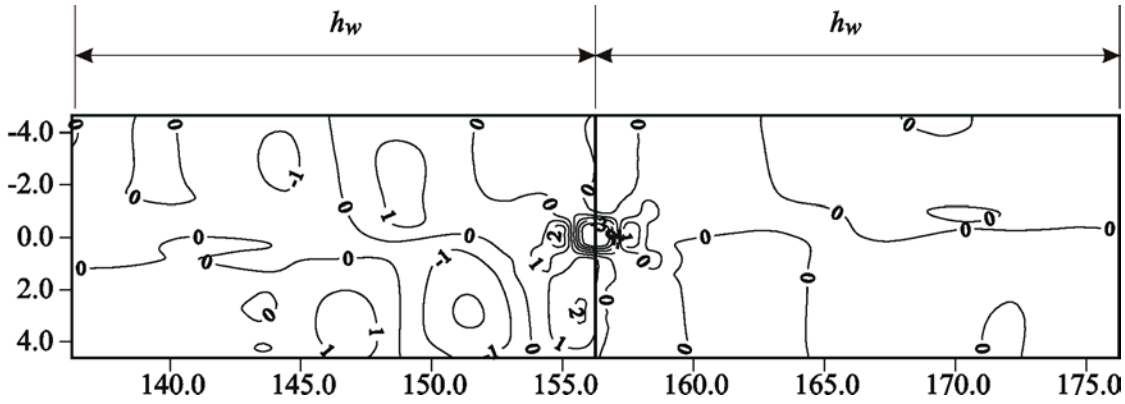

(a) Moment *SM1* (kip-in/in)

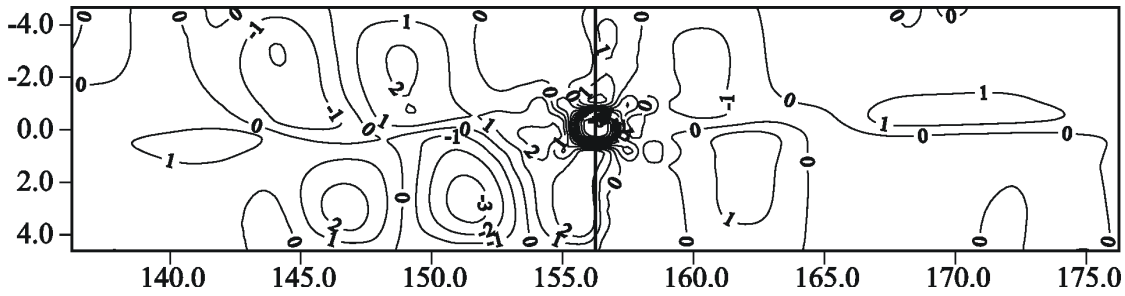

(b) Moment *SM2* (kip-in/in)

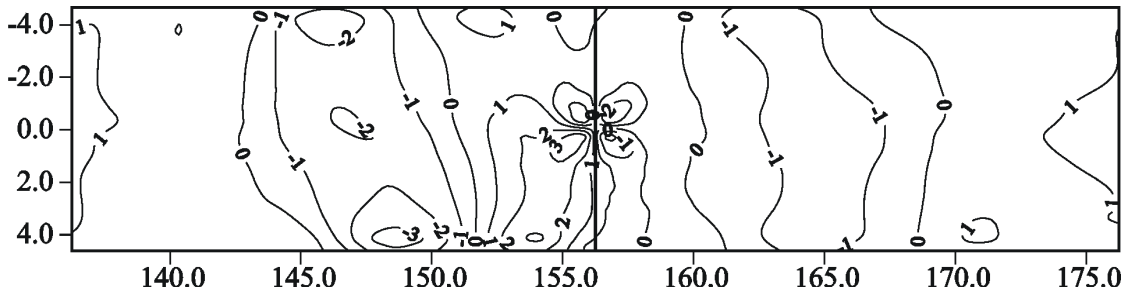

(c) Moment *SM3* (kip-in/in)

Figure 6.11 Top flange moment contours at P_u (Specimen 3)

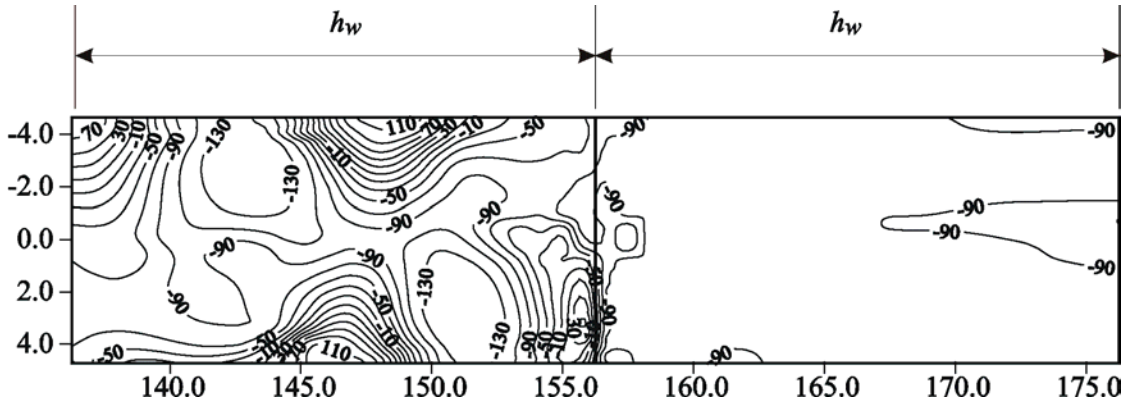

(a) Normal stress σ_{11} (ksi)

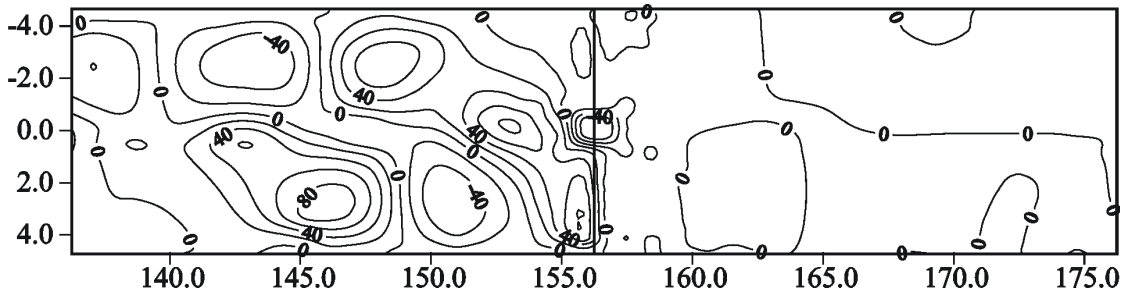

(b) Normal stress σ_{22} (ksi)

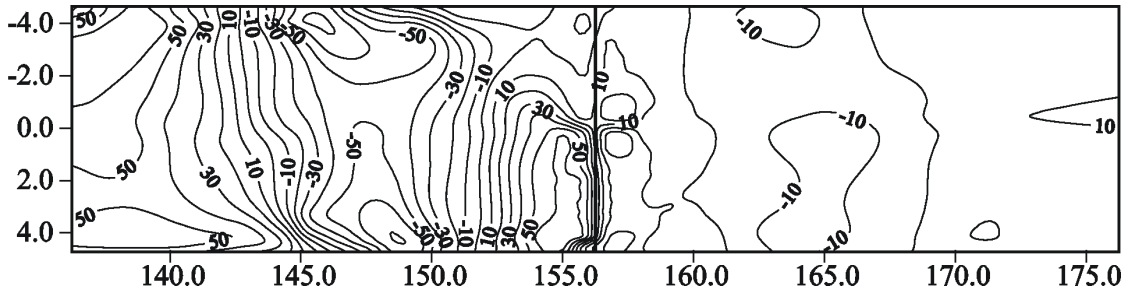

(c) Shear stress σ_{12} (ksi)

Figure 6.12 Top flange, upper surface, stress contours at 90% P_u-post peak (Specimen 3)

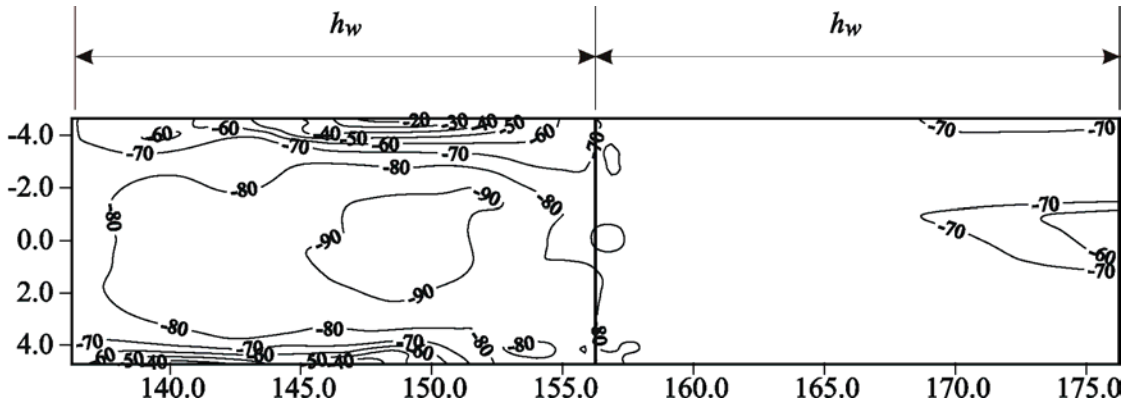

(a) Normal force *SF1* (kip/in)

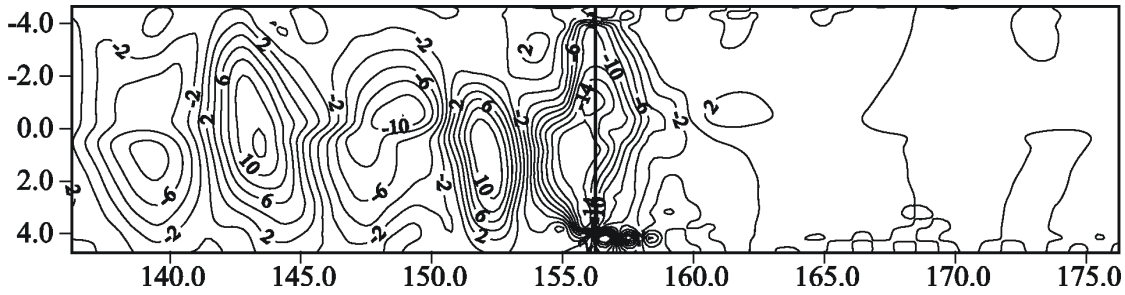

(b) Normal force *SF2* (kip/in)

A

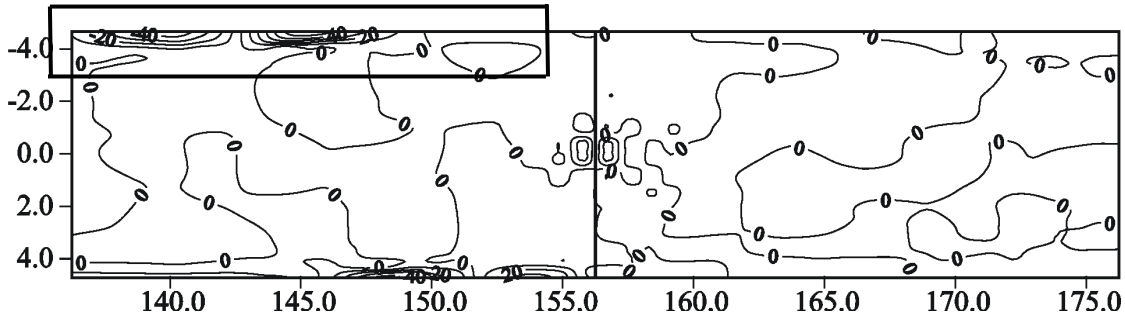

(c) Transverse force *SF4* (kip/in)

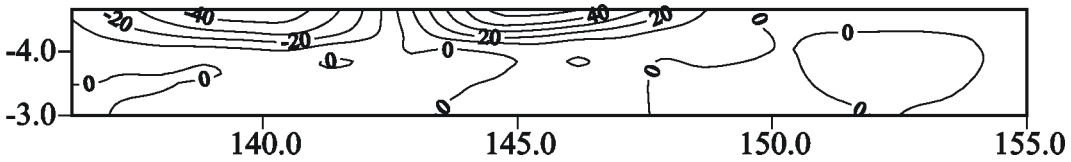

(d) Detail A

Figure 6.13 Top flange force contours at 90% P_u-post peak (Specimen 3)

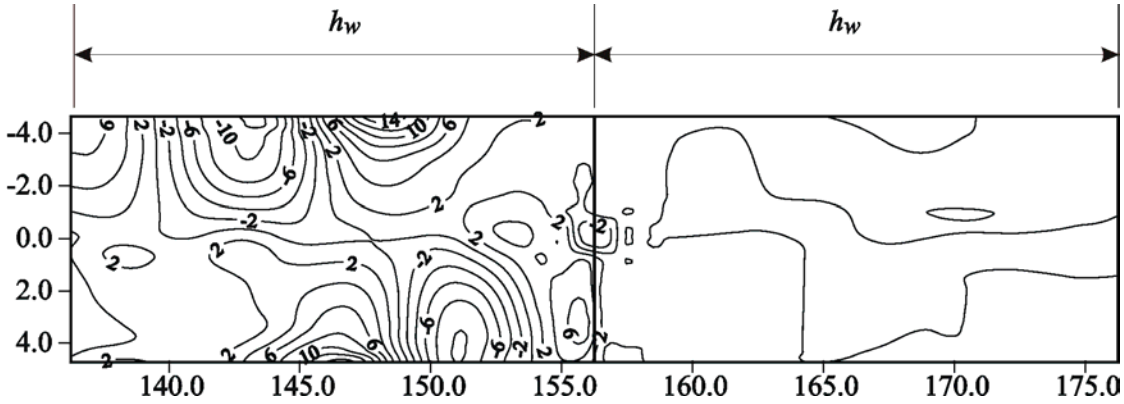

(a) Moment *SM1* (kip-in/in)

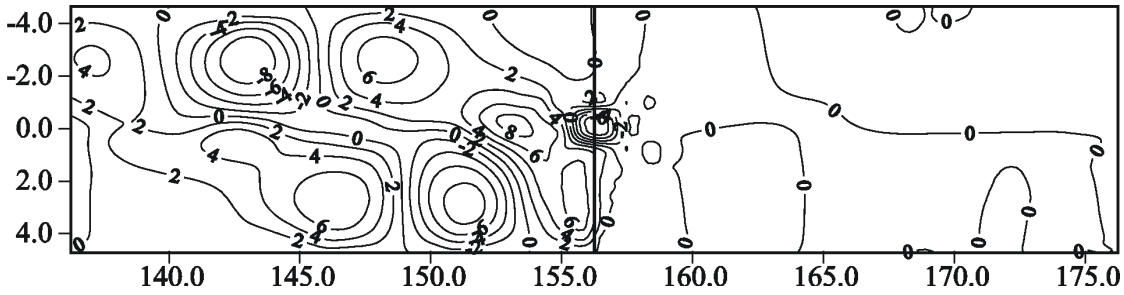

(b) Moment *SM2* (kip-in/in)

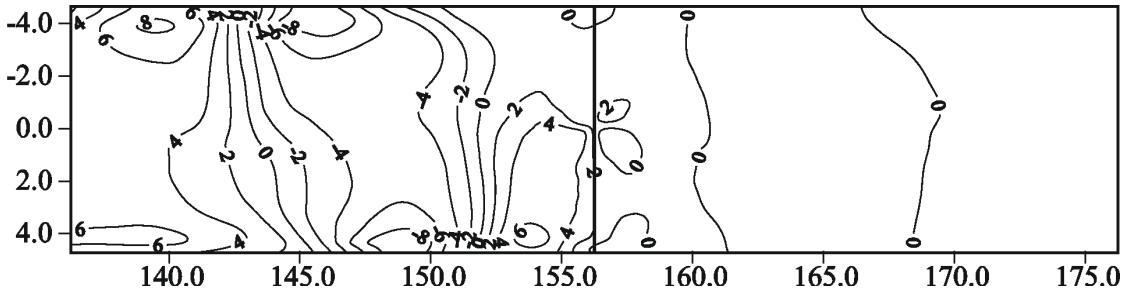

(c) Moment *SM3* (kip-in/in)

Figure 6.14 Top flange moment contours at 90% P_u-post peak (Specimen 3)

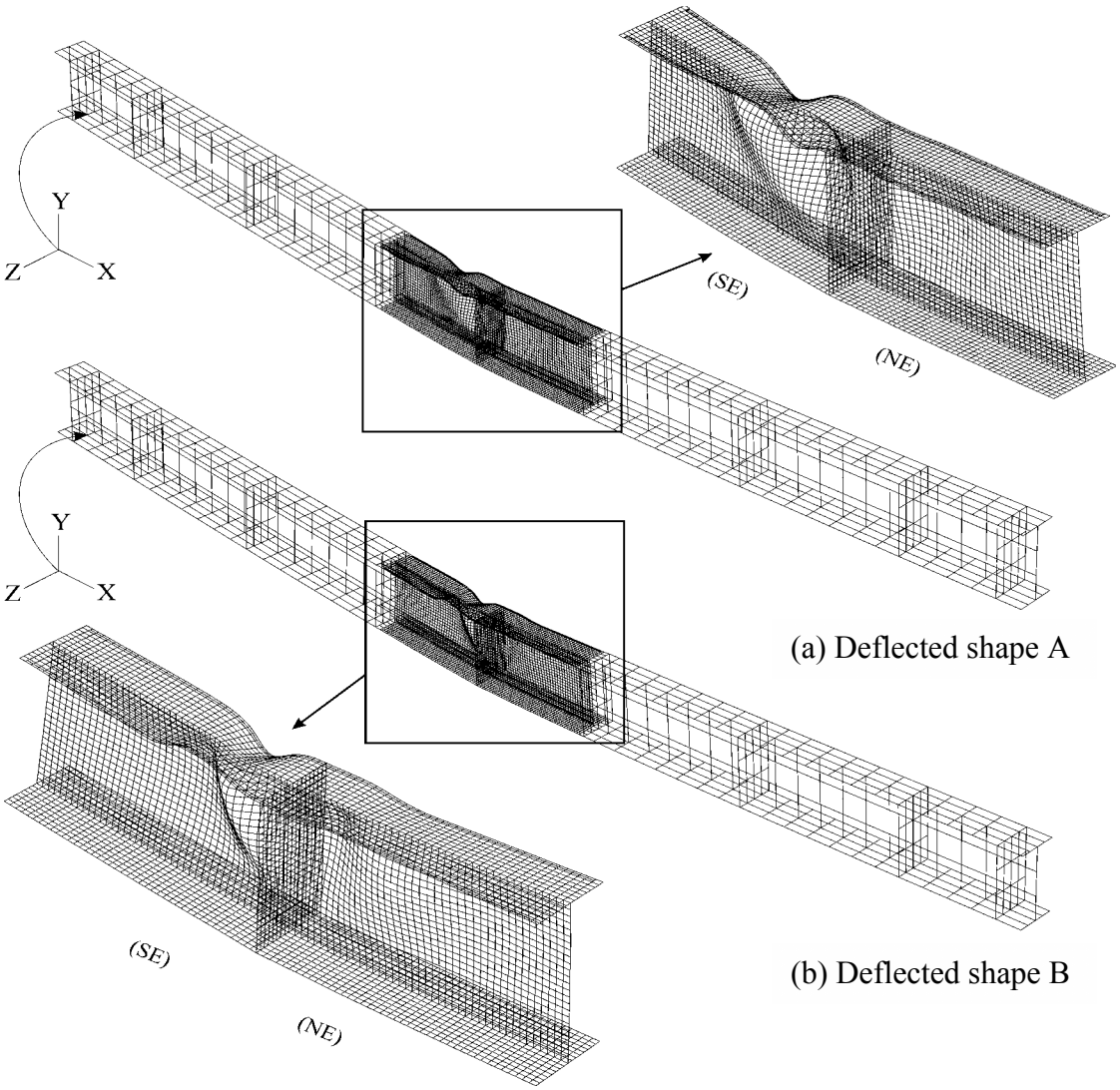

(c) Deflected shape from experiment

Figure 6.15 Deflected shape using different imperfections (at 90% P_u-post peak) and deflected shape from experiment (Specimen 3)

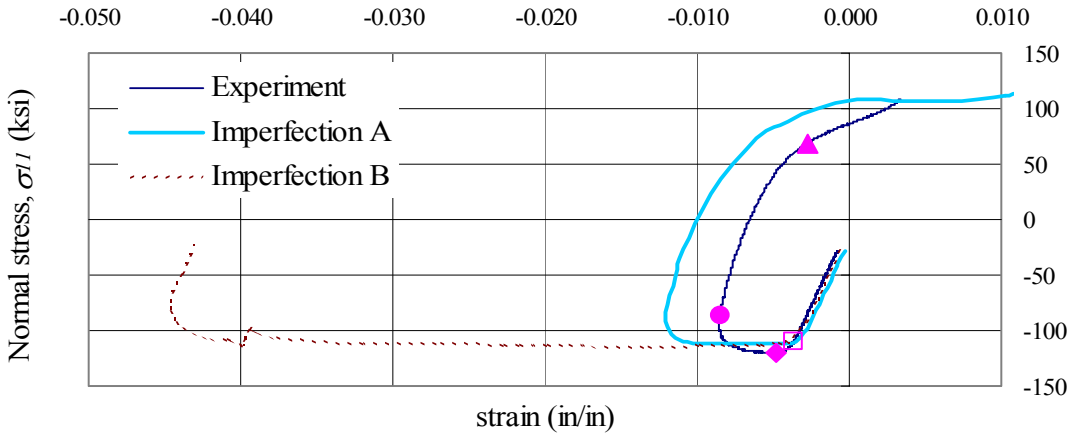

(a) Normal strain, ε_{11}

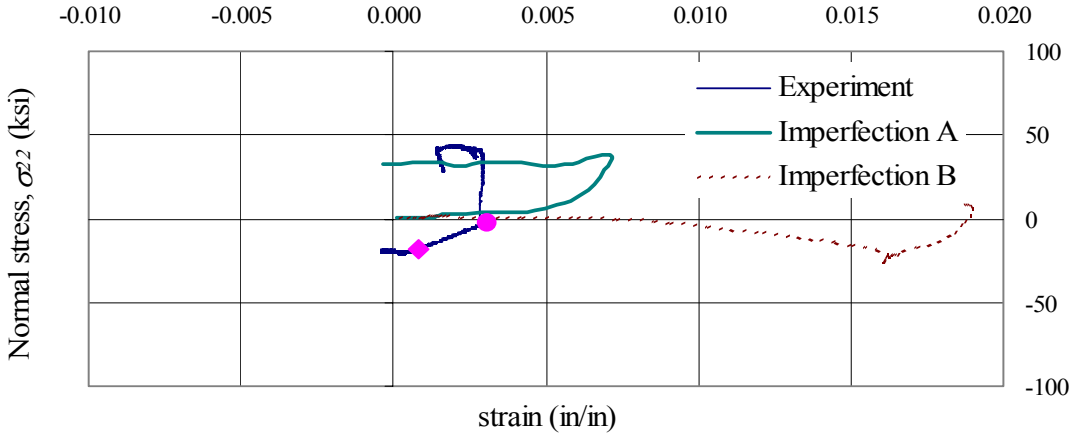

(b) Normal strain, ε_{22}

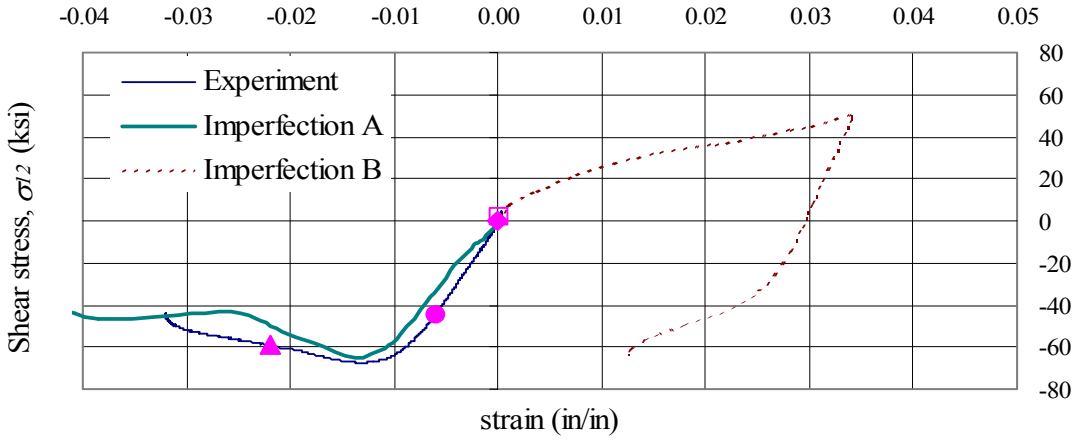

(c) Engineering shear strain, γ_{12}

Figure 6.16 Stress versus strain for different imperfections (section 2-West, Specimen 3)

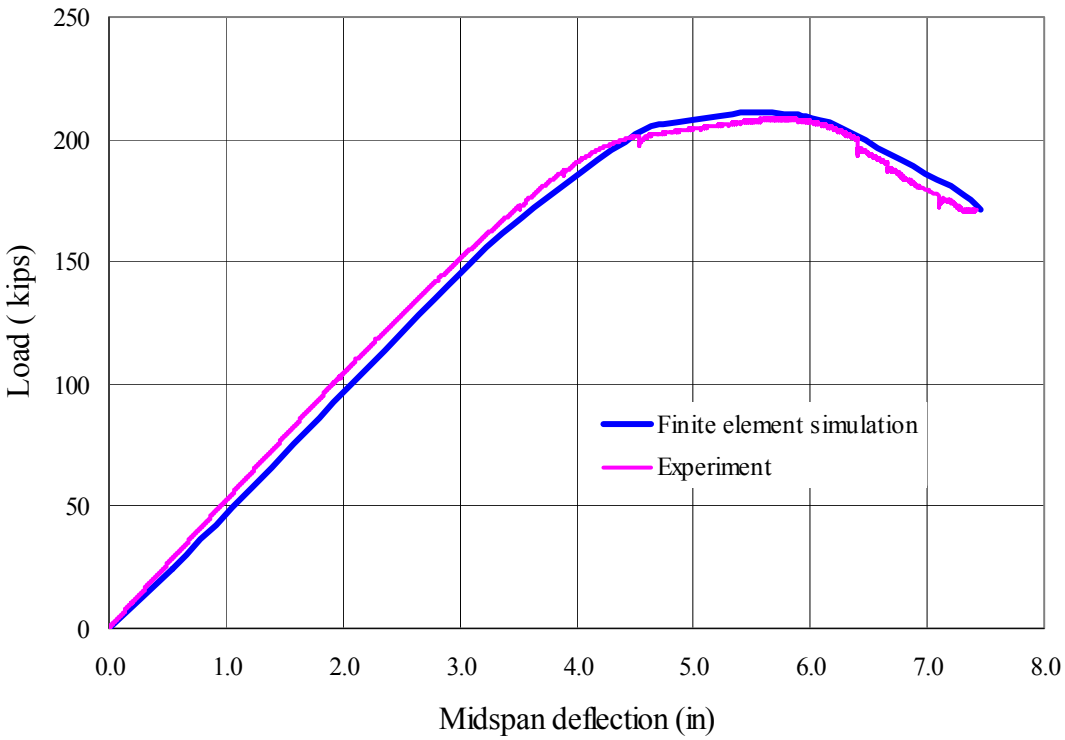

Figure 6.17 Load versus midspan vertical deflection (Specimen 4)

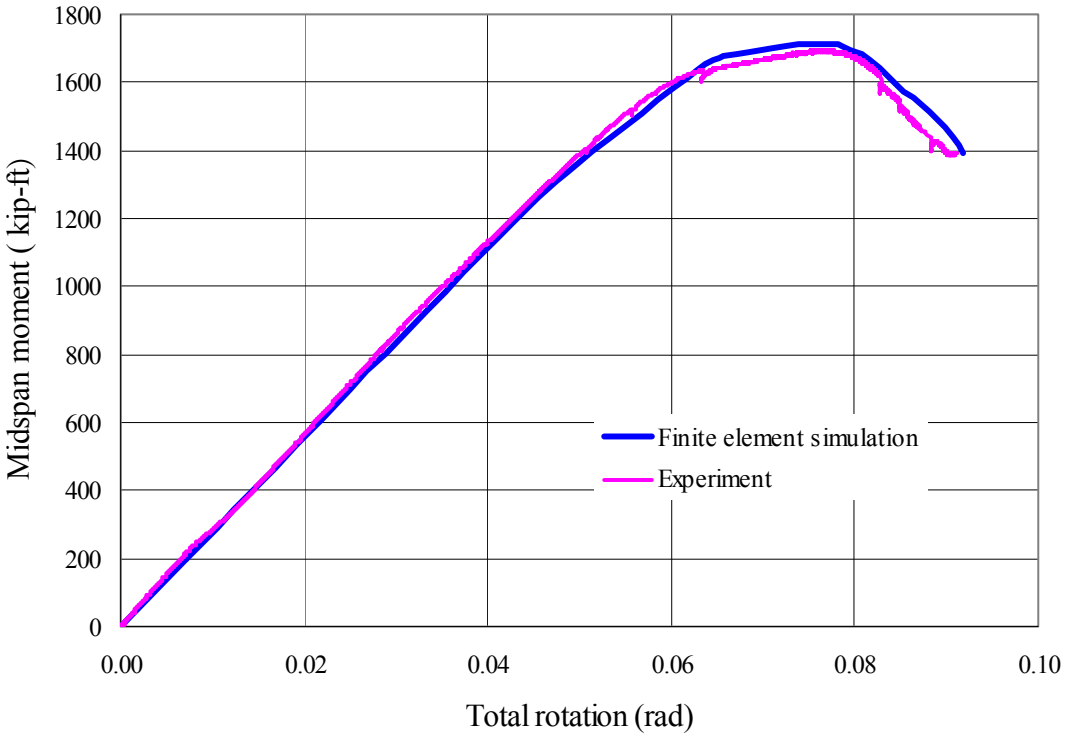

Figure 6.18 Midspan moment versus total rotation (Specimen 4)

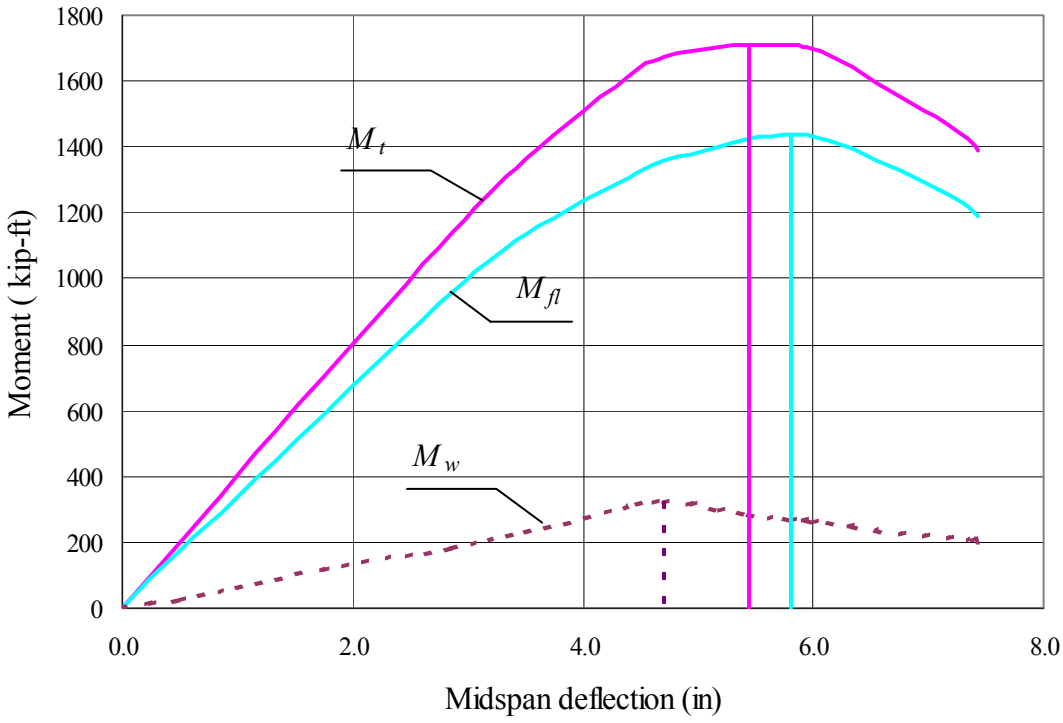

Figure 6.19 Moment components versus midspan vertical deflection (Specimen 4)

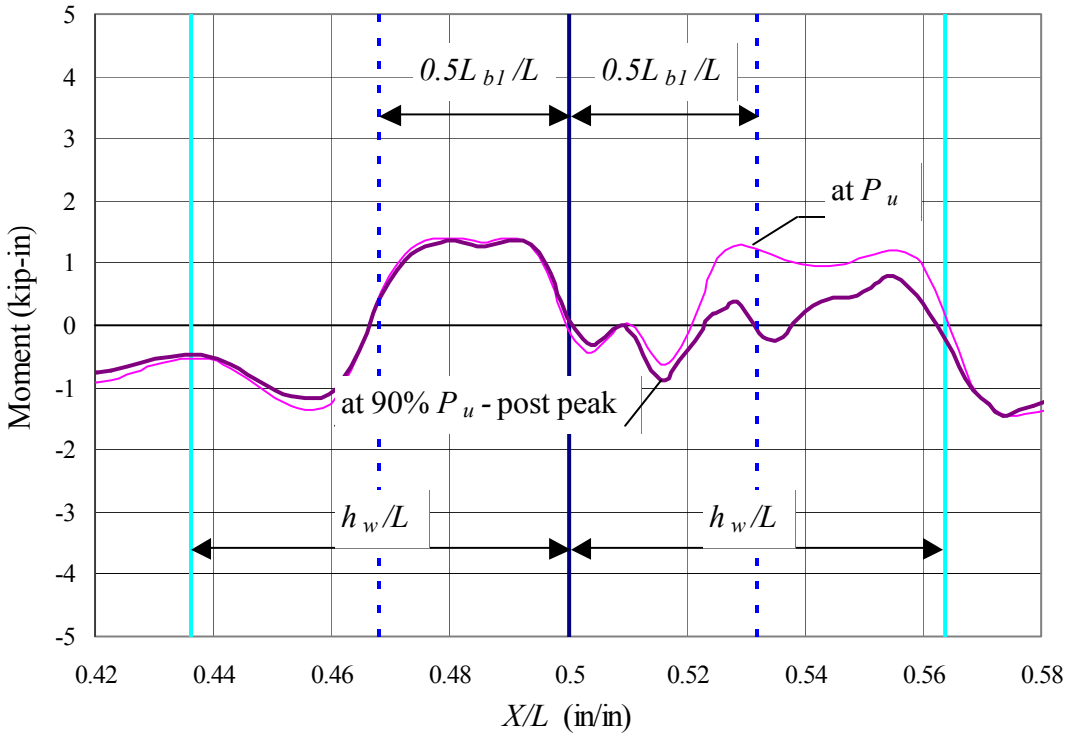

Figure 6.20 Moment (*SM2*) transferred between web and top flange (Specimen 4)

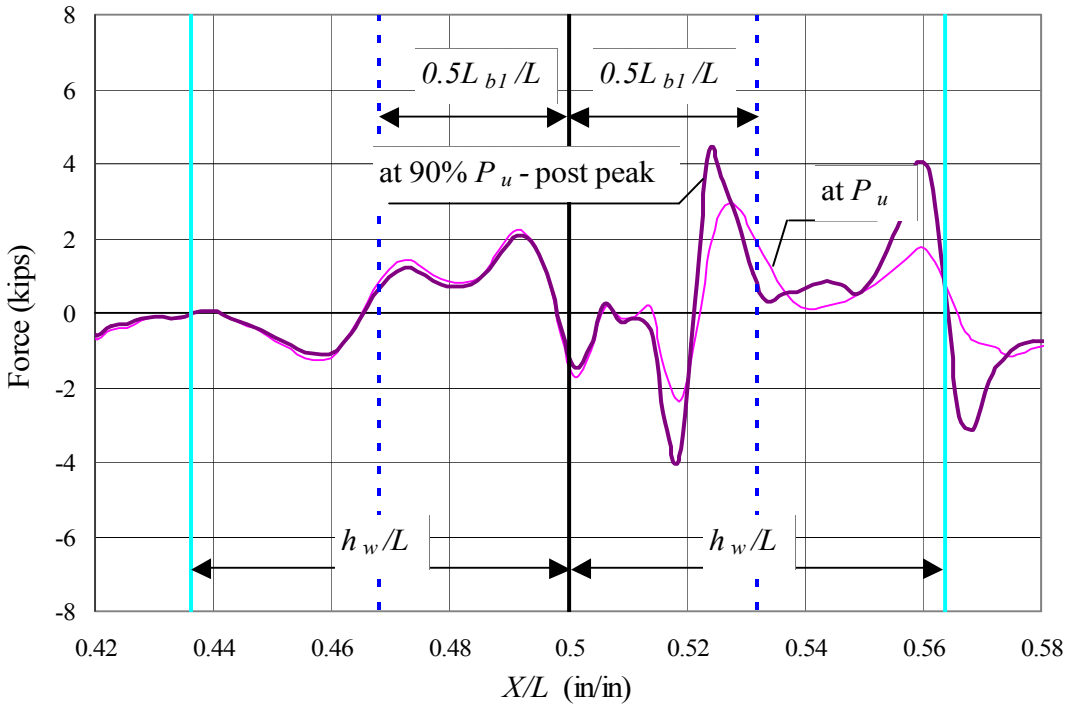

Figure 6.21 Lateral force (*SF5*) transferred between web and top flange (Specimen 4)

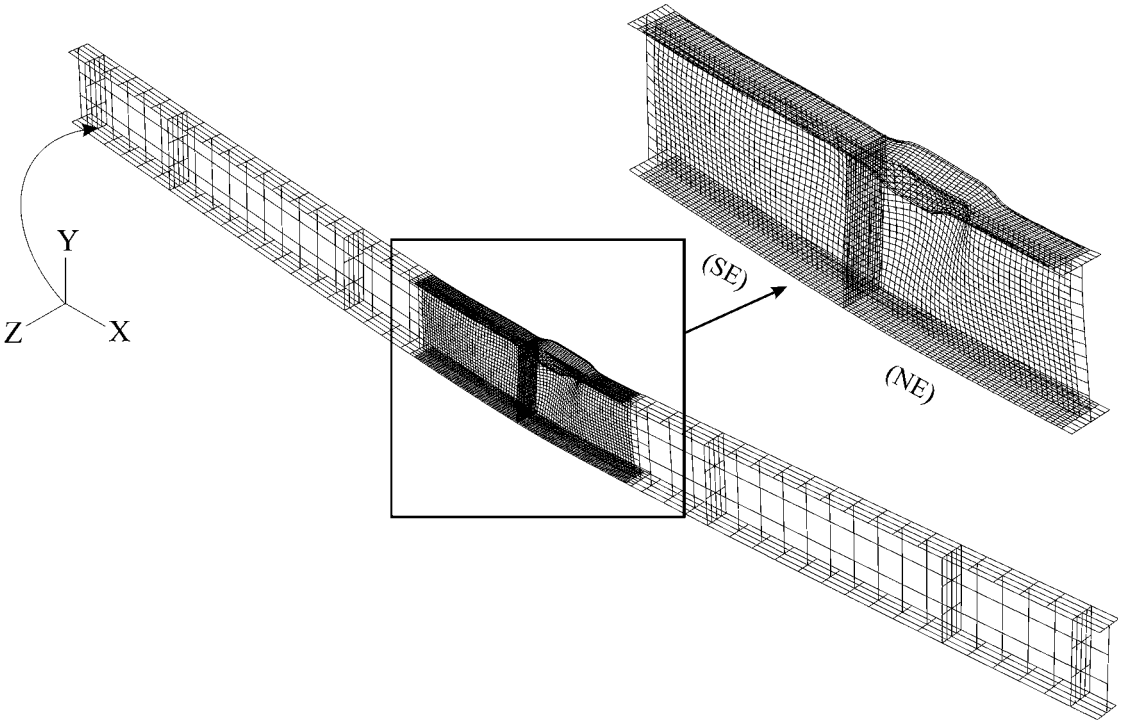

(a) Deflected shape (at 90% P_u-post peak)

(b) Deflected shape from experiment

Figure 6.22 Deflected shape at 90% P_u-post peak and deflected shape from experiment (Specimen 4)

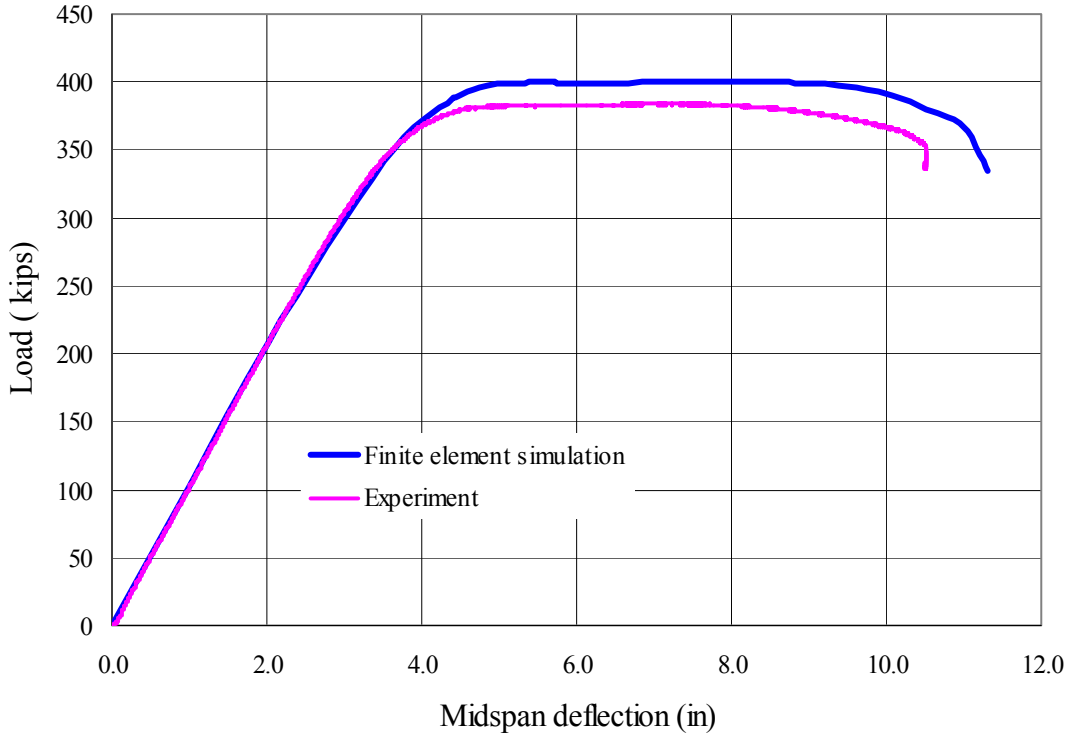

Figure 6.23 Load versus midspan vertical deflection (Specimen 5)

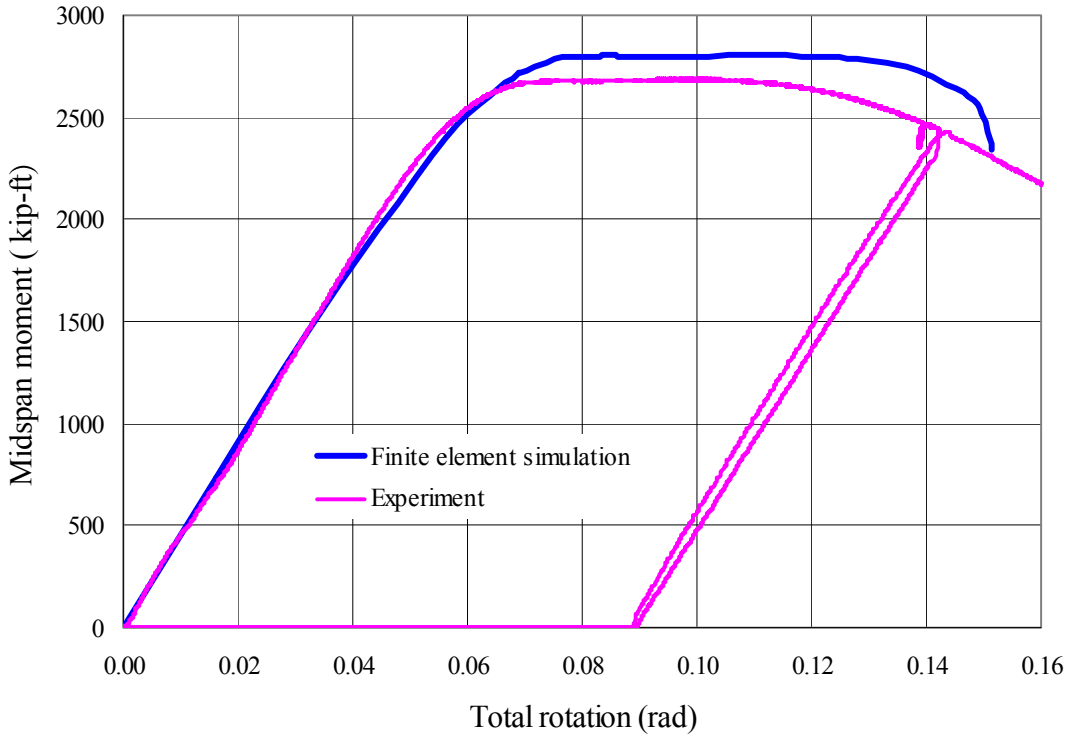

Figure 6.24 Midspan moment versus total rotation (Specimen 5)

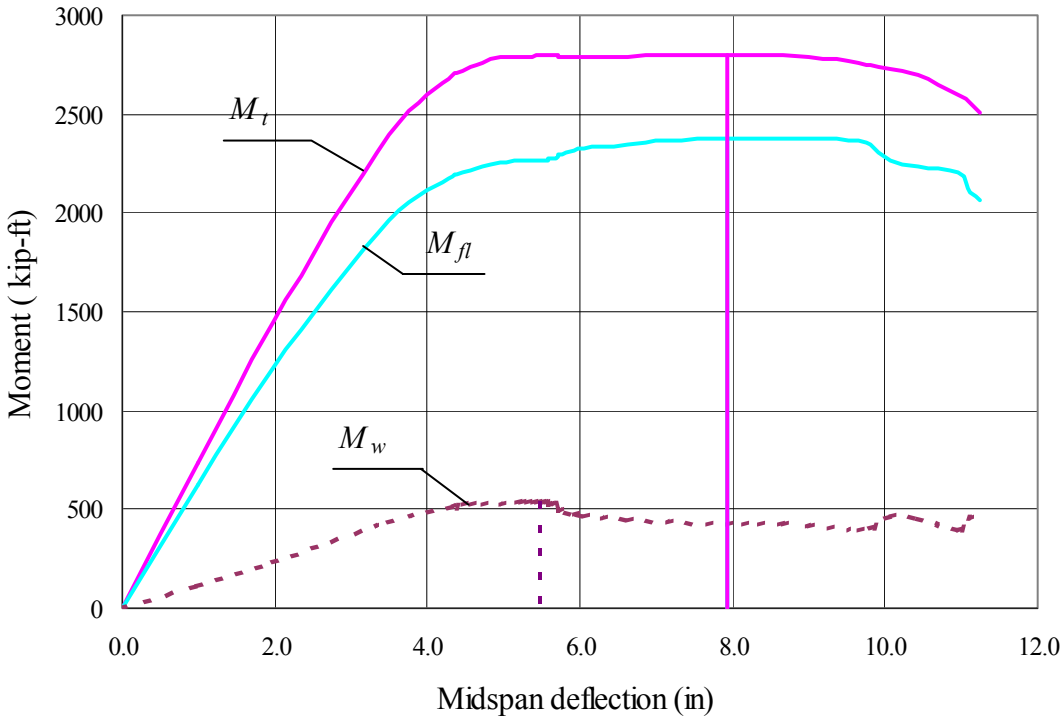

Figure 6.25 Moment components versus midspan vertical deflection (Specimen 5)

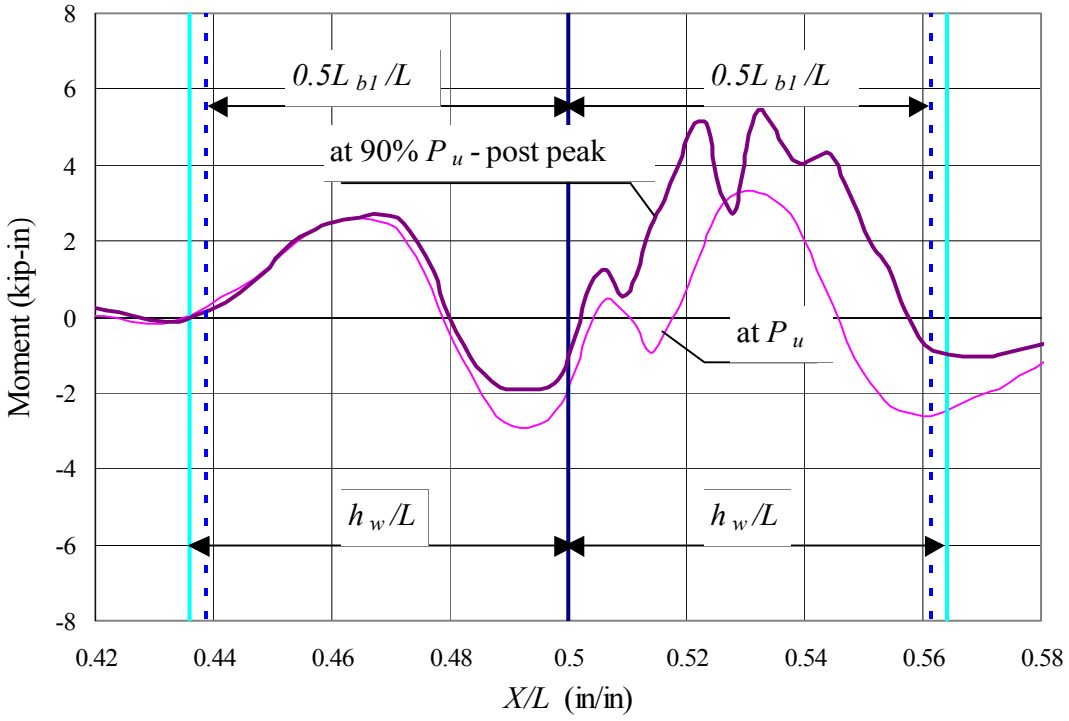

Figure 6.26 Moment (*SM2*) transferred between web and top flange (Specimen 5)

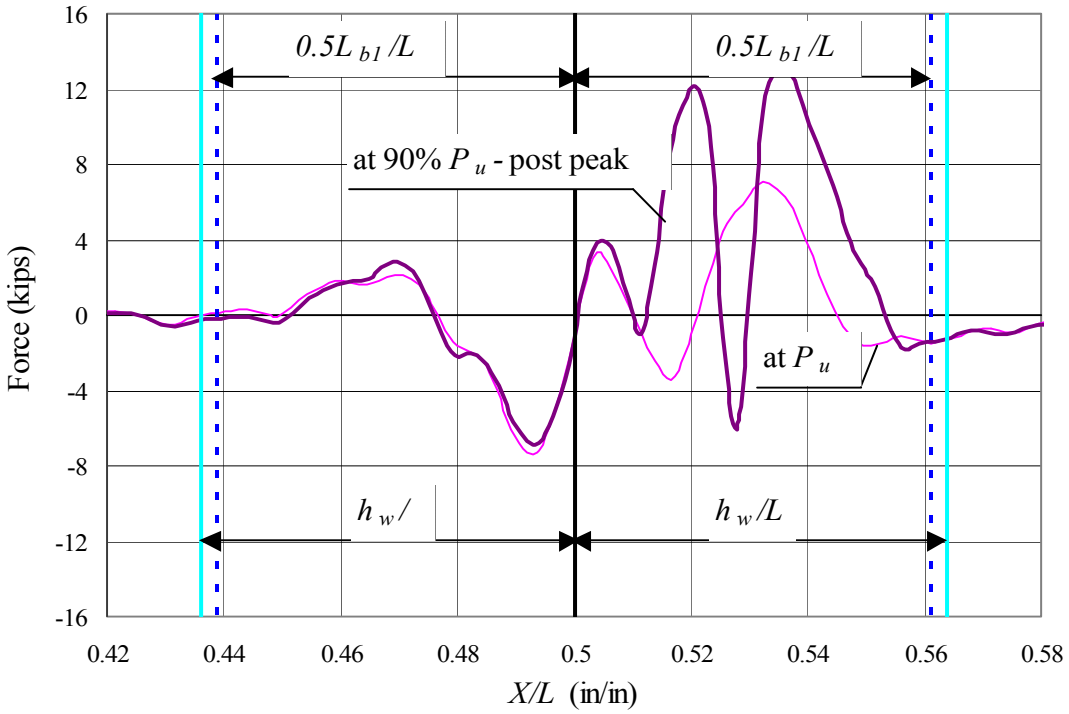

Figure 6.27 Lateral force (*SF5*) transferred between web and top flange (Specimen 5)

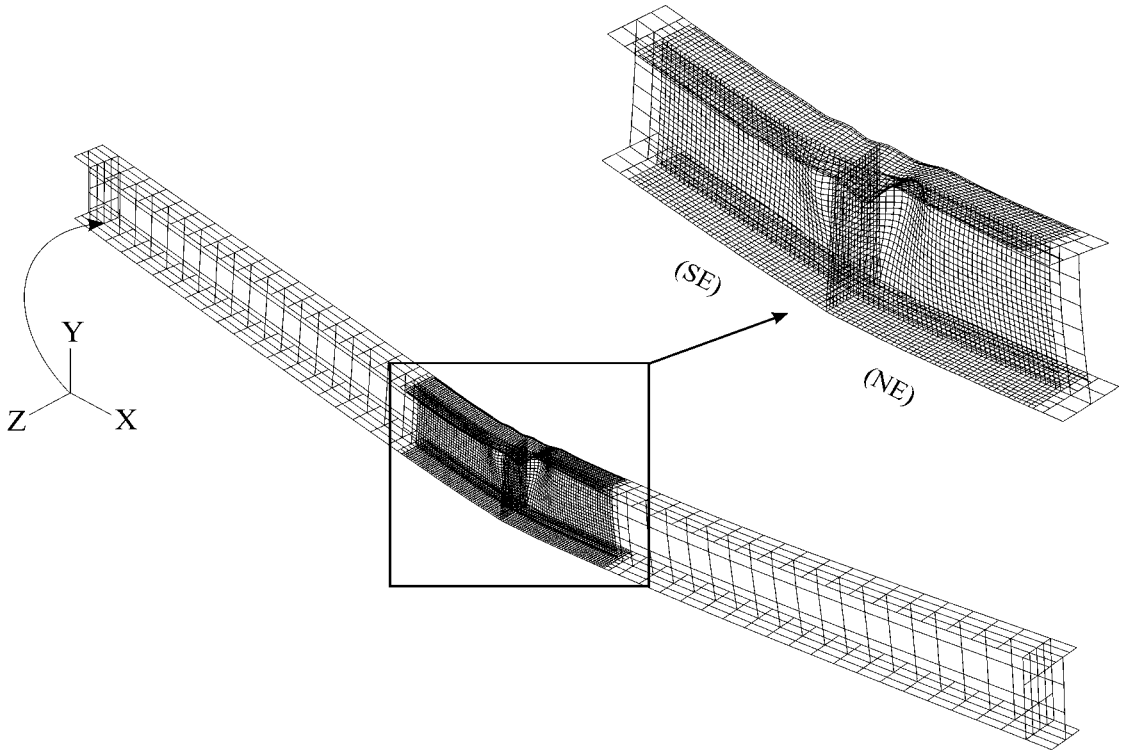

(a) Deflected shape (at 90% P_u-post peak)

(b) Deflected shape from experiment

Figure 6.28 Deflected shape at 90% P_u-post peak and deflected shape from experiment (Specimen 5)

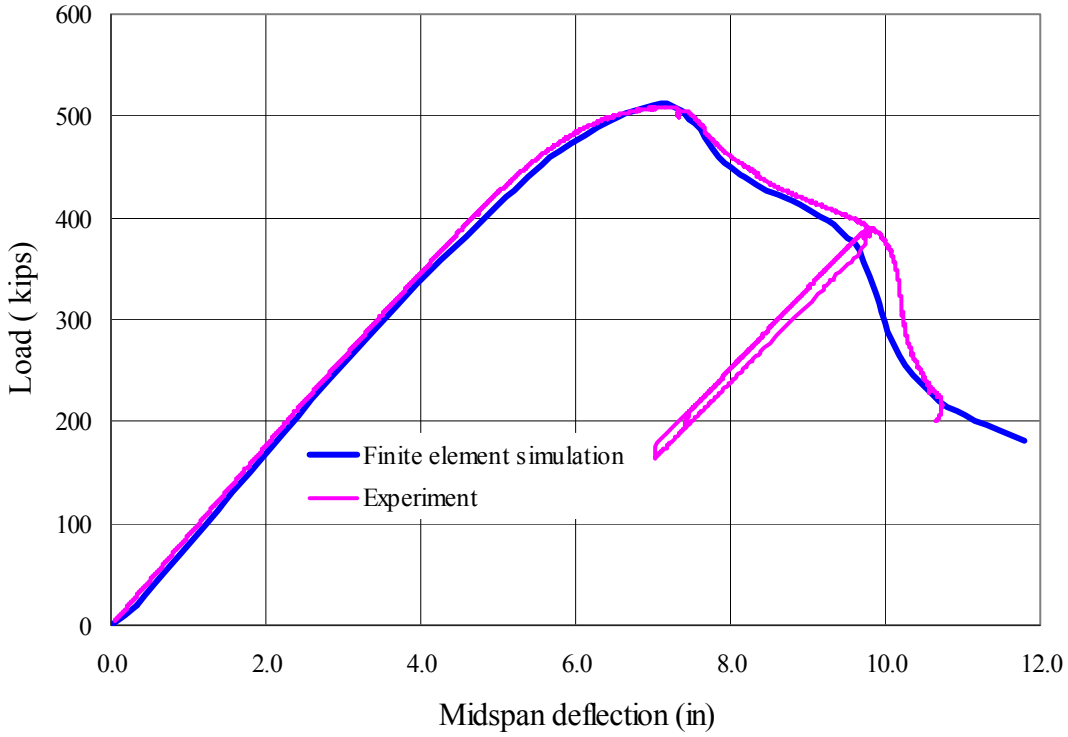

Figure 6.29 Load versus midspan vertical deflection (Specimen 6)

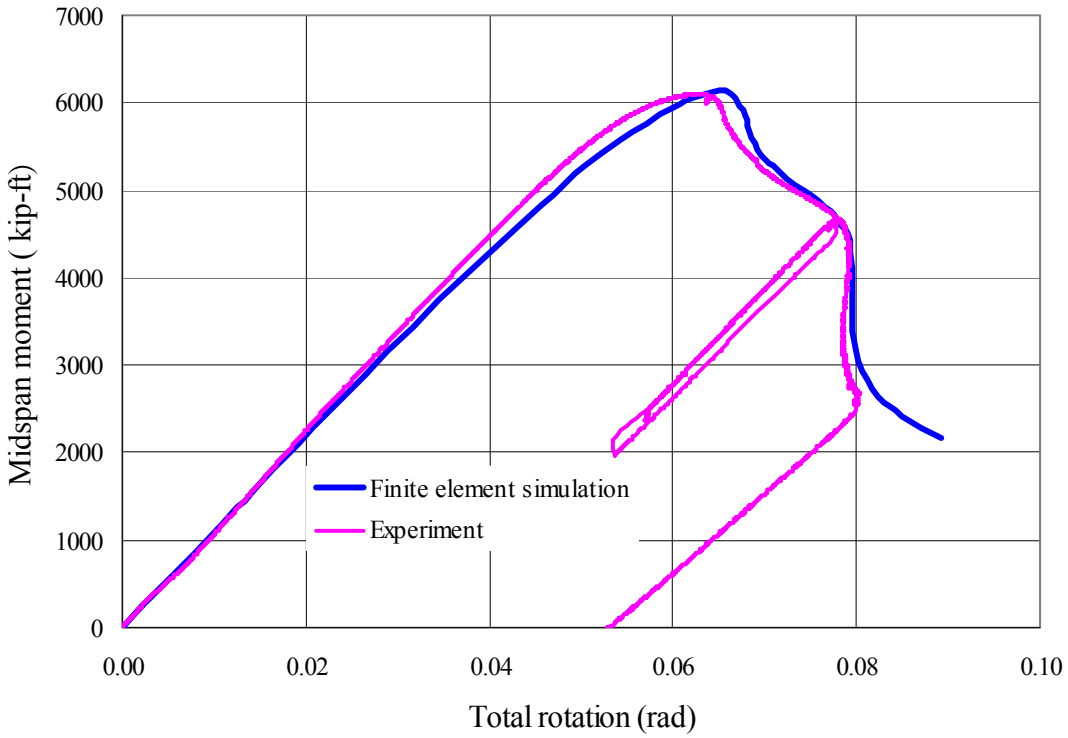

Figure 6.30 Midspan moment versus total rotation (Specimen 6)

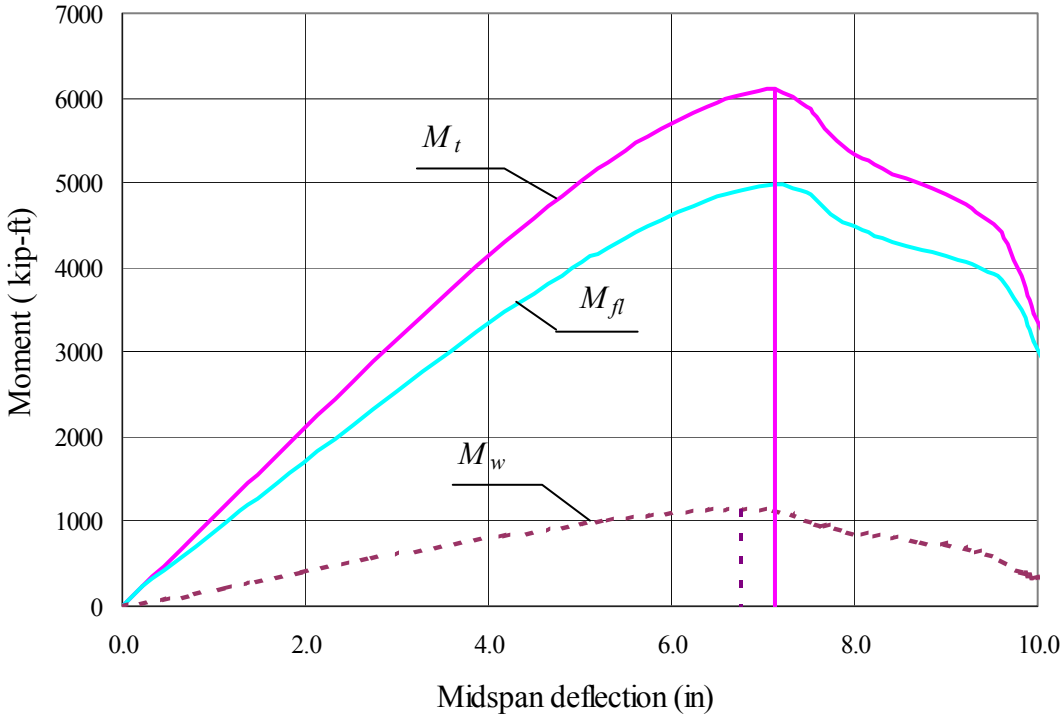

Figure 6.31 Moment components versus midspan vertical deflection (Specimen 6)

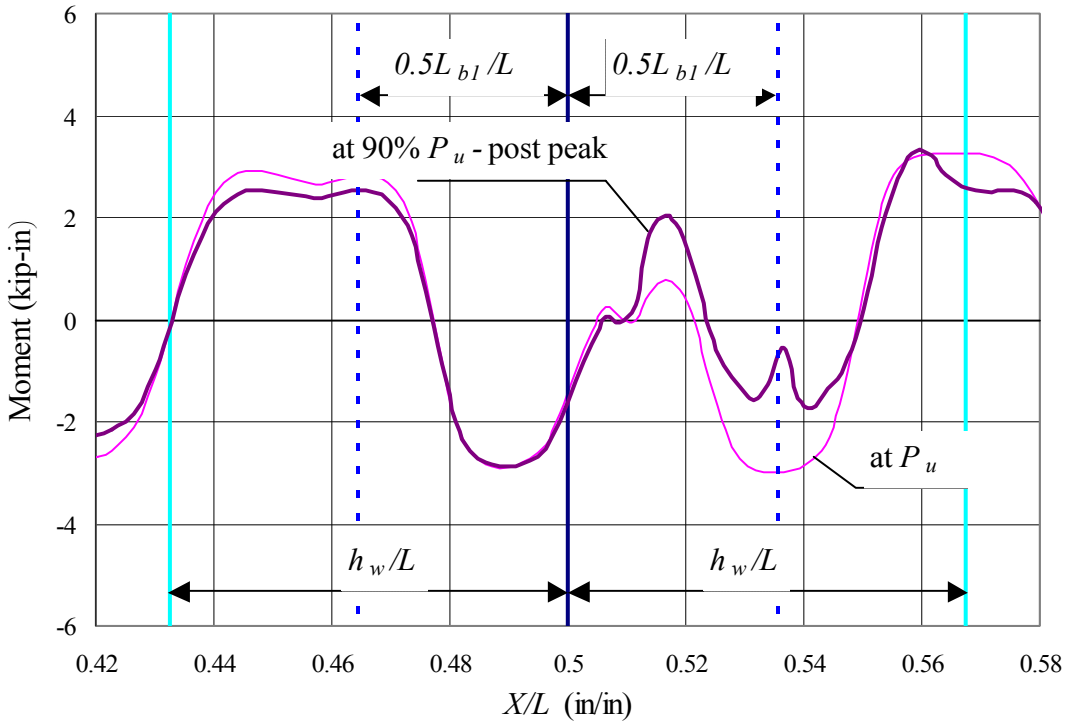

Figure 6.32 Moment (*SM2*) transferred between web and top flange (Specimen 6)

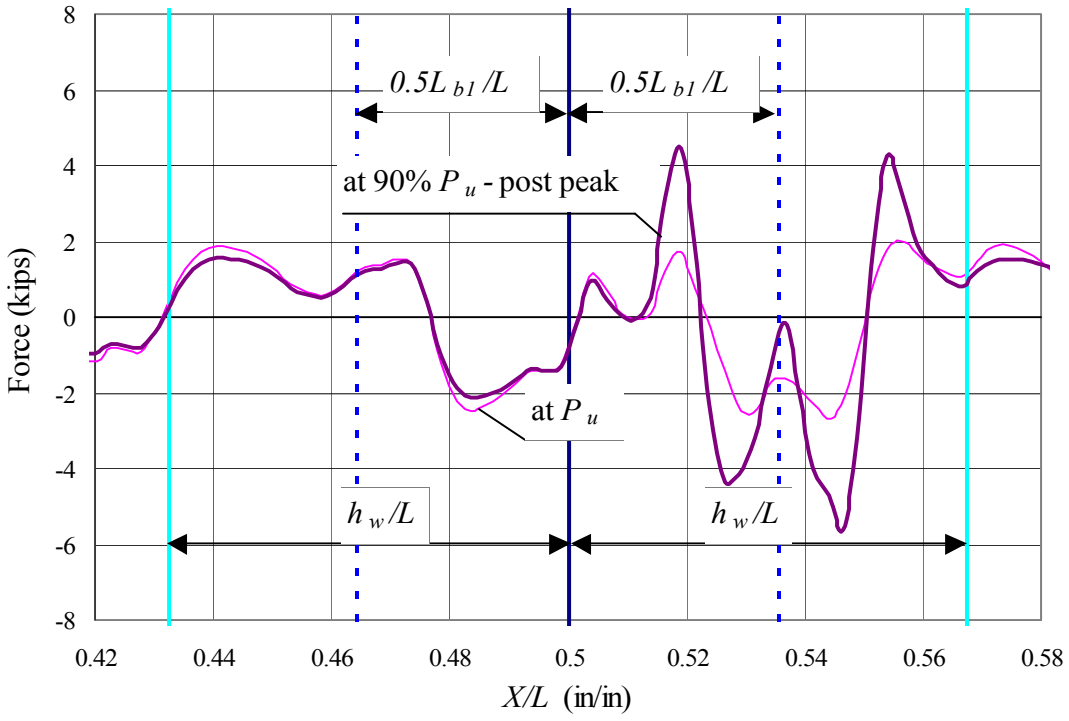

Figure 6.33 Lateral force (*SF5*) transferred between web and top flange (Specimen 6)

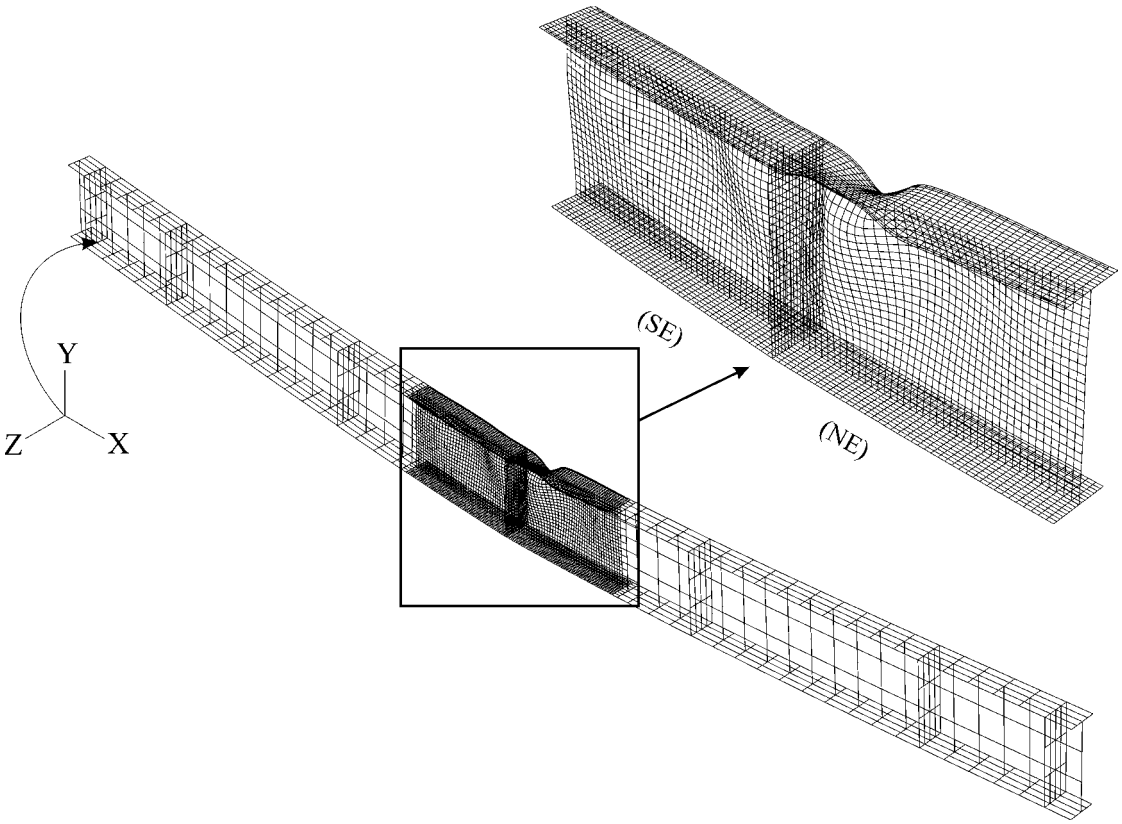

(a) Deflected shape (at 90% P_u-post peak)

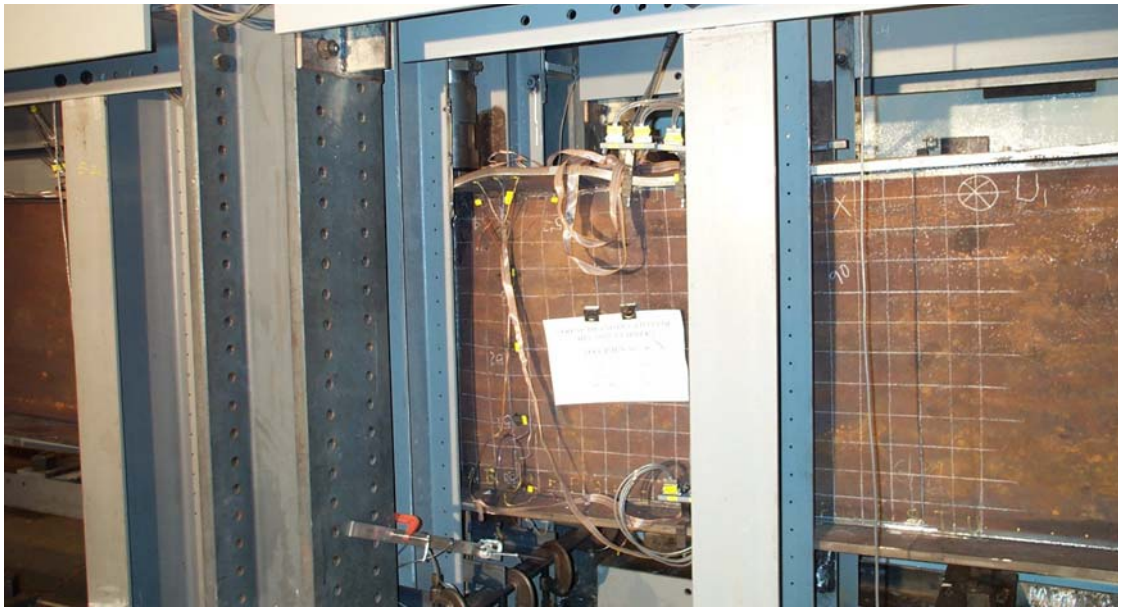

(b) Deflected shape from experiment

Figure 6.34 Deflected shape at 90% P_u-post peak and deflected shape from experiment (Specimen 6)

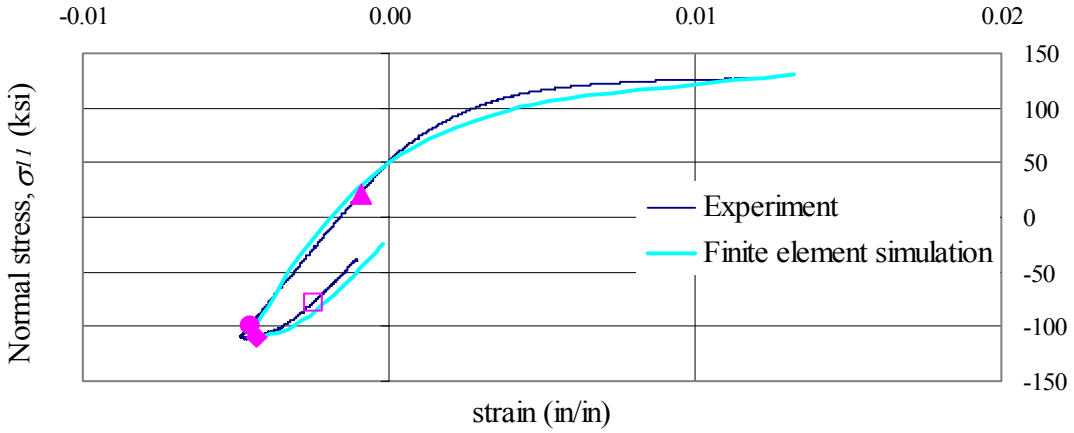

(a) Normal strain, ε_{11}

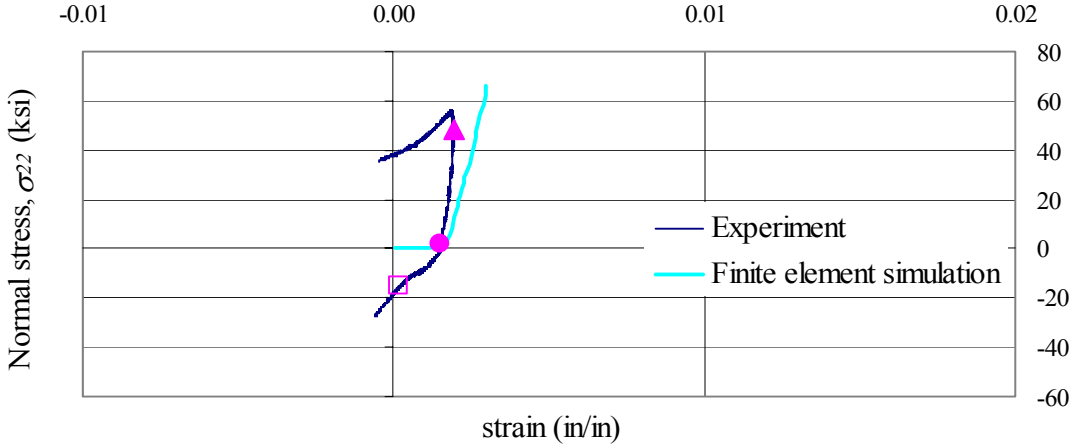

(b) Normal strain, ε_{22}

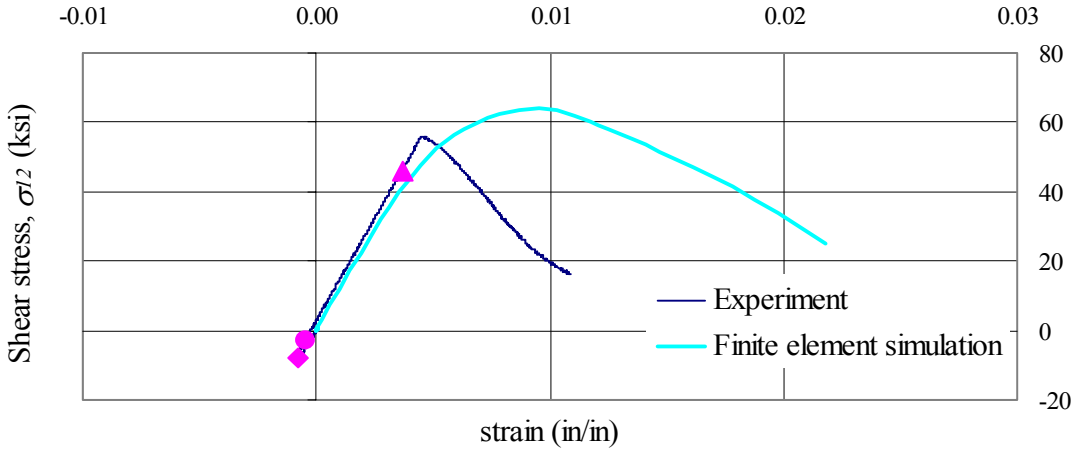

(c) Engineering shear strain, γ_{12}

Figure 6.35 Stress versus strain (section 6-East, Specimen 6)

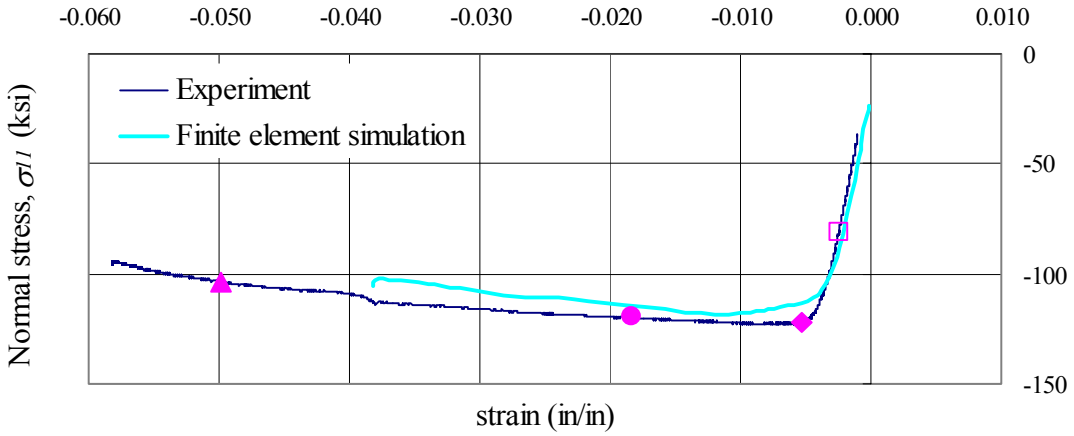

(a) Normal strain, ε_{11}

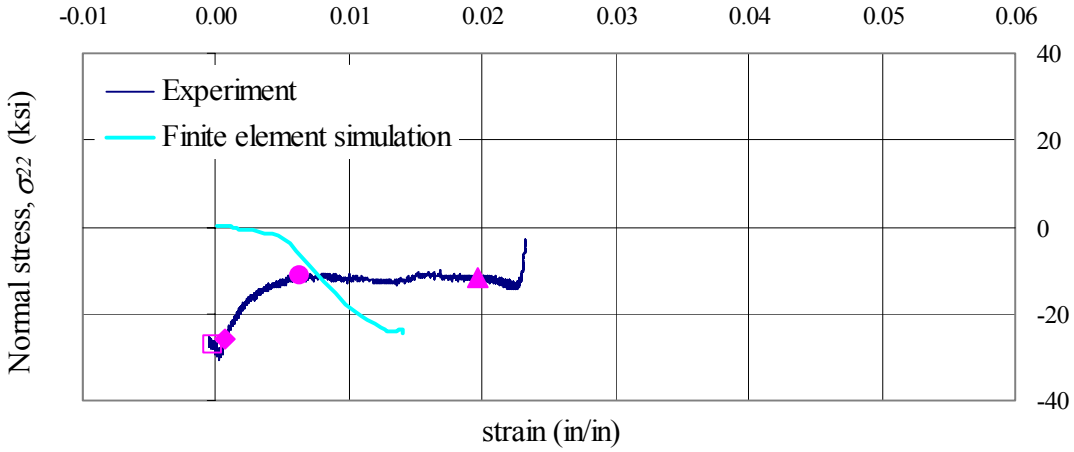

(b) Normal strain, ε_{22}

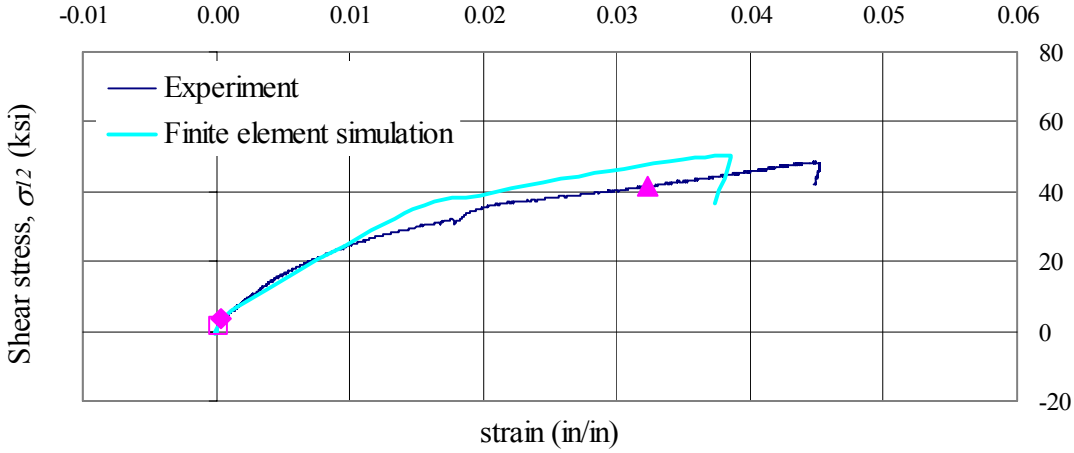

(c) Engineering shear strain, γ_{12}

Figure 6.36 Stress versus strain (section 7-West, Specimen 6)

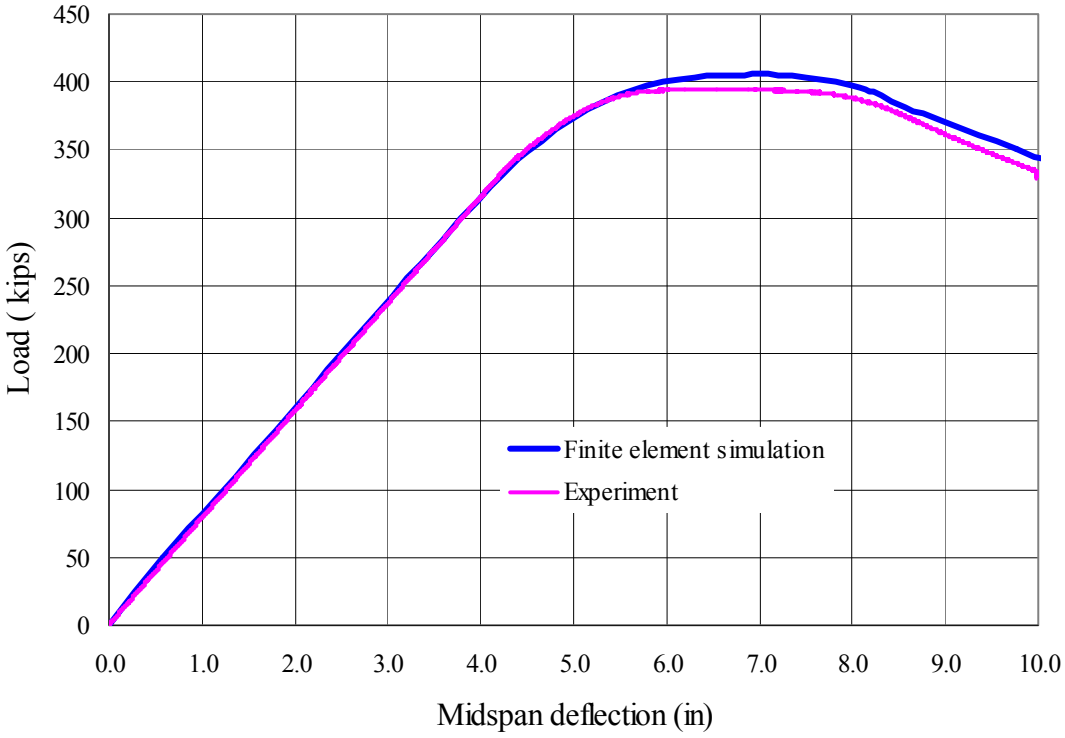

Figure 6.37 Load versus midspan vertical deflection (Specimen 7)

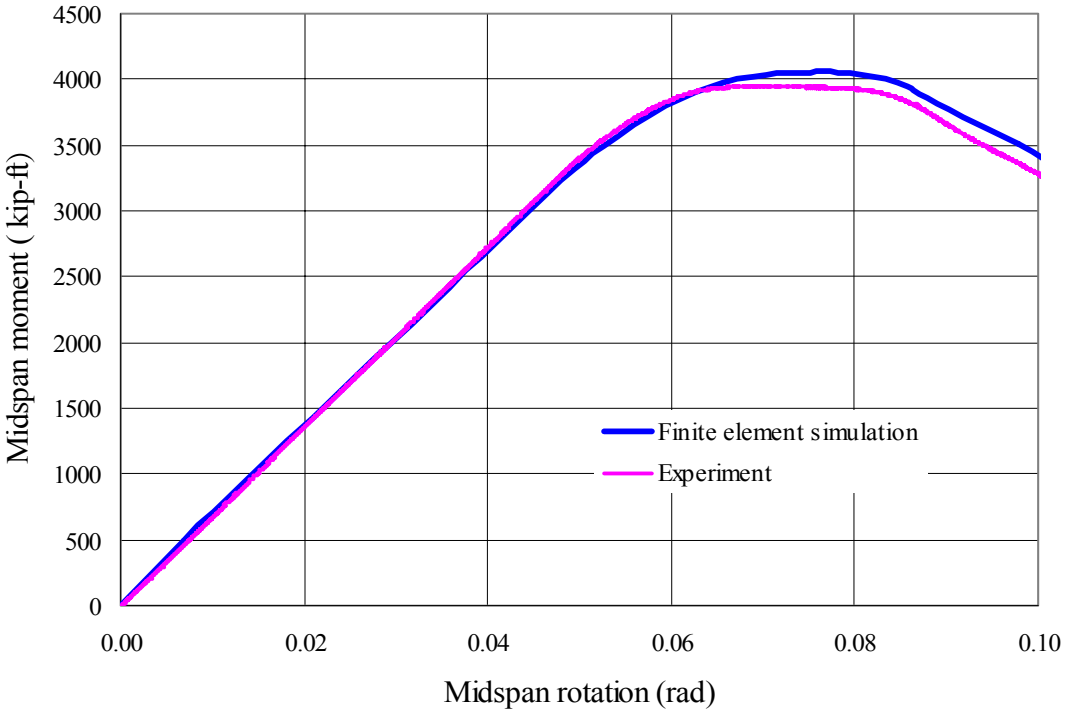

Figure 6.38 Midspan moment versus total rotation (Specimen 7)

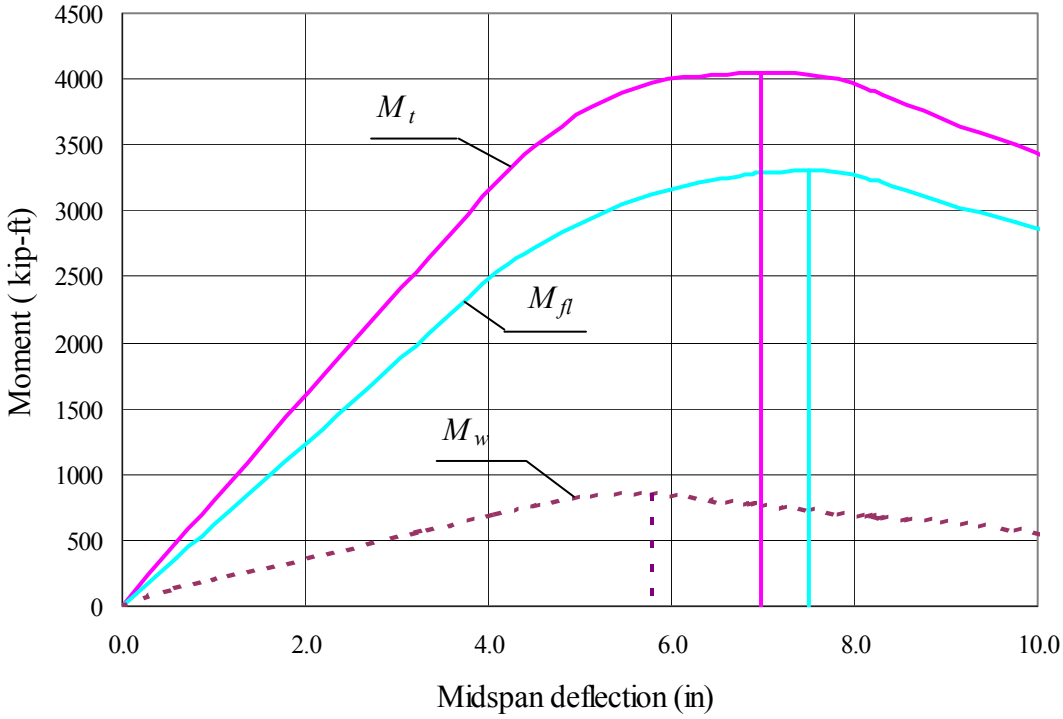

Figure 6.39 Moment components versus midspan vertical deflection (Specimen 7)

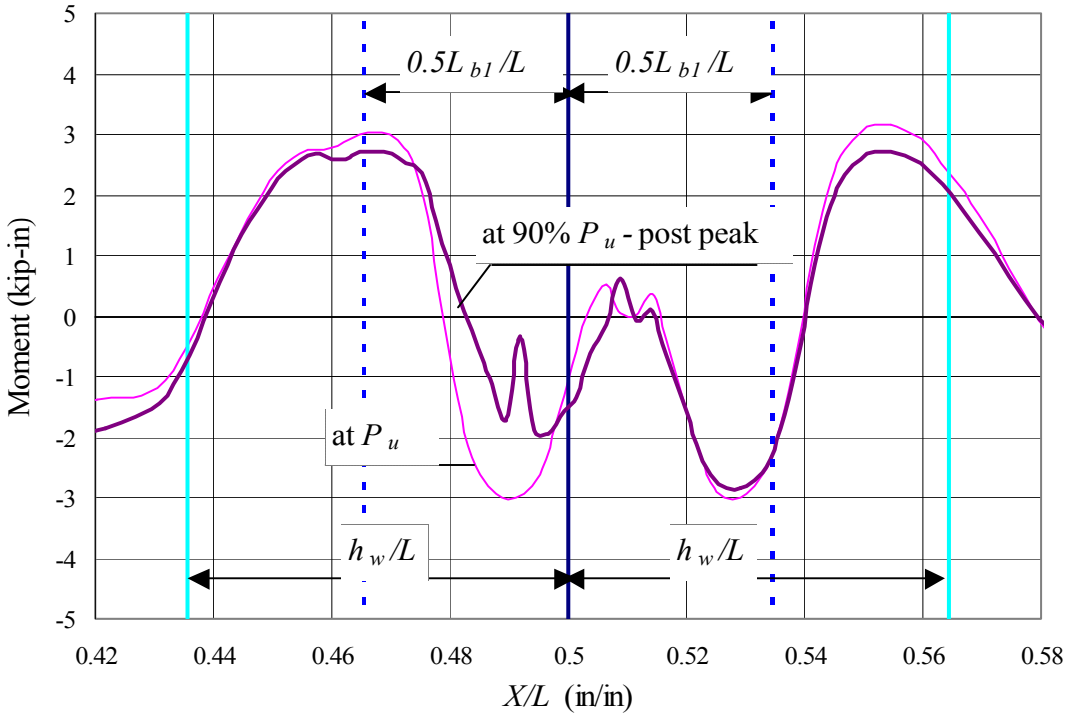

Figure 6.40 Moment (*SM2*) transferred between web and top flange (Specimen 7)

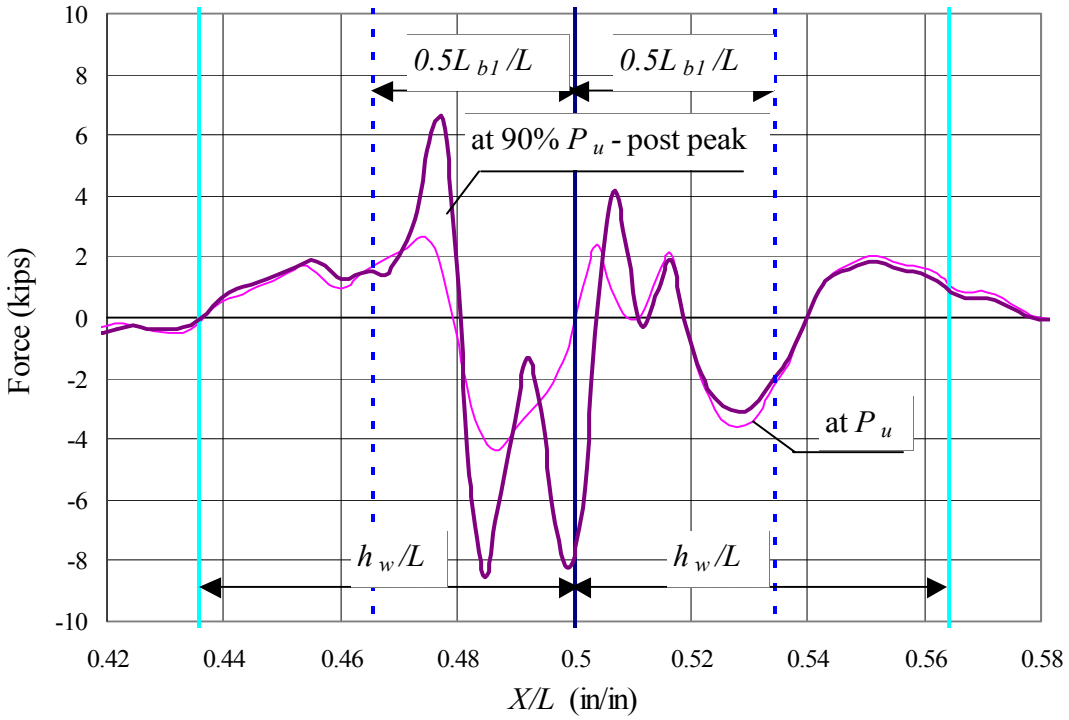

Figure 6.41 Lateral force (*SF5*) transferred between web and top flange (Specimen 7)

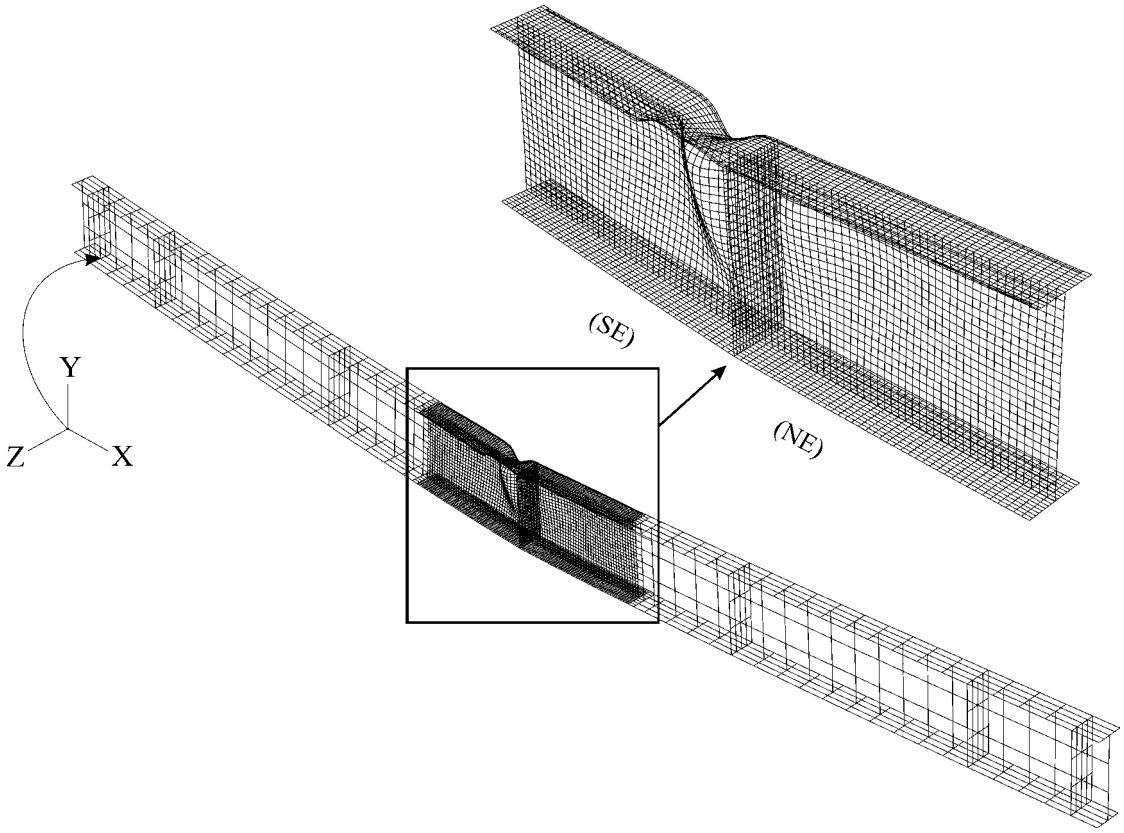

(a) Deflected shape (at 90% P_u-post peak)

(b) Deflected shape from experiment

Figure 6.42 Deflected shape at 90% P_u-post peak and deflected shape from experiment (Specimen 7)

CHAPTER 7 Flexural Strength and Ductility of HPS-100W Bridge I-Girders

7.1 Introduction

The results presented in Chapter 5 show good correlation between the experimental results and the finite element simulation results. Using the finite element model, a parametric study was performed to expand the database for bridge I-girders fabricated from HPS-100W steel. The results of this study are presented in this chapter. Also the effect of residual stresses on the strength and ductility will be discussed.

In this parametric study, the effect of different parameters on the strength and ductility will be studied. These parameters are the normalized flange slenderness, λ_f, the normalized web slenderness, λ_w, and the cross section aspect ratio h_w/b_f. The parametric study results are presented first in this chapter, because in the parametric study one parameter was varied while the other parameters are constant. This is not the case for the experimental specimens, since many factors affected their geometry, as explained in Chapter 4.

The nominal flexural strength of the parametric specimens and the experimental specimens was calculated using two versions of the AASHTO LRFD specifications: the Draft 2004 AASHTO LRFD specifications [AASHTO 2004] and the 2001 AASHTO LRFD specifications [AASHTO 2001]. For each specification version, the flexural strength was calculated twice. In one calculation the flexural strength is limited to the yield moment because of the limit related to the specified minimum yield strength of the steel as discussed in Chapter 1 and 2. In the second calculation the yield strength limit was ignored. The nominal flexural strength calculated using the two versions of the AASHTO LRFD specifications was then compared with the finite element simulations for the parametric specimens and the experimental results for the experimental specimens. Also the plastic rotation capacity calculated using the Draft 2004 AASHTO LRFD specifications [AASHTO 2004] was compared with the results from the finite element simulations for the parametric specimens and the experimental results for the experimental specimens.

7.2 Parametric Study of Flexural Strength and Ductility

A total of twelve parametric specimens were used in this study. These specimens were divided into two groups with each group containing six specimens. In each group the cross section aspect ratio was kept constant. Two values for the flange slenderness and three values for the web slenderness were used to generate the six cross sections of the six specimens in each group. The numbering scheme in each

group is as follows. The first parametric specimen starts with the number 11 and the group number is included to show the cross section aspect ratio. For example, "11-2.5" refers to parametric specimen number 11 in the group with a cross section aspect ratio of 2.5. The selected web slenderness and flange slenderness values are shown in Figure 7.1. The geometry and material properties of the parametric specimens, along with the experimental specimens discussed in Chapter 4, are shown in Table 7.1.

The engineering stress-strain curve used for the parametric study is shown in Figure 7.2. The data for this curve is the average tensile coupon data for the plate with a nominal thickness of 1.0 in (25 mm). The yield stress, 113 ksi (779 MPa), used in calculating the yield and plastic moment, is the 0.2% offset yield stress. The engineering stress-strain curve was converted to the true stress-natural plastic strain curve, shown in Figure 7.3, using the procedure explained in Section 3.3.2. This true stress-natural plastic strain curve was used in the finite element simulations (obtained using ABAQUS).

The finite element model described in Section 6.2 was used in this study. Residual stresses were incorporated using the model described in Section 4.5.3. The first unbraced length, on each side of the midspan, was determined using Equation 4.3.

An initial imperfection with a sine wave in the local-x direction and cosine wave in the local-y direction was introduced to the web. The local-x and y coordinate system is shown in Figure 7.4. Equation 3.2 specifies the surface of the imperfect region. This initial imperfection was introduced to the north of midspan as shown, hatched, in Figure 7.4. The imperfection amplitude, z_0, was taken as the maximum permitted according to the AWS Structural Welding Code [1998] as follows:

for $h_w / t_w < 150$ the maximum imperfection amplitude, $z_0 = h_w / 115$.

The behavior of each specimen is represented by a plot of normalized midspan moment, M/M_p, versus plastic rotation, θ_p. The plastic rotation is calculated by subtracting the elastic rotation from the total rotation, θ_t, using Equation 7.1.

$$\theta_p = \theta_t - \frac{ML}{2EI} \tag{7.1}$$

The total rotation is the sum of the right and left end rotations.

7.2.1 Effect of Flange Slenderness

Figure 7.5 through Figure 7.10 show the effect of flange slenderness, λ_f, on both the flexural strength and ductility, which is represented by plastic rotation. As λ_f

decreases, the flexural strength slightly increases. The flange slenderness, λ_f, has a predominant effect on the plastic rotation capacity. As λ_f decreases, the plastic rotation capacity considerably increases. This considerable increase in plastic rotation capacity is mainly attributed to an increase in the flange torsional resistance as λ_f decreases.

7.2.2 Effect of Web Slenderness

Figure 7.11 through Figure 7.14 show the effect of web slenderness, λ_w, on both the flexural strength and plastic rotation. For the same h_w/b_f, an increase in web slenderness, λ_w, has the effect of reducing the strength and ductility. The reason for this reduction is that as λ_w increases the web buckles earlier, and both sheds primary bending moment to the flanges and applies both twisting moments and lateral forces to the compression flange. These twisting moments and lateral forces help to destabilized the compression flange.

7.2.3 Effect of Cross Section Aspect Ratio

The importance of the cross-section aspect ratio, h_w/b_f , on the plastic rotation capacity and the failure mode was studied by El-Ghazaly [1983], Barth [1996], and Barth and White [1997]. Figure 7.15 through Figure 7.20 show the effect of h_w/bf on the flexural strength and plastic rotation. As h_w/bf is decreased, both flexural strength and plastic rotation capacity considerably increase. The reason for this is that as h_w/b_f decreases, the distance over which the twisting moment and lateral force are applied to the flange by the buckling web decreases (as shown in Section 3.6). The twisting moment disturbs the top flange and increases its torsional instability. The lateral force increases its lateral instability and produces lateral moment in the top flange. Also, this length will contribute to the flange torsional stiffness.

7.3 Strength and Ductility of Experimental Specimens

The geometry and material properties of the experimental specimens are shown in Table 7.1. The experimental and finite element simulation results are compared in Table 7.2. The comparison shows that the finite element simulations accurately predict the flexural strength of the experimental specimens.

7.3.1 Effect of Flange Slenderness

Figure 7.21 through Figure 7.23 show that the flange slenderness, λ_f, has a predominant effect on the plastic rotation capacity. As λ_f decreases, the plastic rotation capacity considerably increases as explained in Section 7.2.1. Note that for the specimens compared in these figures, the h_w/bf is not constant.

7.3.2 Effect of Web Slenderness

Figure 7.24 and Figure 7.25 show the effect of web slenderness, λ_w, on the plastic rotation. Note that for the specimens compared in these figures, the h_w/bf is not constant. As λ_w decreases, the plastic rotation capacity slightly increases in . However, in Figure 7.25 the effect of h_w/bf overrides the effect of λ_w. Even though Specimen 6 has a more slender web, its plastic rotation is grater than that of Specimen 2 because Specimen 6 has a smaller h_w/bf.

7.3.3 Effect of Cross Section Aspect Ratio

Figure 7.26 shows the effect of h_w/b_f on the flexural strength and plastic rotation. As h_w/bf is decreased, both the flexural strength and plastic rotation considerably increase as shown in Section 7.2.3.

7.3.4 Effect of Residual Stresses

Figure 7.27 through Figure 7.31 show the effect of the residual stresses for Specimen 3 through 7, respectively. In each figure, the finite element simulation results (obtained using ABAQUS) with and without the residual stresses are compared with the experimental results. The plots represent midspan moment versus total end rotation. From these figures, it is clear that including the residual stresses in the finite element simulation will provide more accurate results, even though the residual stresses have almost no effect on the flexural strength of cross sections similar to those of the experimental specimens, which have compact or ultra compact flanges and noncompact webs.

7.4 Comparison with Nominal Flexural Strength

The nominal flexural strength of the parametric specimens and the experimental specimens was calculated using two versions of the AASHTO LRFD specifications: the Draft 2004 AASHTO LRFD specifications [AASHTO 2004] and the 2001 AASHTO LRFD specifications [AASHTO 2001]. For each specification version, the flexural strength was calculated twice. In one calculation the flexural strength is limited to the yield moment because of the limit related to the specified minimum yield strength of the steel as discussed in Chapter 1 and 2. In the second calculation the yield strength limit was ignored. The nominal flexural strength calculated using the two versions of the AASHTO LRFD specifications was then compared with the finite element simulations for the parametric specimens and the experimental results for the experimental specimens. Comparison of the calculated nominal flexural strength with the finite element simulation results and the experimental results shows whether the limit related to the steel yield strength can be lifted.

7.4.1 Draft 2004 AASHTO LRFD Bridge Design Specifications

The calculated flexural strength, M_n, according to the Draft 2004 AASHTO LRFD specifications [AASHTO 2004], using either Article 6.10.8 or Appendix A, is shown in Table 7.3 and compared with the ultimate flexural strength, M_u. For the parametric specimens, M_u is obtained from finite element simulation, while for the experimental specimens, M_u is the ultimate moment reached during the experiment. The procedures for calculating the nominal flexural strength, M_n, according to the Draft 2004 AASHTO LRFD specifications [AASHTO 2004] using Article 6.10.8 are explained in Section 2.2.1. The procedures for calculating M_n according to the Draft 2004 AASHTO LRFD specifications [AASHTO 2004] using Appendix A are explained in Section 2.2.2. In calculating M_n, the measured yield strengths of the compression flange steel and the web steel, σ_{yf} and σ_{yw}, respectively, were used instead of the specified minimum yield strengths of the compression flange steel and the web steel, F_{yc} and F_{yw}, respectively.

7.4.2 2001 AASHTO LRFD Bridge Design Specifications

The calculated flexural strength, M_n, according to the 2001 AASHTO LRFD specifications [AASHTO 2001], using either the optional Q formula or Article 6.10.4.2.4, is shown in Table 7.4 and compared with the ultimate flexural strength, M_u. The procedures for calculating the nominal flexural strength, M_n, according to the 2001 AASHTO LRFD specifications [AASHTO 2001] using the optional Q formula are explained in Section 2.3. In calculating M_n, the actual yield strengths of the compression flange steel and the web steel, σ_{yf} and σ_{yw}, respectively, were used instead of the specified minimum yield strengths of the compression flange steel and the web steel, F_{yc} and F_{yw}, respectively.

7.4.3 Comparison of Flexural Strength

From Table 7.3, it is clear that using either Article 6.10.8 or Appendix A of the Draft 2004 AASHTO LRFD specifications [AASHTO 2004] provides a nominal flexural strength, M_n, which is less than the ultimate flexural strength, M_u. However, M_n calculated using Article 6.10.8 was very conservative compared to M_u. In Article 6.10.8, the flexural strength is limited to the yield moment because of the specified minimum yield strength of the steel (i.e. 100 ksi (690 MPa)) exceeds 70 ksi (485 MPa). However, the results in Table 7.3 show that limiting the flexural strength to the yield moment is too conservative. Table 7.3 shows that M_n calculated using Appendix A is a more accurate estimate of M_u, and therefore the limit against using Appendix A for HPS-100W I-girders can be eliminated for girders in negative flexure.

From Table 7.4, it is clear that the optional Q formula of the 2001 AASHTO LRFD specifications [AASHTO 2001] provides M_n that overestimates the ultimate flexural strength, M_u. In almost 60% of the specimens, M_n calculated from the optional Q formula is higher than M_u, and therefore the limit against using the optional Q formula for HPS-100W I-girders can not be eliminated for girders in negative flexure. On the other hand, Article 6.10.4.2.4 of the 2001 AASHTO LRFD specifications [AASHTO 2001] provides M_n which is less than M_u. In Article 6.10.4.2.4, the flexural strength is limited to the yield moment because of the specified minimum yield strength of the steel (i.e. 100 ksi (690 MPa)) exceeds 70 ksi (485 MPa). However, the results in Table 7.4 show that limiting the flexural strength to the yield moment is too conservative.

7.5 Plastic Rotation Capacity

The plastic rotation capacity, θ_{pc}, is determined as the plastic rotation through which the girder can rotate while maintaining the nominal flexural strength calculated from the AASHTO LRFD specifications (as shown in Figure 7.32). Since the optional Q formula, [AASHTO 2001], overestimates the flexural strength of 60% of the specimens, θ_{pc} was not determined using the flexural strength based on this formula. As can be seen from Table 7.3 and Table 7.4, the nominal flexural strength calculated using Article 6.10.8 the Draft 2004 AASHTO LRFD specifications [AASHTO 2004] and Article 6.10.4.2.4 of the 2001 AASHTO LRFD specifications [AASHTO 2001] is the same except for the first three specimens. As a result, θ_{pc} was calculated using the nominal flexural strength calculated according to the Draft 2004 AASHTO LRFD specifications [AASHTO 2004] only and is shown in Table 7.5. In Figure 7.33 through Figure 7.51 three horizontal lines are marked on each plot. The first one represents M/M_p =1.0, the second one represents the nominal flexural strength calculated using Appendix A [AASHTO 2004], and the third one represents the nominal flexural strength calculated using Article 6.10.8 [AASHTO 2004]. It is clear that the nominal flexural strength calculated using Appendix A is higher than that calculated using Article 6.10.8, as shown in Table 7.5. As a consequence, θ_{pc} determined using the nominal flexural strength from Appendix A is lower than that determined using Article 6.10.8.

Note that, according to the Draft 2004 AASHTO LRFD specifications [AASHTO 2004], the plastic rotation limit, θ_{RL}, at which an interior-pier section moment capacity begins to decrease with increasing plastic rotation, θ_p, is as follows:

$$\theta_{RL} = 0.128 - 0.143\frac{b_f}{t_f}\sqrt{\frac{F_y}{E}} - 0.0216\frac{D}{b_f} + 0.0241\frac{D}{t_f}\sqrt{\frac{F_y}{E}} \qquad (7.2)$$

This plastic rotation limit, θ_{RL}, is equivalent to the plastic rotation capacity, θ_{pc}, defined earlier. A comparison between θ_{pc} and θ_{RL} is shown in Table 7.5. This comparison shows that Equation 7.2 provides a conservative estimate of the plastic rotation capacity of an interior-pier section. Note that Equation 7.2 for calculating θ_{RL} was developed for steel with a specified minimum yield strength of 70 ksi (485 MPa) and is shown, in this study, to be applicable also for HPS-100W steel.

Of course the plastic rotation capacity depends on the cross section parameters λ_f, λ_w, and h_w/b_f. As λ_f decreases, θ_{pc} increases as explained in Section 7.2.1. This effect can be seen by comparing θ_{pc} for the following specimen pairs: Specimen 11 and 14; Specimen 12 and Specimen 15; Specimen 13 and Specimen 16.

As λ_w decreases, θ_{pc} increases as explained in Section 7.2.2. This effect can be seen by comparing θ_{pc} for the following sets of specimens: Specimen 11, 12, and 13; Specimen 14, 15, and 16.

As h_w/b_f decreases, θ_{pc} increases as explained in Section 7.2.3. This effect can be seen by comparing θ_{pc} for specimens with the same λ_f and λ_w, but different h_w/b_f. As an example, Specimen 11-2.5 and Specimen 11-3.5 can be compared.

The plastic rotation capacity, θ_{pc}, of the experimental and parametric specimens which reached or exceeded M_p is added to the data shown previously in Figure 2.2 and presented in Figure 7.52 and Figure 7.53. In these figure, θ_{pc} is determined using M_p as the flexural strength. In other words, θ_{pc} is the plastic rotation at which the flexural strength of the I-girder falls below M_p. The ultimate flexural strength, M_u, for Specimen 5 reached M_p and for four parametric specimens reached M_p. Therefore, θ_{pc} versus λ_w for Specimen 5 is shown in Figure 7.52, with the label S, 5, and θ_{pc} versus λ_w for the four parametric specimens 11-2.5, 12-2.5, 14-2.5, and 11-3.5 is shown in Figure 7.52, with the labels S, 11-2.5, S, 12-2.5, S, 14-2.5, and S, 11-3.5, respectively. The wide scatter in the values of θ_{pc} is the result of the difference in h_w/b_f and web imperfection amplitude and location. The effect of h_w/b_f can be seen by comparing θ_{pc} for parametric specimens 11-2.5 and 11-3.5 in Figure 7.52. These two specimens have the same λ_w (and also the same λ_f and web imperfection amplitude and location) but decrease h_w/b_f from 3.5 to 2.5 almost doubles the value of θ_{pc}. The effect of h_w/b_f is directly shown in Figure 7.53. As h_w/b_f decreases, θ_{pc} increases as explained in Section 7.2.3. In Figure 7.53, the wide scatter in the values of θ_{pc} is the result of the difference in λ_w, λ_f, and web imperfection amplitude and location.

However, by comparing θ_{pc} for specimens F&S, 1 and S, 14-2.5, it is clear that when λ_w, λ_f, h_w/b_f, and web imperfection amplitude and location are almost the same, the scatter in the values of θ_{pc} is small.

Table 7.1 Geometry and material properties for experimental and parametric specimens

Specimen	t_f (in)	t_w (in)	b_f (in)	h_w (in)	L (in)	h_w/b_f	h_w/t_w	$b_f/2t_f$	a_r	L/D	E_f (ksi)	σ_{yf} (ksi)	E_w (ksi)	σ_{yw} (ksi)	λ_f	λ_w
1 *	0.775	0.388	9.813	24.000	408.0	2.45	61.9	6.33	1.22	15.97	29000.0	115.0	29000.0	100.0	0.399	3.63
2 *	0.770	0.395	9.813	36.000	600.0	3.67	91.1	6.37	1.88	15.98	29000.0	115.0	29000.0	100.0	0.401	5.35
3	0.759	0.245	9.359	20.000	300.0	2.14	81.6	6.17	0.69	13.94	28967.0	113.4	29067.0	124.4	0.386	5.34
4	0.759	0.245	7.469	25.375	390.0	3.40	103.5	4.92	1.10	14.50	28967.0	113.4	29067.0	124.4	0.308	6.77
5	1.030	0.374	10.063	21.969	336.0	2.18	58.7	4.88	0.79	13.98	29526.0	113.4	28667.0	116.9	0.303	3.75
6	1.030	0.374	12.719	39.688	576.0	3.12	106.1	6.17	1.13	13.80	29526.0	113.4	28500.0	116.9	0.383	6.79
7	1.030	0.374	10.063	31.500	480.0	3.13	84.2	4.88	1.14	14.30	29526.0	113.4	28500.0	116.9	0.303	5.39
11-2.5	1.312	0.500	11.942	29.854	464.0	2.50	59.7	4.55	0.95	14.29	29000.0	113.0	29000.0	113.0	0.284	3.73
12-2.5	1.871	0.500	17.023	42.558	662.0	2.50	85.1	4.55	0.67	14.30	29000.0	113.0	29000.0	113.0	0.284	5.31
13-2.5	2.363	0.500	21.501	53.754	836.0	2.50	107.5	4.55	0.53	14.30	29000.0	113.0	29000.0	113.0	0.284	6.71
14-2.5	0.984	0.500	11.942	29.854	464.0	2.50	59.7	6.07	1.27	14.58	29000.0	113.0	29000.0	113.0	0.379	3.73
15-2.5	1.403	0.500	17.023	42.558	662.0	2.50	85.1	6.07	0.89	14.59	29000.0	113.0	29000.0	113.0	0.379	5.31
16-2.5	1.772	0.500	21.501	53.754	836.0	2.50	107.5	6.07	0.71	14.59	29000.0	113.0	29000.0	113.0	0.379	6.71
11-3.5	0.937	0.500	8.530	29.854	464.0	3.50	59.7	4.55	1.87	14.62	29000.0	113.0	29000.0	113.0	0.284	3.73
12-3.5	1.336	0.500	12.160	42.558	662.0	3.50	85.1	4.55	1.31	14.64	29000.0	113.0	29000.0	113.0	0.284	5.31
13-3.5	1.688	0.500	15.358	53.754	836.0	3.50	107.5	4.55	1.04	14.63	29000.0	113.0	29000.0	113.0	0.284	6.71
14-3.5	0.703	0.500	8.530	29.854	464.0	3.50	59.7	6.07	2.49	14.84	29000.0	113.0	29000.0	113.0	0.379	3.73
15-3.5	1.002	0.500	12.160	42.558	662.0	3.50	85.1	6.07	1.75	14.86	29000.0	113.0	29000.0	113.0	0.379	5.31
16-3.5	1.266	0.500	15.358	53.754	836.0	3.50	107.5	6.07	1.38	14.85	29000.0	113.0	29000.0	113.0	0.379	6.71

* Specimen previously tested by Sause and Fahnestock [2001]

Table 7.2 Experimental and finite element simulation results

Specimen	h_w/b_f	a_r	λ_f	λ_w	M_y (kip-in)	M_p (kip-in)	M_u (Experiment) (kip-in)	M_u (Simulation) (kip-in)	$\frac{M_u \text{ (Simulation)}}{M_u \text{ (Experiment)}}$
1 *	2.45	1.22	0.399	3.63	25030	27250	27958	28296	1.012
2 *	3.67	1.88	0.401	5.35	40700	44740	43110	43491	1.009
3	2.14	0.69	0.386	5.34	17860	19770	19625	19989	1.019
4	3.40	1.10	0.308	6.77	19140	21710	20335	20564	1.011
5	2.18	0.79	0.303	3.75	29010	32310	32270	33663	1.043
6	3.12	1.13	0.383	6.79	69600	77720	73203	73758	1.008
7	3.13	1.14	0.303	5.39	43660	49080	47382	48672	1.027

* Specimen previously tested by Sause and Fahnestock [2001]

Table 7.3 Flexural strength using the Draft 2004 AASHTO LRFD specifications

Specimen	h_w/b_f	a_r	λ_f	λ_w	M_y (kip-in)	M_p (kip-in)	M_u (kip-in)	M_n (Appendix A) (kip-in)	M_n (6.10.8) (kip-in)	M_u/M_y	M_u/M_p	M_u/M_n (Appendix A)	M_u/M_n (6.10.8)
1 *	2.45	1.22	0.399	3.63	25030	27250	27958	26830	24550	1.12	1.03	1.04	1.14
2 *	3.67	1.88	0.401	5.35	40700	44740	43110	40800	39810	1.06	0.96	1.06	1.08
3	2.14	0.69	0.386	5.34	17860	19770	19625	18190	17750	1.10	0.99	1.08	1.11
4	3.40	1.10	0.308	6.77	19140	21710	20335	———	18920	1.06	0.94	———	1.07
5	2.18	0.79	0.303	3.75	29010	32310	32270	32310	29010	1.11	1.00	1.00	1.11
6	3.12	1.13	0.383	6.79	69600	77720	73203	———	68540	1.05	0.94	———	1.07
7	3.13	1.14	0.303	5.39	43660	49080	47382	44580	43660	1.09	0.97	1.06	1.09
11-2.5	2.50	0.95	0.284	3.73	60700	67770	70593	67770	60700	1.16	1.04	1.04	1.16
12-2.5	2.50	0.67	0.284	5.31	169200	185500	188217	173200	169200	1.11	1.01	1.09	1.11
13-2.5	2.50	0.53	0.284	6.71	334400	363000	358616	———	332200	1.07	0.99	———	1.08
14-2.5	2.50	1.27	0.379	3.73	47570	53540	54786	53540	47570	1.15	1.02	1.02	1.15
15-2.5	2.50	0.89	0.379	5.31	131000	144200	142926	134200	131000	1.09	0.99	1.07	1.09
16-2.5	2.50	0.71	0.379	6.71	257300	279900	273141	———	255200	1.06	0.98	———	1.07
11-3.5	3.50	1.87	0.284	3.73	34890	40400	40881	40130	34890	1.17	1.01	1.02	1.17
12-3.5	3.50	1.31	0.284	5.31	94270	106200	103764	96790	94270	1.10	0.98	1.07	1.10
13-3.5	3.50	1.04	0.284	6.71	183300	203200	195750	———	181200	1.07	0.96	———	1.08
14-3.5	3.50	2.49	0.379	3.73	28260	33290	32829	32730	28260	1.16	0.99	1.00	1.16
15-3.5	3.50	1.75	0.379	5.31	74920	85560	80812	77030	74920	1.08	0.94	1.05	1.08
16-3.5	3.50	1.38	0.379	6.71	144200	161700	150692	———	142200	1.05	0.93	———	1.06

* Specimen previously tested by Sause and Fahnestock [2001]

Table 7.4 Flexural strength using the 2001 AASHTO LRFD specifications

Specimen	h_w/b_f	a_r	λ_f	λ_w	M_y (kip-in)	M_p (kip-in)	M_u (kip-in)	M_n (Q formula) (kip-in)	M_n (6.10.4.2.4) (kip-in)	M_u/M_y	M_u/M_p	M_u/M_n (Q formula)	M_u/M_n (6.10.4.2.4)
1 *	2.45	1.22	0.399	3.63	25030	27250	27958	27250	25030	1.12	1.03	1.03	1.12
2 *	3.67	1.88	0.401	5.35	40700	44740	43110	44010	40700	1.06	0.96	0.98	1.06
3	2.14	0.69	0.386	5.34	17860	19770	19625	19770	17860	1.10	0.99	0.99	1.10
4	3.40	1.10	0.308	6.77	19140	21710	20335	21700	18930	1.06	0.94	0.94	1.07
5	2.18	0.79	0.303	3.75	29010	32310	32270	32310	29010	1.11	1.00	1.00	1.11
6	3.12	1.13	0.383	6.79	69600	77720	73203	77100	68780	1.05	0.94	0.95	1.06
7	3.13	1.14	0.303	5.39	43660	49080	47382	49080	43660	1.09	0.97	0.97	1.09
11-2.5	2.50	0.95	0.284	3.73	60700	67770	70593	67770	60700	1.16	1.04	1.04	1.16
12-2.5	2.50	0.67	0.284	5.31	169200	185500	188217	185500	169200	1.11	1.01	1.01	1.11
13-2.5	2.50	0.53	0.284	6.71	334400	363000	358616	359700	332400	1.07	0.99	1.00	1.08
14-2.5	2.50	1.27	0.379	3.73	47570	53540	54786	53540	47570	1.15	1.02	1.02	1.15
15-2.5	2.50	0.89	0.379	5.31	131000	144200	142926	144200	131000	1.09	0.99	0.99	1.09
16-2.5	2.50	0.71	0.379	6.71	257300	279900	273141	277300	255300	1.06	0.98	0.99	1.07
11-3.5	3.50	1.87	0.284	3.73	34890	40400	40881	40400	34890	1.17	1.01	1.01	1.17
12-3.5	3.50	1.31	0.284	5.31	94270	106200	103764	106200	94270	1.10	0.98	0.98	1.10
13-3.5	3.50	1.04	0.284	6.71	183300	203200	195750	201300	181400	1.07	0.96	0.97	1.08
14-3.5	3.50	2.49	0.379	3.73	28260	33290	32829	33290	28260	1.16	0.99	0.99	1.16
15-3.5	3.50	1.75	0.379	5.31	74920	85560	80812	85560	74920	1.08	0.94	0.94	1.08
16-3.5	3.50	1.38	0.379	6.71	144200	161700	150692	160200	142300	1.05	0.93	0.94	1.06

* Specimen previously tested by Sause and Fahnestock [2001]

Table 7.5 Flexural strength and ductility using the Draft 2004 AASHTO LRFD specifications

Specimen	h_w/b_f	λ_f	λ_w	M_u (kip-in)	M_n (Appendix A) (kip-in)	M_n (6.10.8) (kip-in)	M_u/M_n (Appendix A)	M_u/M_n (6.10.8)	θ_{pc} (Appendix A) rad	θ_{pc} (6.10.8) rad	θ_{RL} rad
1 *	2.45	0.399	3.63	27958	26830	24550	1.04	1.14	0.020	0.028	0.008
2 *	3.67	0.401	5.35	43110	40800	39810	1.06	1.08	0.005	0.006	0.005
3	2.14	0.386	5.34	19625	18190	17750	1.08	1.11	0.032	0.033	0.011
4	3.40	0.308	6.77	20335	—	18920	—	1.07	—	0.028	0.017
5	2.18	0.303	3.75	32270	32310	29010	1.00	1.11	0.049	0.090	0.026
6	3.12	0.383	6.79	73203	—	68540	—	1.07	—	0.015	0.009
7	3.13	0.303	5.39	47382	44580	43660	1.06	1.09	0.034	0.037	0.019
11-2.5	2.50	0.284	3.73	70593	67770	60700	1.04	1.16	0.040	0.056	0.027
12-2.5	2.50	0.284	5.31	188217	173200	169200	1.09	1.11	0.037	0.039	0.027
13-2.5	2.50	0.284	6.71	358616	—	332200	—	1.08	—	0.026	0.027
14-2.5	2.50	0.379	3.73	54786	53540	47570	1.02	1.15	0.017	0.029	0.011
15-2.5	2.50	0.379	5.31	142926	134200	131000	1.07	1.09	0.022	0.024	0.011
16-2.5	2.50	0.379	6.71	273141	—	255200	—	1.07	—	0.024	0.011
11-3.5	3.50	0.284	3.73	40881	40130	34890	1.02	1.17	0.022	0.046	0.019
12-3.5	3.50	0.284	5.31	103764	96790	94270	1.07	1.10	0.034	0.037	0.019
13-3.5	3.50	0.284	6.71	195750	—	181200	—	1.08	—	0.035	0.019
14-3.5	3.50	0.379	3.73	32829	32730	28260	1.00	1.16	—	0.025	0.008
15-3.5	3.50	0.379	5.31	80812	77030	74920	1.05	1.08	0.014	0.016	0.008
16-3.5	3.50	0.379	6.71	150692	—	142200	—	1.06	—	0.017	0.008

* Specimen previously tested by Sause and Fahnestock [2001]

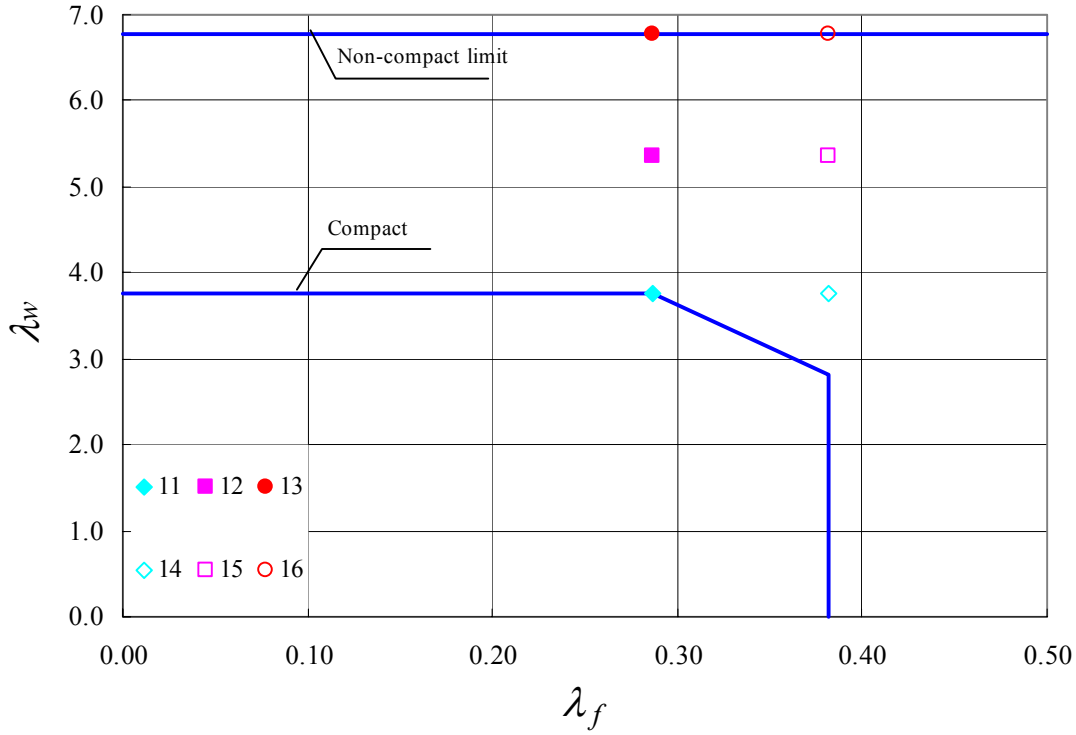

Figure 7.1 Flange and web slenderness for parametric study

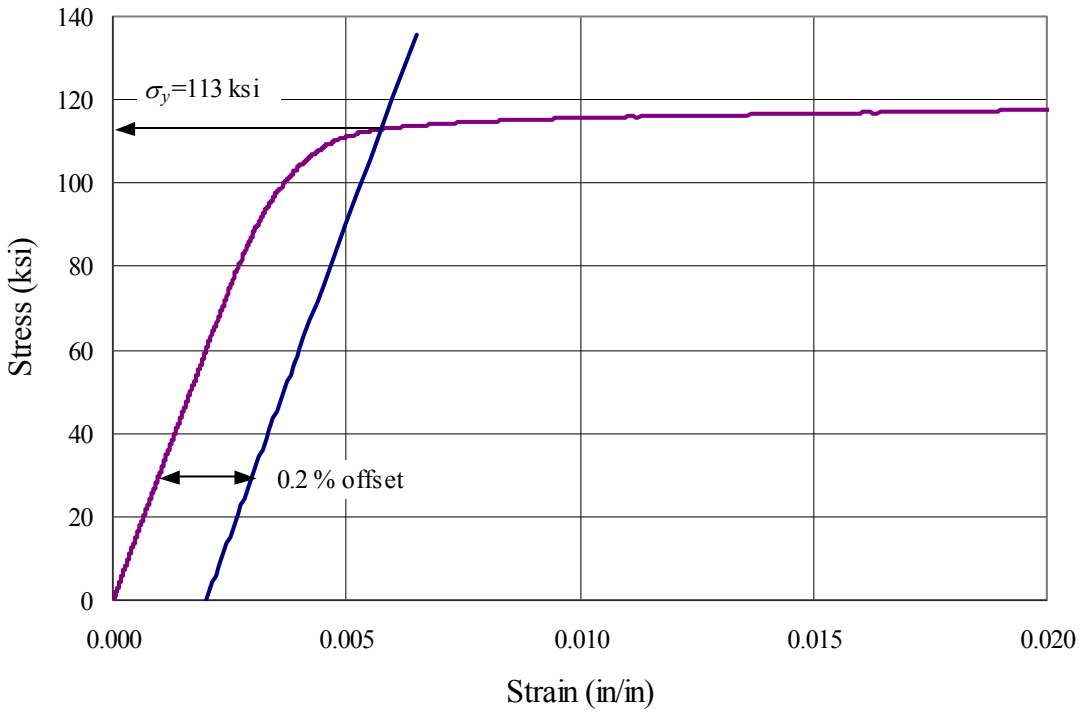

Figure 7.2 Engineering stress versus strain

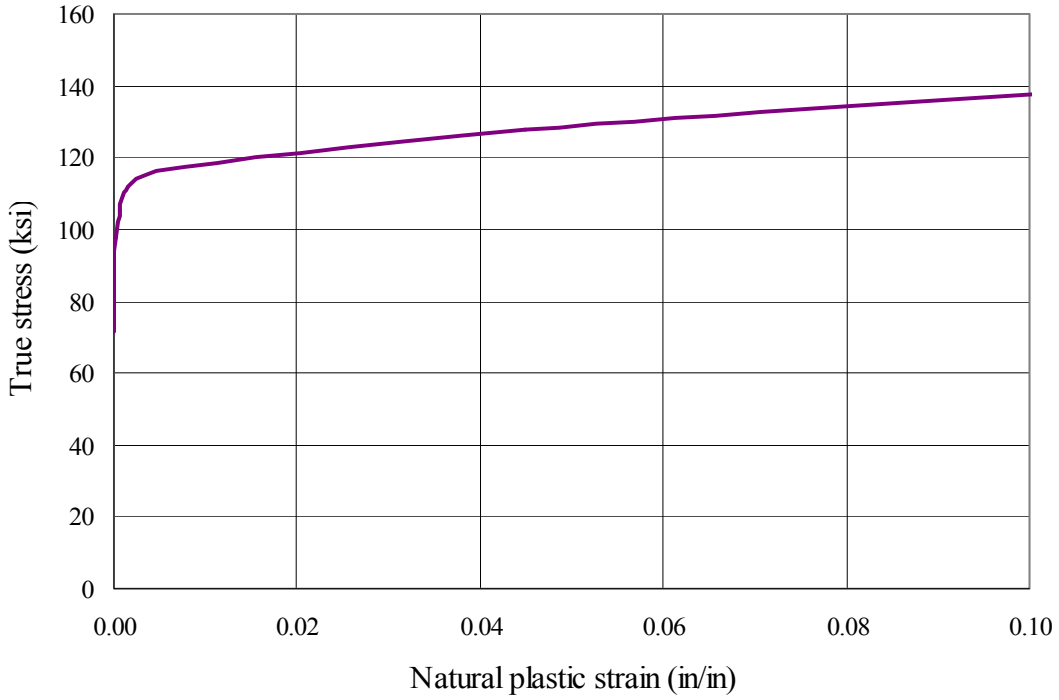

Figure 7.3 True stress versus natural plastic strain

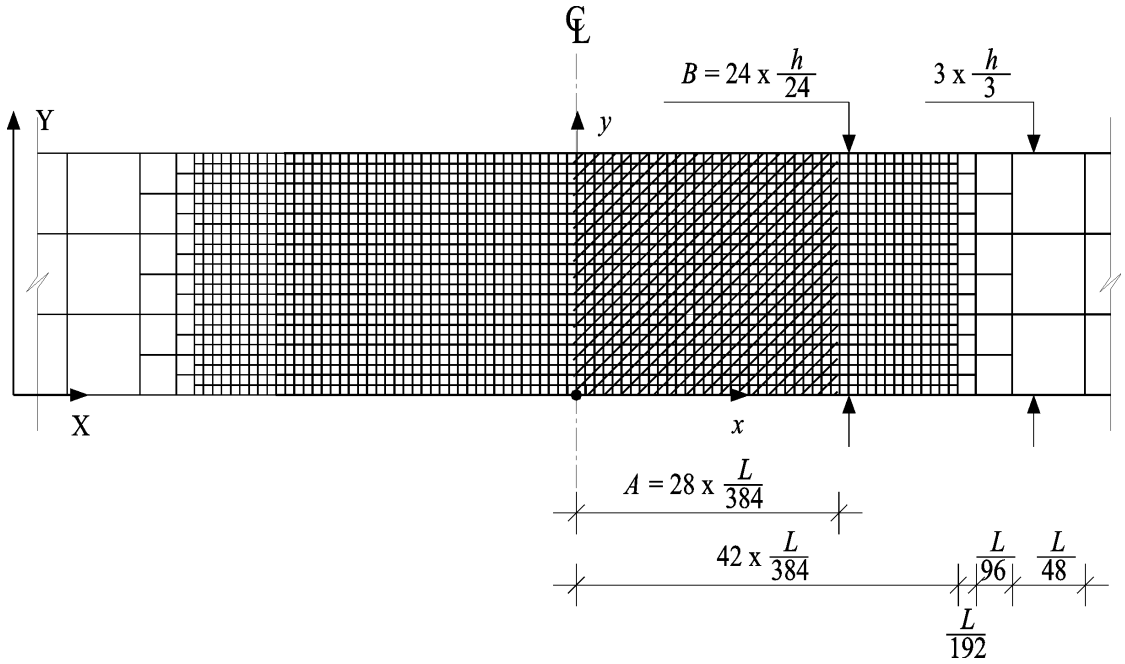

Figure 7.4 Initial imperfection location

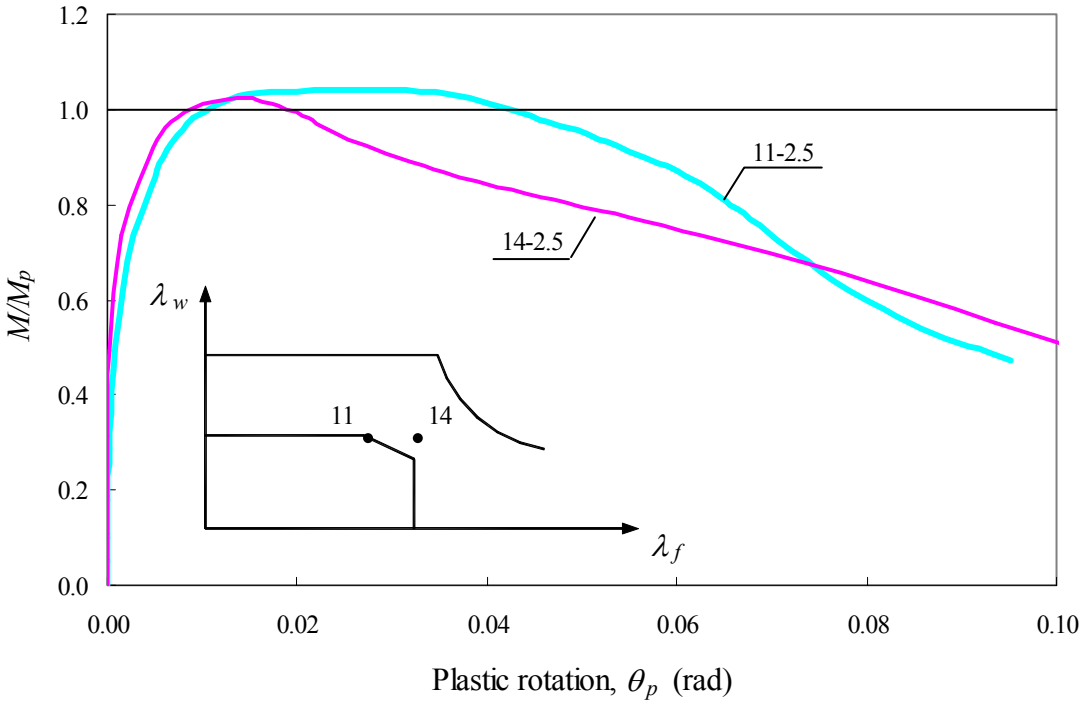

Figure 7.5 Effect of flange slenderness, λ_f

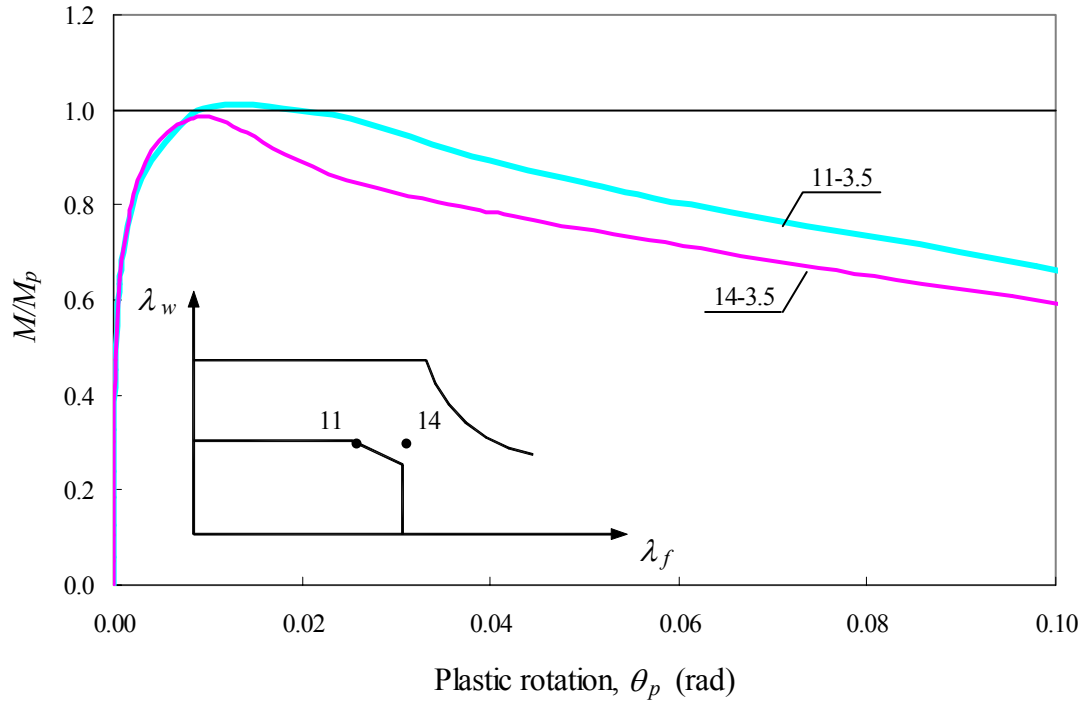

Figure 7.6 Effect of flange slenderness, λ_f

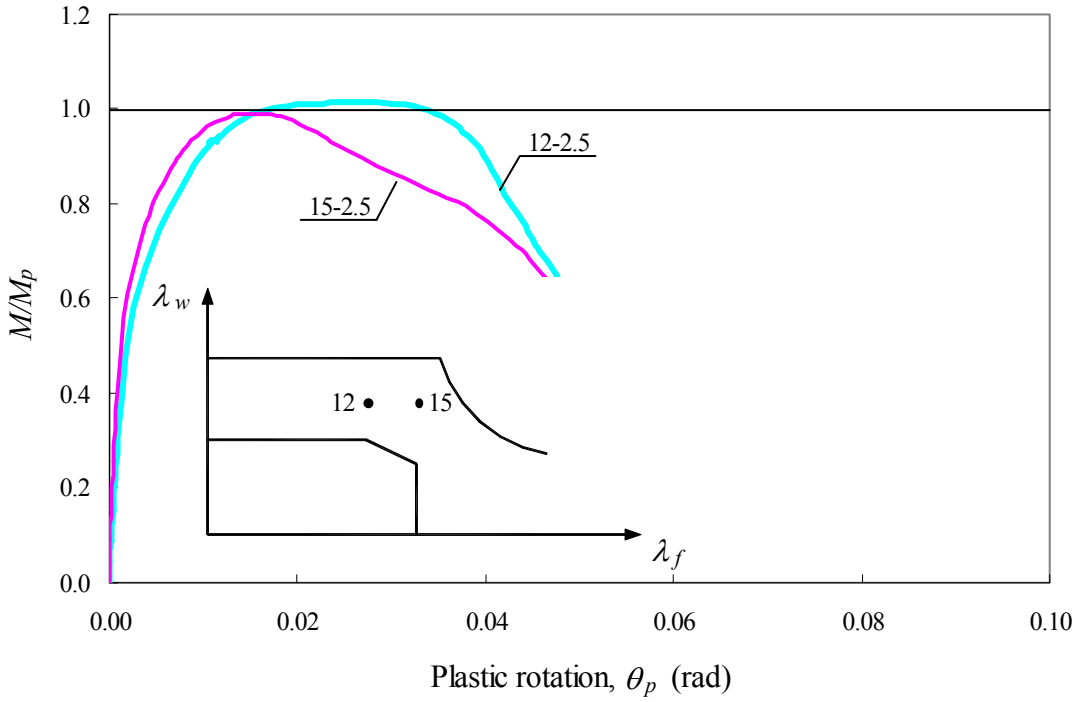

Figure 7.7 Effect of flange slenderness, λ_f

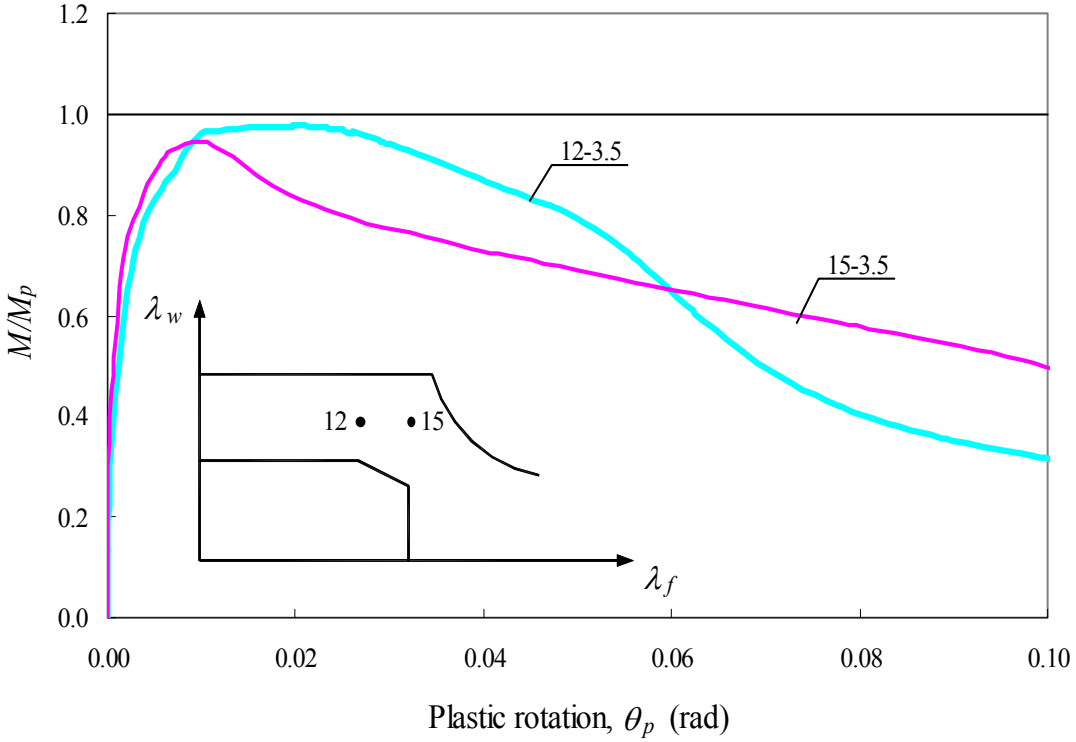

Figure 7.8 Effect of flange slenderness, λ_f

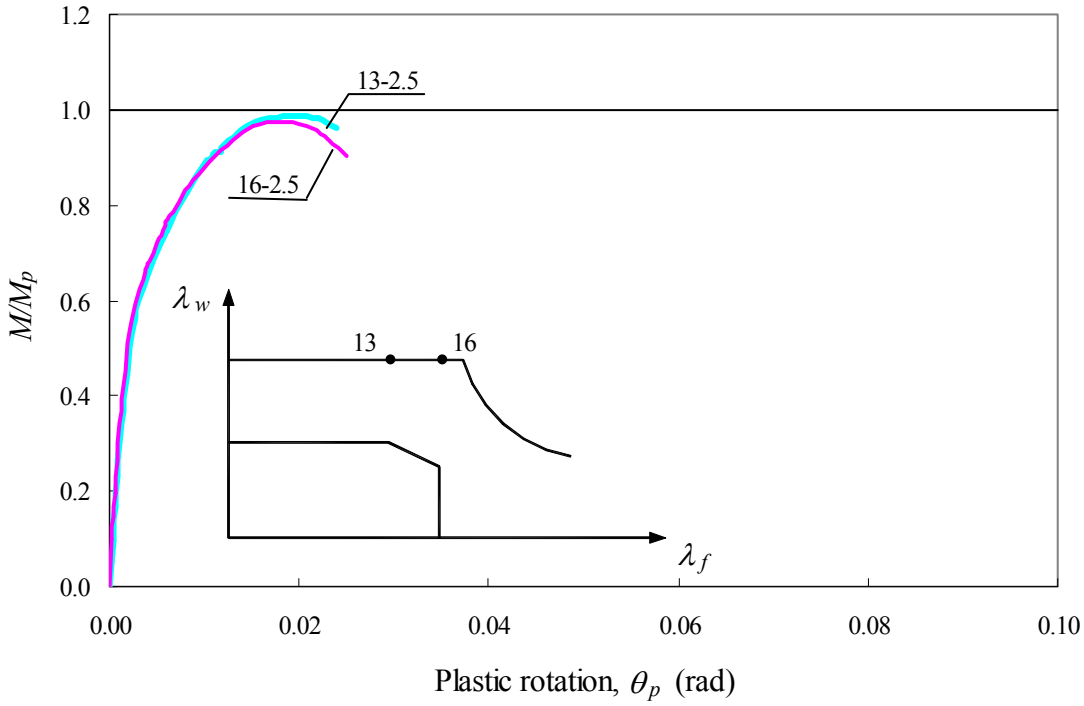

Figure 7.9 Effect of flange slenderness, λ_f

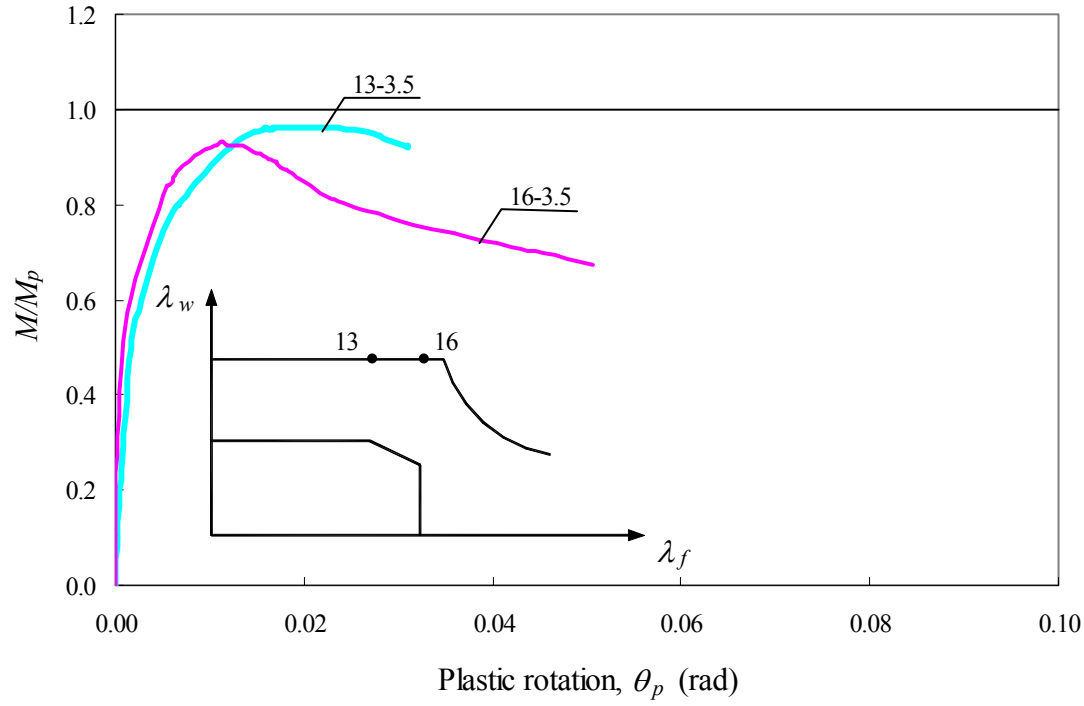

Figure 7.10 Effect of flange slenderness, λ_f

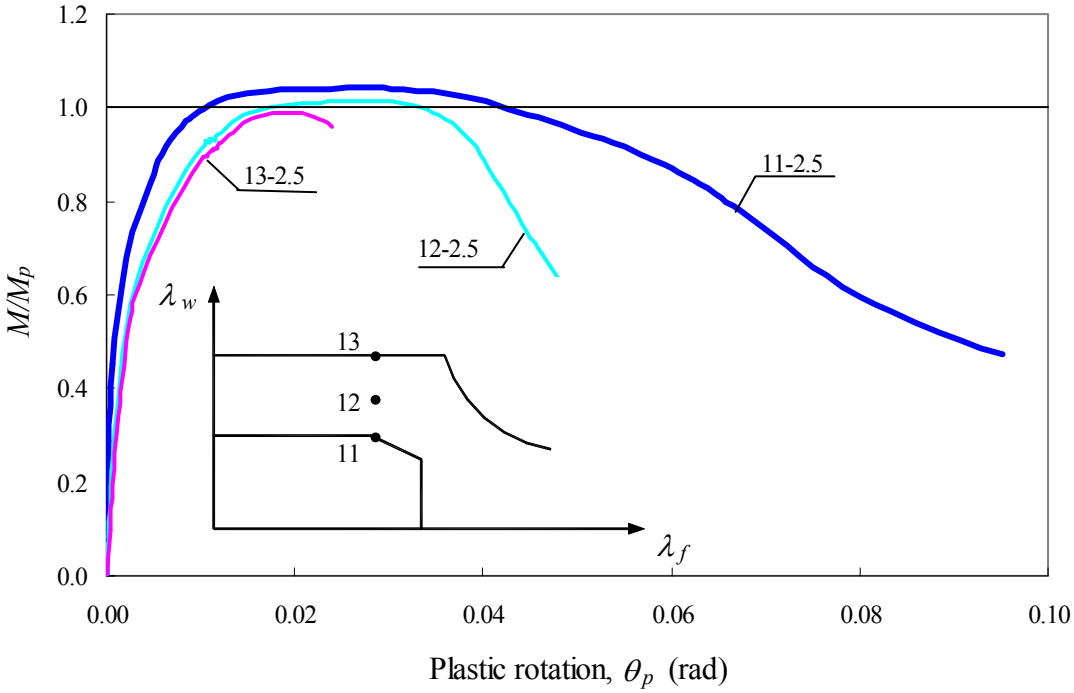

Figure 7.11 Effect of web slenderness, λ_w

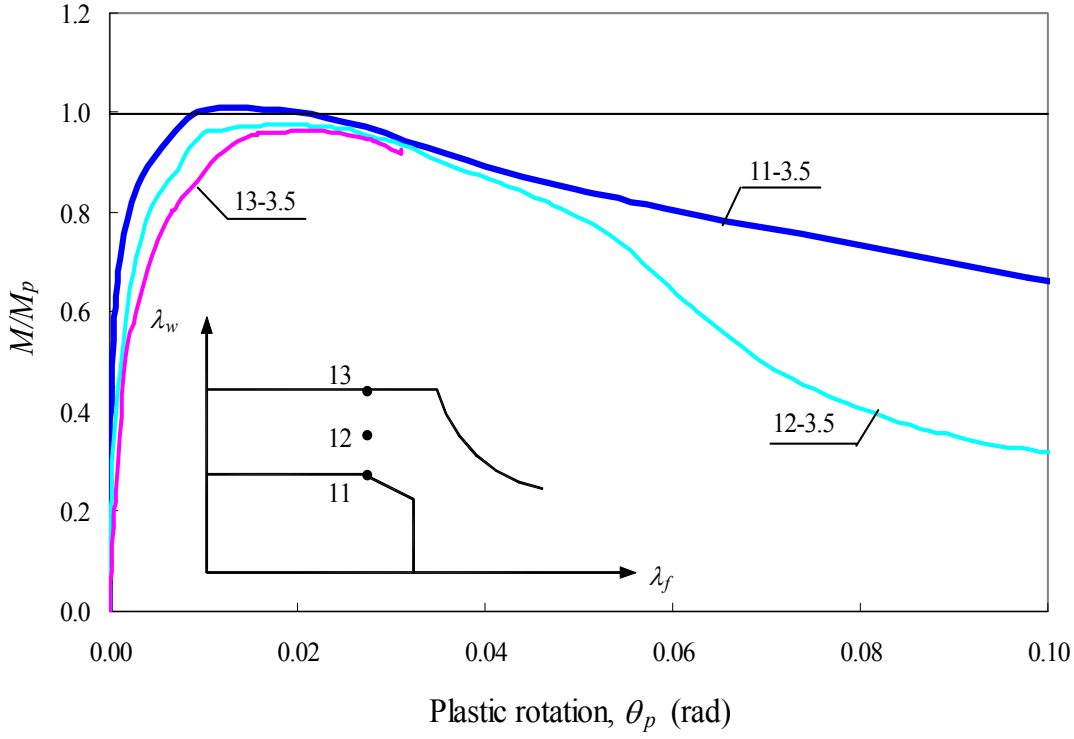

Figure 7.12 Effect of web slenderness, λ_w

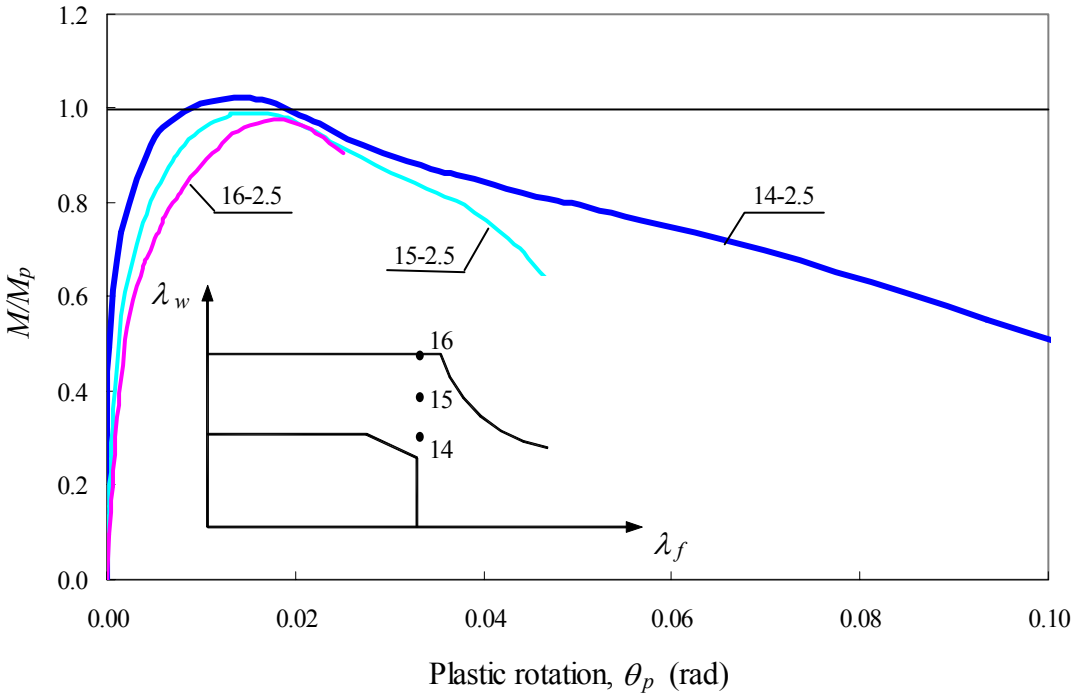

Figure 7.13 Effect of web slenderness, λ_w

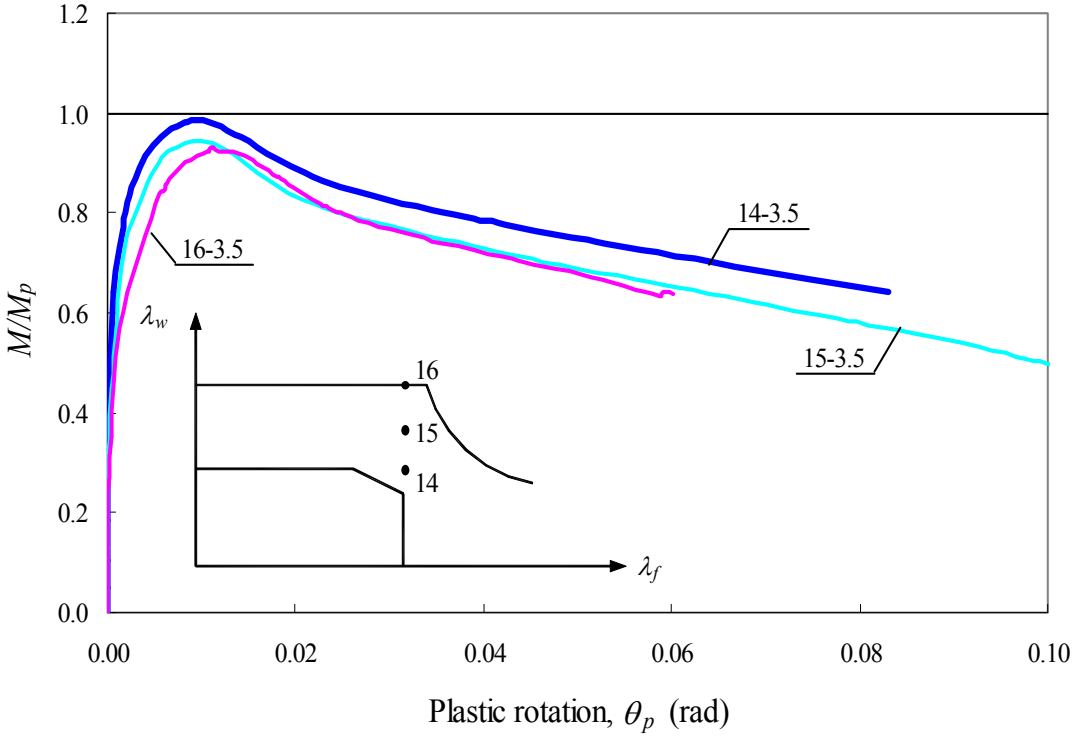

Figure 7.14 Effect of web slenderness, λ_w

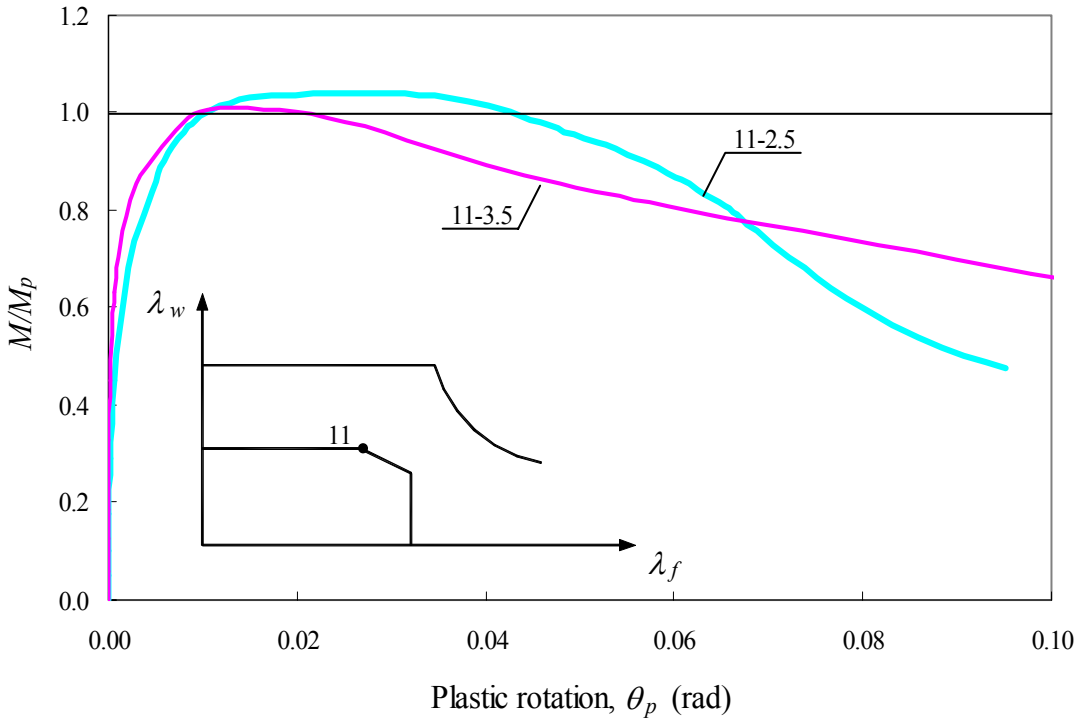

Figure 7.15 Effect of cross section aspect ratio, h_w / b_f

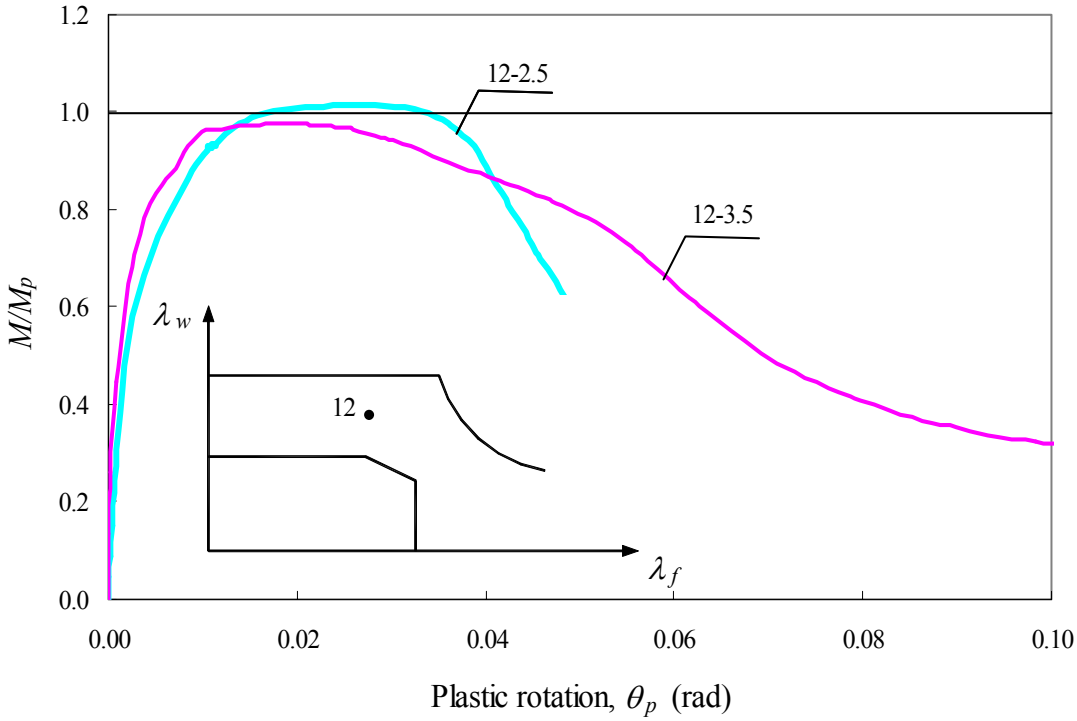

Figure 7.16 Effect of cross section aspect ratio, h_w / b_f

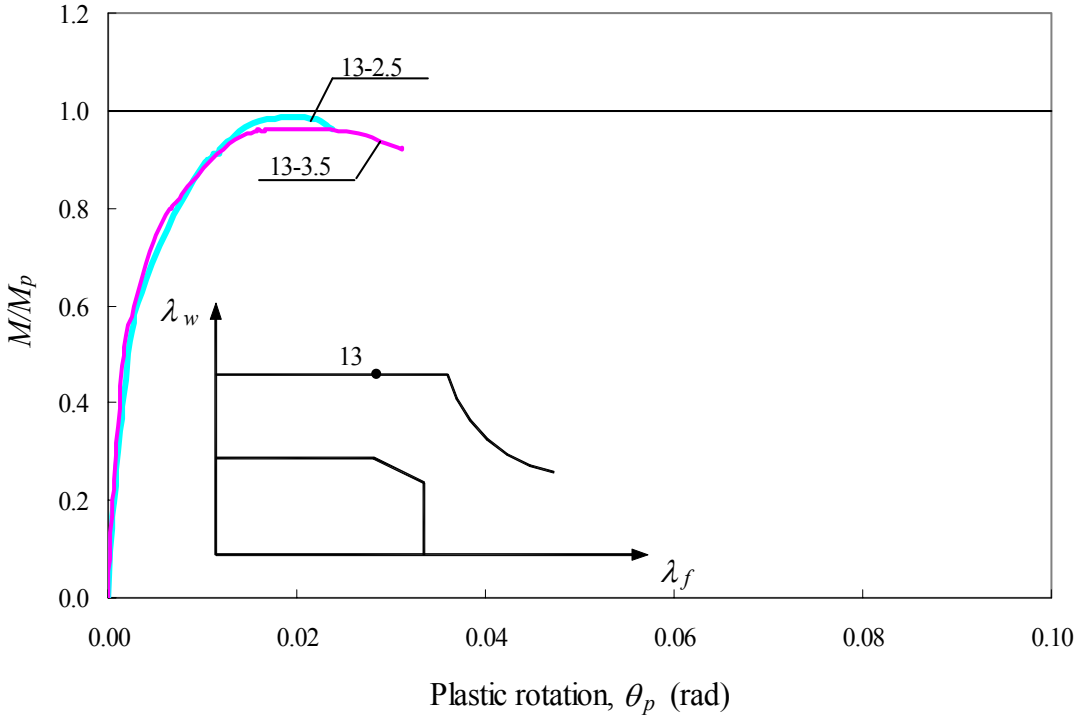

Figure 7.17 Effect of cross section aspect ratio, h_w / b_f

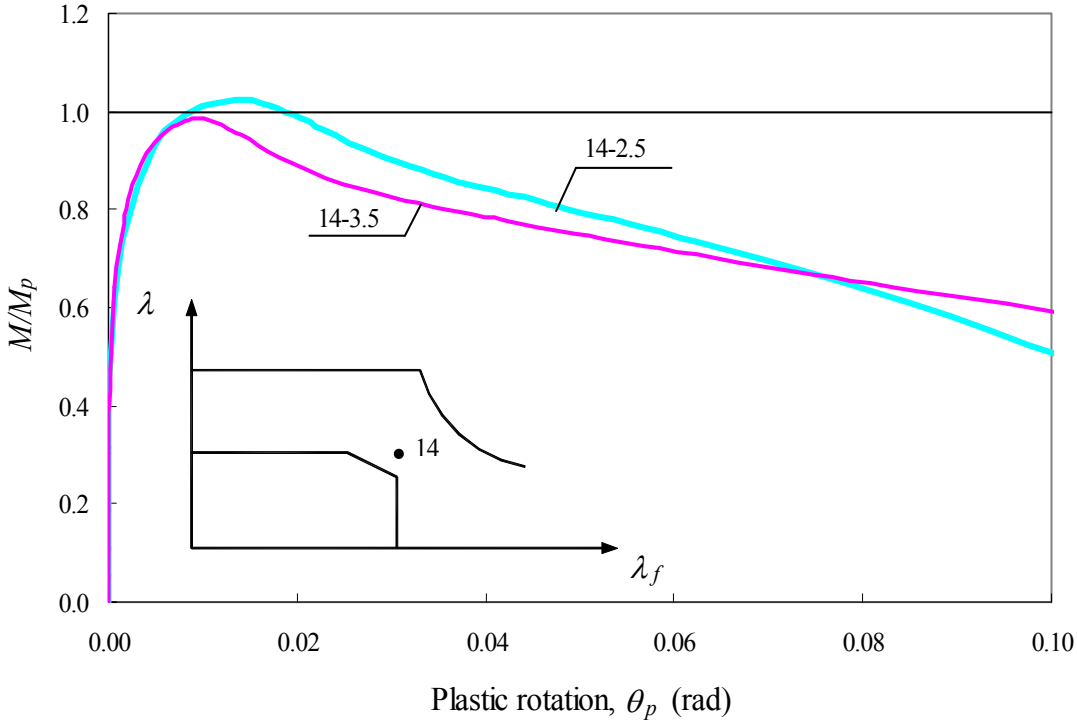

Figure 7.18 Effect of cross section aspect ratio, h_w / b_f

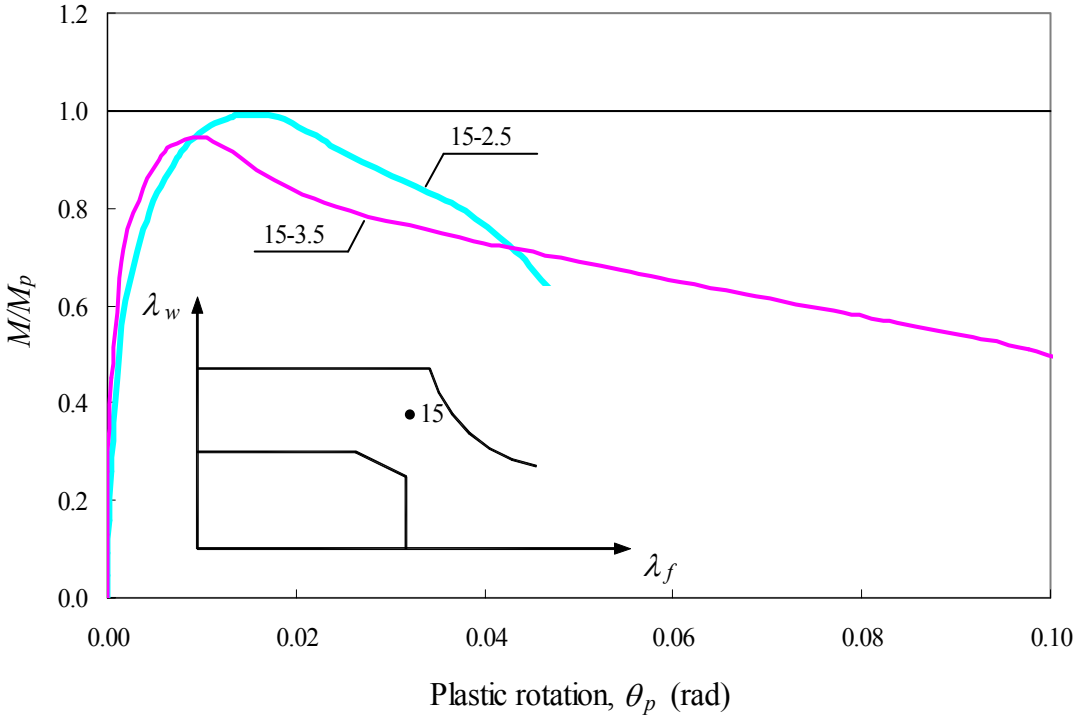

Figure 7.19 Effect of cross section aspect ratio, h_w / b_f

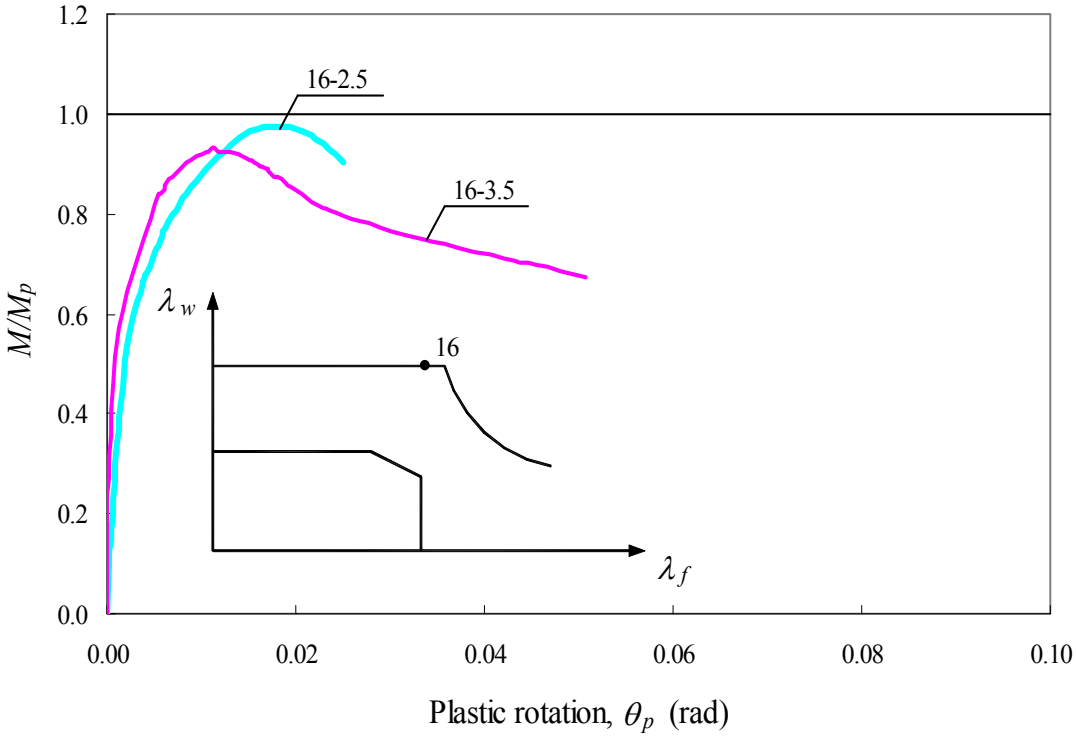

Figure 7.20 Effect of cross section aspect ratio, h_w / b_f

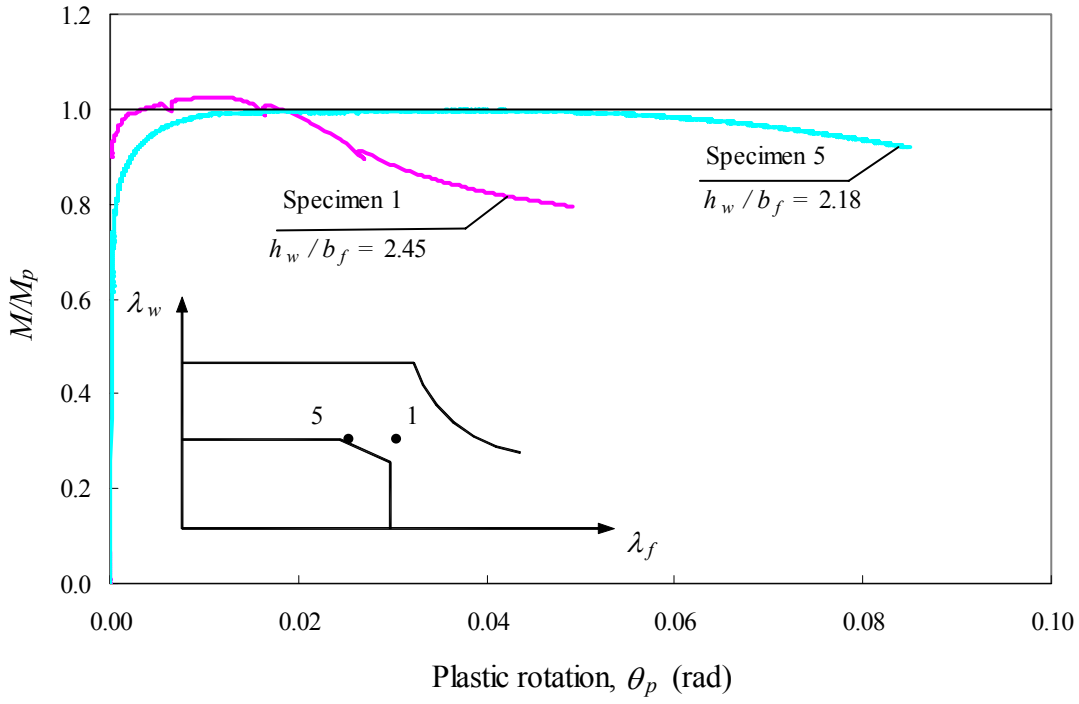

Figure 7.21 Comparison of Specimen 1 and Specimen 5

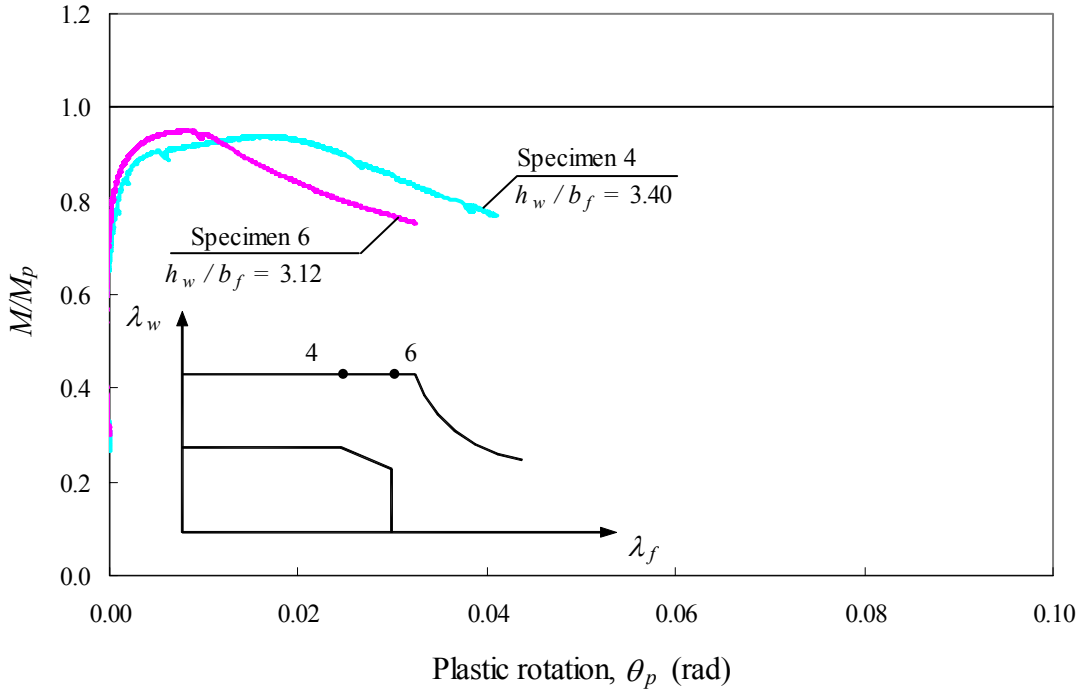

Figure 7.22 Comparison of Specimen 4 and Specimen 6

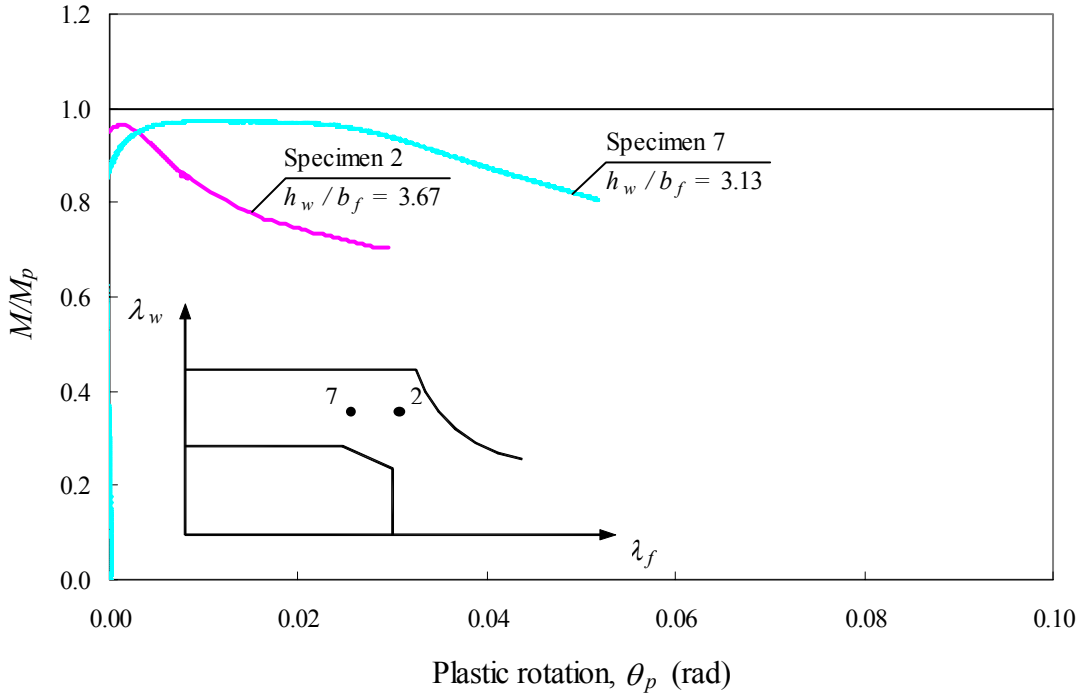

Figure 7.23 Comparison of Specimen 2 and Specimen 7

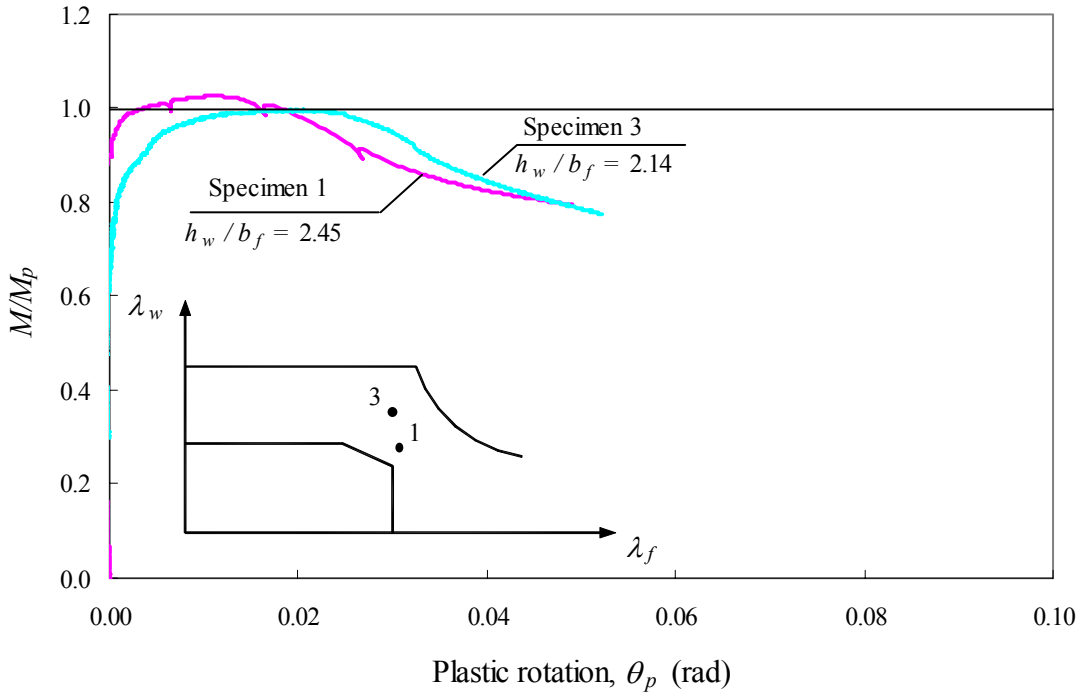

Figure 7.24 Comparison of Specimen 1 and Specimen 3

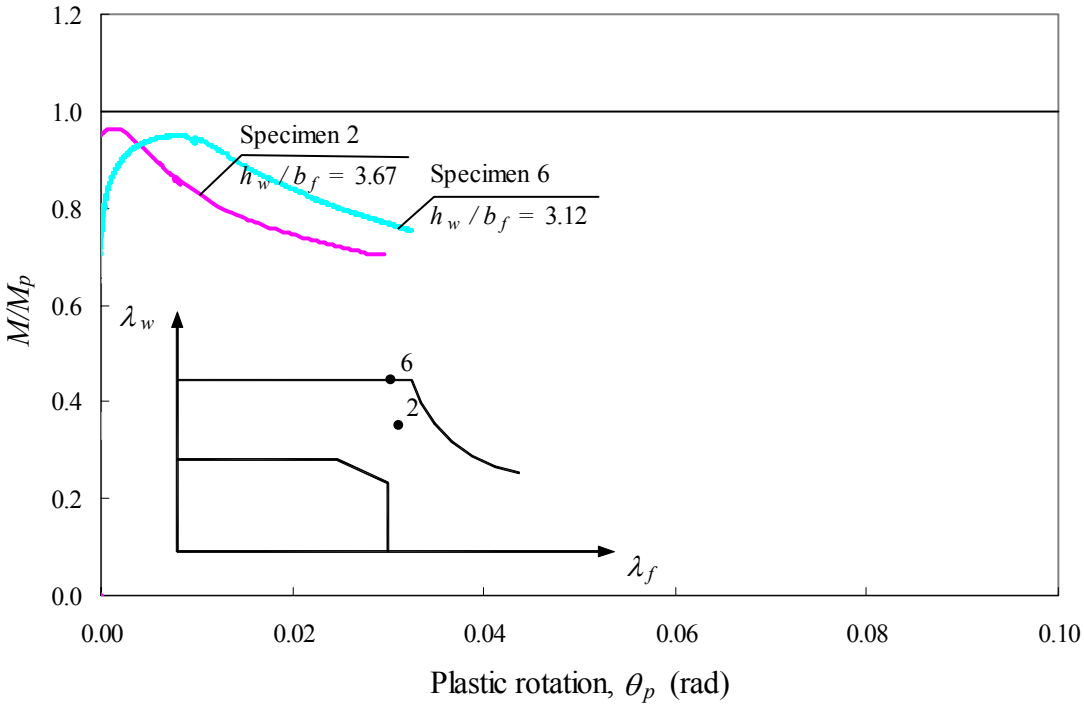

Figure 7.25 Comparison of Specimen 2 and Specimen 6

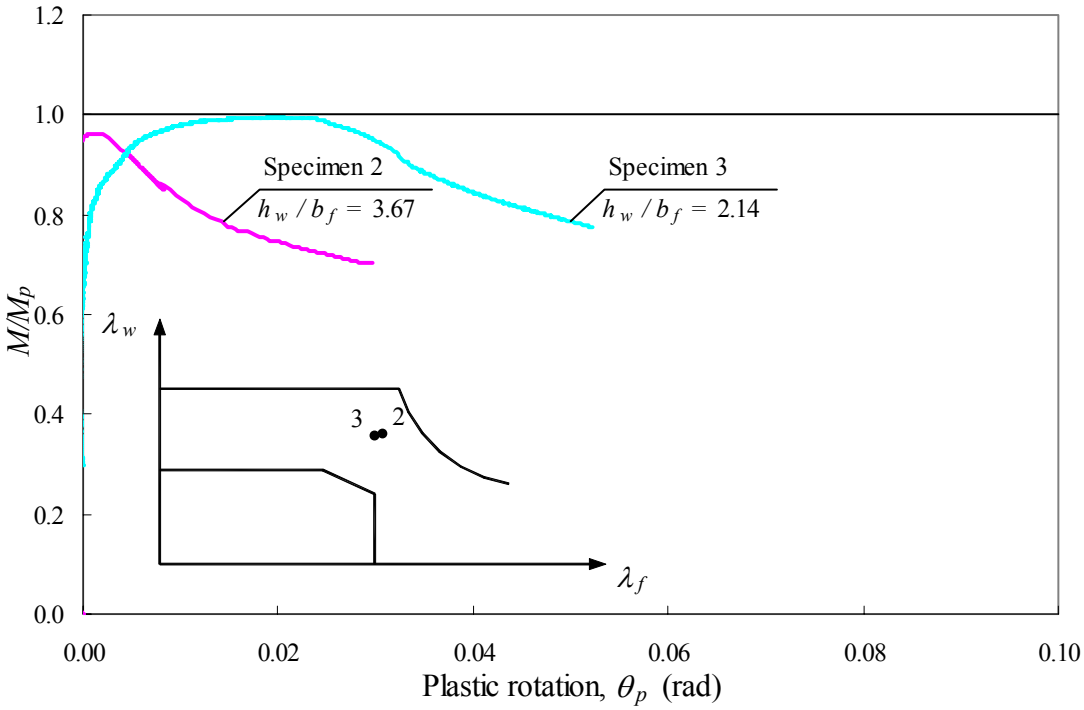

Figure 7.26 Comparison of Specimen 2 and Specimen 3

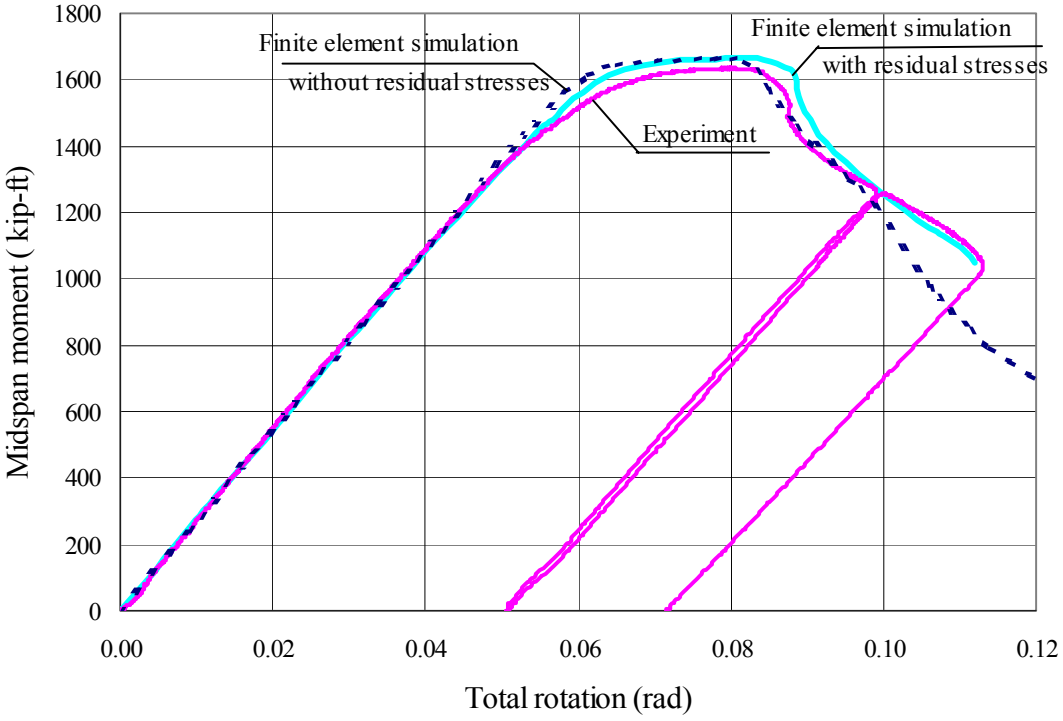

Figure 7.27 Effect of residual stresses (Specimen 3)

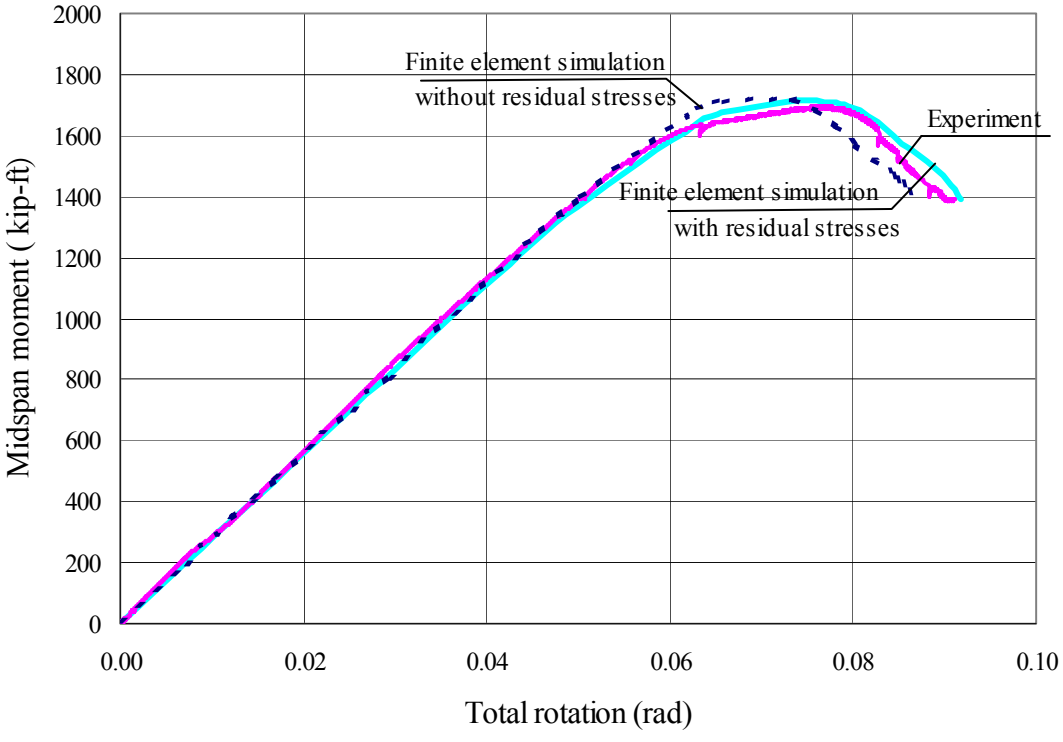

Figure 7.28 Effect of residual stresses (Specimen 4)

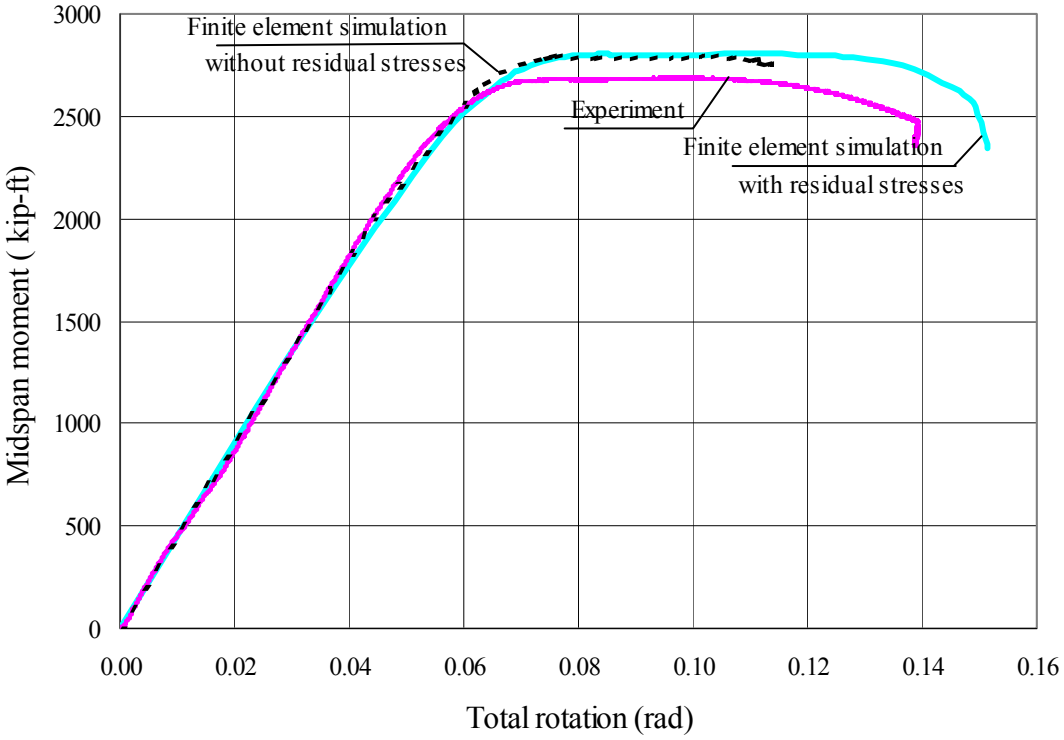

Figure 7.29 Effect of residual stresses (Specimen 5)

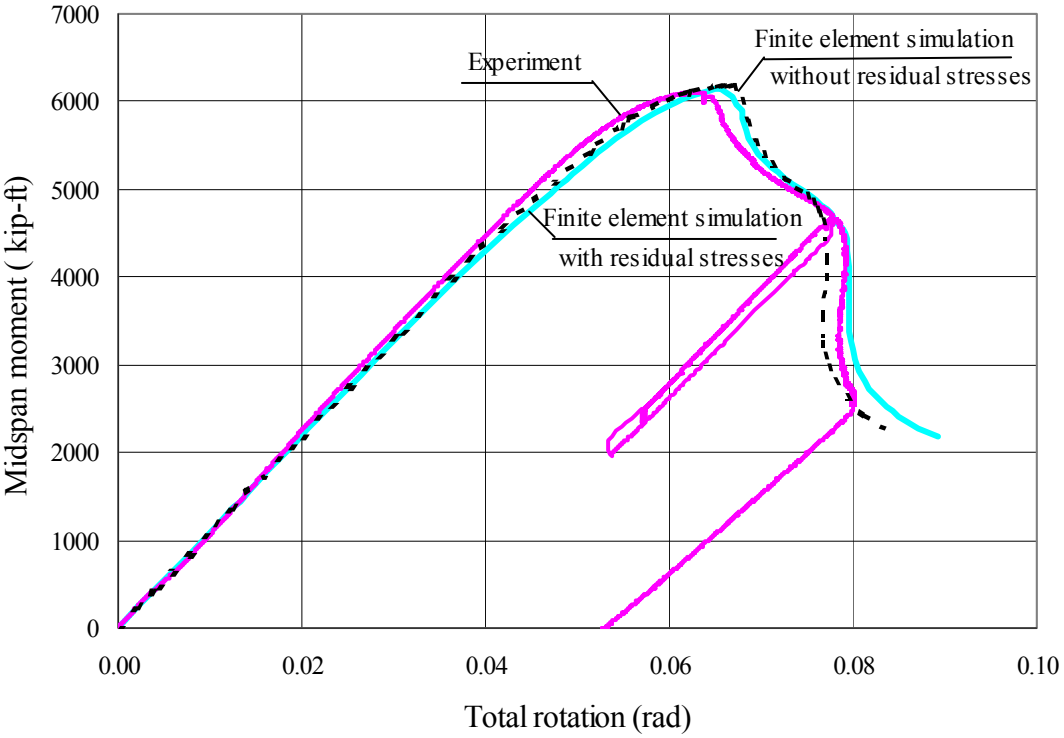

Figure 7.30 Effect of residual stresses (Specimen 6)

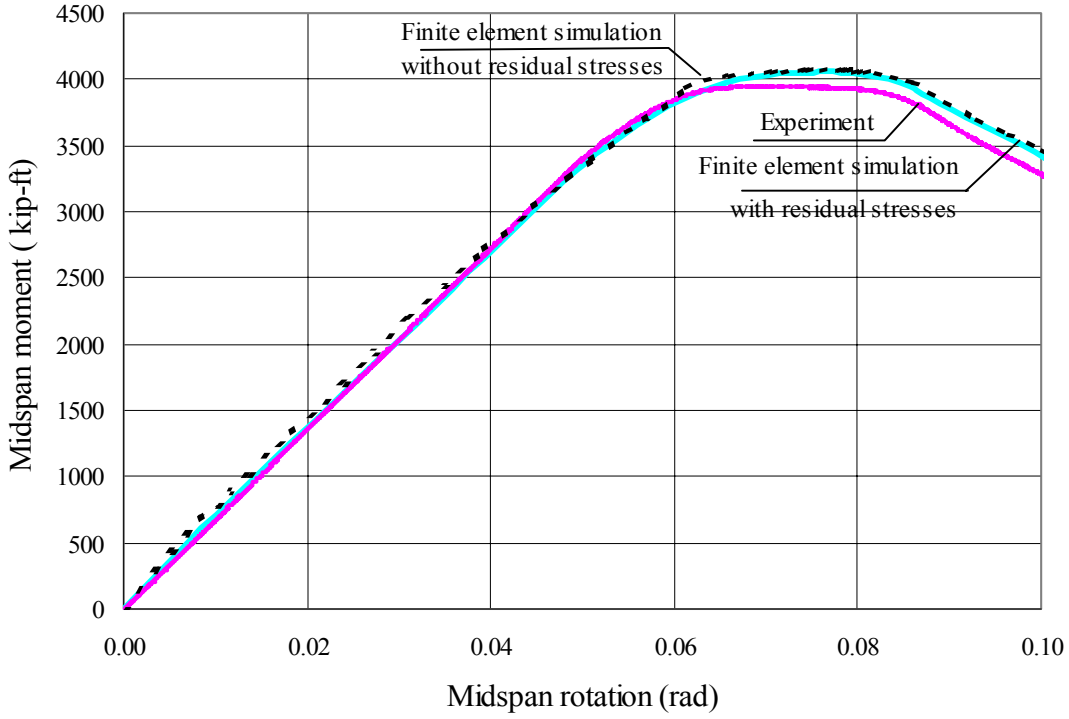

Figure 7.31 Effect of residual stresses (Specimen 7)

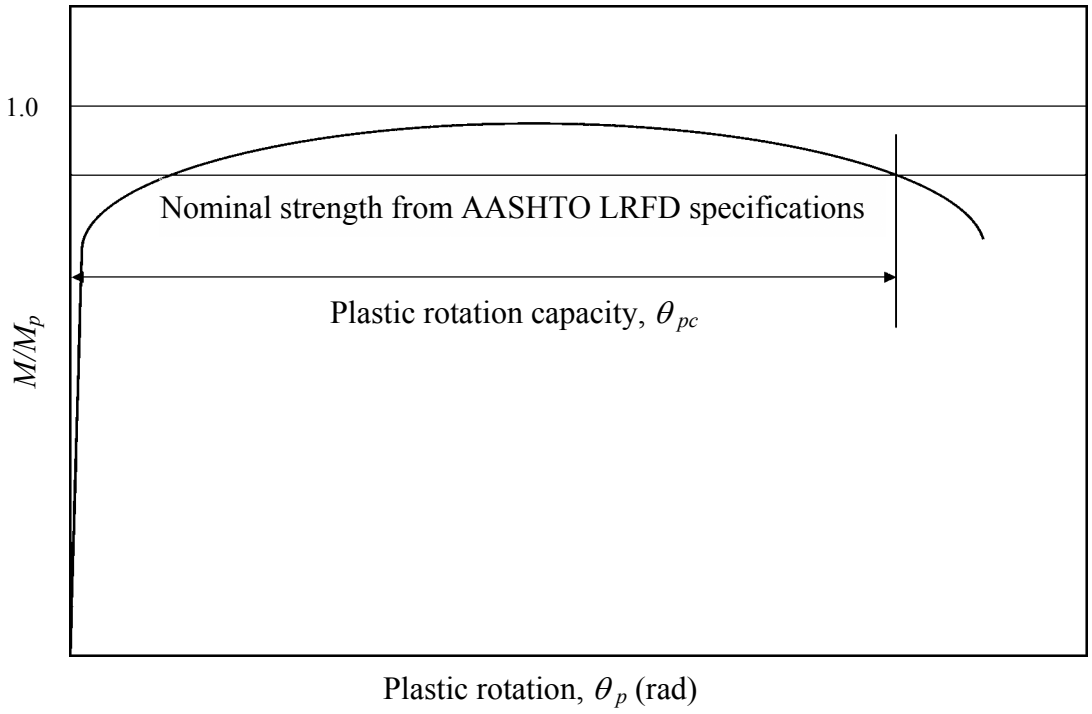

Figure 7.32 Plastic rotation capacity definition

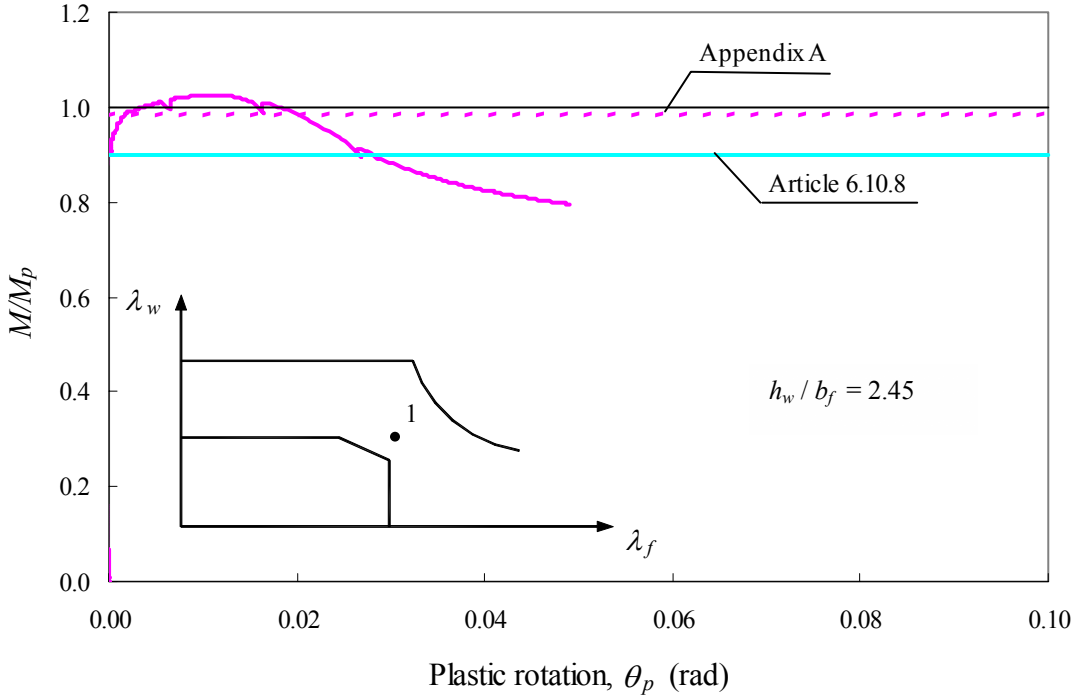

Figure 7.33 Strength and ductility of Specimen 1

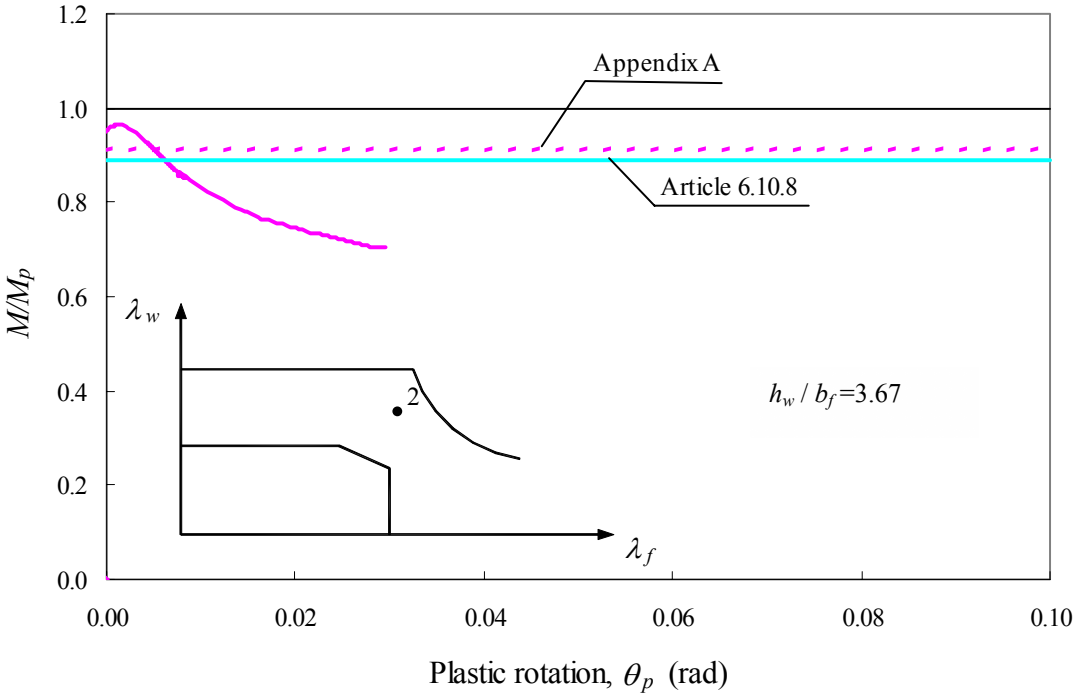

Figure 7.34 Strength and ductility of Specimen 2

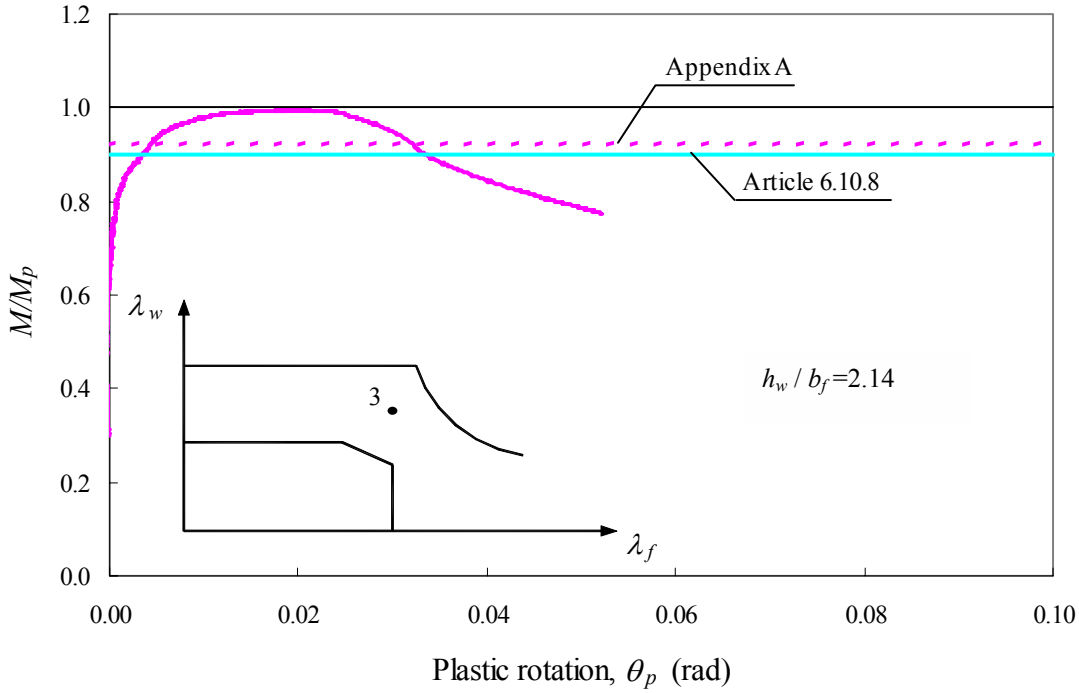

Figure 7.35 Strength and ductility of Specimen 3

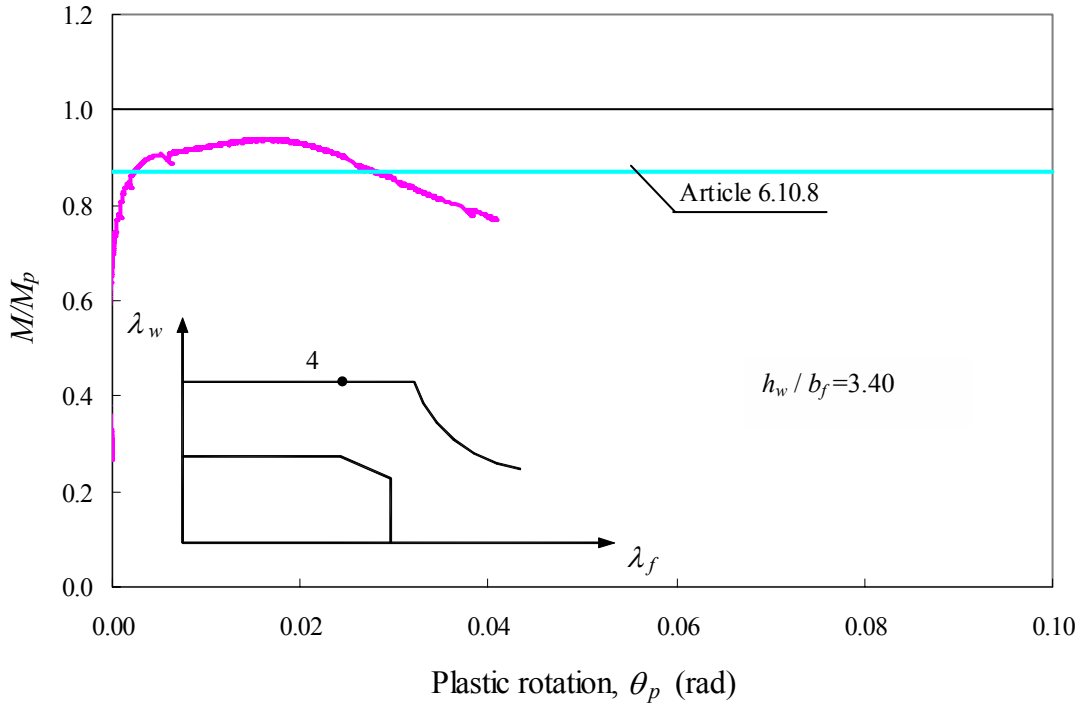

Figure 7.36 Strength and ductility of Specimen 4

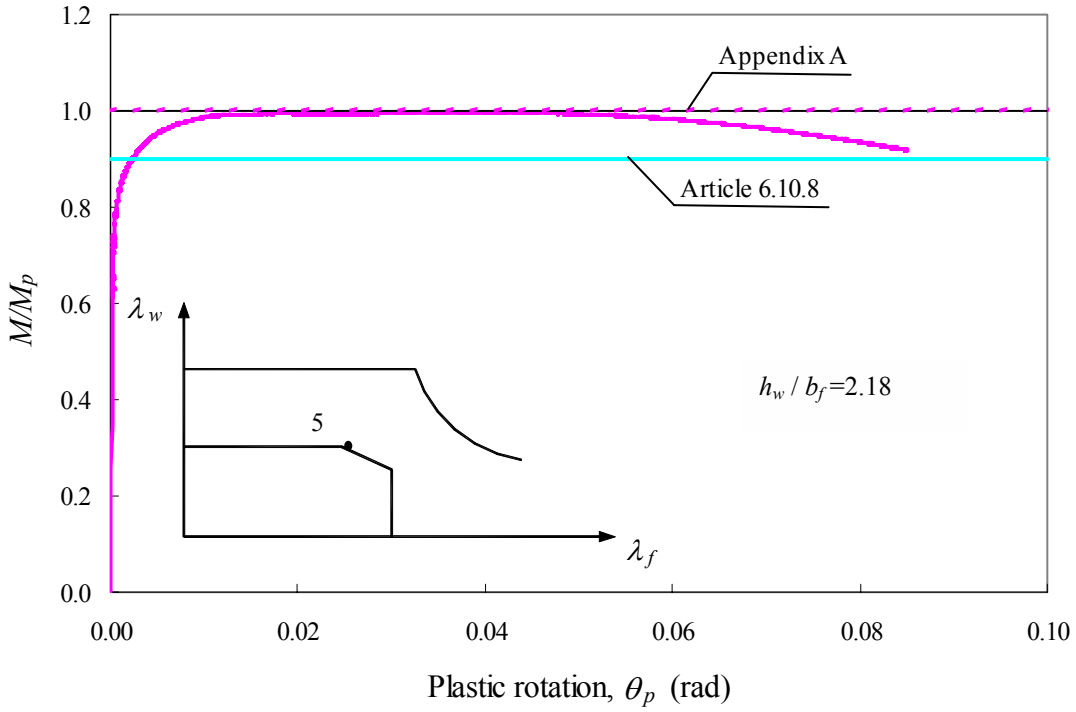

Figure 7.37 Strength and ductility of Specimen 5

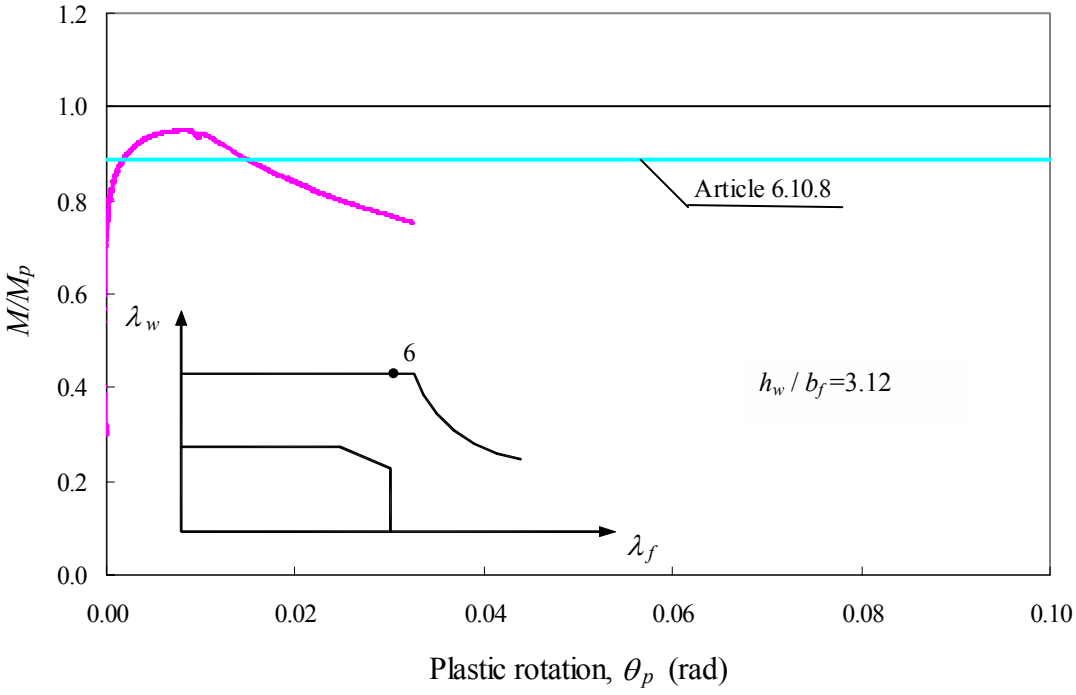

Figure 7.38 Strength and ductility of Specimen 6

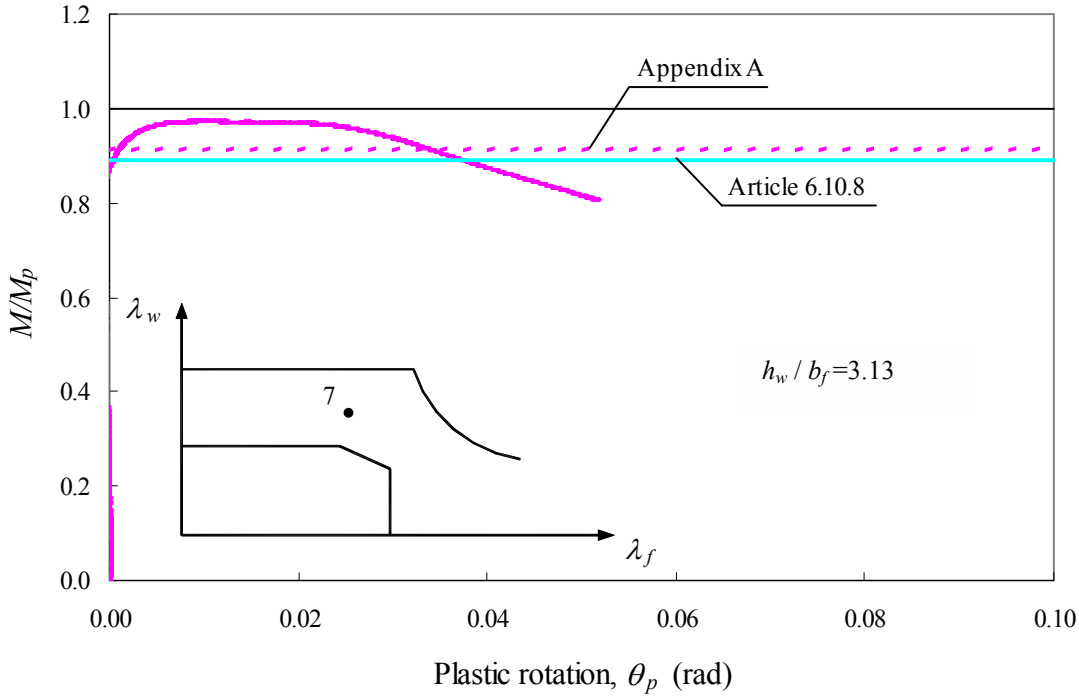

Figure 7.39 Strength and ductility of Specimen 7

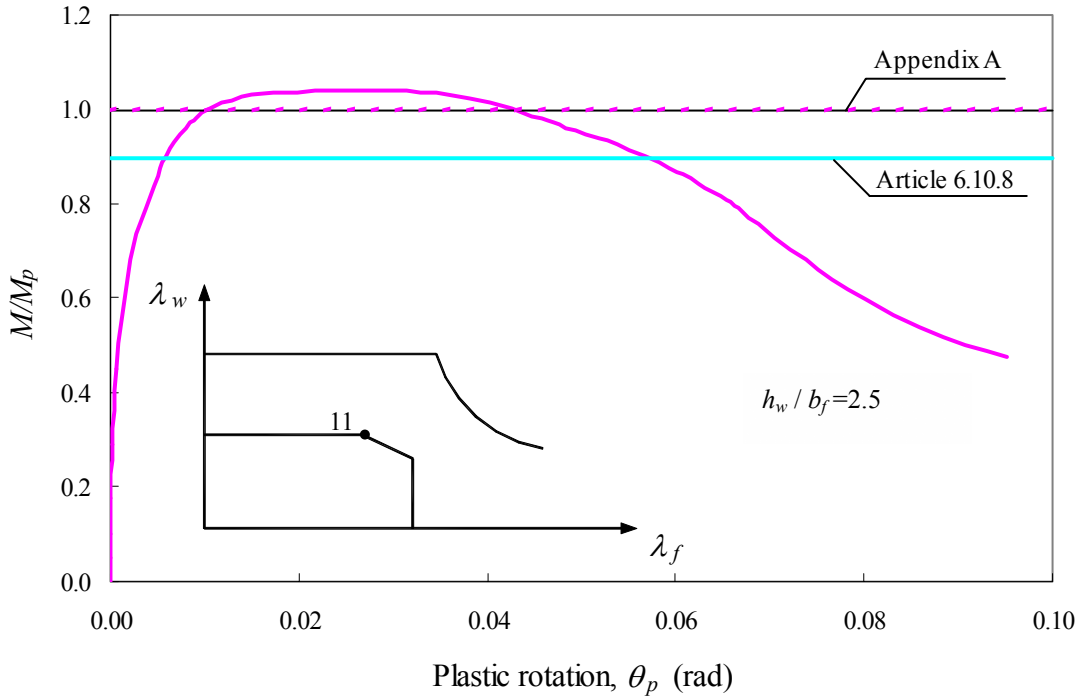

Figure 7.40 Strength and ductility of Specimen 11-2.5

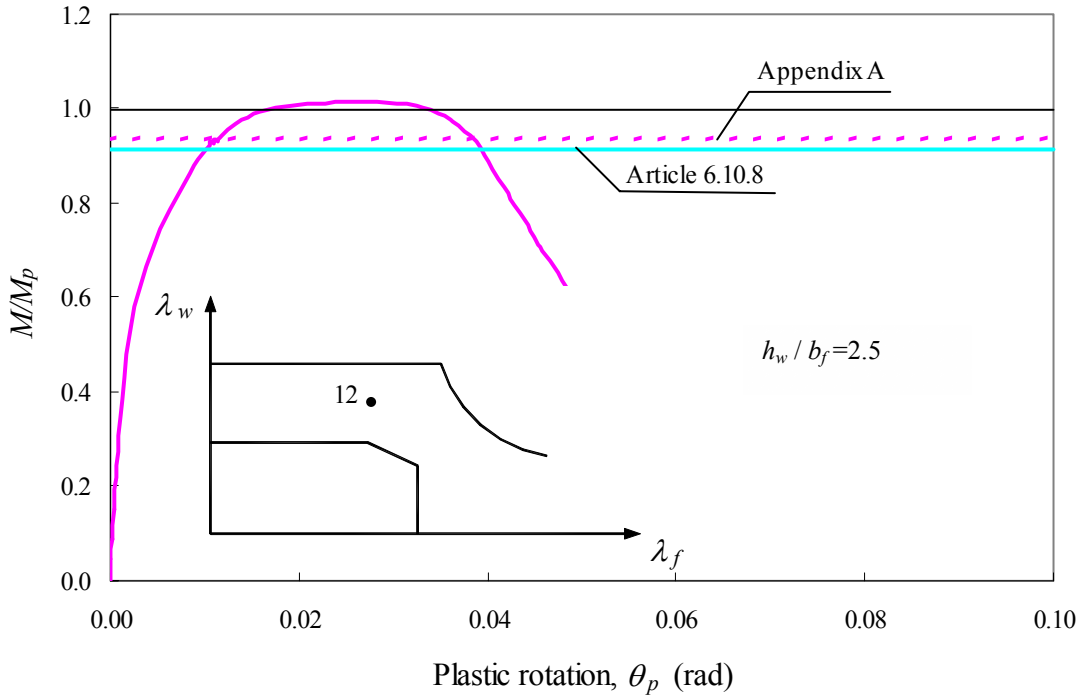

Figure 7.41 Strength and ductility of Specimen 12-2.5

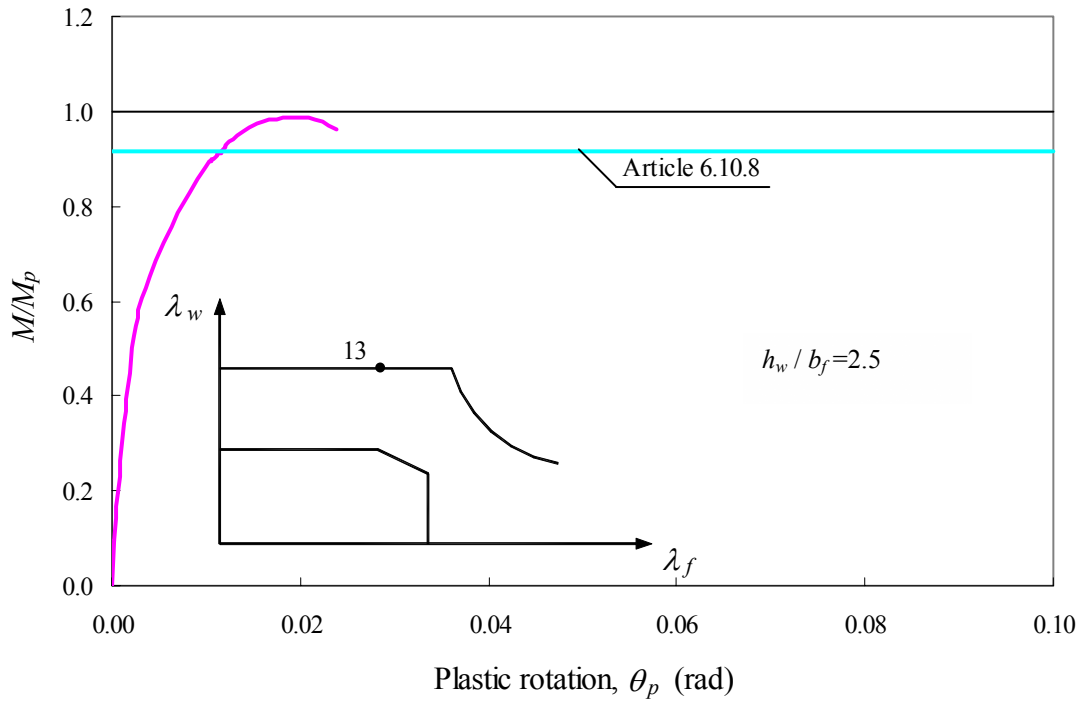

Figure 7.42 Strength and ductility of Specimen 13-2.5

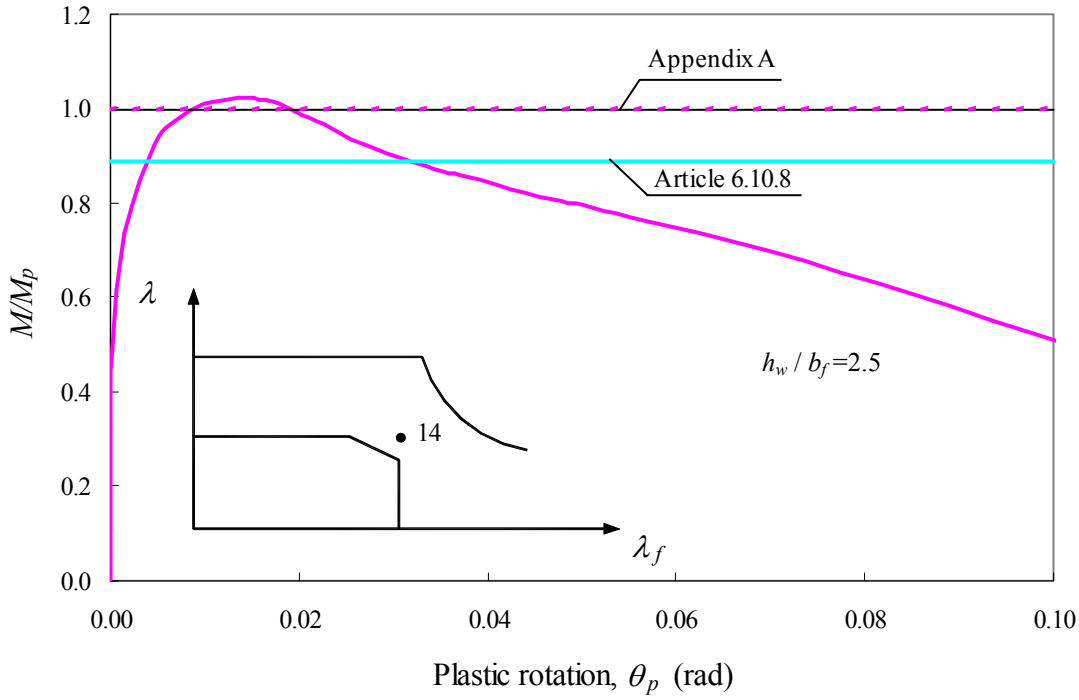

Figure 7.43 Strength and ductility of Specimen 14-2.5

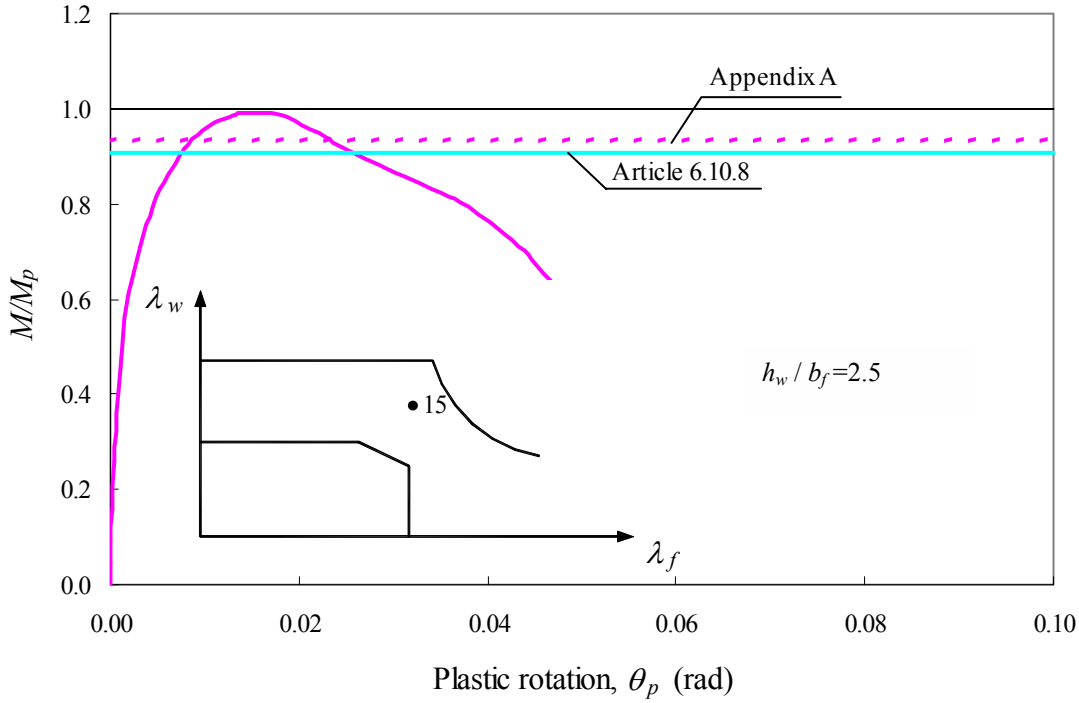

Figure 7.44 Strength and ductility of Specimen 15-2.5

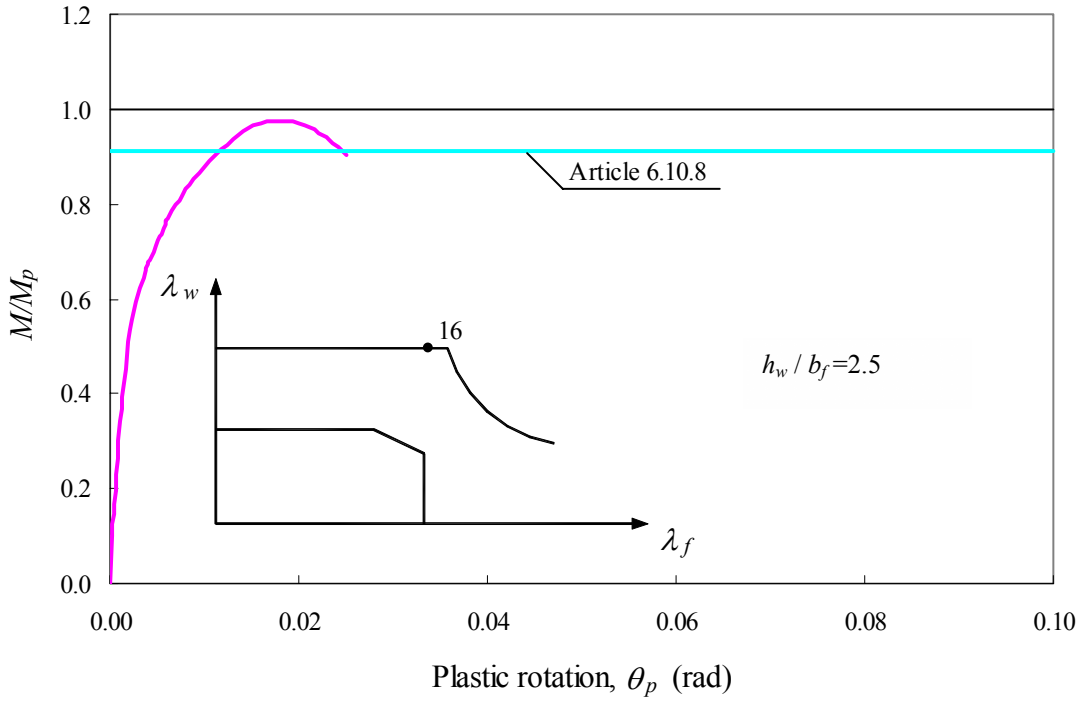

Figure 7.45 Strength and ductility of Specimen 16-2.5

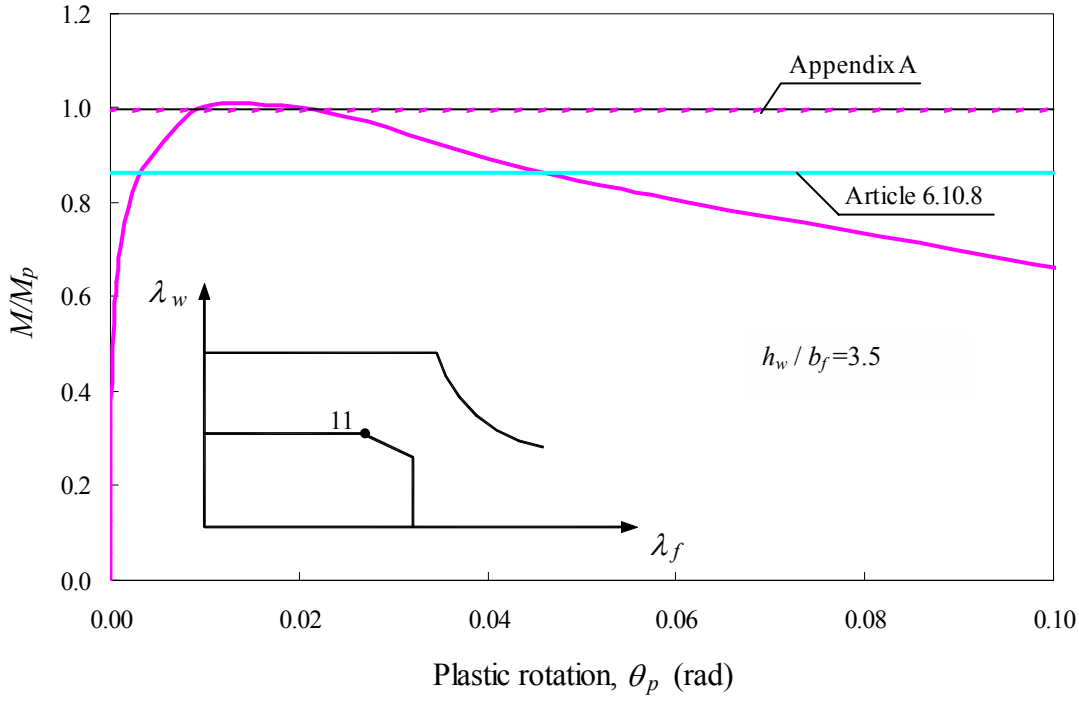

Figure 7.46 Strength and ductility of Specimen 11-3.5

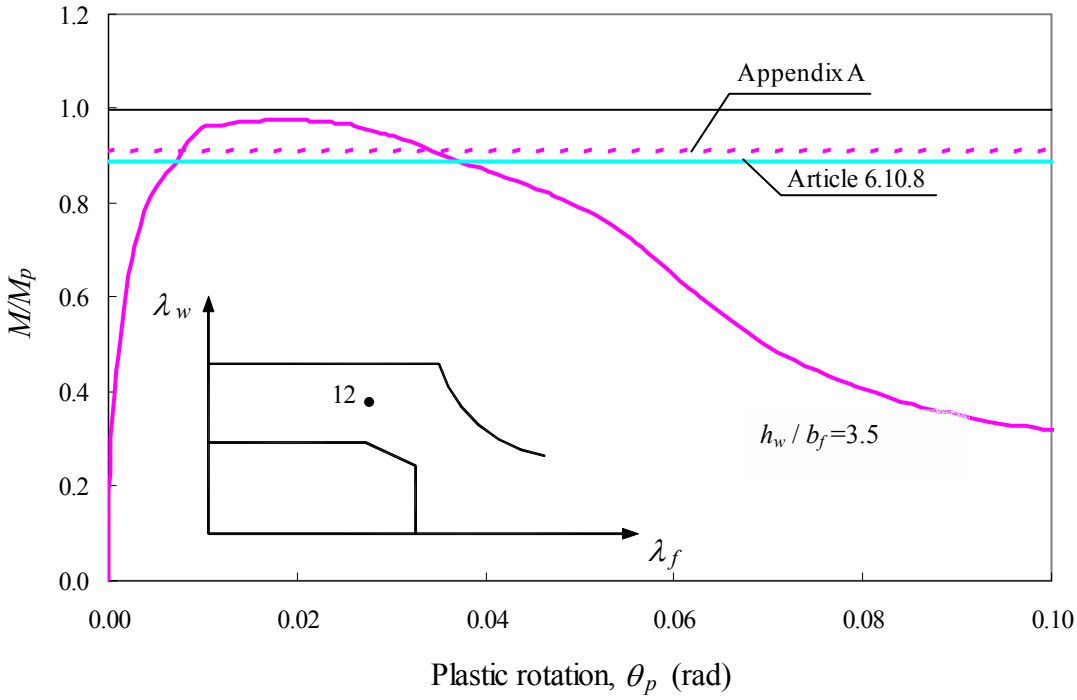

Figure 7.47 Strength and ductility of Specimen 12-3.5

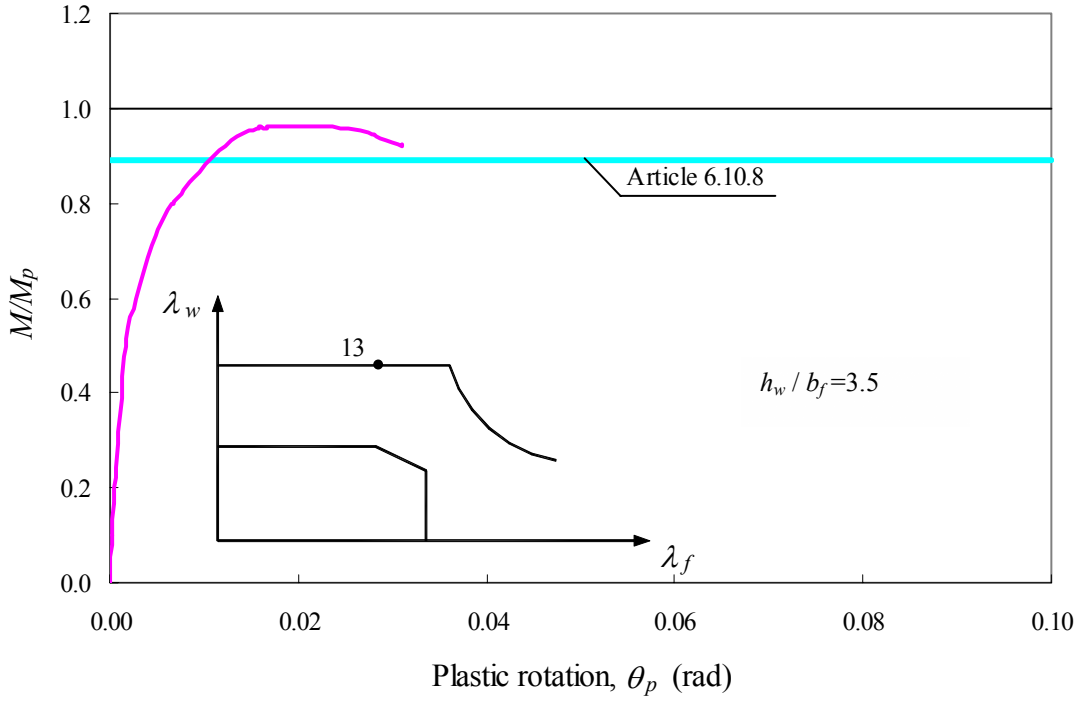

Figure 7.48 Strength and ductility of Specimen 13-3.5

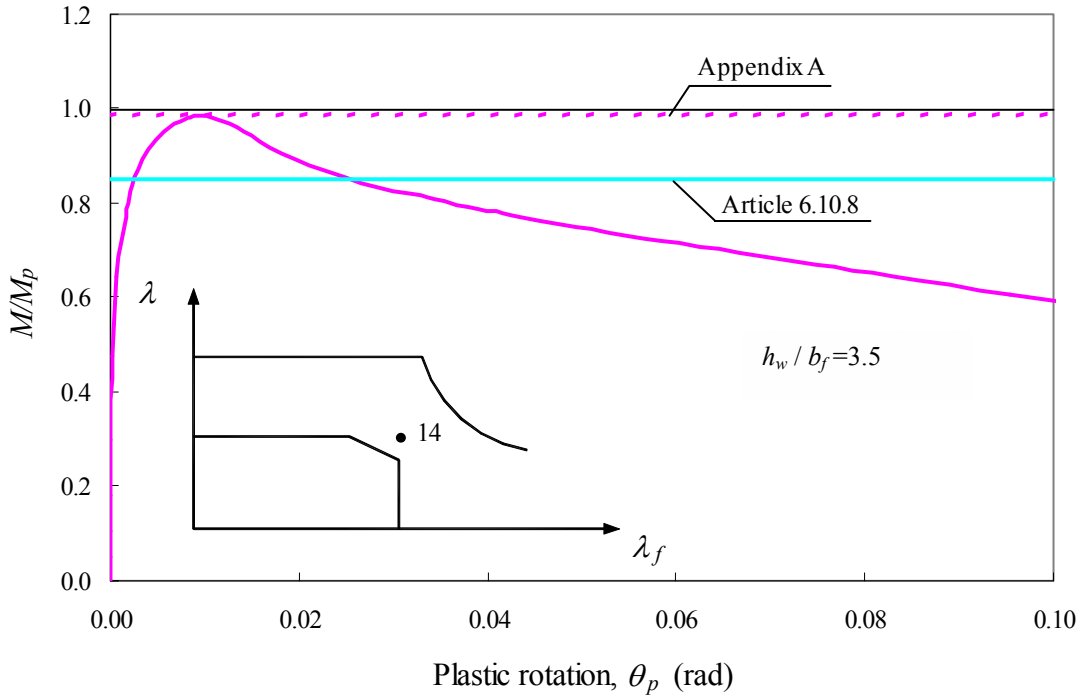

Figure 7.49 Strength and ductility of Specimen 14-3.5

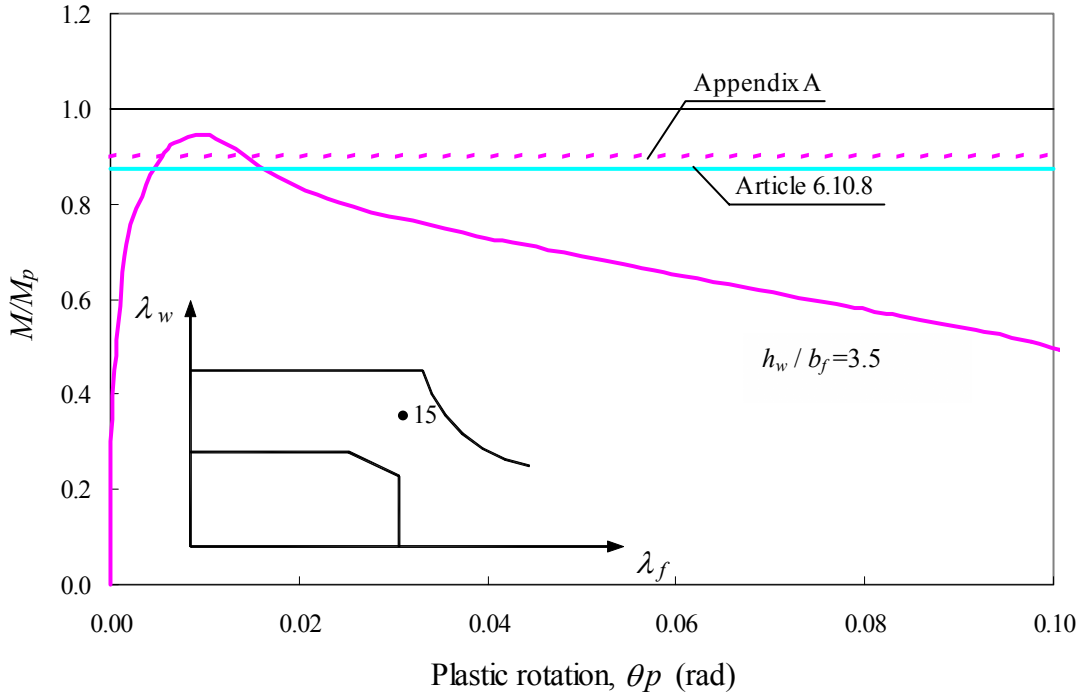

Figure 7.50 Strength and ductility of Specimen 15-3.5

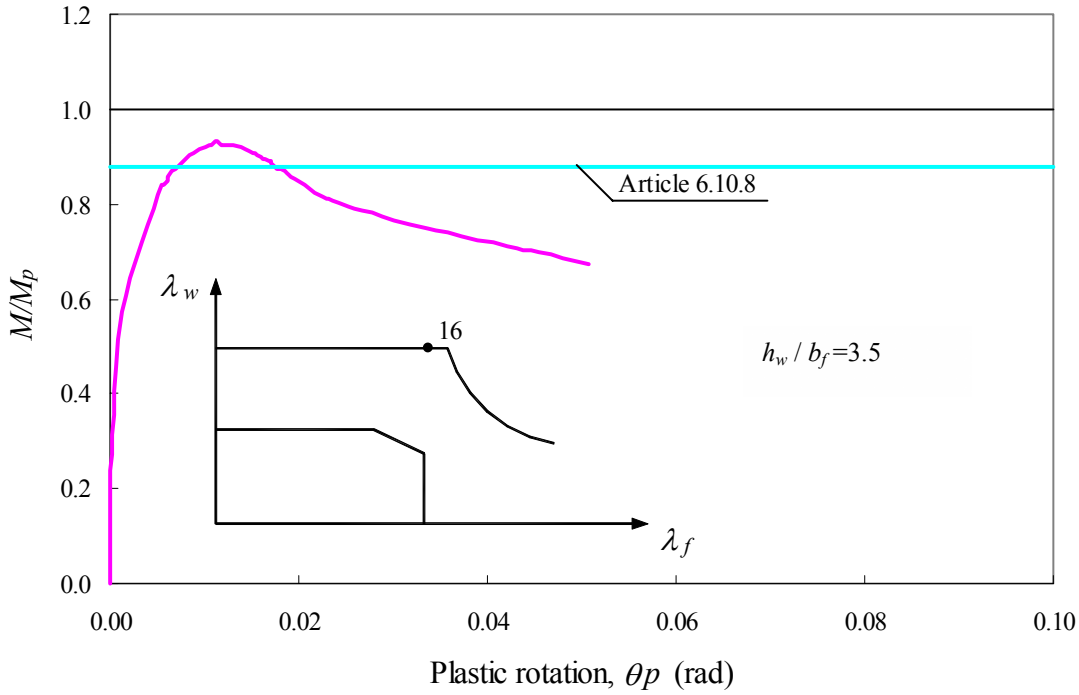

Figure 7.51 Strength and ductility of Specimen 16-3.5

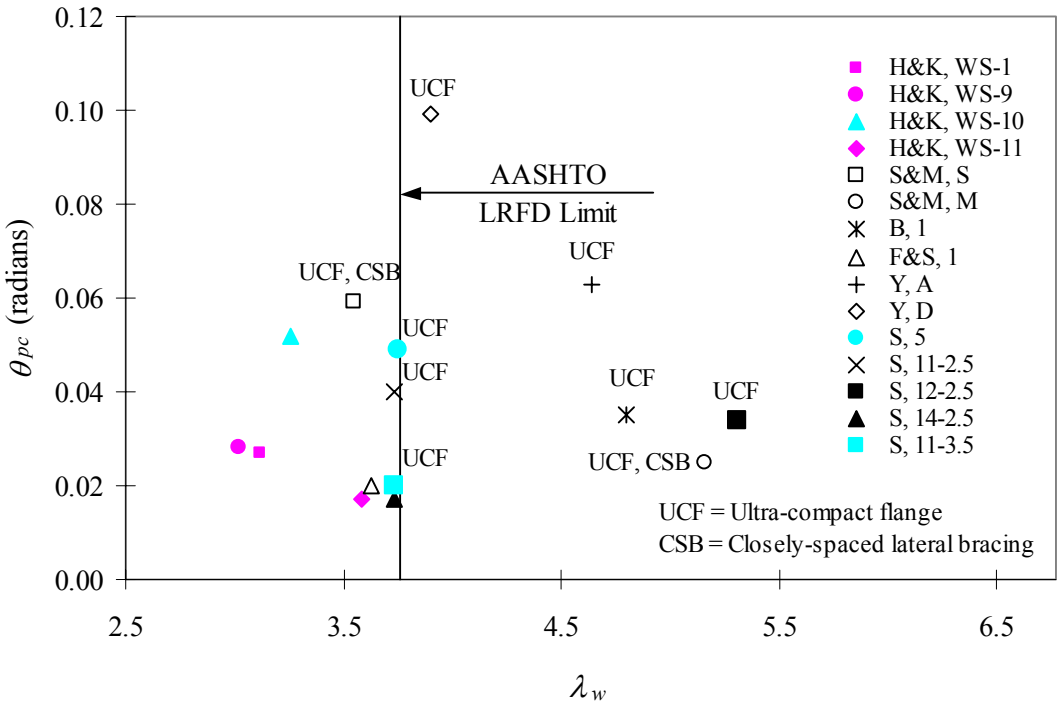

Figure 7.52 Plastic rotation capacity at M_p versus normalized web slenderness

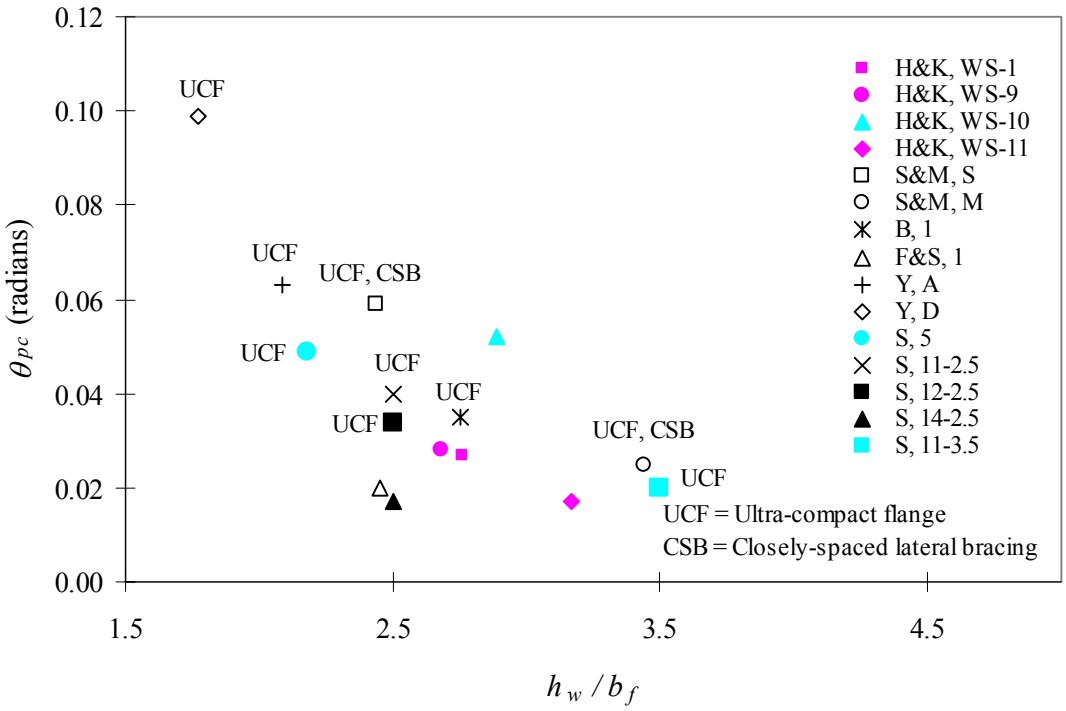

Figure 7.53 Plastic rotation capacity at M_p versus cross section aspect ratio

CHAPTER 8 Summary and Conclusions

8.1 Summary

This research investigated the flexural strength and ductility of highway bridge I-girders fabricated from HPS-100W steel, a new high performance steel with a nominal yield strength of 100 ksi (690 MPa), developed at Lehigh University. This steel has stress-strain characteristics that are different than those of conventional ASTM A709 Grade 50 steel. The applicability of two versions of the AASHTO LRFD Bridge Design Specifications, namely, the Draft 2004 AASHTO LRFD specifications [AASHTO 2004] and the 2001 AASHTO LRFD specifications [AASHTO 2001], for calculating the nominal flexural strength of bridge I-girder fabricated from HPS-100W was investigated. The research integrated experiments, finite element simulations, and a parametric study to provide better understanding of the flexural strength and ductility of HPS-100W bridge I-girders in negative flexure, as controlled by local buckling of the compression flange and web.

In the 1996 AASHTO LRFD specifications, the nominal flexural strength of steel I-girders with a specified minimum yield strength greater than 50 ksi (345 MPa) was limited to the yield moment. However, studies performed by Barth et al. [2000] and Yakel et al. [2002], developed knowledge that enabled this limit on the specified minimum yield strength to be raised to 70 ksi (485 MPa), as is now implemented in the 2001 AASHTO LRFD specifications [AASHTO 2001] and in the Draft 2004 AASHTO LRFD specifications [AASHTO 2004]. The present research is aimed at developing knowledge to enable the current limit in the 2001 AASHTO LRFD specifications to be eliminated, enabling the economic use of HPS-100W.

To initiate the work, a finite element model was developed and verified using the experimental results from two specimens tested by Fahnestock and Sause [1998]. The stress-strain characteristics of the HPS-100W steel used in fabricating these two earlier specimens differed from the stress-strain characteristics of the steel used in the present study. However, the finite element simulations of these two specimens provided information about the main parameters controlling compression flange and web local buckling of I-girders, which control their flexural strength and ductility. These parameters are the compression flange and web slenderness, the cross section aspect ratio, the imperfection amplitude and location, the twisting moment and lateral forces transferred between the web and compression flange, and the residual stresses. The information was used in selecting the properties of the experimental specimens, and motivated the work to accurately measure these parameters prior to testing of these specimens.

Five I-girder experimental specimens were designed, fabricated, and tested. Each specimen was a half-scale model of the pier region of a continuous-span bridge I-girder, with a main span in the range of 150 ft to 350 ft (46 m to 107 m). Prior to fabricating the experimental specimens, tensile coupon specimens were cut from the plates that were used in fabricating these specimens. The thickness of these tensile coupon specimens was measured and the tensile coupon specimens were tested to determine the stress-strain characteristics of this steel. Using this procedure of determining the thickness and stress-strain properties before selecting the experimental specimen geometries, the actual normalized flange and web slenderness of each experimental specimen were made very close to the desired web and flange slenderness. Guided with the plate thickness, stress-strain properties, and knowledge from the finite element simulations of the two specimens tested by Fahnestock and Sause [1998], the geometry of each experimental specimen was selected. The possibility of making comparisons with previously tested specimens was also considered.

After selecting the experimental specimen geometries, more detailed design calculations for each specimen were performed following the 2001 AASHTO LRFD specifications [AASHTO 2001]. The nominal flexural strength, the lateral brace spacing, and the nominal shear resistance were calculated and compared against the requirements. Preliminary finite element simulations were performed on the specimens prior to fabrication to confirm the expected behavior.

After the experimental specimens were fabricated and delivered, the specimen geometry, geometric imperfection, and residual stresses were measured. The residual stresses were measured using the hole-drilling method in accordance with the ASTM Standard Test Method E837 [ASTM 1997]. The instrumentation plan was based on, in part, clustering the strain gages on the compression flange at regions where local flange buckling is expected to occur. These regions were determined from the preliminary finite element simulations of the experimental specimens. Also, to monitor the twisting moment transferred between the web and the flange, strain gages were attached to the web as close as possible to its intersection with the compression flange. To convert strains from the strain gages into stresses after the material had yielded, plasticity theory was used. A plane stress plasticity program was developed for this purpose as a part of this research.

Each of the five experimental specimens was tested to failure under three-point loading to simulate the condition of negative flexure at an interior pier of a continuous span bridge. For each experimental specimen, a finite element simulation was performed and the finite element simulation results were compared with the experimental results. Good correlation between the experimental results and the finite element simulation results was observed, and a parametric study was then performed. In this parametric study, the effect of normalized flange slenderness, λ_f, normalized

web slenderness, λ_w, and cross section aspect ratio, h_w/b_f, on the flexural strength and ductility of I-girders fabricated from HPS-100W was investigated.

The flexural strength from the finite element simulations for the parametric specimens and from the experimental results for the experimental specimens was compared with the nominal flexural strength calculated using two versions of the AASHTO LRFD specifications, namely, the Draft 2004 AASHTO LRFD specifications [AASHTO 2004] and the 2001 AASHTO LRFD specifications [AASHTO 2001]. Comparison of the calculated nominal flexural strength with the finite element simulation results and the experimental results shows whether the specifications which limit the nominal flexural strength of HPS-100W I-girders to the yield moment, can be eliminated. Also the flexural ductility from the finite element simulations for the parametric specimens and the experimental results for the experimental specimens was compared with that calculated using the Draft 2004 AASHTO LRFD specifications [AASHTO 2004].

8.2 Conclusions

This section presents the conclusions from this research. These conclusions are related to: (1) the applicability of the AASHTO LRFD Bridge Design Specifications to the flexural strength and ductility of HPS-100W I-girders, (2) the research methods used in this investigation, (3) the finite element simulations, and (4) the parameters affecting the flexural strength and ductility of HPS-100W I-girders.

Regarding the applicability of the AASHTO LRFD Bridge Design Specifications for calculating the flexural strength and ductility of HPS-100W I-girders, the following conclusions are made:

- Comparison of the flexural strength of the experimental and parametric specimens with the nominal flexural strength, M_n, calculated according to the Draft 2004 AASHTO LRFD specifications [AASHTO 2004], using either Appendix A or Article 6.10.8 of the specifications, shows that these specifications are also applicable for calculating the nominal flexural strength of HPS-100W I-girders in negative flexure.
- The Draft 2004 AASHTO LRFD specifications [AASHTO 2004] define θ_{RL} as the plastic rotation at which the interior-pier section moment begins to decrease with increasing plastic rotation. Comparing the plastic rotation capacity of the experimental and parametric specimens with θ_{RL}, shows that Article B6.6.2.1 of the Draft 2004 AASHTO LRFD specifications [AASHTO 2004] provides a conservative estimate of the plastic rotation capacity.
- The optional Q formula of the 2001 AASHTO LRFD specifications [AASHTO 2001] was not conservative in calculating the nominal flexural strength, M_n, of HPS-100W I-girders in negative flexure. On the other hand, Article 6.10.4.2.4

was conservative in calculating the flexural strength, M_n, of HPS-100W I-girders. This conclusion is based on comparing the flexural strength of the experimental and parametric specimens with the nominal flexural strength calculated according to the 2001 AASHTO LRFD specifications [AASHTO 2001].

Regarding the research methods used in this investigation, the following conclusions are made:

- The procedures followed to execute the experiments proved to be valuable in achieving accurate experimental results, accurate understanding of experimental results, and accurate correlation with finite element simulations. These procedures are summarized as follows: (1) measure the plate thickness and material properties of the specimen plates before fabricating the specimens, (2) select the specimen geometries to satisfy the required slenderness and cross section aspect ratios, (3) perform preliminary finite element simulations, (4) after fabricating the specimens, measure the flange and web imperfections and the residual stresses, as well as the actual flange width and web height, (5) provide the necessary instrumentation to measure the desired strains and other deformations, (6) analyze the experimental data and use a plasticity program to convert the experimentally measured strains to stresses, and (7) perform finite element simulations and compare the results with experimental results in terms of local and global behavior.
- The implementation of a plane stress plasticity program provided a valuable tool for determining stresses from experimentally measured strains, which were used to correlate the complex state of flange stresses observed in the finite element simulations.

From the finite element simulations the following conclusions are made:

- The development and use of an accurate finite element model, verified through previous experimental data, is essential to achieving accurate correlation with the experimental results.
- An accurate finite element model requires, an accurate stress-strain model, accurate flange and web imperfections, and estimations of residual stresses.
- Accurate simulation of local buckling of the compression flange requires a fine mesh in regions where local buckling is expected to occur, especially at the edges of the compression flange.

Regarding the different parameters affecting the flexural strength and ductility of HPS-100W I-girders, the following conclusions are made:

- As the cross section aspect ratio, h_w/b_f, decreases, the plastic rotation capacity, θ_{pc}, increases. As h_w decreases, the length over which the twisting moment and lateral force are applied to the flange by the buckling web decreases. The twisting moment increases the compression flange torsional instability, and the lateral force produces lateral bending in the compression flange. As b_f increases, the flange torsional and lateral stiffness and strength increase.
- The normalized flange slenderness has a slight effect on the flexural strength, as λ_f decreases, the flexural strength slightly increases. However, λ_f has a large effect on the plastic rotation capacity. As λ_f decreases, the plastic rotation capacity considerably increases. The reason for this considerable increase in the plastic rotation capacity is mainly attributed to the increase in the flange torsional resistance as λ_f decreases.
- The normalized web slenderness, λ_w, has an effect on both the flexural strength and ductility. As λ_w increases, the flexural strength and ductility decrease. The reason for this reduction is that as λ_w increases the web buckles earlier. Also the length over which the twisting moment and lateral force are applied to the flange by the buckling web increases as the web height, h_w, increases (which increases λ_w).

8.3 Recommendations for Future Work

This research integrated experiments and finite element simulations to provide better understanding of the flexural strength and ductility of HPS-100W bridge I-girders in negative flexure, as controlled by local buckling of the compression flange and web. However, additional research is recommended. Before removing the restriction that limits the nominal flexural strength of steel I-girders with a specified minimum yield strength greater than 70 ksi (485 MPa) to the yield moment, other flexural strength limit states should be investigated. For example, the flexural strength of composite sections in positive flexure, where the flexural strength may be controlled by fracture of tension flange should be investigated. Other strength limit states should be investigated. For example, I-girder shear strength and the strength of bolted splices should be investigated.

Only five experimental specimens fabricated from HPS-100W steel were tested in this research. Therefore, it is recommended to perform experiments with different plate thickness and geometry than used in the present study. Parametric specimens with values of λ_f, λ_w, and h_w/b_f different than those used in the present study should be investigated.

The experimental specimens in the present study were tested to failure under three-point loading simulating the condition of negative flexure at an interior pier. However, other loading conditions should be investigated, for example, constant moment conditions.

Appendix A Plane Stress Plasticity

To calculate the stresses from the experimental strains, which are beyond the elastic range, a plane stress plasticity algorithm was used. In this appendix, the steps in the plane stress plasticity algorithm are explained. A computer program was developed to implement this algorithm. A comparison between the results obtained using this program and the commercially available finite element program ABAQUS [2002] is presented to validate the program.

A.1 Yield Criterion

The yield criterion defines a surface, which represents the boundary of the current elastic region. If the stress state lies within this boundary, no plastic deformations will take place. On the other hand, when the stress state lies on the boundary, plastic deformations will occur. The Von Mises yield criterion was used in this algorithm because this yield criterion is based on a continuous function. For plane stress problems, Von Mises yield criterion for a nonlinear hardening material is defined by [Crisfield, 1991]:

$$f = \sqrt{\sigma^2{}_{11} + \sigma^2{}_{22} - \sigma_{11}\,\sigma_{22} + 3\,\sigma^2{}_{12}} - \sigma_y(\varepsilon_{ps}) \tag{A.1}$$

$$f = \sigma_e - \sigma_y(\varepsilon_{ps}) \tag{A.2}$$

$$\sigma_e = \sqrt{\sigma^2{}_{11} + \sigma^2{}_{22} - \sigma_{11}\,\sigma_{22} + 3\,\sigma^2{}_{12}} = \sqrt{3J} = \sqrt{\frac{3}{2} S_{ij} S_{ij}} \tag{A.3}$$

where:

σ_e = Effective stress
J = Second stress invariant
S_{ij} = Stress deviator tensor
$d\varepsilon_{ij}^p$ = Plastic strain increment in i-j direction
$\sigma_y(\varepsilon_{ps})$ = Yield stress as a function of the equivalent plastic strain, ε_{ps}

A.2 Plastic Strain

The equivalent plastic strain, ε_{ps}, is defined as:

$$\varepsilon_{ps} = \int d\varepsilon_{ps} \tag{A.4}$$

which is accumulated from the equivalent plastic strain rate [Crisfield, 1991]:

$$d\varepsilon_{ps} = \sqrt{\frac{2}{3} d\varepsilon_{ij}^{p} d\varepsilon_{ij}^{p}} \tag{A.5}$$

For three dimensional plasticity:

$$d\varepsilon_{ps} = \sqrt{\frac{2}{3}\left[d\varepsilon_{11}^{p\,2} + d\varepsilon_{22}^{p\,2} + d\varepsilon_{33}^{p\,2} + 2\left[d\varepsilon_{12}^{p\,2} + d\varepsilon_{23}^{p\,2} + d\varepsilon_{13}^{p\,2} \right] \right]} \tag{A.6}$$

For two dimensional plasticity, $d\varepsilon_{23}^{p} = d\varepsilon_{13}^{p} = 0$.

and since the plastic volumetric strain is zero:

$$d\varepsilon_{33}^{p} = -\left(d\varepsilon_{11}^{p} + d\varepsilon_{22}^{p} \right) \tag{A.7}$$

Therefore:

$$d\varepsilon_{33}^{p\,2} = \left(d\varepsilon_{11}^{p\,2} + d\varepsilon_{22}^{p\,2} + 2\, d\varepsilon_{11}^{p}\, d\varepsilon_{22}^{p} \right) \tag{A.8}$$

Substituting from Equations A.7 and A.8 into Equation A.6 yields:

$$d\varepsilon_{ps} = \frac{2}{\sqrt{3}} (d\varepsilon_{11}^{p\,2} + d\varepsilon_{22}^{p\,2} + d\varepsilon_{11}^{p}\, d\varepsilon_{22}^{p} + d\varepsilon_{12}^{p\,2})^{1/2} \tag{A.9}$$

A.3 Flow Rule

The flow rule is a kinematic assumption for plastic deformation, which provides the ratio or relative magnitudes of the plastic strain increment components. That is, the flow rule defines the direction of the plastic strain increment. The simplest flow rule is defined when yield function and plastic potential function coincide, which is called an associated flow rule:

$$d\varepsilon_{ij}^{p} = \delta\lambda \left(\frac{\partial f}{\partial \sigma_{ij}} \right) \tag{A.10}$$

For two dimensional plasticity,

$$\frac{\partial f}{\partial \sigma_{ij}} = \frac{1}{2\sigma_e}\begin{pmatrix} 2\sigma_{11} - \sigma_{22} \\ 2\sigma_{22} - \sigma_{11} \\ 6\sigma_{12} \end{pmatrix} = a \tag{A.11}$$

$$d\varepsilon_{ij}^{p} = \begin{pmatrix} d\varepsilon_{11}^{p} \\ d\varepsilon_{22}^{p} \\ d\varepsilon_{12}^{p} \end{pmatrix} = \frac{\delta\lambda}{2\sigma_e}\begin{pmatrix} 2\sigma_{11} - \sigma_{22} \\ 2\sigma_{22} - \sigma_{11} \\ 6\sigma_{12} \end{pmatrix} \tag{A.12}$$

where the vector *a* is the normal to the yield surface and $\delta\lambda$ is the plastic strain-rate multiplier, which is a positive constant [Crisfield 1991].

A.4 Constitutive Relationship

The relationship between the changes in stress and the changes in strain is given by [Crisfield 1991]:

$$d\sigma = \begin{bmatrix} d\sigma_{11} \\ d\sigma_{22} \\ d\sigma_{12} \end{bmatrix} = [C]\left(\begin{pmatrix} d\varepsilon_{11} \\ d\varepsilon_{22} \\ d\varepsilon_{12} \end{pmatrix} - \begin{pmatrix} d\varepsilon_{11}^{p} \\ d\varepsilon_{22}^{p} \\ d\varepsilon_{12}^{p} \end{pmatrix}\right) = [C]\left(\begin{pmatrix} d\varepsilon_{11} \\ d\varepsilon_{22} \\ d\varepsilon_{12} \end{pmatrix} - \frac{\delta\lambda}{2\sigma_e}\begin{pmatrix} 2\sigma_{11} - \sigma_{22} \\ 2\sigma_{22} - \sigma_{11} \\ 6\sigma_{12} \end{pmatrix}\right) \tag{A.13}$$

$$[C] = \frac{E}{1-\nu^2}\begin{bmatrix} 1 & \nu & 0 \\ \nu & 1 & 0 \\ 0 & 0 & \dfrac{1-\nu}{2} \end{bmatrix} \tag{A.14}$$

where:

$d\varepsilon_{ij}$ = Total strain increment in i-j direction

A.5 Hardening Rule

The plane stress plasticity algorithm uses nonlinear isotropic hardening, which is based on the assumption that the yield surface expands uniformly without distortion or translation as plastic flow occurs. This expansion of the yield surface is a function of the equivalent plastic strain, ε_{ps}. The hardening behavior is derived from the stress versus strain behavior from a tensile coupon test. In this section, the symbols have over bars to represent stresses and strains from a uniaxial tension test.

Under a uniaxial tension stress, $\bar{\sigma}_{11}$, $d\bar{\varepsilon}_{22}^{p} = d\bar{\varepsilon}_{33}^{p} = -\frac{1}{2} d\bar{\varepsilon}_{11}^{p}$ since there is no plastic volume change. Therefore, $d\varepsilon_{ps} = d\bar{\varepsilon}_{11}^{p}$ and $\sigma_e = \sigma_y(\varepsilon_{ps}) = \bar{\sigma}_{11}(\bar{\varepsilon}_{11}^{p})$, where $\bar{\sigma}_{11}(\bar{\varepsilon}_{11}^{p})$ is the uniaxial stress as a function of the plastic strain obtained from the tensile coupon test. As a result, the relationship between $\sigma_y(\varepsilon_{ps})$ and ε_{ps} can be calculated from the uniaxial stress-plastic strain relationship as follows:

$$\frac{\partial \sigma_y(\varepsilon_{ps})}{\partial \varepsilon_{ps}} = \frac{\partial \bar{\sigma}_{11}(\bar{\varepsilon}_{11}^{p})}{\partial \bar{\varepsilon}_{11}^{p}} = A \tag{A.15}$$

Applying Equation A.12 to the case of uniaxial tension and substituting into Equation A.9, yields [Crisfield 1991]:

$$d\varepsilon_{ps} = \delta\lambda \tag{A.16}$$

The engineering uniaxial stress versus engineering plastic strain curve from the tensile coupon model, developed in Chapter 5, for 3/4 in thick plate is plotted in Figure A.1. Line segments are then fitted to this curve. The slopes of these lines provide the hardening parameter *A* in Equation A.15.

A.6 Consistency Condition

When plastic flow occurs, the stresses must be on the yield surface. In other words, there should be no change in the yield function, *f*.

$$df = \frac{\partial f}{\partial \sigma_{ij}}^{T} d\sigma + \frac{\partial f}{\partial \sigma_y(\varepsilon_{ps})} \frac{\partial \sigma_y(\varepsilon_{ps})}{\partial \varepsilon_{ps}} d\varepsilon_{ps} = 0 \tag{A.17}$$

where:

$$\frac{\partial f}{\partial \sigma_y(\varepsilon_{ps})} = -1 \qquad \text{(from Equation A.2)}$$

$$\frac{\partial \sigma_y(\varepsilon_{ps})}{\partial \varepsilon_{ps}} = A \qquad \text{(from Equation A.15)}$$

Substitution from Equation A.11 and Equation A.16 into Equation A.17 yields [Crisfield 1991]:

$$df = a^T \, d\sigma - A \, \delta\lambda = 0 \tag{A.18}$$

A.7 Updating the State

The starting point in this algorithm is a known state of strains and corresponding stresses which is within the yield surface (elastic) (for example, point A in Figure A.2) or on the yield surface. If the state of strains and corresponding stresses is within the yield surface, the yield function, *f*, given by Equation A.1 will be less than zero. However, if the state of strains and corresponding stresses is on the yield surface, *f* will be zero. The algorithm updates the state of stresses and plastic strains for an applied total strain increment, $\Delta\varepsilon$ which is defined as:

$$\Delta\varepsilon = \begin{pmatrix} \Delta\varepsilon_{11} \\ \Delta\varepsilon_{22} \\ \Delta\varepsilon_{12} \end{pmatrix} \tag{A.19}$$

Part of this total strain increment is elastic and the other part is plastic. The algorithm starts with an elastic predictor, assuming that the applied total strain increment is elastic. With this elastic predictor, the new state of stresses at point B is determined, which will be within the yield surface or outside the yield surface as shown in Figure A.2. Point B will be within the yield surface if *f* (calculated at point B) is less than zero. In this case, the stresses at point B are the updated stresses. If *f* calculated at point B is greater than zero, then point B is outside the yield surface. In this case, plastic correction is needed to return the stresses to the yield surface. The return to the yield surface will be along the normal to the yield function at the elastic predictor point (point B). A truncated Taylor series for the yield function evaluated at point B gives [Crisfield 1991]:

$$f = f_B + \frac{\partial f}{\partial \sigma}^T \Delta\sigma + \frac{\partial f}{\partial \varepsilon_{ps}} \Delta\varepsilon_{ps} = f_B - \delta\lambda \, a_B^T \, C \, a_B - \delta\lambda \, A_B \tag{A.20}$$

Where the subscript *B* shows that the terms are evaluated at B. The truncated Taylor series is used to find the state where the yield function equals zero (i.e., the yield surface) be setting it equal to zero and then solving for the plastic strain multiplier $\delta\lambda$ (which is now incremental rather than differential as shown in Equation A.16).

$$\delta\lambda = \frac{f_B}{a_B^T \, C \, a_B + A_B} \tag{A.21}$$

and the final stresses, σ_C, are given by:

$$\sigma_C = \sigma_B + \Delta\sigma_B = \sigma_B - \delta\lambda\, C\, a_B \tag{A.22}$$

$\Delta\sigma_B$ is calculated using Equation A.23 by setting the total strain $\Delta\varepsilon$ equal to zero, since this total strain has already been applied in moving from point A to point B [Crisfield 1991].

$$\Delta\sigma_B = \begin{bmatrix} \Delta\sigma_{11} \\ \Delta\sigma_{22} \\ \Delta\sigma_{12} \end{bmatrix} = [C]\left(\begin{pmatrix} \Delta\varepsilon_{11} \\ \Delta\varepsilon_{22} \\ \Delta\varepsilon_{12} \end{pmatrix} - \begin{pmatrix} \Delta\varepsilon_{11}^p \\ \Delta\varepsilon_{22}^p \\ \Delta\varepsilon_{12}^p \end{pmatrix}\right) = -[C]\begin{pmatrix} \Delta\varepsilon_{11}^p \\ \Delta\varepsilon_{22}^p \\ \Delta\varepsilon_{12}^p \end{pmatrix} = -\delta\lambda\, C\, a_B \tag{A.23}$$

The final stresses at C may not lie on the yield surface. However, by using iterations, as discussed below, a point on the yield surface can be determined. In some cases, the iteration will not converge or the results may not be accurate. In these cases, the strain increment should be subdivided into subincrements.

A.8 Incremental Plasticity Algorithm

The algorithm begins with a state of strains and stresses at point A and a total strain increment, and updates the state by calculating the state of strains and stresses for another point A within the yield surface or a point C on the yield surface. In this section, the plasticity algorithm [Crisfield 1991] used in this study is explained in detail. The following steps are implemented in this algorithm:

Step 1. Assume an elastic increment and calculate the stresses at point B
$\sigma_B = \sigma_A + C\,\Delta\varepsilon$

Step 2. Determine the equivalent plastic strain at B, which equals that at A
$\lambda_B = \lambda_A = (\varepsilon_{ps})_A$

Step 3. From the linearized curve of stress versus plastic strain calculate $\sigma_y(\varepsilon_{ps})$ and calculate A

Step 4. Calculate the effective stress, σ_e, at point B using Equation A.3

Step 5. Calculate the yield function at point B, f_B, using Equation A.2

Step 6. If $f_B < 0$, the step is elastic, go to Step 1. Otherwise, yielding occurs and go to Step 7

Step 7. Calculate the normal to the yield surface at point B, a_B, using Equation A.11

Note that to return to the yield surface iterations are required and the iteration number is given by the superscript k.

Step 8. For iteration k, calculate $\delta\lambda^k$ using Equation A.21

Step 9. Calculate $\Delta\lambda^k = \Delta\lambda^{k-1} + \delta\lambda^k$ to update the stresses

Step 10. Calculate $\lambda^k = \lambda^{k-1} + \delta\lambda^k$

Step 11. $\sigma^{k+1} = \sigma_B - \Delta\lambda^k \, C \, a_B$

Step 12. From the linearized curve of stress versus plastic strain calculate $\sigma_y(\varepsilon_{ps}^k)$ and A^k using λ^k (note that $\varepsilon_{ps}^k = \lambda^k$)

Step 13. Calculate $f^k = \sigma_e^k - \sigma_y(\varepsilon_{ps}^k)$

Step 14. Check convergence using the following criterion:

$$ABS\left[f^k\right] / \sigma_y(\varepsilon_{ps}^k) \leq 0.000001 \tag{A.24}$$

Step 15. If the convergence criterion is satisfied, the solution has converged, go to Step 1

Step 16. Otherwise, calculate the effective stress, σ_e^{k+1}, using σ^{k+1}

Step 17. Go to Step 8 and repeat Steps 8 through 15 (note that while calculating $\delta\lambda^k$ in Step 8 use the following Equation:

$$\delta\lambda^k = \frac{f^k}{a_B^T \, C \, a_B + A^k} \tag{A.25}$$

A.7 Verification of the Plasticity Algorithm

From the finite element simulations of the experimental specimens using ABAQUS [2002], stresses and strains at selected locations were obtained. The strains were then used as input data for the plane stress plasticity algorithm and the corresponding stresses were calculated using this algorithm. These stresses were then compared with the stresses obtained from ABAQUS [2002] as shown in Figure A.3 and Figure A.4. To improve the accuracy, the strain increment was subdivided into subincrements. In Figure A.3, the effect of the number of subincrements on the accuracy of the results is shown. In these analyses, ten subincrements appear to provide sufficiently accurate results compared with the results from the finite element simulations.

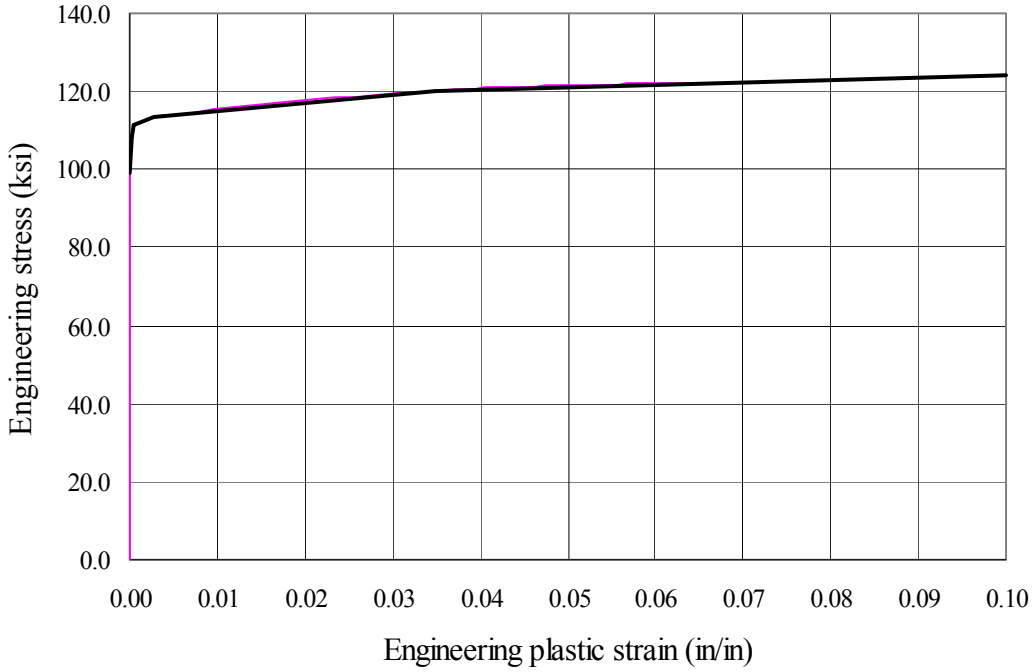

Figure A.1 Engineering stress versus engineering plastic strain

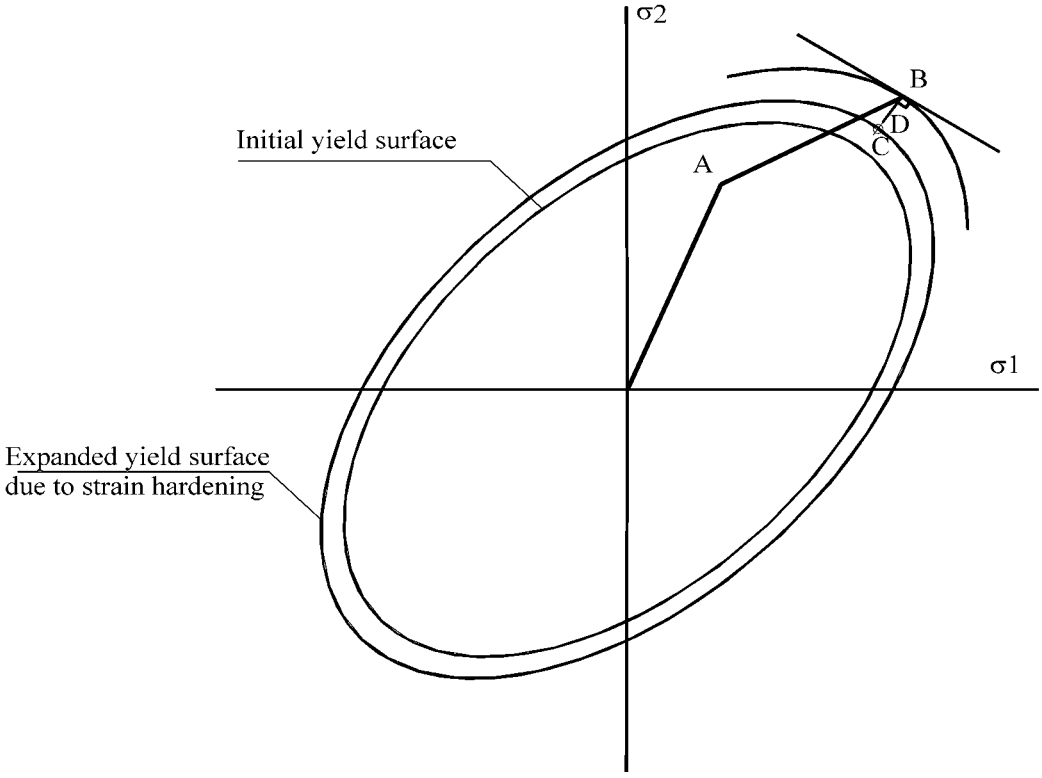

Figure A.2 Returning to the yield surface along the normal at point B

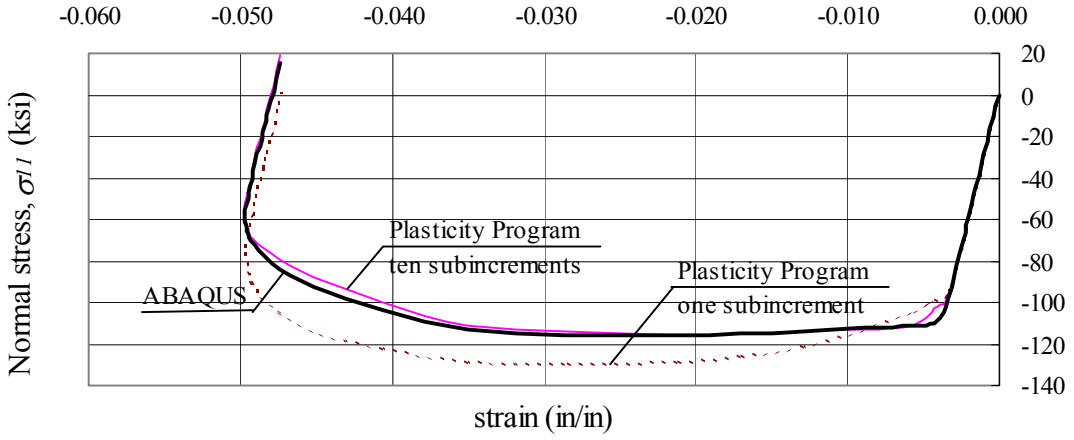

(a) Normal strain, ε_{11}

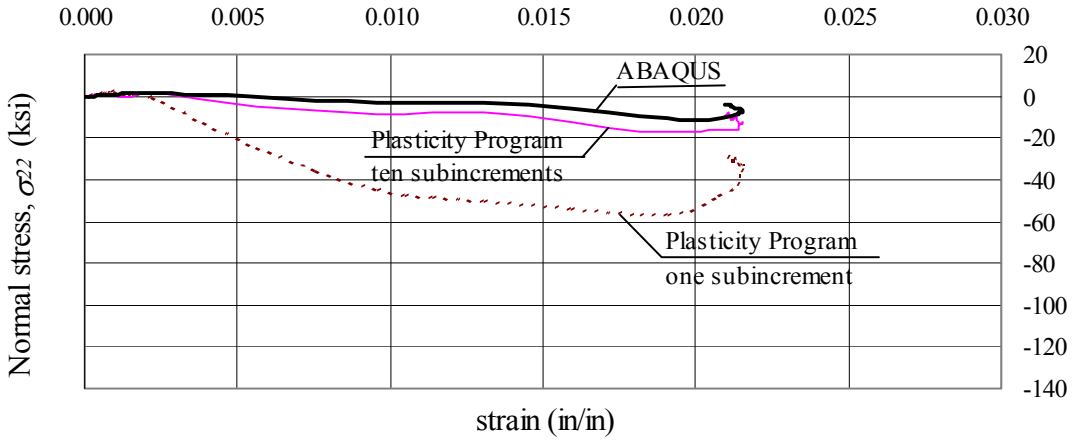

(b) Normal strain, ε_{22}

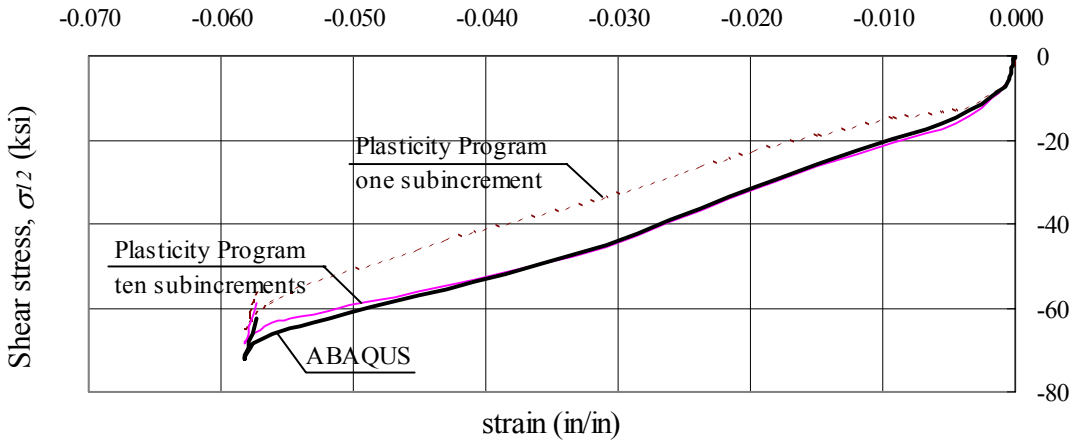

(c) Shear strain, γ_{12}

Figure A.3 Comparison of the results obtained using the plasticity program and ABAQUS showing the effect of the number of subincrements

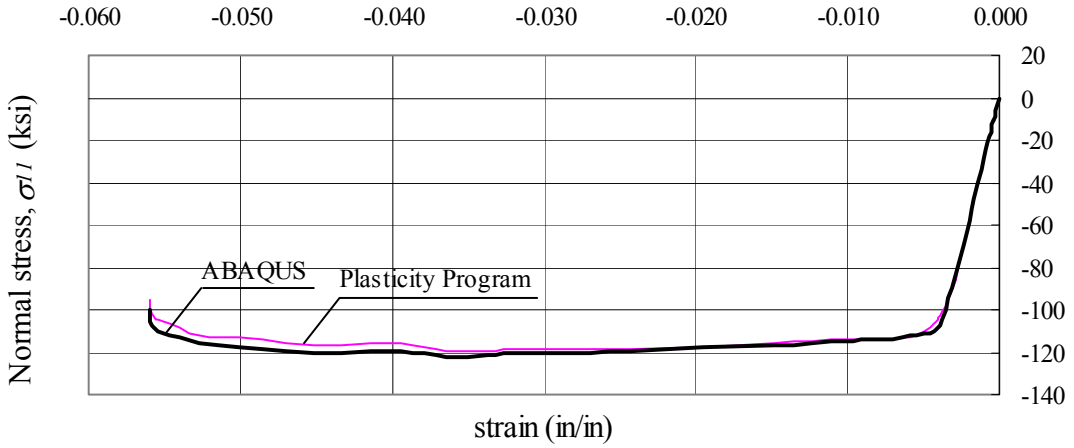

(a) Normal strain, ε_{11}

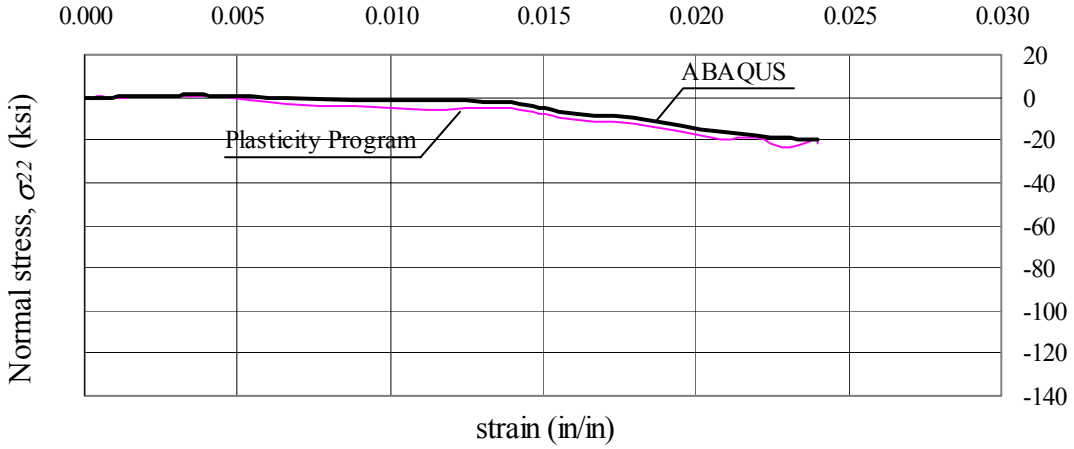

(b) Normal strain, ε_{22}

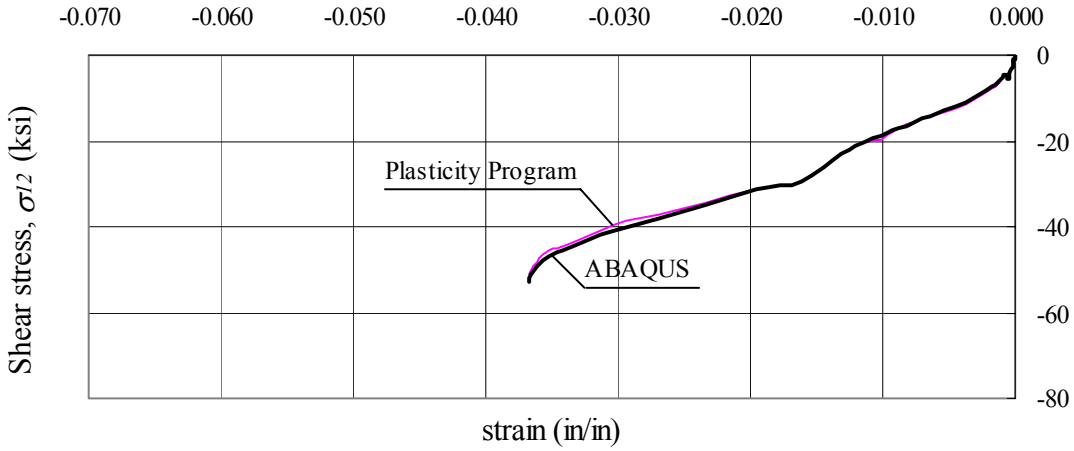

(c) Shear strain, γ_{12}

Figure A.4 Comparison of the results obtained using the plasticity program and ABAQUS

REFERENCES

AASHTO (1996), AASHTO LRFD Bridge Design Specifications – 1996 Interim, American Association of State Highway Transportation Officials, Washington, D. C.

AASHTO (2001), AASHTO LRFD Bridge Design Specifications – 2001 Interim, American Association of State Highway Transportation Officials, Washington, D. C.

AASHTO (2004), Draft, AASHTO LRFD Bridge Design Specifications, American Association of State Highway Transportation Officials, Washington, D. C.

ABAQUS/Standard User's Manual (2002), Version 6.1, Hibbitt, Karlsson and Sorensen, Inc., 100 Medway Street, Providence, Rhode Island, 02906.

ASTM (1994), E837, "Standard Test Method for Determining Residual Stresses by Hole-Drilling Strain-Gage Method," ASTM Standard E837-94a, American Society for Testing and Materials.

ASTM (2001), A370-97a, "Standard Test Methods and Definitions for Mechanical Testing of Steel Products," Annual Book of ASTM Standards, Volume 01.04, Steel-Structural, Reinforcing, Pressure Vessel, Railway, Section 1, pp 167-171.

ASTM (2004), A709/A709M-03a, "Standard Specifications for Carbon and High-Strength Structural Steel Shapes, Plates, and Bars and Quenched-and Tempered Alloy Structural Steel Plates for Bridges," Annual Book of ASTM Standards, Volume 01.04, Steel-Structural, Reinforcing, Pressure Vessel, Railway, Section 1, pp 357-364.

AWS D1.1-98 (1998), Structural Welding Code-Steel, American Welding Society, Miami.

Barth, K. E. (1996), "Moment-Rotation Characteristics for Inelastic Design of Steel Bridge Beams and Girders." Ph.D. Dissertation, Purdue University, West Lafayette, Ind.

Barth, K. E., White, D. W., and Mobb, B. M. (2000), "Negative Bending Resistance of HPS70W Girders." J. Constr Steel Res., vol. 53, 1-31.

Chen, W. F., and Lui, E. M. (1987), Structural Stability, Theory and Implementation. Elsevier, New York.

Crisfield, M. A. (1981), "A Fast Incremental/Iterative Solution Procedure that Handles "Snap-Through"," Computers and Structures, vol. 13, pp 55-62.

Crisfield, M. A. (1983), "An Arc-Length Method Including Line Search and Accelerations," Int. J. Num. Meth. Engng., vol. 19, pp 1269-1289.

Crisfield, M. A. (1991), Nonlinear Finite Element Analysis of Solids and Structures. John Wiley & Sons, New York.

Croce, A. D. (1970), "The Strength of Continuous Welded Girders with Unstiffened Webs." Struct. Research Laboratory Rep. No. 70-2, Dept. of Civ. Engrg., University of Texas at Austin, Austin, Tex.

Earls, C. J., and Shah, B. J. (2002), "High Performance Steel Bridge Girder Compactness," J. Constr Steel Res., vol. 58, 859-880.

El-Ghazaly, H. A., (1984), "Inelastic Interactive Distortional Buckling of W-Shape Steel Beams," Computers and Structures, vol. 19, No. 3, pp 351-368.

Fahnestock, L. A., and Sause, R. (1998), "Flexural Strength and Ductility of HPS-100W Steel I-Girders." ATLSS Rep. No. 98-05, Ctr. for Advanced Technol. for Large Struct. Sys., Lehigh University, Bethlehem, PA.

Gaylord, E. H., Gaylord C. N., and Stallmeyer, J. E. (1992), Steel Structures. McGraw-Hill, New York.

Greco, N. and Earls, C. J. (2003), "Structural Ductility in Hybrid High Performance Steel Beams," Journal of Structural Engineering, ASCE, 129(12), 1584-1595.

Green, P. S. (2000), "The Inelastic Behavior of Flexural Members Fabricated from High Performance Steel." Ph.D. Dissertation, Lehigh University, Bethlehem, PA.

Gross, J. H., Stout, R. D., Dawson, H. M. (1998), "Copper-Nickel High-Performance 70W/100W Bridge Steels – Part II." ATLSS Rep. No. 98-02, Ctr. for Advanced Technol. for Large Struct. Sys., Lehigh University, Bethlehem, PA.

Gross, J.H., Stout, R.D. (2001), "Evaluation of a Production Heat of an Improved Cu-Ni 70W/100W Steel." ATLSS Rep. No. 2001-(01-10), Ctr. for Advanced Technol. for Large Struct. Sys., Lehigh University, Bethlehem, PA.

Holtz N. M. and Kulak, G. L. (1973), "Web Slenderness Limits for Compact Beams." Struct. Engrg. Rep. No. 43, Dept. of Civ. Engrg., University of Alberta, Edmonton, Alta., Canada.

McDermott, J. F. (1969), "Plastic Bending of A514 Beams," Journal of the Structural Division, ASCE, vol. 95, 1851-1871.

Möller, M., Johansson, B., and Collin P. (1997), "A New Analytical Model of Inelastic Local Flange Buckling," J. Constr.. Steel Res., vol. 43, 43-63.

Murray, N. W. (1984), Introduction to The Theory of Thin-Walled Structures. Oxford University Press, New York.

Nickerson, R. L. (1997), "Girder Fabrication Report #3: HPS-100W for Lehigh University by High Steel Structures," Report to the American Iron and Steel Institute.

Onat, E. T. and Druccker, D. C. (1953), "Inelastic Instability and Incremental Theories of Plasticity," J. of the Aeronautical Sciences, vol. 20, 181-186.

Riks, E. (1972), "The Application of Newton's Method to The Problem of Elastic Stability," J. of Applied Mechanics, vol. 39, 1060-1066.

Riks, E. (1979), "An Incremental Approach to The Solution of Snapping and Buckling Problems," International Journal of Solids and Structures, vol. 15, 529-551.

Sause, R. and Fahnestock, L. (2001), "Strength and Ductility of HPS-100W I-Girders in Negative Flexure," Journal of Bridge Engineering, ASCE, vol. 6, 316-323.

Schajer, G. S., "H-DRILL Hole-Drilling Residual Stress Calculation Program," Version 2.20, 2001.

Schilling, C. G. and Morcos, S. S. (1988), "Moment-Rotation Tests of Steel Girders with Ultracompact Flanges," Report on Project 188, American Iron and Steel Institute, Washington, D.C., July.

Timoshenko, S. P. and Goodier, J. N. (1970), Theory of Elasticity. McGraw-Hill, New York.

Trahair, N. S. (1993), Flexural-Torsional Buckling of Structures. CRC Press, London.

Wempner, G. A. (1971), "Discrete Approximations Related to Nonlinear Theories of Solids," International Journal of Solids and Structures, vol. 7, 1581-1500.

Yakel, A. J., Mans, P. and Azizinamini, A. (2002), "Flexural Capacity and Ductility of HPS-70W Bridge Girders," Engineering Journal, AISC, vol. 39, 38-51.